# Experimental and Analytical Studies of Smart Composite Reinforcements and Structures

by

Anastasis Vyron Georgiades

Submitted
In Partial Fulfilment of the Requirements
For the Degree of

DOCTOR OF PHILOSOPHY

Major Subject: Mechanical Engineering

at

DALHOUSIE UNIVERSITY

Halifax, Nova Scotia

May, 2002

# Dalhousie University

# Faculty of Engineering

The undersigned hereby certify that they have examined, and recommend to the Faculty of Graduate Studies for acceptance, the thesis entitled "Experimental and Analytical Studies of Smart Composite Reinforcements and Structures" by Anastasis Vyron Georgiades in partial fulfilment of the requirements for the degree of Doctor of Philosophy.

Dated: May 2nd, 2002

Supervisor: Alexander L. Kalamkarov

External Examiner: Dr. Cheung Poon, NRC

Examiners: Dale Retallack

Guy Kember

# Dalhousie University

# Faculty of Engineering

DATE: May 2nd, 2002

AUTHOR: Anastasis Georgiades

TITLE: Experimental and Analytical Studies of Smart Composite Reinforcements and Structures

MAJOR SUBJECT: Mechanical Engineering

DEGREE: Doctor of Philosophy

CONVOCATION: October, 2002

# DEDICATION

This work is dedicated to Our Lord and Saviour Jesus Christ, Our Holy Mother, Ayia Marina, Ayia Anastasia and Ayios Nectarios for carrying me through all my life.

It is also dedicated to my mother Olga who passed away on November 9th, 2000, but never stopped praying for me. Mom, this thesis is finished because of your prayers from heaven. I love you always.

# TABLE OF CONTENTS

# List of Tables

# LIST OF FIGURES

# Abbreviations and Symbols

## Abbreviations

| | |
|---|---|
| ASTM | American Society for Testing and Materials |
| BG | Bragg Grating |
| BaTiO3 | Barium Titanate |
| CFRP | Carbon Fiber Reinforced Polymer |
| FC/APC | Face Contact/Angled Physical Connector |
| FFT | Fast Fourier Transform |
| FRP | Fiber Reinforced Polymer |
| GFRP | Glass Fiber Reinforced Polymer |
| LVDT | Linear Variable Displacement Transformer |
| MEM | Micro-electro-mechanical |
| NOL | Naval Ordnance Laboratory |
| PAN | Polyacrylonitrile |
| PEEK | Polyetheretherketone |
| PEK | Polyetherketone |
| PEKK | Polyetherketoneketone |
| PPS | Polyphenyle Sulphide |
| PVDF | Piezoelectric material |
| PZT-4 | Piezoelectric material |
| PZT-6B | Piezoelectric material |
| RTM | Resin Transfer Molding |
| SRIM | Structural Reaction Injection Molding |

SMA          Shape Memory Alloy

UV           Ultra Violet

**Variables**

| | |
|---|---|
| $\lambda_0$ | Bragg wavelength |
| $\Delta\lambda$ | Wavelength shift |
| GF | Gauge factor of Bragg Grating sensor |
| $\beta_0$ | Thermo-optic response of Bragg Grating sensor |
| $\Delta T$ | Change in temperature of Bragg Grating sensor |
| $T_{ref}$ | Reference temperature |
| $\varepsilon$ | Mechanical strain |
| | |
| P | Load |
| A | Cross-sectional area of tendon |
| E | Longitudinal tensile modulus of tendon |
| | |
| n | Refractive index of core of Bragg Grating sensor |
| $\nu$ | Poisson's ratio |
| $p_{11}, p_{22}$ | Strain-optic constants |
| | |
| $\beta$ | Temperature sensitivity factor of Bragg Grating sensor |
| $\alpha_o$ | Thermal expansion coefficient of Bragg Grating sensor |
| $\alpha_s$ | Thermal expansion coefficient of substrate |
| | |
| $S_f$ | Fatigue strength |
| $S_e$ | Endurance limit |
| | |
| O ( ) | The first Landau symbol |
| o ( ) | The second Landau symbol |
| | |
| $x_i$ | Macroscopic (slow) variable |
| $y_i$ | Microscopic (fast) variable |
| $\varepsilon$ | A general small (in comparison to unity) parameter |
| | |
| $\sigma_{ij}$ | Stress tensor |
| $u_i$ | Displacement field vector |
| G | Domain of a smart composite structure |
| $\partial G$ | Boundary surface of smart composite structure |
| | |
| $P_{ijk}$ | Actuation stress tensor |
| $R_k$ | Control signal |
| $K_{ij}$ | Thermal expansion stress tensor |
| $\Theta$ | Temperature change |
| $B_{ij}$ | Hygroscopic expansion stress tensor |
| C | Change in moisture content |

| | |
|---|---|
| $C_{ijkl}$ | Elasticity tensor |
| $e_{ij}$ | Strain tensor |
| $f_i$ | Body force vector |
| $N_{ij}^k$ | Homogenization function |
| $N_i^k$ | Homogenization function |
| $M_i$ | Homogenization function |
| $S_i$ | Homogenization function |
| $V_i$ | Homogenization function |
| $\tilde{C}_{ijkl}$ | Effective elastic tensor |
| $\tilde{P}_{ijkl}$ | Effective actuation tensor |
| $\tilde{K}_{ij}$ | Effective thermal expansion tensor |
| $\tilde{B}_{ij}$ | Effective hygroscopic expansion tensor |
| $|Y|$ | Volume of unit cell |
| $\sigma_{ij}^{(k)}$ | $k^{th}$ term in asymptotic expansion of stress field |
| $u_{ij}^{(k)}$ | $k^{th}$ term in asymptotic expansion of displacement field |
| $y_{inner}$ | Inner solution to boundary layer problem |
| $y_{outer}$ | Outer solution to boundary layer problem |
| $\sigma_{i3}$ | Prescribed stress boundary condition |
| $P_i$ | Prescribed stress |
| $P_{i3k}^*$ | Boundary condition actuation tensor |
| $C_{i3kl}^*$ | Boundary condition elasticity tensor |
| $K_{i3}^*$ | Boundary condition thermal expansion tensor |
| $B_{i3}^*$ | Boundary condition hygroscopic expansion tensor |
| $N_i^{(1)kl}$ | Boundary layer elasticity homogenization function |
| $N_i^{(1)k}$ | Boundary layer actuation homogenization function |
| $M_i^{(1)}$ | Boundary layer thermal expansion homogenization function |
| $S_i^{(1)}$ | Boundary layer hygroscopic expansion homogenization function |
| $u_i^{(1,2)}$ | Boundary layer displacement vector |

| | |
|---|---|
| $\tilde{C}_{ij}$ | Effective elasticity coefficients in contracted notation |
| $\tilde{P}_{ij}$ | Effective actuation coefficients in contracted notation |
| $\tilde{K}_i$ | Effective thermal expansion coefficients in contracted notation |
| $\tilde{B}_i$ | Effective hygroscopic expansion coefficients in contracted notation |
| | |
| $A_{ijk}$ | Elasticity integration constants |
| $B_{ij}$ | Piezoelectricity integration constants |
| $\varepsilon_{ij}$ | Dielectric permittivity |
| $\sigma_x$ | x-directed stress |
| $\sigma_y$ | y-directed stress |
| $\varepsilon_x$ | x-directed strain |
| $\varepsilon_y$ | y-directed strain |
| $D_i$ | Thermal expansion integration constants |
| | |
| $\delta$ | Thickness (non-dimensional) of smart composite plate |
| $\delta h_1$ | Width (non-dimensional) of unit cell of smart composite plate |
| $\delta h_2$ | Length (non-dimensional) of unit cell of smart composite plate |
| $S^+$ | Top surface of smart composite plate |
| $S^-$ | Bottom surface of smart composite plate |
| $\Omega_\delta$ | Region of unit cell of smart composite plate |
| $n_i^+$ | Outward unit vector normal to the surface of unit cell of smart composite plate |
| $n_i^+$ | Inward unit vector normal to the surface of unit cell of smart composite plate |
| $N_i^+$ | Normalized outward vector normal to the surface of unit cell of smart composite plate |
| $N_i^-$ | Normalized inward vector normal to the surface of unit cell of smart composite plate |
| $\omega^\pm$ | Length of normalized outward (or inward) vector normal to the surface of unit cell of smart composite plate |
| $z$ | fast non-periodic variable pertinent to smart composite plate |
| $p_\alpha$ | surface traction vector along tangential plate direction |
| $p_3$ | surface traction vector along transverse plate direction |
| $r_\alpha$ | Auxiliary surface traction vector along tangential plate direction |
| $r_3$ | Auxiliary surface traction vector along transverse plate direction |
| $P_\alpha$ | Body force vector along tangential direction of smart composite plate |
| $P_3$ | Body force vector along transverse direction of smart composite plate |
| $f_\alpha$ | Auxiliary body force vector along tangential direction of smart composite plate |

| | |
|---|---|
| $g_3$ | Auxiliary body force vector along transverse direction of smart composite plate |
| $d_{ijk}^{(r)}$ | Piezoelectric strain tensor |
| $\beta_{ij}^{(c)}$ | Hygroscopic expansion strain tensor |
| $\alpha_{ij}^{(\theta)}$ | Thermal expansion strain tensor |
| | |
| $L_{ijk}$ | Differential operator |
| $D_{jk}$ | Differential operator |
| $c_{ijk}$ | Differential operator |
| | |
| $U_i^{kl}$ | Displacement function for smart composite plate |
| $\varepsilon_{k\alpha}^{(0)}$ | Strain function for smart composite plate |
| $v_i^{(1)}$ | Homogeneous displacement function for smart composite plate |
| | |
| $P_{ij}^*$ | Piezoelectric differential operator |
| $K_i^*$ | Thermal expansion differential operator |
| $B_i^*$ | Hygroscopic expansion differential operator |
| | |
| $T^{(0)}$ | 1$^{st}$ term in temperature change variation |
| $T^{(1)}$ | 2$^{nd}$ term in temperature change variation |
| $C^{(0)}$ | 1$^{st}$ term in moisture change variation |
| $C^{(1)}$ | 2$^{nd}$ term in moisture change variation |
| $R^{(0)}$ | 1$^{st}$ term in electric field variation |
| $R^{(1)}$ | 2$^{nd}$ term in electric field variation |
| | |
| $V_i^{kl}$ | Displacement function for smart composite plate |
| $U_i^k$ | Piezoelectric displacement function for smart composite plate |
| $V_i^k$ | Piezoelectric displacement function for smart composite plate |
| $W_i$ | Thermal displacement function for smart composite plate |
| $X_i$ | Thermal displacement function for smart composite plate |
| $Y_i$ | Hygroscopic displacement function for smart composite plate |
| $A_i$ | Hygroscopic displacement function for smart composite plate |
| | |
| $b_{ij}^{\alpha\beta}$ | Elasticity unit cell function for smart composite plate |
| $b_{ij}^{*\alpha\beta}$ | Elasticity unit cell function for smart composite plate |
| $d_{ij}^k$ | Piezoelectricity unit cell function for smart composite plate |

| | |
|---|---|
| $d_{ij}^{*k}$ | Piezoelectricity unit cell function for smart composite plate |
| $\Theta_{ij}$ | Thermal expansion unit cell function for smart composite plate |
| $\Theta_{ij}^{*}$ | Thermal expansion unit cell function for smart composite plate |
| $\Lambda_{ij}$ | Hygroscopic expansion unit cell function for smart composite plate |
| $\Lambda_{ij}^{*}$ | Hygroscopic expansion unit cell function for smart composite plate |
| $\left\langle b_{ij}^{\alpha\beta} \right\rangle$ | Effective elastic coefficient for smart composite plate |
| $\left\langle b_{ij}^{*\alpha\beta} \right\rangle$ | Effective elastic coefficient for smart composite plate |
| $\left\langle d_{ij}^{k} \right\rangle$ | Effective piezoelectric coefficient for smart composite plate |
| $\left\langle d_{ij}^{*k} \right\rangle$ | Effective piezoelectric coefficient for smart composite plate |
| $\left\langle \Theta_{ij} \right\rangle$ | Effective thermal expansion for smart composite plate |
| $\left\langle \Theta_{ij}^{*} \right\rangle$ | Effective thermal expansion for smart composite plate |
| $\left\langle \Lambda_{ij} \right\rangle$ | Effective hygroscopic expansion for smart composite plate |
| $\left\langle \Lambda_{ij}^{*} \right\rangle$ | Effective hygroscopic expansion for smart composite plate |
| $N_1$ | Force per unit length for thin plate |
| $N_2$ | Force per unit width for thin plate |
| $N_{12}$ | Force per unit length for thin plate |
| $Q_1$ | Force per unit length for thin plate |
| $Q_2$ | Force per unit width for thin plate |
| $M_1$ | Moment per unit length resultant for thin plate |
| $M_2$ | Moment per unit width resultant for thin plate |
| $M_{12}$ | Moment per unit length resultant for thin plate |
| $v_1$ | x-directed displacement of middle plane of plate |
| $v_2$ | y-directed displacement of middle plane of plate |
| $w$ | z-directed displacement of middle plane of plate |
| $\tau_{11}$ | bending curvature of middle plane of plate in x-z plane |
| $\tau_{22}$ | bending curvature of middle plane of plate in y-z plane |
| $\tau_{12}$ | twisting curvature of middle plane of plate |
| $A_{ij}$ | Extensional stiffness matrix of composite laminate |
| $B_{ij}$ | Coupling stiffness matrix of composite laminate |
| $D_{ij}$ | Bending stiffness matrix of composite laminate |
| $\mathbf{N}^{T}$ | Thermal force vector for composite laminate |
| $\mathbf{M}^{T}$ | Thermal moment vector for composite laminate |
| $\mathbf{N}^{M}$ | Hygroscopic force vector for composite laminate |

| $\mathbf{M}^M$ | Hygroscopic moment vector for composite laminate |
| $\mathbf{N}^M$ | Hygroscopic force vector for composite laminate |
| $\mathbf{N}^R$ | Piezoelectric force vector for composite laminate |
| $\mathbf{M}^R$ | Piezoelectric moment vector for composite laminate |
| | |
| $\Omega_1$ | First region of unit cell of wafer-reinforced plate |
| $\Omega_2$ | Second region of unit cell of wafer-reinforced plate |
| $\Omega_3$ | Third region of unit cell of wafer-reinforced plate |
| | |
| $E_1$ | Young's modulus of orthotropic material in principal direction 1 |
| $E_2$ | Young's modulus of orthotropic material in principal direction 2 |
| $E_3$ | Young's modulus of orthotropic material in principal direction 3 |
| $G_{12}$ | Shear modulus of orthotropic material |
| $G_{13}$ | Shear modulus of orthotropic material |
| $G_{23}$ | Shear modulus of orthotropic material |
| $\nu_{12}$ | Poisson's ratio of orthotropic material |
| $\nu_{13}$ | Poisson's ratio of orthotropic material |
| $\nu_{23}$ | Poisson's ratio of orthotropic material |
| | |
| $F_1^{(w)}$ | Cross-sectional area of region 1 of wafer-reinforced smart composite plate |
| $F_2^{(w)}$ | Cross-sectional area of region 2 of wafer-reinforced smart composite plate |
| $S_1^{(w)}$ | $1^{st}$ moment of area of region 1 of wafer-reinforced smart composite plate relative to middle surface of region 3 |
| $S_2^{(w)}$ | $1^{st}$ moment of area of region 2 of wafer-reinforced smart composite plate relative to middle surface of region 3 |
| $J_1^{(w)}$ | $2^{nd}$ moment of area of region 1 of wafer-reinforced smart composite plate relative to middle surface of region 3 |
| $J_2^{(w)}$ | $2^{nd}$ moment of area of region 2 of wafer-reinforced smart composite plate relative to middle surface of region 3 |
| | |
| $\tau_{ij}$ | Hygroscopic expansion functions for wafer-reinforced plate |
| $t_i$ | Hygroscopic boundary condition functions for wafer-reinforced plate |
| $\bar{\tau}_{ij}$ | Hygroscopic expansion functions for wafer-reinforced plate |
| $\bar{t}_i$ | Hygroscopic boundary condition functions for wafer-reinforced plate |
| $\tau_{ij}^k$ | Piezoelectric functions for wafer-reinforced plate |
| $t_i^k$ | Piezoelectric boundary condition functions for wafer-reinforced plate |
| $\bar{\tau}_{ij}^k$ | Piezoelectric functions for wafer-reinforced plate |
| $\bar{t}_i^k$ | Piezoelectric boundary condition functions for wafer-reinforced plate |

| | |
|---|---|
| $\dot{\mathbf{r}}$ | Position vector |
| $\mathbf{I}$ | Linear momentum |
| $\rho$ | Density of deformed configuration |
| $\rho_i$ | Density of undeformed configuration |
| $\mathbf{t}$ | Traction per unit surface area |
| $\mathbf{F}_s$ | Total surface forces |
| $\mathbf{p}$ | Resultant body force per unit volume |
| $\mathbf{B}_s$ | Total body forces |
| $\mathbf{F}_{net}$ | Total surface forces |
| $G_i$ | Initial configuration |
| $\mathbf{u}$ | Displacement |
| $\dot{\mathbf{u}}$ | Velocity |
| $\ddot{\mathbf{u}}$ | Acceleration |

# ACKNOWLEDGEMENTS

The author would like to thank Dr. Alex Kalamkarov for his supervision, guidance and support throughout the duration of this research, as well as Dr. Retallack and Dr. Kember for serving on the guiding committee.

I would particularly like to thank Dr. Douglas MacDonald, Mr. Steven Fitzgerald, and Mr. Aniruddha Chahande for their tremendous help. Thanks are also extended to Mr. Gobinda Saha and Mr. Krishna Challagulla.

Especially, I would like to thank all my teachers, and professors that had taught me from the first day of kindergarten school to this last day of University. I will never be able to repay the favour, but I am sure God will. God bless you all.

# ABSTRACT

This thesis discusses experimental and analytical aspects of active and passive smart composite materials.

For the experimental purposes of the work, Bragg Grating and Fabry Perot fiber optic strain sensors are embedded in glass- and carbon-fiber-reinforced polymer tendons during pultrusion. The intended application is to embed these smart tendons in civil engineering structures wherein they would act as concrete reinforcements, replacing steel and overcoming the associated corrosion problems. As well, by virtue of the embedded sensors, these tendons would provide remote for health monitoring of these structures. To verify the operation of the embedded sensors, mechanical tests were performed at room temperatures as well as at low (-40°C) and high (+80°C) temperature extremes. The reliability assessment of the fiber optic sensors further involved a detailed examination of their fatigue and creep behavior as well as the combined effect of sustained loads and aggressive chemical solutions. The purpose of these latter tests is to closely simulate conditions encountered in concrete. Other aspects of the work dealt with the use of the fiber optic sensors to monitor the pultrusion process as well as tests performed to investigate the effect of the embedded sensors on the structural integrity of the host composite material.

For the analytical aspects of this thesis, the asymptotic homogenization method was used to develop mathematical models pertaining to (active) smart composite structures with a periodic array of embedded actuators. To make the model more comprehensive, thermal and hygroscopic expansion effects were included. Asymptotic homogenization takes a boundary value problem which is characterized by rapidly oscillating coefficients, and replaces it with a simpler one containing some effective coefficients. This homogenized problem is much more amenable to analytic and numerical treatment than the original one. The effectiveness of the derived models was illustrated by means of two- and three-dimensional examples. The asymptotic homogenization methodology was used also to develop mathematical models describing the behavior of smart composite plates with rapidly varying thickness and a large number of embedded actuators. This model was applied to wafer-reinforced piezoelectric plates. These are plates reinforced with mutually perpendicular ribs or stiffeners. The stiffeners themselves, may, if desired also exhibit piezoelectric characteristics.

# 1.0 INTRODUCTION

Interest in composite materials has led in recent years to their integration within such areas as the aerospace industry, civil engineering, transportation, medicine, and sports. At the same time, significant advances in MEMS, telecommunications and other fields, significantly facilitated the development of new and highly effective sensors and actuators. It would seem natural therefore that the ever-expanding field of composite materials would seek ways to take advantage of and encompass these advancements in actuator and sensor technology. The merger of these domains gave birth to the so-called "smart composite materials". Smart composites are adaptive structures which incorporate sensors and/or actuators. Depending on their type, smart composites may be classified as passive or actively controlled. Passive smart materials incorporate sensors that provide information on their state and integrity, while their actively controlled counterparts incorporate both sensors and actuators and they can perform self-adjustment or self-repair as conditions change.

This thesis discusses experimental and analytical aspects of smart composite materials. The experimental aspects of this thesis are focused on fabrication, processing, testing and evaluation of pultruded smart carbon fiber and glass fiber reinforced tendons with embedded Fabry Perot and Bragg Grating sensors. This work has been conducted for the purposes of ISIS Canada Project T3.4 on smart reinforcements and connectors. ISIS Canada is a National Network of Centres of Excellence which combines the efforts of many researchers from across the country in order to develop advanced technologies for the civil engineering infrastructure. The long-term objective pertinent to the smart tendons described in this thesis is to embed them in structures such as bridges and overpasses, wherein they would replace steel as the primary concrete reinforcement and at the same time monitor the health of these structures by virtue of the embedded fiber optic sensors.

The use of smart composite structures will be greatly facilitated if the effective properties and coefficients such as elastic, piezoelectric, thermal expansion and hygroscopic expansion can be predicted at the design stage. Consequently, for the purposes of the analytic aspects of this thesis, mathematical models characterizing the behavior of smart composites with a large number of embedded actuators are developed and applied.

Three models are derived. The first model pertains to a smart composite with homogeneous boundary conditions and the second model modifies the first one by prescribing stress boundary conditions on part of the boundary surface of the smart structure. It is shown that the two models differ in what amounts to "boundary-layer" solutions. The mathematical framework on which the two models are developed is that of perturbation expansions and asymptotic homogenization.

The third mathematical model pertains to smart composite plates with rapidly varying thickness and a periodic array of embedded actuators. This model is again developed on the basis of asymptotic homogenization and is used to analyze, among others, wafer-reinforced piezoelectric plates. These are plates reinforced with mutually perpendicular ribs or stiffeners. Both the base plate and/or the stiffeners may exhibit piezoelectric effects.

In summary Chapters 2-6 describe various aspects of the experimental work conducted on (passive) pultruded glass and carbon fiber reinforced composite tendons with embedded fiber optic sensors, and Chapters 7-12 present the development and application of the various mathematical models pertaining to active smart structures. Finally, Chapter 13 concludes this work.

# 2.0 LITERATURE REVIEW

## 2.1 Introduction to Smart Composite Materials

Recent years have witnessed a steadily increasing volume of applications of advanced composite materials in the fields of civil engineering, transportation and marine engineering. Among the properties that make composite materials attractive for such applications include high strength-to-weight ratio, corrosion resistance, enhanced (or reduced) thermal and electrical conductivity, and good survivability in high-temperature environments. More important however is the fact that engineers have the ability to modify and adapt existing manufacturing techniques for the purpose of tailoring the mechanical properties of composites so as to meet the design objectives and criteria of the intended applications.

The last decade has seen a shift in the focus of the application of composite materials from the aerospace industry to the larger-volume civil engineering field. However, the task of replacing or strategically complimenting traditional materials such as steel and concrete with this new class of materials is complicated by the fact that composites lack reliable data pertinent to their long-term behavior.

One method of compensating for the lack of longer-term data for a particular application is to monitor the condition of a structure continuously using "smart materials". A smart material is a structure characterized by all of the following fourfold functions [Udd, 1995, page ix]. The first function is to monitor certain basic manufacturing parameters such as temperature, pressure, viscosity and others during the manufacturing process using sensors embedded in the structure. Fiber optic sensors are commonly used for this purpose. Quite often the sensors can be embedded in the part during the fabrication of the composite structure itself. In other cases, the sensors can be surface mounted. Surface

mounting however, means that the sensors are more susceptible to damage and eventual failure. The second function of smart structures is to be able to perform a post-fabrication evaluation of the various parts of the composite structure. It is imperative of course that this evaluation not compromise the integrity of the structure in any appreciable way. This all-important requirement often restricts the size and number of the sensing elements that can be embedded in a composite part, see Georgiades [1998, pages 51-56] for a literature review. The third function of smart structures is the ability to incorporate the sensors in a central monitoring network that can be used to continuously assess the system with the object of determining whether the intended performance goals are being achieved over time. A smart structure that meets the above three criteria is often referred to as a "passive" smart structure. If in addition, the structure is able to respond to external disturbances such as change in load, temperature, moisture content etc. by altering the natural frequency, shape, degree of polarization, or any other characteristic by means of a suitable array of actuators, then the structure is termed an "active" smart material.

Jain and Sirkis [1994], compared, for obvious reasons, active smart structures to biological systems. In their work they defined the goal of smart-structures technology as being to "reproduce biological functions in load bearing structural systems. These biological functions would include a skeletal system to provide load bearing capability, a nervous system which is a network of embedded or attached sensors to monitor the state of the structure, a motor system to provide adaptive response, an immune system to provide healing capability and a neural system to provide learning and decision making functions." Shape-memory alloys, magnetostrictives, and particularly piezoelectric materials are considered as suitable candidates for use as actuators in smart composite systems.

The use of smart composite materials will be greatly facilitated if, in addition to the broadening of the knowledge base pertaining to their long-term behavior, their effective properties and coefficients such as the elastic, thermal expansion and other coefficients

can be predicted at the design stage. To achieve this goal, mathematical models characterizing their behavior will have to be developed. Appropriately, subsequent sections of this thesis will describe experimental and analytical aspects of passive and active smart composite materials.

## 2.2 Composite Materials

Composite materials are defined in the Engineered Materials Handbook [1987] as "a combination of two or more materials differing in form or composition on a macroscale. The constituents retain their identities; that is they do not dissolve or merge completely into one another although they act in concert. Normally, the components can be physically identified and exhibit an interface between one another."

Typically, composites are two-phase systems with one phase, the reinforcement, being embedded in a continuous matrix phase. The reinforcement, being stronger and stiffer than the matrix, is responsible for the load-carrying characteristics of the composite material. For the composite to be an effective load-carrier, however, the stresses must be transferred from one reinforcement to another and this is the primary responsibility of the matrix. The matrix also serves to protect the reinforcements and, for the case of fibrous composites, to hold them in a particular orientation. The latter is very important because the macroscopic properties of the composite largely depend upon the orientation of the reinforcements.

Composite materials can be classified in accordance with the nature of the matrix [Schwartz, 1996a, page 10]. Thus we have polymer-matrix, metal-matrix, and ceramic-matrix composites, and carbon-carbon composites. Another classification methodology divides composites according to the type of the reinforcement [Engineered Materials Handbook, 1987]. This gives rise to fiber-reinforced, particle-reinforced and laminated

composites. The fiber-reinforced composites may contain continuous (long) or discontinuous (short) fibers.

Fiber-reinforced composites contain fibers with lengths that are much larger than their cross-sectional directions. Common examples of such fibers include glass, carbon, aramid and silicon carbide. Discontinuous or short fiber composites are characterized by the fact that their properties, such as strength and stiffness, depend upon the length of the reinforcements (sometimes also called whiskers). The short fibers can be oriented in a preferred direction, which results in the composite exhibiting orthotropic behavior, or can be randomly embedded so that the composite behaves like a quasi-isotropic material. On the other hand, the mechanical properties of continuous-fiber composites are independent of the length of the fibers. The fibers can be oriented in a preferred direction, such as in the direction of load application for uniaxially loaded members, or can be oriented at right angles to one another giving rise to crossply fiber composites. Continuous fiber composites tend to be stronger and stiffer than their short fiber counterparts but become impractical when the final product is to have a complicated profile. In this case, discontinuous-fiber composites are much more attractive and can be produced rather quickly and inexpensively.

Particle-reinforced composites consist of particles (often called particulates) of different sizes such as spheres, flakes and rods randomly embedded within the expanse of the matrix. All the dimensions of particulate reinforcements are of roughly equal size and this feature renders the pertinent composites macroscopically isotropic, also by virtue of the random distribution of the particles in the matrix. Particulates are used in a broad range of applications and are cheaper than the other types of reinforcements. The most common types of particulates are silicon carbide (SiC), Aluminum Oxide ($Al_2O_3$) and Boron Carbide ($BC_4$). Since mechanical properties such as strength and stiffness are enhanced with an increase in the length of the reinforcements, particle-reinforced composites are not as strong as their whisker-reinforced or fiber-reinforced counterparts.

Finally, laminated composites are those composed of two or more layers of the reinforcement, with each layer having two of its dimensions much larger than the third. Examples of laminated composites are bimetals, clad metals, plywood and formica [Daniel and Ishai, 1994, page 20].

The ever-increasing popularity of advanced composites in practically all engineering applications can be attributed to a number of benefits, the most important of which are: high strength-to-weight ratio, high-stiffness-to-weight ratio, advanced survivability in harsh (acidic or alkaline) environments, enhanced toughness and fracture characteristics, improved friction and wear properties, and varying degrees of thermal and electric conductivity. As well, in addition to the fact that close tolerances and optimum surface finish can be integrated directly into the fabrication stage without the need to resort to post-fabrication machining, composite materials can be tailored to achieve a broad range of thermal expansivities in compliance with the specific applications at hand. [Engineered Materials Handbook, 1988, page 36]. Thus composite materials have been successfully integrated with the civil, construction, marine, aerospace and medical fields. Such applications are expected to increase as the confidence of scientists and engineers in composite materials grows through an increase in the appropriate knowledge bases.

## 2.2.1 Reinforcing Fibers

Although a broad range of both fibrous and particulate reinforcements are available for use in the manufacture of composite materials, the focus of attention in recent years has been directed towards fibrous reinforcements. Fibers, the most important constituent of composite materials, have a significant influence on such macroscopic properties of the end product as strength, stiffness, toughness, density, electrical and thermal conductivity, wear resistance, as well as other issues such as chemical compatibility with different resin systems, ease of fabrication and cost of production. There are a number of naturally

occurring minerals which may be used for the production of composites, the most important of which probably has been asbestos. The best source of asbestos is a mineral called chrysotile [Matthews and Rawlings, 1994] which is a hydrated magnesium silicate, $Mg_3Si_2O_5(OH)_4$. Chrysotile fibers can be up to several centimeters in length and have a very good strength-to-weight ratio and a high elastic modulus.

Although chrysotile and other forms of asbestos have been exploited commercially, most practical composites are fabricated using synthetic organic and inorganic fibers. The subsequent sections discuss some of the most common types of synthetic fibers.

### 2.2.1.1 Glass Fibers

Hopper

Furnace

Platinum
Bushing

Filament Collecting and
Size Applicator

Collet

Winding Head Unit
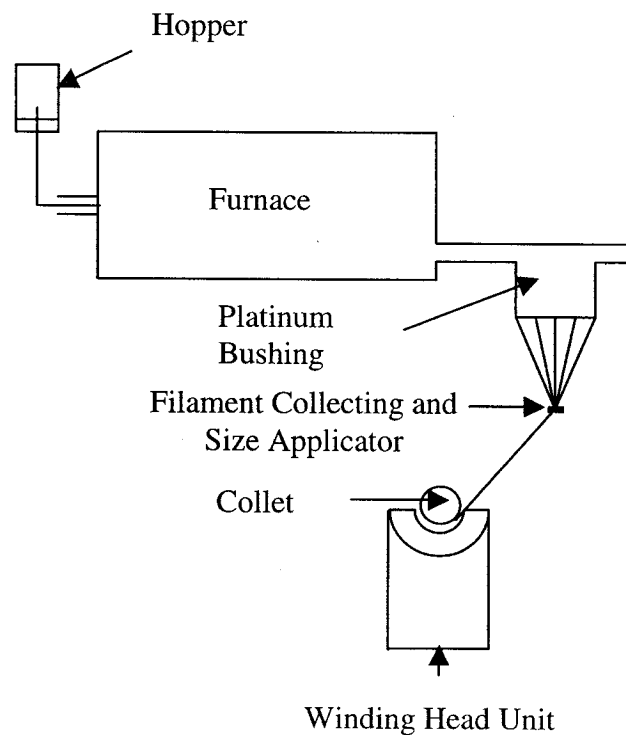
**Figure 2-1:** Conventional fabrication procedure for glass fibers [Chawla, 1993]

Glass fibers are the most commonly encountered type of fiber reinforcement. The chemical composition of glass fibers is essentially the same as that of the common glass, silicon dioxide (silica-$SiO_2$) being the main constituent. Unlike common glass however, commercially available glass fibers only contain small amounts of sodium and potassium oxides. This means that glass fibers exhibit enhanced corrosion resistance and have a better surface finish [Schwartz, 1997]. Glass fibers exhibit an attractive combination of both the well-known glass properties such as hardness and transparency and as the desired reinforcement characteristics such as high strength-to-weight ratio and ease of processability.

The most common types of glass fibers are E-glass and S-glass. E-glass is available as continuous fibers or chopped strands and is the cheapest among all commercial types of reinforcement. S-glass has superior properties to those of E-glass, primarily as a consequence of its more stringent compositional requirements. However, the higher manufacturing costs incurred restrict its applications primarily to aerospace projects. There is a less expensive form of S-glass available, however, known as S-2 glass, with similar mechanical properties to those of regular S-glass but with a different coating. Another less common type of glass fibers is C-glass, which is known for its superior chemical resistance. It is used therefore in highly corrosive environments.

A simplified schematic of the fabrication procedure for glass fibers is shown in Figure 2-1 [Chawla, 1993]. The raw materials are melted and then fed into an electrically-heated platinum bushing that has a number of holes at its base. The molten glass flows through the holes under gravity, forming continuous filaments which are subsequently passed around a rotating collet, drawn at a speed that varies from 1 to 2 km min$^{-1}$ and finally wound on a drum [Chawla, 1993]. Before winding, the glass fibers are treated with a polymeric emulsifier for protection against foreign agents.

## 2.2.1.2 Carbon Fibers
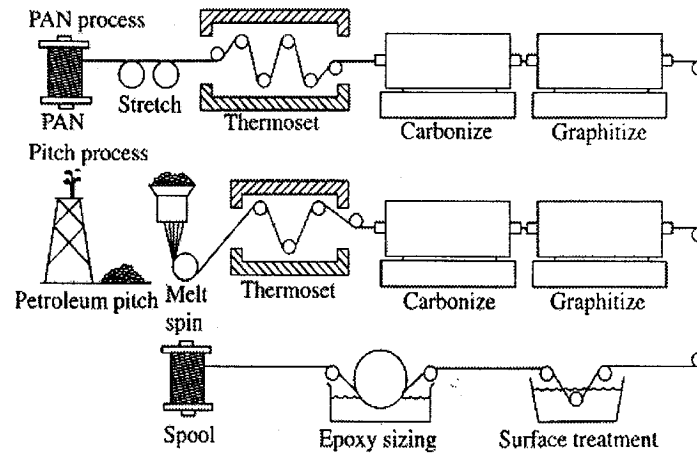


**Figure 2-2:** Processing polyacrylonitrile (PAN) and pitch-based carbon fibers [Swanson, 1997]

Carbon fibers are available with a wide range of tensile moduli ranging from 207 GPa to over 1000 GPa [Schwartz, 1997]. They are characterized typically by very high strength-to-weight and stiffness-to-weight ratios, and are thus used extensively in the aerospace industry where weight saving is critical (and certainly deemed more important than cost of production). In general, carbon fibers with intermediate tensile moduli have high tensile and compressive strength, whereas their high-modulus counterparts exhibit lower strength. High-strength grades are made from a PAN (polyacrylonitrile) fiber precursor that is heat-treated and converted to carbon by pyrolysis. Low-strength grades are made from a pitch precursor at a lower cost. A schematic of the PAN and pitch processes is shown in Figure 2-2 [Swanson, 1997]. The main disadvantages of carbon fibers are low impact strength and a relatively high electrical (and thermal) conductivity which renders them unsuitable for some applications.

### 2.2.1.3 Aramid Fibers

Aramid fibers are made from aromatic polyamides (polymers with long chains). Aromatic compounds are characterized by the presence of the benzene ring, a hexagonal arrangement of carbon atoms bonded to one another as well as to hydrogen atoms. Aramid fibers were originally developed in the early 1970's by Du Pont to replace steel in radial tires [Weeton et. al, 1987] but have since been used in a wide range of applications. Aramid fibers have a high tensile strength and modulus and a low density. They exhibit particularly enhanced toughness and impact strength, and for this reason they are currently the material of choice for bulletproof vests and other accessories. Other advantages of aramid fibers are that they burn with difficulty and have a glass transition temperature of about 360°C [Matthews and Rawlings, 1994]. Consequently they can be used for extended periods of time in high-temperature environments. They have a high thermal capacity, a low coefficient of thermal expansion and low electrical and thermal conductivities.

The most common commercial names for aramid fibers are Kevlar (by Du Pont), Twaron (by Akzo) and Technora (by Teijin).

### 2.2.1.4 Polyethylene Fibers

Polyethylene fibers are commercially available in a variety of trade names, the most common of which are Spectra (Allied Signal) and Dyneema (DSM). They are made of long hydrocarbon chains with each carbon atom bonded to two other carbon and two hydrogen atoms.

Polyethylene fibers have the highest specific strength of all commercial fibers, and also exhibit very low moisture absorption and good resistance to chemical attack. This makes

them particularly attractive for marine applications. Polyethylene fibers are also characterized by high impact resistance. On the other hand, their susceptibility to creep at temperatures above 100°C and their low melting point (135°C) prevents their use in high temperature applications.

### 2.2.1.5 Boron Fibers

Boron fibers are made by chemical vapor deposition of boron onto a carbon or tungsten substrate. Boron-fiber reinforced composites have superior mechanical properties when compared to their carbon-fiber counterparts. In addition to a high tensile modulus, boron composites exhibit excellent compressive strength, and this makes them attractive for applications where buckling resistance is required. On the other hand, the high costs incurred in the manufacture of boron fibers limits their use primarily to aerospace applications.

### 2.2.2 Tensile Properties of Commercial Reinforcing Fibers

**Table 2-1:** Tensile properties of common fibers and steel [Mallick, 1988]

| Fiber | Typical Diameter (μm) | Density (Mg/m$^3$) | Tensile Modulus (GPa) | Tensile Strength (GPa) | Failure Strain (%) |
|---|---|---|---|---|---|
| E-glass | 10 | 2.54 | 72.4 | 3.45 | 4.8 |
| S-glass | 10 | 2.49 | 86.9 | 4.30 | 5.0 |
| Carbon | 7 | 1.85 | 344.5 | 2.34 | 0.58 |
| Kevlar | 11.9 | 1.45 | 131 | 3.62 | 2.8 |
| Boron | 140 | 2.70 | 393 | 3.1 | 0.79 |
| Steel | - | 3.08 | 207 | 0.58 (average) | - |

Table 2-1 [Mallick, 1988] compares the tensile properties of some commercially available reinforcing fibers, and Figure 2-3 clearly demonstrates the superiority of these fibers over some common metals, with respect to specific tensile strength and specific tensile modulus [Schwartz, 1997].
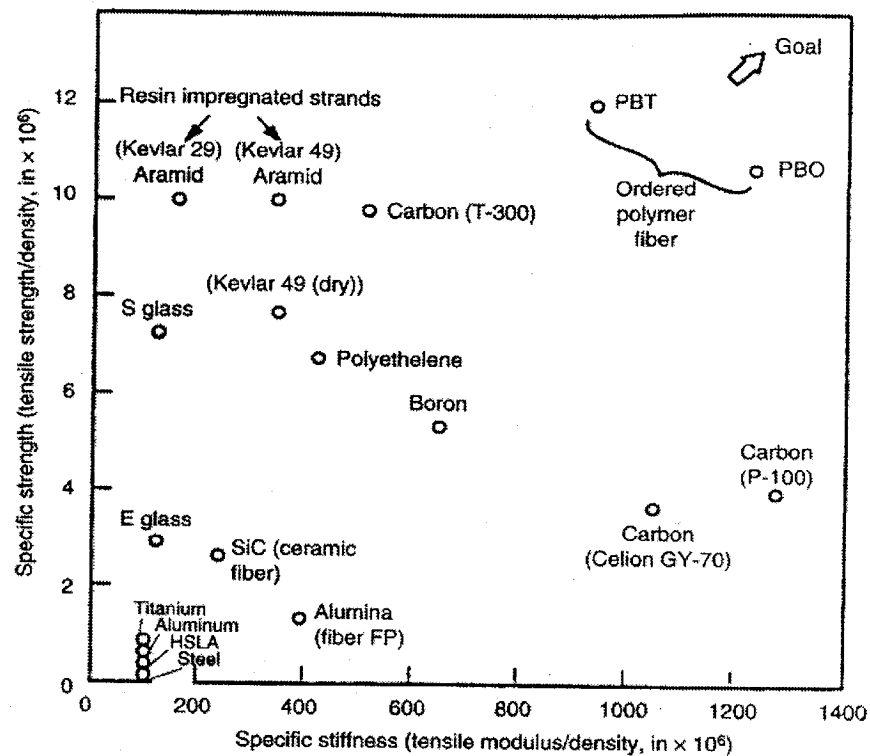


**Figure 2-3:** Specific tensile strength and specific tensile modulus of advanced fibers [Schwartz, 1997]

In addition to the reinforcing fibers, the other component of a composite structure is the matrix which serves to hold the fibers together, to keep them in the proper orientation, to protect them from harsh environments and more importantly to transfer the load between the fibers. As well, typically, the matrix is responsible for the shear strength of the composite and provides resistance to crack initiation and propagation. The most common matrix materials are polymeric which can be classified as either thermoplastics or thermosets. They will be discussed in subsequent sections.

## 2.2.3 Matrix Systems

### 2.2.3.1 Thermoplastic Polymeric Matrices

**Table 2-2:** Tensile properties of thermoplastic resins [Harvey, 1993]

| Polymer | Tensile Strength (MPa) | Tensile Modulus (MPa) |
|---|---|---|
| PEEK | 92-103 | 3.1-3.8 |
| PEK | 105 | 4 |
| PEKK | 102 | 4.5 |
| PPS (amorphous) | 65.5-82.2 | 4.3 |
| K-Polymer | 102 | 3.8 |
| N-Polymer | 110 | 4.1 |
| LARC-TPI | 113-163 | 3.5-4.5 |
| Eymid Imides | 91.1 | 4.1 |
| Durimid | 138-153 | 3.4-4.4 |
| Polyamideimides | 136-185 | 3.3-4.5 |
| Polyetherimides | 100-105 | 3-3.1 |
| PBI | 160 | 5.8 |

In a thermoplastic polymer, the individual molecules are held together by weak forces such as Van der Waals bonds. As a consequence of the relative weakness of these bonds as compared to the chemical covalent bonds, thermoplastic resins will soften when high temperatures are applied and will regain their rigidity on cooling. The advantages of thermoplastics are enhanced processability, attractive toughness and fracture characteristics, large failure strains, high vibration damping coefficients, and reduced moisture absorption. The latter is very important because moisture absorption can deteriorate the performance of composites in two ways. First, moisture absorption causes the matrix to swell up, and this change in shape is resisted by the much stiffer reinforcing fibers. Consequently residual stresses are developed and the load-carrying capacity of the composite is reduced. As well, moisture absorption reduces the glass transition temperature of the polymeric matrix, causing deterioration in the mechanical properties of the composite and limiting its use to lower temperature applications [Gibson, 1994].

The main disadvantage of thermoplastics is the high viscosity of the molten resin, which makes it difficult to incorporate fibers. As well, thermoplastic resins are more susceptible to creep, especially at elevated temperatures. Some common types of thermoplastic resins include polyetheretherketone (PEEK), polyetherketoneketone (PEKK), polyetherketone (PEK), and polyphenyle sulphide (PPS). Table 2-2 [Harvey, 1993, page 202] shows the tensile properties of some common types of thermoplastic resins.

## 2.2.3.2 Thermoset Polymeric Matrices

Table 2-3: Properties of thermoplastics and thermosets [Matthews and Rawlings, 1994; Schwartz, 1997]

| Property | Thermosets | Thermoplastics |
|---|---|---|
| Young's Modulus (GPa) | 1.3-6.0 | 1.0-4.8 |
| Tensile Strength (MPa) | 20-180 | 40-190 |
| Fracture Toughness $K_{IC}$ (MPa m$^{1/2}$) | 0.5-1.0 | 1.5-6.0 |
| Maximum Service Temperature (°C) | 50-450 | 25-230 |
| Melt Viscosity | Very low | High |
| Fiber Impregnation | Easy | Difficult |

In a thermoset polymer, the molecules are held together by strong covalent bonds which form a network of cross-links between the molecules. Once these cross-links are created during polymerization (setting of the resin), they cannot be reshaped by subsequent heating. Thermosets typically contain one or more types of catalyst (curing agent) in addition to the resin itself. It is the chemical reaction between the curing agents and the thermosetting resin that marks the onset of the consolidation of a composite, and quite often the application of heat is needed. In general, thermosets are stiffer than thermoplastics, have better creep characteristics, and can be used in higher-temperature environments. As well, they have a lower viscosity when molten, which facilitates the

integration of the fibers. On the other hand, they have lower toughness and fracture characteristics. Table 2-3 [Matthews and Rawlings, 1994, page 171; Schwartz, 1996, page 46] compares some of the properties of thermosetting and thermoplastic resins.

The most common types of thermosetting resins are polyester resins, vinylester resins, epoxies, phenolics, and polyimides. Of these, the polyester resins are the most common and least expensive. They have low viscosity, which facilitates processability and fiber impregnation. Epoxies have better mechanical properties than polyesters and exhibit excellent resistance to most chemicals [Schwartz, 1997]. On the other hand, higher thermal-expansion and hygroscopic-expansion coefficients lead to dimensional instability and the generation of residual stresses in the resulting composites. Because phenolics are inexpensive and have good fire resistance, they are used in environments where fire regulations are more stringent. Vinylester resins have higher tensile strength than polyesters and also low viscosity and fast cure rates. However, their adhesive strength is not as high as that of epoxy resins [Schwartz, 1997]. Finally, polyimides are more expensive than epoxies or polyesters, but their superior thermal stability makes them attractive for high-temperature applications. Table 2-4 [Matthews and Rawlings, 1994, page173; Mallick, 1988, page 56] shows a comparison of the density and tensile properties of thermosetting resins.

**Table 2-4:** Comparison of properties of thermosets [Matthews and Rawlings, 1994; Mallick, 1988]

| Property | Epoxy | Polyester | Phenolic | Polyimide | Vinylester |
|---|---|---|---|---|---|
| Density (Mg/m$^3$) | 1.1-1.4 | 1.1-1.5 | 1.3 | 1.2-1.9 | 1.12-1.32 |
| Tensile Modulus (GPa) | 20-180 | 40-190 | 4.4 | 3-3.1 | 3-3.5 |
| Tensile Strength (GPa) | 35-90 | 45-85 | 50-60 | 80-190 | 73-81 |

## 2.3 Fabrication of Composite Materials

Composite materials were manufactured traditionally by the hand lay-up method. However, other methods have since evolved and gained popularity; examples include pultrusion, filament winding, injection molding and many others. The following sections will describe briefly the most common fabrication procedures.

### 2.3.1 Hand Lay-up Method
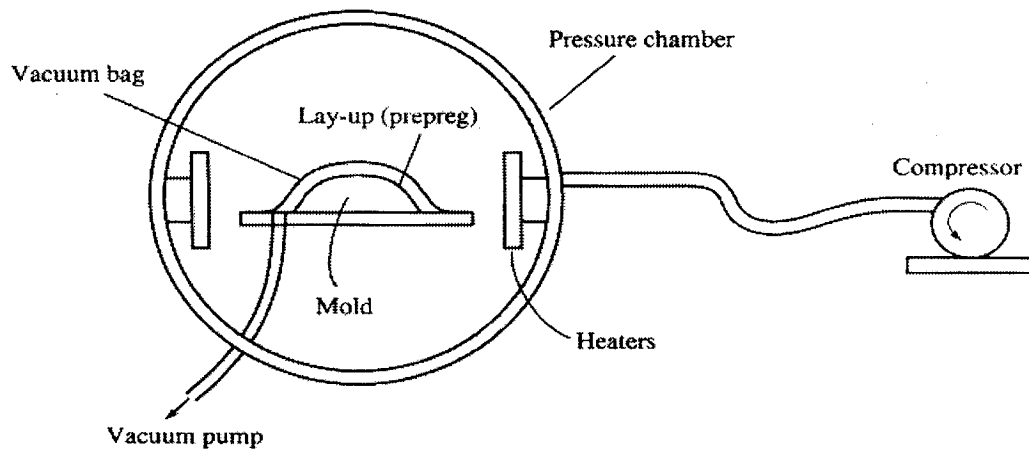


**Figure 2-4:** Autoclave molding [Gibson, 1994]

Hand lay-up is the cheapest and oldest of all of the manufacturing processes, and it can produce parts with complicated profiles. The surface of a mold having the shape of the part to be manufactured is first coated with adequate mold release compounds, to prevent permanent bonding of the consolidated product. Then, unidirectional plies are manually laid-up onto the mold and are subsequently saturated with resin. Sometimes, instead of applying the resin to the laminae after they are laid up, one can use preimpregnated thin sheets called prepregs. The part is then cured in an autoclave. An autoclave, see Figure 2-4 [Gibson, 1994], is essentially a specialized pressure vessel into which the part is placed

and cured under predetermined conditions of temperature and pressure. The process of preparing a laid-up part for autoclave is called vacuum bagging and requires the use of special apparatus such as a breather, a bleeder, a separator and others.

The main problem associated with the hand lay-up method is that it is time-consuming and labor-intensive. The mechanical quality of the finished product depends heavily on the skill of the operator during both the actual lay-up and the preparation of the vacuum bag. On the other hand, the incorporation of sensors such as fiber optic sensors, and actuators such as shape memory alloy wires or piezoelectric films, within composite materials is straightforward with the hand lay-up method. This, in conjunction with the ease of egress of, say, the sensor leads from the consolidated product, makes hand lay-up one of the most efficient procedures for the production of smart composite materials.

## 2.3.2 Filament Winding

Filament winding is used to produce hollow cylindrical or tubular parts. It involves the continuous pulling of fibers from a set of spools through a resin bath. The saturated fibers then pass through an array of rollers that serve to squeeze out excess resin from the fibers. The rollers are fitted with tensioning control to ensure uniform tension across the fibers. The fiber rovings are then positioned on a rotating mandrel. A simplified schematic of the filament winding process is shown in Figure 2-5 [Gibson, 1994]. Filament winding can be classified as helical or polar. In helical winding, the fibers are first placed on a horizontally translating surface, which subsequently positions them on a rotating mandrel. In polar winding, a feeding units moves around a slowly rotating mandrel [Mallick and Newman, 1990].
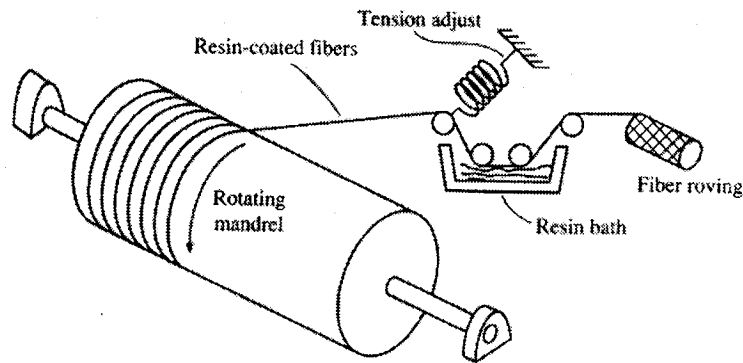
**Figure 2-5:** Filament winding process [Gibson, 1994]

## 2.3.3 Pultrusion

Pultrusion is an automated process that can be used to produce long prismatic parts. The basic principle of operation of the pultrusion process is quite simple, but the underlying thermomechanical processes that occur inside the die are very complex.

In the pultrusion of thermosetting resin composites, the fiber rovings are pulled continuously from an array of spools or creel into a resin bath that also contains catalysts, promoters and mold-release compounds. The fibers are impregnated thoroughly with resin, and are subsequently directed towards the die through a set of guides. These guides serve to orient the fibers and also to squeeze out excess resin so that the fibers are uniformly saturated. The fibers then enter the die, which typically is fitted with a set of strip heaters attached to the top and bottom surfaces. These strip heaters provide the necessary thermal zones within the die needed to initiate and complete the consolidation process. The processes which go on inside the die are as follows [Sumerak, 1985; Vaughan and Hacket, 1991]. First, the strip heaters raise the temperature of the die walls. When the resin is in the liquid phase, it is at a lower temperature than the die walls and thus heat transfer takes place inward, i.e. from the die to the resin. The heat absorption by

the resin further lowers its viscosity and this promotes an even more uniform fiber saturation or "wet-out". The chemical catalysts mixed with the resin use this thermal energy to initiate the curing process. This is a highly exothermic reaction and the heat released gradually brings the temperature of the resin to a value which is higher than that of the surrounding die walls. At this point the heat transfer direction is reversed, with thermal energy flowing from the resin to the die. Consequently, the viscosity of the resin begins to increase and soon the so-called "gel region" is reached. The peak exotherm is reached within this gel zone. The degree of cure progresses to the point where shrinkage allows the part to detach from the die walls; the presence of a suitable mold release is crucial for this detachment to occur. The consolidated product finally exits the die and is cut to the desired length. The pullers which move the product usually are hydraulic, and they come in various forms such as hand-over-hand or contacting-wheels. A schematic of the pultrusion process is shown in Figure 2-6 [Kalamkarov et al., 2000].

Data Acquisition & Strain
Monitoring Unit

Fabry Perot Sensor Lead

Roller Pulling
Mechanism

Die With
ElectricStrip
Heaters

Fiber
FeedCard
System

Resin Wet-Out Bath

Carbon Fiber
Roving Creels
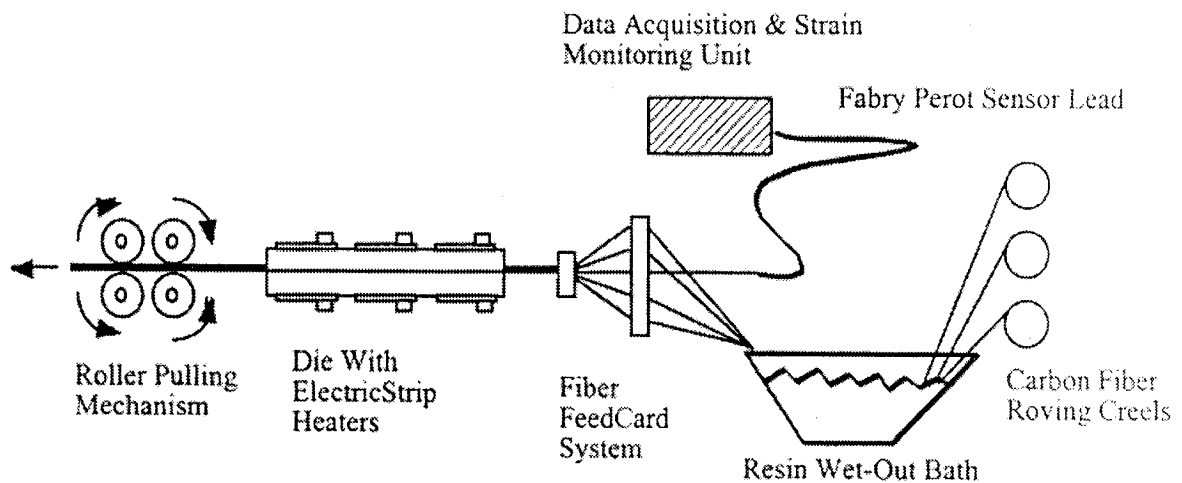
**Figure 2-6:** Pultrusion process for production of smart composite

Fiber optic and other types of sensors, as well as actuators, can be embedded readily in a composite part, provided they are protected from the harsh conditions that exist in the die such as the fiber compaction pressure. Figure 2-6 illustrates the ingress of a Fabry Perot fiber optic sensor in a pultruded composite part [Kalamkarov et al, 2000].

The structural integrity of the consolidated product will partly depend upon the overall pressure profile that exists in the die. This is a function of a number of processing parameters, the most important of which are the volume fractions of the fibers and resin, the tolerance to which the die is machined, the die cross-sectional profile, the coefficient of thermal expansion of the fibers and of the resin, and the variation in the thermal expansion coefficient and the viscosity of the mixture from the onset of the curing process through the gelation stages. Thus a comprehensive characterization of the pultrusion process cannot take place without a thorough understanding of the pressure profile in the die.

A number of researchers have attempted to assess experimentally the influence of such variables as pulling speed, constituent volume fractions, die temperature, the presence of different catalysts etc. on the mechanical integrity of the pultruded product. MacDonald [1989] examined the effect of different processing parameters on the quality of pultruded cylindrical glass rods and rectangular glass bars using a phenolic resin. It was found that the optimal cure temperature for the composites was 180°C and the optimal resin injection pressure was around 40-50 psi. The desired fiber pulling speed was 40 cm/min and pultrusion rates higher than 50 cm/min jeopardized the mechanical properties of the end product. It was also discovered that the use of a large weight fraction of the glass reinforcement (75%) prevented resin seepage/scale problems in the die. As well, the use of silane and caustic soda additives in the resin mixture improved the overall mechanical properties of the product. More importantly, however, the strength of the composite depended very strongly on the degree of cure. In particular, a 90% or more degree of cure was necessary for the composite to develop its full strength. A 60% degree of cure meant that the resulting composite was only half as strong in flexure and shear.

The characterization and optimization of the process variables that govern the pultrusion process have been the subjects of investigation by many researchers over the last decade. Vaughan et al. [1989] employed a series of statistical experiments to examine the

interaction among the various parameters, and used the results obtained to optimize the pultrusion process for any mechanical characteristic such as tensile strength or shear strength. Lackey [1992] used similar statistical techniques to examine the effect of pulling speed, fiber volume fraction and die temperature profile on the flexural strength and short-beam shear strength of pultruded glass/epoxy and graphite/epoxy composites. The effects of these same variables on the Iosipescu shear strength of pultruded glass/epoxy and graphite/epoxy composites was assessed by Theobald et al. [1998]. The influence of the pertinent variables on the dynamic characteristics (elastic modulus and damping coefficient) of pultruded graphite/epoxy composites was investigated by Mantena et al. [1992] and Kowsika et al. [1996].

## 2.3.4 Resin Transfer Molding
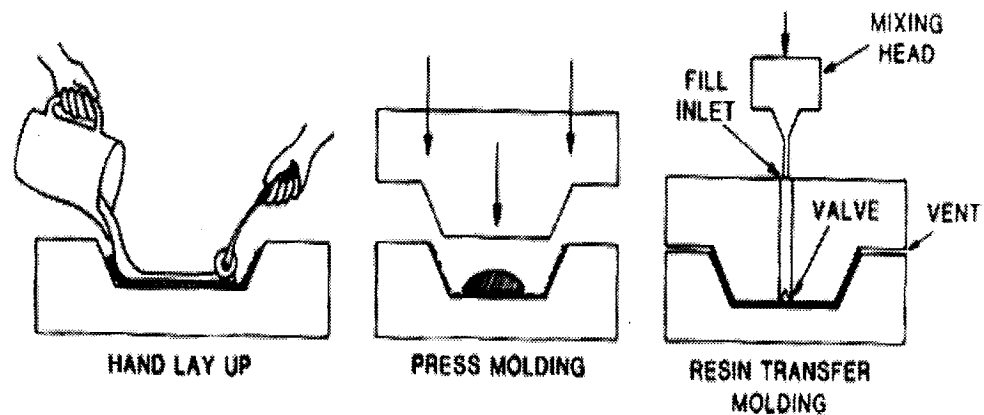


**Figure 2-7:** Schematic of the resin transfer molding (RTM) process [Mallick and Newman, 1990]

Resin transfer molding (RTM) has the capability of producing composite parts of varying size and complexity. A simplified schematic of the process is shown in Figure 2-7 [Mallick and Newman, 1990]. The dry fibers or prepregs are laid up into the lower half of a mold. The mold is then tightly sealed and resin is injected into the cavity until the

reinforcements are fully saturated. The resin is subsequently allowed to cure (at room temperature or in autoclave) and finally the product is removed. Post-fabrication curing may be necessary to ensure that the composite develops its full strength. A very similar technique is the structural reaction injection molding (SRIM). The essential difference between RTM and SRIM is that in the former the resin and the catalyst are mixed prior to injection in the mold, whereas in the latter they are mixed as they are being injected.

## 2.3.5 Injection Molding
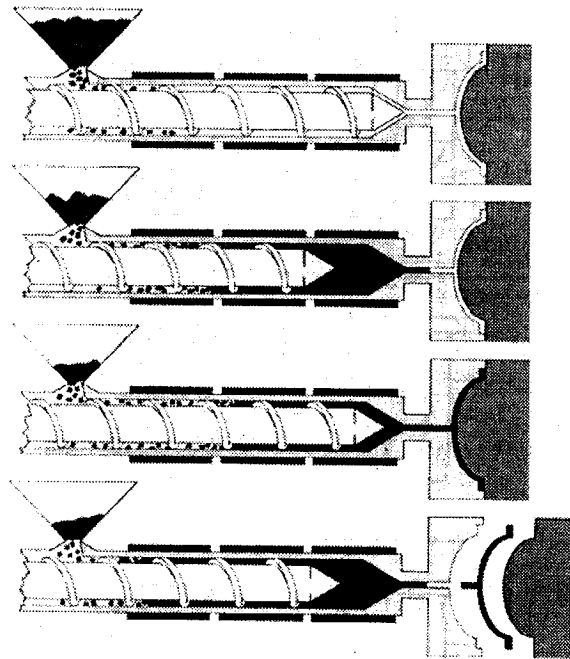


**Figure 2-8:** Schematic of the injection molding process [Wright, 1991]

Injection molding involves injecting a fluid plastic material into a closed mold. In thermoplastic injection molding, a thermoplastic material is melted and forced into a closed mold which is relatively cool. When the resin cures the mold is opened and the consolidated product is removed. In thermosetting injection molding the resin is injected

into a warm mold. After the curing process, the mold is opened and the composite is removed [Handbook for Infrastructure Applications of Composite Materials, 1998, page 24]. A schematic of the injection-molding process is shown in Figure 2-8 [Wright, 1991, page 92].

## 2.4 Overview of Fiber Optic Sensors

### 2.4.1 Optical Fibers

This thesis will deal with various aspects of smart composite materials. The first smart composites to be discussed in the sequel will be pultruded glass- and carbon-fiber reinforced rods with embedded Fabry Perot or Bragg Grating fiber optic sensors. Therefore, a brief review of common types of fiber optic sensors is warranted.
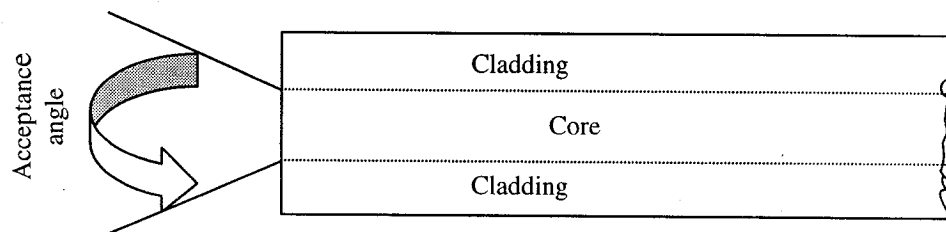
**Figure 2-9:** Schematic of an optical fiber

The two basic components of an optical fiber (see Figure 2-9) are the inner part, or core, and the outer part, or cladding. The refractive index of the core is slightly greater than that of the cladding so that light entering the fiber and striking the core/cladding interface at an angle greater than the pertinent critical angle will undergo total internal reflection and travel down the fiber. Hence, for light to be confined within the core, it must fall within the acceptance angle as shown in Figure 2-9.

There are three types of optical fibers available: step-index (multimode), graded-index (multimode) and single-mode fibers. A mode is a stable propagation state in a fiber. The electromagnetic fields in the light waves reinforce one another to produce stable propagation states only when light travels along certain paths. Each of these propagation states is called a mode. As their name suggests, single mode fibers only carry one mode of light, whereas step index and graded index fibers can carry many modes. The three types of optical fibers are shown diagrammatically in Figure 2-10 [Guide to Fiber Optics System Design, 1996].
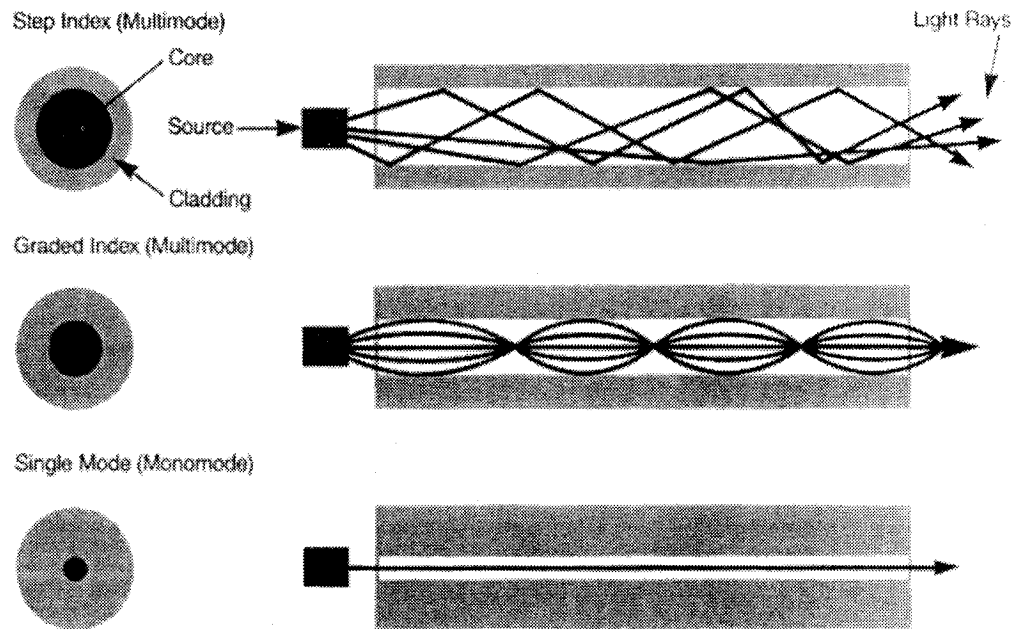


**Figure 2-10:** The three types of optical fiber [Guide to Fiber Optics System Design, 1996]

The next few sections will describe briefly the principles of operation of some fiber optic sensors, particularly the ones that are being used or have the potential to be used for smart composite structures. They are the Microbend, the Fabry Perot and the Bragg Grating sensors. The Fabry Perot and Bragg Grating sensors are the ones used for the purposes of this thesis.

## 2.4.2 Intrinsic and Extrinsic Fiber Optic Sensors

The term "fiber optic sensors" covers a whole spectrum of optical devices that operate in many different ways. The advantages of fiber optic sensors that make them particularly attractive for smart composite applications are light weight, and a small size that enables them to be embedded in many composite structures without significant deteriorating effects on the integrity of the host material. As well, fiber optic sensors are immune to electromagnetic interference, and can operate in high and low temperature environments. Fiber optic sensors are very sensitive and some, like the Bragg Grating sensor, can be constructed to output absolute readings, making the need for repeated calibration obsolete.
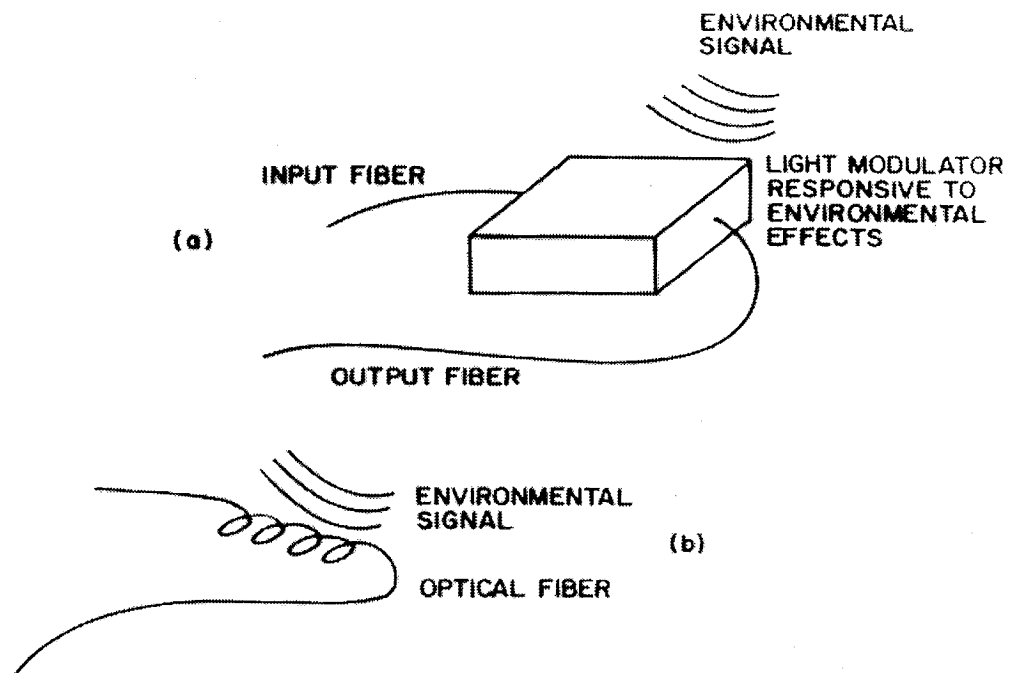


**Figure 2-11:** Fundamentals of (a) extrinsic and (b) intrinsic fiber optic sensors [Udd, 1991]

Fiber optic sensors can be classified as extrinsic or intrinsic, as shown in Figure 2-11 [Udd, 1991]. In extrinsic sensors, modulation of light in response to environmental

changes occurs in a separate device and the optical fiber only acts as a carrier of the light to and from the modulator. In intrinsic sensors, modulation occurs within the fiber itself. Fiber optic sensors can monitor many variables including temperature, pressure, mechanical strain, linear and angular displacement, change in conductivity and many others.

## 2.4.3 Microbend Sensor

This is one of the most popular types of optic sensors, and can be used to measure pressure, force, strain and other parameters. Its principle of operation is based on the fact that when light rays strike a bend in a multimode fiber, those rays in higher modes may strike the core/cladding interface at an angle that is lower than the critical angle. Consequently, they will not undergo total internal reflection and they will be attenuated. Light rays in lower modes are less susceptible to attenuation but may switch to higher modes further along the fiber and may leak out as well.
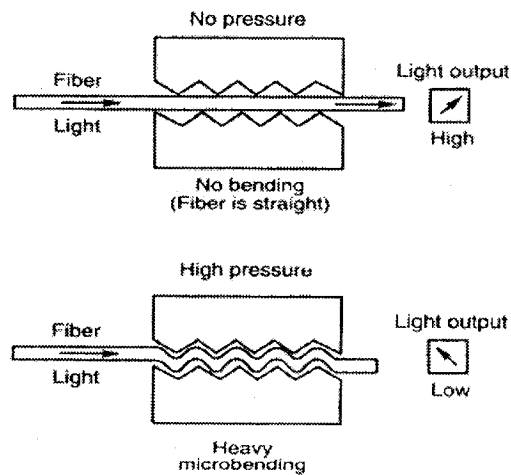


**Figure 2-12:** Principle of operation of microbend sensor [Hecht, 1993]

Figure 2-12 shows the principle of operation of a microbend sensor [Hecht, 1993]. A fiber is located between a pair of grooved plates. When there is no pressure acting on the top plate, the fiber is fairly straight and a strong signal is detected. When the plate is subjected to a pressure, microbends are induced along the length of the fiber so that some of the light leaks out and the optical power transmitted to the detector is diminished. The higher the applied pressure, the more extensive is the degree of microbending and consequently the lower is the transmitted power.

## 2.4.4 Fabry Perot Sensor
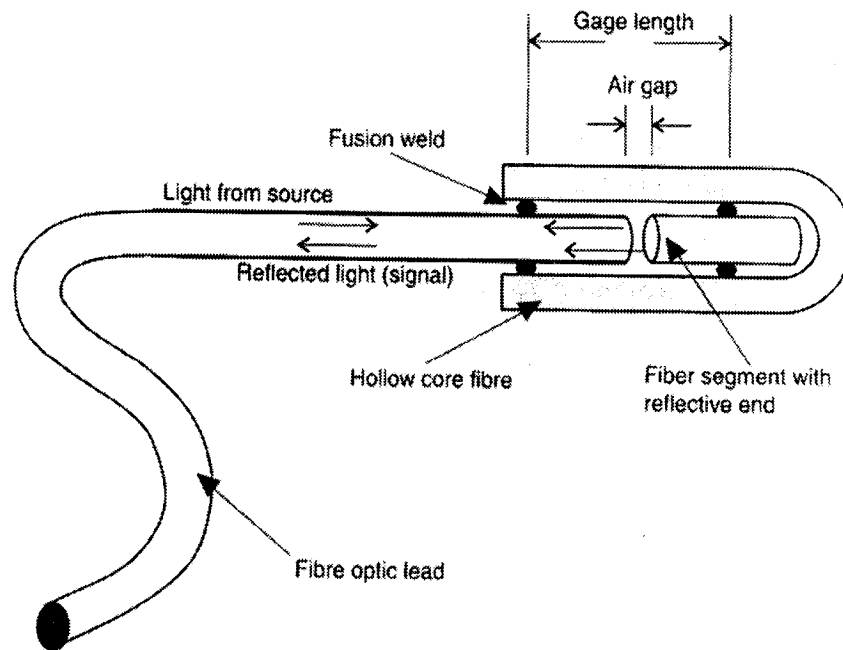


**Figure 2-13:** Fabry Perot sensor [Kalamkarov et al., 2000]

Interferometric sensors are among the most popular sensors in use today. Their principle of operation is based on changes in the effective length of a fiber. The effective length of

an optical fiber depends not only on the physical length (which may change as a result of mechanical or thermal strain), but also on the refractive index.

The most common interferometric sensor used with smart materials is the Fabry Perot sensor shown schematically in Figure 2-13 [Kalamkarov et al., 2000]. Fabry Perot sensors were first used as temperature transducers and demonstrated high accuracy. They generally consist of two reflective surfaces separated by a transparent medium. The transmittance of the interferometer depends vitally on the proper spacing between these reflectors, as well as on the wavelength of light [Udd, 1991].

The principle of operation of a Fabry Perot sensor is best explained by reference to Figure 2-13. Light from a source such as a laser or a light-emitting diode (LED) is coupled into the lead-in fiber, the end-portion of which is encapsulated into another hollow core fiber of slightly larger diameter. Another small fiber segment with a reflective surface is also fusion-welded to the inside of the hollow fiber. The lead-in fiber and the fiber with the reflective surface are separated by a small air gap. Light from the source reaching the end of the lead-in fiber will be mostly transmitted, but a small portion will be reflected back. The light transmitted across the air gap will be reflected off the reflecting fiber. Thus the incident light splits into two beams, one of which travels a larger distance than the other by an amount equal to twice the length of the air gap. The two reflected beams will therefore be out of phase and this results in interference. Mechanical or thermal strain at the location where the Fabry Perot sensor is embedded or attached will change the length of the air gap and hence the interference pattern of the two reflected beams. Hence, the detected signal can be used to compute strain.

Fabry Perot sensors are very attractive for smart composite applications because their extremely small size allows them to be embedded easily into composite materials, for example in pultruded glass- and carbon-fiber reinforced tendons [Georgiades, 1998]. As well, they are very sensitive in the direction parallel to the fiber axis and quite insensitive

in the perpendicular direction. Fabry Perot sensors can be used to measure mechanical strain [Georgiades, 1998], and if desired they can be designed with temperature compensation. The Fabry Perot sensors embedded in the pultruded rods at the Smart Composites Processing Lab at Dalhousie University are multimode sensors operating at a wavelength of 1300 nm.

## 2.4.5 Bragg Grating Sensor

Another class of sensors is constructed by creating a pattern of refractive-index differentials directly onto the core of the fiber. This may be achieved by directing two laser beams operating in the ultraviolet from the side. An interference pattern results, with alternating bright and dark fringes as shown in Figure 2-14 [Udd, 1995], which resembles a diffraction grating. At the regions of constructive interference, the intensity of light is high enough to cause optical damage at the sights occupied by germanium atoms. This changes the index of refraction of the core material, and creates a periodic pattern known as a Bragg Grating. Appropriately, the pertinent sensors are called Bragg Grating sensors.
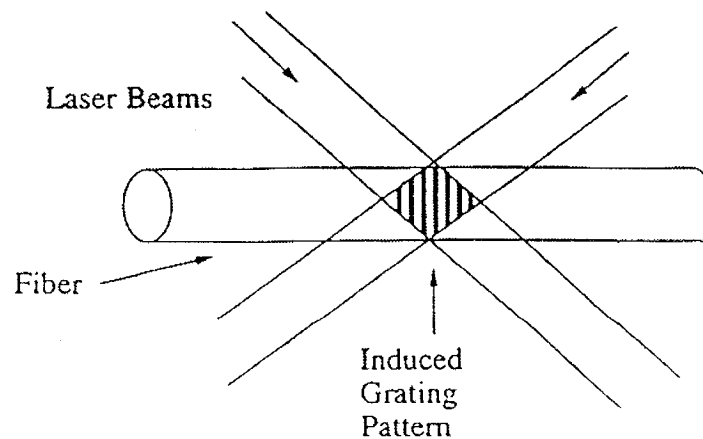


**Figure 2-14:** Bragg Grating sensor [Udd, 1995]

Broadband or
Tunable Source

Optical Fiber          Grating Sensor

Index of Refraction

Optical Spectrum Analyzer
or Photedetector

Incident Light          Reflected Light          Transmitted Light

$\lambda_0$          $\lambda$          $\lambda_0$          $\lambda$          $\lambda_0$          $\lambda$
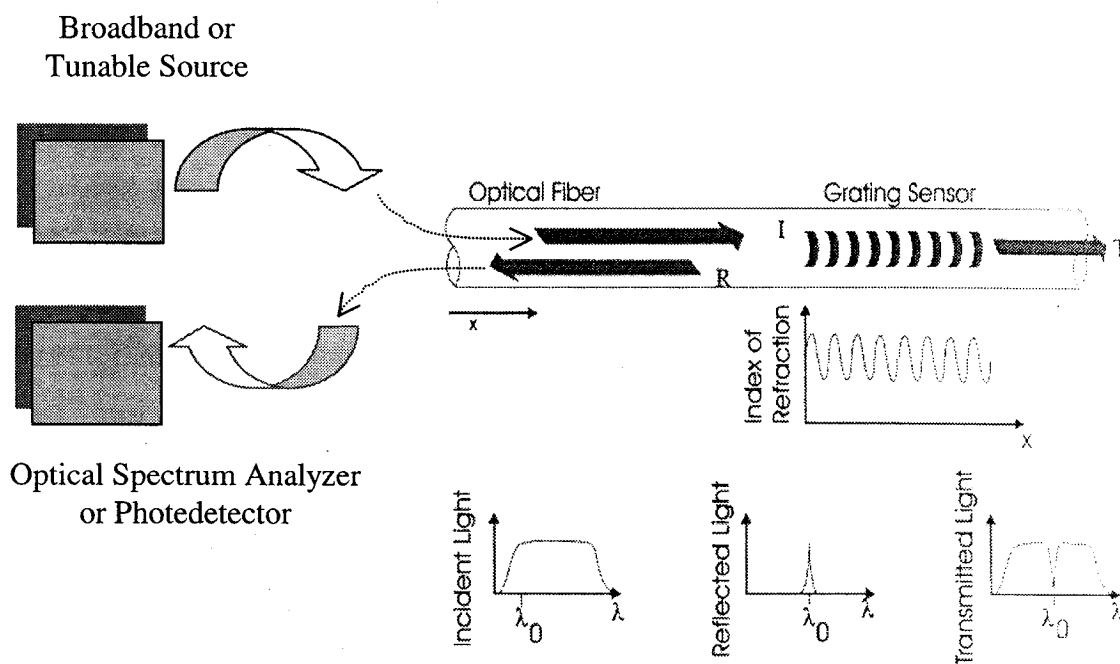
**Figure 2-15:** Schematic of Bragg Grating sensor response [Tennyson, 2001]

Fiber gratings selectively reflect certain wavelengths and transmit others as shown in Figure 4-15 [Tennyson, 2001]. The reflected wavelength will be a function of the index of refraction of the core as well as the spacing of the grating. Changes in temperature or pressure will cause a change in the refractive index of the core material and hence cause a shift in the narrow-band reflected light. A change in temperature will also induce a thermal strain that will change the spacing of the grating. A similar effect will be imparted by a mechanical strain. Consequently, thermal and/or mechanical strains will cause a change in the peak reflected wavelength. This wavelength shift provides the basis of operation of Bragg Grating sensors, as shown in Figure 2-16 [FLS 3100 Operation Manual, 1998]. The main advantages of Bragg Grating sensors, other than their small size, are a linear response and ease of manufacture. As well, being absolute sensors, they do not require recalibration. Typically, optical fibers are supplied with a protective coating such as polyimide or acrylate. However, Bragg Gratings often will be manufactured with the coating around the sensor portion removed to facilitate surface bonding or embeddement.

## Sensor Reflectivities
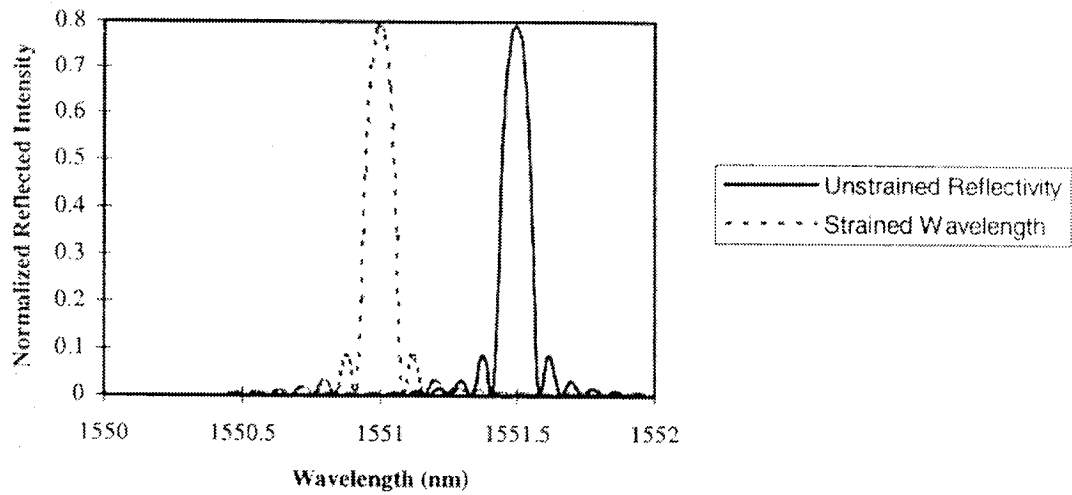


**Figure 2-16:** Strained and unstrained reflectivities [FLS 3100 Operation Manual, 1998]

To determine the mechanical strain ε from a Bragg Grating sensor the following equation may be used [Tennyson, 2001]:

$$\frac{\Delta\lambda}{\lambda_0} = GF \times \varepsilon + \beta_0 \Delta T \qquad (2\text{-}1)$$

where $\lambda_0$ is the Bragg wavelength and $\Delta\lambda$ the wavelength shift (see Figures 2-15 and 2-16]. GF, the gauge factor, and $\beta_0$, the thermo-optic response of the grating at fabrication, are supplied by the manufacturer. Finally, $\Delta T$ is the change in temperature on the grating with respect to $T_{ref}$, a reference temperature of the sensor at calibration (supplied by manufacturer).

The Bragg Grating sensors used at the Smart Composites Processing Lab at Dalhousie University are of the single-mode type, operating at a Bragg wavelength of around 1300 nm.

Other sensors that are being employed today are the polarization sensors. They work on the principle that certain fibers have different refractive indices for differently polarized light. They have been used to measure pressure, displacement, acceleration and other variables [Udd, 1991]. Other fiber optic sensors are based on the photoelastic effect, the Sagnac interferometer, the Mach-Zehnder inteferometer, the Michelson Interferometer etc. [Udd, 1991]. Fiber optic technology has grown tremendously over the past twenty years, as evidenced by the fact that since 1980 there has been a steady, almost exponential decrease in the cost of fiber optic components. For example, the cost of laser diodes has fallen from around $3000 to a mere $3 and the cost of a single-mode fiber has gone from $10 to $0.10 per meter [Udd, 1991, page 5]. It is anticipated that in the very near future, fiber optic sensors, perhaps together with micro-electro-mechanical (MEM) sensors, will enjoy widespread use in essentially all fields of health, engineering, and telecommunications.

## 2.5 Civil Engineering Applications of Passive Smart Materials

In Section 2.1 a distinction was made between passive smart materials and active (or adaptive) smart materials. Passive smart materials incorporate sensors that provide information on their state and integrity, while actively controlled smart materials incorporate both sensors and actuators and they can perform self-adjustment or self-repair as conditions change. Chapters 3-6 of this thesis will deal with the production and assessment of pultruded glass- and carbon-fiber reinforced tendons with embedded Fabry Perot and Bragg Grating sensors. The objective is to use these and other similar passive smart composites as prestressing tendons, cables or rebars in bridges, overpasses, dams and other structures. Appropriately, Section 2.5 will discuss briefly some civil engineering applications of passive smart materials and/or structures using fiber optic sensors. Active smart materials will be dealt with in chapters 7-12 of the thesis.

One of the biggest incentives in applying fiber optic sensor technology to the infrastructure has been the monitoring of large structures such as bridges and dams. Their economic and environmental impact is so pronounced that a concise assessment of the structures and their foundations is of paramount importance. Vurpillot et al. [1996] installed a large number of fiber optic deformation sensors together with thermocouples and conventional strain gages in the concrete deck and steel girders of a highway bridge near Lausanne, Switzerland. Their objective was to monitor the bridge during the first hours after concreting and to perform a strain analysis of the bridge under the action of static and dynamic loads (in the form of heavy trucks).
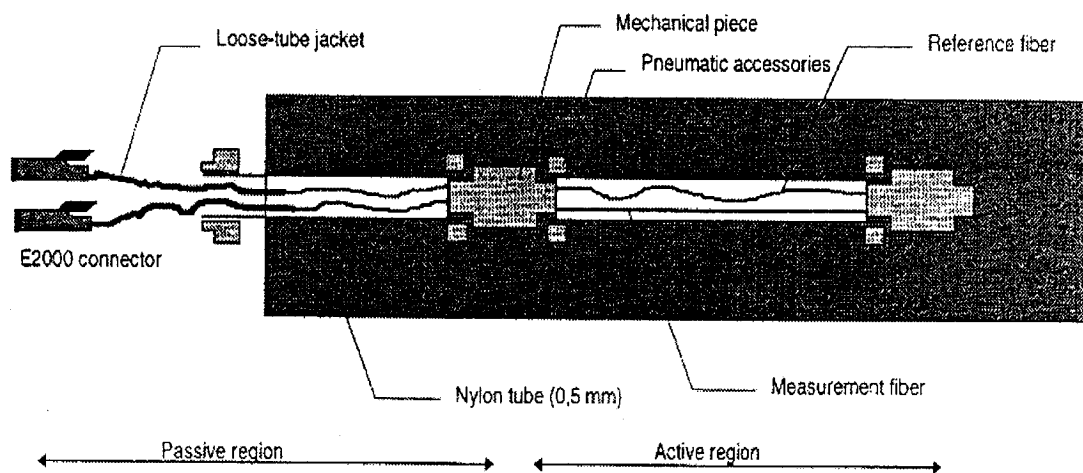


**Figure 2-17:** Schematic of fiber optic sensor [Vurpillot et al., 1996]

The salient features of the sensor system used are shown in Figure 2-17. It consists of two single-mode optical fibers. One fiber, the measurement fiber, is prestrained and anchored between two mechanical pieces that serve to transmit the displacement of the deck to the optical fiber. Prestraining the measurement fiber allows it to detect both tensile and compressive strains. The second fiber, the reference fiber, is located free in the tube and is not affected by mechanical displacements of the deck, and it will detect only thermal expansions. Clearly, the combination of the two sensors renders the overall smart

arrangement temperature-independent. The fibers are coated with a thin layer of acrylate and are encapsulated in a 0.5 mm nylon tube.
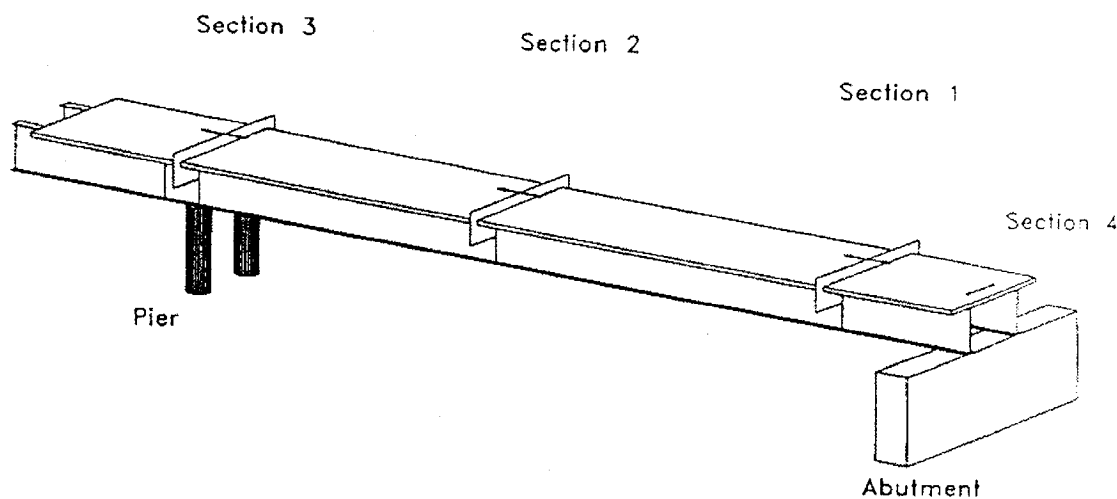


**Figure 2-18:** Placement of fiber optic sensors [Vurpillot et al., 1996]

Figure 2-18 [Vurpillot et al., 1996] shows the details of the installation of the sensors. Sections 1, 2, and 3 have 8 sensors each, monitoring the deck along the axis of the bridge, and section 4 has 4 sensors that monitor the deck in a direction perpendicular to the bridge axis. The sensor installation was very expedient, taking only half a day.

As stated earlier, the first objective of this project was to assess the deck after concreting. The shrinkage measurements of the concrete deck indicated that during the thermal expansion phase (the first few hours after concreting) the peak strains attained were about 0.06%. During the shrinkage (cooling) phase the fiber optic sensor measurements exhibited discontinuities, indicative of crack formation eight days after concreting. Hence, we see that similar experiments have the potential of providing valuable insight into the underlying fundamentals of steel-concrete interaction as well as on the current strain state of a structure. The load test, which was conducted four months after concreting, involved locating 25-ton trucks on the deck according to six different load patterns labeled a, b, c, d, e, and f with each load pattern repeated 3 times. Figure 2-19 shows the displacement output from one of the sensors. The repeatability of the readings

from this sensor is evident. The authors thus concluded that such a smart system is well suited for bridge monitoring. As well, it was observed that the overall precision of the fiber optic sensors would be increased if an integrated (rather than an external) optic coupler were used.

Fiber optic sensor measurement
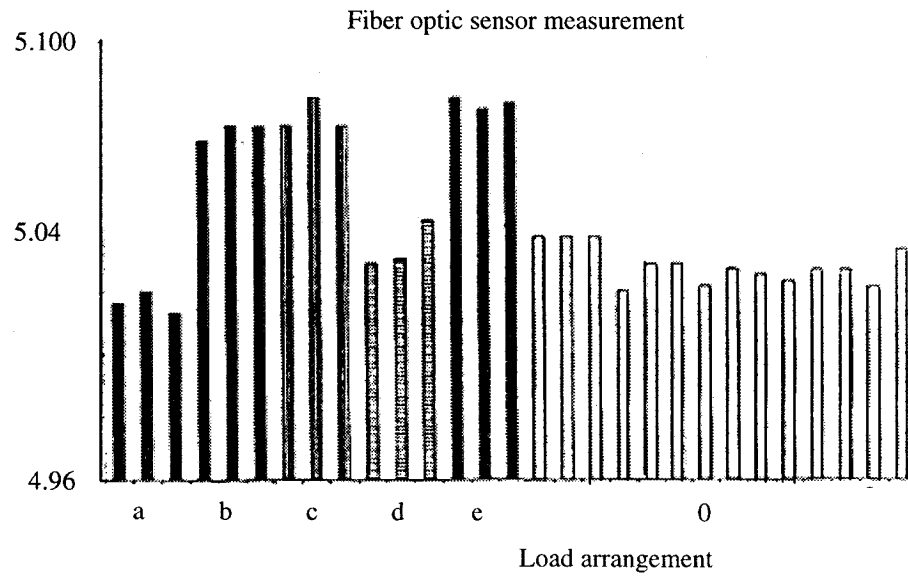
Figure 2-19: Displacement output from fiber optic sensor [Vurpillot et al., 1996]
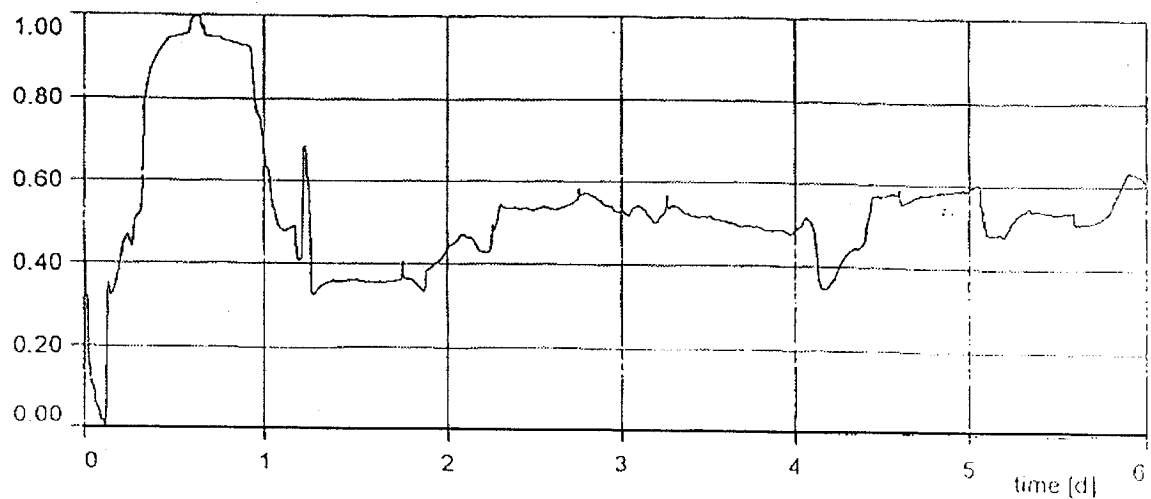
Figure 2-20: Strain behavior for 6 days following concrete pouring [Habel and Hofmann, 1994]

The potential of using fiber optic sensors with the objective of monitoring civil engineering structures was also demonstrated by Habel and Hofmann [1994], who embedded Fabry Perot fiber optic sensors in the reinforced walls of a new sewage treatment project. The sensors were placed inside a cement mortar body and subsequently attached to the cage of the steel reinforcement. The wall was then concreted and the strain data were acquired. Figure 2-20 shows the strain behavior recorded by one of the Fabry Perot sensors for the first six days following concrete pouring.
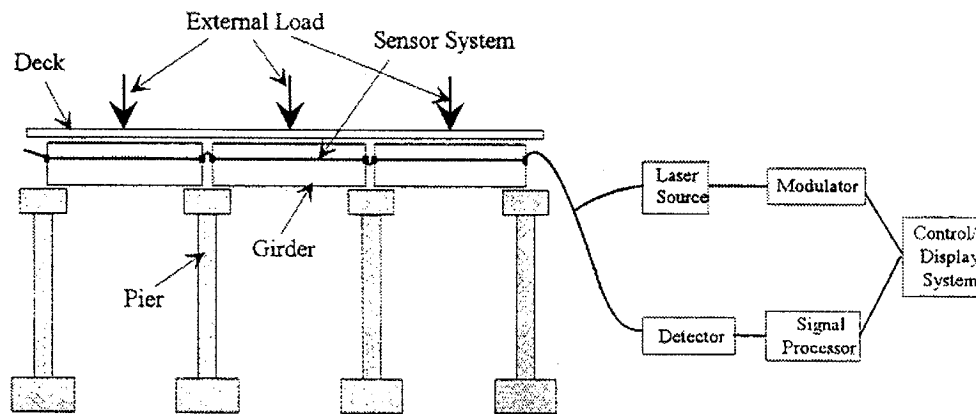


**Figure 2-21:** Health monitoring system for a bridge instrumented with Fabry Perot sensors [Kim et al., 1997]

The first attempt at introducing smart elements (using fiber optic sensors) into real bridges in the Republic of Korea was made by Kim et al. [1997]. Their study involved performing diagnostic tests of the Sungsan Bridge (in Seoul), the busiest motorway bridge in the country carrying a traffic load of about 200,000 vehicles per day. Three spans were chosen for testing with the Fabry Perot sensors, along with accelerometers and foil gages attached to a steel girder at midspan, as shown in Figure 2-21. Static and dynamic tests were performed using a 30-ton truck and the results were recorded.

Typical plots are shown in Figure 2-22. The top graph shows the strain signature from the Fabry Perot sensor due to the static load, and the other two graphs pertain to truck

velocities of 10 km/h and 20 km/h. The potential for strain monitoring using fiber optic sensors is evident.

Strain Signature

↓



Static Load Test



truck velocity =10 km/h

truck velocity =20 km/h
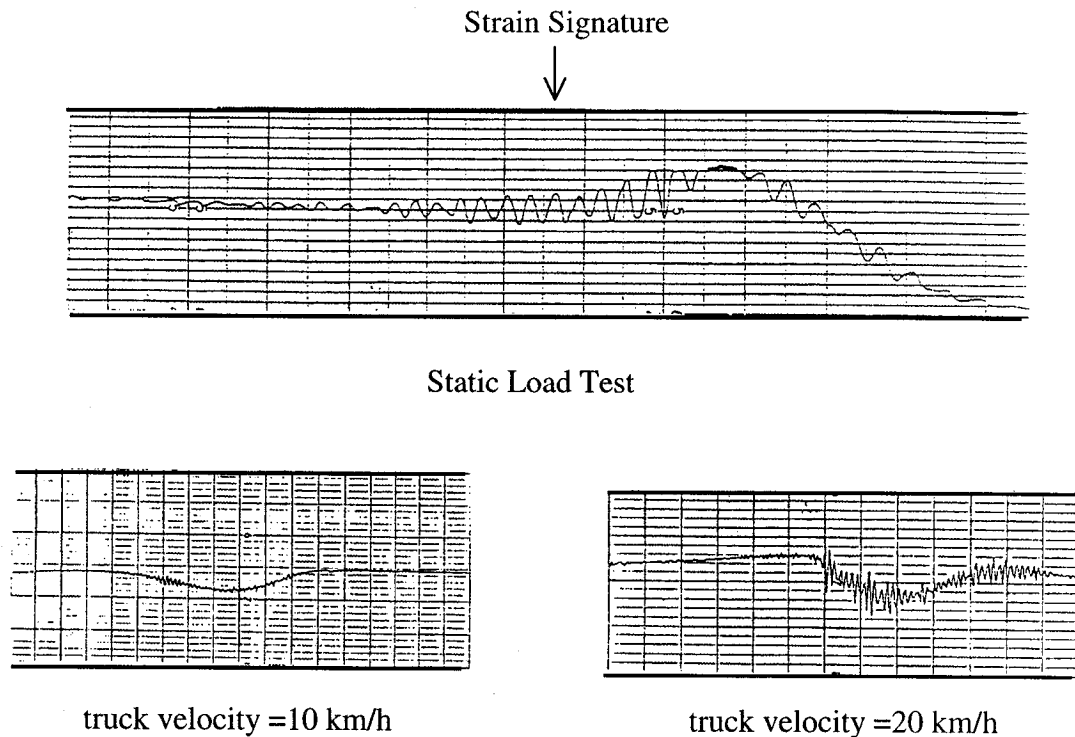
**Figure 2-22:** Response of Fabry Perot sensors due to static and dynamic loads [Kim et al., 1997]

Nellen et al. [1997] reported one of the earliest known applications of smart composite structures, pertaining to the monitoring the Storck's stay cable bridge in Winterhur, Switzerland. Two novel carbon fiber reinforced cables equipped with strain gages, temperature sensors and Bragg Grating fiber optic sensors had previously been installed in the bridge.

A schematic of the Storck's Bridge is shown in Figure 2-23. Each CFRP cable has a length of 35 m and consists of 241 5 mm-diameter wires arranged in a hexagonal manner inside a polymer tube. Each CFRP cable has 7 Bragg Grating (BG) sensors and 6 resistance strain gages (RSG). Three Bragg Grating sensors (BG1, BG4, and BG7) are bonded to wires on the outer periphery of the array as shown in Figure 2-24. The

remaining sensors (BG2, BG3, BG5, and BG6) are used as temperature compensators on dummy wires that will not carry any load.
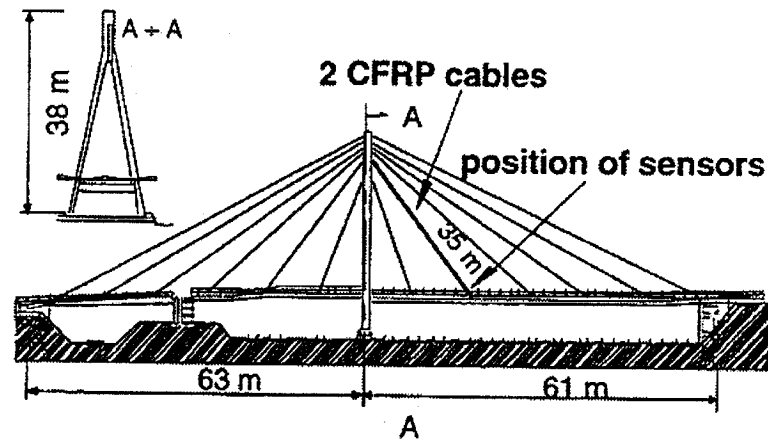


**Figure 2-23:** Schematic of Storck's Bridge with smart CFRP cables [Nellen et al., 1997]
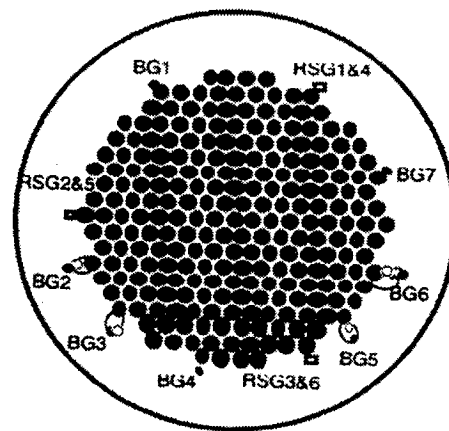


**Figure 2-24:** Cross-Section of smart CFRP cable [Nellen et al., 1997]

Figure 2-25 shows the monitoring of the bridge during different phases. In particular eight different events are represented on the graph. These are:

" 1. The sensors are applied and the cables ready for shipment.
2. The cables are fixed to the bridge; no load is applied.
3. A first load which is used as reference load is applied to the cables.
4. The bridge is concreted and gains most of its weight.
5. The load distribution on all cables is adjusted.

6. The load on the cables was measured with a hydraulic press for comparison.
7. Measurements made two days before the bridge opening.
8. Measurements on a typical winter day."
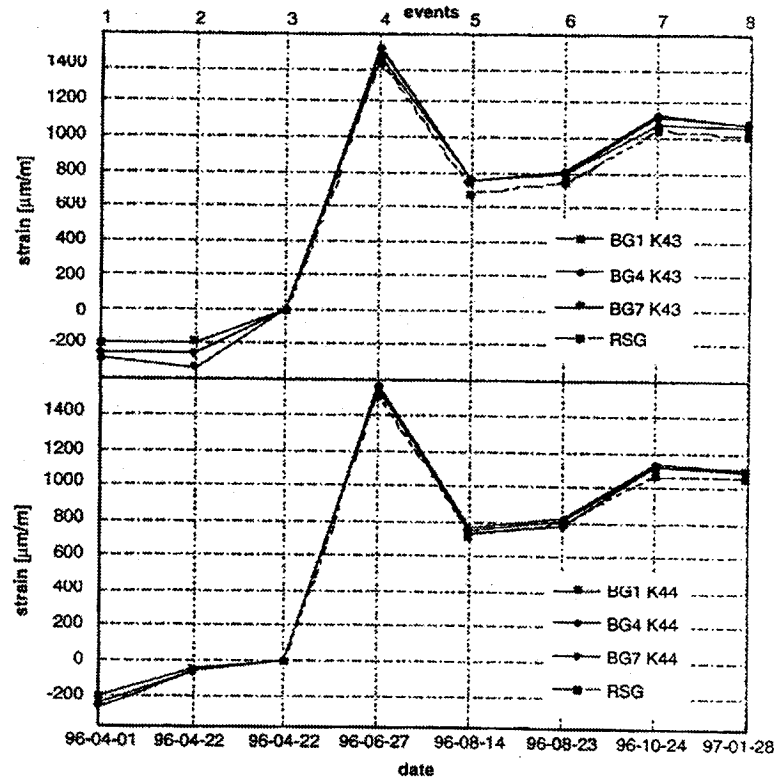


**Figure 2-25:** Monitoring of bridge using smart CFRP cables [Nellen et al., 1997]

The top graph in Figure 2-25 shows the strain output from the four Bragg Grating sensors in one smart cable, and the bottom graph pertains to the other cable. One noteworthy feature of the graphs is the excellent agreement between the fiber optic sensors and the strain gages. It is thus clear that Bragg Grating sensors have great potential in monitoring civil engineering structures in terms of strain measurements and temperature compensation.

Tennyson et al. [2001] describe the use of what are referred to as "long gauge sensors" as well as Bragg Grating sensors for strain monitoring of different structures in Canada. The

long gauge sensor is an interferometric sensor and operates on a similar principle to that of a Fabry Perot sensor. Since the sensing element is essentially a flexible optical sensor, the long gauge sensor can vary in length from a few cm to tens of meters. This allows the sensor to be employed in many interesting configurations, such as, for example, around a composite column wrap to measure circumferential strain. The authors demonstrated the feasibility of having fiber optic smart components monitor large structures by bonding Bragg Grating sensors and long gauge sensors to composite rebars embedded into the concrete repair of the Centre St. Bridge in Calgary, Alberta. The authors also used long gauge sensors to monitor the strain state in the pier columns of the Portage Creek Bridge in Victoria, British Columbia. Since this bridge was designated a "disaster route", it became necessary to reinforce the columns that were designed prior to the introduction of the new seismic design guidelines in 1982. Figure 2-26 shows a schematic of a column with FRP wrap and bonded long gauge sensors.
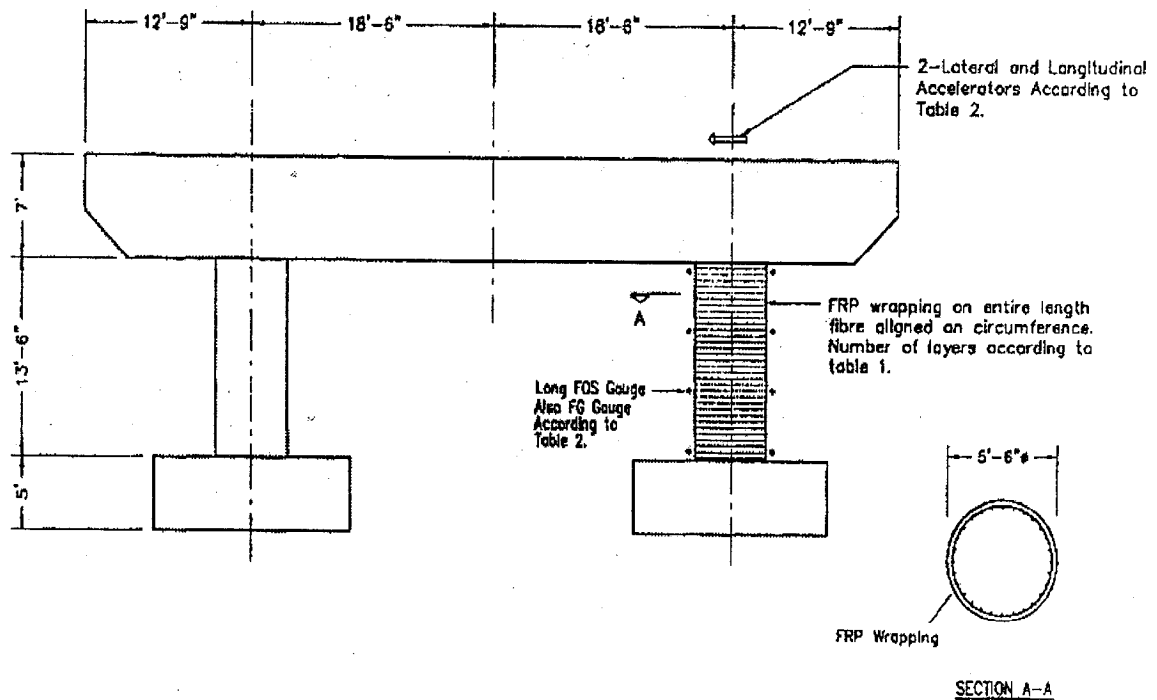


**Figure 2-26:** Schematic of column with composite overwrap and long gauge sensors [Tennyson et al., 2001]

The examples described in this section represent only a few select cases of smart elements being integrated within various civil engineering structures. In some of the above-mentioned projects, as well as in others (see for example Mufti et al., 2001, Newhook et al., 2001) the fiber optic sensors are used in conjunction with composite materials. In fact, smart composites are one of the most rapidly evolving fields with applications not only in civil and structural engineering, but also in medicine, sports, space research, machine design and control and many other fields. The impact of smart composite materials undoubtedly will become more pronounced as the pertinent knowledge base expands and scientists and engineers become more comfortable with their long-term behavior.

# 3.0 EXPERIMENTAL MATERIALS, PROCESSES, AND EQUIPMENT

## 3.1 Introduction

During the last few years, countries worldwide have been agonizing over the problem of rehabilitating the huge volume of their steel-reinforced concrete structures, and the ever-corroding steel has added a new dimension to the world's infrastructure problems. Due to the severity of its climatic conditions, Canada is in a more critical situation than most other countries. ISIS Canada, a Network of Centres of Excellence, was created to combat this problem and it combines the work of hundreds of researchers throughout the country. ISIS stands for Intelligent Sensing for Innovative Structures. "ISIS Canada research enables infrastructure to be built and rehabilitated using innovative materials that are tremendously lighter, stronger, and longer lasting. In addition, structures can be engineered to monitor and communicate the stresses and strains they encounter on a daily basis. An engineer could arrive at work one morning to a message resembling E-mail, warning of damage that could have a cost in human lives. Without even visiting the site, those responsible will recognize the problem and be able to respond immediately." [ISIS Canada Annual Report, 1996].

This thesis research has primarily been funded by ISIS. Chapters 4-6 deal with the fabrication, processing and reliability assessment of pultruded smart CFRP and GFRP tendons with embedded fiber optic sensors. The long-term objective is to use these tendons as both rebars and strain monitors in civil engineering structures. Such materials eventually will replace steel as the primary concrete reinforcement, and at the same time provide the strain data from the integrated fiber optic sensors to enable us to correct problems before they become insurmountable. Appropriately, this chapter describes, in

some detail, the experimental materials, processes and equipment used in the various aspects of this research.

## 3.2 Pultrusion

Central to the current study is the fabrication of carbon- and glass-fiber reinforced polymer (FRP) tendons using pultrusion. 9.5 mm-diameter rod stock was produced using a customized pultrusion machine designed and built at the Smart Composites Processing Lab at Dalhousie University. The pultrusion setup is shown in Figure 3-1 [Kalamkarov et al., 1997]. The reinforcing fibers (E-glass or carbon) are pulled from a regular array of spools into a tool-steel die. Prior to entering the die, the fibers pass through a set of fiber-feed polyethylene guides and then through a dip-type bath that contains the resin and appropriate catalysts and mold-release compound. The fibers are thoroughly saturated with resin and subsequently pass through another fiber feed guide with two sets of holes arranged in horizontal lines. The holes in this guide help to squeeze out excess resin from the fiber rovings so that there is an even distribution around the cross-section of each one. The reinforcements then pass through another set of guides that has holes arranged in a circular pattern. This guide finally leads the fibers into the die. It should be noted that one roving traverses a straight path through the guides and into the center of the die. This center roving is used to carry the optical fiber sensor in the cases where a sensor is required to be embedded in the composite rod. The pulling force is maintained by a set of counter-rotating wheels fitted with a thick layer of rubber. A groove is machined into the center of the rubber to help guide the consolidated rod as it exited the die.

The glass fiber rovings used are continuous E-glass filaments formed into a single end reinforcement, free from catenary and treated with 0.45 nominal wt% sizing which is silane-based and compatible with most resin systems. The carbon rovings (see Figure 3-2) used had a standard epoxy-based sizing. The rods were produced using a urethane modified bisphenol-A based vinylester resin system known for its good mechanical properties and excellent processability. Two types of organic peroxide catalysts were

used to cure the resin, di-peroxydicarbonate and tert-butyl peroxybenzoate, commonly known as TBPB. Adequate release from the die was achieved by using an internal lubricant. The mechanical properties of the vinylester resin system are given in Table 3-1.
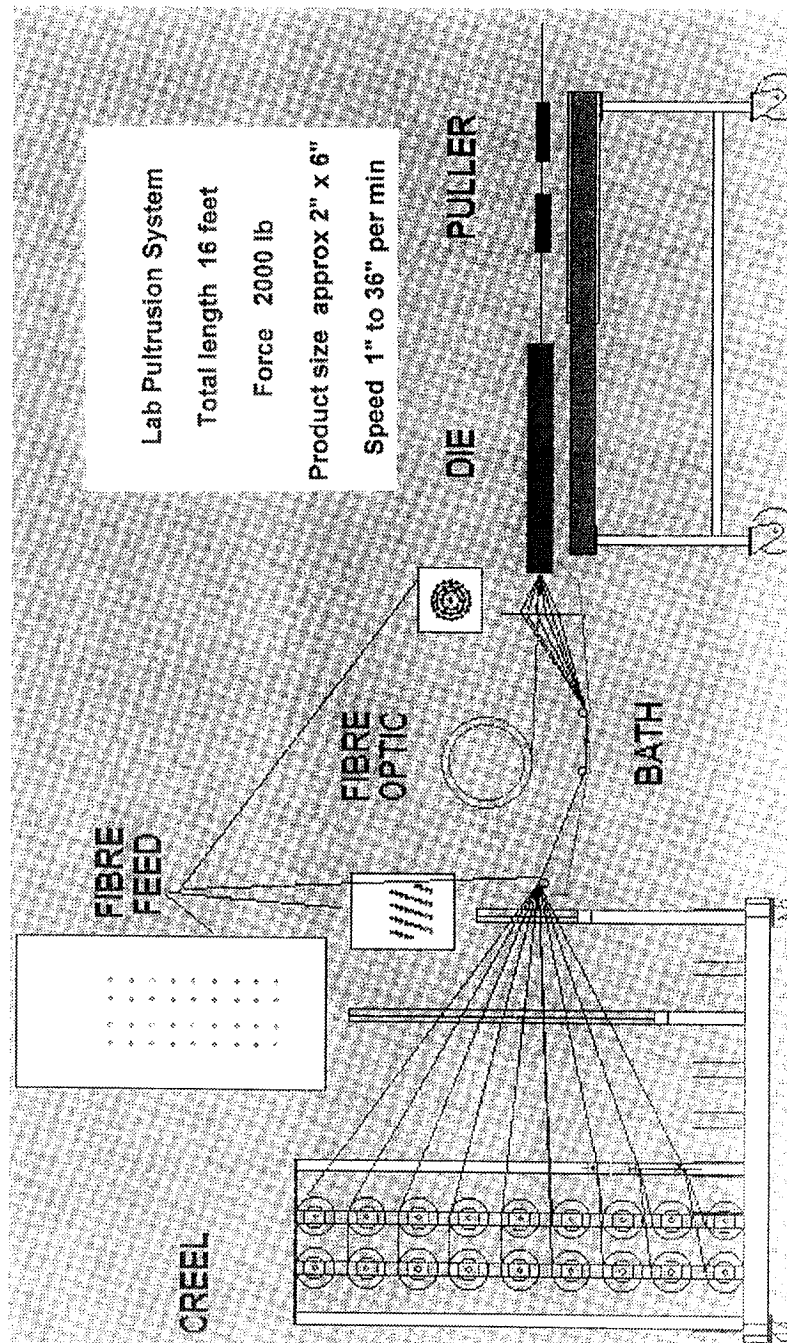


**Figure 3-1:** Pultrusion setup at Dalhousie University [Kalamkarov et al., 1997]

The properties of the carbon- and glass-fiber rovings which contained a sizing compatible with the vinylester resin system are given in Tables 3-2 and 3-3 respectively. The 9.5 mm-diameter GFRP rods were pultruded with a 64% reinforcement volume ratio and the CFRP rods were pultruded with a 62.5% volume ratio. These figures correspond to 22 rovings for carbon and 26 rovings for glass. Six strip heaters attached in pairs of two on the top and bottom surfaces of the die provided three thermal zones, one near the die entrance (120°C), one in the middle region of the die (150°C), and one near the exit (120°C). The operator of the pultrusion machine can adjust the pultrusion rate by means of an integrated speed controller. However, it was found that a pulling speed of around 25 cm per minute produces good-quality rods. The color of the GFRP tendons permitted a visual inspection of any defects. As far as the quality of the CFRP rods was concerned, a simple manual hardness test proved sufficient.
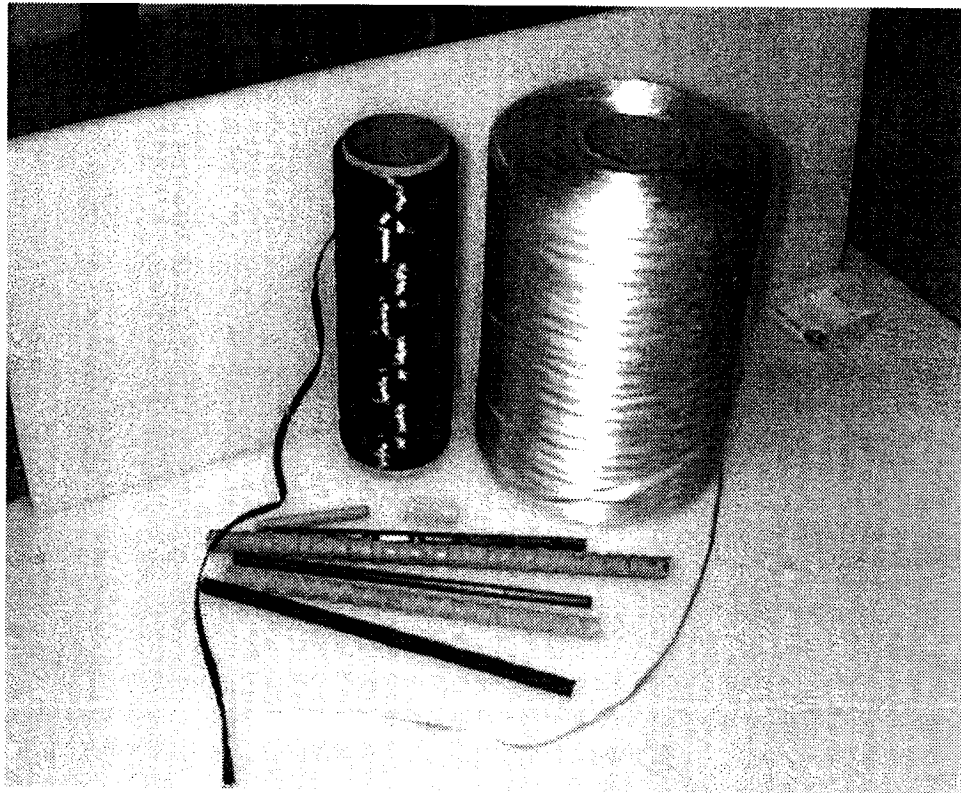


**Figure 3-2:** Carbon and glass fiber spools together with pultruded CFRP and GFRP tendons

**Table 3-1:** Properties of vinylester resin

| Property | Value | Units |
|---|---|---|
| Young's Modulus | 3.0 | GPa |
| Tensile Strength | 73* | MPa |
| Poisson's Ratio | 0.4 | |

\* - Values taken from literature for similar materials

**Table 3-2:** Properties of carbon fiber rovings

| Property | Value | Units |
|---|---|---|
| Axial Modulus | 227 | GPa |
| Radial Modulus | 70* | GPa |
| Tensile Strength | 3500 | MPa |
| Poisson's Ratio | 0.3* | |

\* - Values taken from literature for similar materials

**Table 3-3:** Properties of glass fiber rovings

| Property | Value | Units |
|---|---|---|
| Axial Modulus | 73* | GPa |
| Radial Modulus | 73* | GPa |
| Tensile Strength | 2760 | MPa |
| Poisson's Ratio | 0.22* | |

\* - Values taken from literature for similar materials

Figure 3-3 shows the overall pultrusion setup of the Smart Materials Centre, Dalhousie University. The creel system loaded with glass fiber spools, the fiber guides and the pultrusion die are clearly visible. A vent, seen above the machine, is an integral part of any pultrusion lab due to the strong odor of the chemicals involved in the process. Figures 3-4 and 3-5 show a close up views of two storage shelves. One holds carbon fiber spools and the other has some of the chemicals added to the resin. Notice also in Figure 3-5 a spool with polyimide-coated optical fiber. Figure 3-6 shows glass fiber rovings passing through holes machined in the polyethylene guides and Figure 3-7 is a close up view of the creel loaded with glass fibers spools. Figures 3-8, 3-9, and 3-10 show glass fibers guided into the die. Figures 3-11 and 3-12 show close up views of the die with the strip heaters and their ceramic cap insulators, and Figure 3-13 shows the inside of the controller box with the temperature controllers clearly visible. Figure 3-14 shows a pultruded carbon rod exiting the pulling wheels and Figures 3-15 and 3-16 a pultruded glass rod.
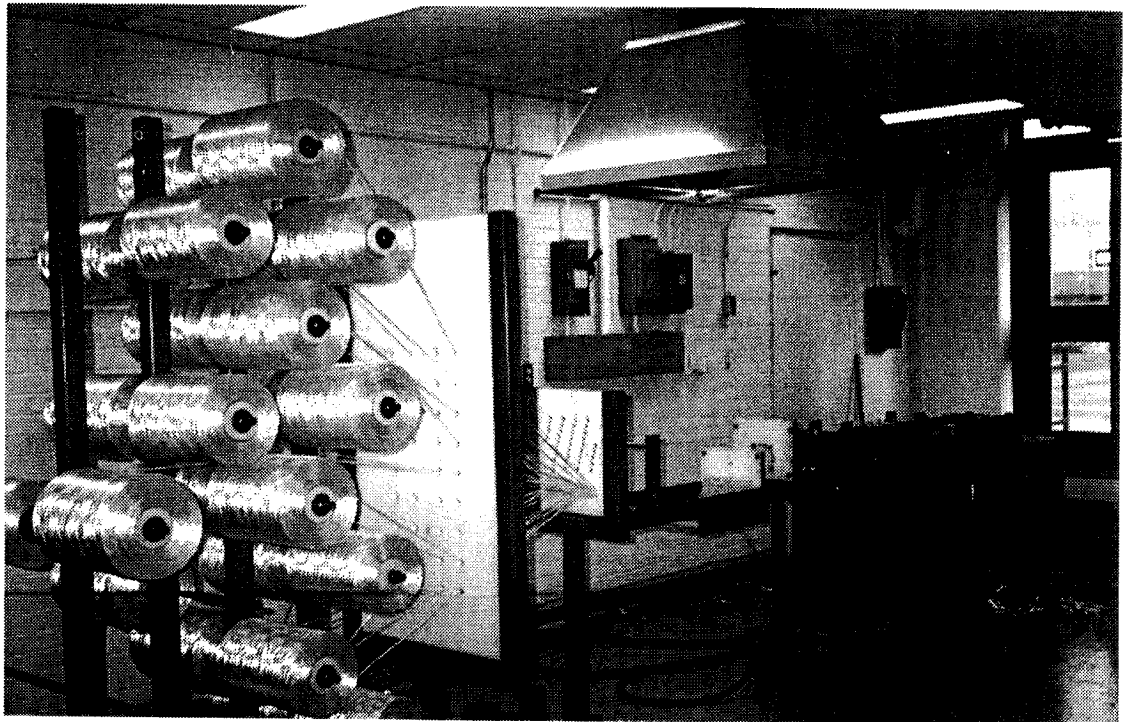


**Figure 3-3:** Overall pultrusion setup at Dalhousie University
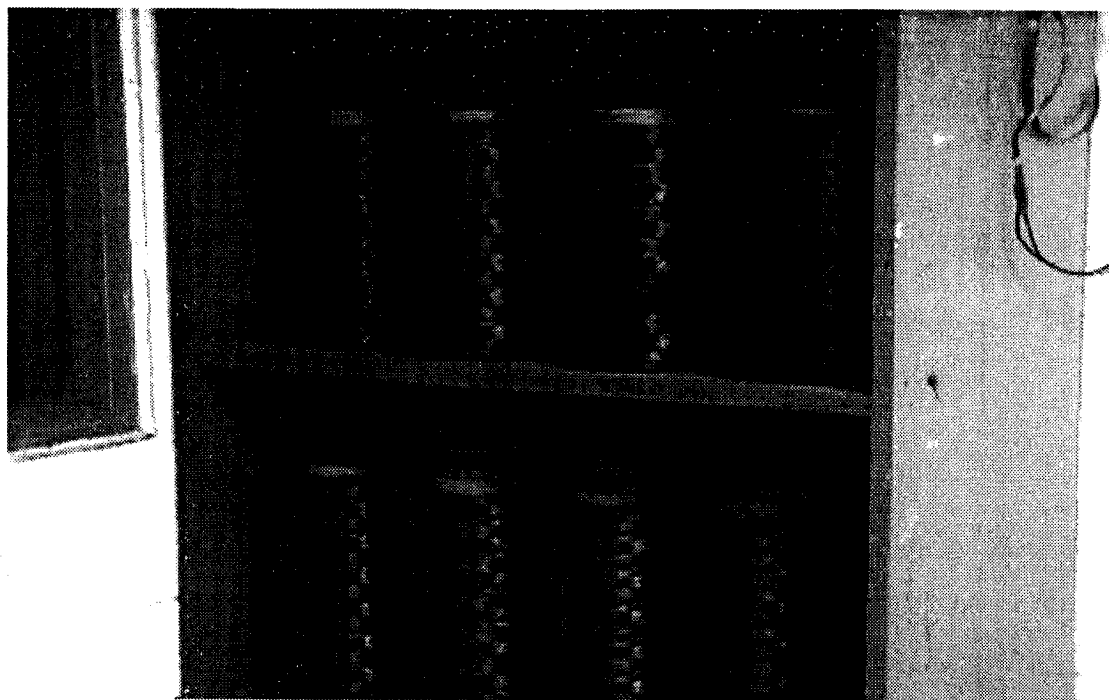
**Figure 3-4:** Storage cabinet with carbon fiber spools in pultrusion lab
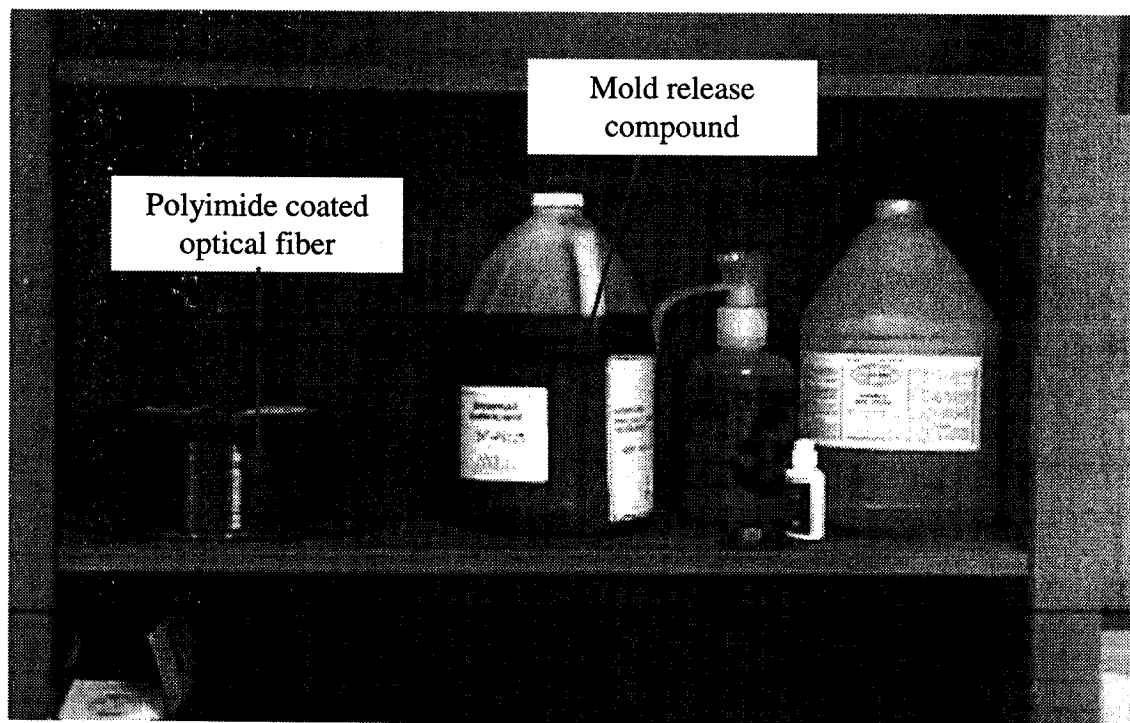


**Figure 3-5:** Storage shelf with some of the resin additives
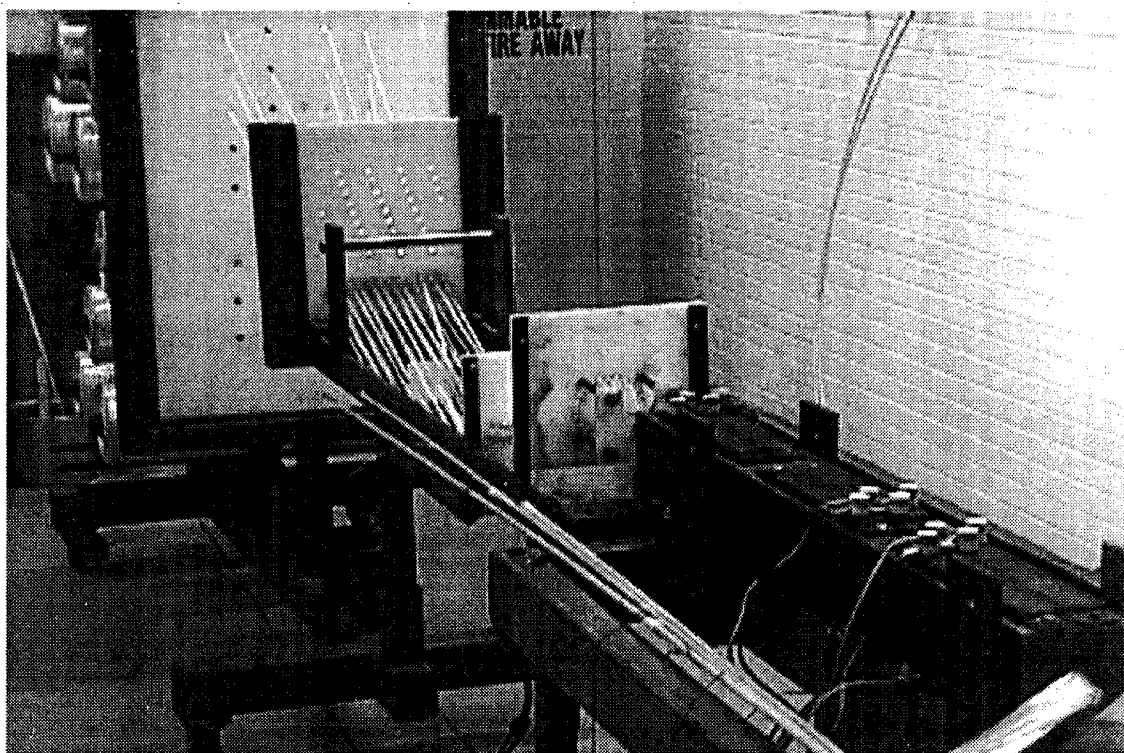
**Figure 3-6:** Glass fiber rovings from the creel are being pulled towards the die
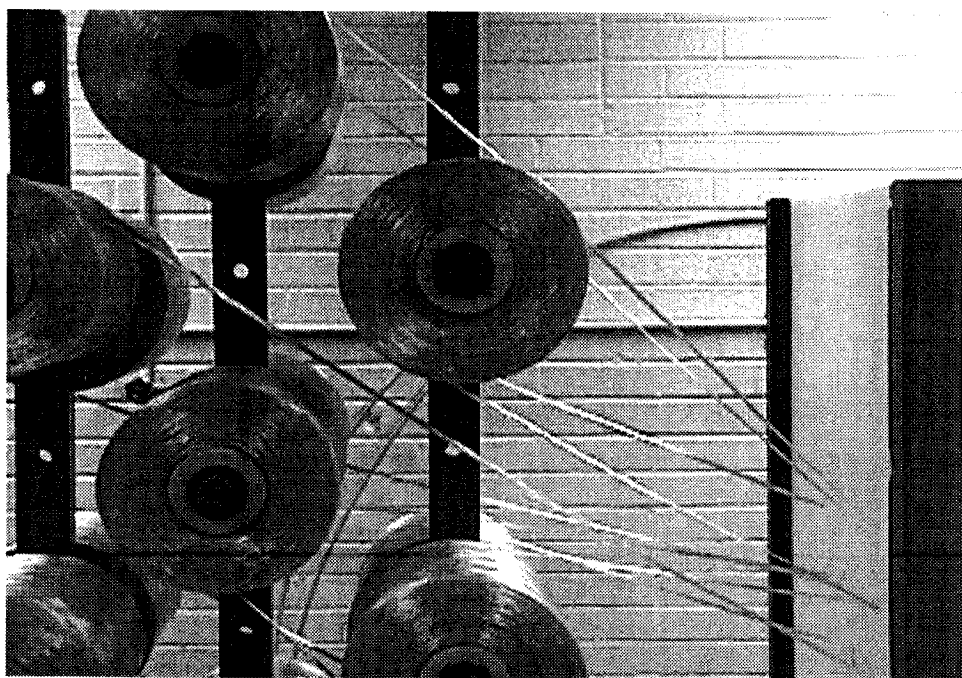


**Figure 3-7:** Close up view of creel with glass fiber spools
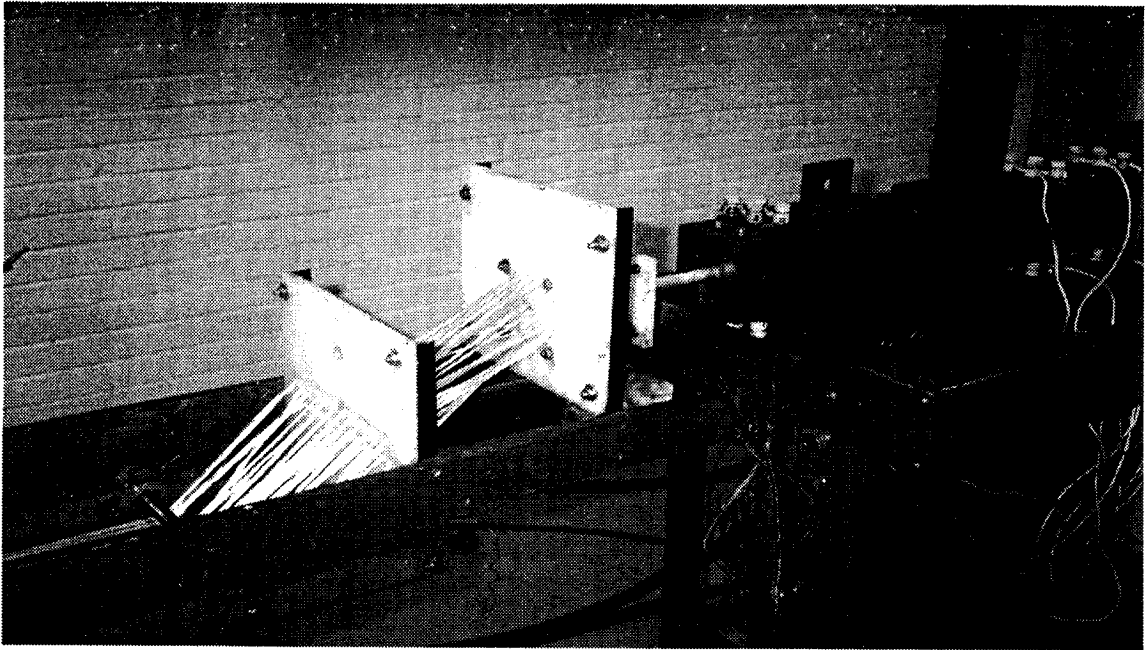
**Figure 3-8:** Close up view of glass fiber rovings guided into the die
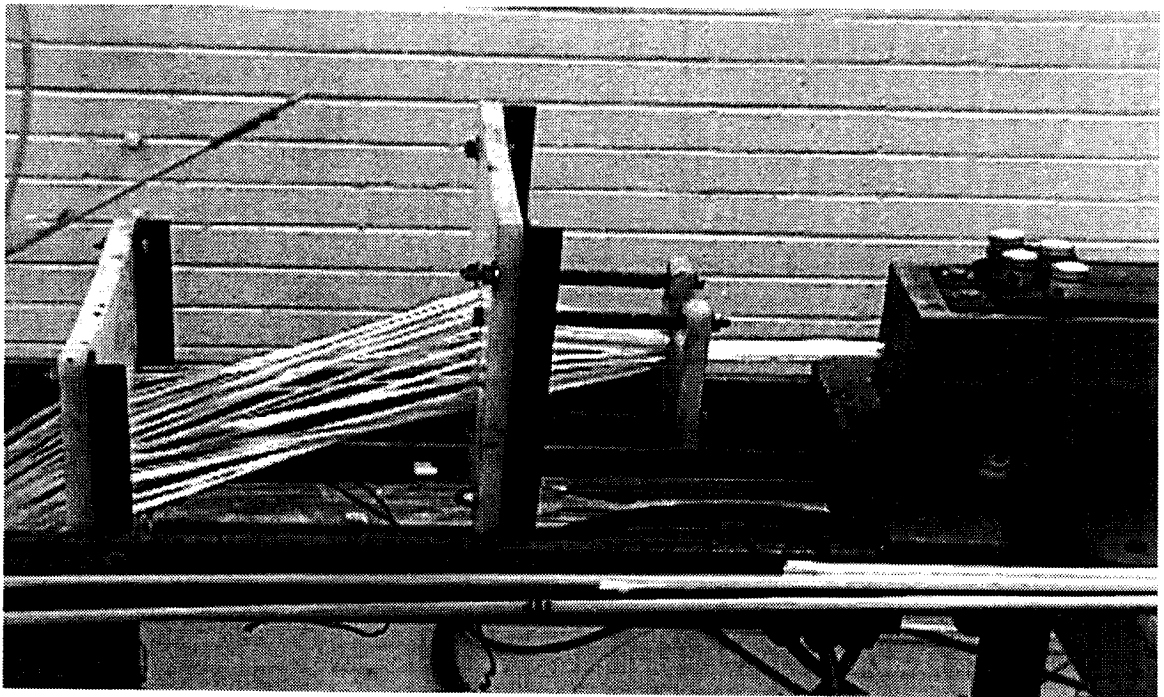


**Figure 3-9:** Glass fiber rovings enter the die
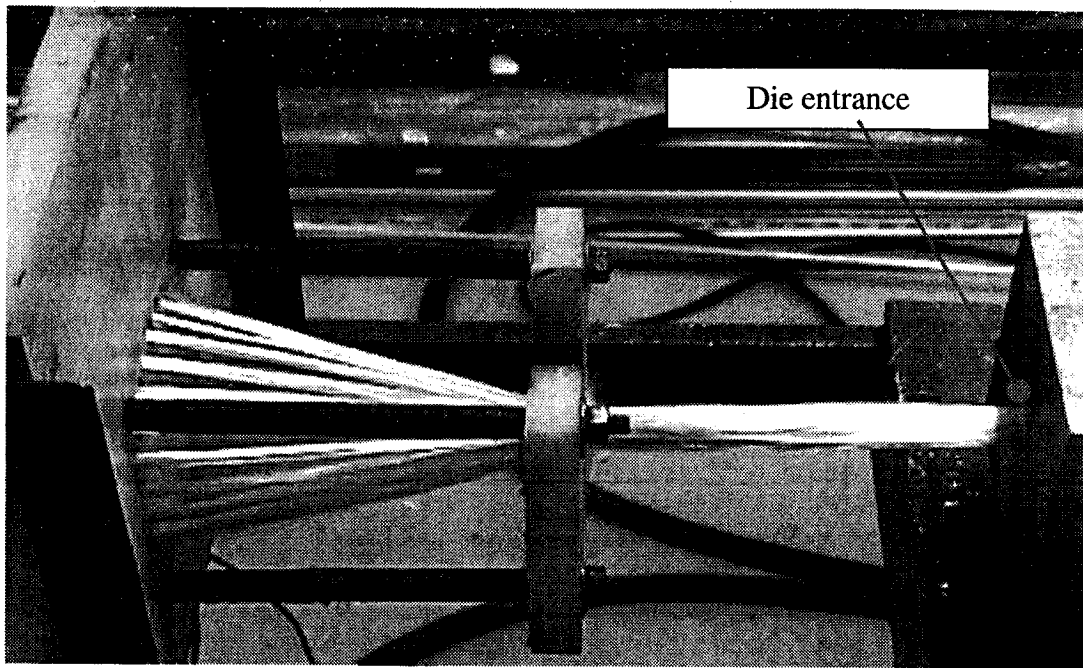
**Figure 3-10:** Glass fiber rovings pass through last two guides and enter the die
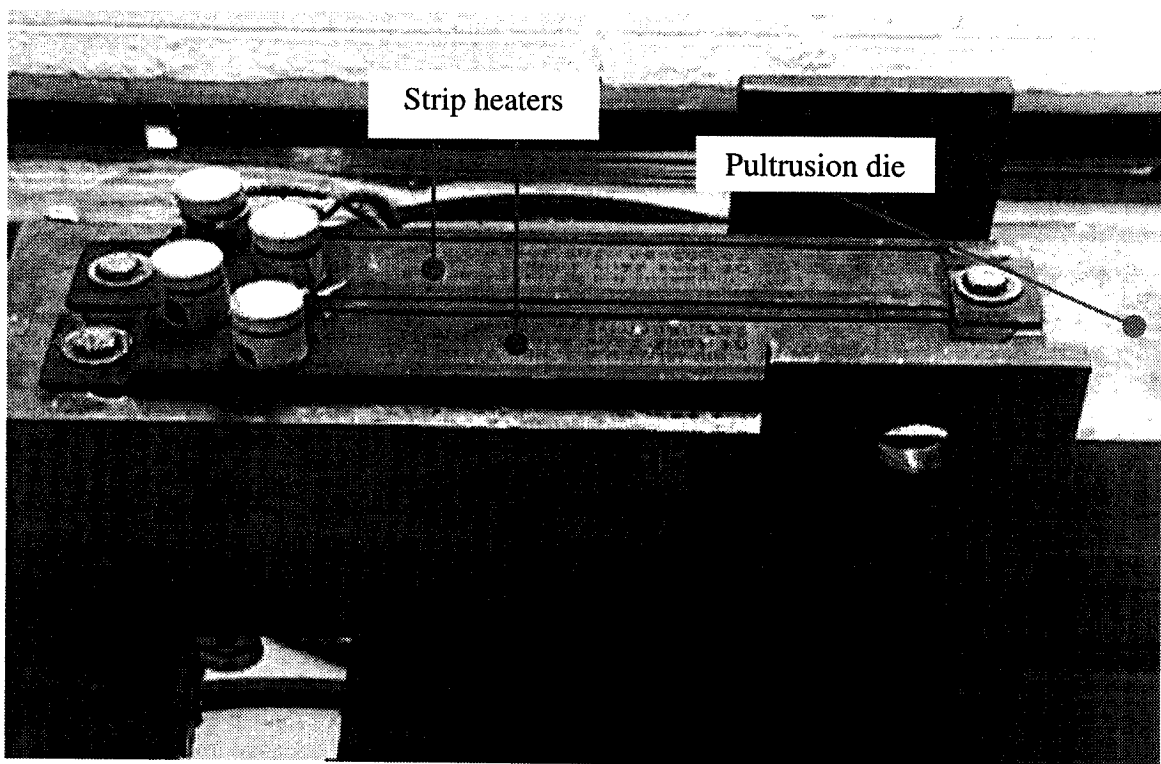


**Figure 3-11:** Close up of the die shows two strip heaters
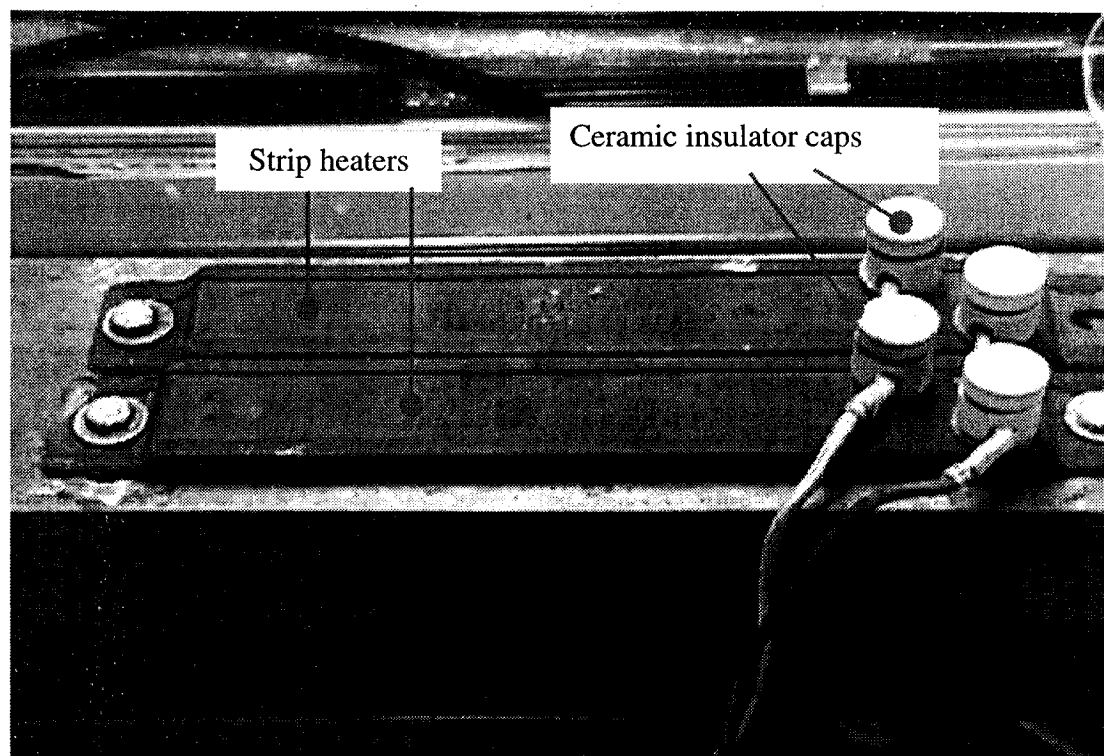
**Figure 3-12:** The strip heaters and their ceramic insulators
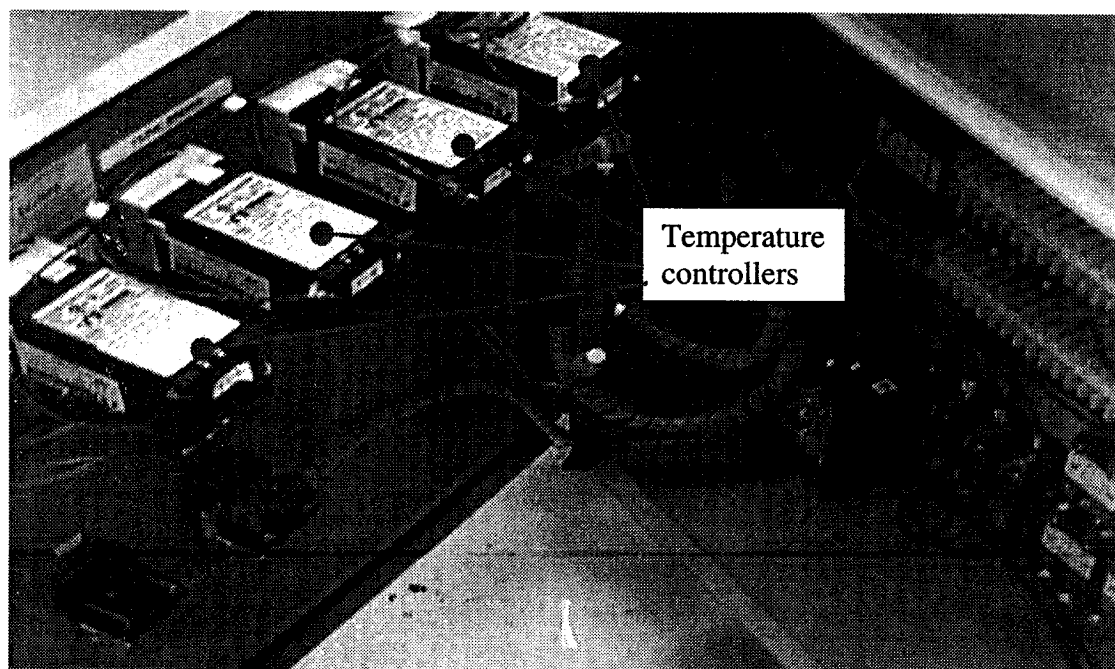


**Figure 3-13:** Inside the pultrusion controller box

Figure 3-14 shows a pultruded carbon rod exiting the pulling wheels and Figures 3-15 and 3-16 a pultruded glass rod.



**Figure 3-14:** Pultruded carbon rod exiting the die



**Figure 3-15:** Pultruded glass rod exiting the die and entering wheels
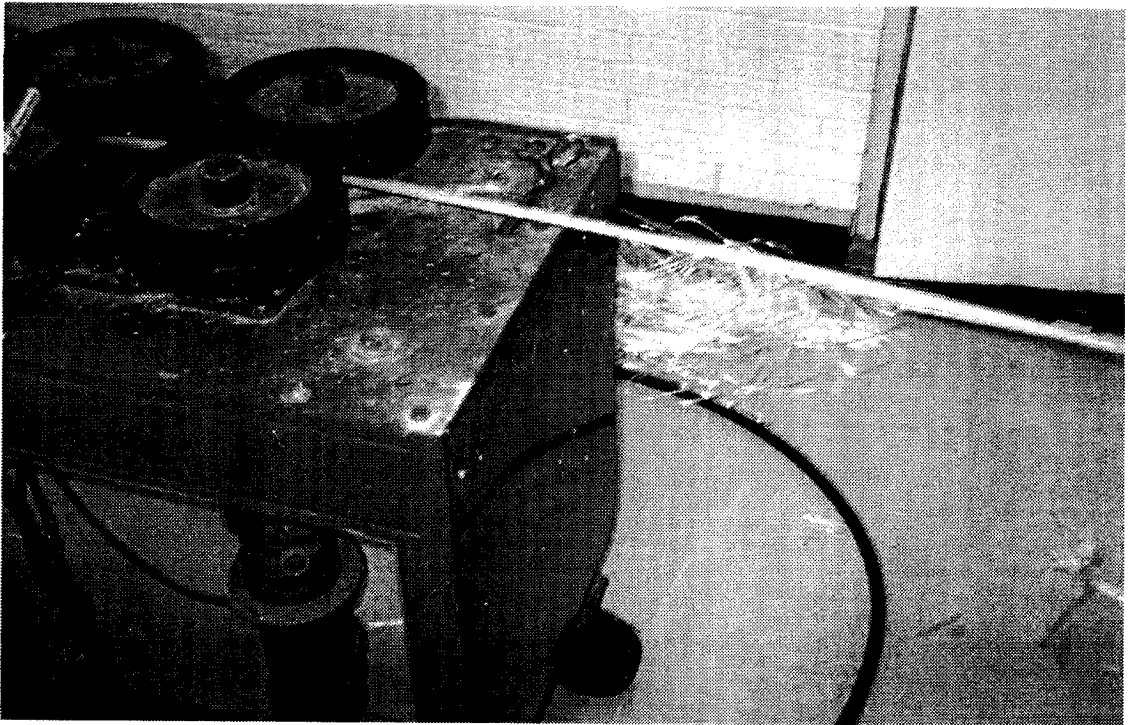
**Figure 3-16:** Pultruded glass rod exiting the wheels

## 3.3 Fiber Optic Connector Attachment

The next few chapters deal with different issues related to pultruded GFRP and CFRP smart tendons with embedded fiber optic sensors. The main objective is to incorporate these tendons into civil structures wherein they will replace steel as the principal concrete reinforcement. As well, the integrated fiber optic sensors will provide designers and maintenance engineers with the desired feedback on the strain state of the structure.
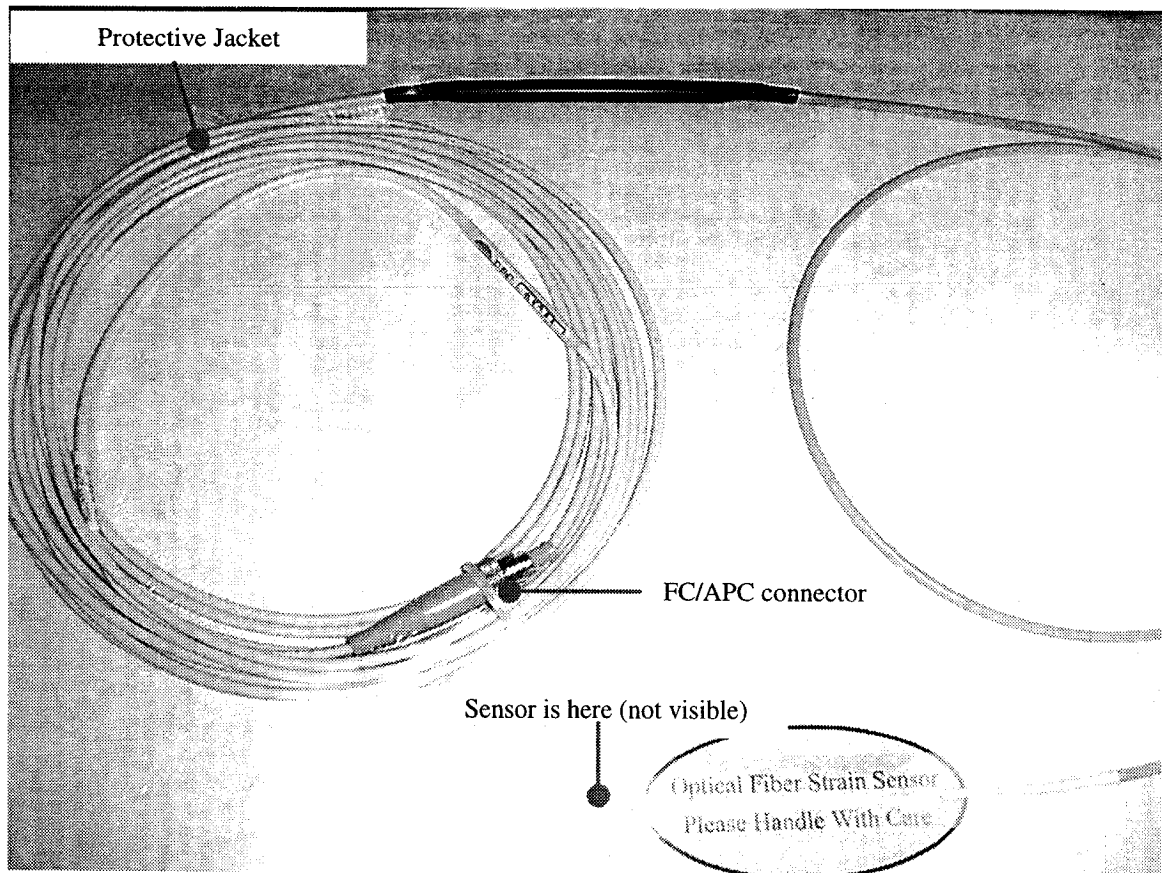


**Figure 3-17:** Bragg Grating sensor prepackaged assembly

Two types of fiber-optic sensors were used; Bragg Grating sensors and Fabry Perot sensors. The Fabry Perot sensors used in these experiments were rated for ± 3000, ± 5000, or 0-10000 microstrain (µε), while their Bragg Grating counterparts were rated for

± 5000 με. The sensors were acquired as prepackaged assemblies, with the sensing element being located at the front end of an optical fiber of approximately 2.0-3.0 meters total length. The optical fiber was coated with a thin layer of polyimide to protect it against the high temperatures encountered in the pultrusion die. This polyimide coating is the contact surface between the optical fiber and the host GFRP or CFRP material. It is thus imperative that the polyimide material be chemically compatible with the vinylester resin so that a good bond between sensor and host is achieved. Bragg Grating sensors cost about $200 each and Fabry Perot sensors about $220 each. A FIZ10 demodulation unit (purchased for about $4000) was used to record strains from Fabry Perot sensors and a BIS card (purchased for about $6000) was used to record strains from the Bragg Grating sensors.
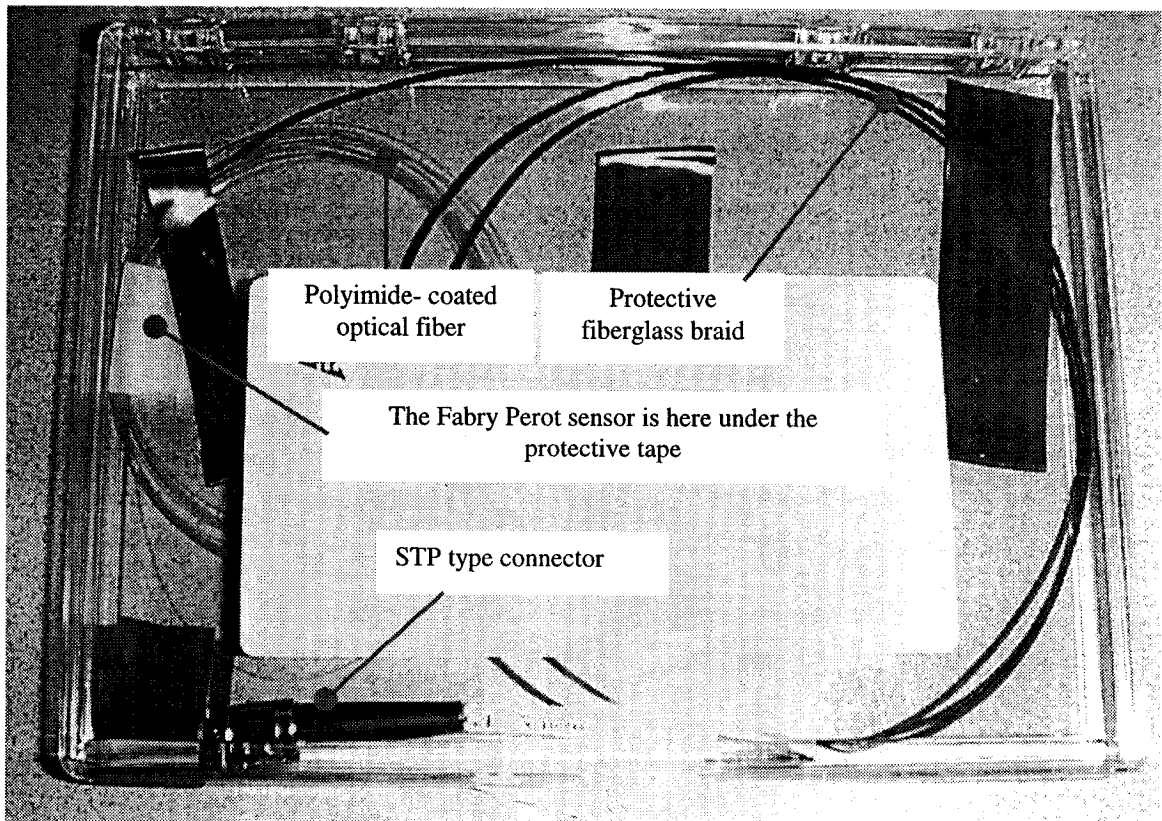


**Figure 3-18:** Fabry Perot sensor prepackaged assembly

To connect the optical fiber lead to the appropriate demodulator, however, required a different type of connector for each of the two sensors. In particular, a Face Contact/Angled Physical Connector (FC/APC) was used for the Bragg Grating sensors and an ST type connector was used for the Fabry Perot sensors. This section will describe briefly the procedure for installing the FC/APC connector. It is essentially a three-stage procedure beginning with the removal of the polyimide coating over the small portion of the fiber on which the connector will be installed, proceeding with the installation and assembly of the connector proper, and ending with the polishing of the fiber end. The procedure for an ST connector only differs in the type of polisher used. In particular, polishing the FC/APC connector requires an angled polisher, whereas the polishing of the ST connector requires a flat polisher.



An FC/APC Connector used with Bragg Grating sensors

Dust cap    Ferrule    Strain-relief jacket

Housing
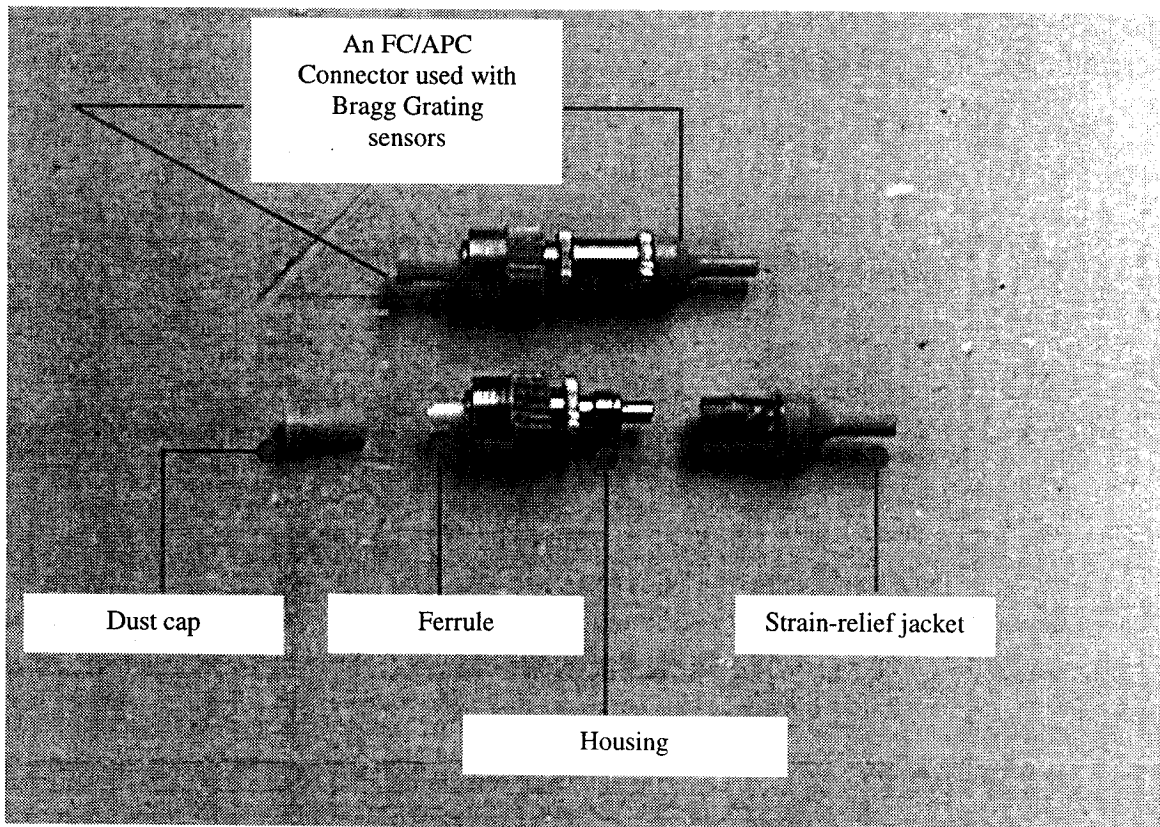
**Figure 3-19:** Photograph of an FC/APC connector with the various components shown separately

An FP/APC connector is depicted in Figure 3-19, wherein the individual components are also shown. The dust cap covers and protects the ferrule when the connector is not affixed to the demodulating unit. The ferrule is the white ceramic tip and serves to align the optical fiber. It has a small hole bored along its length, with a diameter only slightly larger than that of the fiber. The spacing between the ferrule and the optical fiber is necessary for the epoxy to flow freely around the fiber and permanently bond it to the ferrule. The housing is the metallic part that holds the ferrule on one end, and the strain-relief jacket on the other end. As its name suggests, the strain relief jacket protects the optical fiber against accidental cleavage.
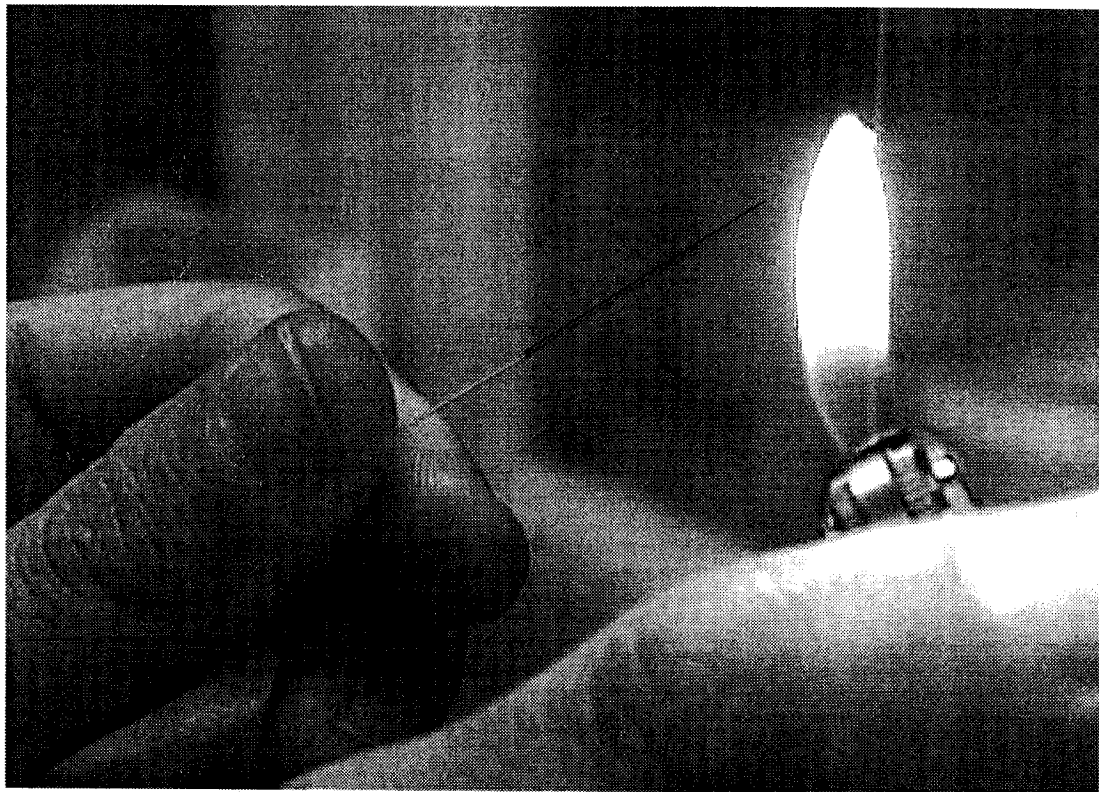


**Figure 3-20:** Removal of polyimide coating by rapid heating

The first step in the connector-installation process is the removal of the polyimide coating from a small portion of the optical fiber. There are essentially two methods for achieving this [Lane et al., 1996]. The first method simply involves passing the optical fiber

through an open flame in order to burn off the polyimide as shown in Figure 3-20. The carbonized polyimide material then is removed easily by acetone-wetted tissue paper [Lane et al., 1996]. This method is very quick and convenient, but comes with the disadvantage that it renders the optical fiber very brittle and consequently susceptible to breakage. The other method involves dipping the optical fiber in hot concentrated sulphuric acid (heated to around 130°C) for a few minutes until the coating is dissolved, see Figure 3-21 [Lane et al., 1996]. This method is time-consuming, requires a fume hood and is hazardous. Thus, it is rarely used.
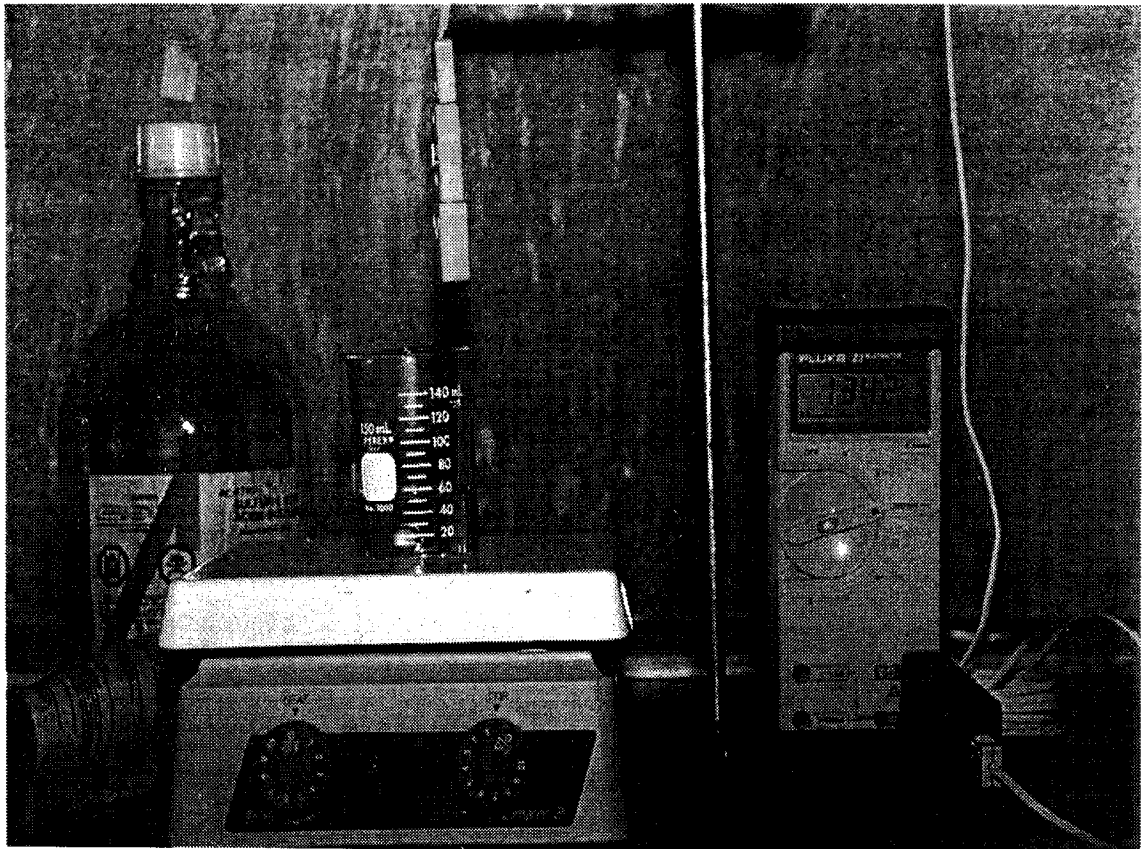


**Figure 3-21:** Removal of polyimide coating from optical fiber by dipping in hot concentrated sulphuric acid [Lane et al., 1996]

The next step in the procedure is to make a suitable epoxy mixture by mixing a resin with a suitable hardener. Using a hypodermic needle, two or three drops of the mixed epoxy are injected into the ferrule of the connector. The uncoated optical fiber then is gently

inserted into the ferrule from the opposite end of the housing (see Figure 3-19), and finally the strain-relief jacket is screwed back onto the housing. The whole assembly then is heated at about 150°C for a few minutes (Figure 3-22) to ensure that the resin cures and bonds the fiber to the ferrule. At the Smart Processing and Instrumentation Lab, Dalhousie University, we use an epoxy which changes to red ( from colorless) on curing, thus signaling the end of the process.
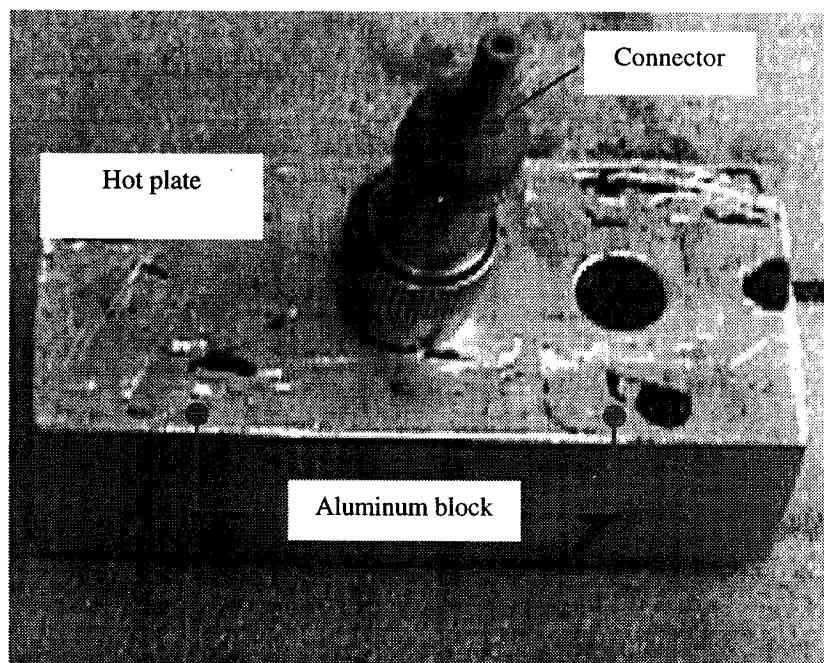


**Figure 3-22:** The fiber connector is mounted in a heated aluminum block to cure the resin which bonds the optical fiber to the ferrule

The last step in the FC/APC connector installation involves a four-stage wet polishing procedure utilizing 30-$\mu$m, 5-$\mu$m, 1-$\mu$m, and sub-micron lapping films [Lane et al., 1996]. An Ultra Tek model 8801 fiber polisher is used as shown in Figure 3-23. As mentioned above, the procedure for installing an ST type connector (pertinent to Fabry Perot sensors) is identical to the one described above. The only difference is that, since the ST connector is flat (and not angled), the Ultra Tek polisher cannot be used. Instead, a simple manual flat-end polisher must be used, as shown in Figure 3-24.
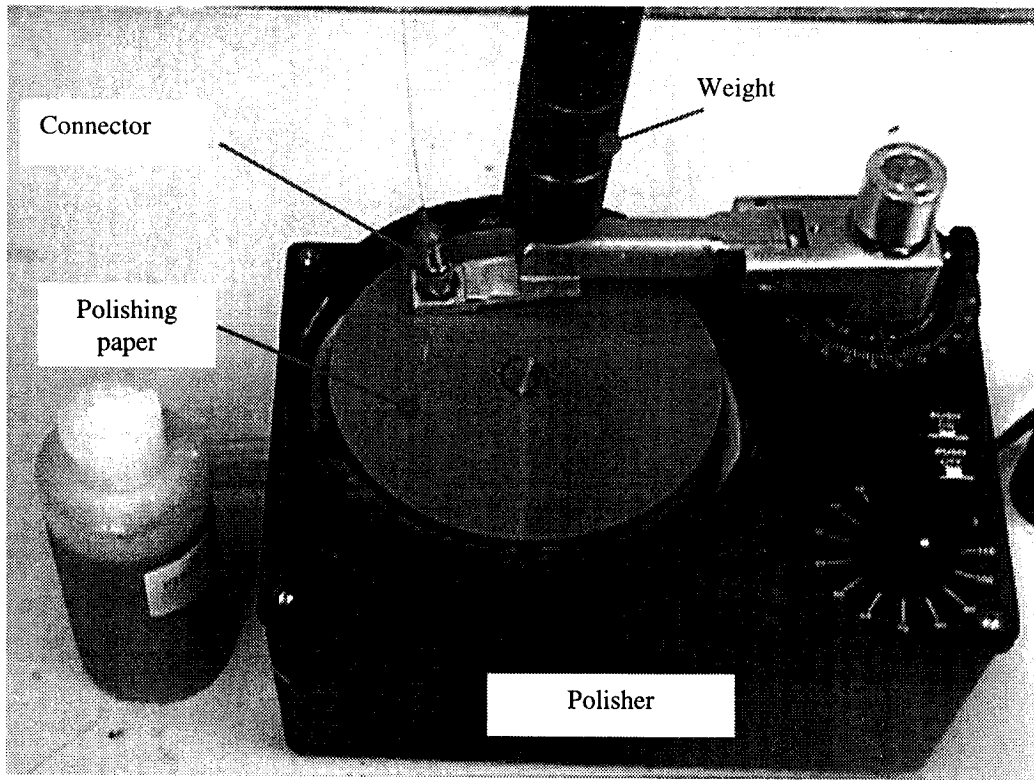
**Figure 3-23:** The Ultra Tek Model 8801 fiber optic polisher and some accessories
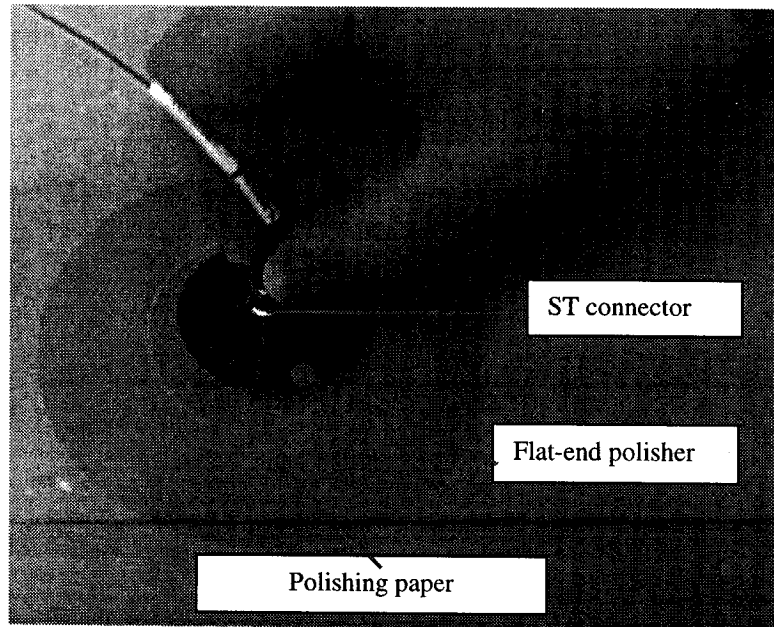


**Figure 3-24:** The flat-end hand-held fiber optic polisher for ST connectors

## 3.4 Fabry Perot Sensor Prereinforcement

Bragg Grating sensors were embedded in both GFRP and CFRP tendons during pultrusion without any problems. With the Fabry Perot sensors, however, the situation was slightly more complicated. The first attempts to embed a Fabry Perot sensor in a carbon tendon led to the failure of all sensors, see Georgiades [1998] for more details. What was unique about these failures, however, was the fact they occurred some time after the consolidated rod exited the die and the pultrusion wheels and had cooled down. In other words, the Fabry Perot sensor survived the high temperature and pressure conditions inside the pultrusion die, as well as the passage through the pulling wheels, but failed shortly thereafter.
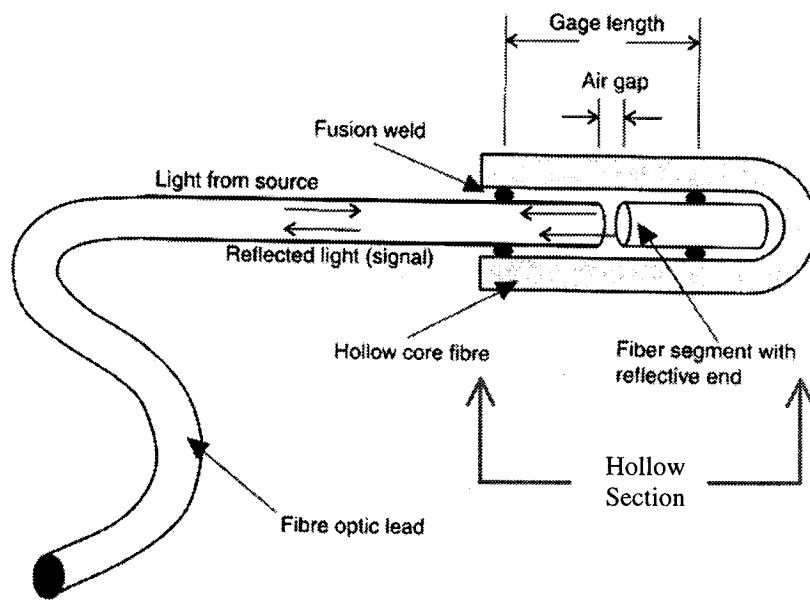


**Figure 3-25:** Fabry Perot sensor [Kalamkarov et al., 2000]

This post-fabrication failure was attributed to radial shrinkage of the composite rod when it cooled down to room temperature after exiting the die, causing a large pressure to be exerted on the sensor. The origin of this radial pressure is the large difference between the radial coefficients of thermal expansion of the rod (estimated to be about 29 x $10^{-6}$

m/m °C) and the sensor (about 0.5 x $10^{-6}$ m/m °C). This effect is similar to the forces developed when shrink fitting metal jackets on thick-walled pressure vessels. By examining the schematic of the Fabry Perot sensor from Figure 2-13 reproduced above as Figure 3-25 for convenience, one can see that this pressure could be significant enough to cause the hollow section of the sensor to collapse.

To overcome this problem, it was found that Fabry Perot sensors had to be prereinforced. The procedure for prereinforcement will be outlined in this section. Figure 3-26 shows all the materials involved in the process. In particular, one will need, in addition to the sensor, a straight metallic rod, some high-temperature tape, a thin piece of teflon tube (with diameter equal to about 1 mm), a glass fiber or carbon fiber roving, and a small amount of resin and suitable hardener. The resin used during the installation of the fiber optic connectors, as described in the previous section, is a suitable candidate.
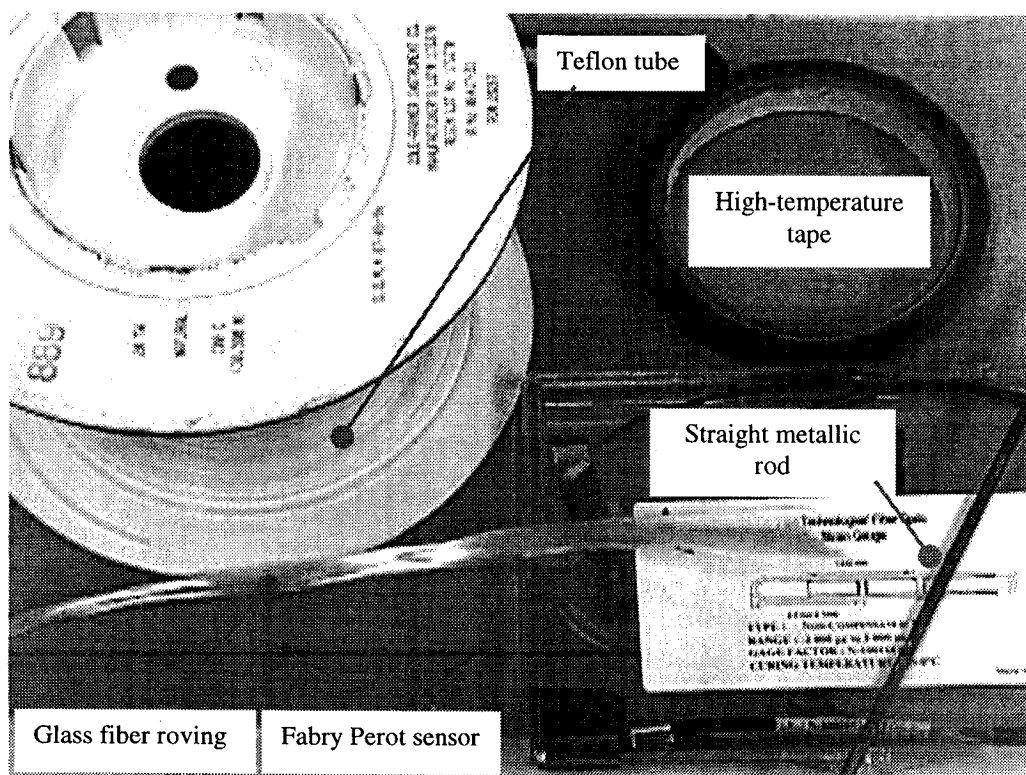


**Figure 3-26:** Materials needed for prereinforcement of Fabry Perot sensors
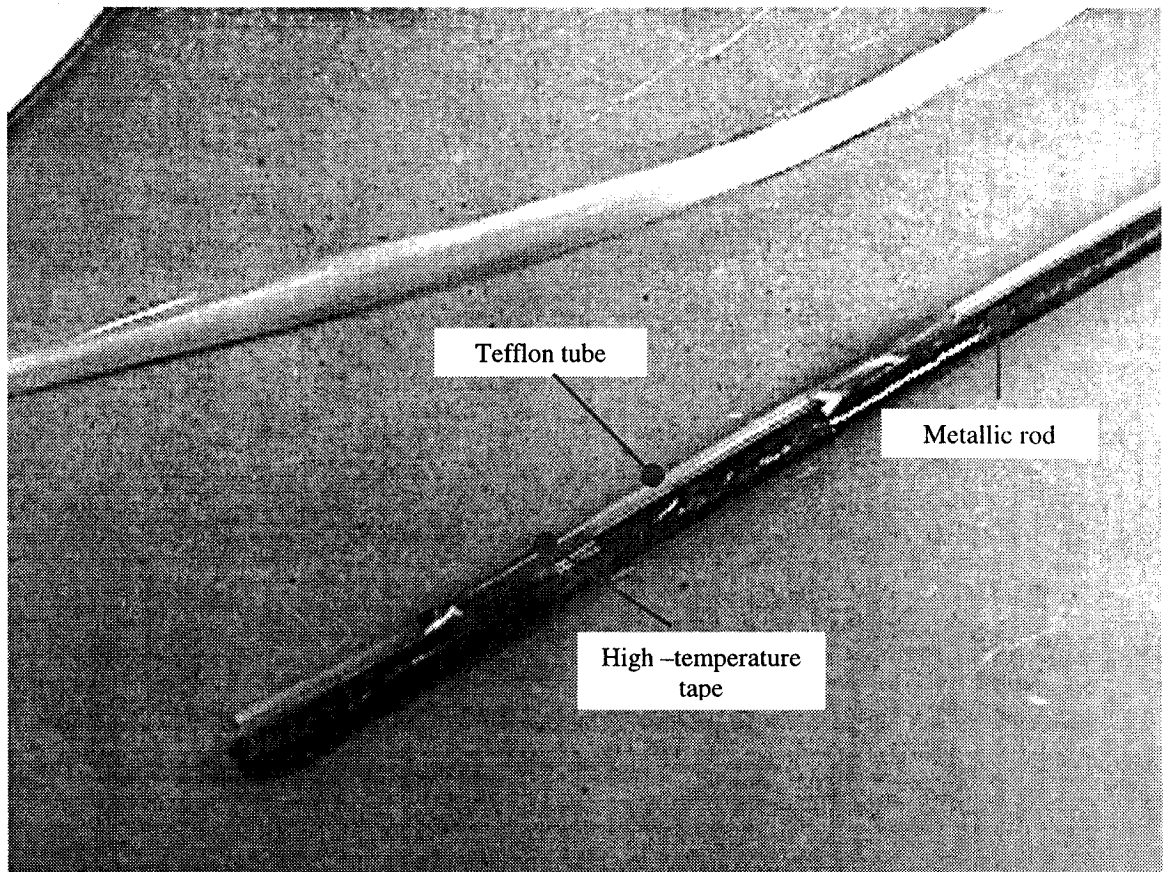
**Figure 3-27:** The teflon tube is affixed to the metallic rod

The first step in the process is to cut a small piece of tefflon tube and attach it firmly to the metallic rod as shown in Figure 3-27. The importance of ensuring that the tube is straight when attached to the rod cannot be overemphasized. This tube eventually will be the enclosure for the Fabry Perot sensor, and unless it is free from regions of any significant curvature, this would lead to the fracture of the sensor. Subsequently, a few strands from the glass-fiber roving are removed and passed through the teflon tube as shown in Figure 3-28. The amount of glass reinforcement that can pass through the tubing essentially depends upon the skill of the person. However, too few strands will mean that the sensor will not be sufficiently reinforced. The glass-fiber strands are then pulled from the opposite end of the tube until the length hanging outside the tube equals the length of the tube.
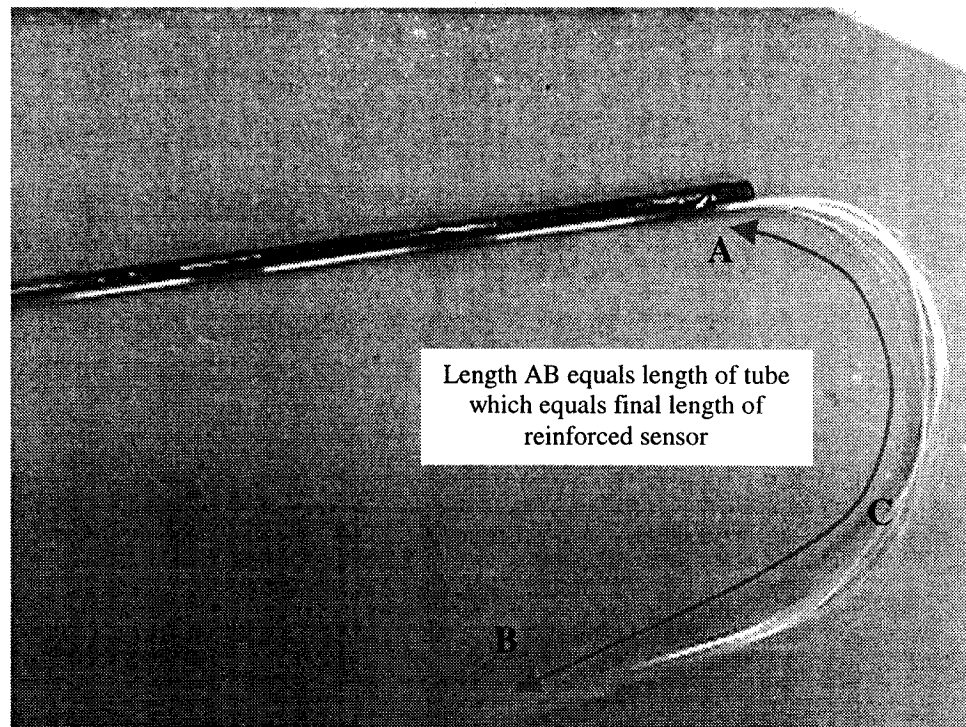
**Figure 3-28:** Passing of the fiber strands through the tube

Length AB equals length of tube which equals final length of reinforced sensor
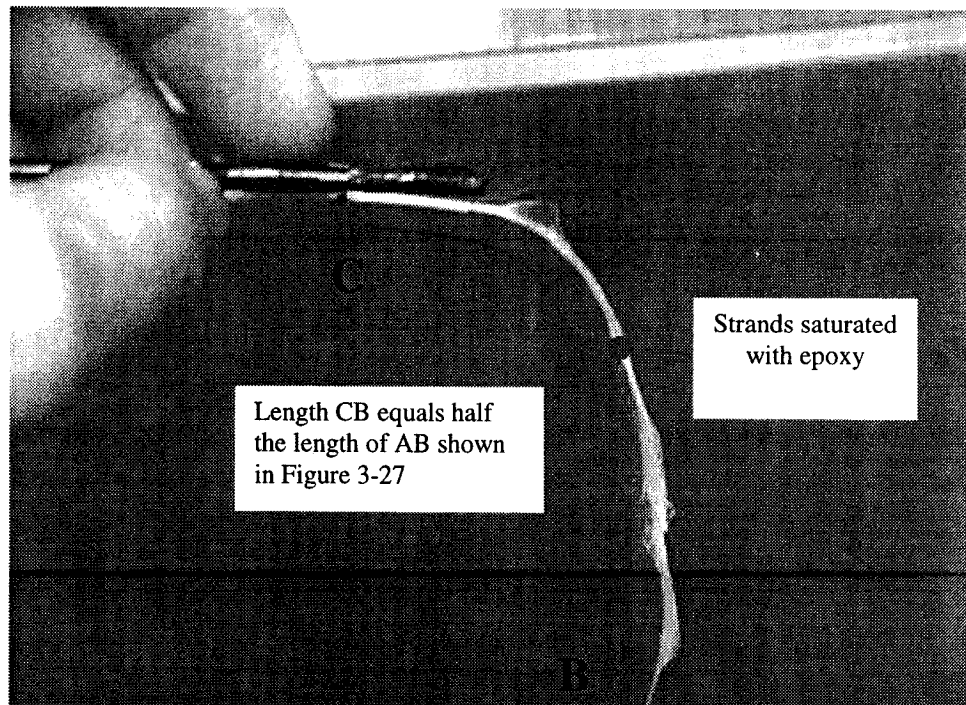


**Figure 3-29:** Saturating the fibers with epoxy resin

Length CB equals half the length of AB shown in Figure 3-27

Strands saturated with epoxy

The next step in the procedure is to mix the resin and a suitable hardener to make an epoxy mixture, and to use this to saturate the glass fiber strands. Then the soaked fibers are pulled halfway into the tube from the opposite end (see Figure 3-29). It is now time to reinforce the sensor. The Fabry Perot sensor is threaded carefully just inside the tube, in the middle of the hanging fiber bundle as shown in Figure 3-30. The fiber bundle is then pulled all the way into the tube (from the opposite end) thus dragging the sensor with it as well. At this point, the sensor is located halfway along the teflon tube, surrounded by resin-soaked glass fibers.
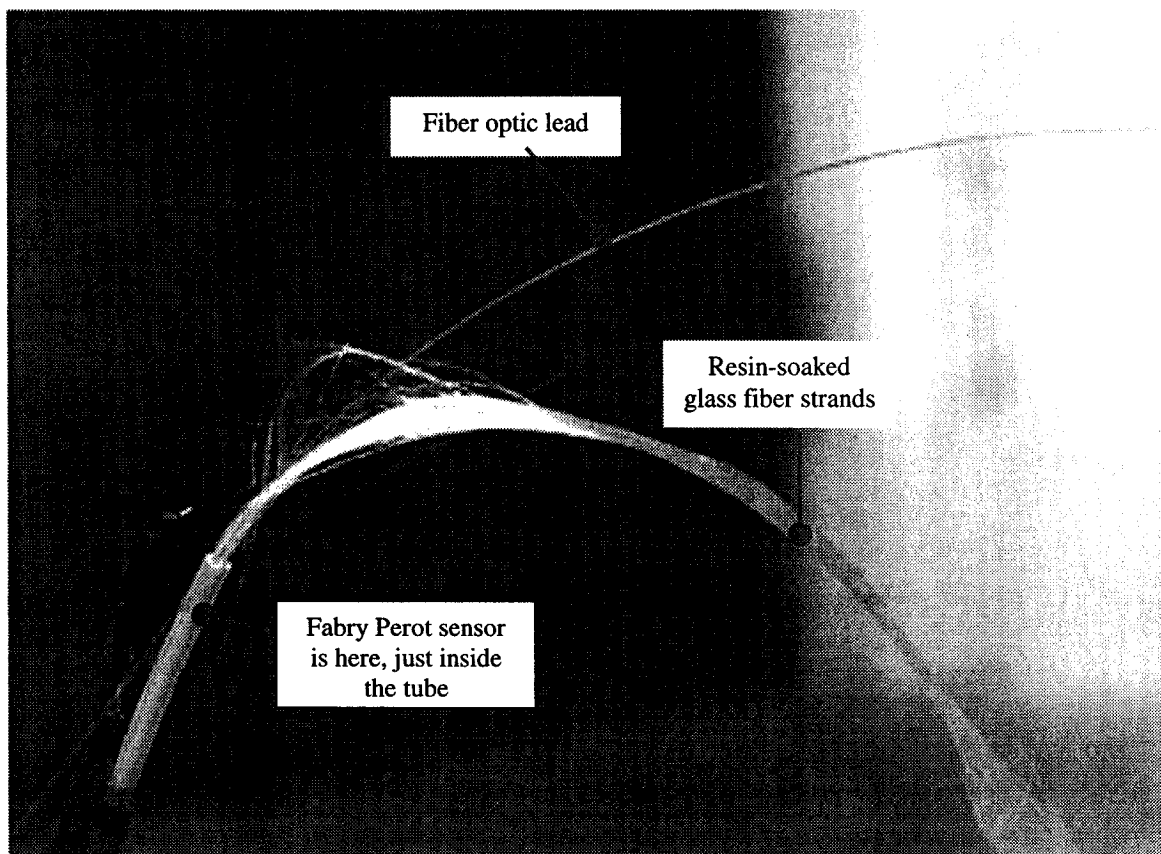


**Figure 3-30:** The Fabry Perot sensor is gently threaded just inside the tube

The final step in the procedure involves heating the tube on a hot plate at 150°C for about 5 minutes until the resin is cured (Figure 3-31). The consolidated rod is then carefully removed from the tube with the aid of a blade.
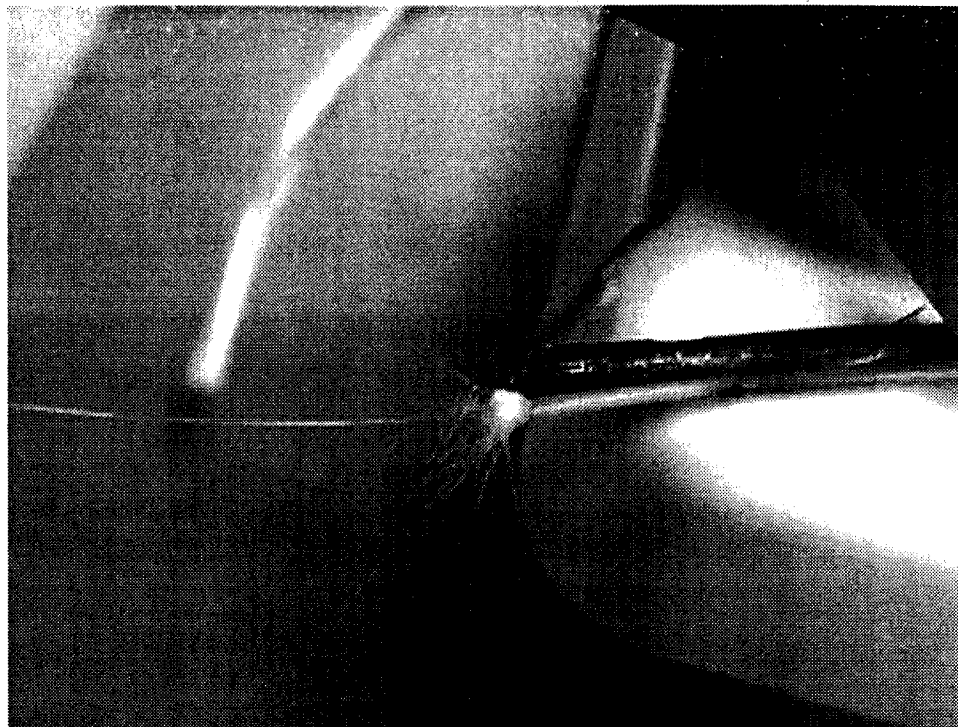
**Figure 3-31:** The teflon tube is heated on a hot plate to cure the resin
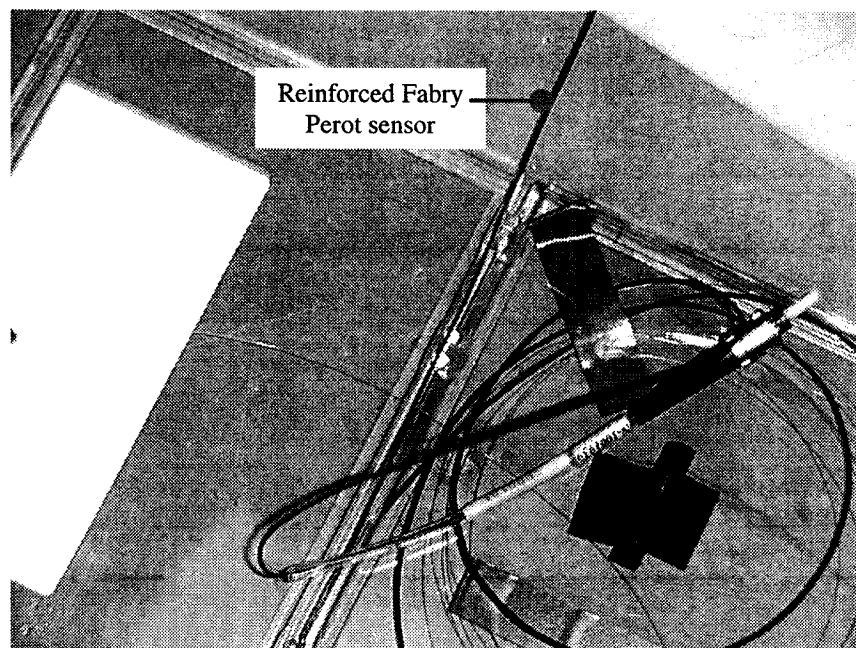


**Figure 3-32:** The reinforced Fabry Perot sensor

Fiberglass composite microtube with the embedded Fabry Perot sensor
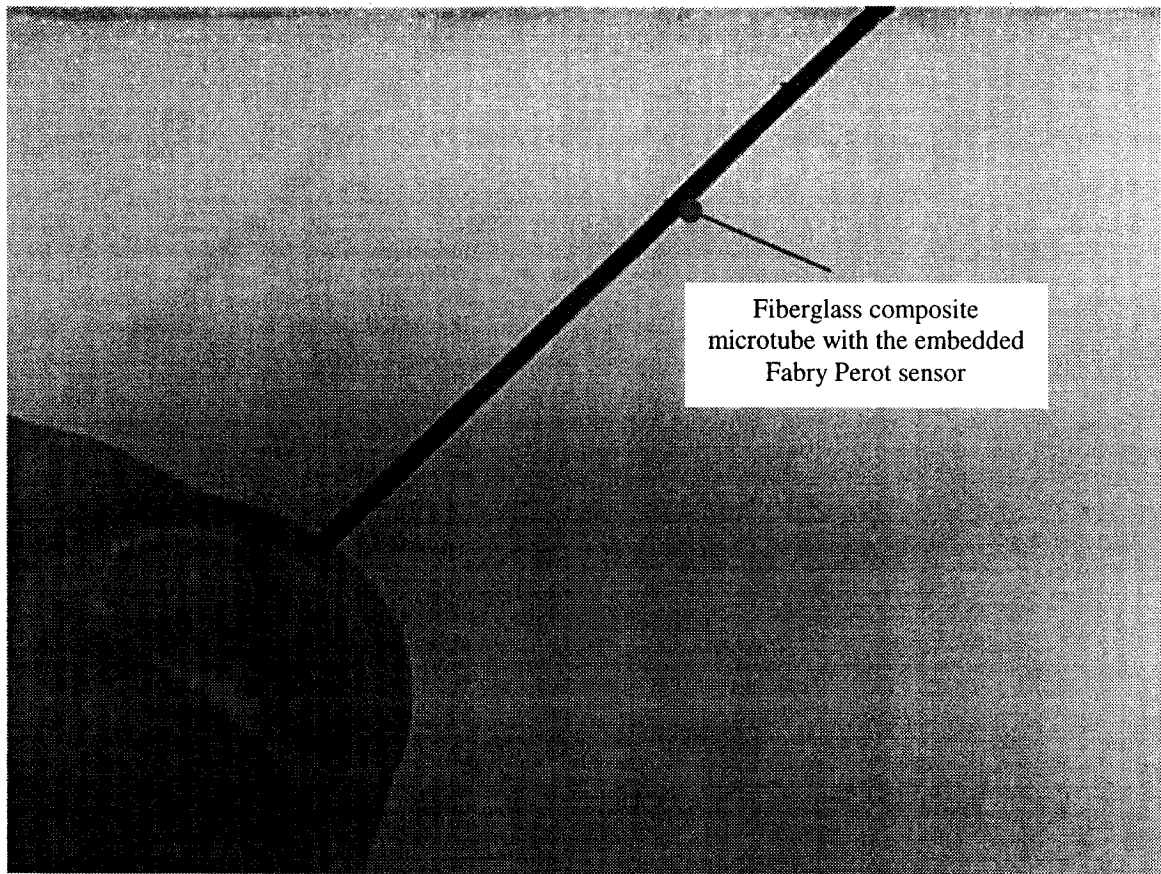
**Figure 3-33:** The fiberglass microtube encompassing and protecting the Fabry Perot sensor.

The final reinforced sensor is shown in Figures 3-32 and 3-33. Thus, the overall procedure amounts to encasing the Fabry Perot sensor in a glass-fiber composite microtube. It was found that this prereinforced Fabry Perot sensor could be embedded much more easily into a GFRP or CFRP tendon than its unreinforced counterpart, and more importantly it did not fail after cooling down. In fact, all the prereinforced Fabry Perot sensors subsequently pultruded survived the pultrusion process and remained operational. Before closing this section, it should be mentioned that the reinforcement procedure outlined produced a fiberglass microtube with the understanding that it would be later embedded in a GFRP. If instead, a Fabry Perot sensor is to be embedded in a CFRP, then the composite microtube will be made from carbon fiber strands using an otherwise unchanged procedure.

## 3.5 Application of Grips to the Tendons for Mechanical Testing

One of the objectives of the work described in this thesis is to perform a reliability assessment of the embedded Fabry Perot and Bragg Grating sensors under different environmental and load conditions. For example, one wants to know how the sensors will perform in high- or low-temperature environments, andr how they will react to fatigue loads. As well, it is important to collect data that reflect the repeatability of the sensor readings and to compare their values with corresponding values from conventional strain-measuring devices such as extensometers and foil gauges.
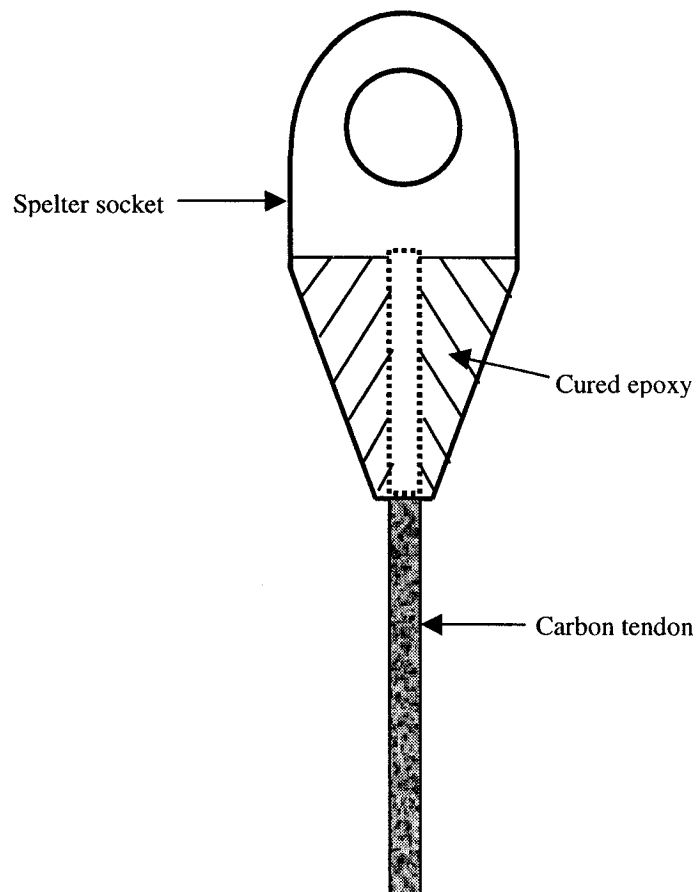


**Figure 3-34:** Spelter socket used to grip the smart tendons in a load frame
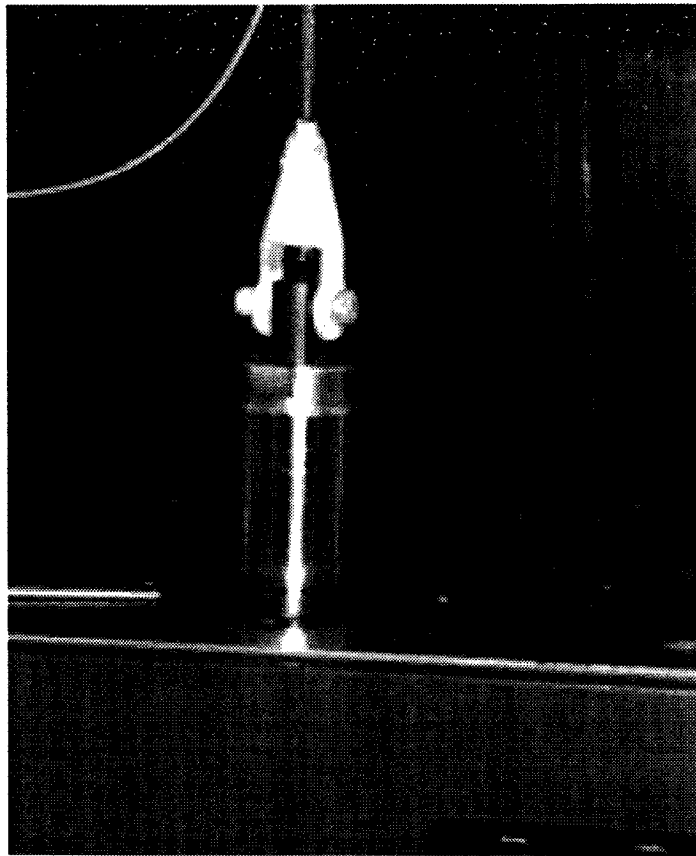
**Figure 3-35:** Spelter socket attaching the lower end of a pultruded carbon tendon to an Instron machine

To meet these objectives, the pultruded smart tendons would have to be tested in a suitable load frame such as an Instron machine. However, in order to perform this testing it was necessary to grip directly onto the sample without damaging the fiber optic lead that exited one end of the tendon. Thus, the standard wedge grips supplied with the Instron were found to be unsuitable, and a special type of fixture known as an open spelter socket was used instead. A schematic of the Spelter socket is shown in Figure 3-34, and a photograph of an actual socket attaching a pultruded carbon tendon to an Instron machine is shown in Figure 3-35. There is a central hole running along the length of the spelter socket, and this allows the pultruded tendon to be inserted inside without any difficulty and without compromising the fiber optic lead. The tendon is then held in place by means of a strong adhesive such as a resin and its hardener. If the adhesive

strength of the resin of choice is high enough, then the tendons can be subjected to very large tensile loads without encountering any slipping of the grips. However, the overall procedure (as will be described in subsequent paragraphs) for installing the sockets can be quite time consuming. Other types of grips, such as the "wire fingers" were also considered (Figure 3-36) but these were later rejected because they tend to slip at relatively low tensile loads.
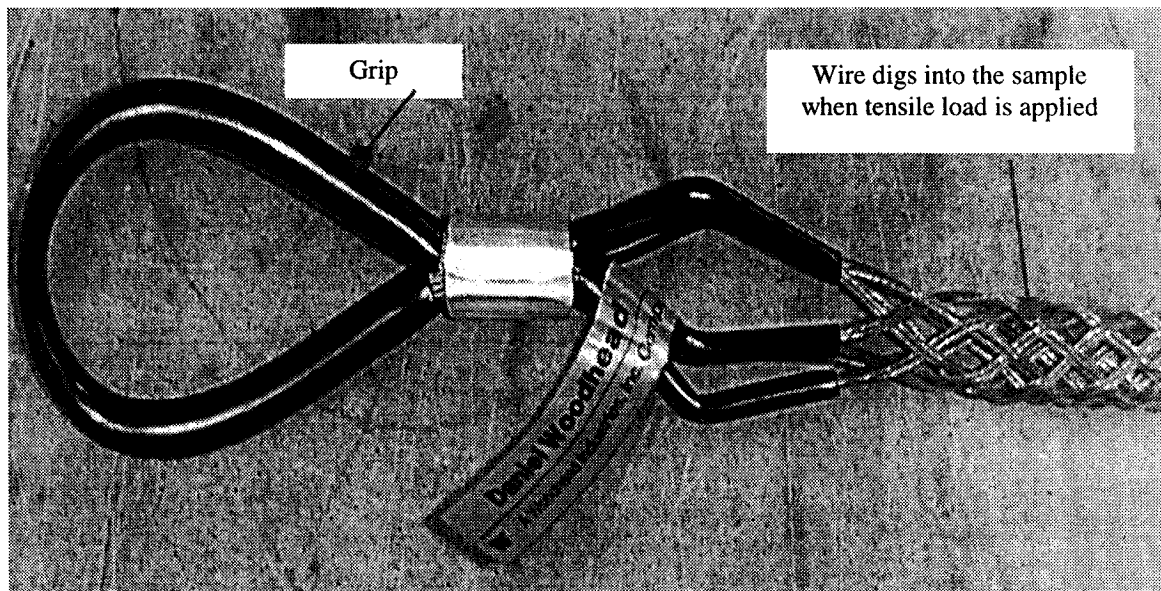


**Figure 3-36:** "Wire fingers" grips

Before explaining how the spelter socket is added to a tendon, the issue of protecting the fiber-optic lead must be addressed. When a pultruded smart tendon exits the pulling wheels of the pultrusion machine, the fiber optic lead protrudes out of its end. If this lead fractures (and it is quite vulnerable), then the embedded sensor is of no use. To avoid this problem, a protective jacket is used, which is slipped around the fiber. This jacket, shown in Figure 3-37, consists of three components: a white inner tube, aramid fiber strands, and an outer rubber jacket. The optical fiber is threaded into the inner tube, and is protected against accidental pulling by the aramid fiber strands. Finally, the outer jacket offers protection against accidental treading on the fiber, and more importantly provides strain relief at the point of exit of the lead from the composite rod.
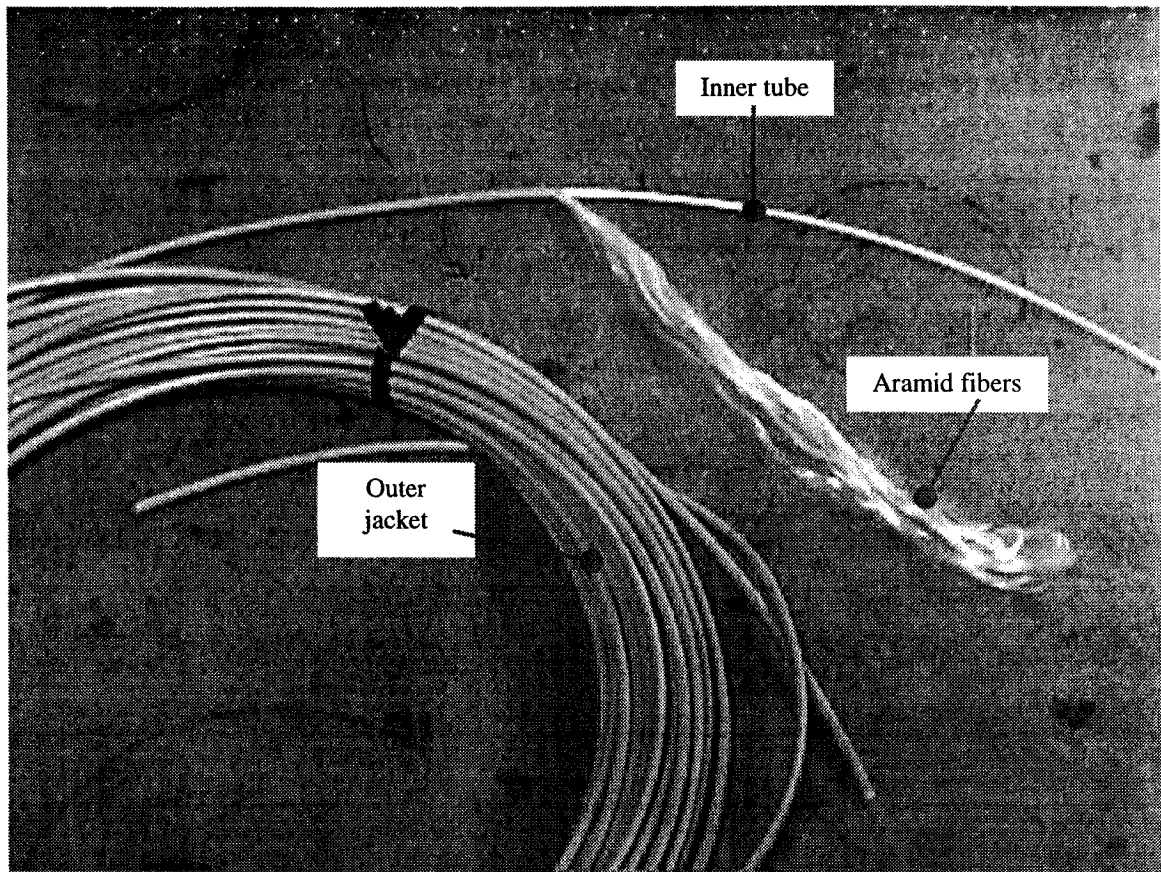
**Figure 3-37:** Jacket used to encase and protect fiber optic lead

The steps involved in protecting the fiber optic lead are the following. First the fiber is gently slipped into the jacket and guided to the other end through the inner tube. The jacket is then pushed as far as possible through the uncured bundle of reinforcing fibers at the back end of the composite tendon. This is shown in Figure 3-38. This bundle is then tied together by a thread, and stiffened by applying a strong resin/hardener combination. A good way to ensure satisfactory resin saturation of all the fibers in this bundle is to inject the resin using a hypodermic needle. This is shown in Figure 3-39.

The last step in the process is the application of the spelter sockets. The sockets are attached one at a time using the same resin/hardener that was mentioned above. Essentially, the socket is held in place and then the mixed resin is poured in from the top

and allowed to cure at room temperature overnight. A piece of plasticene holds the resin within the confines of the socket. Figure 3-40 illustrates these steps.
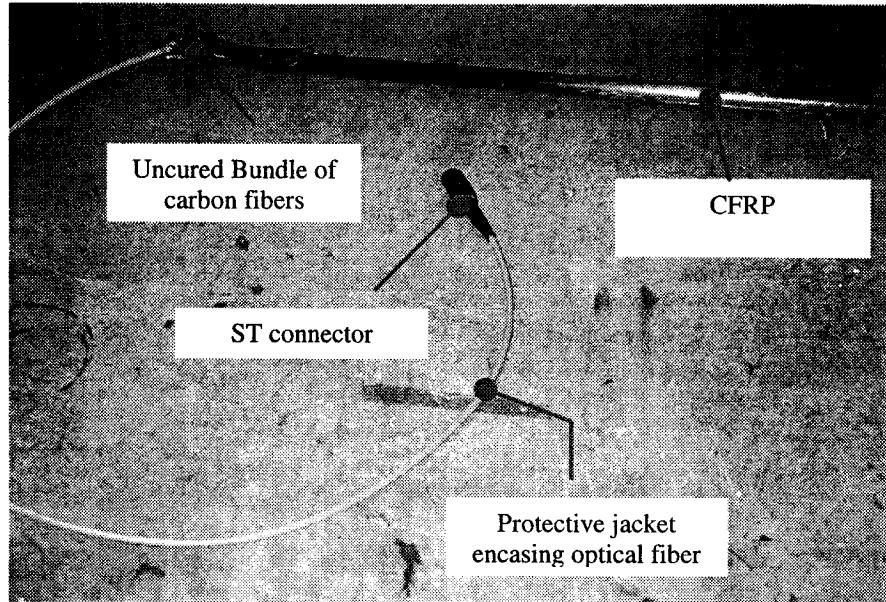


**Figure 3-38:** CFRP smart tendon with a jacket to protect its fiber optic lead
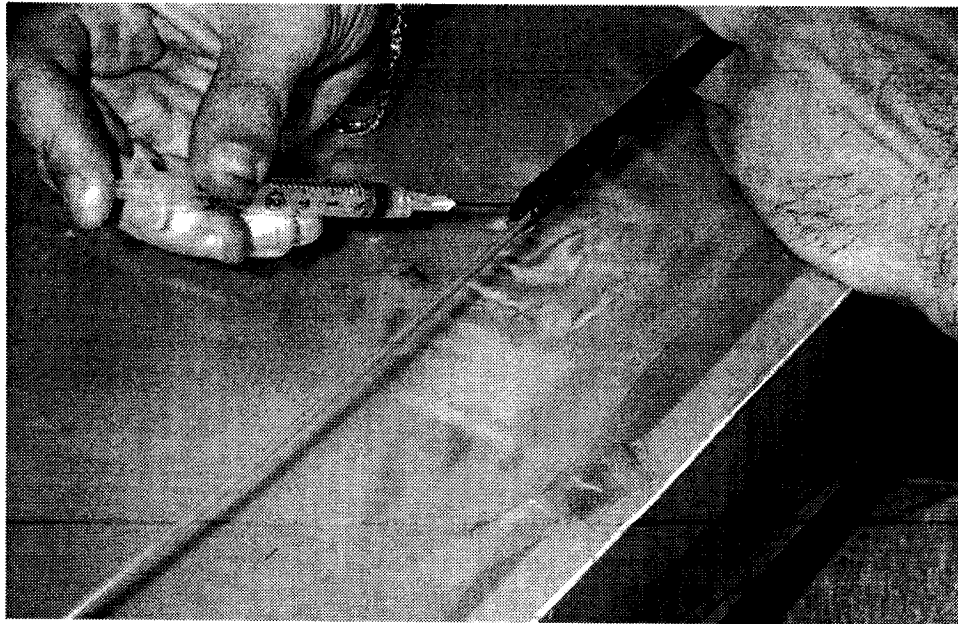


**Figure 3-39:** Injecting resin to cure a carbon fiber bundle at the end of a CFRP tendon and attach a protective jacket for strain relief
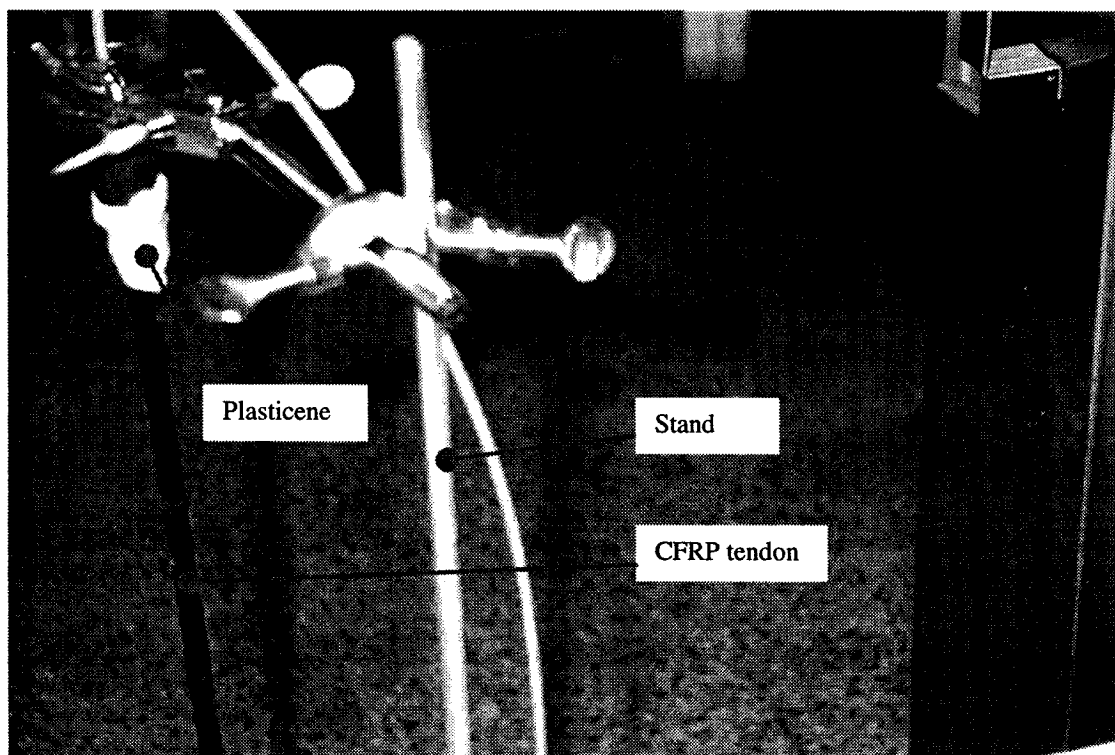
**Figure 3-40:** Attaching a spelter socket to a CFRP tendon

## 3.6 Mechanical Testing of Pultruded Tendons

Following the fabrication of the pultruded composite tendons, a comprehensive reliability study was undertaken. This involved subjecting the tendons to various types of loads in different ambient conditions. Much of the testing was done with the aid of a load frame at the Experimental Mechanics Lab, Dalhousie University. The load frame used was an Instron Model 1321 controlled by an Instron 8500 series controller and fitted with a 45 kN load cell. The overall setup is shown in Figures 3-41 and 3-42. Figure 3-43 shows a close-up of the Instron frame.
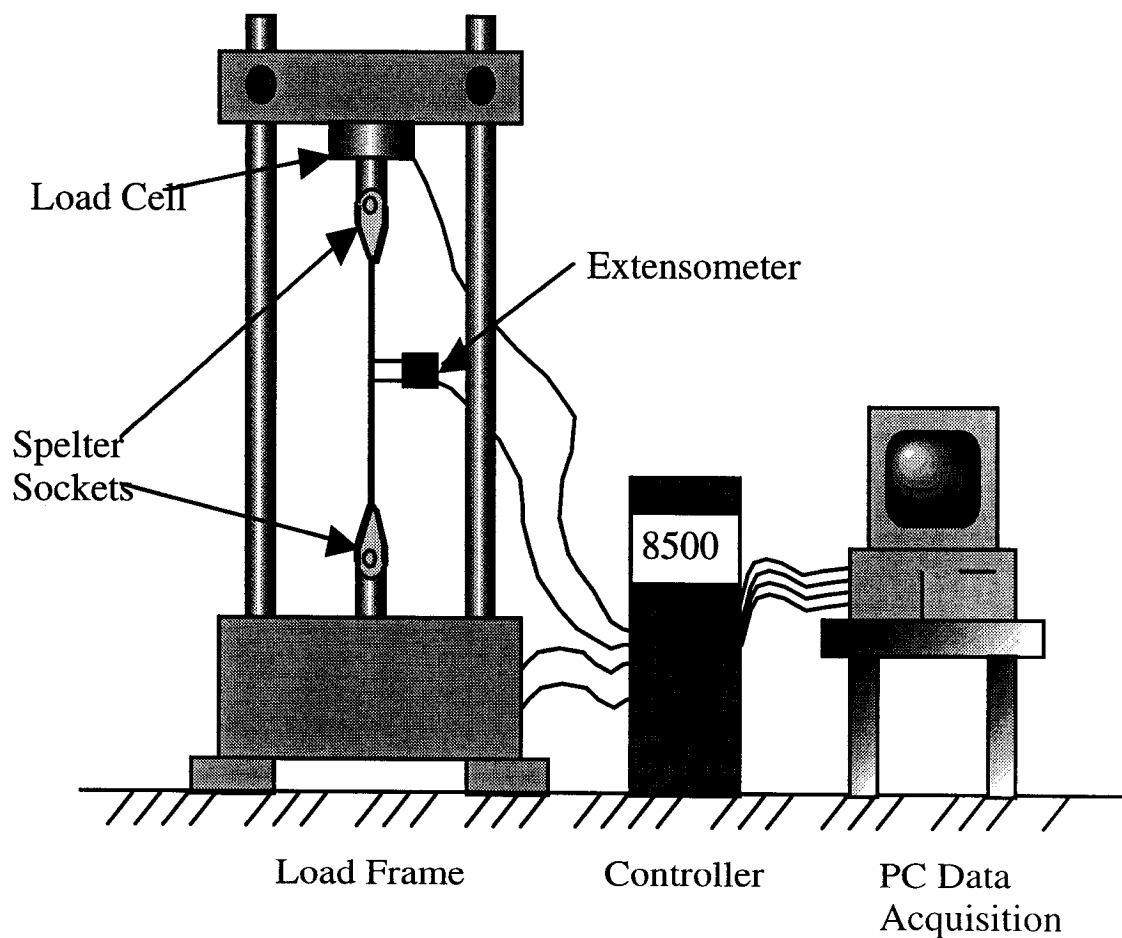


**Figure 3-41:** Instron machine and controller at Experimental Mechanics Lab, Dalhousie University [Kalamkarov et al., 1998]
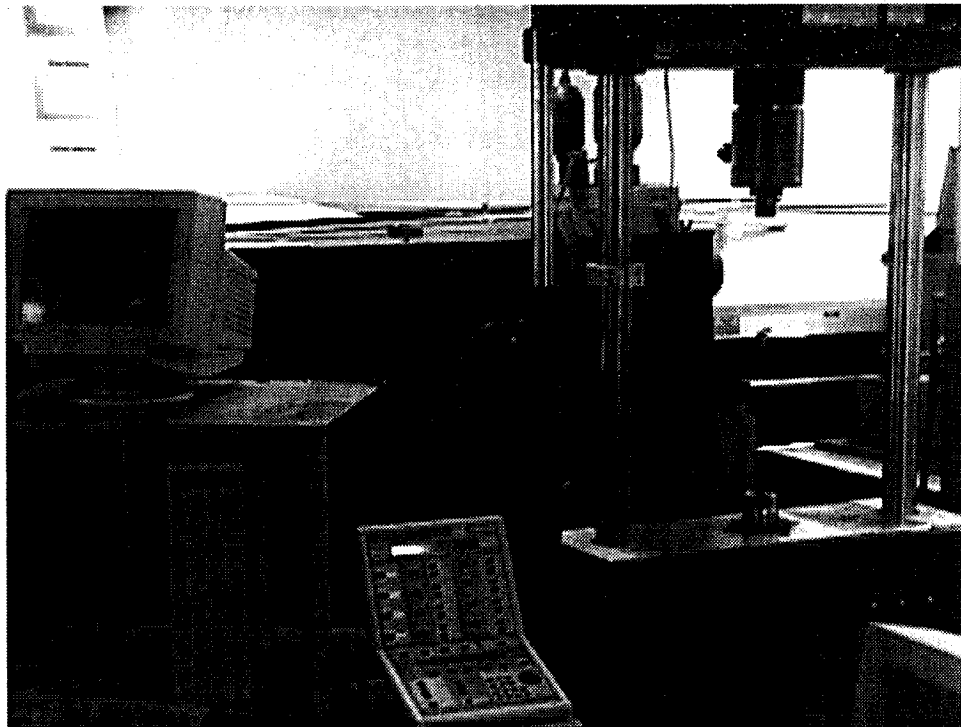
**Figure 3-42:** Overall setup for mechanical testing



**Figure 3-43:** Instron machine used for tension loading of pultruded tendons

To assess the performance of the embedded fiber optic sensors, the pultruded tendons were subjected to two types of loads: sinusoidal and trapezoidal. The following load vs. time graphs (Figures 3-44, 3-45) show the characteristics of the load waveforms.
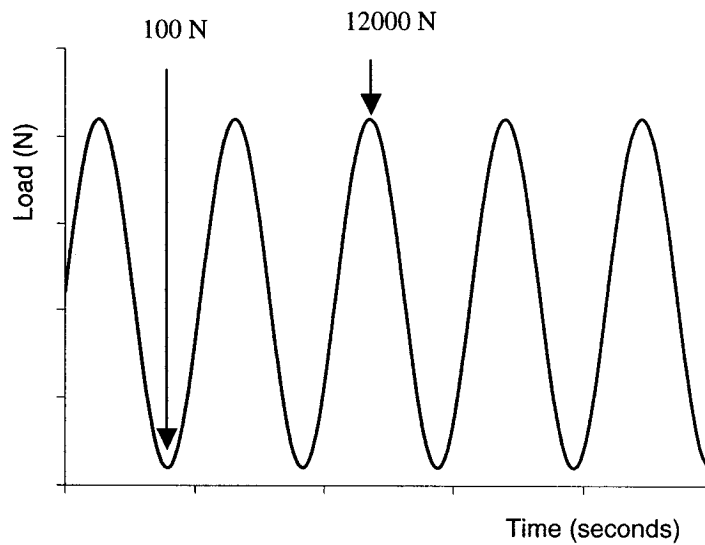


**Figure 3-44:** Sinusoidal tension load applied to tendons
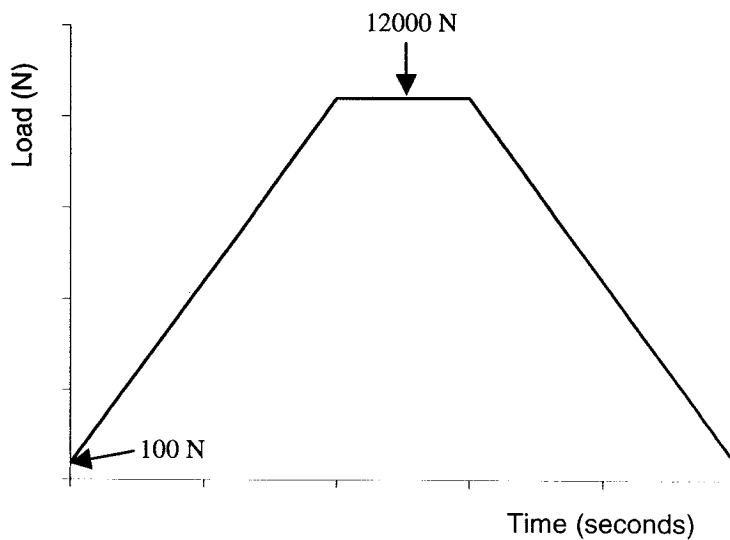


**Figure 3-45:** Trapezoidal tension load applied to tendons

For the trapezoidal waveform, the load was ramped up to its peak value (typically 7-12 kN) from a small preload level of around 100 N. The rate of load application was 90 N/sec. The tendons were held at this load level for 20 seconds and then the load was ramped back down to the starting load at a rate of 90N/sec. For the sinusoidal waveform, the frequency of the applied load was one cycle per minute (0.0167 Hz) for five cycles. Slow load rates were chosen because it was desired to avoid any fatigue effects for these tests. To verify the accuracy of the strain values from the embedded Fabry Perot and Bragg Grating sensors, we also attached an extensometer to the surface of the tendons as shown in Figure 3-46.
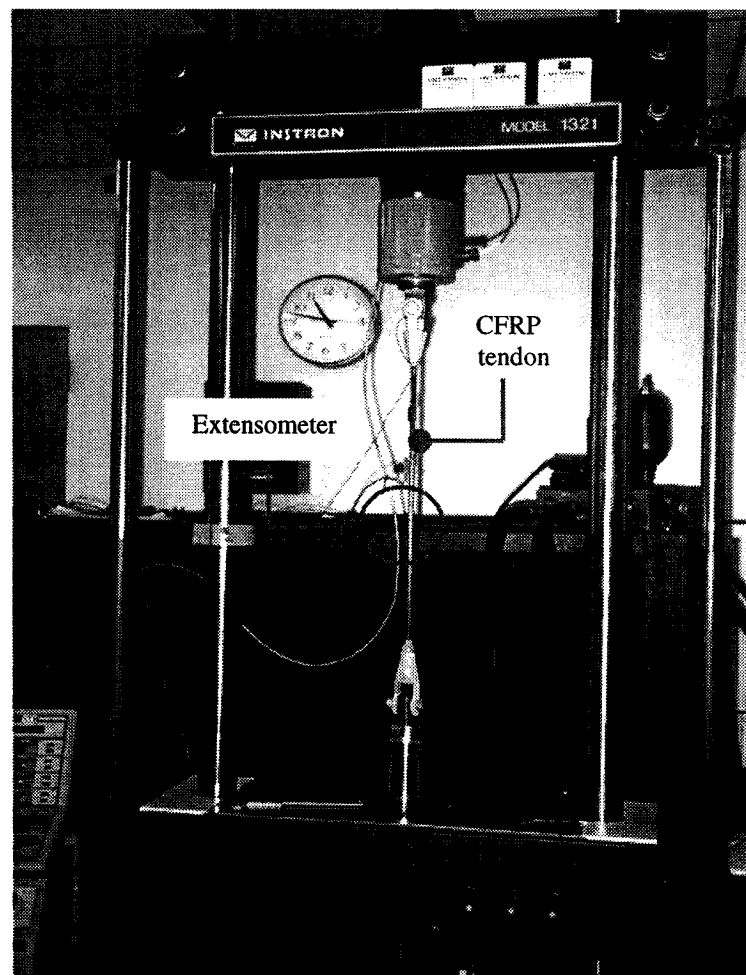


**Figure 3-46:** Strain from a Fabry Perot sensor embedded in a CFRP tendon and an externally affixed extensometer

Thus, during testing, four analogue signals were read into the data acquisition program. They were the three voltage signals from the extensometer, the load cell, and an LVDT (linear variable displacement transformer), and a strain signal from the Bragg Grating or Fabry Perot sensor. FLS 2000 and FIZ 10 demodulation units were used to record strain from the Bragg Grating and Fabry Perot sensor respectively (see Figure 3-47).



**Figure 3-47:** FIZ 10 demodulation unit for Fabry Perot sensors

In addition to tests performed in ordinary laboratory conditions, the reliability assessment of the smart tendons required that tests be done in hot and cold environments. Specialized equipment such as an environmental chamber fitted with a temperature controller had to be used, and consequently these tests were performed at the laboratories of the PSC Analytical company in Dartmouth, Scotia. Figure 3-48 shows the overall setup at PSC Analytical, that includes an MTS model 8540RM load frame (with a capacity of 400 kN), an Instron Series IX controller, and an Instron temperature chamber fitted with its own

controller. A thermocouple monitored the temperature in the chamber. Figure 3-49 shows the temperature chamber and its controller, and Figures 3-50 and 3-51 show close-up views of a glass tendon being tested at $-40^{\circ}C$.
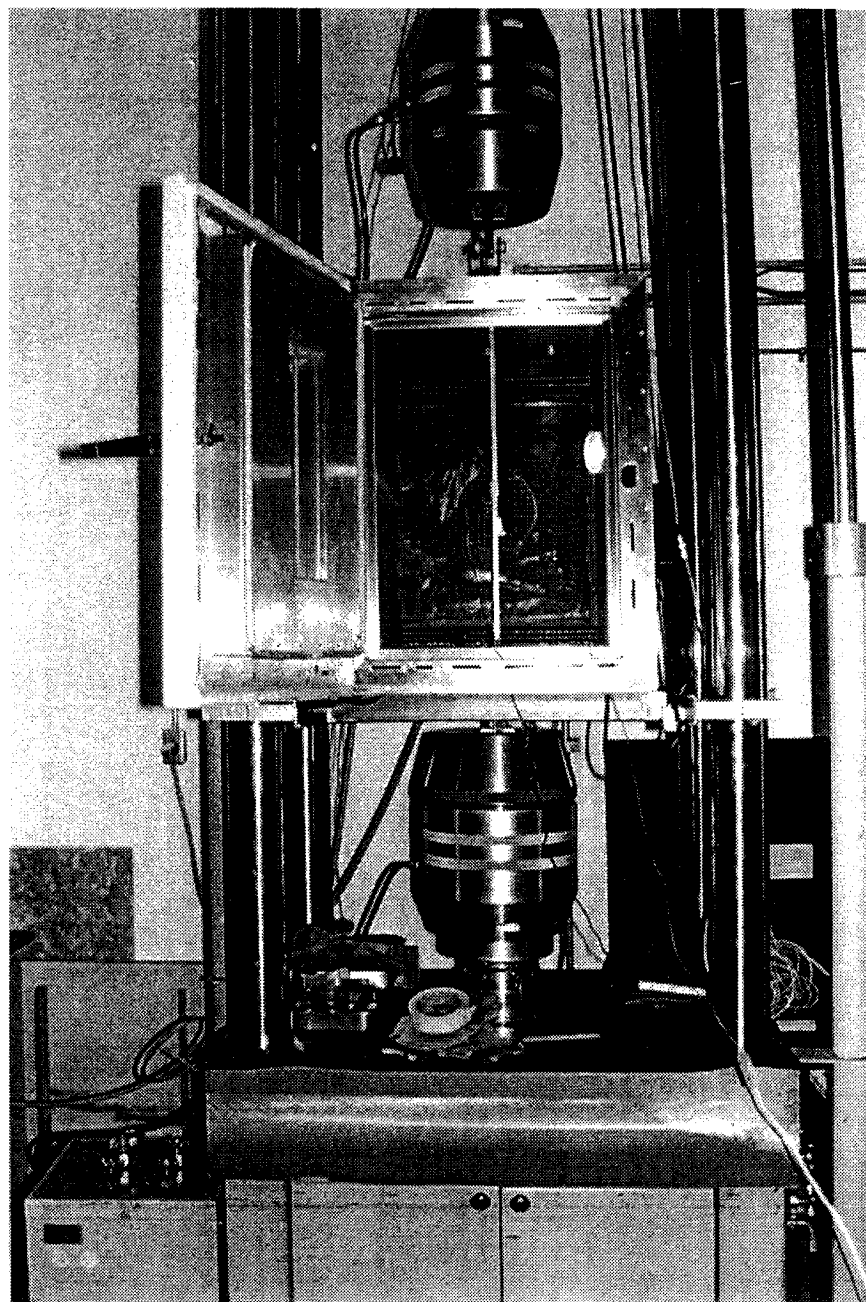


Figure 3-48: Load frame and temperature frame at PSC Analytical

**Figure 3-49:** Temperature frame and controller at PSC Analytical
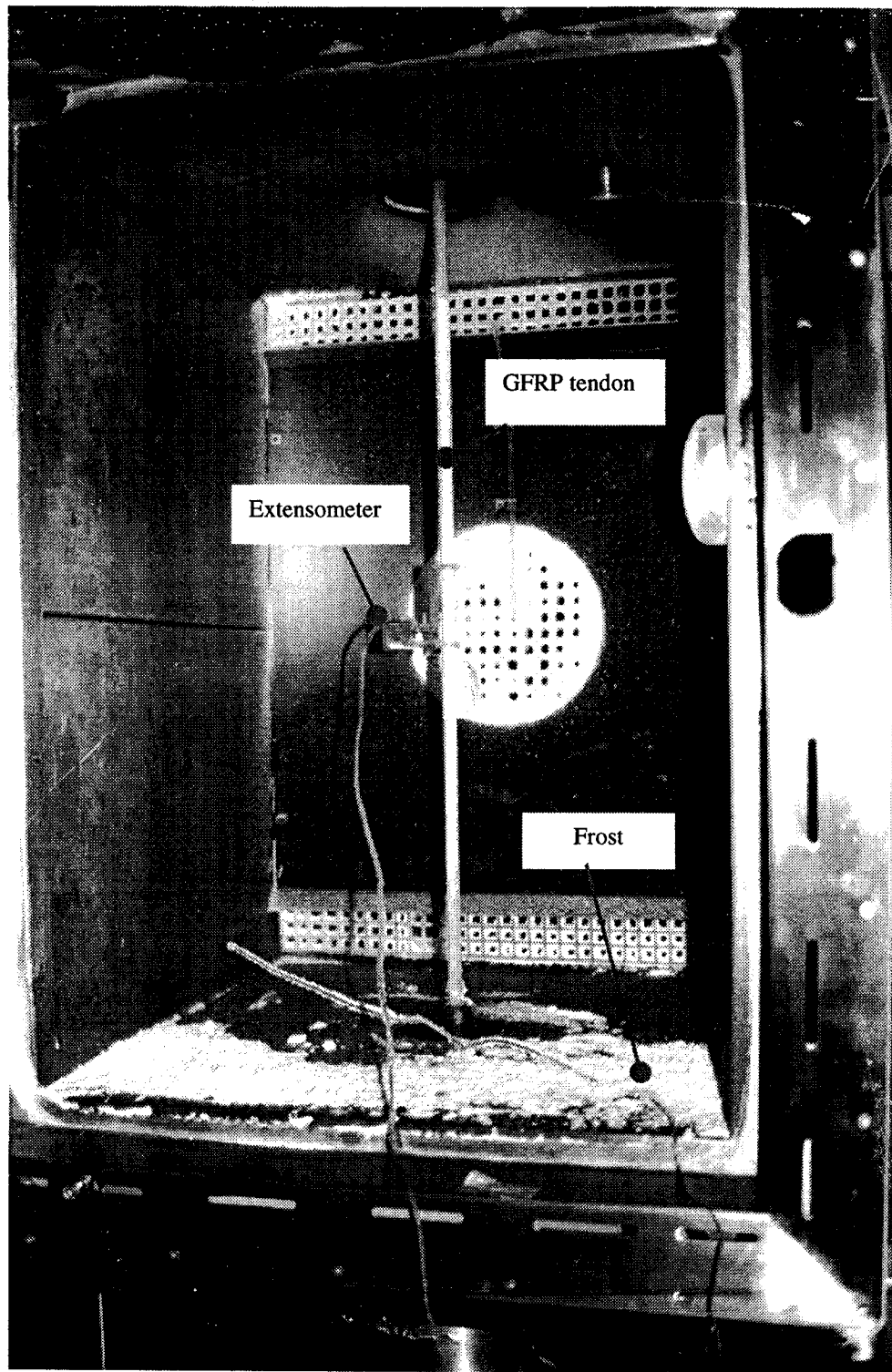
**Figure 3-50:** GFRP tendon during testing at −40°C
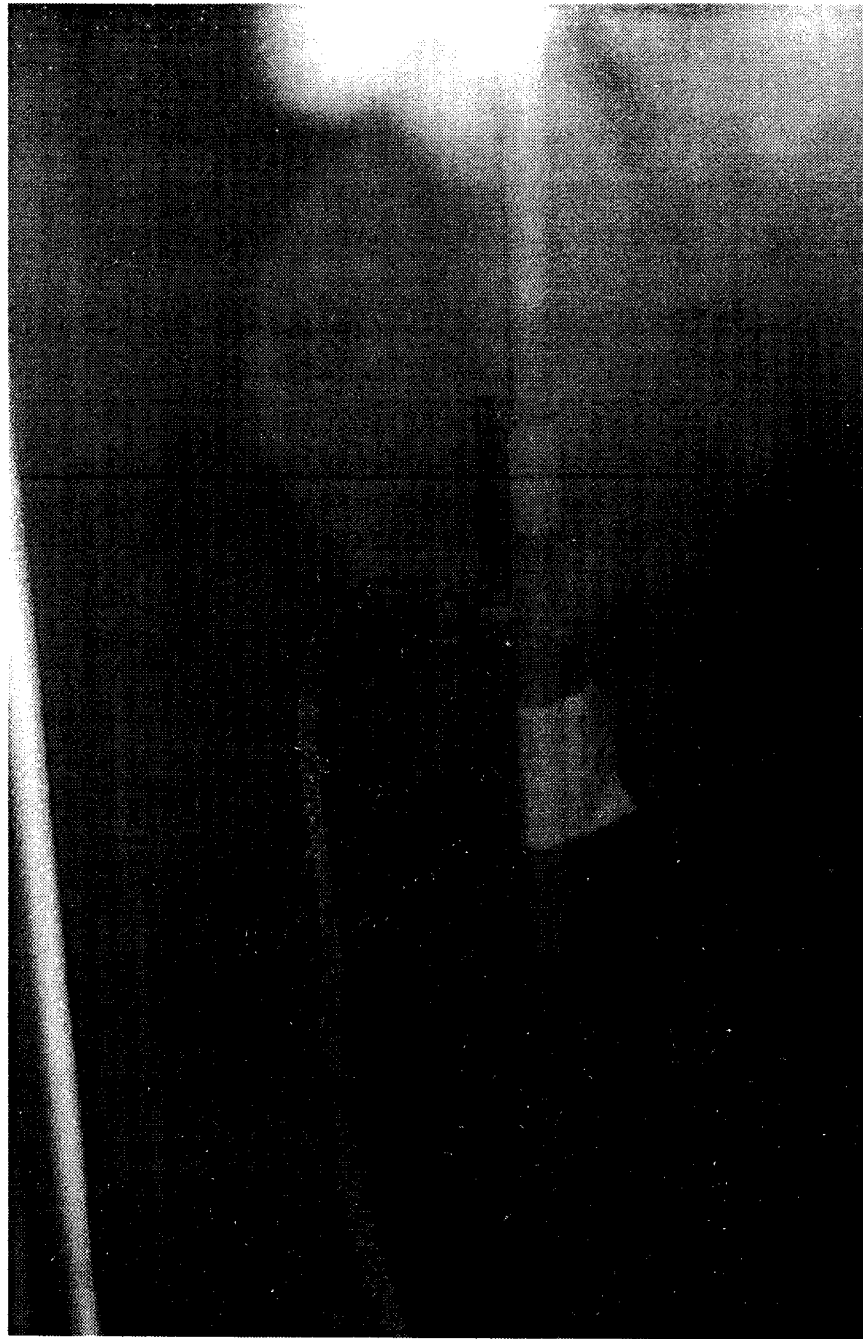
**Figure 3-51:** Close-up view of a GFRP tendon during testing at –40°C

In addition to static tests at various temperatures, the behavior of the sensors when the tendons in which they are embedded are subjected to fatigue or creep loads was examined. More details from these tests will be given in subsequent chapters.

# 4.0 MANUFACTURING, PROCESSING AND RELATED ISSUES

## 4.1 Introduction

The first objective of this research was to undertake a comprehensive reliability study of the smart pultruded FRP tendons. This will include tensile tests in high-temperature and low- temperature ambient conditions, fatigue tests, short-term creep tests, and longer-term creep tests in alkaline environments. Before dealing with these tests however, a few other issues should be addressed. These are (a) a micromechanical investigation of the smart tendons, (b) sensor embeddement and pultrusion monitoring, and (c) tension testing of the pultruded tendons under ordinary laboratory conditions. Details regarding the first issue are given by Kalamkarov and MacDonald [1997], and the other two issues are discussed by Georgiades [1998]. A brief account of this work will be given in this chapter.

## 4.2 Micromechanical Study of Smart Tendons
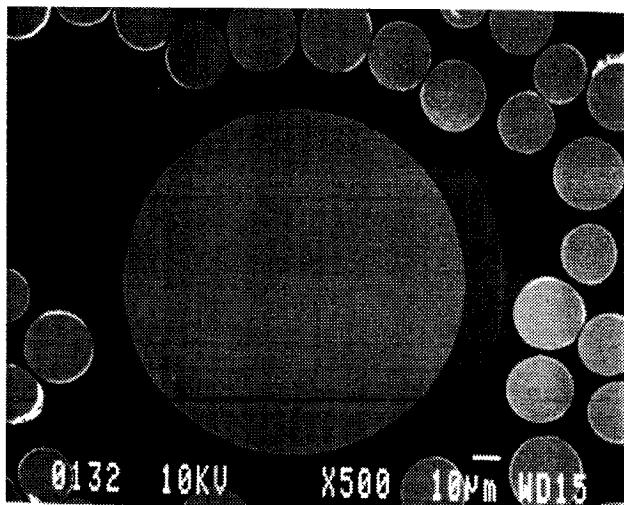


**Figure 4-1:** SEM micrograph shows excellent interface between polyimide coated optical fiber and host material [Kalamkarov and MacDonald, 1997]

Optical fibers usually are supplied with an outer buffer coating for added protection, and consequently the bond strength between the embedded fiber and the host material will depend upon the features of this coating. In particular, two noteworthy features are the extent of chemical compatibility between the buffer coating and the surrounding matrix, and also the ability of this coating to sustain the elevated temperatures encountered in the pultrusion die. Two common types of coating materials are polyimide and acrylate.
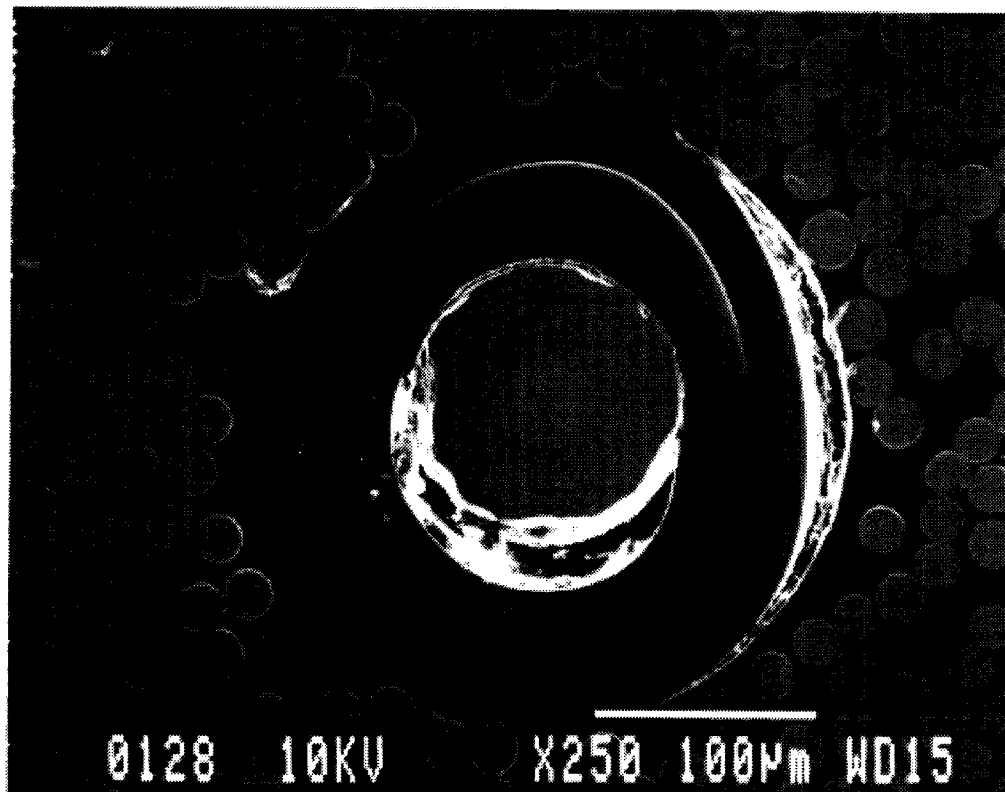


**Figure 4-2:** SEM micrograph shows debonding between acrylate coated optical fiber and host material [Kalamkarov and MacDonald, 1997]

To compare the relative merits of these buffers, a polyimide-coated single-mode optical fiber with an overall diameter of 155 microns and an acrylate-coated multimode fiber with an overall diameter of 250 microns were pultruded in GFRP and CFRP rods [Kalamkarov and MacDonald, 1997]. The SEM micrograph in Figure 4-1 shows an excellent interface between the polyimide coated optical fiber and the host material.

Figure 4-2 shows however extensive debonding between acrylate-coated optical fibers and the surrounding matrix. The above results show that acrylate-coated optical fibers cannot withstand the temperatures in the die (over 150°C) and consequently only polyimide-coated ones were used for further research.

Another related issue that is of paramount importance is the effect of the embedded fiber on the mechanical integrity of the composite tendon. For this purpose, tensile and shear tests were carried out in accordance with ASTM D3916 and ASTM D4475 respectively, using an MTS Model 850RM load frame driven by an Instron controller [Kalamkarov and MacDonald, 1997]. The results obtained are summarized in Tables 4-1 and 4-2.

**Table 4-1:** Tensile properties of GFRP and CFRP tendons [Kalamkarov and MacDonald, 1997]

| Material | Ultimate Strength (MPa) | Standard Deviation (MPa) | Tensile Modulus (GPa) | Standard Deviation (GPa) |
|---|---|---|---|---|
| **Glass FRP** | | | | |
| No Optical fiber | 902 | 126 | 48.2 | 1.1 |
| One Polyimide fiber | 949 | 55 | 47.3 | 0.7 |
| **Carbon FRP** | | | | |
| No Optical fiber | 1245 | 118 | 140.8 | |
| One Optical fiber | 1246 | 56 | 144.2 | 3.4 |

As Table 4-1 shows, the tensile modulus and strength of the GFRP and CFRP tendons are essentially unaffected by the presence of one optical fiber. The most probable reason for this is that, for such unidirectional composites, the reinforcing fibers are practically solely responsible for the tensile properties [Kalamkarov, 1992]. Table 4-2 however, shows that the embeddement of optical fibers has a small degrading effect on the shear properties of GFRP tendons. Also, the decrease in shear strength becomes more pronounced as the number of embedded optical fibers increases. On the other hand, the shear strength of

CFRP tendons did not seem to be affected by the presence of a single embedded optical fiber.

**Table 4-2:** Shear properties of GFRP and CFRP tendons [Kalamkarov and MacDonald, 1997]

| Material | Shear Strength (MPa) | Standard Deviation (MPa) |
|---|---|---|
| **Glass FRP** | | |
| No Optical fiber | 29.3 | 1.3 |
| One Polyimide fiber | 27.2 | 1.1 |
| Two Polyimide fibers | 25.4 | 1.0 |
| One acrylate fiber | 29.2 | 2.2 |
| | | |
| **Carbon FRP** | | |
| No Optical fiber | 29.7 | 1.6 |
| One Optical fiber | 29.5 | 1.5 |

Before closing this section, let us mention that the different aspects regarding the embeddement of optical fibers in composites have been the subject of research for many years. Leka and Bayo [1989], Davidson et al., [1989], Jensen and Pascual [1990], Carman et al., [1993], Lee et al. [1995], among others, used experimental techniques to assess the effect of embedding different numbers of different-sized optical fibers on the tensile, shear and fatigue properties of composite laminates. Sirkis and Singh [1994], Tay and Wilson [1989], Eaton et al. [1994], and others used finite element techniques to investigate the issue. The general results were that embedded optical fibers are not likely to have a significant effect on the mechanical properties of a composite part if the optical fibers have a small diameter and are embedded in a direction that is parallel to the orientation of the reinforcing fibers. As well, the fewer the number of embedded fibers, the less pronounced is the impact. Finally, the better the degree of chemical compatibility of the fiber coating with the surrounding matrix, the lower are the stress and strain concentrations imparted to the matrix.

## 4.3 Sensor Ingress and Pultrusion Monitoring

As a first attempt at embedding a sensor in a pultruded CFRP rod, an unmodified Fabry Perot sensor was added to the fiber feed side of the pultrusion process. The forward end of the sensor was bonded to a carbon fiber roving to ensure that it would traverse the die. From the location where it was bonded, the sensor had to pass through two polyethylene guide cards, in and out of the pultrusion die, and finally through the two sets of pulling wheels when the CFRP tendon had consolidated. At this point, the resin bath was drained and the pultrusion process stopped to enable the connector to pass through the die.

The result of the first trial was a CFRP rod with an embedded Fabry Perot sensor. However, when the sensor lead was coupled to the demodulator, it was discovered that this sensor was no longer operational. This failure was originally attributed to one of two possible factors. The first was simply that the sensor was not handled with due care and thus it was damaged either through contact with the polyethylene guides or at the entrance of the die. The second was that the sensor failed because it could not sustain one or more of the conditions prevailing inside the die, namely high temperature, resin cure and associated residual stresses, or the compaction pressure from the surrounding reinforcing fibers. To test the latter theory, it was decided to conduct a number experiments that would subject the Fabry Perot sensor to each of the variables mentioned above, hoping to isolate the one that was primarily responsible for the sensor failure.

To test whether fiber compaction pressure was crushing the Fabry Perot sensors, a sensor was passed through the die but with the die heaters switched off and the resin bath completely devoid of any resin [Georgiades, 1998]. The results indicated that fiber compaction pressure alone was not high enough to cause any damage to the sensor. The experiment was then repeated, but this time the heaters were switched on and the die was allowed to reach steady state at the same temperatures as for a normal pultrusion run. For this experiment also, no resin was used. Once again, the Fabry Perot sensor survived the

process and this led to the conclusion that the high temperatures encountered inside the die were not responsible for the sensor failure. The third experiment using the same sensor was a normal pultrusion run. The carbon fiber rovings were pulled through the resin bath and into the heated die through the fiber feed guides [Georgiades, 1998]. The sensor did survive the pultrusion but failed shortly thereafter, with the reason for this failure not obvious. In fact, all subsequently used Fabry Perot sensors met with the same fate.
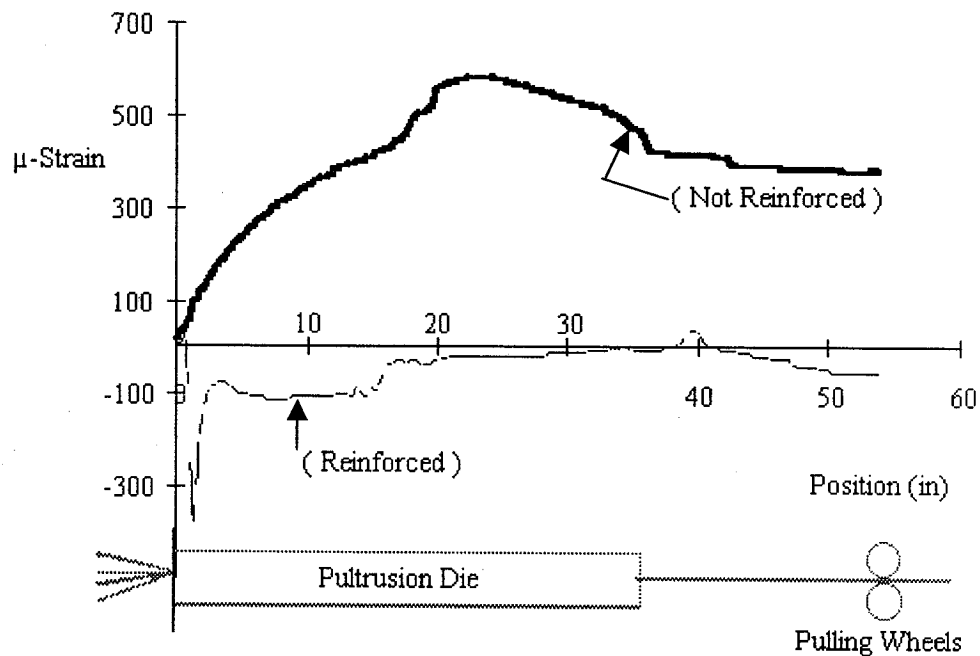


**Figure 4-3:** Comparison of output from reinforced and unreinforced Fabry Perot sensors during pultrusion [Georgiades, 1998]

These post-fabrication failures were attributed to the radial shrinkage of the composite tendon as it cooled down from the die temperature to room temperature [Kalamkarov et al., 1998]. This shrinkage, in turn exerts an external pressure on the hollow portion of the Fabry Perot sensor (see Figure 3-24), causing it to collapse. To avoid this failure it became necessary to prereinforce the sensor [Kalamkarov et al., 1998]. Figure 4-3 [Georgiades, 1998] shows the strain output from a prereinforced sensor together with the output from an unreinforced sensor. Subsequently, all Fabry Perot sensors were

prereinforced and this ensured their successful pultrusion in both GFRP and CFRP tendons. The reliability experiments described in the next chapter and pertaining to Fabry Perot sensors all involved prereinforced sensors. The detailed prereinforcement procedure was given in Section 3.4 of this thesis.
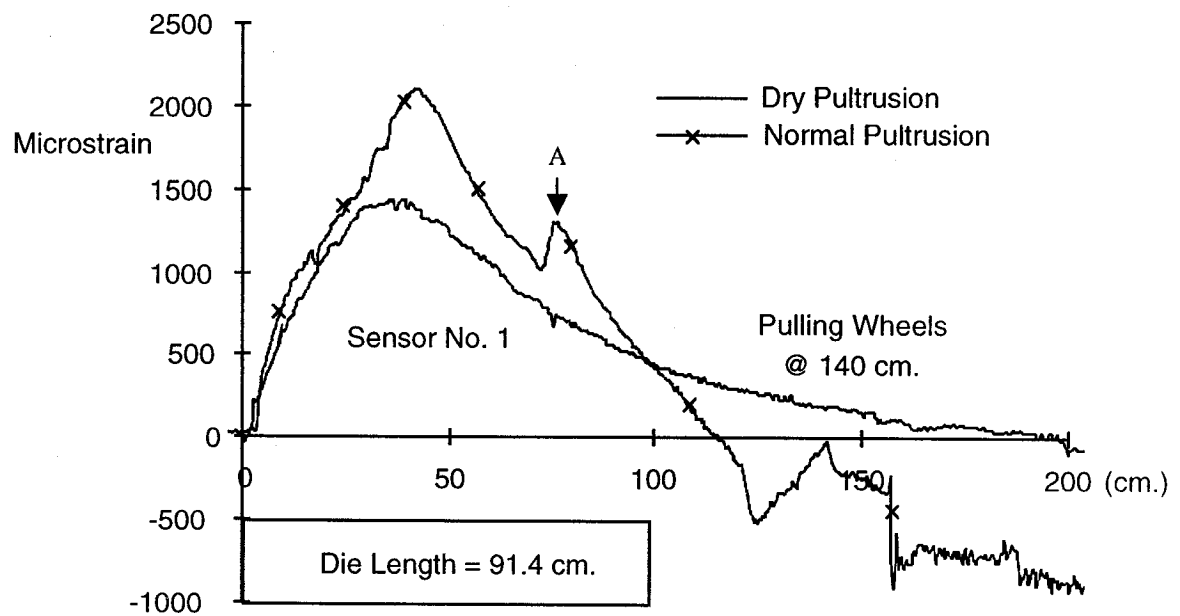


**Figure 4-4:** Comparison of output from Bragg Grating sensor during normal and dry pultrusion [Georgiades, 1998]

Unlike Fabry Perot sensors, Bragg Grating sensors showed enhanced survivability in the pultrusion process and hence it was not deemed necessary to prereinforce them. Nonetheless, Bragg Grating sensors were also subjected to dry (no resin) pultrusion runs [Georgiades, 1998]. Figure 4-4 shows the strain plots from the dry and normal pultrusion experiments superimposed. The differences between the two plots are caused by the curing of the resin. For example, the peak strain attained during normal pultrusion is about 800 microstrain higher than the corresponding value encountered in dry pultrusion. This difference is caused by the chemical processes that accompany the curing of the resin are highly exothermic, and the heat energy released induces a higher thermal strain. It is also noteworthy to observe that once the pultruded rod has exited the die and cooled

to the ambient temperature, the strains recorded by the embedded sensor do not return to zero as for the case of the dry run. These are the process-induced residual strains, which are "locked in". Finally, one of the most interesting features of Figure 4-4 is the sudden spike at point A. This possibly represents the location where the consolidated rod detaches itself from the walls of the die, at which point there could be a transition of forces from shear at the rod/die interface to the much larger tensile force in the rod itself. Thus figures such as 4-3 and 4-4 can give valuable insight as to complex phenomena that take place inside the pultrusion die, and which are otherwise extremely difficult to predict analytically or numerically. More details regarding the experiments described in this section can be found in the author's MASc. thesis [Georgiades, 1998].

## 4.4 Mechanical Testing in Laboratory Conditions

The next natural phase in the research involved testing the pultruded tendons in order to characterize the behavior of the embedded sensors. This was accomplished by applying various loads while continuously monitoring the strain from the sensors. The accuracy and reliability of the Fabry Perot and Bragg Grating sensors was verified by comparing the results with those obtained from a conventional extensometer which was clipped to the outside of the tendons, as described previously in Section 3.6. Care was exercised not to exceed the strain limit on either the extensometer or the sensor.

The smart GFRP and CFRP tendons were subjected to the two load waveforms described in Section 3.6. The first was a trapezoidal waveform, whereby the load was ramped up to a peak level at a rate of 90 N/sec, held at the peak level for 20 seconds, and then ramped back down at the same rate as for ramp-up. Prior to the beginning of each test, a small preload was imparted to the rods to keep them straight. The second waveform to which the tendons were subjected was a sinusoidal one, which typically involved five or six cycles of applied load at a frequency of 0.0167 Hz (1 cycle per minute).

**Figure 4-5:** Strain from extensometer and embedded Bragg Grating sensor in a GFRP tendon subjected to a sinusoidal load [Georgiades, 1998]
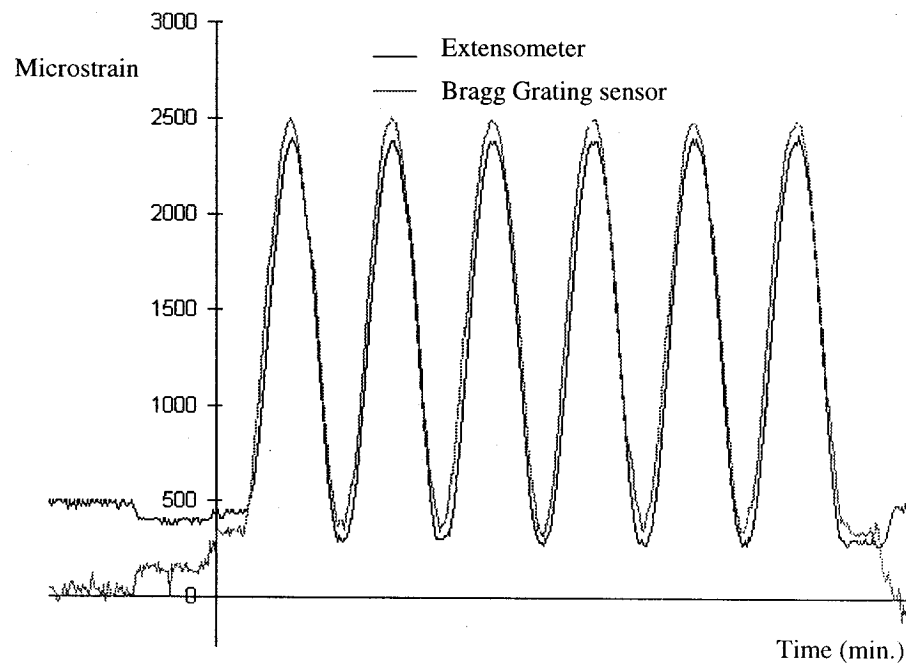


**Figure 4-6:** Strain vs. time plot from extensometer and embedded Bragg Grating sensor in a GFRP tendon subjected to a sinusoidal load [Georgiades, 1998]

Figure 4-5 shows the strain output from an extensometer and a Bragg Grating sensor embedded in a GFRP tendon. The amplitude of the applied sinusoidal load was 5 kN. The figure shows a very good agreement between the extensometer and the sensor, although the extensometer is more consistent than the Bragg Grating sensor, and its data exhibit less scatter as the load is cycled [Georgiades, 1998]. The excellent degree of conformity between the two strain-monitoring devices is perhaps more evident in Figure 4-6, which replots the data from Figure 4-5 as microstrain vs. time. The discrepancy between the sensor and the extensometer does not exceed 100 microstrain (about 4% discrepancy) and this only occurs at the peak load. Figure 4-6 also illustrates the high degree of repeatability of the two devices. Indeed, both the extensometer and the Bragg Grating sensor attain the same peak in every cycle.
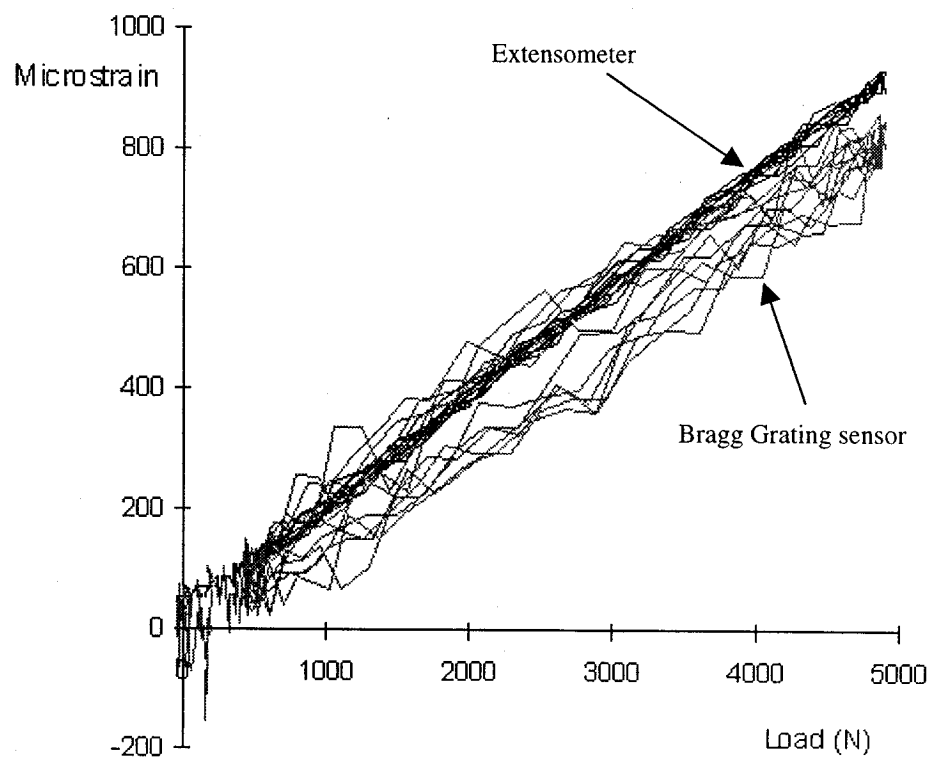
Figure 4-7: Strain from extensometer and embedded Bragg Grating sensor in a CFRP tendon subjected to a sinusoidal load [Georgiades, 1998]

Figure 4-7 shows the results from another sinusoidal test, this time performed on a CFRP tendon [Georgiades, 1998]. The embedded sensor again was of the Bragg Grating type. It is evident that there is a good agreement between the sensor and the extensometer throughout the entire load range. However, the degree of scatter in the sensor data is higher than that corresponding to the extensometer values.



**Figure 4-8:** Strain vs. time plot from extensometer and embedded Bragg Grating sensor in a CFRP tendon subjected to a sinusoidal load [Georgiades, 1998]

Figure 4-8 shows the data from Figure 4-7 plotted as strain vs. time. The conformance between the Bragg Grating sensor and the extensometer is evident once again. As well, both strain-monitoring devices are very consistent, peaking at essentially the same strain value with each cycle.

**Figure 4-9:** Strain from extensometer and embedded Fabry Perot sensor in a GFRP tendon subjected to a trapezoidal load [Georgiades, 1998]

A GFRP tendon with an embedded Fabry Perot sensor was also subjected to sinusoidal and trapezoidal loads. The results from a trapezoidal test are shown in Figure 4-9 [Georgiades, 1998]. Unlike the tests corresponding to Figures 4-5 to 4-8, the peak load in this trapezoidal test was allowed to reach 7kN in magnitude. It is seen that the agreement between the extensometer and the Fabry Perot sensor is very good, and that the discrepancy between the two strain-monitoring devices increases from negligible at low load levels to about 150 microstrain (about 7.5%) at the peak applied load. The amount of scatter was negligible for both the sensor and the extensometer. The data from Figure 4-9 are plotted as microstrain vs. time in Figure 4-10. This graph too indicates a high degree of conformity between the strain outputs from the extensometer and the Fabry Perot sensor.

**Figure 4-10:** Strain vs. time plot from extensometer and embedded Fabry Perot sensor in a GFRP tendon subjected to a trapezoidal load [Georgiades, 1998]



**Figure 4-11:** Strain vs. time plot from extensometer and embedded Bragg Grating sensor in a CFRP tendon subjected to a trapezoidal load

Similar tests were performed on CFRP tendons with the embedded Fabry Perot sensors. A more extensive account on the mechanical performance of the smart pultruded FRP tendons at room temperature can be found in the author's MASc. Thesis [Georgiades, 1998]. We close this section by showing the results from a very interesting trapezoidal test in Figure 4-11. In this test, a CFRP tendon with an embedded Bragg Grating sensor is being subjected to a trapezoidal load waveform when the spelter socket on one end suddenly slips and the load drops abruptly to zero. As Figure 4-11 shows, the Bragg Grating signal, unlike the corresponding extensometer signal, goes directly to zero with no "bounce".

# 5.0 RELIABILITY ASSESSMENT OF THE PULTRUDED SMART TENDONS

## 5.1 Introduction

Fiber-optic sensors and smart composite materials have shown great promise in replacing or strategically complimenting traditional materials such as steel and concrete and conventional strain-monitoring devices such as extensometers and foil gauges. However, the full potential of any new material system cannot be realized until researchers and engineers attain a level of confidence with regards to long-term behavior. It is precisely the fact that smart composite materials have been the "new kid on the block" that has slowed their progression into new domains of application. Quite simply there are not enough data characterizing their long-term behavior. For civil and marine applications, the composite materials will be exposed to humidity, chemical environments, low and high temperature extremes, dynamic loads, as well as mechanical stress.

The overall performance of fiber-optic sensors depends to a large extent on whether they are surface mounted or embedded. It is clear that embedded sensors have an added level of protection against friction and wear as well as chemical attack. On the other hand, embedding the sensors often requires some sophistication pertaining to changes that must be effected in the composite manufacturing process. More importantly, embedding a fiber optic sensor will inevitably mean that unless the associated lead is recovered from the composite, the sensor cannot be coupled to the demodulator. Despite its paramount importance, the issue of fiber-optic lead egress or recovery has not yet been adequately addressed.

To fully assess environmental effects on smart composite structures, one must consider both the individual components and the overall system. The manufacturers of the Fabry

Perot sensors used in this work specify that the sensors are reliable over the temperature range of $-40°C$ to $+125°C$ [RocTest Ltd., 1997]. Specifications for the Bragg Grating sensors used in the various experiments indicate that accuracy is maintained only up to 80°C. It has been shown by Erdogan et al. [1994] that the decay of reflectivity in an optical fiber is fairly small at temperatures up to 300°C, and that losses are negligible over a span of 50 years if the temperature is maintained below 80°C. However, an adverse combination of high temperature and moisture exposure might lead to decay in reflectivity, which in turn would lead to some scatter in the signal from such devices as Fabry Perot and Bragg Grating sensors. On the other hand, it is possible to construct specialized sensors that can be used exclusively in high-temperature environments. However, such customized sensors come with a high price tag which limits their use to mainly aerospace applications. For example, Wang et al., [1994] constructed and tested a sapphire fiber-based polarimetric optical sensor based on the polarization-maintaining characteristics of a sapphire fiber. Sapphire ($Al_2O_3$) can perform very well under adverse conditions and in temperatures up to 2000°C, and the resulting sensor was demonstrated for temperature measurement up to 1200°C with a 2°C resolution [Wang et al., 1994]. Gunther et al., [1994] used a sputtering technique to deposit nickel-based super alloy coatings on optical fibers, rendering them operational in temperatures approaching 1000°C.

Temperature, humidity and other environmental factors affect not only the sensors themselves but also the buffer coatings. An excellent survey was performed by Leka and Bayo [1989], who discussed the findings of many researchers with regard to fiber optic ingress in composite materials and other related issues. Among the results reported was the fact that acrylate-coated optical fibers could not sustain temperatures in excess of 85°C, whereas polyimide-coated optical fibers could withstand temperatures in excess of 350°C. The same conclusions were reached by Kalamkarov and MacDonald [1997], in attempting to embed polyimide-coated and acrylate-coated optical fibers in composite rods during pultrusion. The SEM micrographs in Figures 4-1 and 4-2 illustrate this point.

Another closely-related issue is the susceptibility to chemical attack. The question which immediately arises is whether the superiority exhibited by polyimide buffers over their acrylate counterparts in elevated–temperature environments suggests a similar trend in acidic or alkaline environments. Habel et al., [1994] demonstrated that optical fibers and their coatings are particularly susceptible to chemical attack when exposed to certain agents. It was discovered that, in a reversal of roles, polyimide coatings were degraded as a consequence of exposure to solutions with pH values greater than 11, whereas acrylate coatings were only slightly affected. This is a very important issue, because civil and structural engineering applications inevitably will expose fiber optic sensors to cement mixtures which are alkaline in nature. Thus, polyimide-coated optical fibers are not suitable for direct contact with concrete. However, when embedded in a composite, the extra level of protection offered by the matrix might render the resulting smart material suitable for incorporation in concrete structures, wherein it could monitor the health of such structures.

With respect to the overall system, one should consider the effect of the environment on a smart composite material over an extended period of time. The environmental behavior of composite materials alone has been the subject of investigation for some time. For example, it is known that moisture absorption can deteriorate the performance of composites in two ways [Gibson, 1994]. Firstly, moisture absorption causes the matrix to swell up, and these dimensional changes are resisted by the much stiffer reinforcing fibers. In turn, this creates residual stresses and limits the load-carrying capacity of the composite member. Secondly, moisture absorption reduces the glass transition temperature of the matrix, which leads to a corresponding reduction in the composite properties. The effects of moisture absorption are very similar to the effects of temperature increase. Contrary to composite materials themselves, the overall effects of temperature change and moisture absorption on the embedded fiber optic sensors have not been characterized.

In addition to the environmental impact on smart composites, it is imperative that one also considers the influence of fatigue loads. With respect to fatigue behavior, it is of interest to determine whether the embedded sensors maintain their accuracy and repeatability after thousands or millions of cycles of applied load. From a structural point of view, one is also concerned with the potentially degrading effects that the embedded sensor might have on the fatigue life of the composite.

A comprehensive reliability analysis of smart composite materials must also include a study of the effects of creep and stress relaxation on their mechanical performance. Particularly, and in addition to the behavior of the composite itself, one must understand how the embedded sensor will react to prolonged periods of sustained load. As well, it is necessary to assess the combined long-term effects of creep loads and environmental exposure on the composites. For the CFRP and GFRP rods described in this thesis, such long-term testing can be designed to simulate conditions encountered in concrete structures wherein they may be used as rebars or prestressing tendons.

The present chapter will give a detailed account of the reliability assessment performed on the smart pultruded FRP tendons. The testing regime will include the following:

1. temperature tests on GFRP tendons with embedded Fabry Perot sensors
2. temperature tests on CFRP tendons with embedded Fabry Perot sensors
3. temperature tests on GFRP tendons with embedded Bragg Grating sensors
4. temperature tests on CFRP tendons with embedded Bragg Grating sensors
5. fatigue tests on GFRP tendons with embedded Fabry Perot sensors
6. fatigue tests on CFRP tendons with embedded Fabry Perot sensors
7. fatigue tests on GFRP tendons with embedded Bragg Grating sensors
8. fatigue tests on CFRP tendons with embedded Bragg Grating sensors
9. short-term creep tests on GFRP tendons with embedded Fabry Perot sensors
10. short-term creep tests on CFRP tendons with embedded Fabry Perot sensors
11. long-term creep tests on GFRP tendons with embedded Fabry Perot sensors
12. long-term creep tests on CFRP tendons with embedded Fabry Perot sensors.

In the above list, item 1 was covered in the author's MAsc. Thesis [Georgiades, 1998]. However, for the sake of completeness, item 1 will also be included in this chapter.

## 5.2 Temperature Tests on GFRP tendons with Embedded Fabry Perot sensors
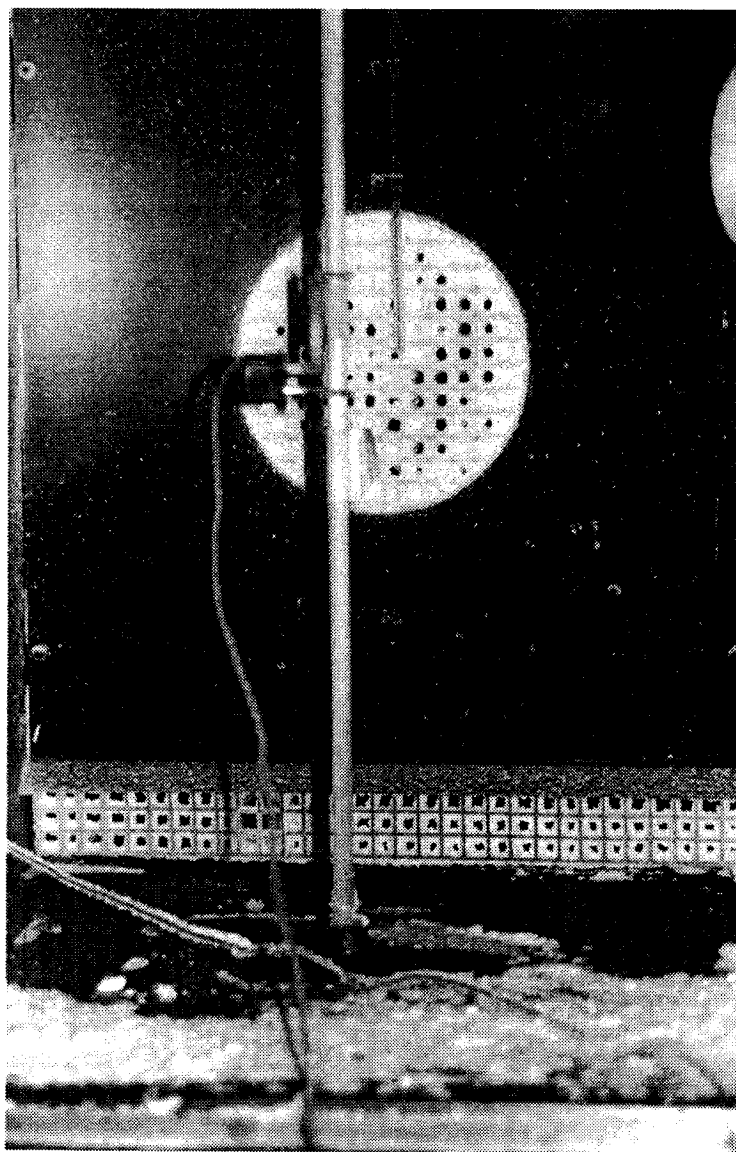


**Figure 5-1:** The pultruded GFRP tendon during temperature testing

As mentioned before, the long-term objective is to embed the smart pultruded GFRP and CFRP rods in large structures, wherein they would monitor the health of the critical members of those structures and at the same time act as concrete reinforcements. For such applications it is imperative that the sensors behave reliably irrespective of ambient temperature fluctuations. Consequently, the smart tendons produced at Dalhousie

University were subjected to trapezoidal and sinusoidal tests at temperatures that varied from –40°C to +60°C. These tests were conducted at the "PSC Analytical" company in Dartmouth, Nova Scotia, using a 400kN-capacity MTS model 8540RM load frame controlled by an Instron Series IX controller, and an Instron temperature chamber.
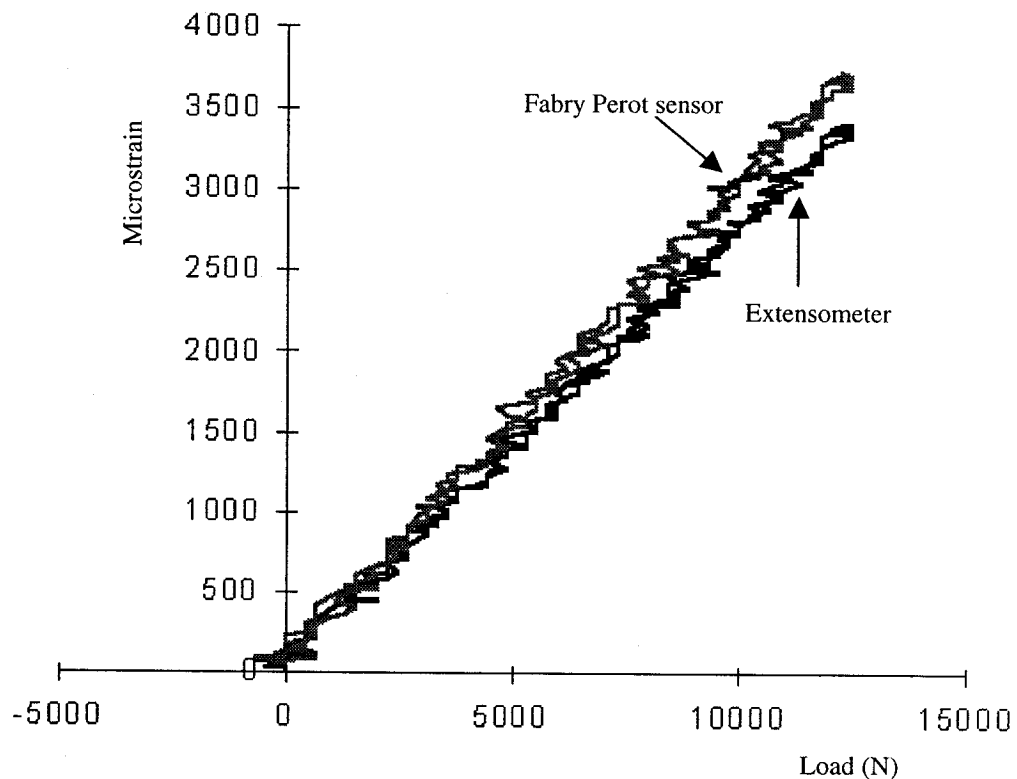


**Figure 5-2:** Strain from extensometer and embedded Fabry Perot sensor in a GFRP tendon subjected to a trapezoidal load at 40°C [Georgiades, 1998]

First a GFRP tendon was prepared with an embedded Fabry Perot sensor (Figure 5.1). It was then mounted into the temperature chamber and an extensometer was clipped to its surface. The temperature chamber was heated to 40°C and allowed to reach steady state as indicated by a thermocouple located inside the chamber. The tendon then was given a small preload (a few N) to keep it straight, and subsequently was subjected to a trapezoidal test. The specifics of this trapezoidal waveform were as follows: (1) A ramp-up to 12,000 N at a rate of 90 N/sec, (2) a steady load level at 12,000 N for 30 seconds

and (3) a ramp-down to the original preload at a rate of 90N/sec. At the beginning of this test and prior to the application of any load, it was observed that the strain reading of the Fabry Perot sensor was about 110 µε (microstrain). This was a purely thermal strain caused by the expansion of the glass tendon. This thermal strain was factored out of both the sensor and the extensometer strain readings, by nulling the two strain-monitoring devices after the temperature in the chamber had reached steady state and just before any load application. This was repeated for all subsequent temperature tests.
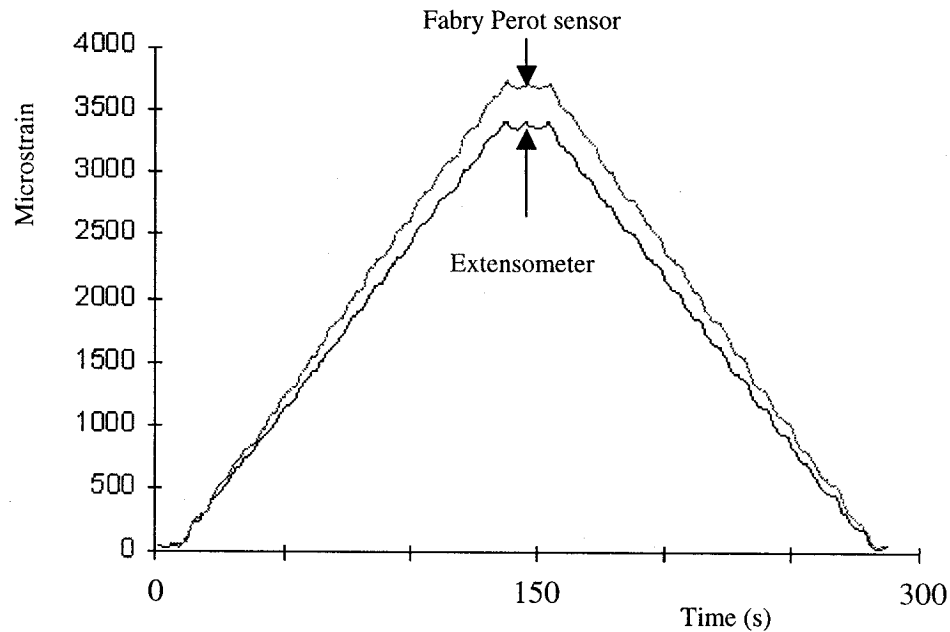


**Figure 5-3:** Strain vs. time plot from extensometer and embedded Fabry Perot sensor in a GFRP tendon subjected to a trapezoidal load at 40°C [Georgiades, 1998]

The results from this test are shown as microstrain vs. load in Figure 5-2 and microstrain vs. time in Figure 5-3. It is seen from these two figures that the maximum discrepancy between the two strain-monitoring devices is about 9% at the maximum applied load, and that the extensometer readings are consistently lower than the sensor readings. A possible reason for this is that there could be a slight misalignment between the spelter sockets and the rod so that the extensometer reads compressive bending strains in addition to the tensile axial strains.
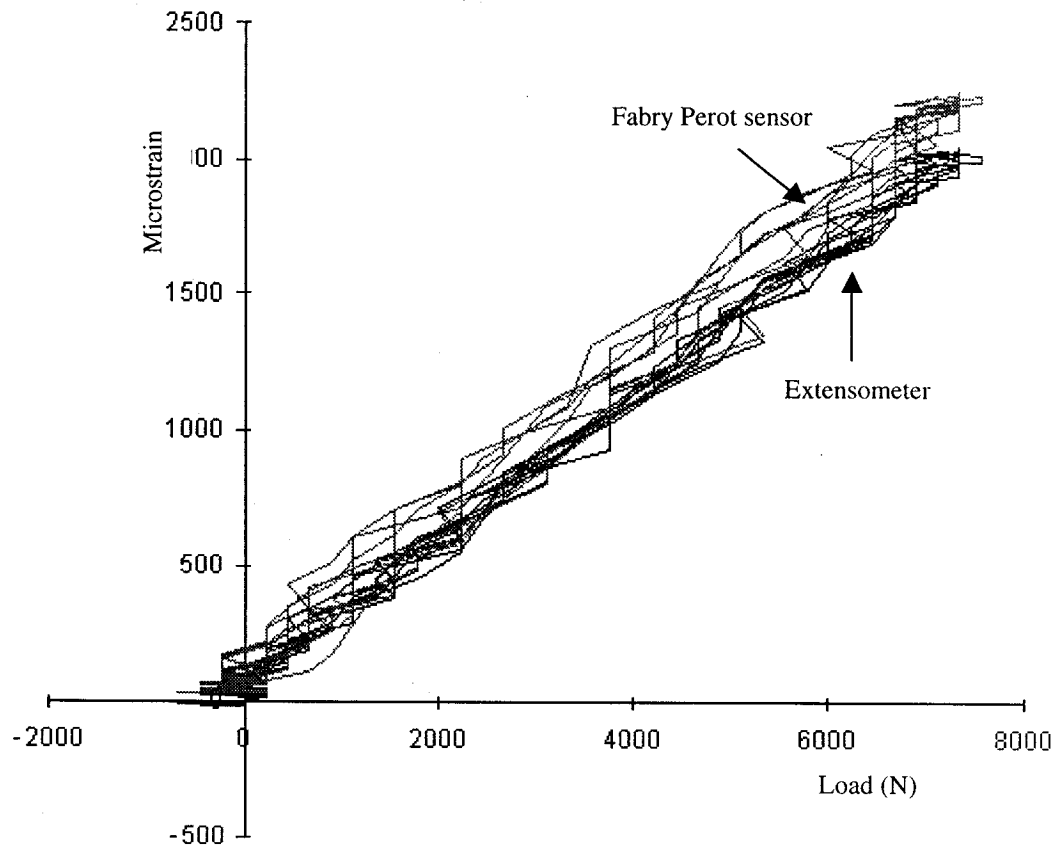
**Figure 5-4:** Strain from extensometer and embedded Fabry Perot sensor in a GFRP tendon subjected to a sinusoidal load at 40°C [Georgiades, 1998]

The same GFRP tendon was then subjected to a sinusoidal load with frequency of 1 cycle per minute and amplitude of 7,000 N. The temperature in the chamber was still at 40°C. Figure 5-4 shows the results from this test plotted as microstrain vs. load. It is seen that the amount of scatter in the sensor readings is greater than that pertaining to the extensometer. The two devices agree well with one another, although a more quantitative assessment of the relative discrepancy can be made after consulting Figure 5-5, which plots microstrain vs. time. As with the trapezoidal test, the discrepancy between the two devices is around 9% at the peak load. Figure 5-5 also shows that both the extensometer and the Fabry Perot sensor are very consistent and repeatable, reaching the same values in each cycle.
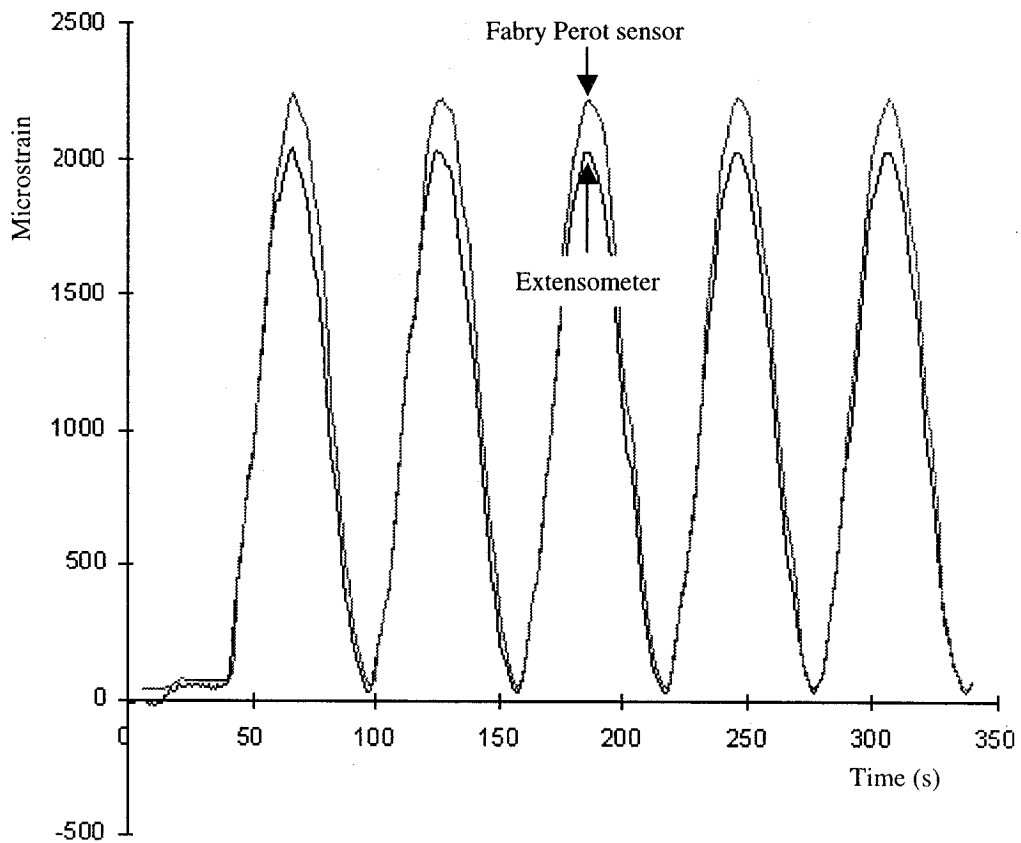
**Figure 5-5:** Strain vs. time plot from extensometer and embedded Fabry Perot sensor in a GFRP tendon subjected to a sinusoidal load at 40°C [Georgiades, 1998]

With the temperature in the chamber maintained at 40°C, the GFRP tendon was subjected to another sinusoidal load, but this time the amplitude of the waveform was selected to be 12,000 N. This is the same amplitude as for the trapezoidal tests of Figures 5-2 and 5-3. The results from this new sinusoidal test are shown in Figures 5-6 and 5-7 (load vs. microstrain and microstrain vs. time). It is evident from these figures that the sensor and the extensometer agree well with one another (about 10% discrepancy).

Thus, based on the results so far, one can conclude that Fabry Perot sensors embedded in GFRP tendons, performed quite well at 40°C, and that their accuracy and consistency was not affected by this high temperature.
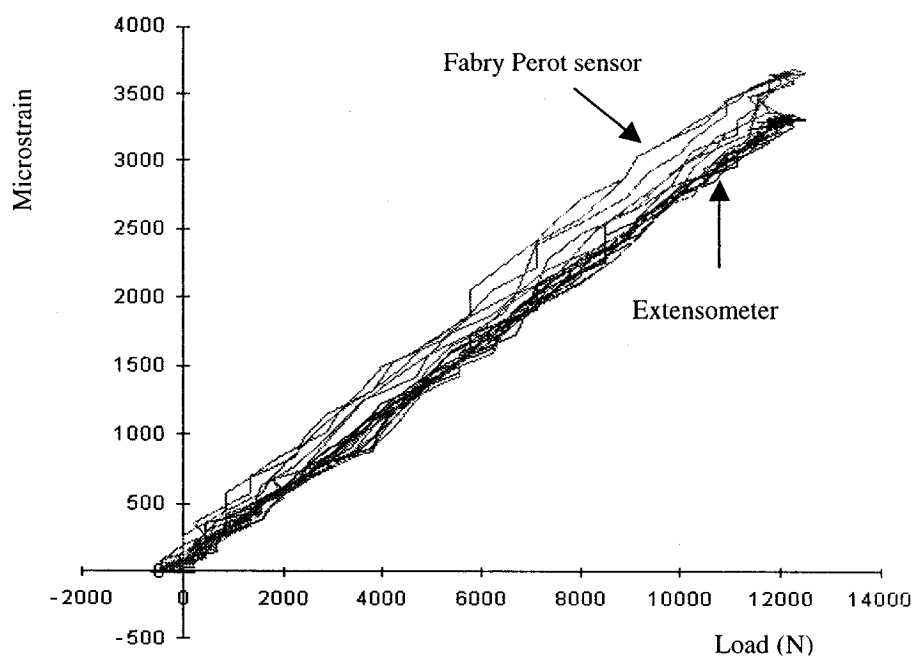
**Figure 5-6:** Strain from extensometer and embedded Fabry Perot sensor in a GFRP tendon subjected to a sinusoidal load at 40°C [Georgiades, 1998]
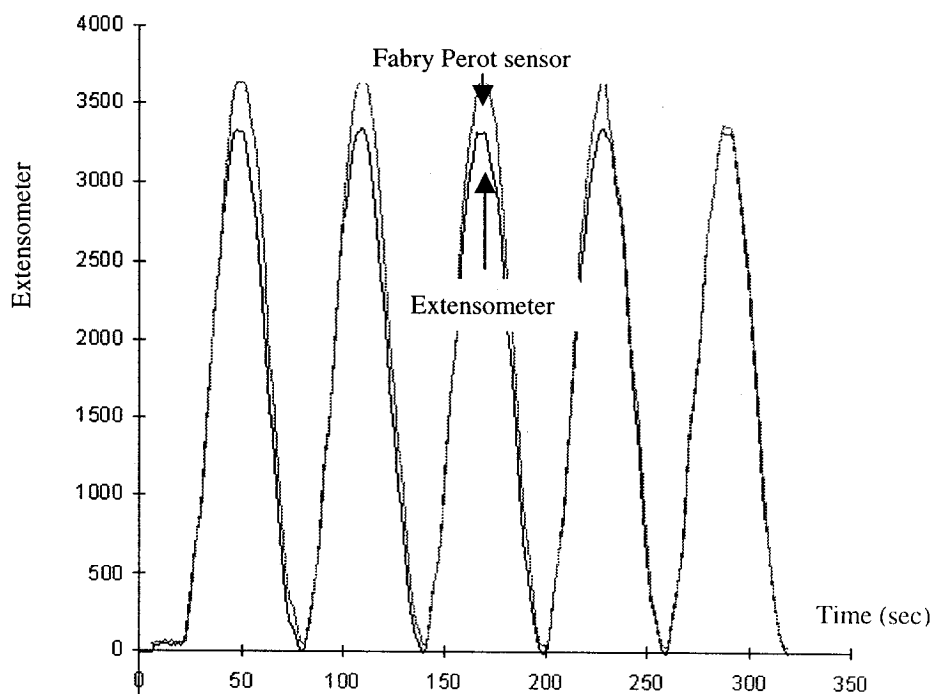


**Figure 5-7:** Strain vs. time plot from extensometer and embedded Fabry Perot sensor in a GFRP tendon subjected to a sinusoidal load at 40°C [Georgiades, 1998]
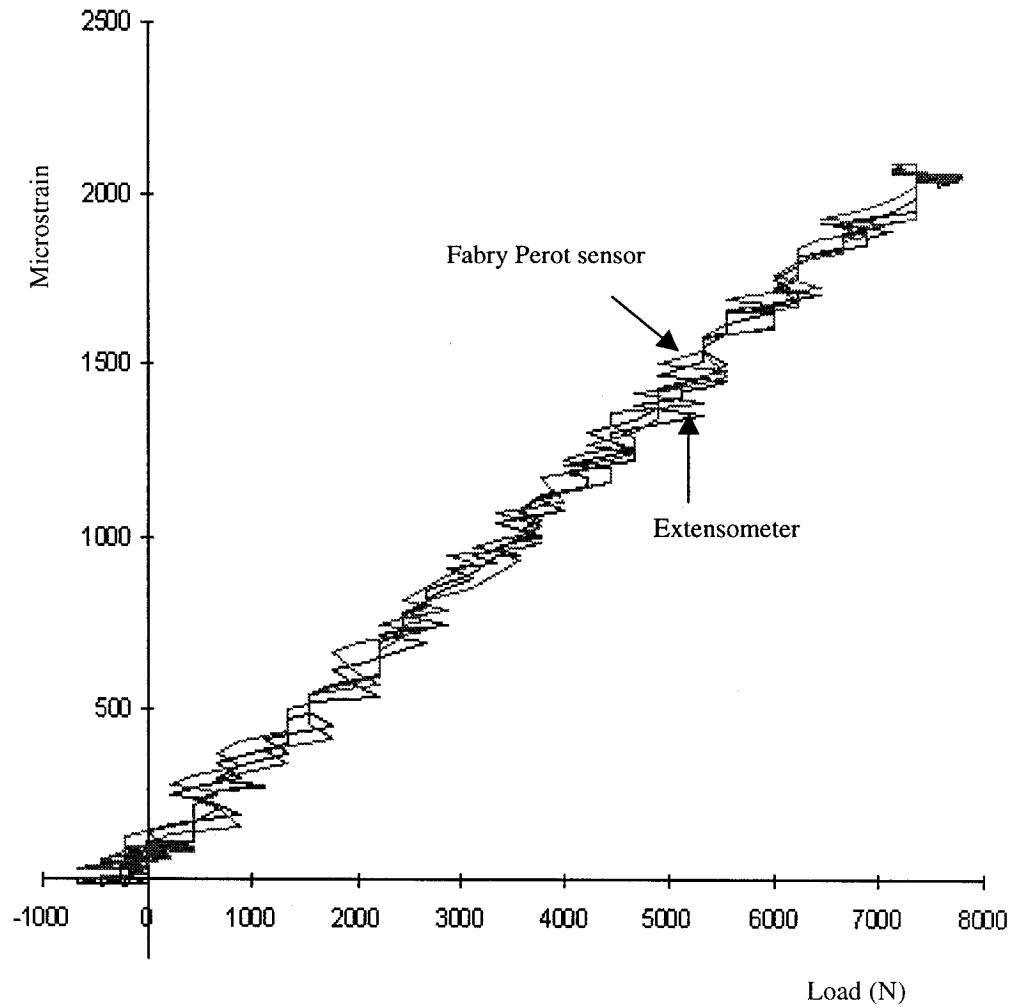
**Figure 5-8:** Strain from extensometer and embedded Fabry Perot sensor in a GFRP tendon subjected to a trapezoidal load at 60°C [Georgiades, 1998]

The temperature chamber was subsequently heated to 60°C and allowed to reach equilibrium, and the GFRP tendon was subjected to two sinusoidal and trapezoidal tests. The first set of tests had a peak load amplitude of 8 kN, while the amplitude of the last set was 13 kN. The microstrain vs. load plot pertaining to the first trapezoidal test is shown in Figure 5-8. It can be observed that the extensometer and the Fabry Perot sensor agreed extremely well with one another. The negligible discrepancy between the two devices is even more evident in the microstrain vs. time graph of Figure 5-9.

Figures 5-10 and 5-11 correspond to the first sinusoidal test. They too indicate a remarkable degree of conformance between the two strain-monitoring devices. Figures 5-12 and 5-13 depict the outcome of the higher-amplitude trapezoidal test, and Figures 5-14 and 5-15 pertain to the corresponding sinusoidal test. The same conclusion can be reached from these tests as for the previous ones. Fabry Perot sensors and extensometers agree extremely well with one another even at temperatures as high as 60°C.

To sum up, the temperature tests performed thus far on the smart GFRP tendons with embedded Fabry Perot sensors indicate that they remain extremely reliable and accurate in high-temperature environments.
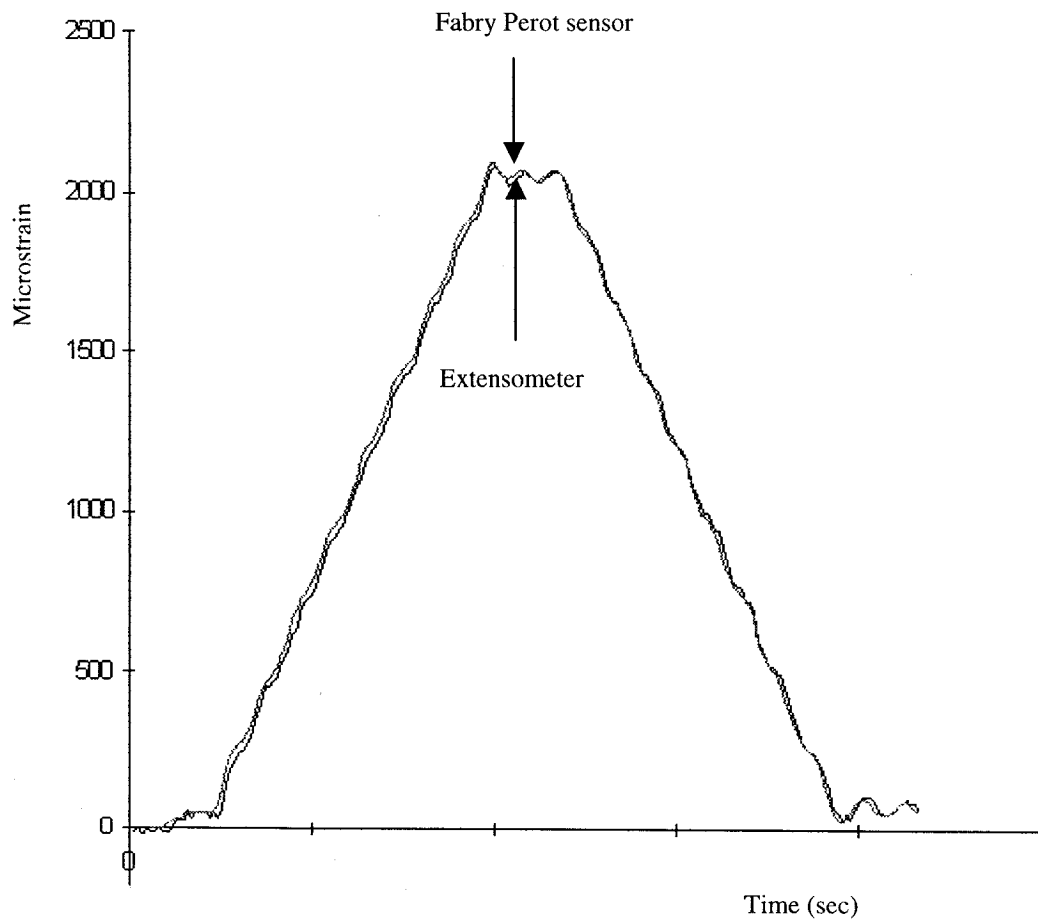
**Figure 5-9:** Strain vs. time plot from extensometer and embedded Fabry Perot sensor in a GFRP tendon subjected to a trapezoidal load at 60°C [Georgiades, 1998]
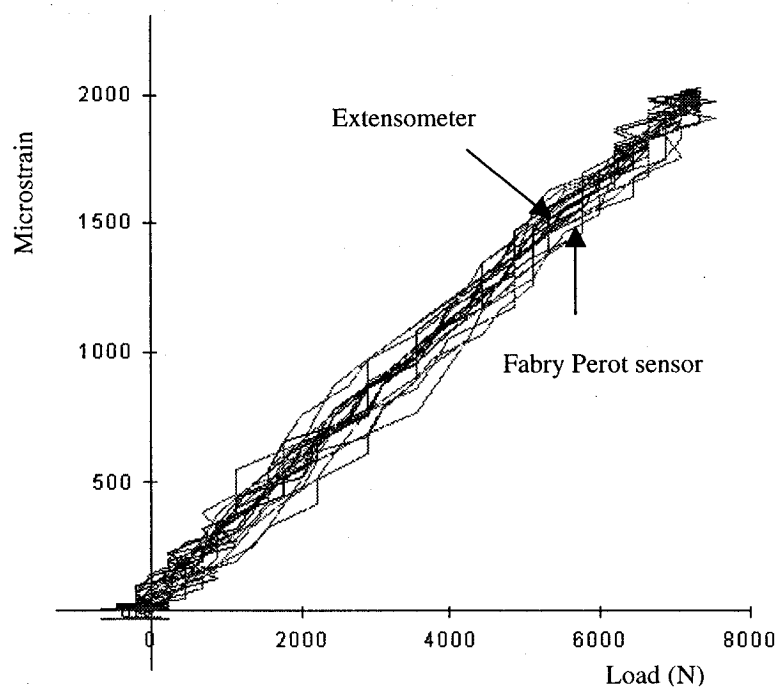
**Figure 5-10:** Strain from extensometer and embedded Fabry Perot sensor in a GFRP tendon subjected to a sinusoidal load at 60°C [Georgiades, 1998]
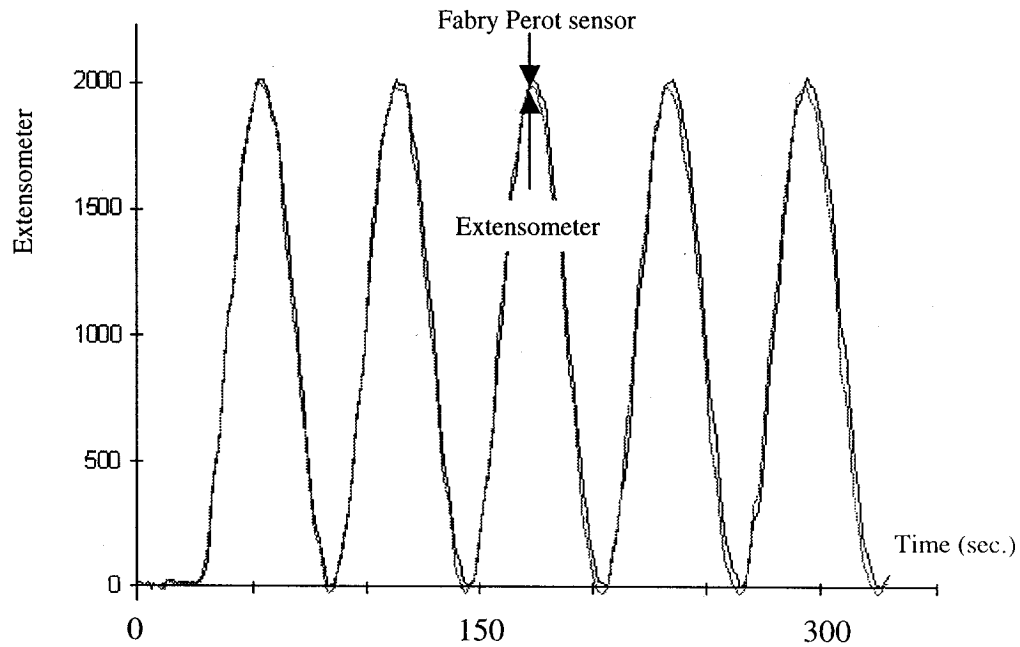


**Figure 5-11:** Strain vs. time plot from extensometer and embedded Fabry Perot sensor in a GFRP tendon subjected to a sinusoidal load at 60°C [Georgiades, 1998]
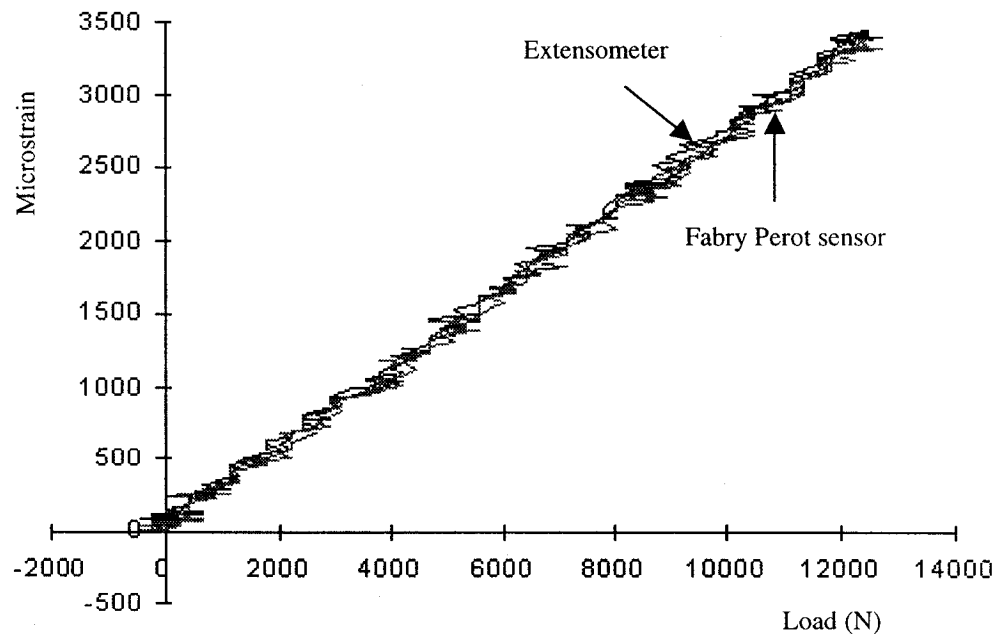
**Figure 5-12:** Strain from extensometer and embedded Fabry Perot sensor in a GFRP tendon subjected to a trapezoidal load at 60°C [Georgiades, 1998]
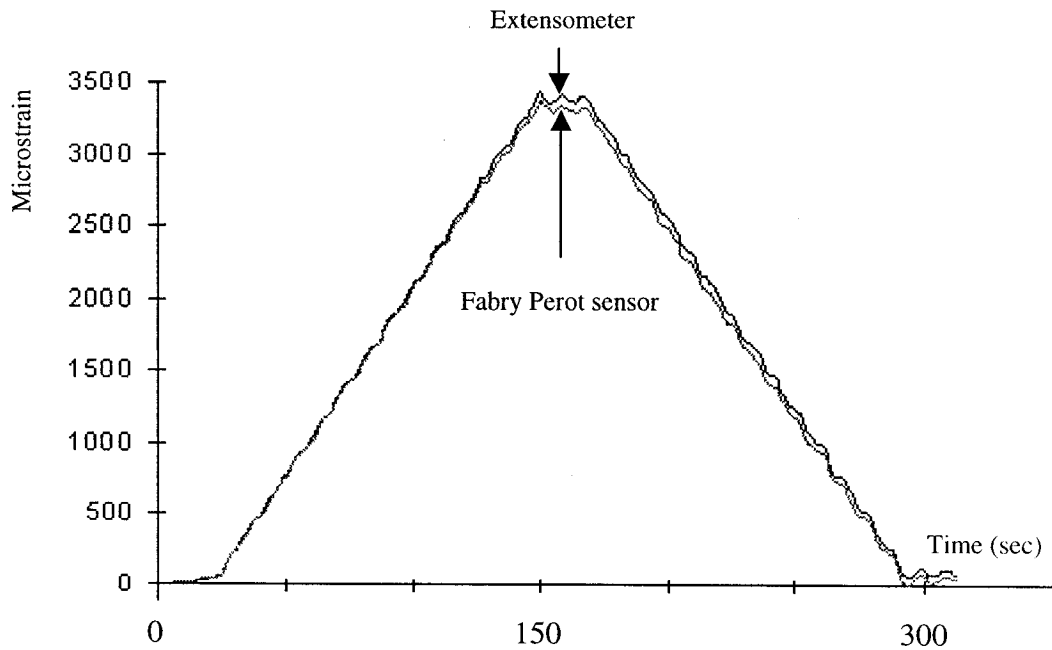
**Figure 5-13:** Strain vs. time plot from extensometer and embedded Fabry Perot sensor in a GFRP tendon subjected to a trapezoidal load at 60°C [Georgiades, 1998]
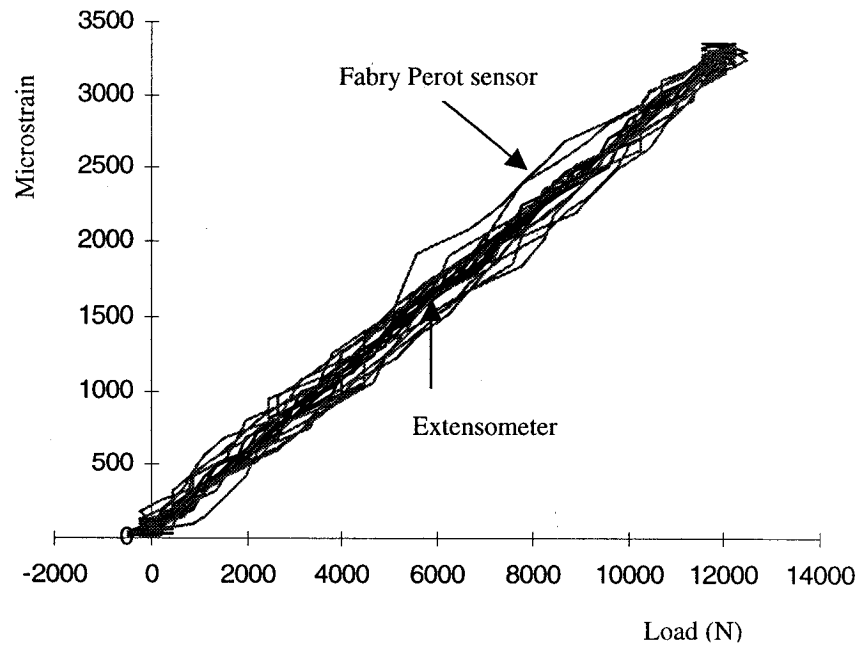
**Figure 5-14:** Strain from extensometer and embedded Fabry Perot sensor in a GFRP tendon subjected to a sinusoidal load at 60°C [Georgiades, 1998]
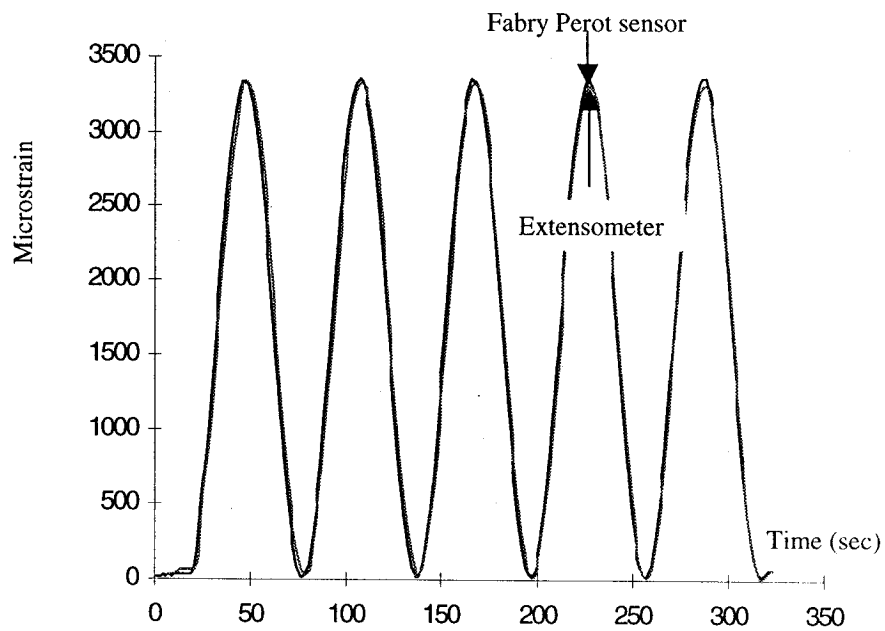


**Figure 5-15:** Strain vs. time plot from extensometer and embedded Fabry Perot sensor in a GFRP tendon subjected to a sinusoidal load at 60°C [Georgiades, 1998]

Subsequent to the high-temperature tests, the temperature chamber was cooled down (use was made of a carbon dioxide supply) and allowed to reach steady state at 0°C. The GFRP tendon was then subjected to sinusoidal and trapezoidal load waveforms as was done during previous tests. The amplitude of the first trapezoidal and sinusoidal tests was 8 kN, and the amplitude of the other two tests was 13 kN.
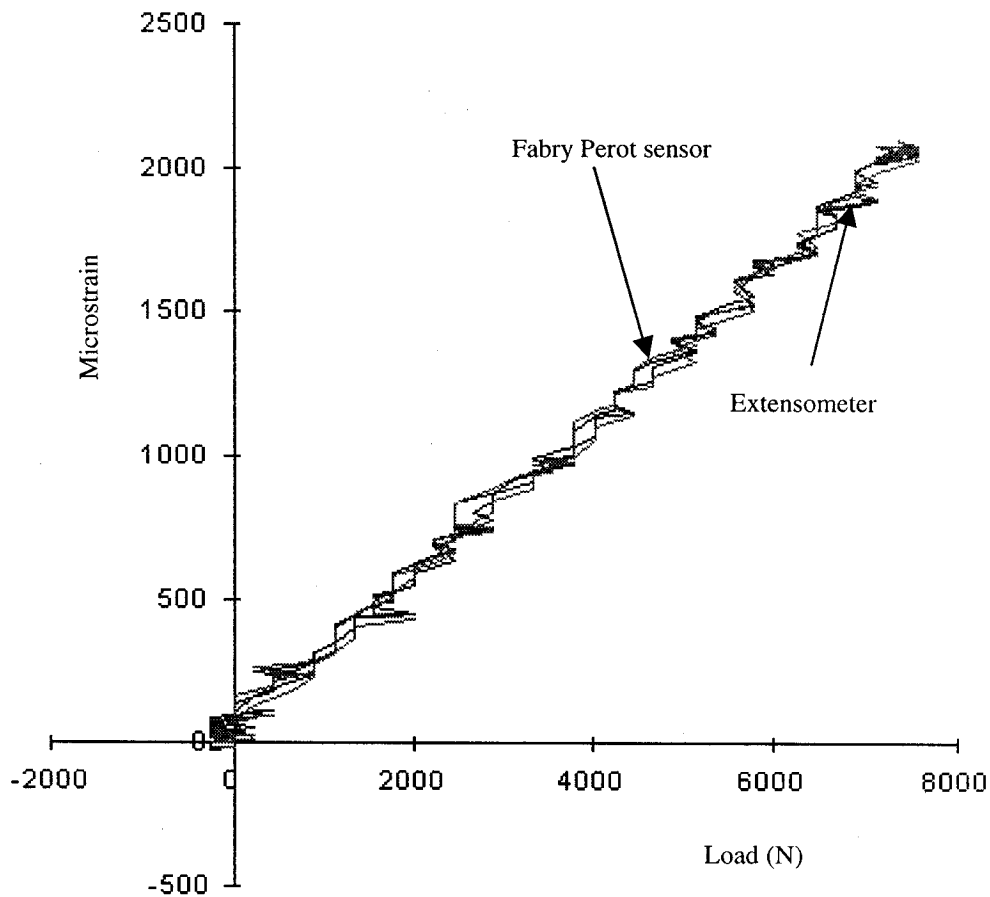


**Figure 5-16:** Strain from extensometer and embedded Fabry Perot sensor in a GFRP tendon subjected to a trapezoidal load at 0°C [Georgiades, 1998]

The microstrain vs. load results for the first trapezoidal test are shown in figure 5-16. As for the high temperature tests, the degree of conformance between the embedded Fabry Perot sensor and the extensometer is remarkable. Figure 5-17 is a plot of microstrain vs. time for the same test.
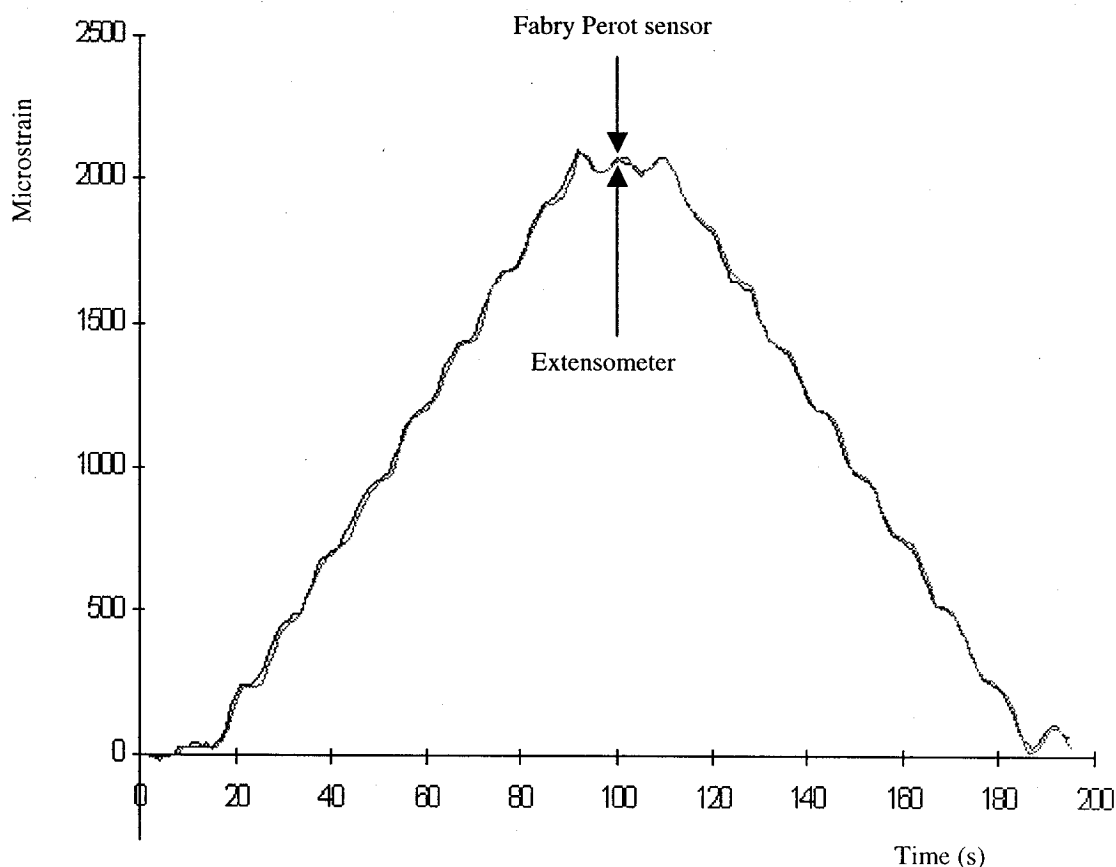
**Figure 5-17:** Strain vs. time plot from extensometer and embedded Fabry Perot sensor in a GFRP tendon subjected to a trapezoidal load at 0°C [Georgiades, 1998]

Since the thermal strains were factored out of all readings, one may compare Figures 5-16 and 5-17 with corresponding Figures 5-8 and 5-9. It is clear that the two sets of figures are essentially the same, and this reiterates the remarkable consistency and repeatability of the Fabry Perot sensor. It behaves just as reliably at 60°C, as it does at 0°C. The same conclusion is reached by observing the results pertaining to the first sinusoidal test at 0°C, Figures 5-18 and 5-19, and then comparing them with the corresponding Figures 5-10 and 5-11.

Figures 5-20 to 5-33 show the results from some of the remaining tests performed at 0°C, -20°C, and -40°C. They all support the conclusion that Fabry Perot sensors perform extremely well at low temperatures. Thus, on the basis of all the temperature tests

performed on the smart GFRP tendon, one can see that embedded Fabry Perot sensors perform just as accurately in the "-40°C to +60°C " range as they do at room temperature, and high or low temperatures do not represent an obstacle to their performance.
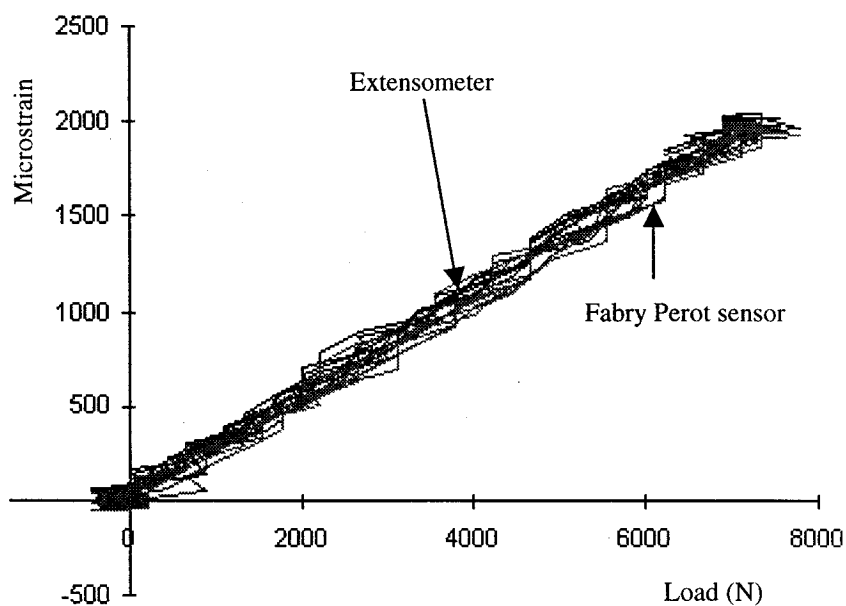


**Figure 5-18:** Strain from extensometer and embedded Fabry Perot sensor in a GFRP tendon subjected to a sinusoidal load at 0°C [Georgiades, 1998]
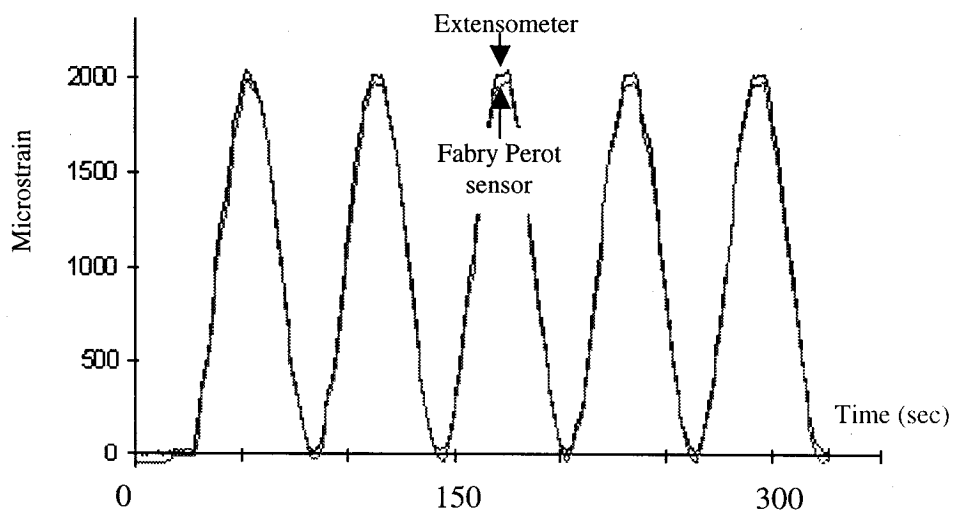


**Figure 5-19:** Strain vs. time plot from extensometer and embedded Fabry Perot sensor in a GFRP tendon subjected to a sinusoidal load at 0°C [Georgiades, 1998]
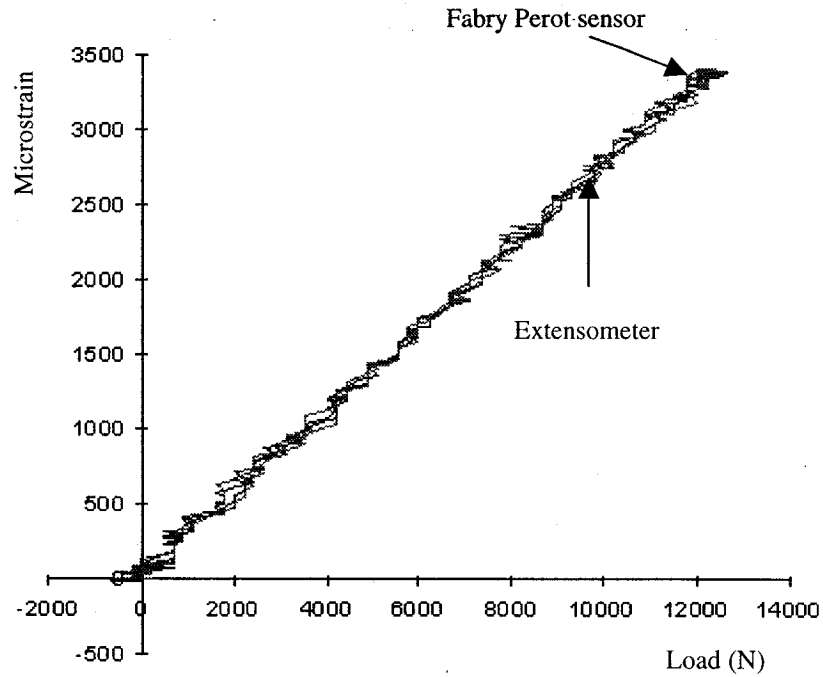
**Figure 5-20:** Strain from extensometer and embedded Fabry Perot sensor in a GFRP tendon subjected to a trapezoidal load at 0°C [Georgiades, 1998]
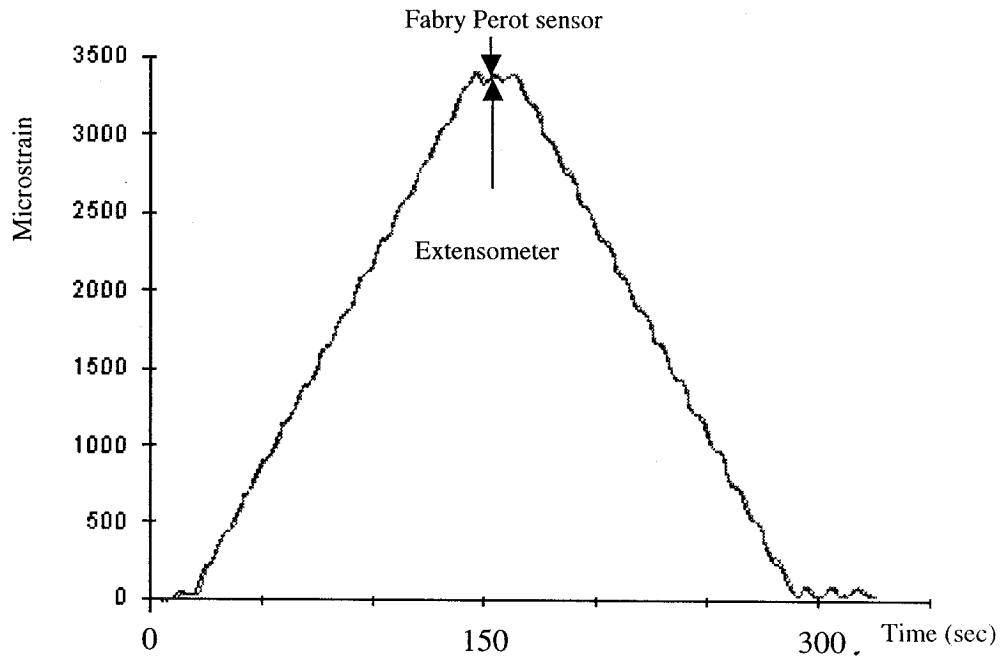


**Figure 5-21:** Strain vs. time plot from extensometer and embedded Fabry Perot sensor in a GFRP tendon subjected to a trapezoidal load at 0°C [Georgiades, 1998]
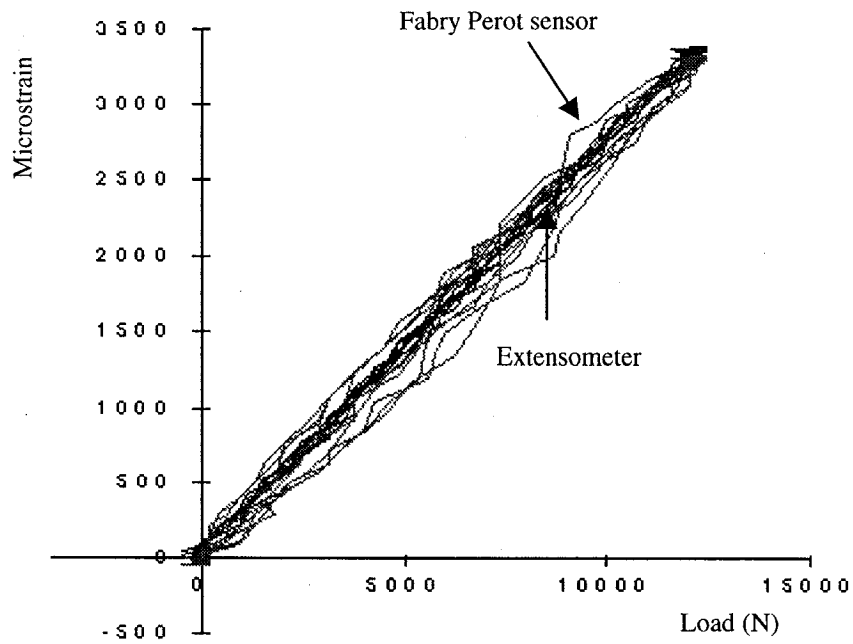
**Figure 5-22:** Strain from extensometer and embedded Fabry Perot sensor in a GFRP tendon subjected to a sinusoidal load at $0^{\circ}C$ [Georgiades, 1998]



**Figure 5-23:** Strain vs. time plot from extensometer and embedded Fabry Perot sensor in a GFRP tendon subjected to a sinusoidal load at $0^{\circ}C$ [Georgiades, 1998]
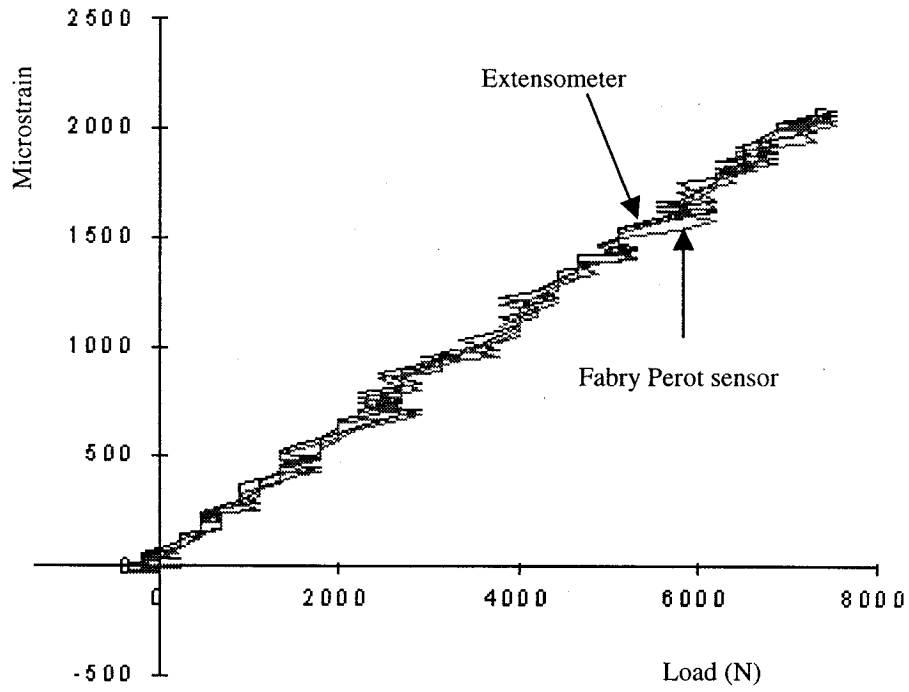
**Figure 5-24:** Strain from extensometer and embedded Fabry Perot sensor in a GFRP tendon subjected to a trapezoidal load at -20°C [Georgiades, 1998]



**Figure 5-25:** Strain vs. time plot from extensometer and embedded Fabry Perot sensor in a GFRP tendon subjected to a trapezoidal load at -20°C [Georgiades, 1998]

**Figure 5-26:** Strain from extensometer and embedded Fabry Perot sensor in a GFRP tendon subjected to a trapezoidal load at -20°C [Georgiades, 1998]



**Figure 5-27:** Strain vs. time plot from extensometer and embedded Fabry Perot sensor in a GFRP tendon subjected to a trapezoidal load at -20°C [Georgiades, 1998]

**Figure 5-28:** Strain from extensometer and embedded Fabry Perot sensor in a GFRP tendon subjected to a trapezoidal load at -40°C [Georgiades, 1998]



**Figure 5-29:** Strain vs. time plot from extensometer and embedded Fabry Perot sensor in a GFRP tendon subjected to a trapezoidal load at -40°C [Georgiades, 1998]
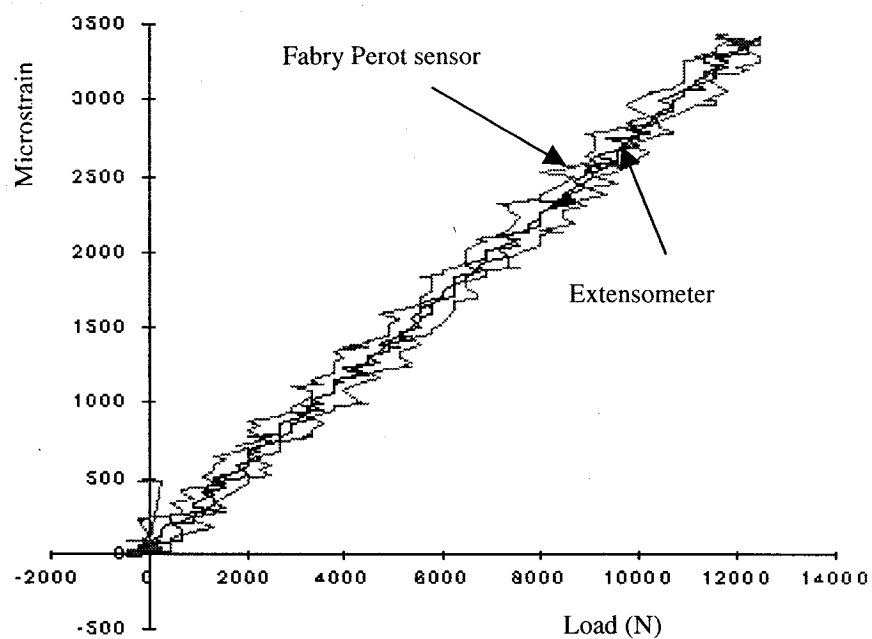
**Figure 5-30:** Strain from extensometer and embedded Fabry Perot sensor in a GFRP tendon subjected to a trapezoidal load at -40°C [Georgiades, 1998]
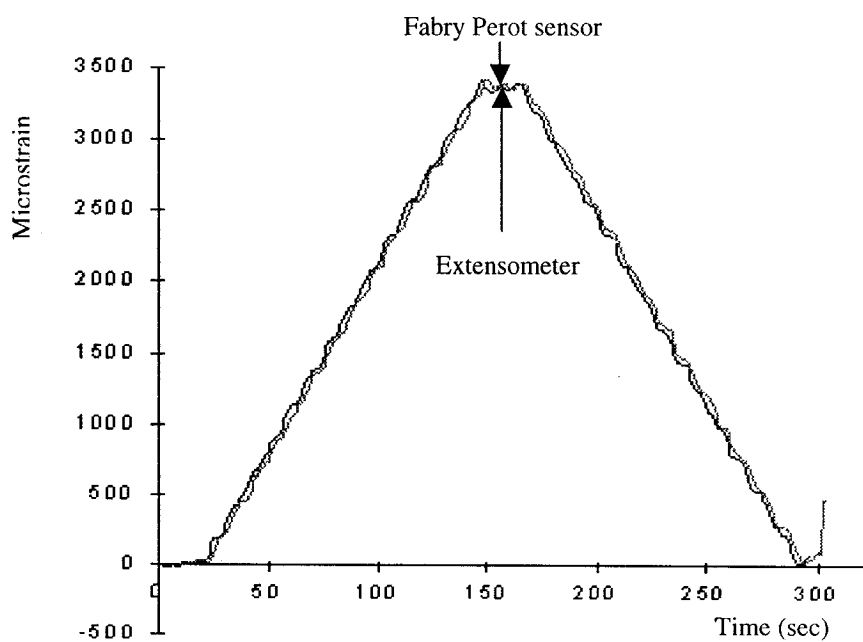


**Figure 5-31:** Strain vs. time plot from extensometer and embedded Fabry Perot sensor in a GFRP tendon subjected to a trapezoidal load at -40°C [Georgiades, 1998]
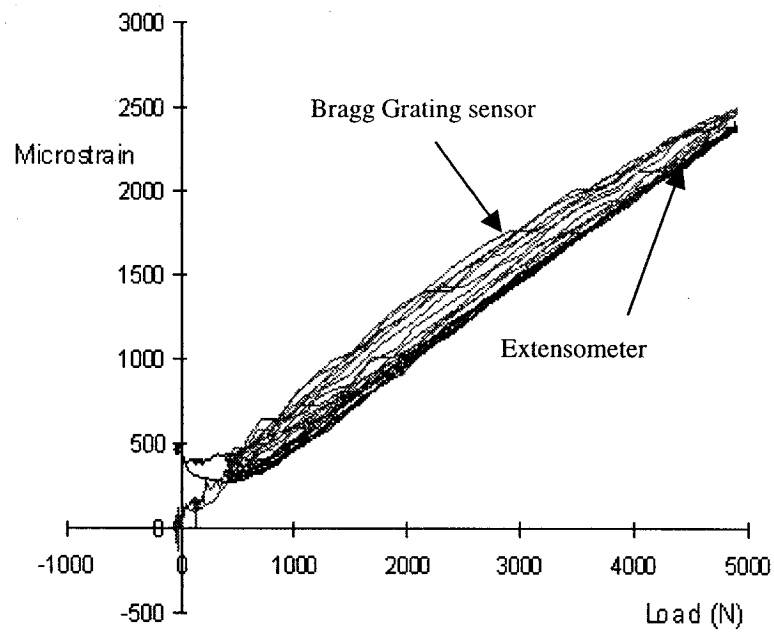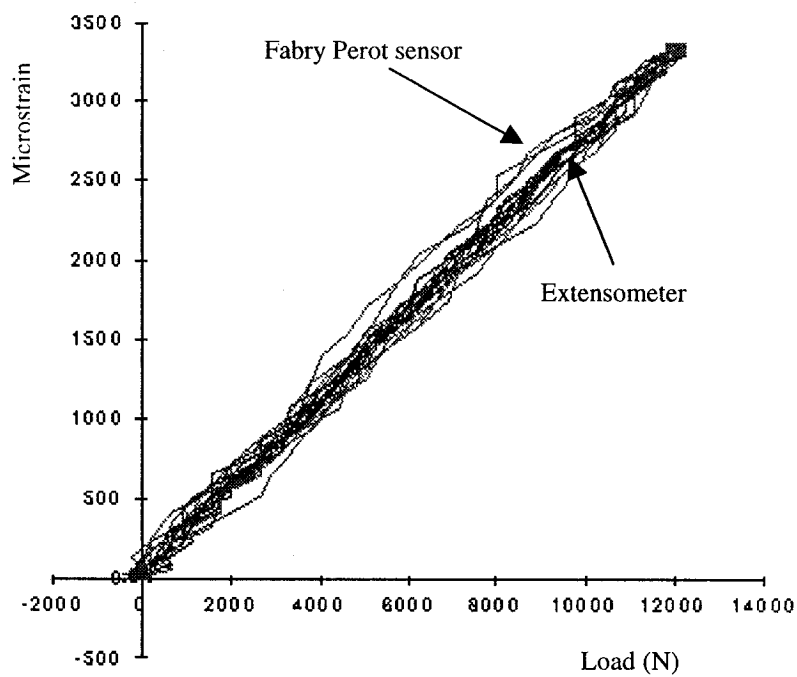
**Figure 5-32:** Strain from extensometer and embedded Fabry Perot sensor in a GFRP tendon subjected to a sinusoidal load at -40°C [Georgiades, 1998]



**Figure 5-33:** Strain vs. time plot from extensometer and embedded Fabry Perot sensor in a GFRP tendon subjected to a sinusoidal load at -40°C [Georgiades, 1998]

## 5.3 Temperature Tests on CFRP Tendons with Embedded Fabry Perot Sensors

The experiments described in the previous pages all indicated that Fabry Perot sensors embedded in GFRP tendons performed very well under conditions of high or low temperature. To further assess the behavior of these sensors, it was decided to repeat the testing protocol with a CFRP tendon and an embedded sensor. Thus, a Fabry Perot sensor was prereinforced according to the procedure described in Section 3.4 and then embedded in a CFRP rod during pultrusion. The smart tendon was subsequently cut to the desired length, and had two spelter sockets fitted at the ends as described in Section 3.5. The sensor fiber optic lead was protected by a Kevlar-reinforced jacket (see Section 3.5). The final product was now ready for testing, and was mounted in the same MTS frame at "PSC Analytical" as its glass counterpart. Sinusoidal and trapezoidal load waveforms were then preprogrammed on the Instron controller and testing began.
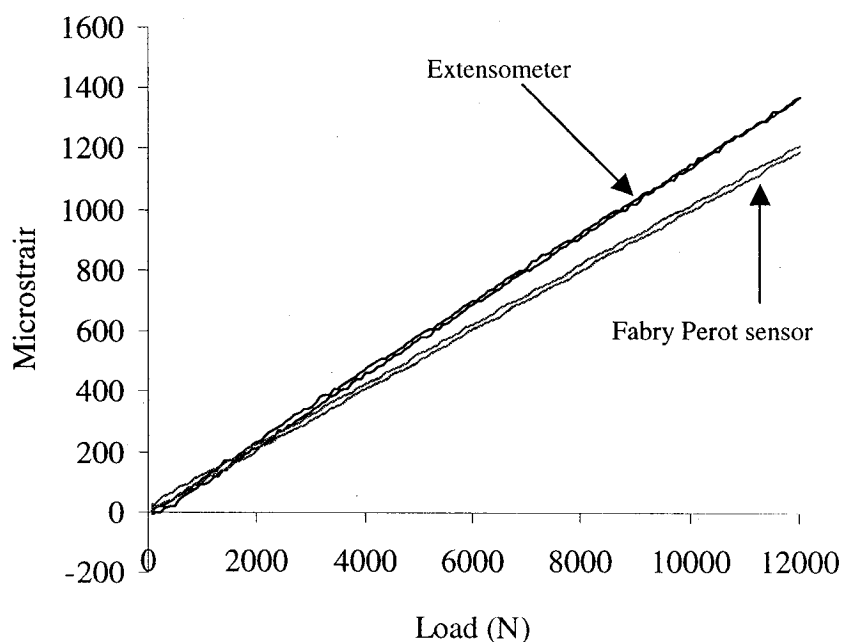
**Figure 5-34:** Strain from extensometer and embedded Fabry Perot sensor in a CFRP tendon subjected to a trapezoidal load at room temperature
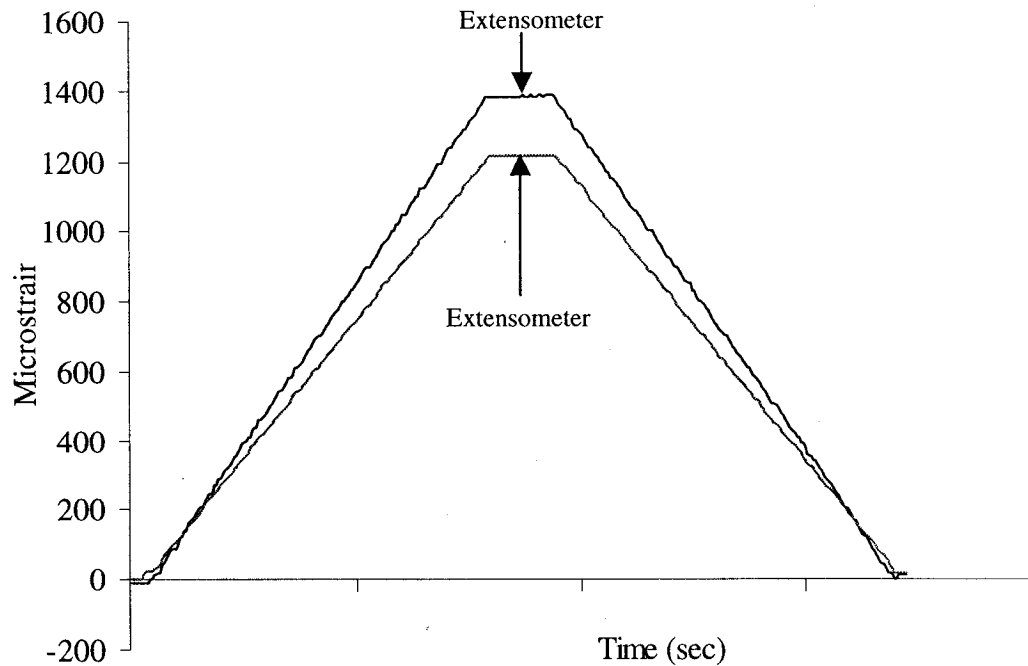
**Figure 5-35:** Strain vs. time plot from extensometer and embedded Fabry Perot sensor in a CFRP tendon subjected to a trapezoidal load at room temperature

The first set of tests involved trapezoidal and sinusoidal loads at ordinary laboratory conditions (26°C). Figure 5-34 is a microstrain vs. load plot pertaining to the trapezoidal test. There is a discrepancy of around 150 microstrain between the extensometer and the Fabry Perot sensor, with the extensometer readings being higher. One possibility that could explain this is a misalignment between the spelter sockets and the tendon. Reference to the procedure for attachment of the spelter sockets in Section 3.5 will show that it is quite difficult to align them perfectly with the rod. In fact, for most of the pultruded tendons used during the research, there was some misalignment present. Consequently, when the tendon is mounted in the load frame, it will also experience bending strains in addition to the axial ones. Thus, if the extensometer is attached on the side that experiences tensile flexural stresses, it will record larger strains. The Fabry Perot sensor however, will be insensitive to bending since it is embedded in essentially the middle of the rod. The results from the remaining tests will shed more light as to whether

this is a viable explanation for the observed discrepancy. Figure 5-35 is a microstrain vs. time plot of the same data.



**Figure 5-36:** Strain from extensometer and embedded Fabry Perot sensor in a CFRP tendon subjected to a sinusoidal load at room temperature

The smart tendon was then subjected to a sinusoidal test at room temperature. The microstrain vs. load plot is shown in Figure 5-36 and the microstrain vs. time plot in Figure 5-37. One can observe from these plots that the extensometer readings are a little higher than the corresponding sensor readings, the discrepancy being equal to about 120 microstrain at the peak applied load. The level of this discrepancy is similar to that pertaining to the trapezoidal test (Figures 5-34 and 5-35) which further indicates that the extensometer is "picking up" flexural strains in addition to axial strains. These flexural

strains could be avoided by moving the extensometer around the tendon (for example four locations spaced at 90° intervals) and averaging the results.
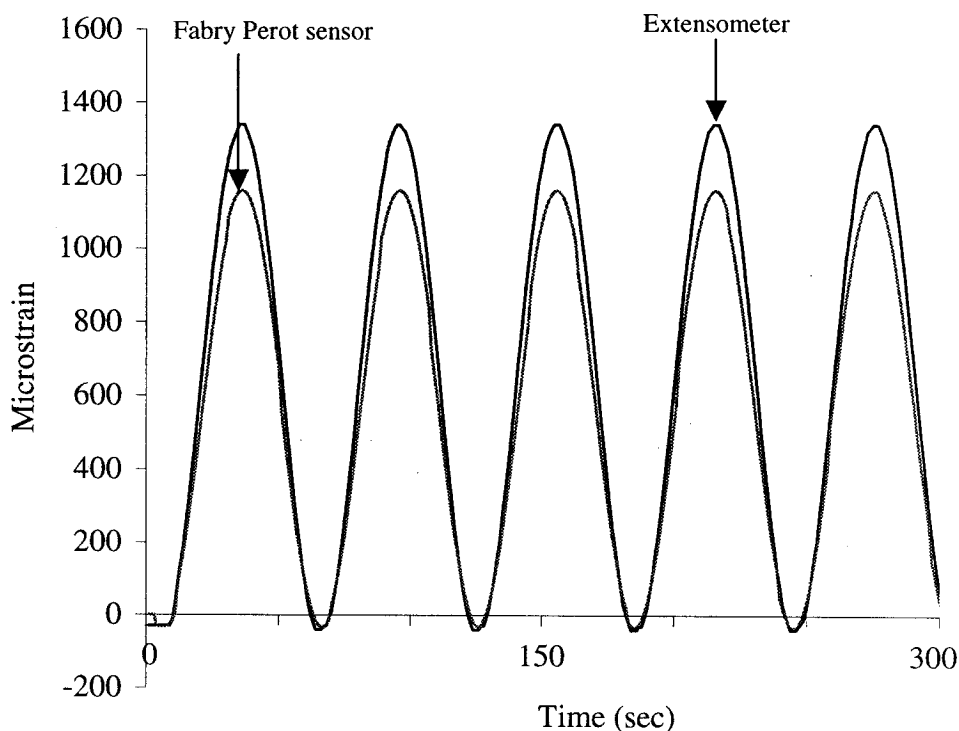


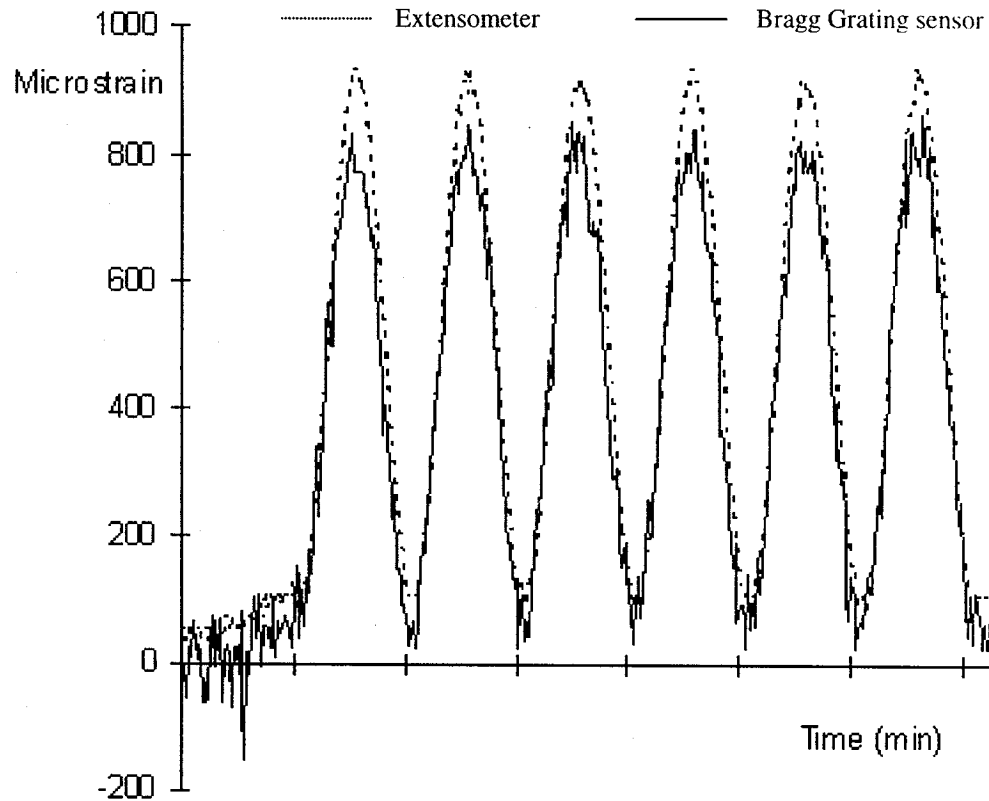**Figure 5-37:** Strain vs. time plot from extensometer and embedded Fabry Perot sensor in a CFRP tendon subjected to a sinusoidal load at room temperature

The temperature in the chamber was subsequently raised to 40°C and allowed to reach steady state. The thermal strain induced by this temperature increase was factored out of both the extensometer and the sensor outputs, as was done for the case of the GFRP tendon in the previous section. The tendon was then subjected to the same sinusoidal and trapezoidal tests as those performed at room temperature. The results from the trapezoidal test are shown in Figures 5-38 and 5-39 and those from the sinusoidal test are shown in Figures 5-40 and 5-41. Comparison of these with Figures 5-34 to 55-37 will reveal essentially the same extensometer and Fabry Perot readings. Thus, raising the temperature to 40°C does not seem to affect the consistency and reliability of the

embedded Fabry Perot sensor, which exhibits a good degree of conformance with the extensometer. The extensometer readings are in both cases about 140 microstrain higher, indicating that it was indeed clipped on the "tension" side of the tendon's bending.
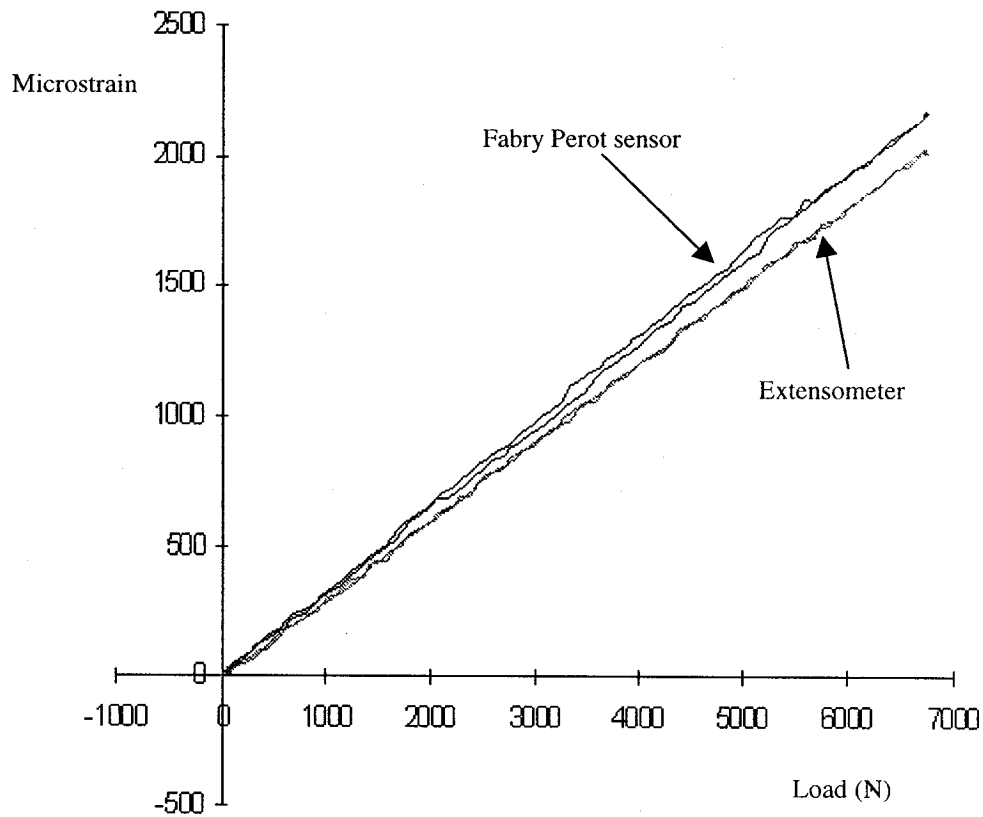


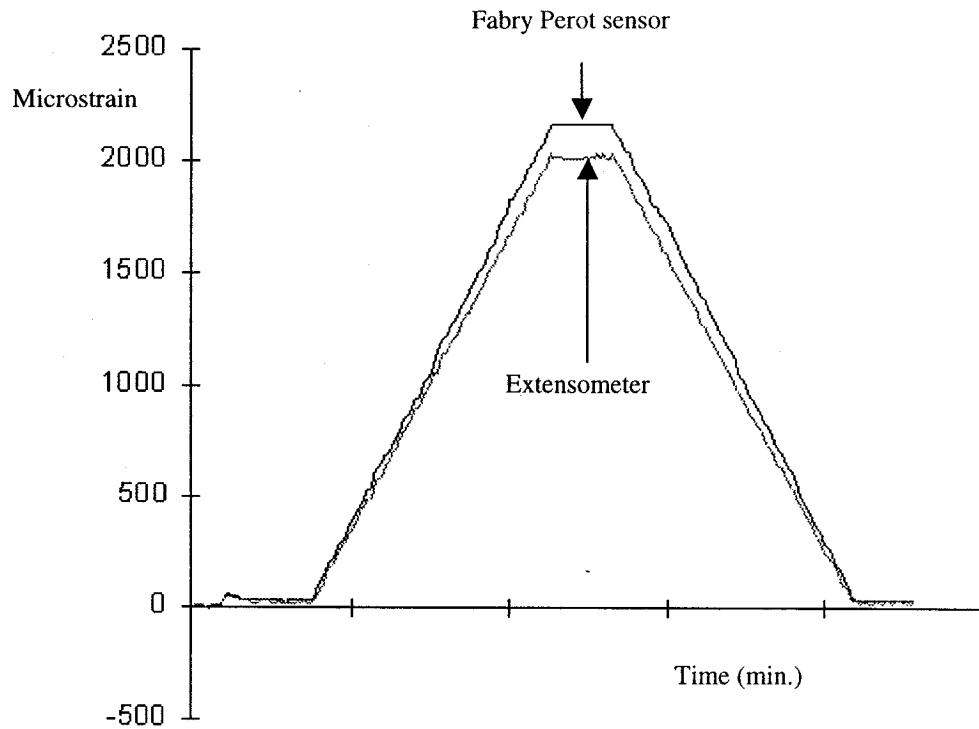**Figure 5-38:** Strain from extensometer and embedded Fabry Perot sensor in a CFRP tendon subjected to a trapezoidal load at 40°C



**Figure 5-39:** Strain vs. time plot from extensometer and embedded Fabry Perot sensor in a CFRP tendon subjected to a trapezoidal load at 40°C
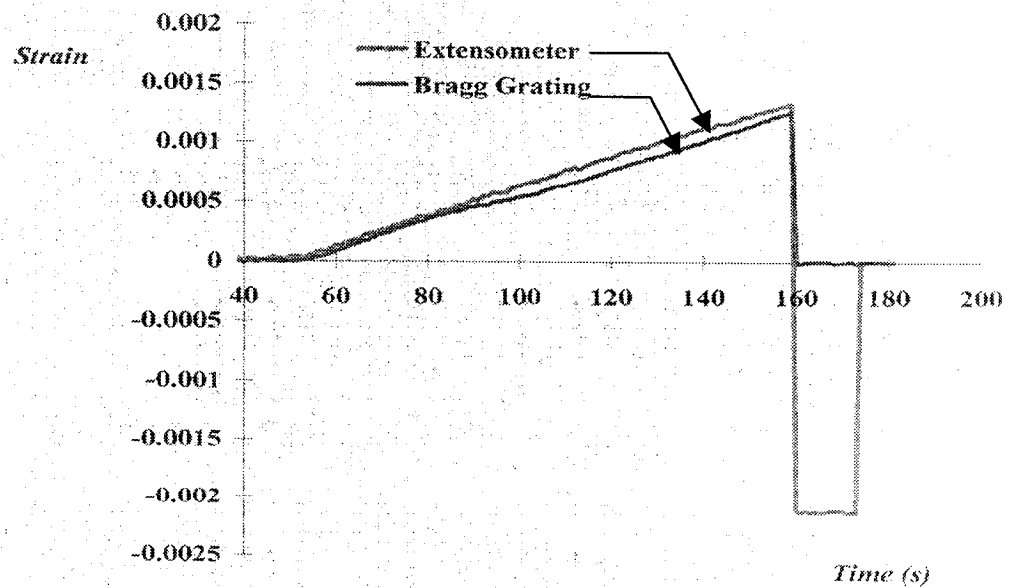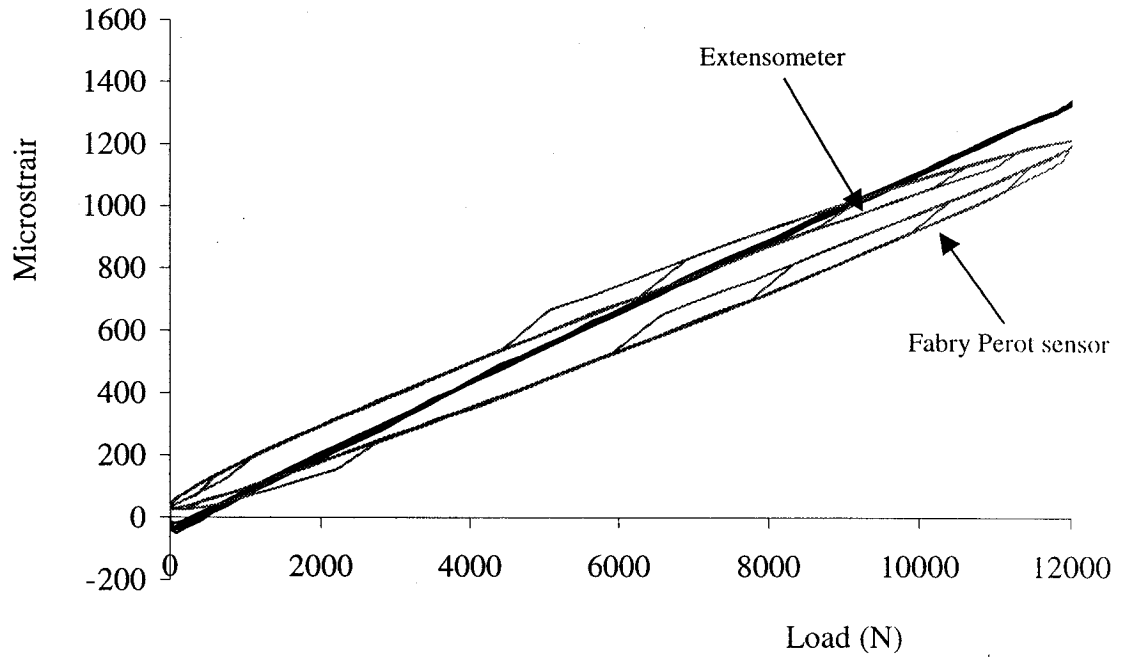
**Figure 5-40:** Strain from extensometer and embedded Fabry Perot sensor in a CFRP tendon subjected to a sinusoidal load at 40°C
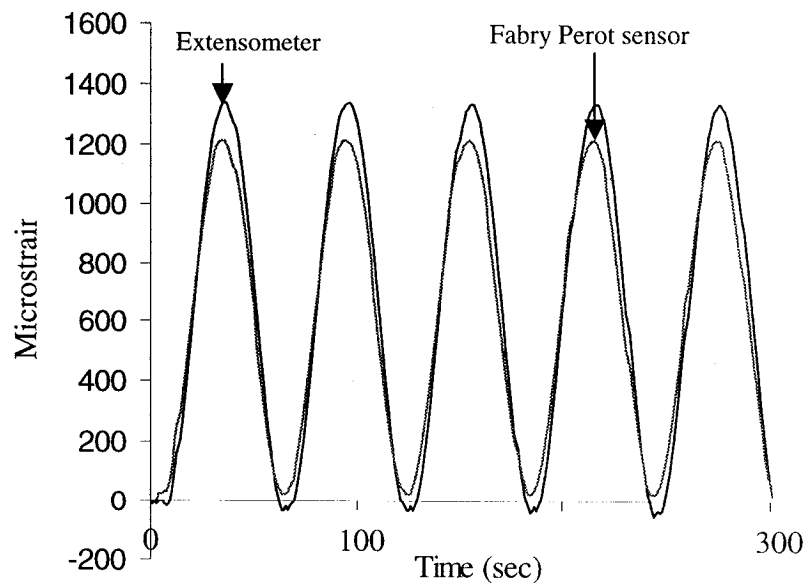


**Figure 5-41:** Strain vs. time plot from extensometer and embedded Fabry Perot sensor in a CFRP tendon subjected to a sinusoidal load at 40°C

Subsequently to the high temperature tests, the carbon dioxide supply was switched on and the chamber was gradually cooled down to 0°C, at which point it was allowed to reach steady state as evidenced by the thermocouple readings recorded by the data acquisition program. The same tests that were conducted at high temperatures would now be conducted at low temperatures as well. Figure 5-42 shows the microstrain vs. load results pertaining to a trapezoidal test at 0°C.
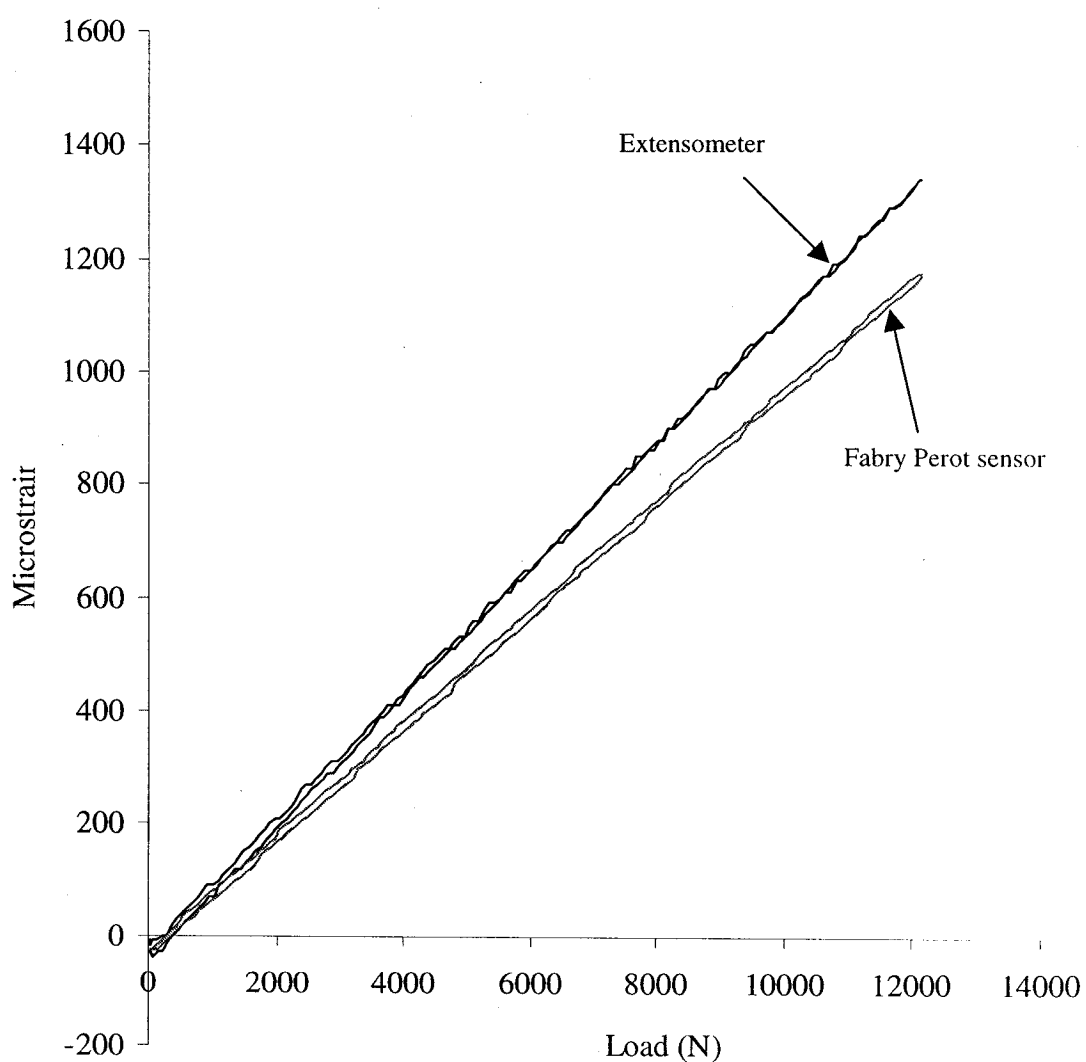


**Figure 5-42:** Strain from extensometer and embedded Fabry Perot sensor in a CFRP tendon subjected to a trapezoidal load at 0°C

As for the previous tests one can observe that there is a good agreement between the extensometer and the Fabry Perot sensor, the discrepancy between the two increasing as the load is increased. As the corresponding microstrain vs. time graph of Figure 5-43 shows the discrepancy at the peak load is around 170 microstrain.
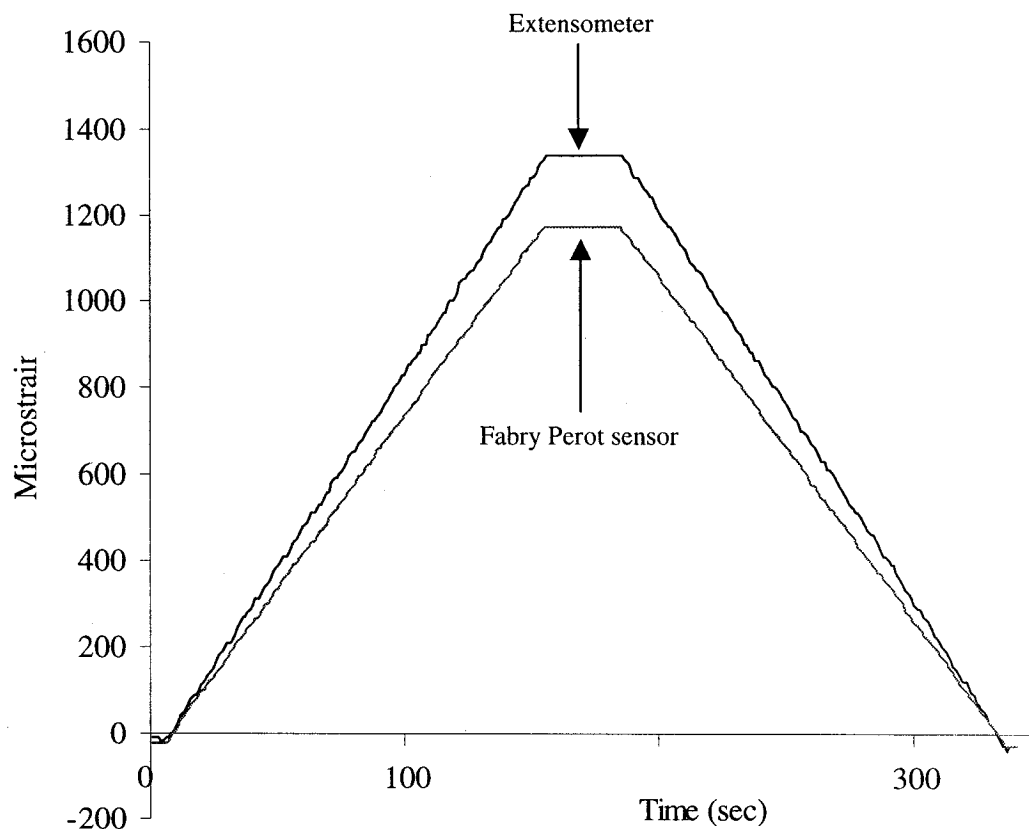


**Figure 5-43:** Strain vs. time plot from extensometer and embedded Fabry Perot sensor in a CFRP tendon subjected to a sinusoidal load at 0°C

It can be observed from a comparison of Figures 5-42 and 5-43 with corresponding sets such as Figures 5-34 and 5-35 or Figures 5-38 and 5-39, that the Fabry Perot sensor is very consistent and repeatable irrespective of the ambient temperature.

Figures 5-44 and 5-45 show the results from the sinusoidal test at 0°C.
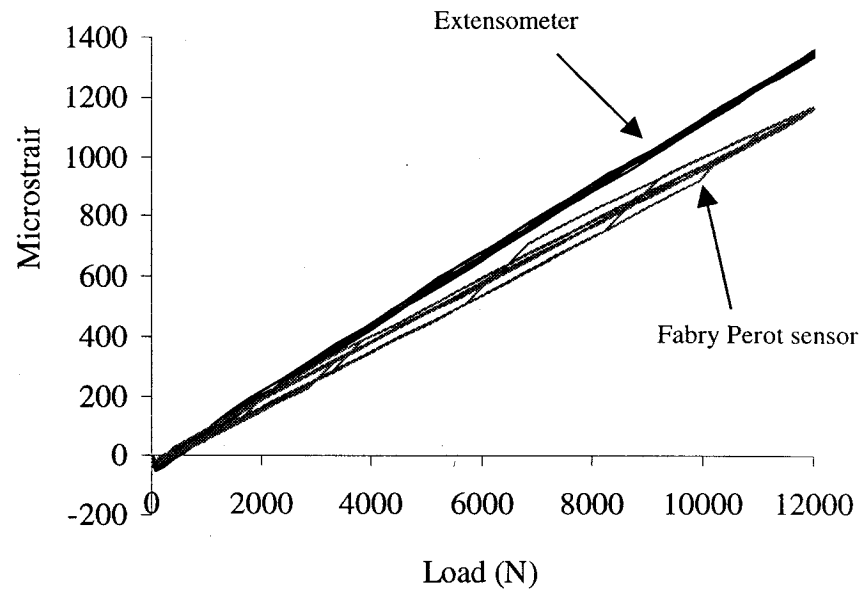


**Figure 5-44:** Strain from extensometer and embedded Fabry Perot sensor in a CFRP tendon subjected to a sinusoidal load at 0°C
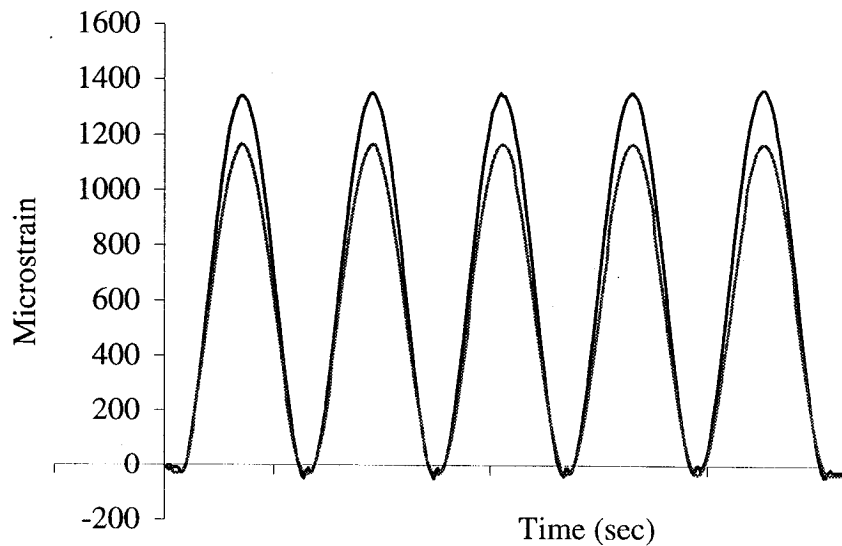


**Figure 5-45:** Strain vs. time plot from extensometer and embedded Fabry Perot sensor in a CFRP tendon subjected to a sinusoidal load at 0°C

Figures 5-46 to 5-53 depict the results from the remaining tests performed at temperatures equal to –20°C and –40°C.
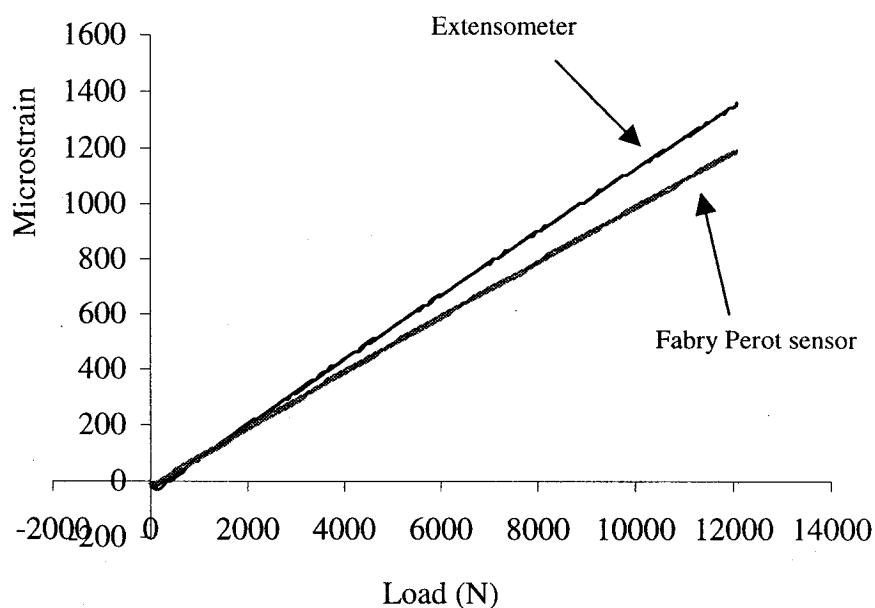


**Figure 5-46:** Strain from extensometer and embedded Fabry Perot sensor in a CFRP tendon subjected to a trapezoidal load at -20°C
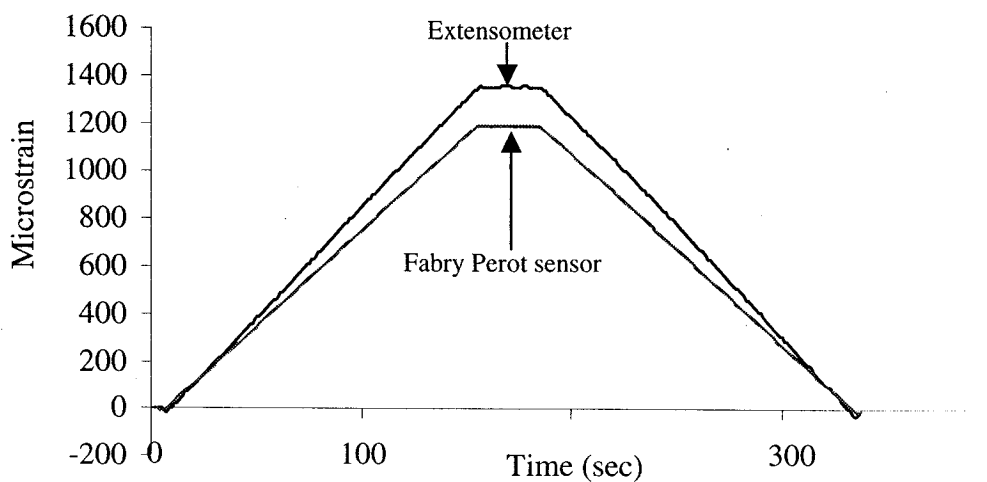


**Figure 5-47:** Strain vs. time plot from extensometer and embedded Fabry Perot sensor in a CFRP tendon subjected to a trapezoidal load at -20°C
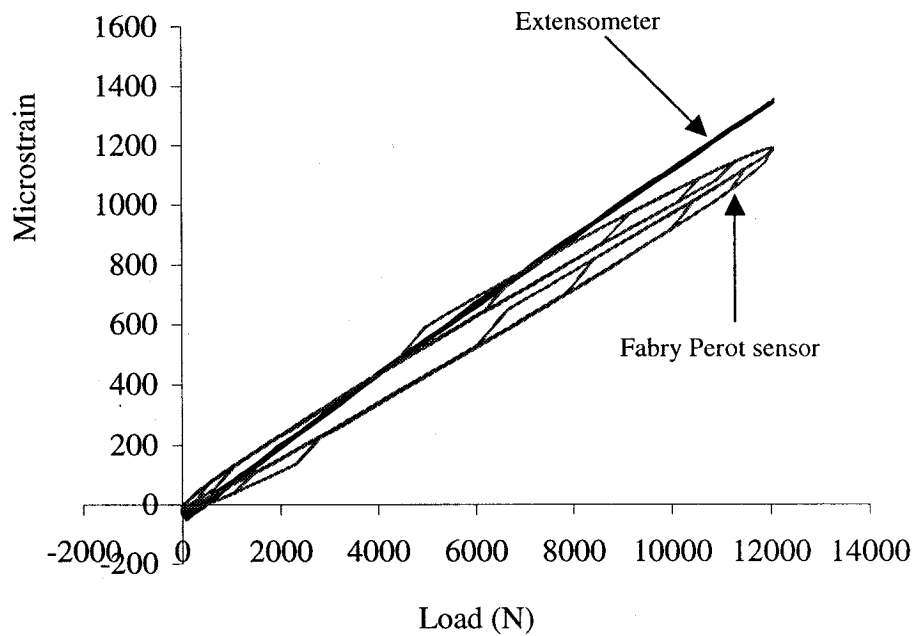
**Figure 5-48:** Strain from extensometer and embedded Fabry Perot sensor in a CFRP tendon subjected to a sinusoidal load at -20°C
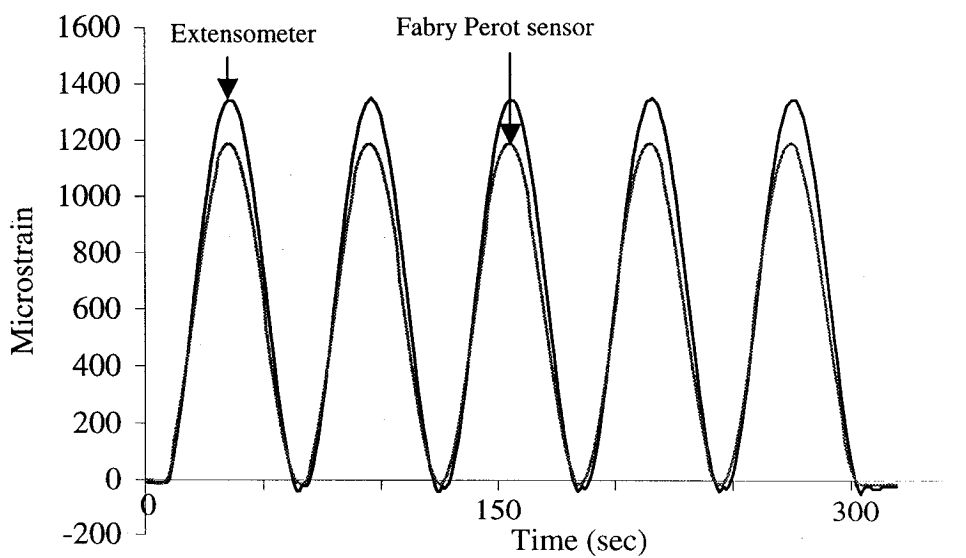


**Figure 5-49:** Strain vs. time plot from extensometer and embedded Fabry Perot sensor in a CFRP tendon subjected to a sinusoidal load at -20°C
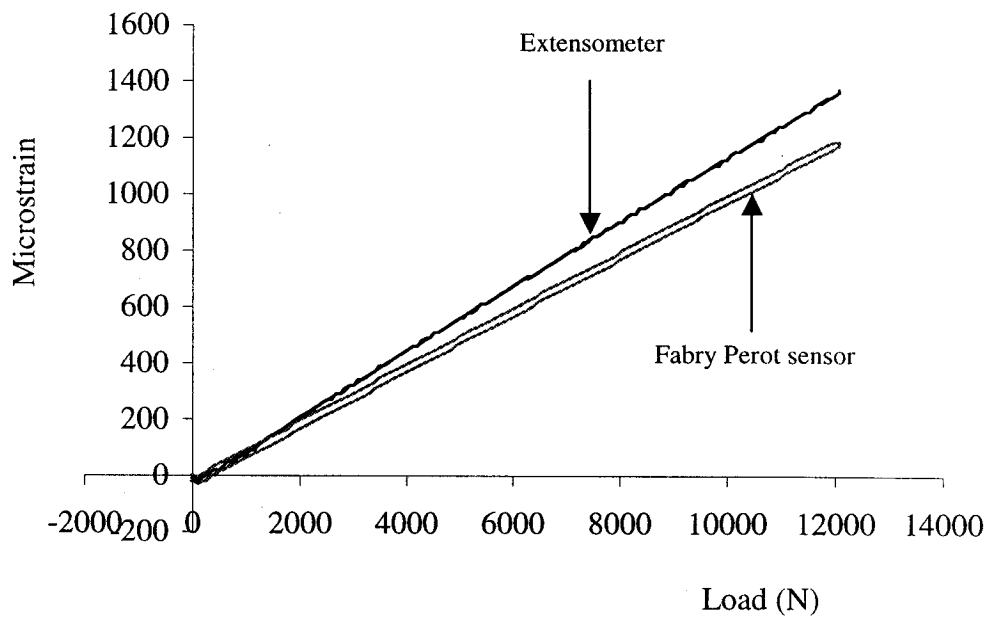
**Figure 5-50:** Strain from extensometer and embedded Fabry Perot sensor in a CFRP tendon subjected to a trapezoidal load at -40°C
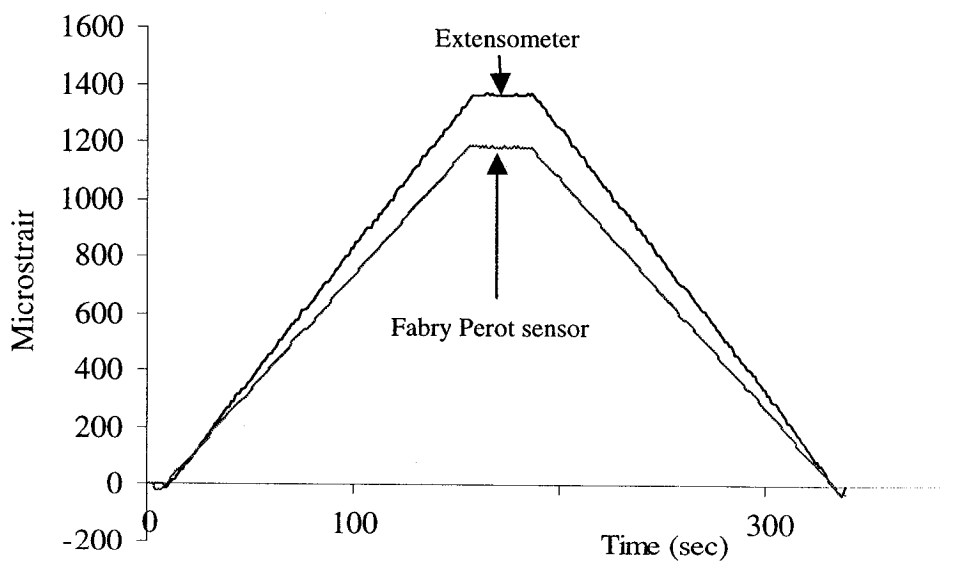


**Figure 5-51:** Strain vs. time plot from extensometer and embedded Fabry Perot sensor in a CFRP tendon subjected to a trapezoidal load at -40°C
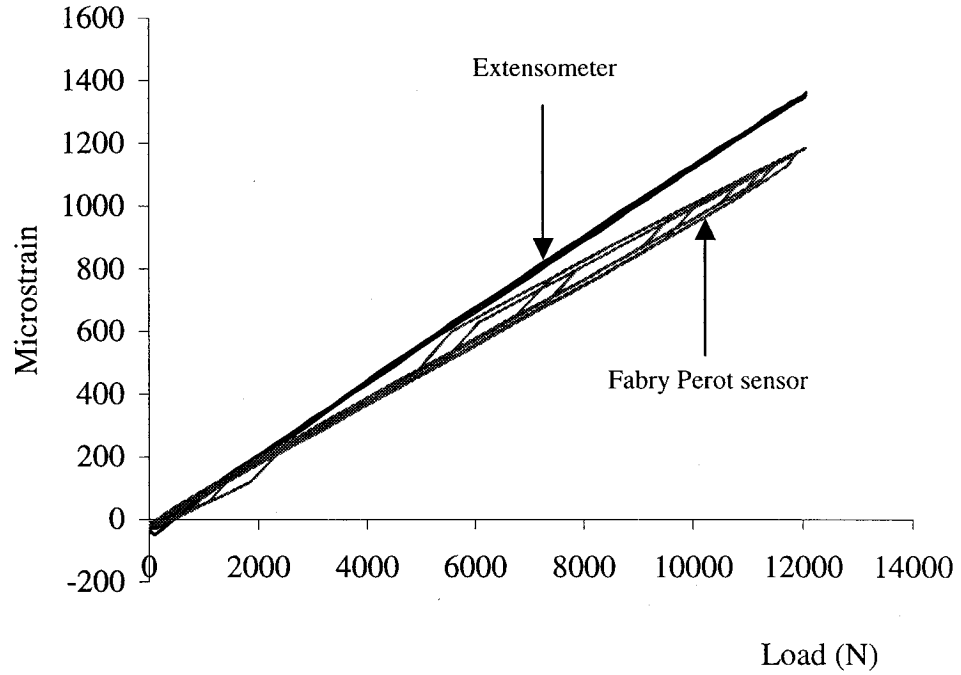
**Figure 5-52:** Strain from extensometer and embedded Fabry Perot sensor in a CFRP tendon subjected to a sinusoidal load at -40°C
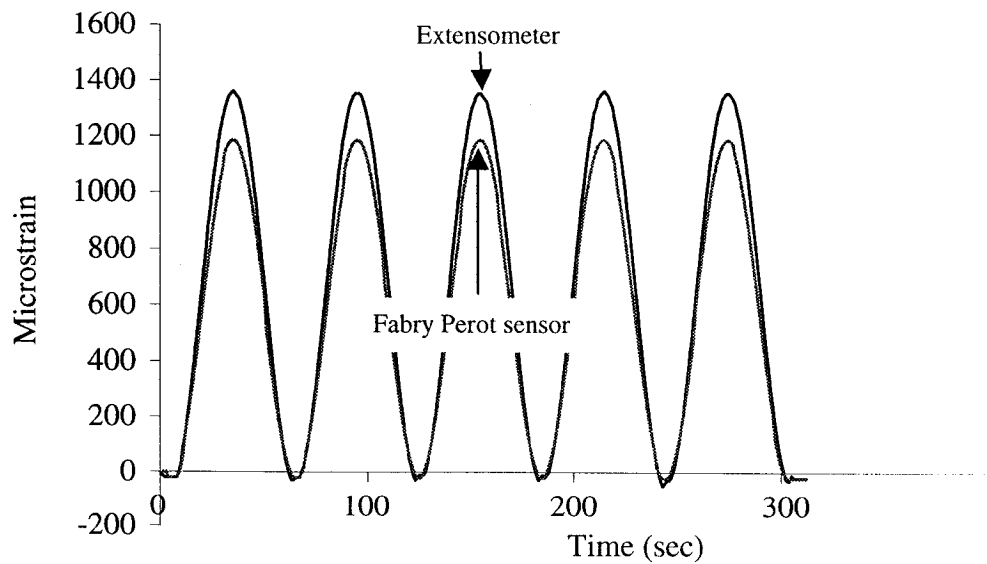


**Figure 5-53:** Strain vs. time plot from extensometer and embedded Fabry Perot sensor in a CFRP tendon subjected to a sinusoidal load at -40°C

On completion of the temperature tests on the smart CFRP tendons, it was evident that the embedded Fabry Perot sensor performed very well at both high and sub-zero temperatures. The sensor exhibited remarkable consistency and repeatability, so that the strain output from a test at a particular temperature was essentially indistinguishable from that pertinent to the same test performed at a different temperature.

Furthermore, it was observed that whereas the sensor readings agreed well with the corresponding extensometer readings, there was, nevertheless, a discrepancy of about 140-180 microstrain between the two strain-monitoring devices. It was surmised that the most likely reason behind this discrepancy was the misalignment between the spelter sockets and the extensometer. Thus, the test frame was imparting a small bending load on the CFRP tendon, in addition to the desired axial load. This idea was further reinforced by the fact that the discrepancy between the two devices was increasing almost linearly with a corresponding increase in the load.

It would be of interest to compare the two strain outputs with the theoretical output obtained by using:

$$\varepsilon = \frac{P}{AE} \tag{5.1}$$

where P is the mechanical load (N), A is the cross-sectional area of the tendons (9.5 mm$^2$), and E is the longitudinal tensile modulus of the CFRP tendons with an embedded sensor (see Table 4-1). Figures 5-54 and 5-55 show the results from another test performed on the CFRP tendon. It is seen that even though the discrepancy between the extensometer and the Fabry Perot sensor was still around 150 microstrain at the peak load, the discrepancy between the theoretical and the sensor readings was negligible. Thus, one is reasonably confident that the extensometer readings during the tests described in this section represent a combination of tensile and flexural strains, and that the Fabry Perot output is indeed very accurate.

Consequently, on the basis of the results obtained in Sections 5.2 and 5.3, it is clear that Fabry Perot sensors embedded in GFRP and CFRP tendons perform just as accurately and reliably in high- and low-temperature environments as they do under ordinary laboratory conditions.
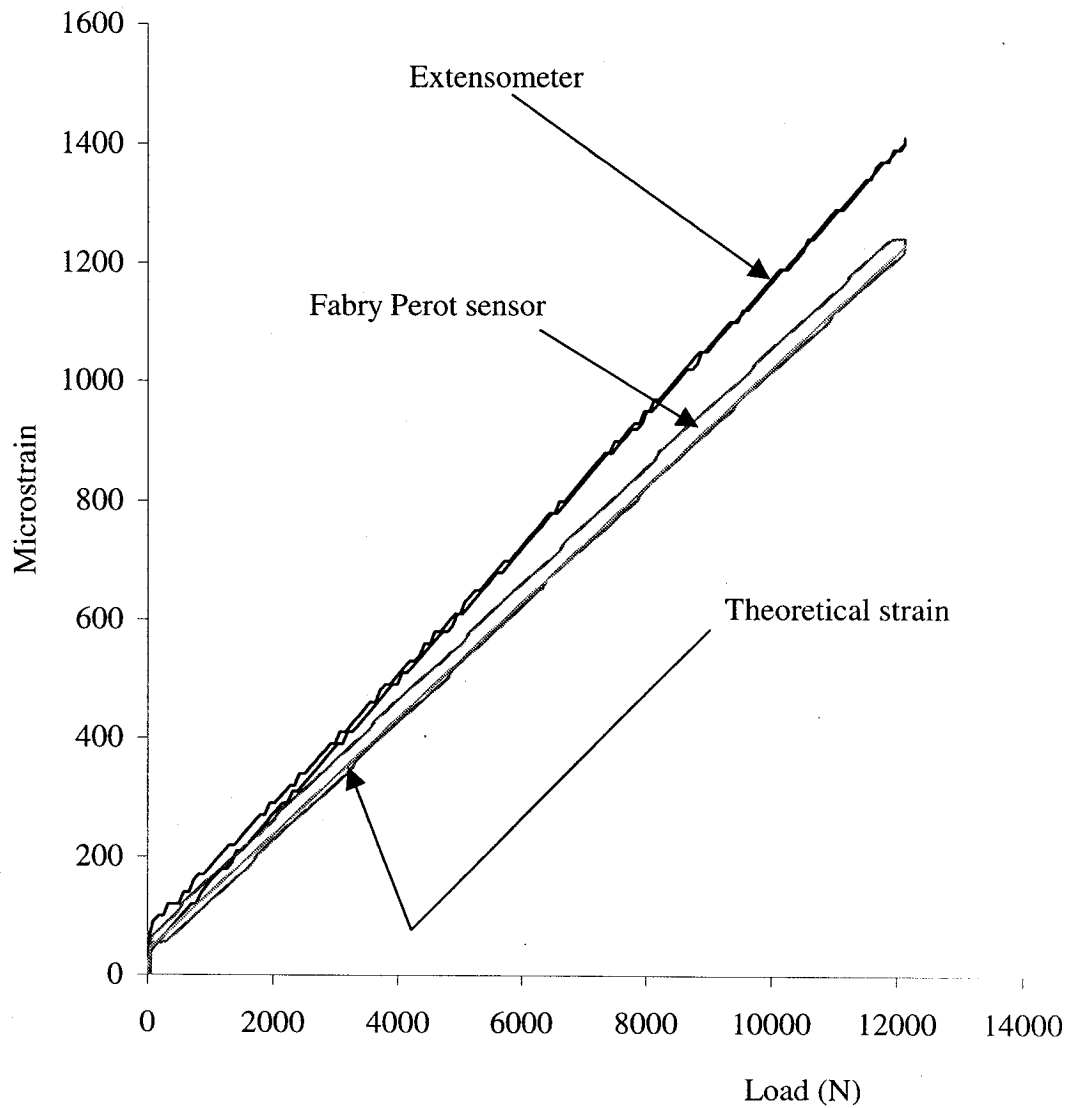


**Figure 5-54:** Strain from extensometer and embedded Fabry Perot sensor in a CFRP tendon subjected to a trapezoidal load
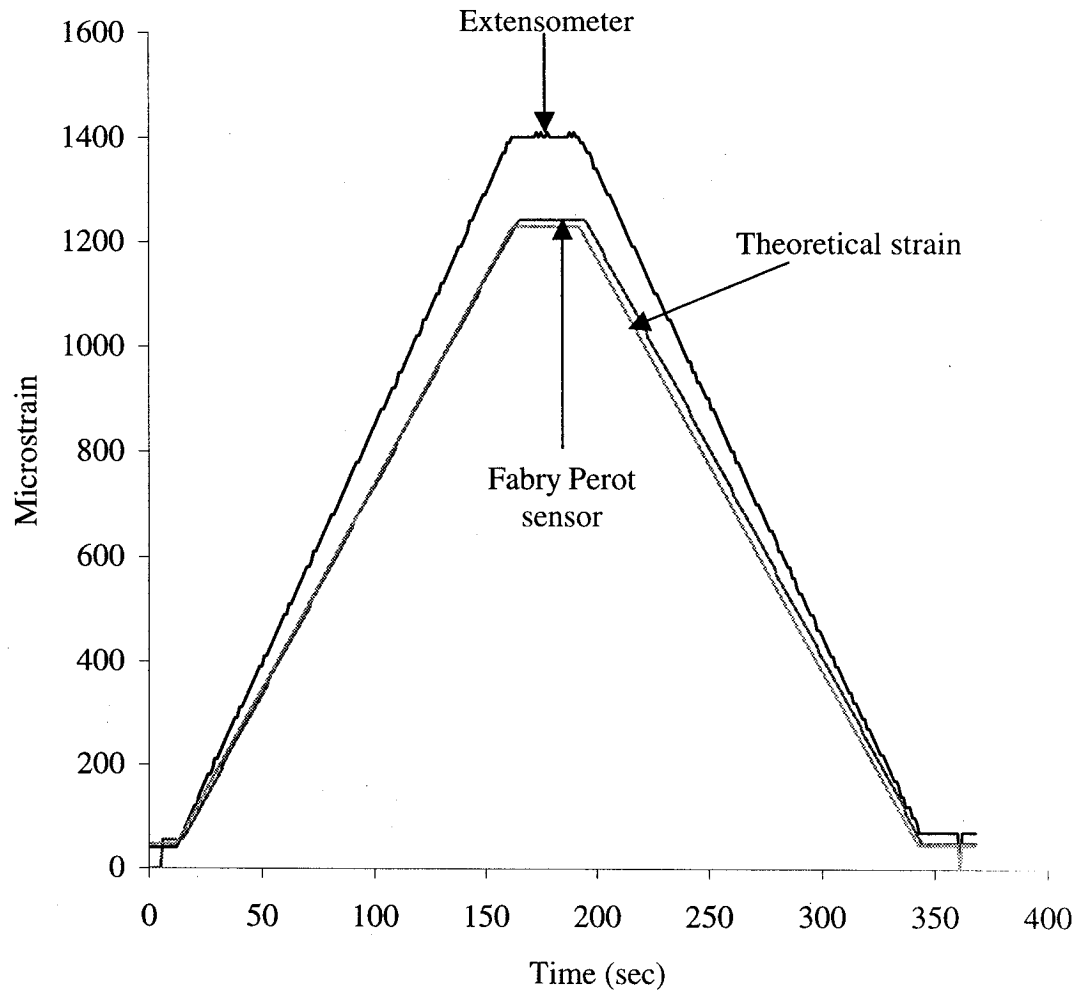
**Figure 5-55:** Strain vs. time plot from extensometer and embedded Fabry Perot sensor in a CFRP tendon subjected to a trapezoidal load

## 5.4 Temperature Tests on GFRP Tendons with Embedded Bragg Grating Sensors

### 5.4.1 Introduction

Among the sensors commonly used to monitor the health of civil engineering structures are Bragg Grating sensors. Davis et al. [1997] employed such sensors to monitor the dynamic strain response of an in-service I-10 interstate bridge in Las Cruces, New Mexico. One of the two sensors used (flange sensor) was attached along the lower flange of the girder, while the other (web sensor) was placed vertically on the web of the same girder.
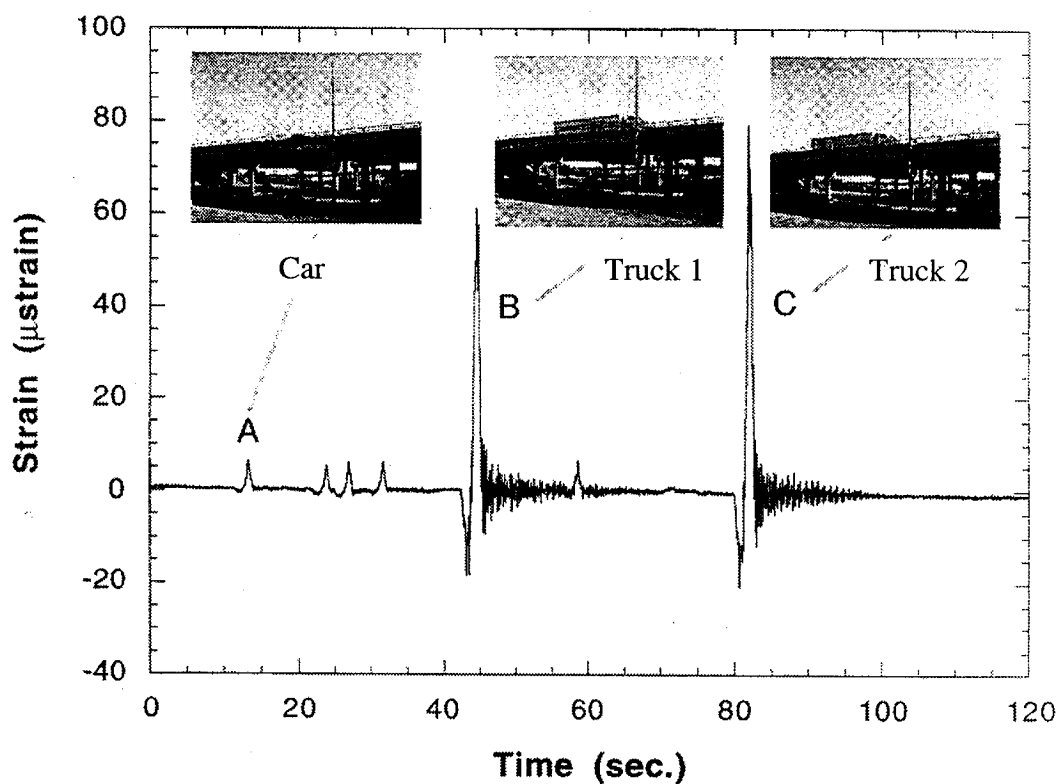


**Figure 5-56:** Flange sensor data over a span of 2 minutes [Davis et al., 1997]

Figure 5.56 shows the strain output from the flange sensor over a time span of two minutes. During this time, five cars and two big trucks passed over the bridge, and the

passage of each vehicle is clearly evident by the corresponding spikes on the strain output of Figure 5-56. The five spikes produced by the cars are all similar and have an amplitude of around 6 microstrain, but the magnitudes of the two spikes corresponding to the trucks are quite different due to the significant weight difference between the two vehicles. It is also of interest to note that there is an appreciable compressive strain prior to the expected tensile spike accompanying the passage of each truck. This strain is due to the fact that as the trucks are traveling over the bridge span before the instrumented one, the sensor span lifts slightly up putting the lower flange in compression which manifests itself as a negative reading of the sensor. Then, when the truck passes over the instrumented span, the flange goes into tension and this is picked up by the Bragg Grating sensor.
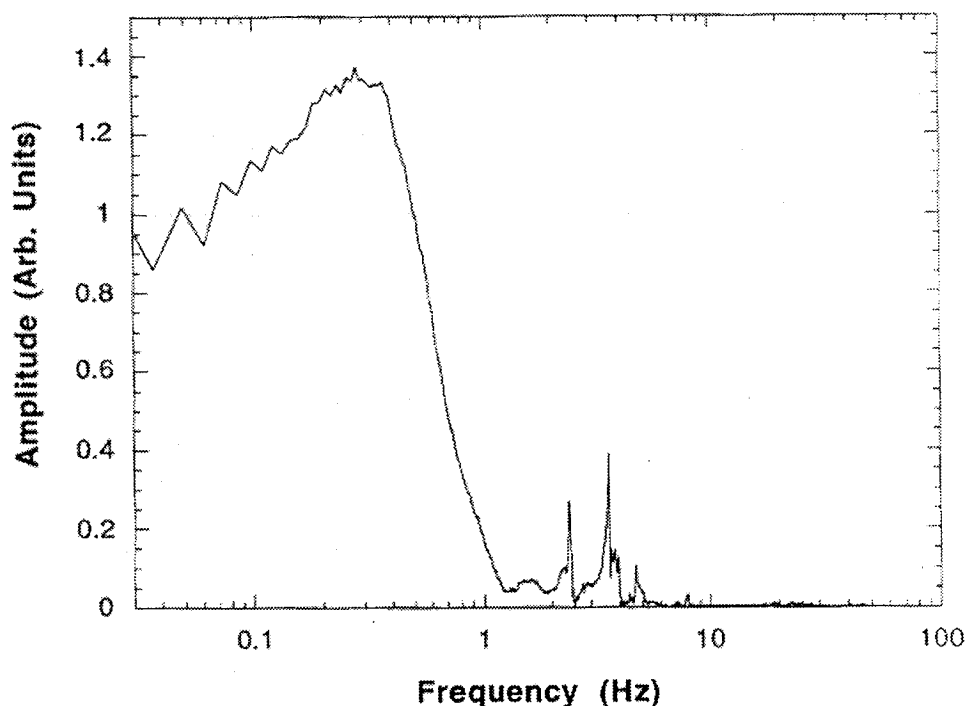


**Figure 5-57:** FFT of flange sensor strain data for truck C [Davis et al., 1997]

Figure 5-57 shows the FFT (Fast Fourier Transform) data pertaining to the passage of truck C. The strong peak at 0.3 Hz is probably due to the fundamental mode of longitudinal vibration of the bridge span with the installed Bragg Grating sensor [Davis et

al., 1997]. Figures 5-58 and 5-59 show the strain data and corresponding FFT respectively, obtained by the web sensor when a truck passes over the bridge.
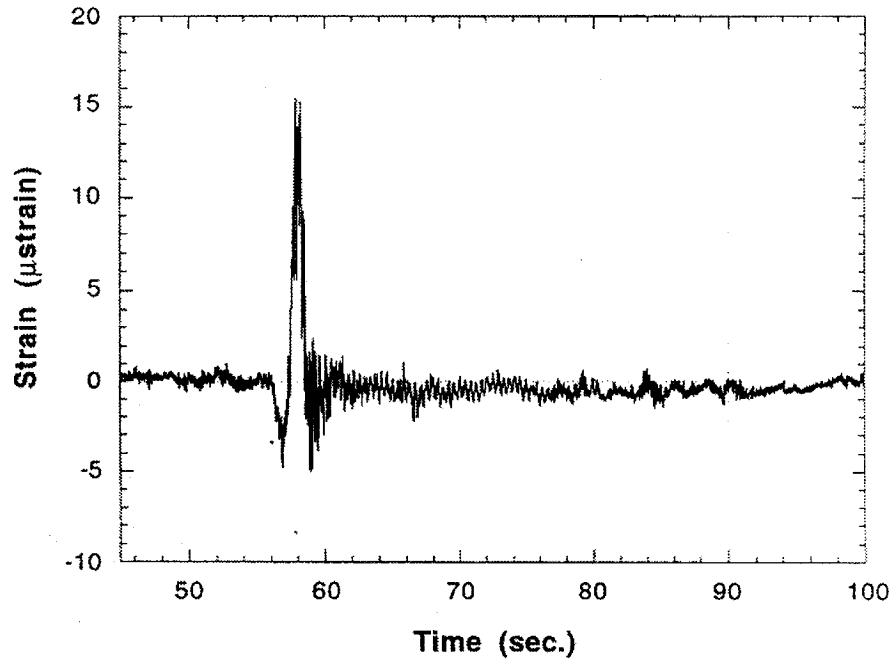


**Figure 5-58:** Web sensor data as truck passes over bridge [Davis et al., 1997]
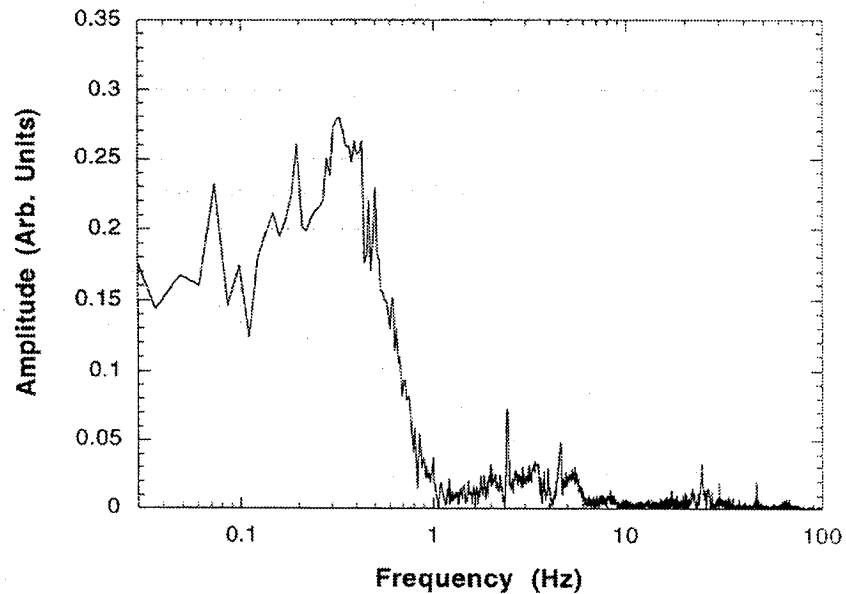


**Figure 5-59:** FFT of web sensor strain due to passage of a truck [Davis et al., 1997]

It is clear therefore that Bragg sensor measurements like the ones presented can be used to (a) characterize vehicle types by their strain signature (b) perform weight measurements of large trucks without having to stop the vehicle, and more importantly (c) monitor important structural elements of the bridge.

More recently, Udd et al., [2001] used Fiber Gratings to monitor the Horsetail Falls Bridge in the Colombia River Gorge National scenic area. Although the first sensors were installed to monitor traffic on the bridge, similar arrangements can be used to perform structural and health monitoring.

To install the sensors, one asphalt and one concrete test pad were constructed and slots were cut into them to accommodate the sensors. The slots were then cleaned, dried and lined with a thin layer of epoxy. The sensors were then installed and the slot was then filled with more epoxy. Finally, the epoxy was cured using large portable heaters [Udd et al., 2001].
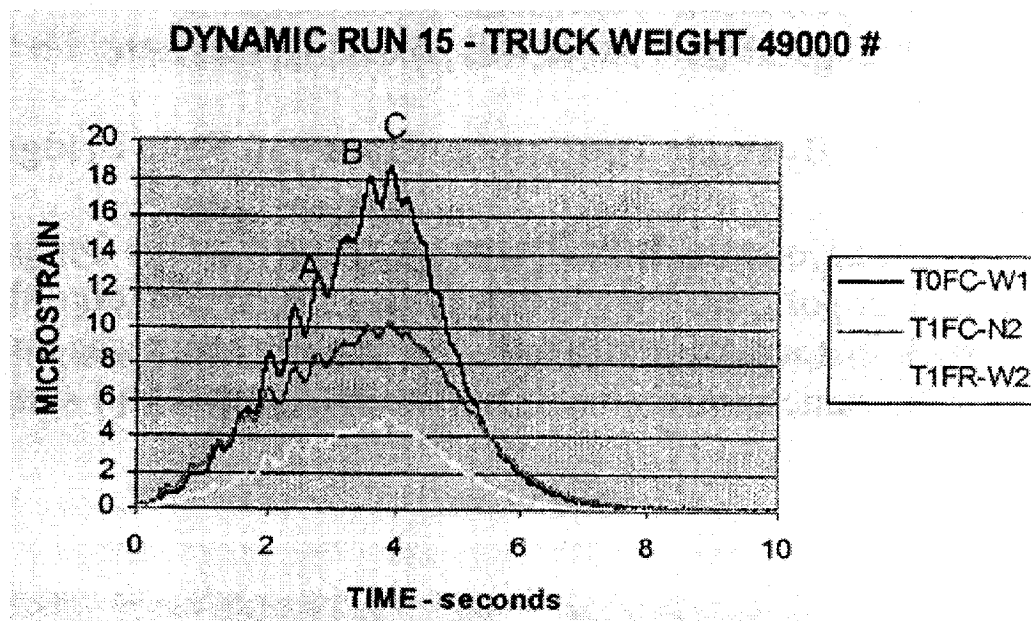


**Figure 5-60:** Output from three sensors due to passage of fully loaded truck [Udd et al., 2001]

Figure 5-60 shows the strain output from three fiber grating sensors when a truck passes over a test pad. Figure 5-61 shows how such sensors can be used to distinguish between different vehicle types.

## HORSETAIL FALLS BRIDGE
## VEHICLE CLASSIFICATION DEMONSTRATION
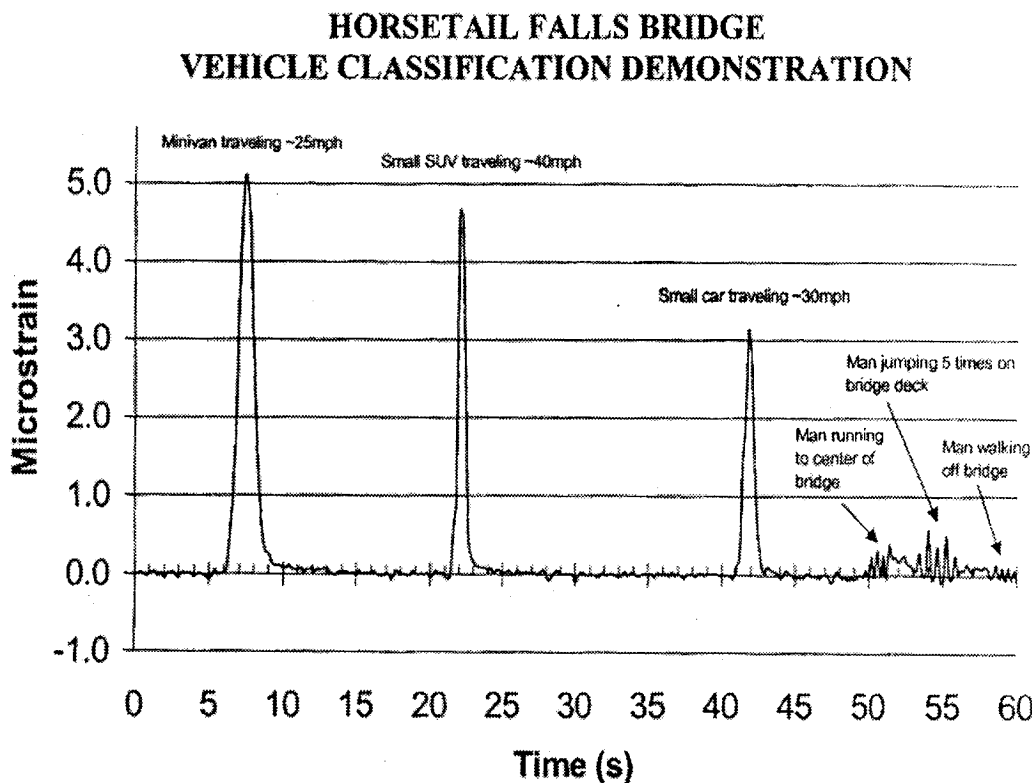


**Figure 5-61:** Output from fiber grating sensor which demonstrates vehicle classification [Udd et al., 2001]

The two papers described in this section demonstrate the viability of using Bragg Grating sensors to measure strain and consequently to monitor the strain state of various structures. However, for the work described in the first paper [Davis et al., 1997], the sensors were bonded to the outside of the structure where they would be vulnerable to damage. As far as the work described in the second paper is concerned [Udd et al., 2001], labor-intensive and time-consuming installation procedures were required. Both of these problems could be avoided if the sensors were embedded in GFRP or CFRP rebars which could be installed in the bridges at the time of construction, using the same procedure as

the one used for installing conventional steel rebars. In fact, the instrumented FRP rebars can replace steel altogether, thus eliminating corrosion problems. Examples of such rebars are the ones described in this thesis. In Section 4.4, the results from some mechanical tests performed on GFRP and CFRP tendons with embedded Bragg Grating sensors were described. These tests however, were performed in the laboratory under normal temperature conditions. If these tendons are to be embedded in concrete they will encounter much more adverse climatic conditions. Hence, it is necessary to assess the behavior of these embedded sensors in high- and low-temperature situations. In Section 5.3, extensive testing on GFRP and CFRP tendons with embedded Fabry Perot sensors, indicated that these sensors are completely reliable in the "$-40^{\circ}C$ to $+60^{\circ}C$" temperature range. In this section, similar testing will be performed on embedded Bragg Grating sensors.

## 5.4.2 Demodulation Unit for Bragg Grating sensors

For all the experiments involving Bragg Grating sensors described in Chapter 4, i.e. pultrusion monitoring and testing at room temperature, a BIS 1000PC demodulator [Electrophotonics Corporation, 1996] was used to read and record strains. However, the demodulator software system was prone to unexpected crashes that often led to loss of experimental data and significant downtime. For this reason, an upgraded demodulator, the FLS 3100, was acquired from the Electrophotonics Corporation [Electrophotonics Corporation, 1998]. The FLS 3100 is custom-designed unit that can handle up to eight plug-in modules with an independent analog output for each module. It can accommodate four to 128 channels with a frequency response of 1 kHz on all channels and 0 to 5 VDC (temperature) and 0 to 10 VDC (strain) analog outputs. The particular model used for the purposes of the experiments described in the sequel only included one module. The front panel of the module, see Figure 5-62, consists of an FC/APC bulkhead connector for connection of the sensor, a type T Thermocouple connector for temperature measurement, and indicators for low signal, out-of-range signal, and power on/off.
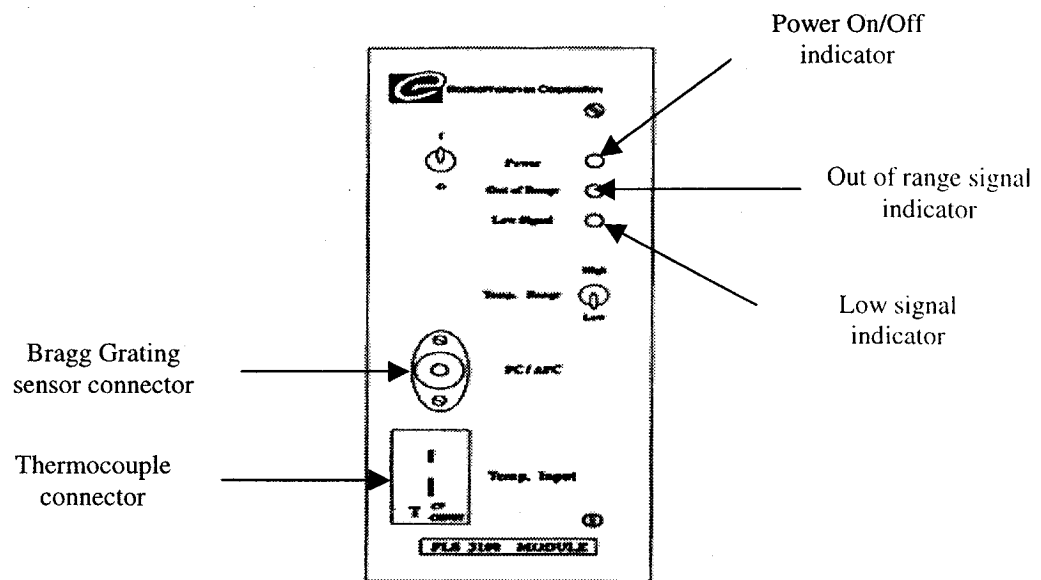
**Figure 5-62:** FLS 3100 front panel layout [Electrophotonics Corporation, 1998]

The operation of a Bragg Grating sensor was described in Section 2.4.5. The wavelength shift in the Bragg signal is given by [Electrophotonics Corporation, 1998]:

$$\frac{\Delta\lambda}{\lambda_o} = GF \times \varepsilon + \beta \times \Delta T \tag{5.2}$$

where $\Delta\lambda$ is the wavelength shift and $\lambda_o$ is the Bragg center wavelength (see Figures 2-15 and 2-16). The Gauge Factor, GF, reflects the strain sensitivity of the grating wavelength and accounts both for the change in length due to mechanical strain, and for changes in the refractive index of the core (on which the grating is etched) due to the strain-optic effect [Electrophotonics Corporation, 1998]. The value of GF is provided by the manufacturer and is calculated from [Electrophotonics Corporation, 1998]:

$$GF = \frac{n^2}{2}\left[p_{11} - v(p_{11} + p_{12})\right] \tag{5.3}$$

where n is the refractive index of the core, $\nu$ is Poisson's ratio, and $p_{11}$, $p_{12}$ are the strain-optic constants. The thermal strain, reflected by a thermal wavelength shift, is due to the thermooptic response of the grating, and to the difference between the values of the thermal expansion coefficients of the sensor ($\alpha_o$) and the substrate ($\alpha_s$). For our purposes the substrate is of course either the GFRP or the CFRP tendon in which the sensor is embedded. The temperature sensitivity factor, $\beta$, which appears in equation (5.2) is given by [Electrophotonics Corporation, 1998]:

$$\beta = \beta_o + GF \times (\alpha_s - \alpha_o) \qquad (5.4)$$

where $\beta_o$ is the thermooptic response coefficient provided by the manufacturer. To calculate the total strain due to mechanical and thermal effects, $\beta = \beta_o$ is entered in equation (5.2). To compensate for the thermal strain and only record mechanical strain, the total value of $\beta$ from equation (5.4) is substituted into equation (5.2). For the experiments pertaining to the Fabry Perot sensors, we manually factored out the thermal strains by nulling the embedded sensor prior to any load application. For the experiments involving Bragg Grating sensors, we achieved the same result by using the full value for $\beta$ from equation (5.4).

The FLS 3100 provides analog output from a 50-pin connector and three signals are needed for accurate measurements (see Figure 5-63). The strain signal is 0 to 10 volts, the Internal Self Calibration Signal is 0 to 5 volts, and the thermocouple signal is 0 to 5 volts. Figure 5-64 shows the specification sheet for the FLS 3100 module used for the experiments that will be described in Section 5.4.3, and Figure 5-65 is the calibration sheet (provided by the manufacturer). Note that $a_0$, $a_1...a_{15}$, $b_1$ and $b_2$ are calibration parameters needed to calculate the wavelength shift (from the output analog signals) which in turn is used to calculate strain.
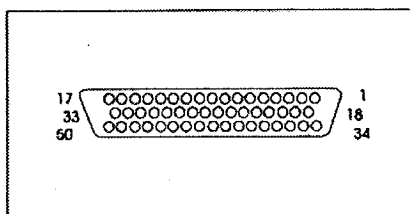
| Channel: | 1 | 2 | 3 | 4 | 5 | 6 | 7 | 8 |
|---|---|---|---|---|---|---|---|---|
| FGS Strain | 18 | 20 | 22 | 24 | 26 | 28 | 30 | 32 |
| Internal Self Calibration | 34 | 36 | 38 | 40 | 42 | 44 | 46 | 48 |
| Thermocouple | 2 | 4 | 6 | 8 | 10 | 12 | 14 | 16 |
| Ground | 19 | 21 | 23 | 25 | 27 | 29 | 31 | 33 |
| Ground | 35 | 37 | 41 | 43 | 45 | 47 | 49 | |

**Figure 5-63:** Pin configuration for 50-pin analog output connector [Electrophotonics Corporation, 1998]

# SPECIFICATION SHEET

**Model No:**    **FLS 3100 Module**
**Serial No:**    **01146**

## Input:

|  |  |
|---|---|
| Thermocouple | T-type; Miniature panel jack |
| Fiber Grating Sensor | FC / APC |
| Power | 90-240 VAC ( 50/60 Hz) ( supplied to the in-line power supply ) |

## Output:

Signal Output

1. FGS Strain ( orange )
2. Common ground ( brown )
3. Internal Self Calibration ( red )
4. Thermocouple ( green )

Warm up:            35 minutes

Analog signal

| | |
|---|---|
| Range | 9.94 V to 0.89 V |
| Avg.p-p noise | < 6.2mV @ 4.788V |

## Optical Characteristics:

| | |
|---|---|
| Wavelength Range | 9300 pm |
| Center wavelength | 1309236 pm |
| Max. Lead Sensitivity | < +/- 2 $\mu\varepsilon$ |
| Stability over 15 hours | < +/- 15 $\mu\varepsilon$ |

**Figure 5-64:** Specification sheet for FLS 3100 module [Electrophotonics Corporation, 1998]

**ElectroPhotonics Corporation**

## Calibration Certificate

**Model: FLS 3100**
**Serial No. 01146**
**Analog signal to strain conversion :**
    (see manual for equations and detailed discussion of data conversion)
**Non - linear data processing:**
    Input:

| | |
|---|---|
| Analog Signal | 9.940 V to 0.890 V |

    Output:

| | |
|---|---|
| Strain Range | 8450 $\mu\varepsilon$ (@ GF=0.77, $\lambda_0$=1310000 pm) |
| Non-linearity | < 0.25 % over ( 8450 $\mu\varepsilon$ ) |

**Linear data processing:**
    Input:

| | |
|---|---|
| Analog Signal | 7.230 V to 2.520 V |

    Output:

| | |
|---|---|
| Strain Range | 3720 $\mu\varepsilon$ ( @ GF=0.77, $\lambda_0$=1310000 pm ) |
| Non-linearity | < 0.52 % (over 3720 $\mu\varepsilon$) |

Curve-fit Parameters:

| | | | |
|---|---|---|---|
| $a_0$ | 1309385.379 | $d_0$ | 1313627.151 |
| $a_1$ | -9.1002592E+01 | $d_1$ | -848.7543126 |
| $a_2$ | -3.3113098E-02 | | |
| $a_3$ | -3.9064205E-02 | | |
| $a_4$ | -5.2357688E-04 | | |
| $a_5$ | 1.5489706E-04 | | |
| $a_6$ | 1.9178943E-06 | | |
| $a_7$ | -4.1047027E-07 | | |
| $a_8$ | -1.2833503E-09 | | |
| $a_9$ | 6.0345176E-10 | | |
| $a_{10}$ | -2.4443571E-12 | | |
| $a_{11}$ | -5.0630968E-13 | | |
| $a_{12}$ | 4.9145159E-15 | | |
| $a_{13}$ | 2.2618996E-16 | | |
| $a_{14}$ | -3.2657857E-18 | | |
| $a_{15}$ | -4.3009841E-20 | | |
| $a_{16}$ | 8.5481625E-22 | | |
| $a_{17}$ | 6.3898444E-25 | | |
| $a_{18}$ | -4.6220059E-26 | | |
| $b_1$ | 234.980 | | |
| $b_2$ | 733.285 | | |
| $c$ | 0.050 | | |
| $S_{IREF}$ | 2.0268 | | |

**Figure 5-65:** Calibration sheet for FLS 3100 module [Electrophotonics Corporation, 1998]

### 5.4.3 Sinusoidal and Trapezoidal Tests Performed on GFRP Tendons with Embedded Bragg Grating Sensors in Varying Temperature Environments

It was decided to begin the testing program with Bragg Grating sensors embedded in GFRP tendons. As mentioned in Chapter 4, Bragg Grating sensors showed enhanced survivability in the pultrusion process, and therefore there was no need to prereinforce them according to the procedure outlined in Section 3.4 for Fabry Perot sensors. As a result, the Bragg Grating sensor was embedded without modification in the GFRP tendon during pultrusion.
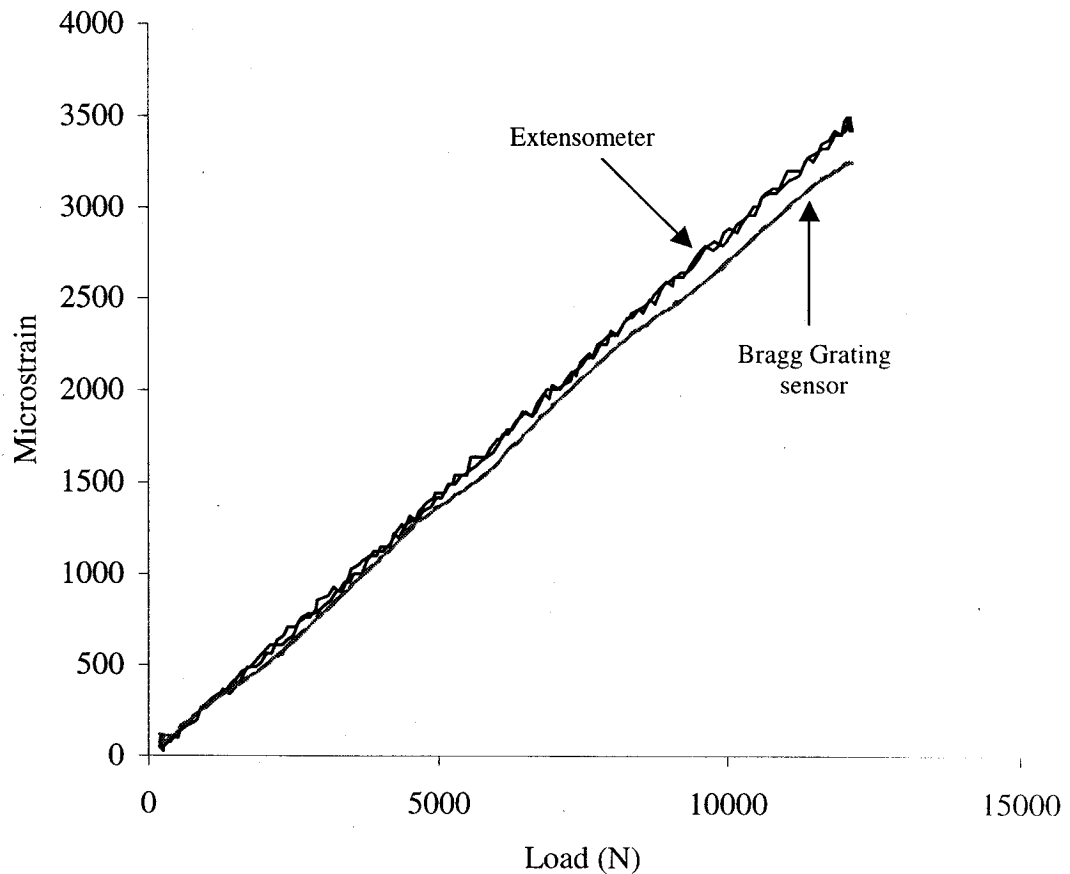
**Figure 5-66:** Strain from extensometer and embedded Bragg Grating sensor in a GFRP tendon subjected to a trapezoidal load at room temperature

Like the tests performed on smart FRP tendons with embedded Fabry Perot sensors, the trapezoidal and sinusoidal tests to be described in the sequel were conducted at PSC Analytical using the same 400 kN-capacity MTS model 8540RM load frame and Instron Series IX controller, and an integrated temperature chamber with its own Instron controller. The load parameters, i.e. the amplitude of both waveforms and the frequency of the sinusoidal waveform were the same as for the tests described in Section 5.3.
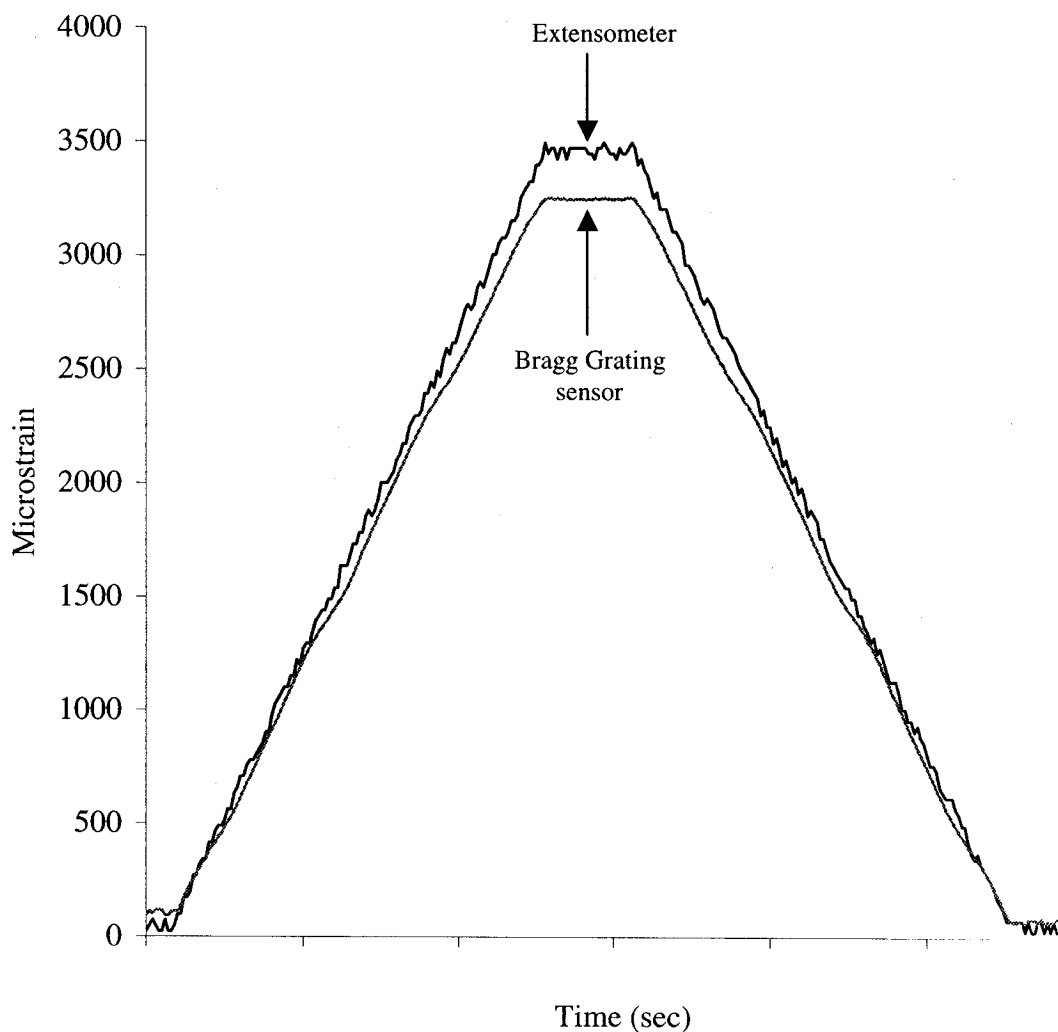
**Figure 5-67:** Strain vs. time plot from extensometer and embedded Bragg Grating sensor in a GFRP tendon subjected to a trapezoidal load at room temperature

The first test was a trapezoidal load performed in ordinary laboratory conditions before the temperature of the chamber was raised. The results are plotted in Figure 5-66. As shown in the figure, there is a very good degree of conformance between the Bragg Grating sensor and the extensometer, the discrepancy between the two being about 250 microstrain (or 7.5%) at the peak applied load. The good agreement between the values from the two strain-monitoring devices is also evident from the microstrain vs. time plot of Figure 5-67. One feature that is evident in both of these figures is the small amount of "waviness" associated with the trend lines. This is not to be attributed to the sensor or the extensometer, but rather to the large-capacity load cell that was used for these tests. The load cell used for the tests of the previous section was of much smaller capacity (100 kN) and hence there was much less wandering from the mean trend line.
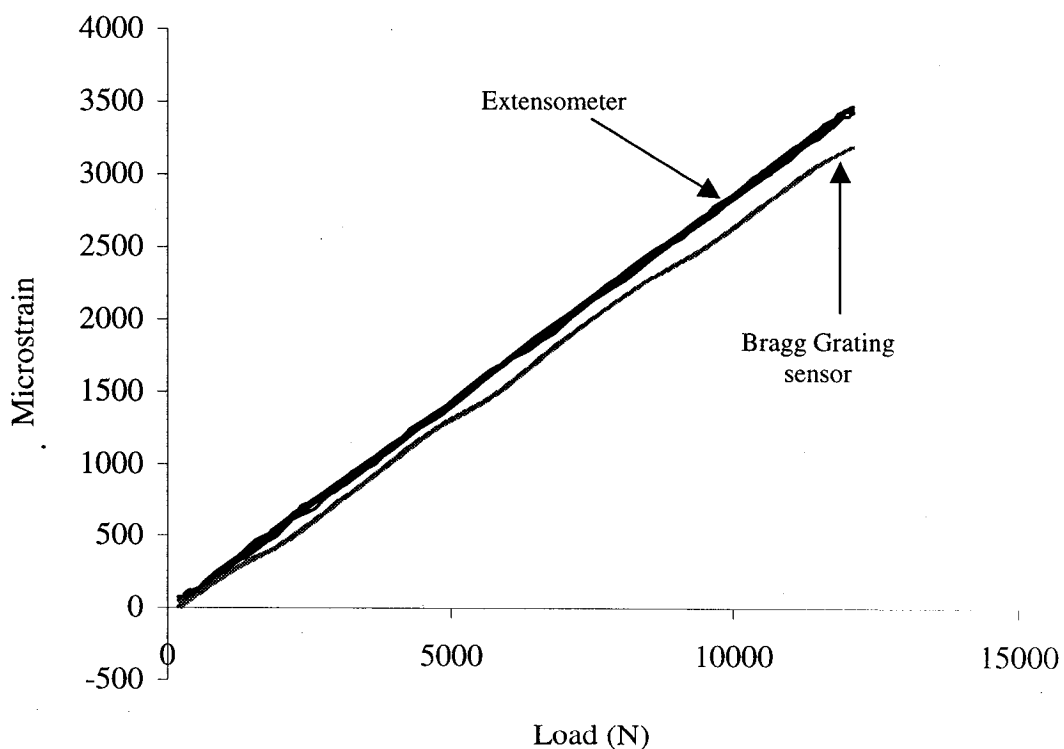
**Figure 5-68:** Strain from extensometer and embedded Bragg Grating sensor in a GFRP tendon subjected to a sinusoidal load at room temperature

The smart GFRP tendon was subsequently subjected to a sinusoidal load at room temperature. The load vs. strain plot in Figure 5-68 again shows a very good agreement between the sensor and the extensometer with a corresponding discrepancy of about 8% at the peak applied load. The data from Figure 5-68 are plotted as microstrain vs. time in Figure 5-69.
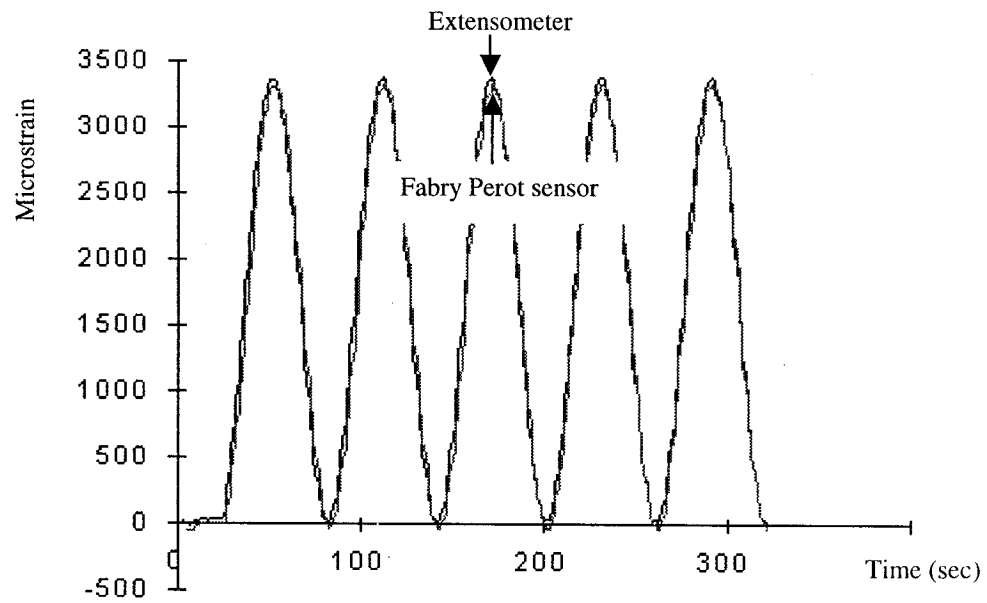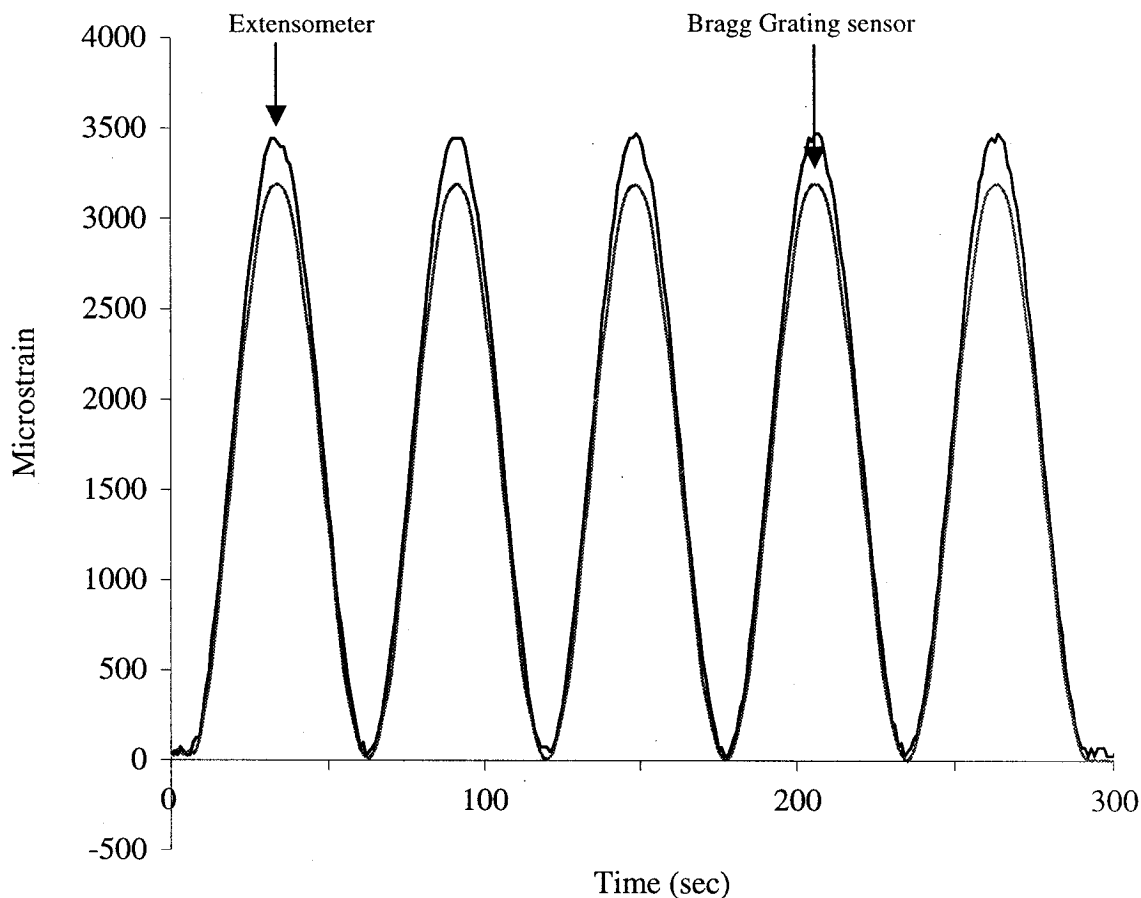
**Figure 5-69:** Strain vs. time plot from extensometer and embedded Bragg Grating sensor in a GFRP tendon subjected to a sinusoidal load at room temperature

The temperature chamber was then heated to 40°C and allowed to reach steady state. The smart tendon was then subjected to the same trapezoidal and sinusoidal loads as those performed at room temperature. The results are shown in Figures 5-70 to 5-73.
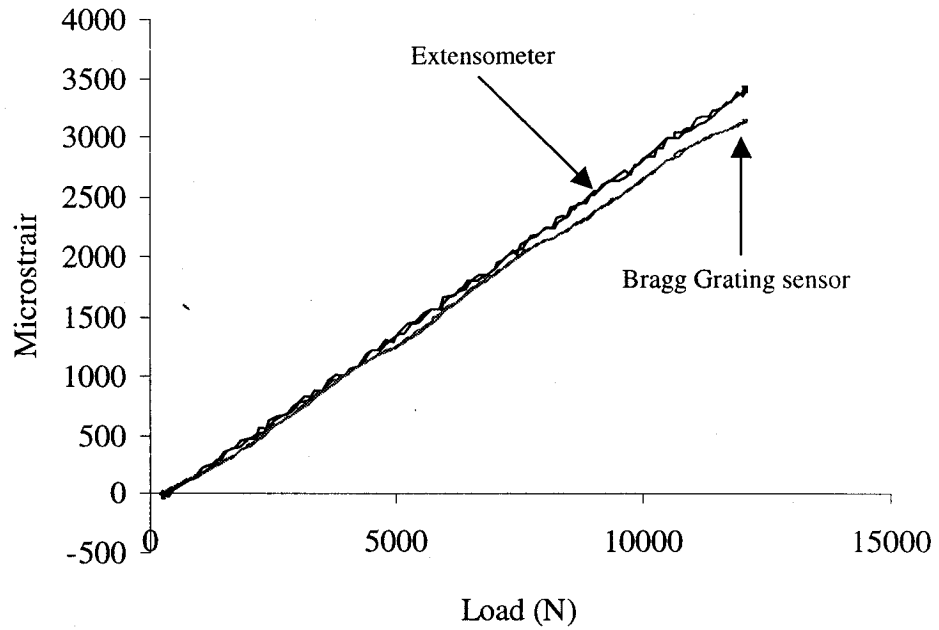
**Figure 5-70:** Strain from extensometer and embedded Bragg Grating sensor in a GFRP tendon subjected to a trapezoidal load at 40°C
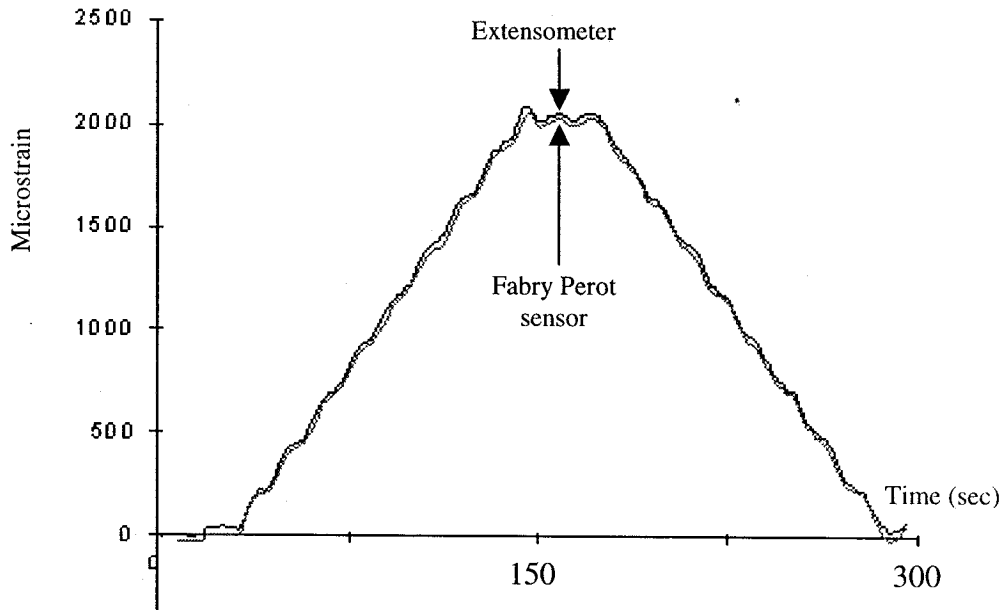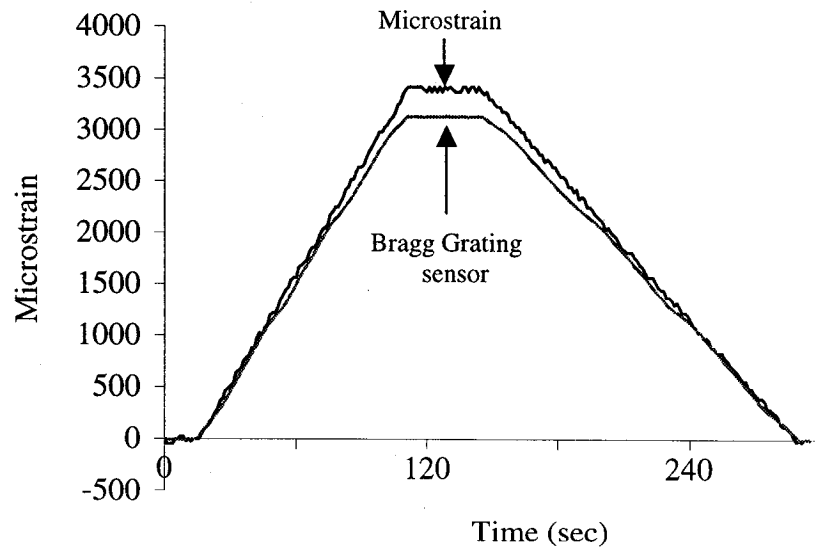


**Figure 5-71:** Strain vs. time plot from extensometer and embedded Bragg Grating sensor in a GFRP tendon subjected to a trapezoidal load at 40°C
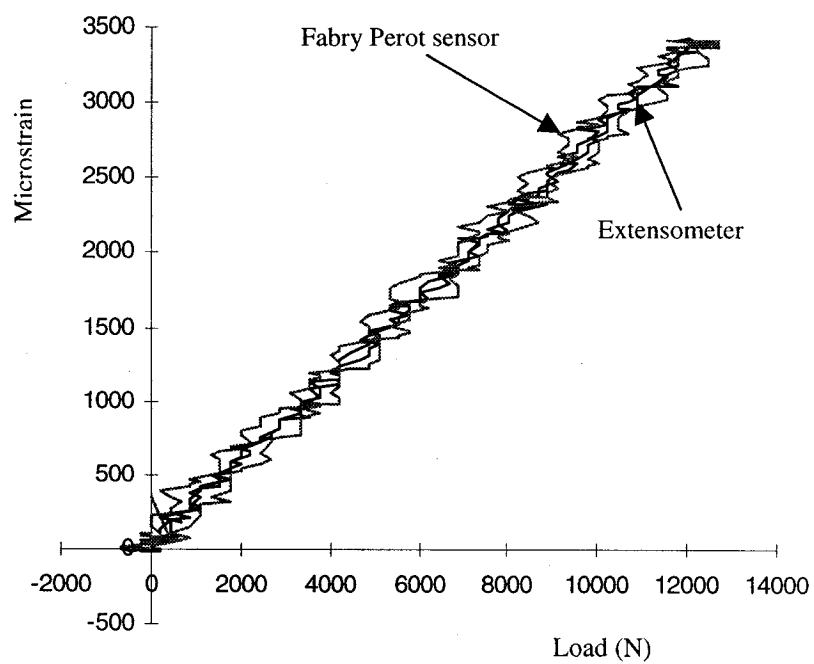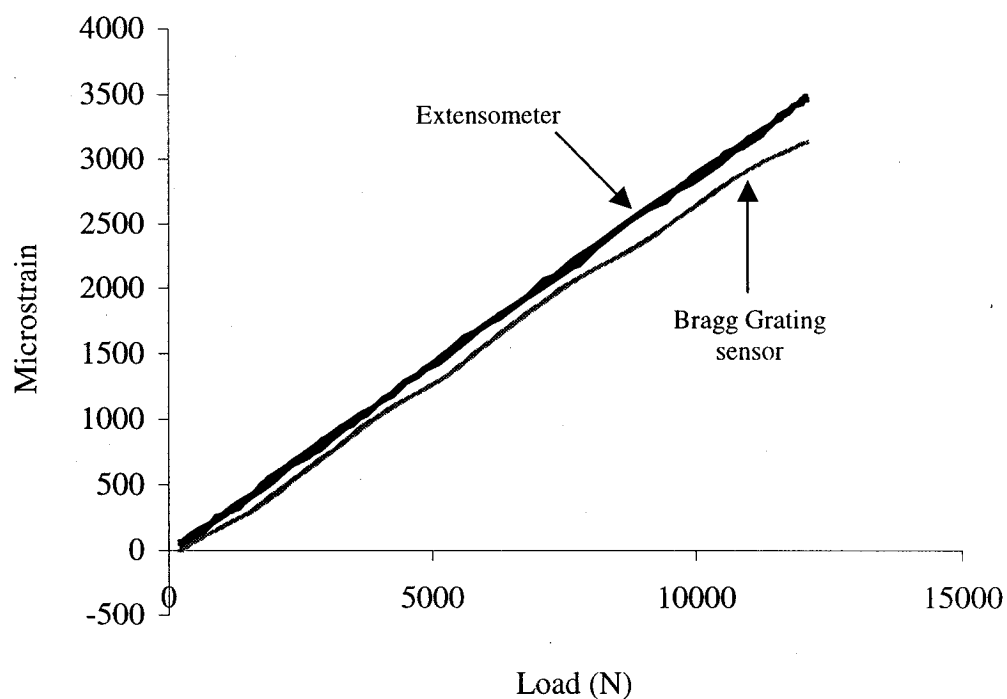
**Figure 5-72:** Strain from extensometer and embedded Bragg Grating sensor in a GFRP tendon subjected to a sinusoidal load at 40°C
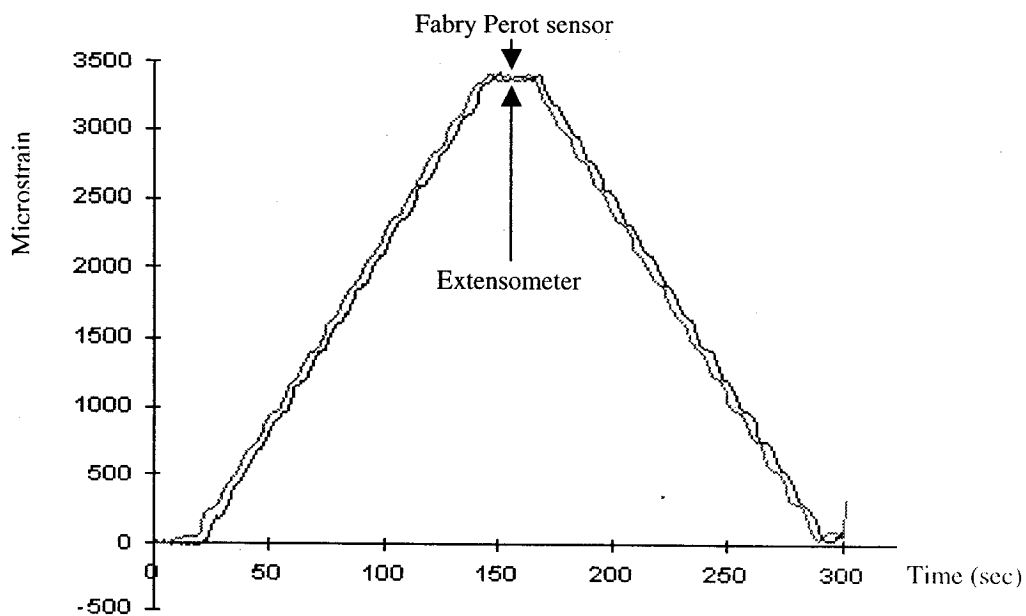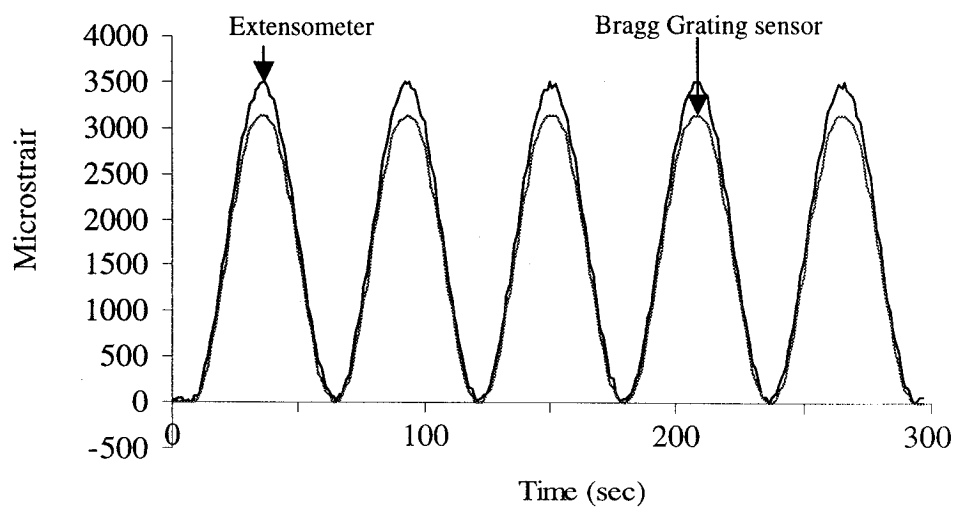


**Figure 5-73:** Strain vs. time plot from extensometer and embedded Bragg Grating sensor in a GFRP tendon subjected to a trapezoidal load at 40°C
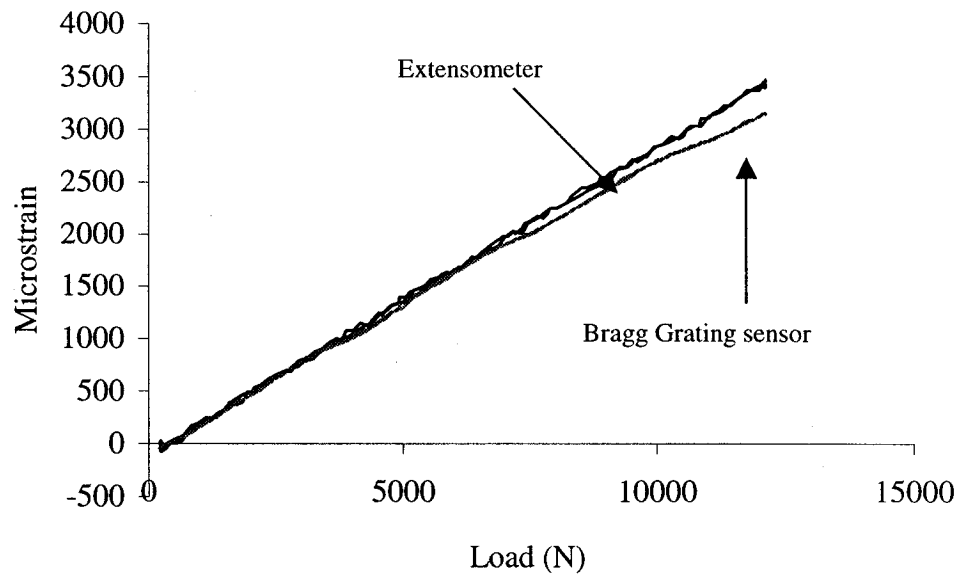
**Figure 5-74:** Strain from extensometer and embedded Bragg Grating sensor in a GFRP tendon subjected to a trapezoidal load at 60°C
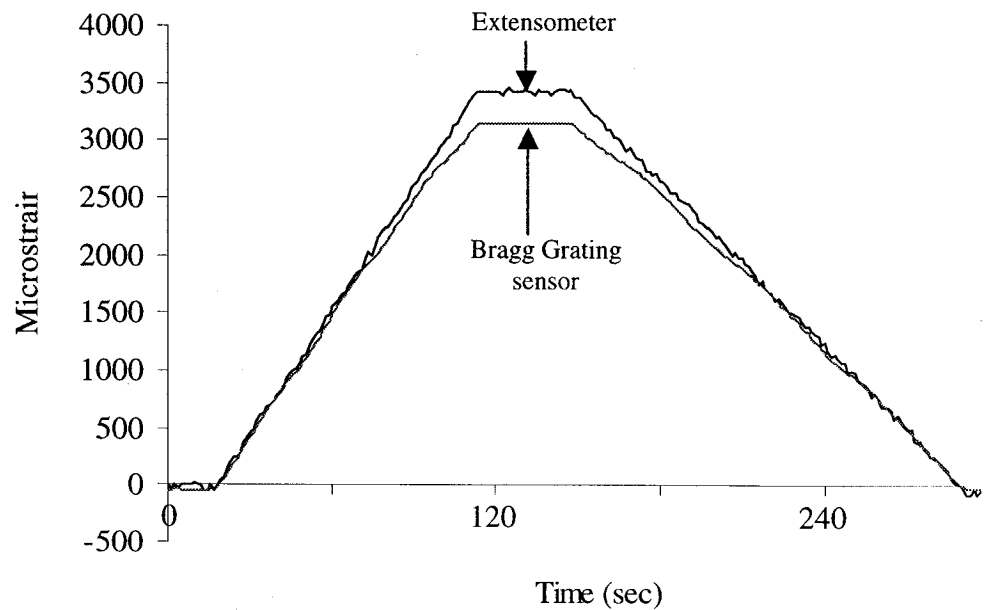


**Figure 5-75:** Strain vs. time plot from extensometer and embedded Bragg Grating sensor in a GFRP tendon subjected to a trapezoidal load at 60°C
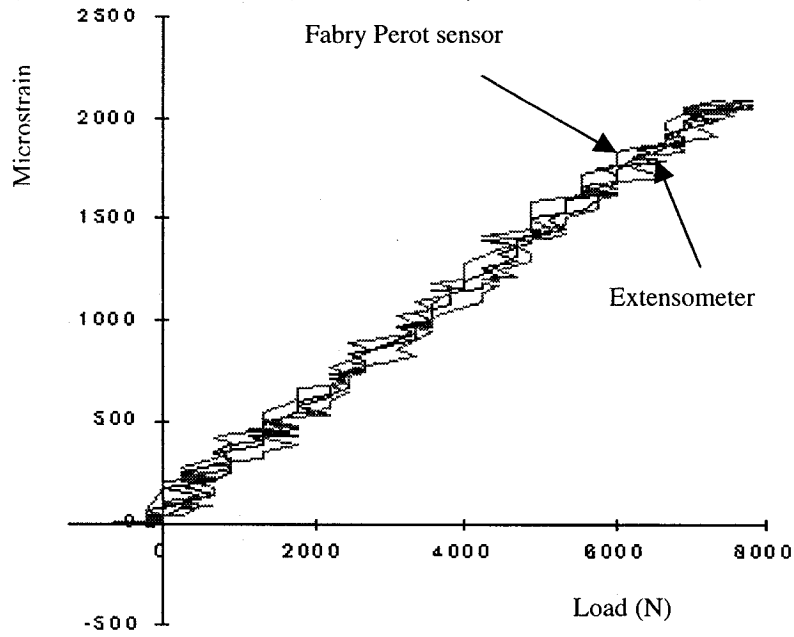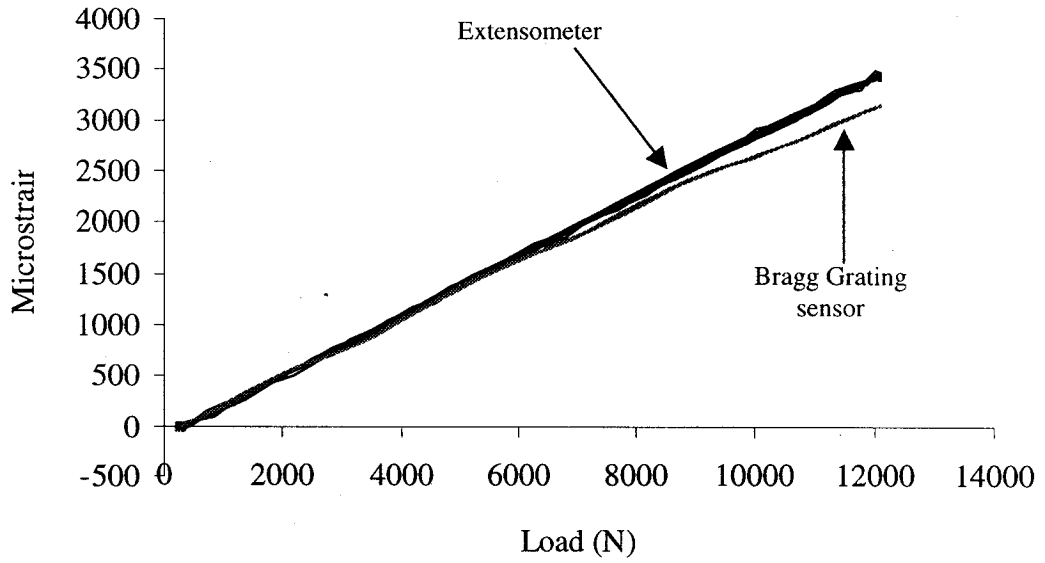
**Figure 5-76:** Strain from extensometer and embedded Bragg Grating sensor in a GFRP tendon subjected to a sinusoidal load at 80°C
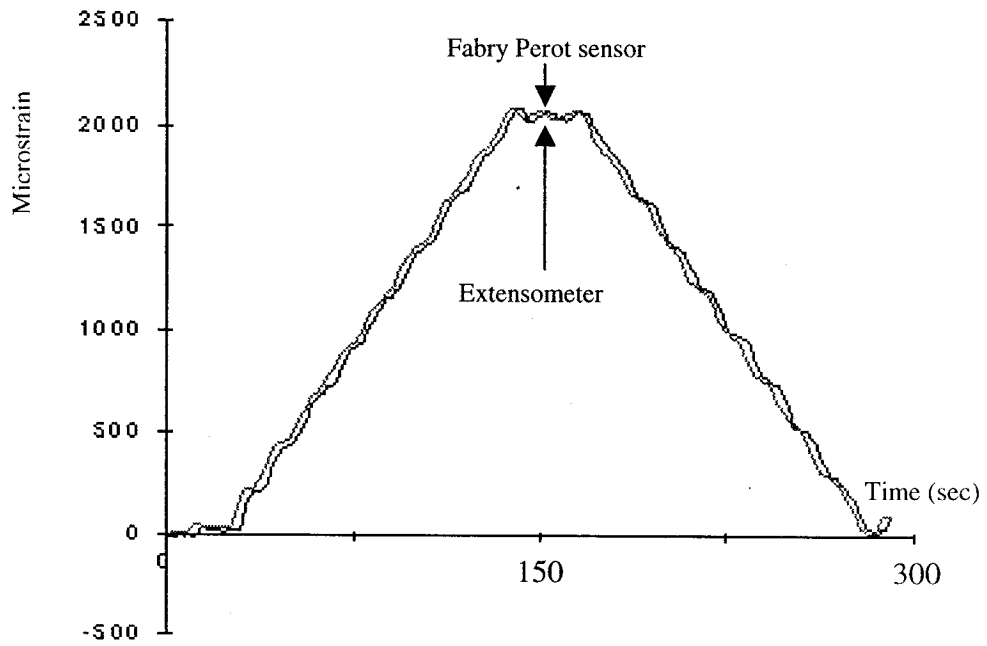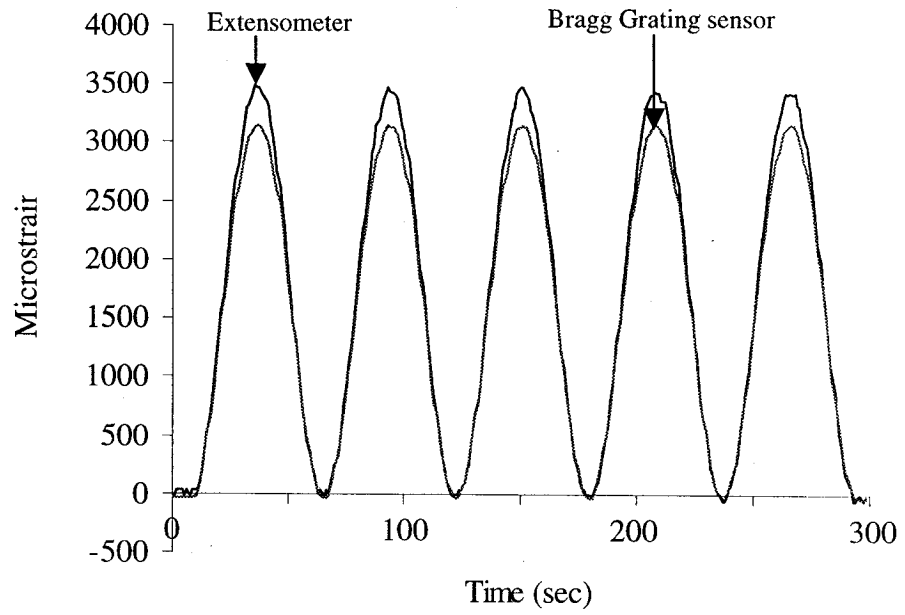


**Figure 5-77:** Strain vs. time plot from extensometer and embedded Bragg Grating sensor in a GFRP tendon subjected to a sinusoidal load at 80°C

Subsequently to the tests at 40°C, the temperature of the chamber was raised first to 60°C and then to 80°C, and trapezoidal and sinusoidal tests were performed at each temperature. The results of some of these tests are plotted in Figures 5-74 to 5-77. The same conclusions can be drawn from these plots as from the previous ones. Bragg Grating sensors embedded in GFRP tendons are very consistent and reliable even at temperatures as high as 80°C and produce strain data that conform very well with corresponding extensometer data.

On completion of the testing at 80°C, the temperature chamber was gradually cooled down. When its temperature stabilized at 0°C, the testing was resumed. The first load to which the tendon was subjected was a trapezoidal one and the load vs. strain results from this test are given in Figure 5-78.
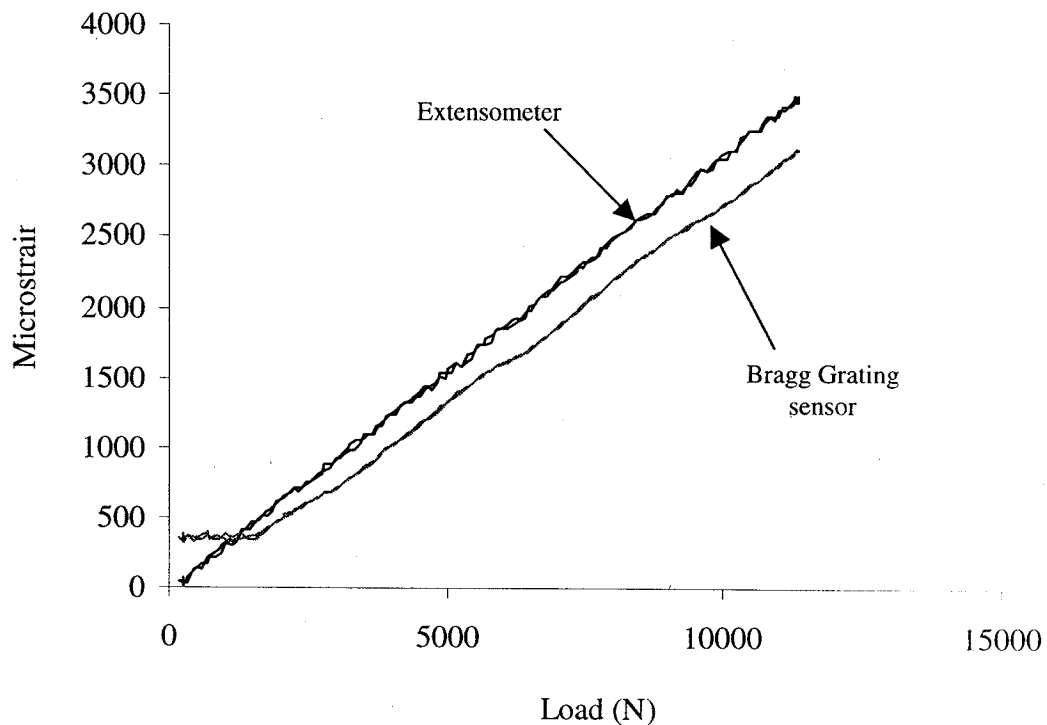


**Figure 5-78:** Strain from extensometer and embedded Bragg Grating sensor in a GFRP tendon subjected to a trapezoidal load at 0°C

Figure 5-78 shows that there is a good agreement between the extensometer and the embedded Bragg Grating sensor, except for low strain values, less than 350 microstrain. On examining the raw data sheet, there was no apparent error signal such as a "low signal" or "no signal" warning from the demodulator at low strain levels. It was simply recording erroneous results. The same conclusions can be drawn from the microstrain vs. time plot in Figure 5-79.
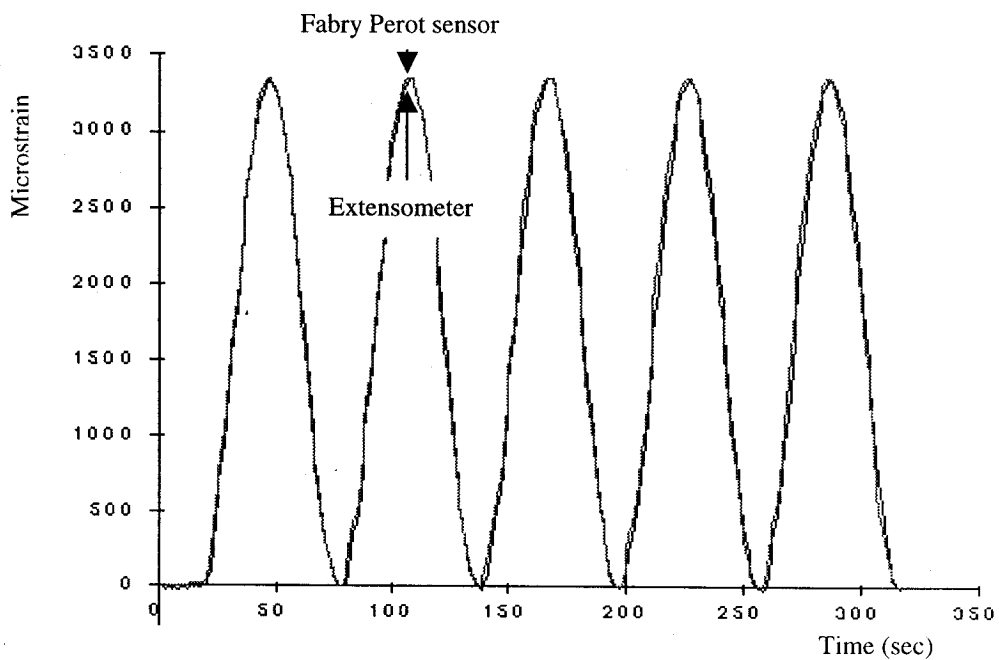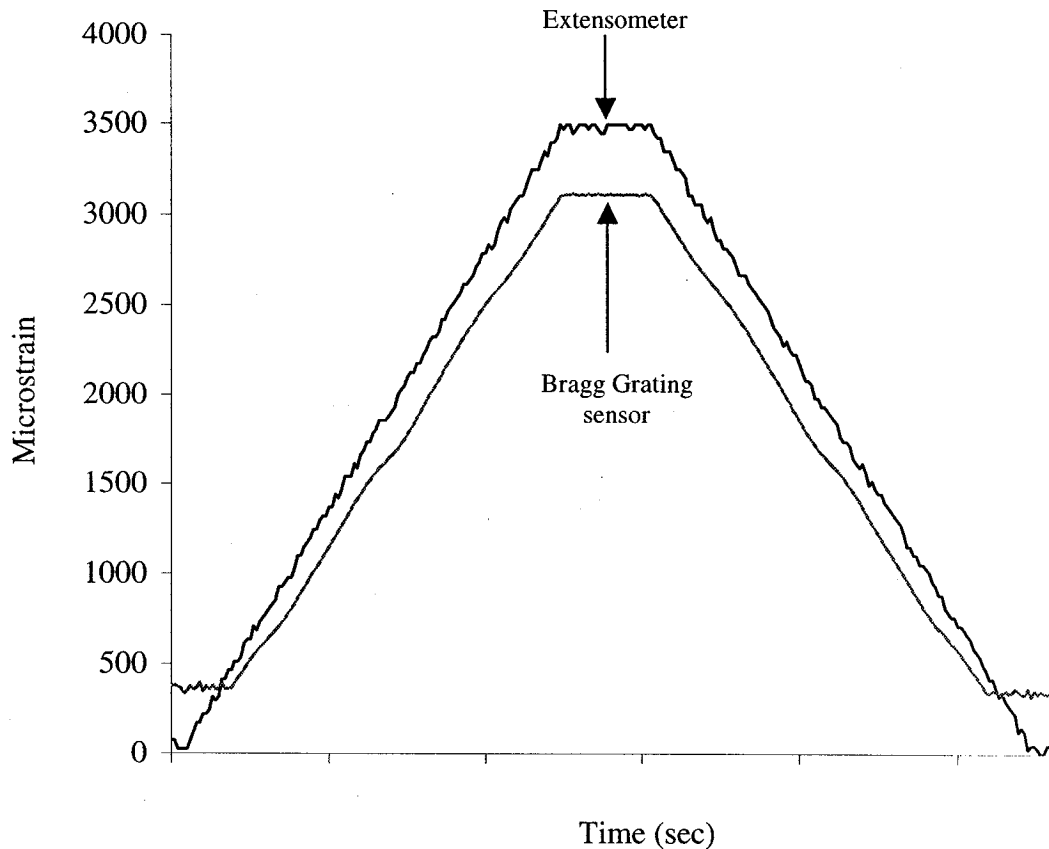


**Figure 5-79:** Strain vs. time plot from extensometer and embedded Bragg Grating sensor in a GFRP tendon subjected to a trapezoidal load at 0°C

The same GFRP tendon was subsequently subjected to a sinusoidal load at 0°C, as well as at sub-zero temperatures. The results, as shown in Figures 5-80 to 5-83, are characterized by the same problem as Figures 5-78 and 5-79.
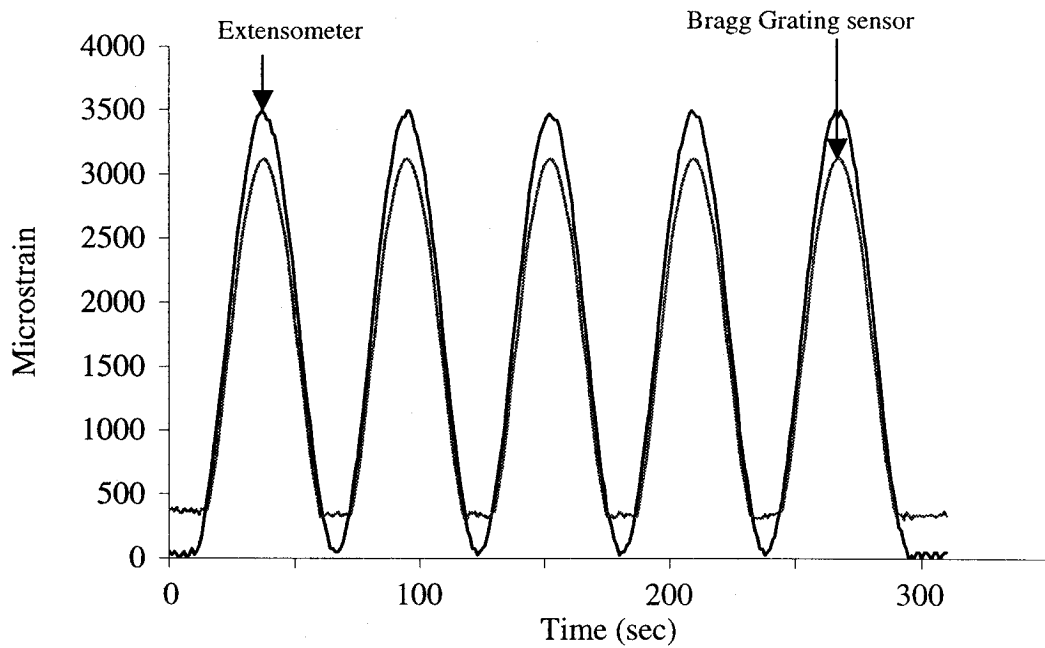
**Figure 5-80:** Strain vs. time plot from extensometer and embedded Bragg Grating sensor in a GFRP tendon subjected to a sinusoidal load at 0°C
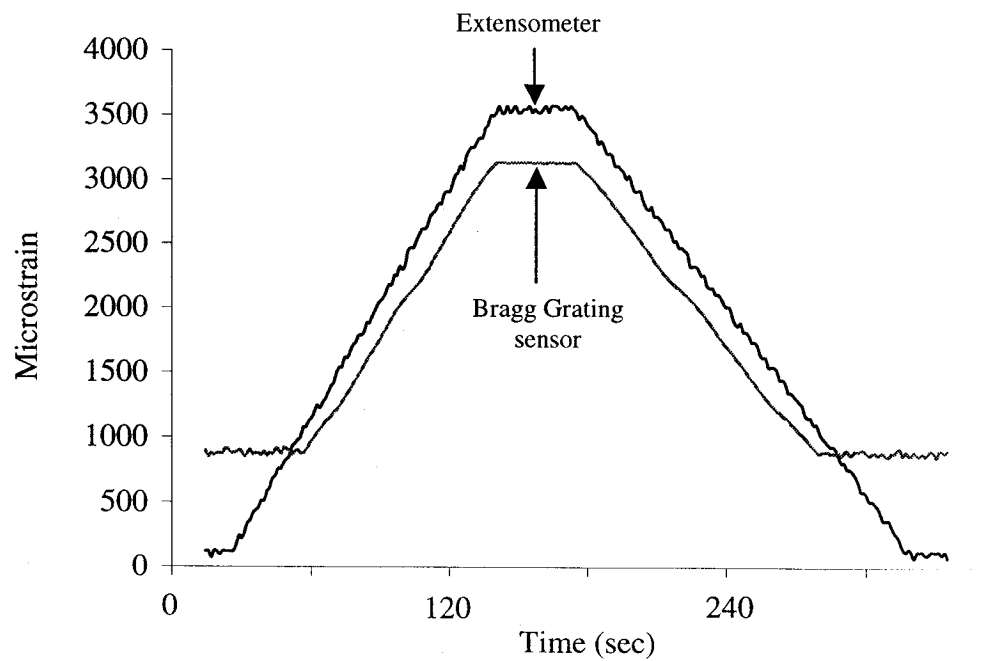


**Figure 5-81:** Strain vs. time plot from extensometer and embedded Bragg Grating sensor in a GFRP tendon subjected to a trapezoidal load at -40°C
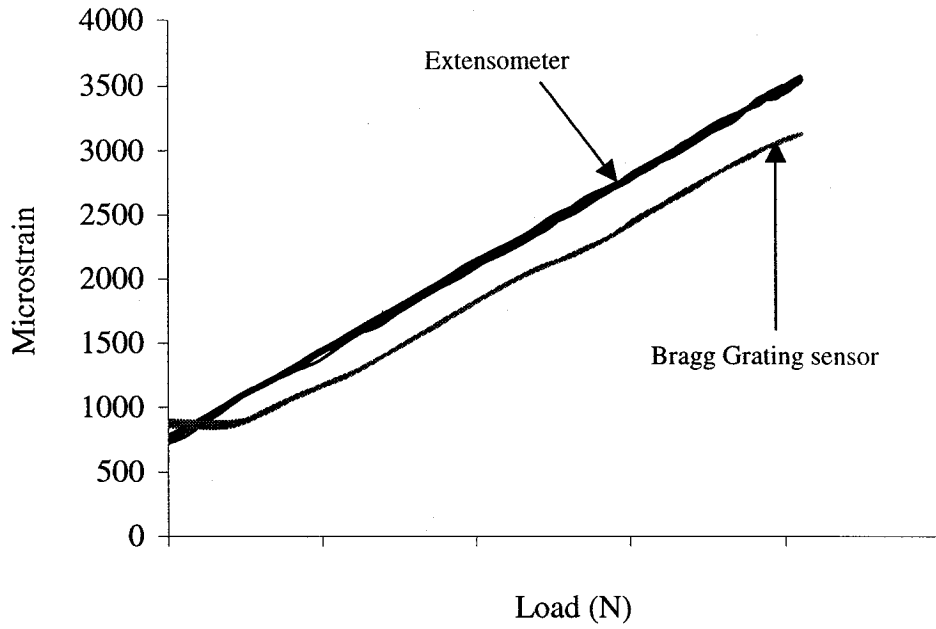
**Figure 5-82:** Strain from extensometer and embedded Bragg Grating sensor in a GFRP tendon subjected to a sinusoidal load at -40°C
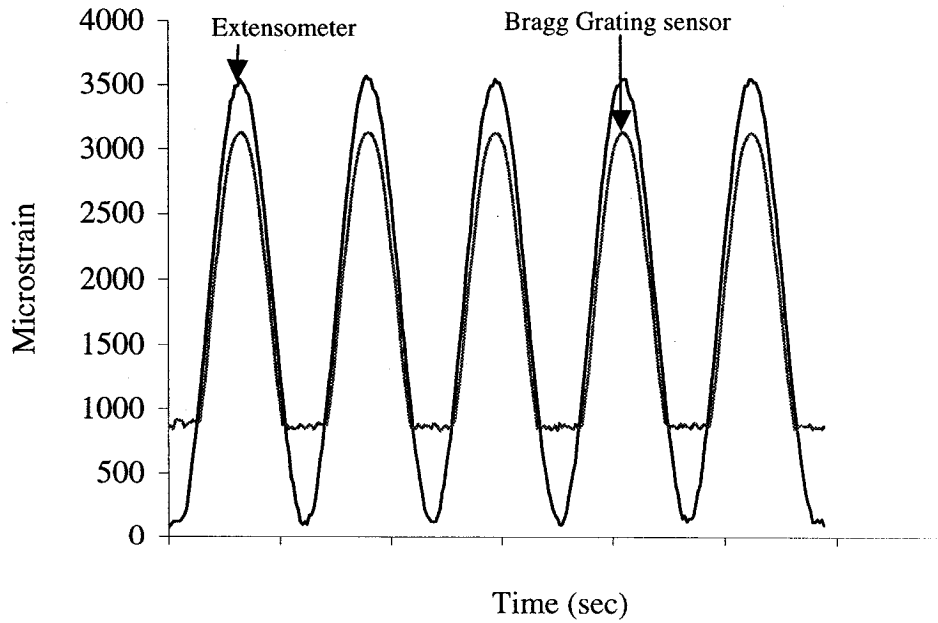


**Figure 5-83:** Strain vs. time plot from extensometer and embedded Bragg Grating sensor in a GFRP tendon subjected to a sinusoidal load at -40°C

## 5.5 Temperature Tests on CFRP Tendons with Embedded Bragg Grating Sensors
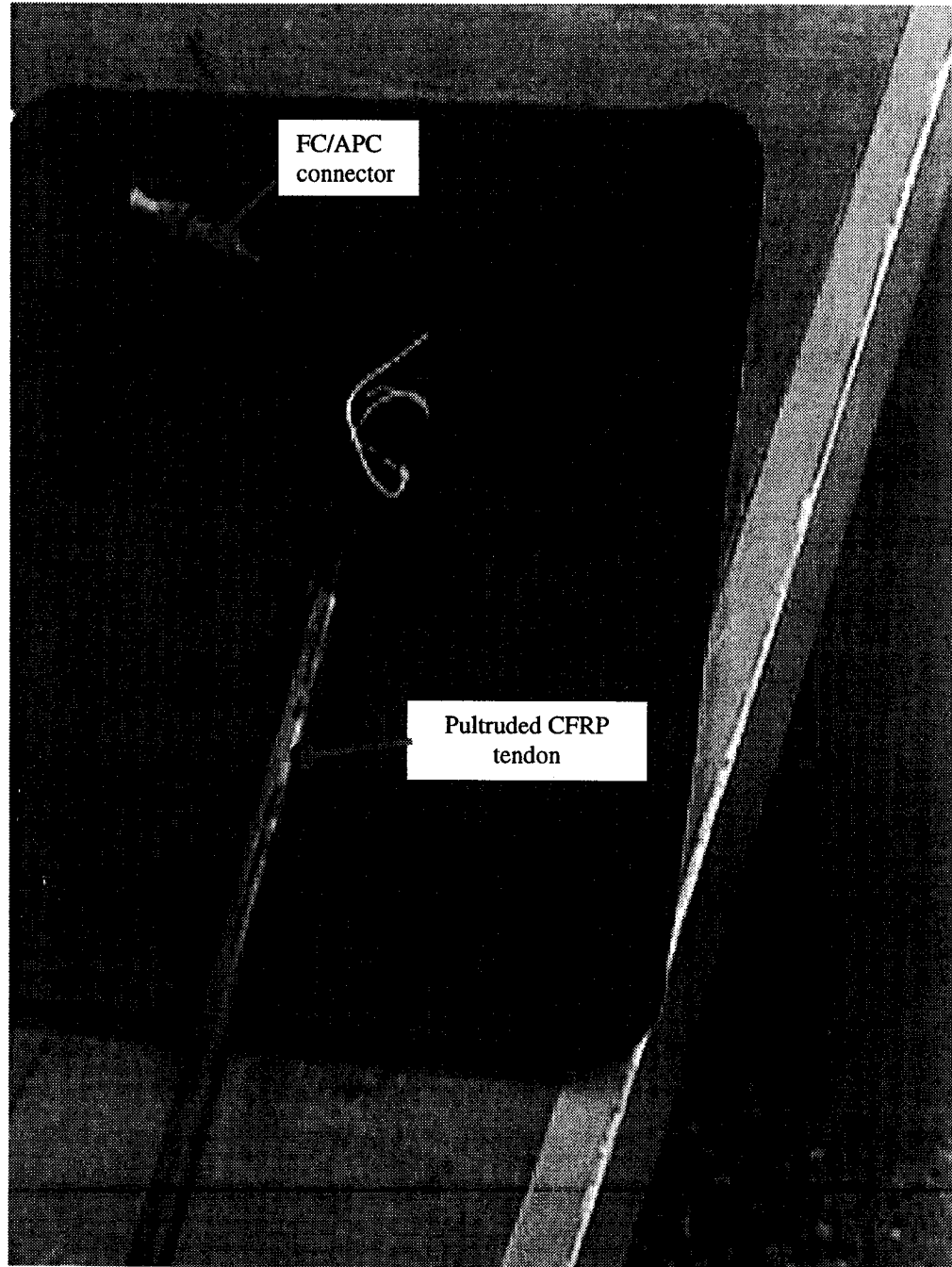


**Figure 5-84:** Pultruded CFRP tendon with embedded Bragg Grating sensor
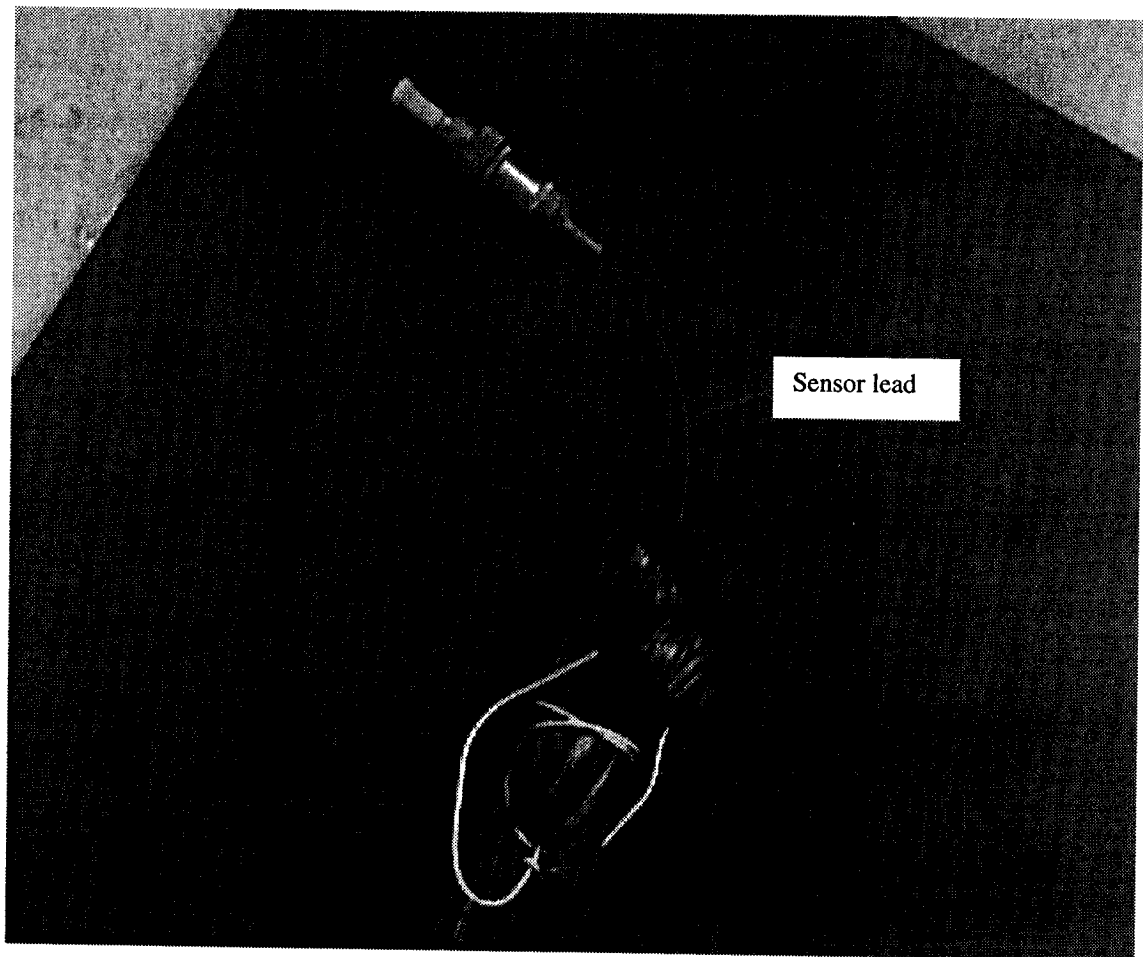
**Figure 5-85:** Close-up view of the end of CFRP tendon with an embedded Bragg Grating sensor

The same testing program that was described in the previous section for the case of a smart GFRP tendon was also conducted on a pultruded CFRP tendon with an embedded Bragg Grating sensor.

The tendon was first subjected to a trapezoidal waveform (with the same parameters as those described in previous sections) at room temperature and the results of this test are shown in Figures 5-86 and 5-87.
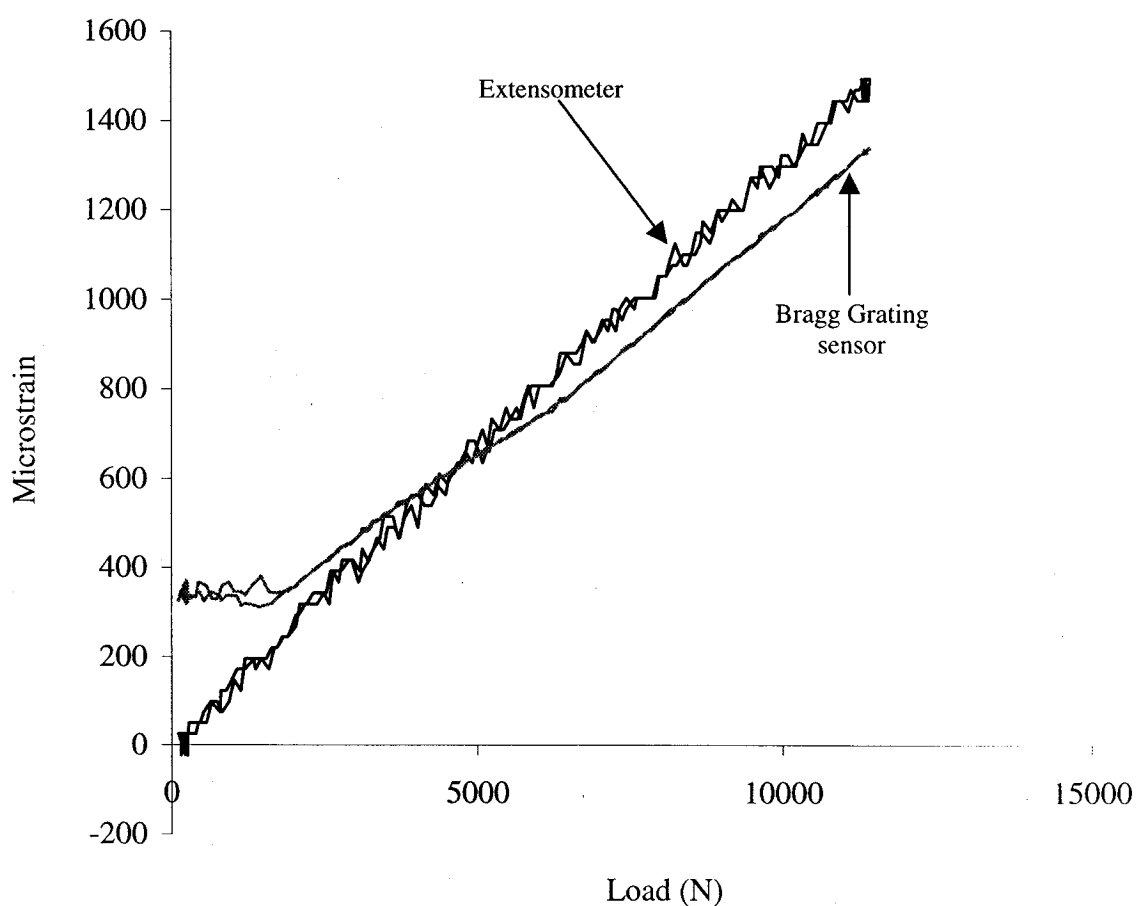


Figure 5-86: Strain from extensometer and embedded Bragg Grating sensor in a CFRP tendon subjected to a trapezoidal load at room temperature
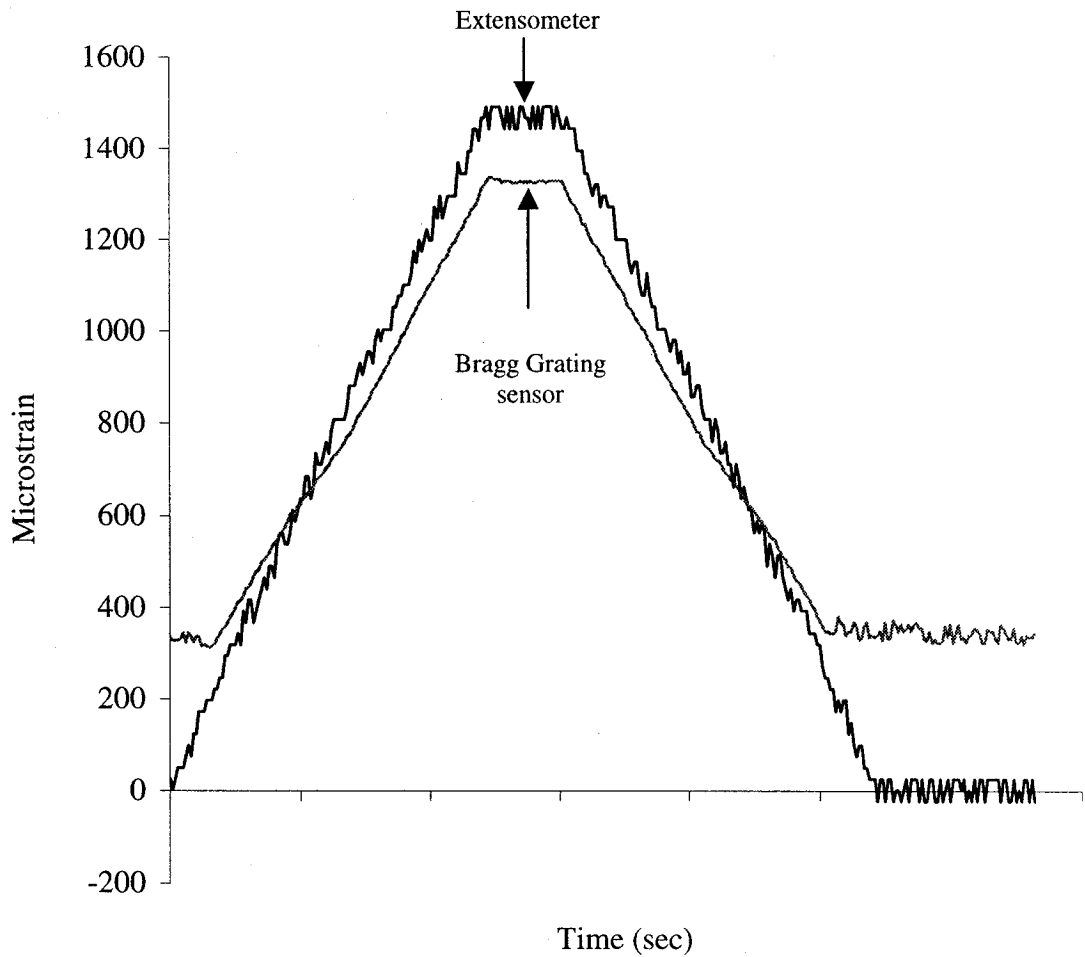
**Figure 5-87:** Strain vs. time plot from extensometer and embedded Bragg Grating sensor in a CFRP tendon subjected to a trapezoidal load at room temperature

It is seen in Figures 5-86 and 5-87 that even though the extensometer and the embedded Bragg grating sensor agree well with one another, the FLS 3100 demodulator could not record any strain values below about 350 microstrain. This is the same as the problem encountered during testing of the GFRP tendon at low temperatures (Figures 5-78 to 5-83). Again, no explanation can be given for this and no error signal was recorded in the data acquisition program. The problem is even more evident in the results of the sinusoidal test at room temperature, shown in Figures 5-88 and 5-89.
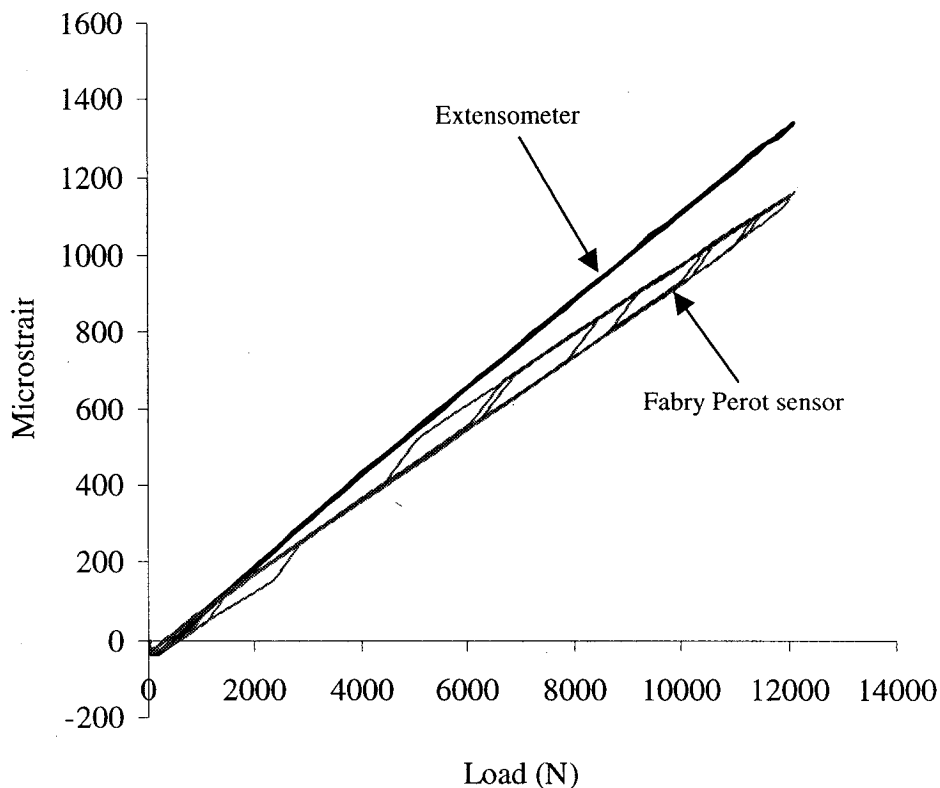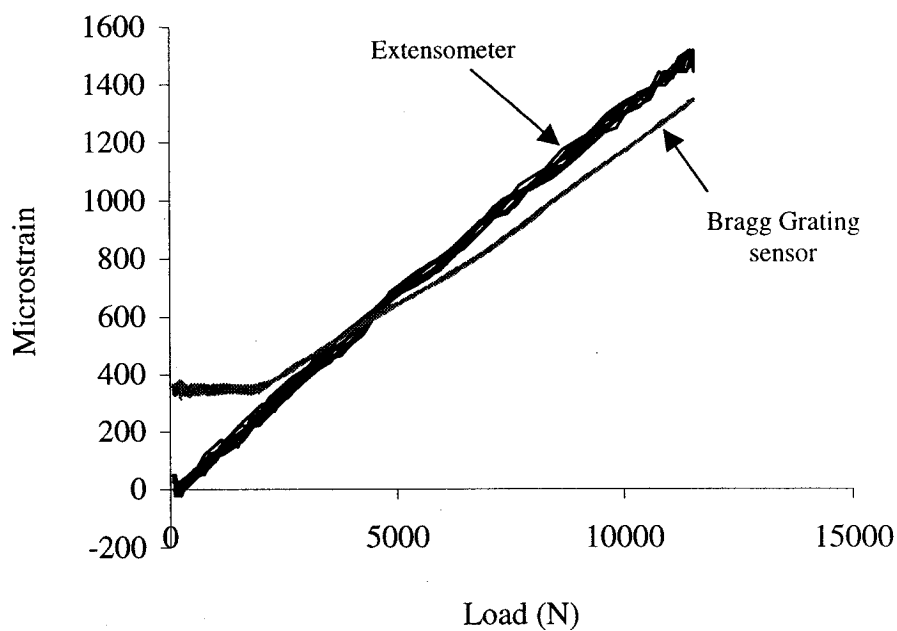
**Figure 5-88:** Strain from extensometer and embedded Bragg Grating sensor in a CFRP tendon subjected to a sinusoidal load at room temperature
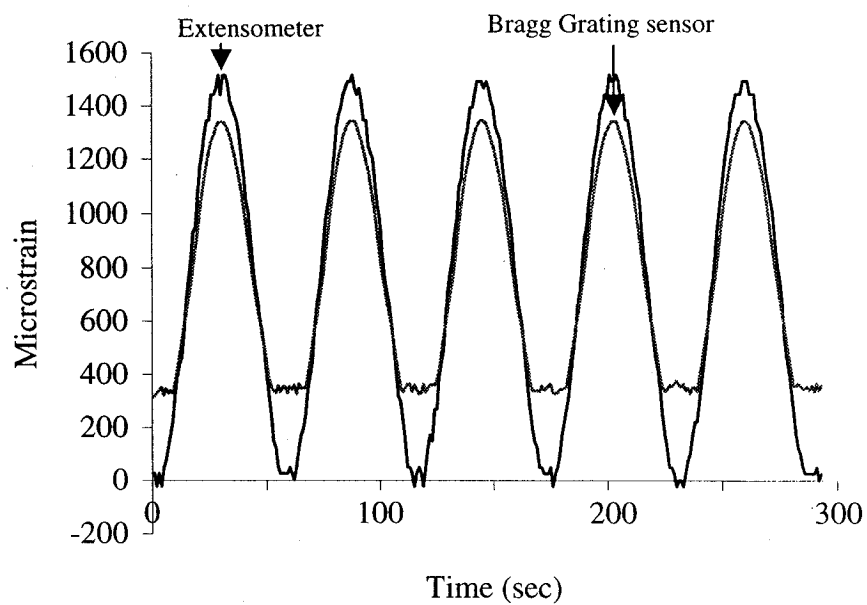


**Figure 5-89:** Strain vs. time plot from extensometer and embedded Bragg Grating sensor in a CFRP tendon subjected to a sinusoidal load at room temperature
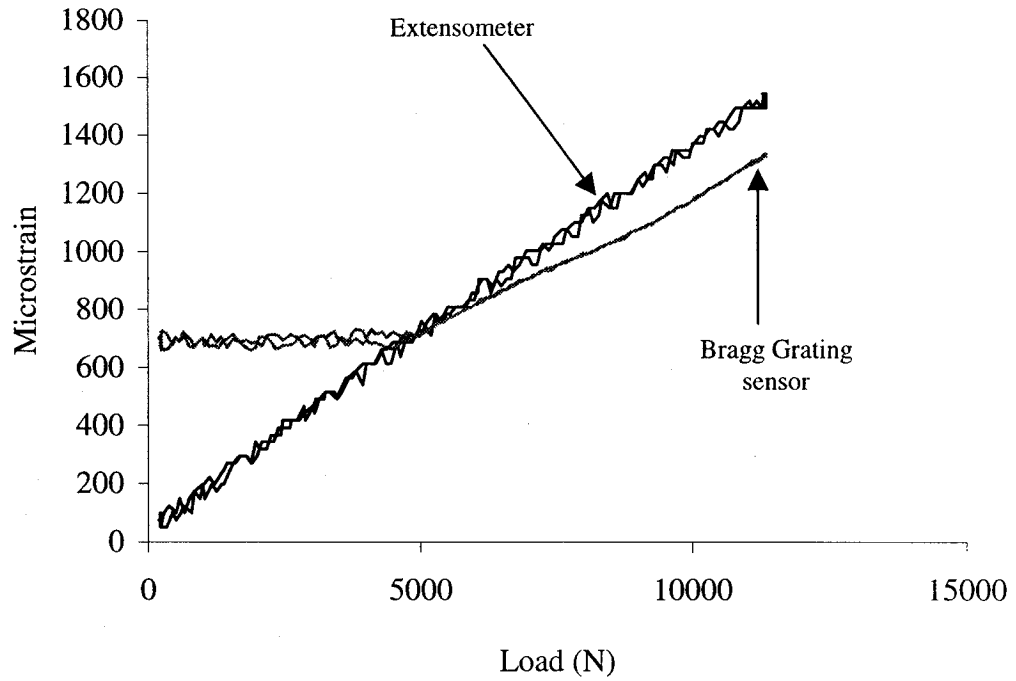
**Figure 5-90:** Strain from extensometer and embedded Bragg Grating sensor in a CFRP tendon subjected to a trapezoidal load at –20°C
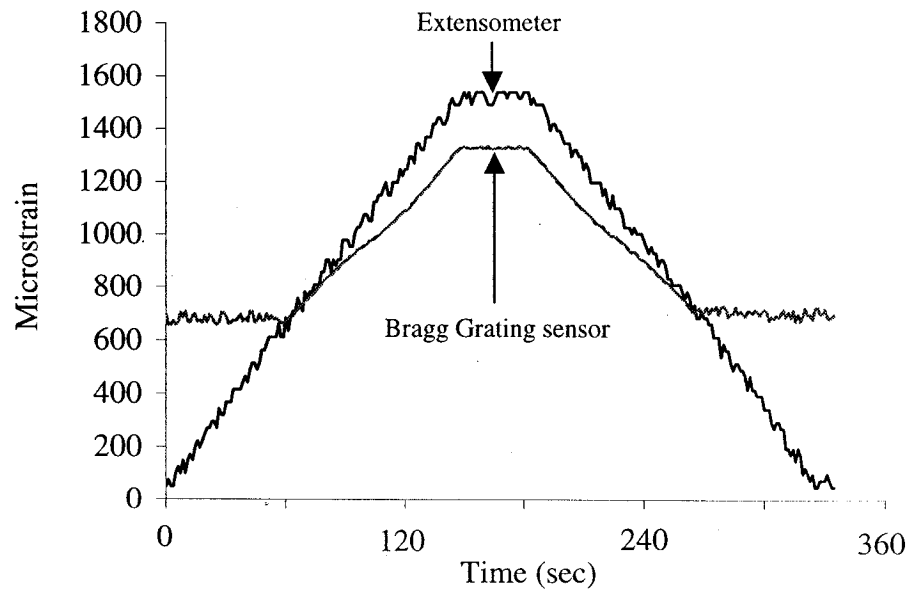


**Figure 5-91:** Strain vs. time plot from extensometer and embedded Bragg Grating sensor in a CFRP tendon subjected to a trapezoidal load at –20°C
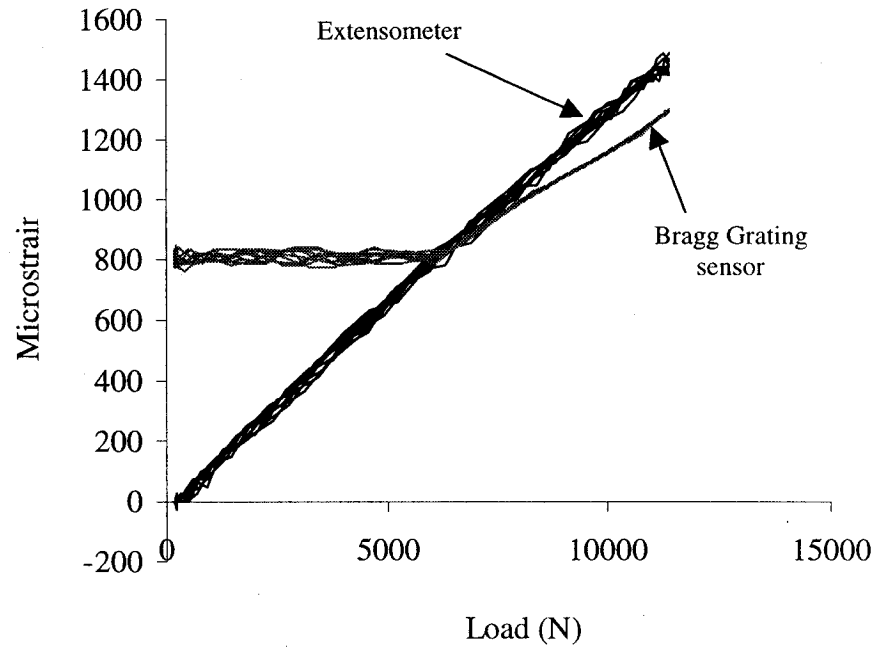
**Figure 5-92:** Strain from extensometer and embedded Bragg Grating sensor in a CFRP tendon subjected to a sinusoidal load at –40°C
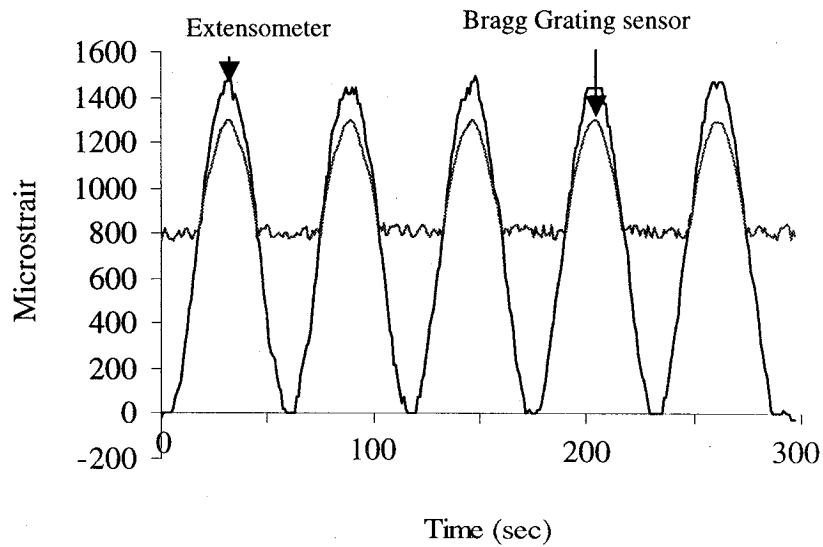


**Figure 5-93:** Strain vs. time plot from extensometer and embedded Bragg Grating sensor in a CFRP tendon subjected to a sinusoidal load at –40°C
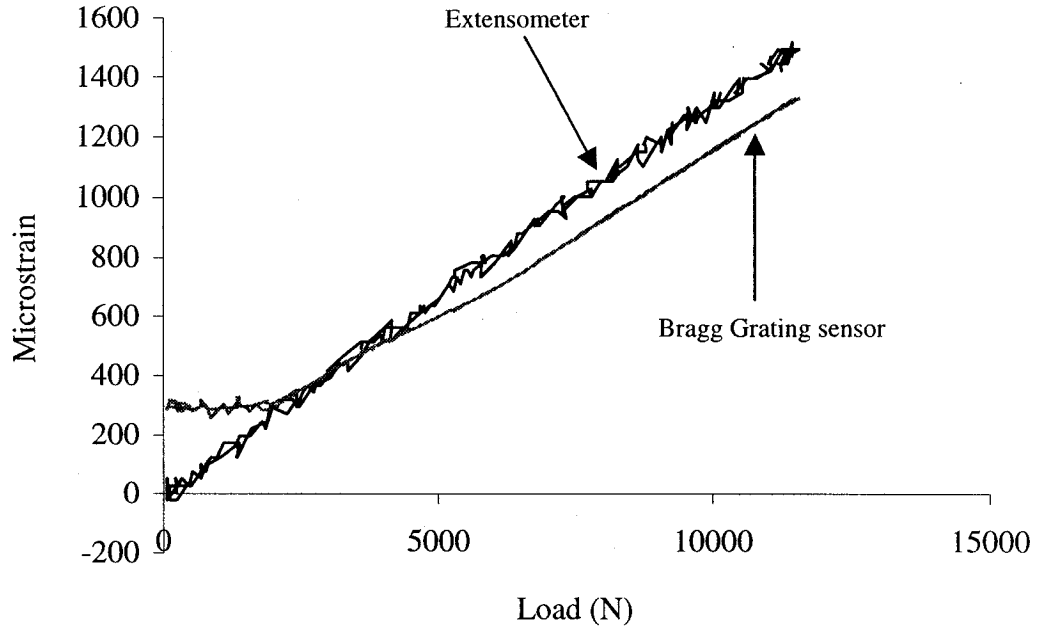
**Figure 5-94:** Strain from extensometer and embedded Bragg Grating sensor in a CFRP tendon subjected to a trapezoidal load at 40°C



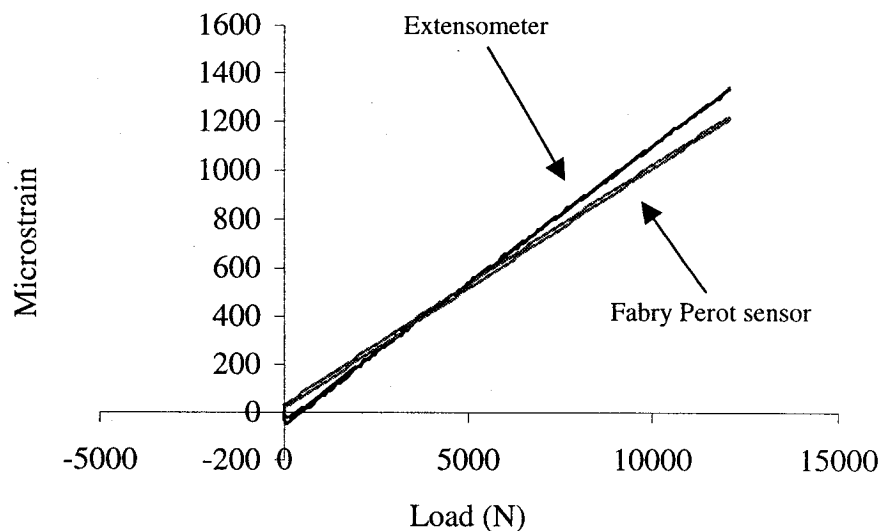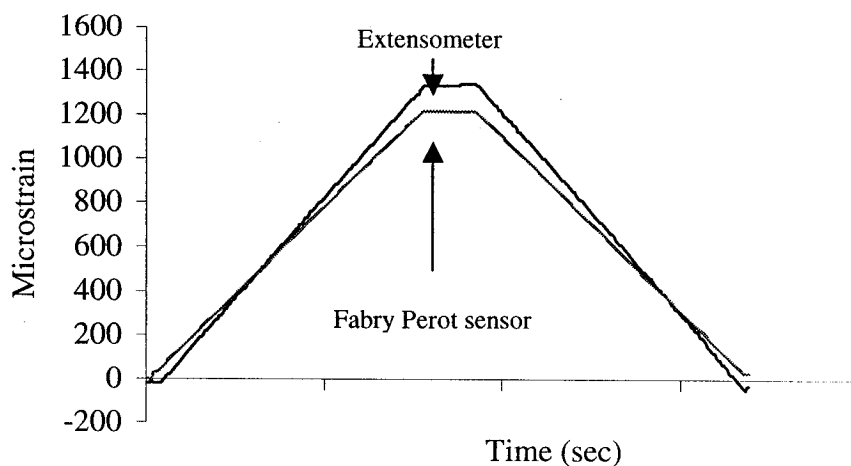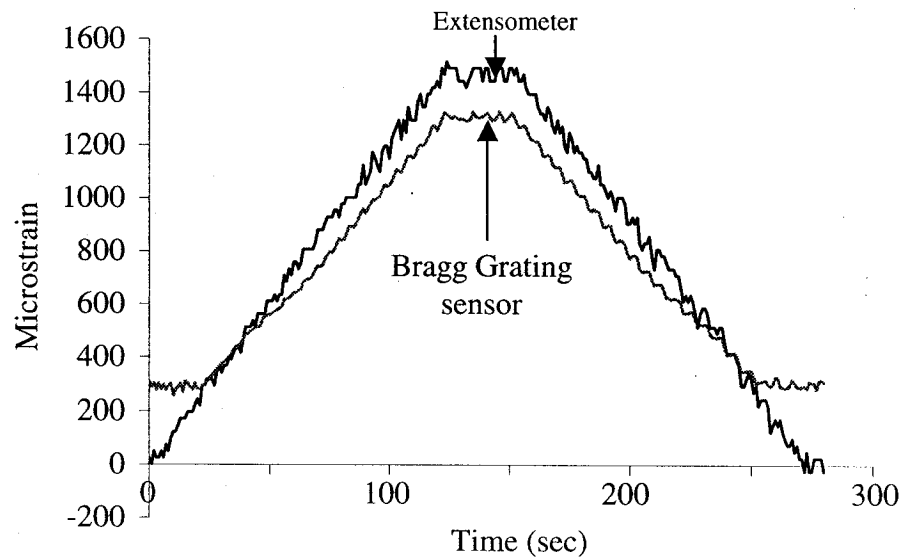**Figure 5-95:** Strain vs. time plot from extensometer and embedded Bragg Grating sensor in a CFRP tendon subjected to a trapezoidal load at 40°C
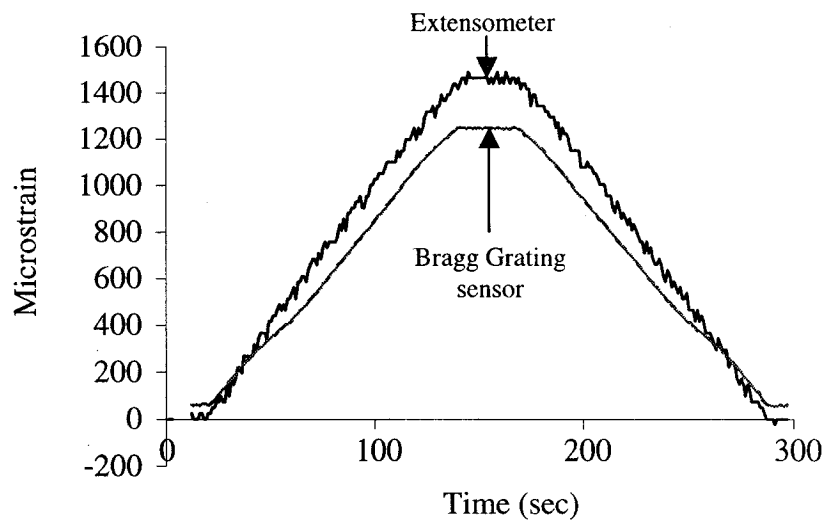
**Figure 5-96:** Strain vs. time plot from extensometer and embedded Bragg Grating sensor in a CFRP tendon subjected to a trapezoidal load at 60°C

On completion of the tests at room temperature, the smart tendon was subjected to sinusoidal and trapezoidal load waveforms at low and high temperatures. As is evident from the results in Figures 5-90 to 5-96, the demodulator kept recording properly only the high strain values. This problem seemed to be more prevalent at low temperatures. Nevertheless, the sensor and the extensometer conformed well to one another at high load levels.

The observed problem with the demodulator was not the only one that was encountered during the research. Another perhaps more significant difficulty had to do with the fact that the "zero" strain level of the Bragg Grating sensor was not retained every time the sensor was disconnected from the FLS 3100 unit. It is known that Bragg Grating sensors, like their Fabry Perot counterparts, are absolute sensors. Thus, when "zeroed" at a particular load value (usually at no load), they maintain that particular reference, so that a non-zero signal is indicative of either mechanical or thermal strain. Indeed, this was observed for the case of Fabry Perot sensors. Bragg Grating sensors however, "lost track" of their zero reference point every time they were disconnected from the demodulator!

Thus, at the onset of a different test, and before any load was applied, the demodulator was showing a non-zero value. Other researchers who used the same demodulator (at the University of Sherbrooke for instance) were also faced with similar problems. Following a large volume of complaints regarding various problems associated with the demodulator, the manufacturer eventually recalled all FLS 3100 models.

### 5.5.1 Synopsis of Temperature Tests on Smart Tendons with Embedded Bragg Grating Sensors

Based on the results of Sections 5.4 and 5.5, one may conclude that Bragg Grating sensors embedded in GFRP tendons provided accurate readings in high-temperature environments. For the tests at low temperatures, the Bragg Grating sensors only gave a reliable strain output at the peak load levels. At low applied loads, the sensors recorded erroneous results. Similar conclusions may be drawn from the tests performed on Bragg Grating sensors embedded in CFRP tendons. For both high- and low-temperature tests, the sensor strain values conformed to extensometer readings only at high load levels. At low stress levels, the sensors did not respond reliably, and the situation seemed to worsen as the ambient temperature was lowered. It is now believed that this odd behavior is attributed to the demodulator rather than the Bragg Grating sensor itself. For all high- and low-temperature tests (as per the room-temperature tests), some of the difference between the embedded sensors and the extensometers is attributed to the misalignment between the spelter sockets and the axis of the tendons.

## 5.6 Fatigue Behavior of Smart Pultruded GFRP and CFRP tendons

### 5.6.1 Introduction

The determination of a conventional stress-strain diagram of a material which conveys information such as Young's modulus, proportional limit, yield strength, ultimate tensile strength and others is obtained by loading the specimen slowly, thus allowing ample time for the stresses to distribute themselves more or less evenly. As well, the specimen is typically loaded to failure. Loading of this nature is called 'static'.

In many practical applications, however, it happens that components of a machine part or structure are subjected to stresses that are not monotonically increasing or decreasing, but are instead varying periodically, often at a high frequency. A typical example is that of a rotating shaft, transmitting power from a high-speed motor to one or more loads. In addition to torsional stresses, the material of the shaft also experiences cyclic flexural or bending stresses. During the first half-cycle of any revolution the top fibers of the shaft might experience tension (and the bottom ones compression), and during the second half cycle the situation reverses, with the top fibers experiencing compression and the bottom fibers experiencing tension. If the motor imparts a speed of 10 Hz to the shaft, then the stresses experienced by the fibers completely reverse themselves ten times each second. Loads of this nature are called alternating or cyclic loads. Different types of cyclic stresses are illustrated in Figure 5-97 [Shigley, 1986].

It is known that when a part is subjected to a sufficiently large number of cycles of load, it fails at stress levels significantly lower than its ultimate strength and sometimes even its yield strength, and that the failure is incurred suddenly and without warning. As well, ductile materials (such as most metals) may fail in a brittle-like fashion when subjected to cyclic loads for extended periods of time. Appropriately, this failure mode is termed

fatigue failure, and the properties of a material associated with its behavior under conditions of prolonged cyclic loads are called fatigue properties.
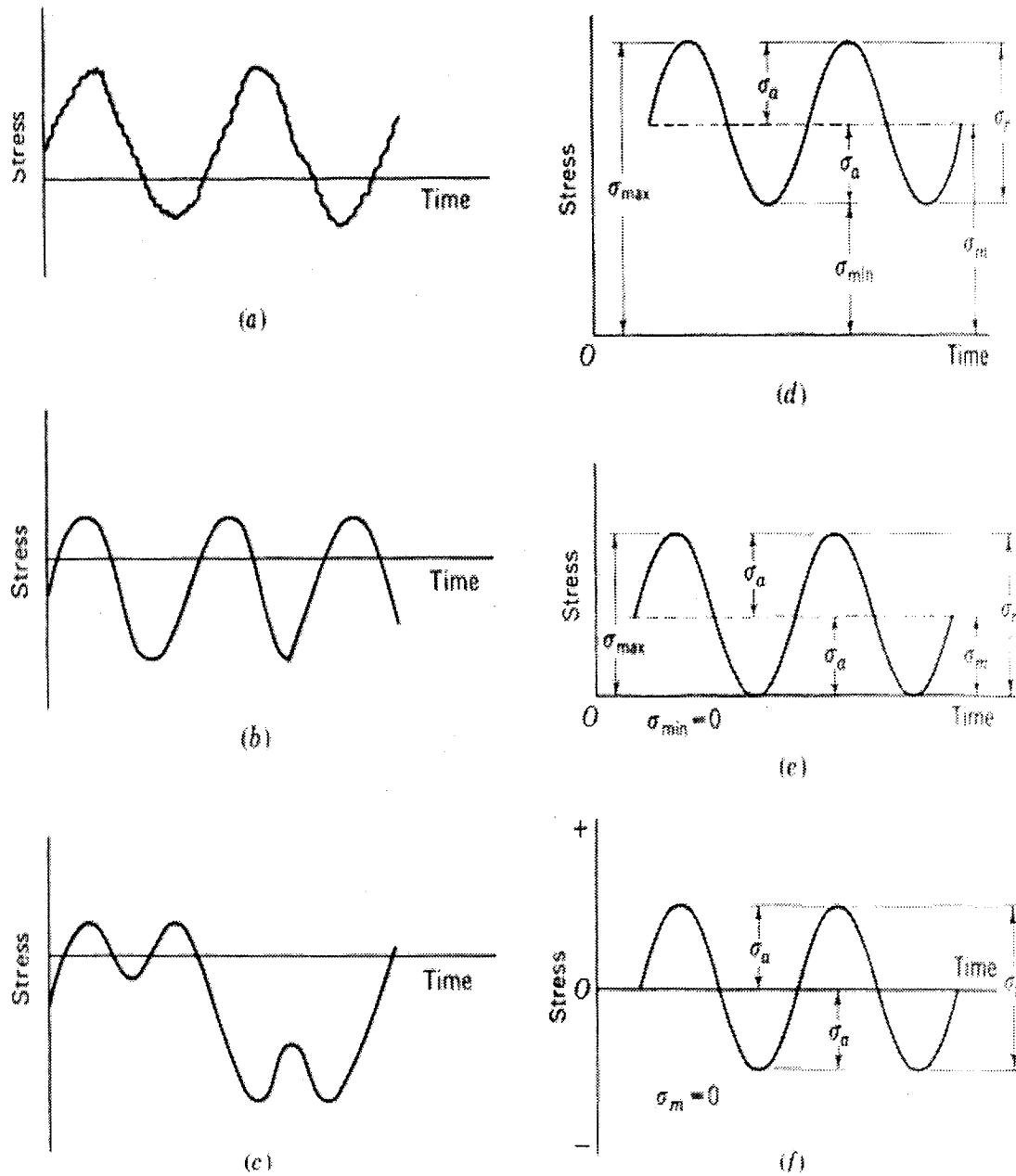


**Figure 5-97:** Some stress-time relations: (a) fluctuating stress with high frequency ripple; (b) and (c) nonsinusoidal fluctuating stress; (d) sinusoidal fluctuating stress; (e) repeated stress; (f) completely reversed sinusoidal stress [Shigley, 1986]
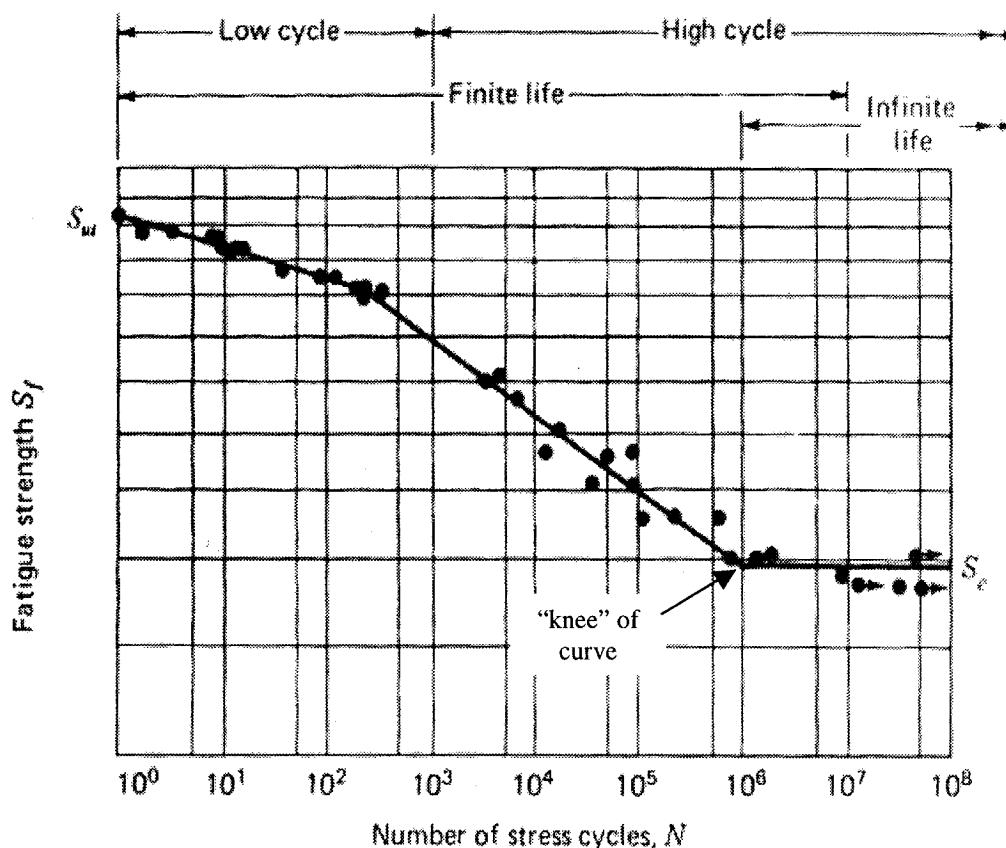
**Figure 5-98:** An S-N diagram plotted from the results of completely reversed axial fatigue tests. Material: chromium-molybdenum steel, normalized; $S_{ut}$ = 800 MPa; $S_e$ = 338 MPa [Shigley, 1986]

The fatigue behavior of a material is characterized by a plot of stress amplitude to failure vs. number of cycles to failure, called an S-N diagram (see Figure 5-98). This diagram is obtained by subjecting a carefully machined specimen to cyclic stresses of different amplitude until failure occurs. The study of fatigue failure that occurs after 1000 cycles or less is called low-cycle fatigue, while high-cycle fatigue examines failure after more than 1000 cycles [Shigley, 1986]. In the case of steels, a "knee" occurs on the S-N plot and this defines the fatigue limit or endurance limit, $S_e$. For stress levels lower than the endurance limit, fatigue failure will not occur irrespective of the number of applied cycles. The most common apparatus used for obtaining the S-N curves is called an R. R.

Moore rotating beam fatigue tester. A schematic of a Moore tester is shown in Figure 5-99 [Juvinall and Marshek, 1991].
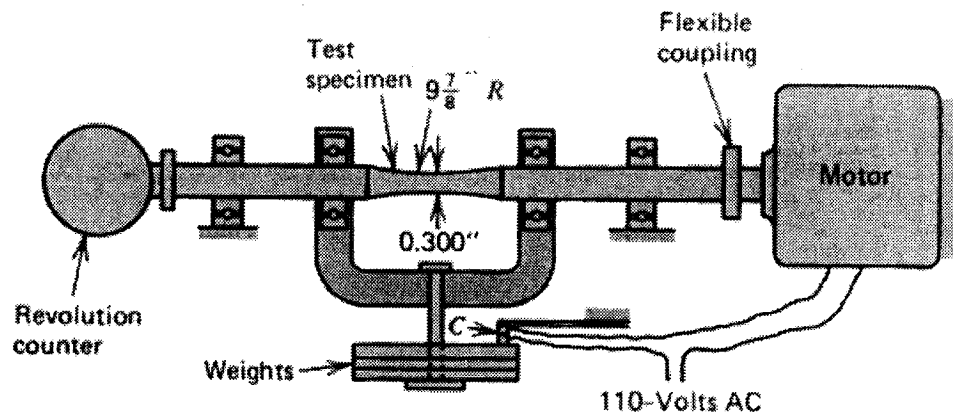
Figure 5-99: R.R. Moore rotating beam fatigue-testing machine [Juvinall and Marshek, 1991]
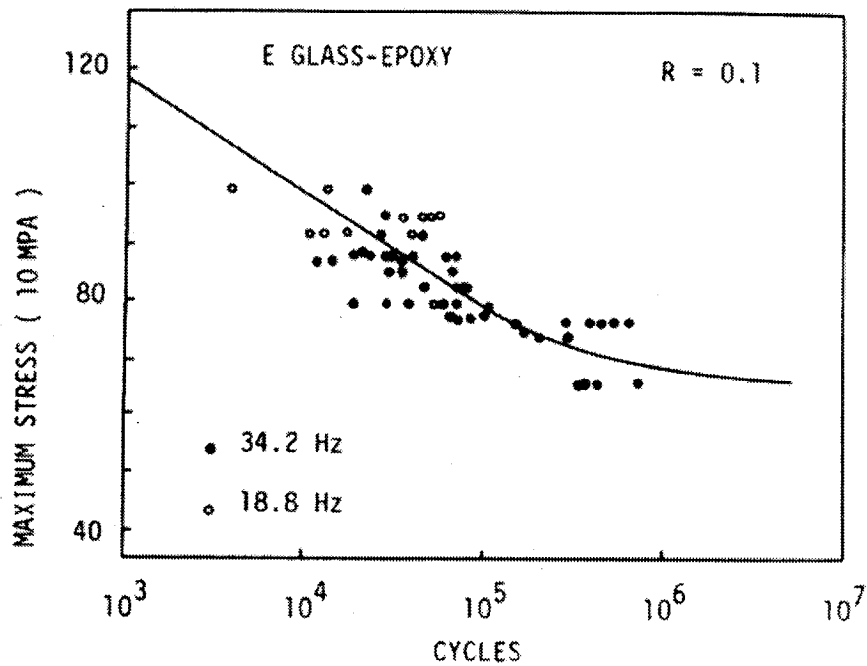
Figure 5-100: Tension-tension S-N diagram for a 0° E-glass/Epoxy laminate [Mallick, 1988]

For most fiber-reinforced composite materials, the characteristic "knee" marking the fatigue limit is not observed. However, the slope of the S-N curve at low stress levels (large number of cycles) is significantly reduced, and consequently, it is customary to give the fatigue strength of composite materials at a large number of cycles, typically 1 million cycles [Schwartz, 1996]. S-N curves for E-glass/epoxy and carbon/epoxy laminates subjected to tension-tension fatigue are shown in Figures 5-100 and 5-101 respectively [Mallick, 1988]. The stress ratio, R, in these figures is the ratio of maximum to minimum stress.
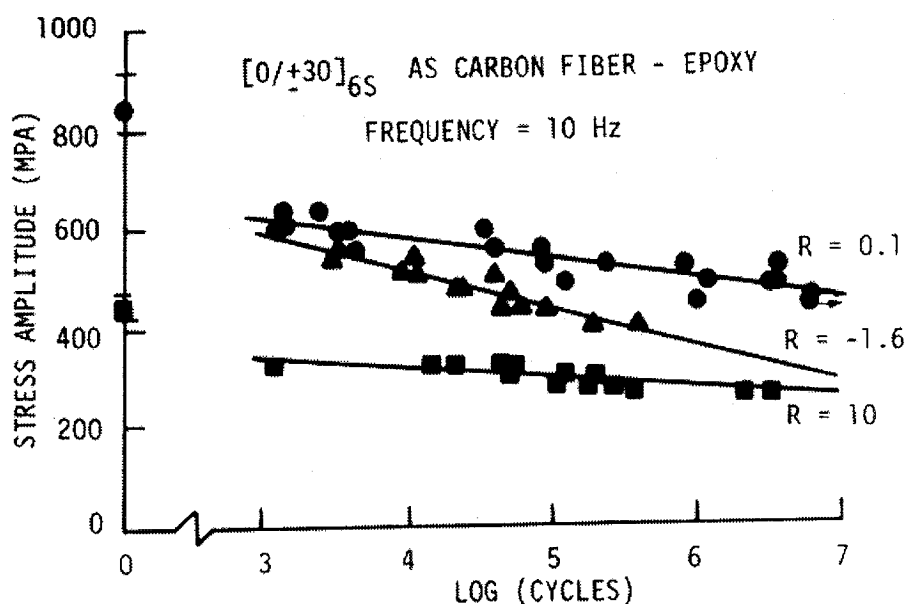


**Figure 5-101:** S-N diagrams for [0/±30]$_{6s}$ carbon/epoxy laminates at various stress ratios. [Mallick, 1988]

Studies [Schwartz, 1996] have shown that composite materials exhibit far superior fatigue resistance to those of metals. One reason for this has to do with the fact that internal flaws in metals act as sites where a crack may initiate and subsequently propagate when the metal part is subjected to cyclic loads. A composite material, however, is less vulnerable to flaws and internal defects, because the large number of

fibers create redundant load paths [Schwartz, 1996]. The superior fatigue-resistance characteristics of composites over metals such as steel and aluminum is evident in Figure 5-102. It should be noted that the "stress density" on the lower axis of the figure is the ratio of applied stress to material density.
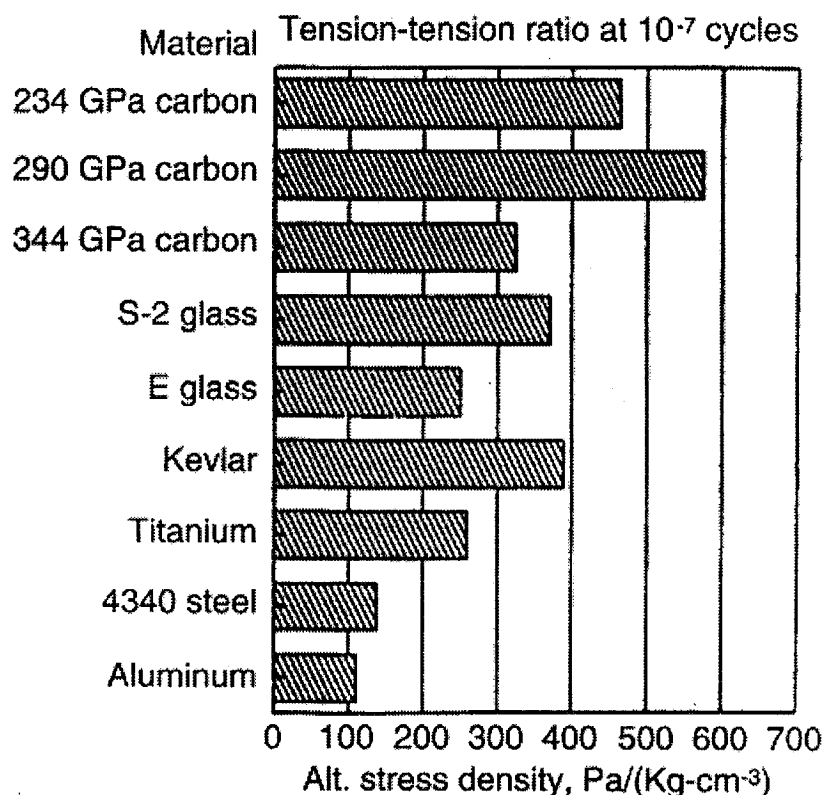


**Figure 5-102:** Fatigue of composites [Schwartz, 1996]

Issues related to fatigue of composites have been studied extensively by many researchers. Mallick et al. [1986] investigated fatigue damage in notched pultruded E-glass/polyester rods with a 75% (wt) reinforcement fraction. The specimens had a diameter of 18 mm and a length of 102 mm, and were characterized by a sharp machined 60° V-notch in the middle. The specimens were tested in an R. R. Moore tester, and the results indicated that the tensile strength of the material was reduced from 690 MPa (as determined from conventional static tests) to 240 MPa. This represents a 60% loss of

strength. Ramkumar and Tossavainen [1986] investigated the fatigue strength of bolted laminates. The AS1/3506 graphite/epoxy specimens were made up of 20, 40, 60 plies in different stacking configurations, with the fibers oriented along the $0^\circ$, $\pm 45^\circ$, $\pm 90^\circ$ directions. Constant-amplitude fatigue tests were conducted at a frequency of 10Hz, with stress ratios of 0 (tension-tension fatigue), -1(completely reversed tension-compression fatigue), and $\infty$ (compression-compression fatigue. Tension-tension fatigue results indicated that the maximum bearing strength was reduced by at most 15% as compared to the static counterpart depending upon the static configuration of the laminate. Similar results were obtained for the compression-compression tests, but for the completely reversed fatigue tests, the overall reduction in strength was up to 50% compared to the static case.

For the current research, it is of interest to assess (a) the impact of an embedded fiber-optic sensor and associated lead on the fatigue properties of the host composite material, and (b) the effect of cyclic loads on the reliability and accuracy of the embedded sensor. Lee et al., [1995] investigated the effect of embedded fiber optic sensors on the fatigue behavior of composite laminates. For their experiments, the authors fabricated two unidirectional and cross-ply glass/epoxy laminates in which they embedded optical fibers with 125 micron diameters. It was determined that the fatigue life for each configuration of crossply and unidirectional laminates was significantly reduced as a result of the embedded optical fibers, and that the effect was more pronounced for the cases of the laminates with a larger number of embedded fibers. It should be mentioned, however, that in these tests the applied fatigue loads were about 70% of the laminate tensile strength (in static conditions) for both stacking configurations. When considering typical safety factors of structural design, it is clear that such a level of applied cyclic load is too high.

Alavie et al. [1994] investigated the reliability of Bragg Grating sensors bonded onto the surface of the CFRP tendons inside a prestressed concrete girder. It was found that the

sensors were not affected by 320,000 cycles of applied load showing excellent stability and durability (see Figure 5-103).
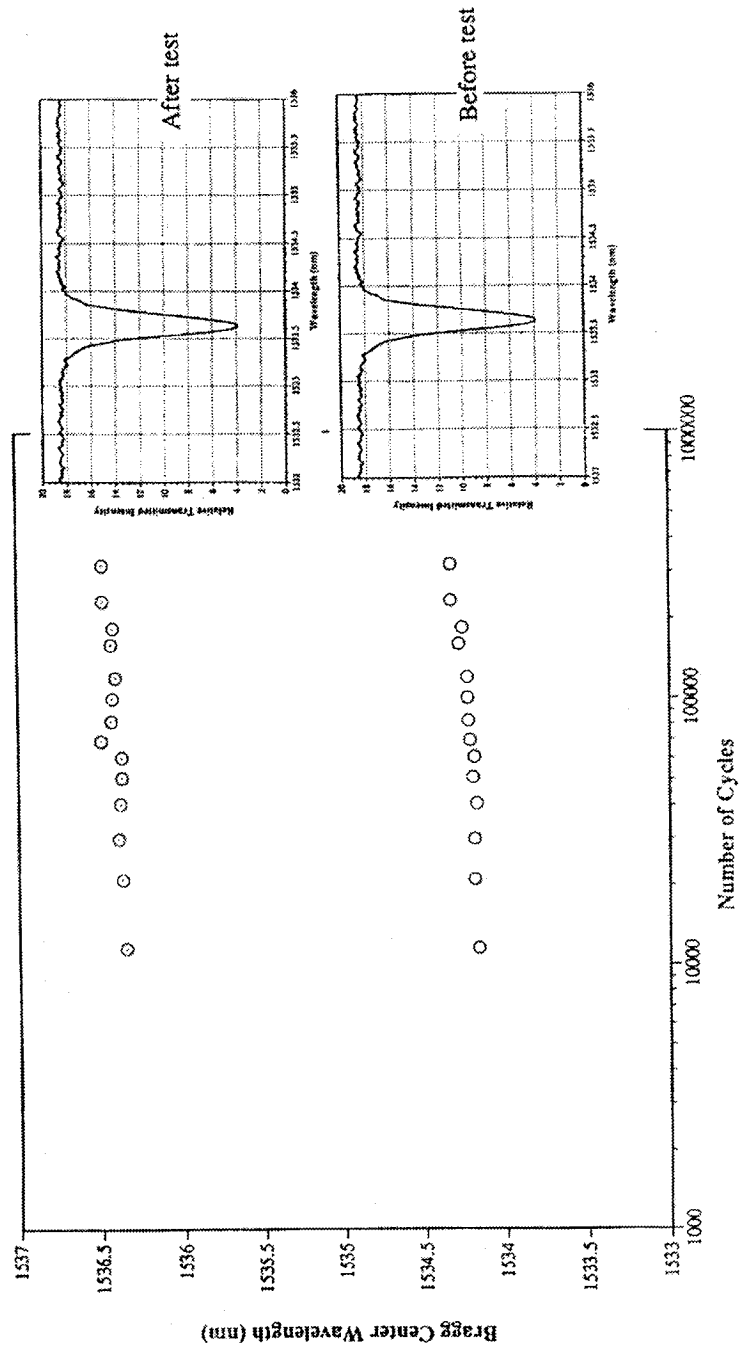


**Figure 5-103:** Fatigue behavior of fiber sensors over 320,000 cycles of 0 to 2000 $\mu\varepsilon$ [Alavie et al., 1994]

Carman and Mitrovic [1994] investigated the performance of a carbon/SiC woven composite system subjected to long- term mechanical fatigue, with a Fabry-Perot sensor. In particular, the authors monitored the reduction in stiffness, and their results indicated that Fabry Perot sensors functioned extremely reliably during long-term fatigue loading of up to 1,000,000 cycles, giving results that conformed very well to conventional extensometers (Figure 104). On the contrary, resistance foil gauges deteriorated fairly rapidly.
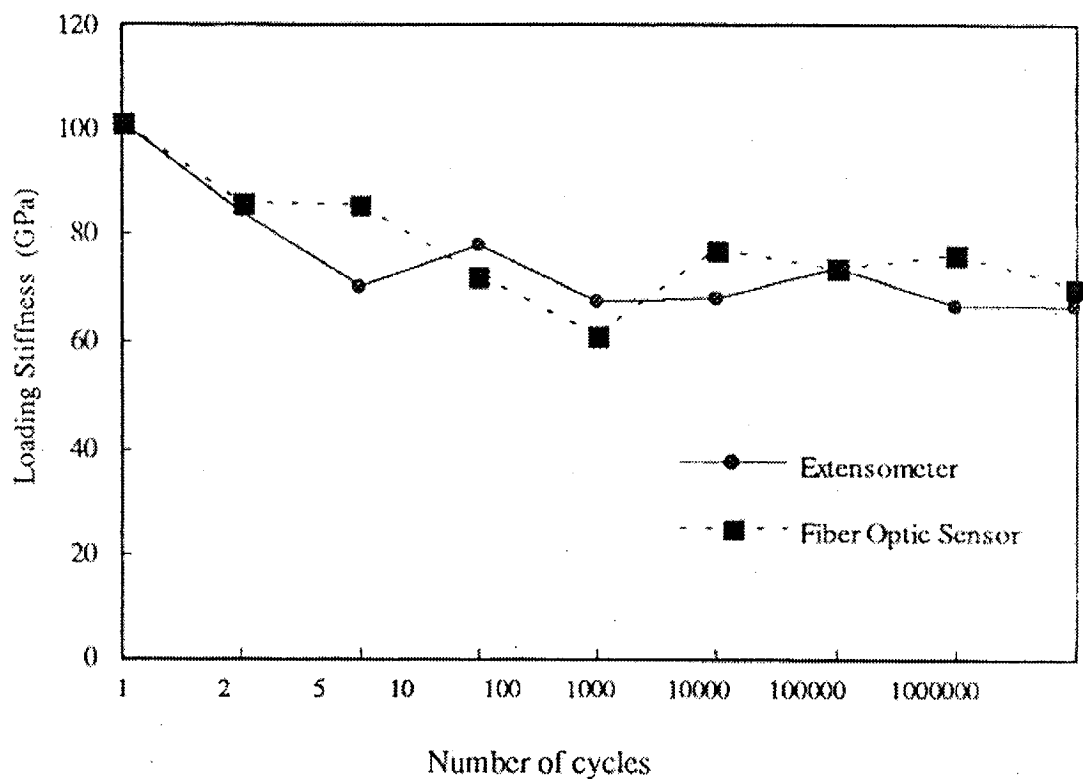


Figure 5-104: Loading stiffness vs. number of cycles for C-SiC composite (comparison of two results: extensometer-fiber optic strain sensor [Carman and Mitrovic, 1994]

Gu and Ansari [2000] successfully demonstrated the use of a multi-gauge-distributed sensor to detect cracks and measure deformations in concrete structures. It was shown that these sensors do not exhibit any hysteresis and therefore can be used for monitoring civil engineering structures that are subjected to fatigue loads.

## 5.6.2 Tension-Tension Fatigue Testing

The tension-tension fatigue cycling test is conducted according to ASTM D3479/D3479M [2001]. The specimen can be tested by subjecting it either to in-plane axial stress at a specified frequency (procedure A) or to in-plane axial strain again at a specified frequency.



**Figure 5-105:** Tension (and fatigue) test specimen drawing [ASTM D3039/D3039M]

The test sample is a thin flat rectangular prismatic strip mounted into the grips of a testing machine such as an Instron. Although many material configurations such as multidirectional laminates can be tested without tabs, it is strongly recommended that

tabs be used (see Figure 5-105) when fatigue testing of unidirectional laminates is to be undertaken [ASTM D3479]. The geometry and dimensions of the test specimen (including tabs) is the same as for the standard tensile test for polymer matrix composite materials and are given in Table 5-1 [ASTM D3039].

**Table 5-1:** Tensile (and fatigue) specimen geometry recommendations [ASTM D3039]

| Fiber Orientation | Width (mm) | Overall Length (mm) | Thickness (mm) | Tab Length (mm) | Tab Thickness (mm) |
|---|---|---|---|---|---|
| 0° unidirectional | 15 | 250 | 1.0 | 56 | 1.5 |
| 90° unidirectional | 25 | 175 | 2.0 | 25 | 1.5 |
| Balanced and symmetric | 25 | 250 | 2.5 | - | - |
| Random-Discontinuous | 25 | 250 | 2.5 | - | - |

## 5.6.3 Experimental Procedure

The fatigue tests were performed on the MTS load frame used for the temperature tests described in the previous sections. The pultruded tendons were subjected only to tension-tension fatigue with a maximum load of 11 kN and a minimum load of 7 kN. This gives a stress ratio, R, (ratio of minimum to maximum load) of 0.64. The load waveform had a frequency of 1 Hz. The first experiments were conducted on GFRP and CFRP tendons with embedded Fabry Perot sensors. As mentioned before, a FIZ 10 demodulation unit is used to record the strain values from the embedded sensor. The number "10" in the name of the demodulator designates the rate at which the unit can acquire data per second. Thus FIZ 10 can acquire 10 samples per second whereas FIZ 100 (also provided by the manufacturer of the Fabry Perot sensors) can sample at 100 Hz. It was decided to select 10 data points per second for the purposes of the experiments described in this thesis. Testing was performed for up to about 300,000 cycles. The main parameters characterizing the fatigue loads used are summarized in Figure 5-106.

R = 0.64

Max. Load = 11 kN

1 second

Load (N)

Min. Load = 7 kN

Time
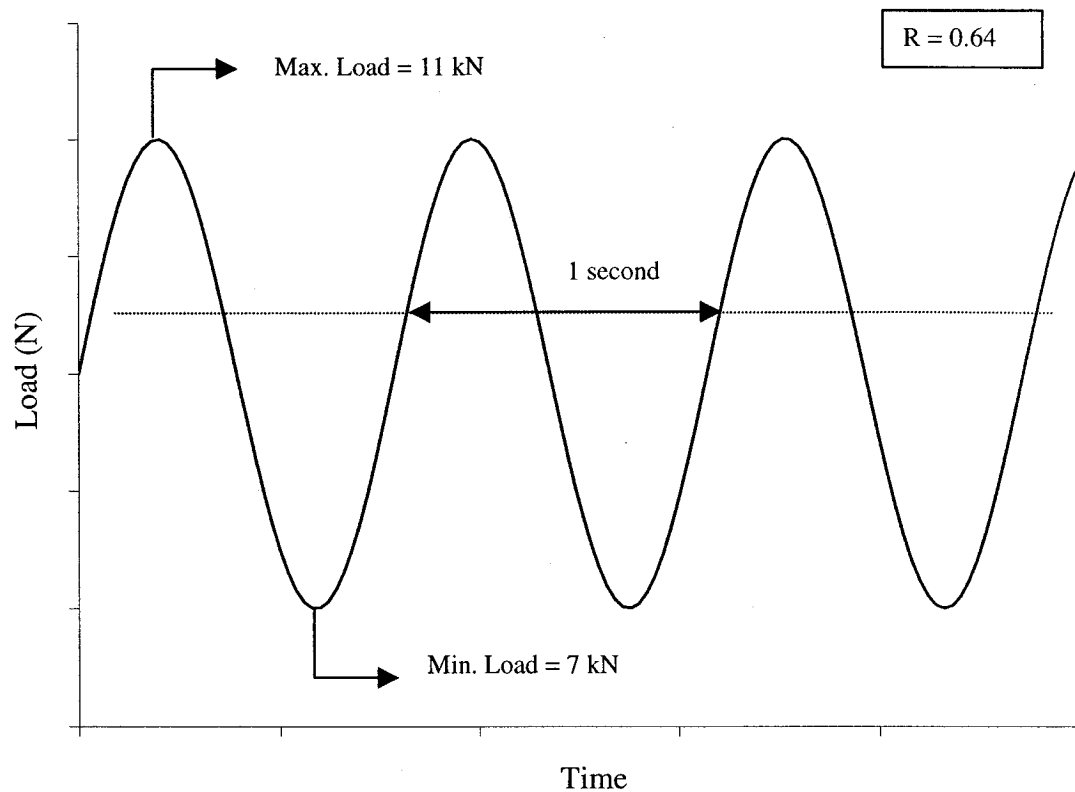
**Figure 5-106:** Testing parameters for the fatigue tests

## 5.6.4 GFRP and CFRP Tendons with Embedded Fabry Perot Sensors

First a GFRP tendon with an embedded Fabry Perot sensor was tested. Figure 5-107 shows the results after 200 load cycles had elapsed. Two features are worth mentioning. The first one is that after 200 cycles the extensometer and the Fabry Perot sensor agree very well with one another. However, it is still too early in the testing phase to conclude on the ability of embedded Fabry Perot sensors to monitor cyclic loads. The second feature is that the FIZ 10 is not recording at the 10 samples-per-second rate as it was supposed to. In fact, an examination of the raw data sheet will reveal that interspersed with actual strain readings were many "no signal" indications. However, there were enough data points recorded at the peaks of the waveforms to be able to draw firm

conclusions with regard to the capability of the sensors themselves. For the purposes of plotting the graphs, the "no signal" points were simply ignored.
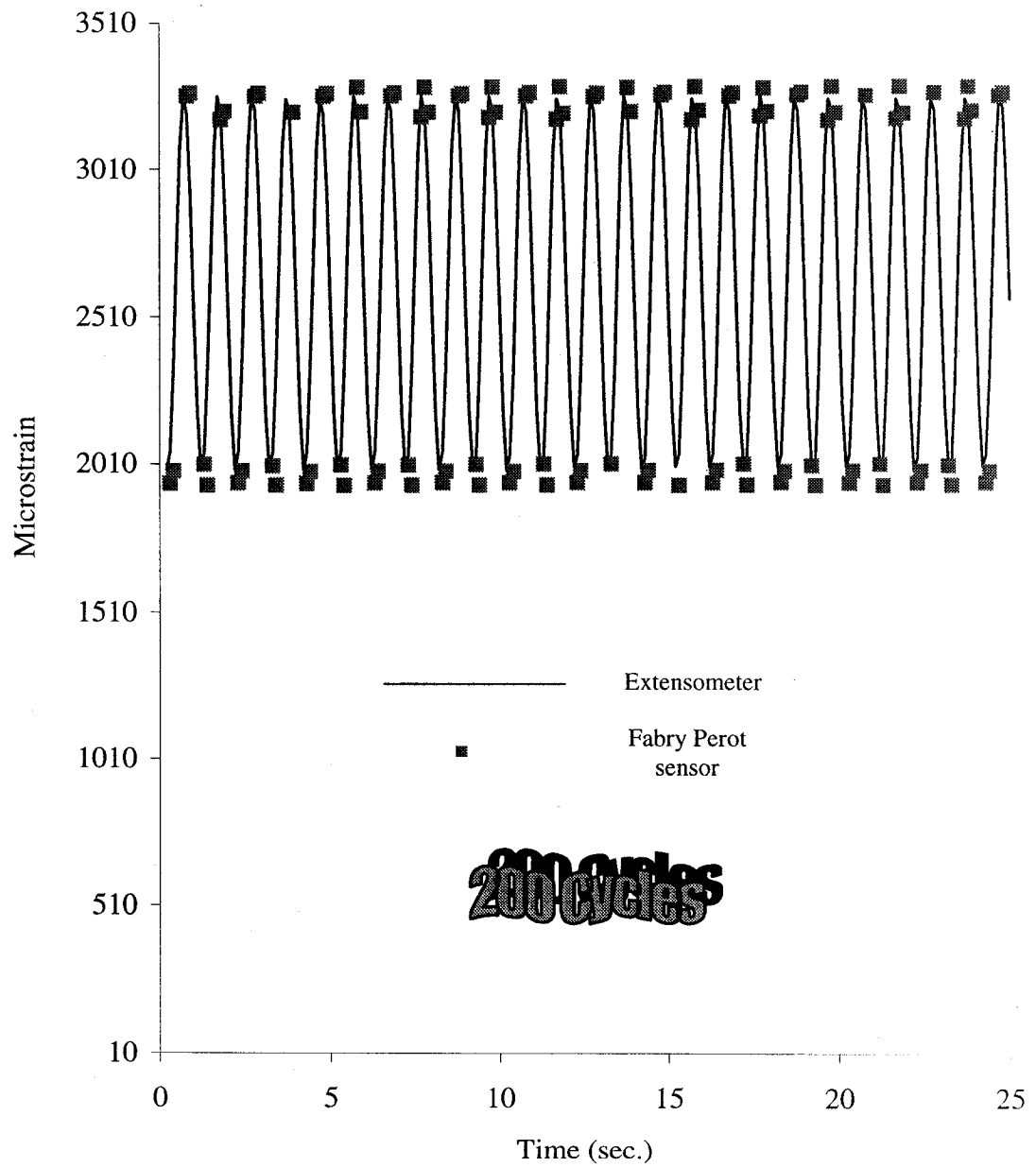


**Figure 5-107:** Strain from extensometer and Fabry Perot sensor in a GFRP tendon subjected to a fatigue load for 200 cycles

Figure 5-108 shows the results after 900 cycles.
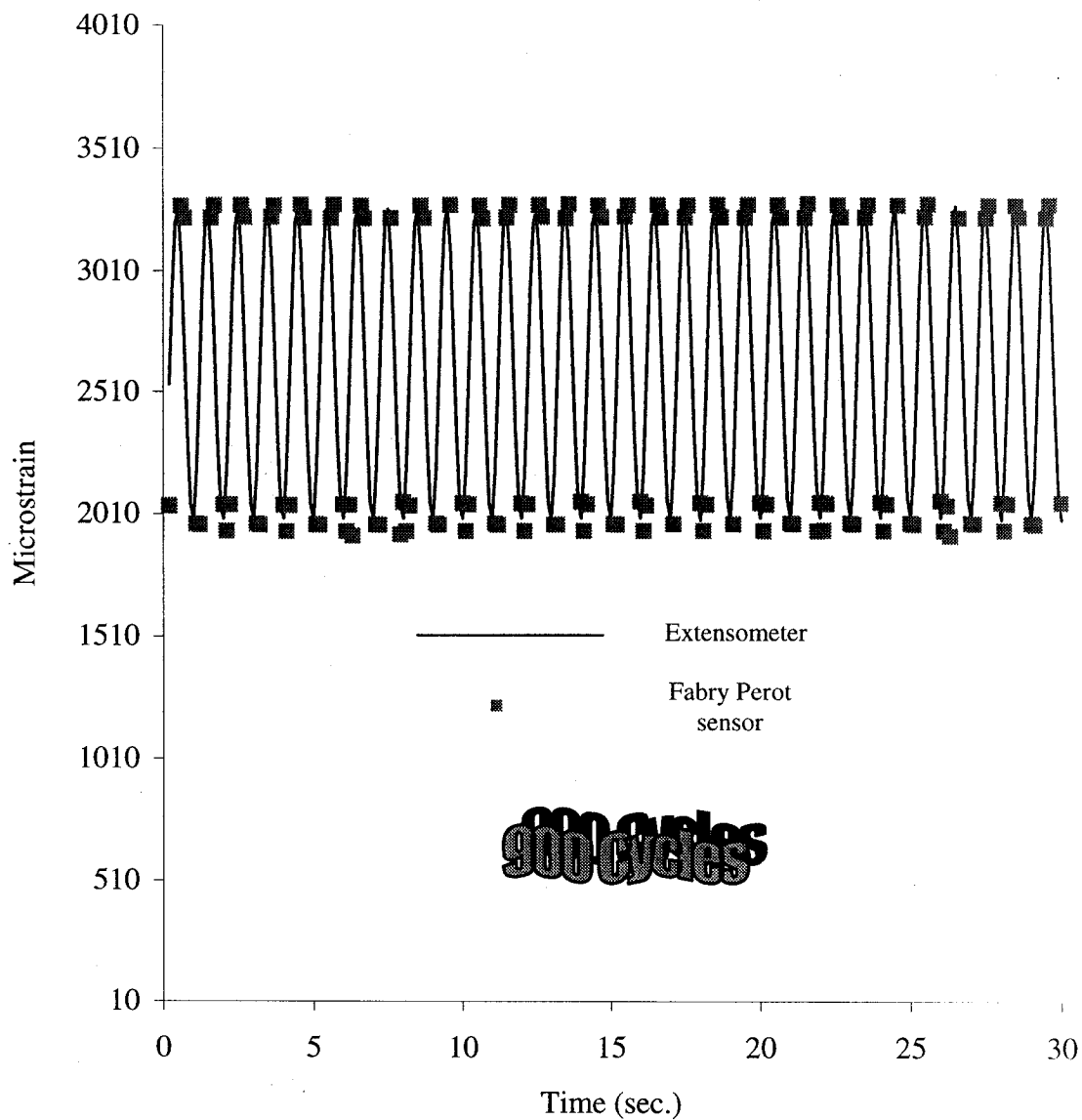


**Figure 5-108:** Strain from extensometer and Fabry Perot sensor in a GFRP tendon
subjected to a fatigue load for 900 cycles

The GFRP tendon was left in the frame overnight, and the next day (after about 100, 000
cycles had elapsed) the results were checked and plotted again.
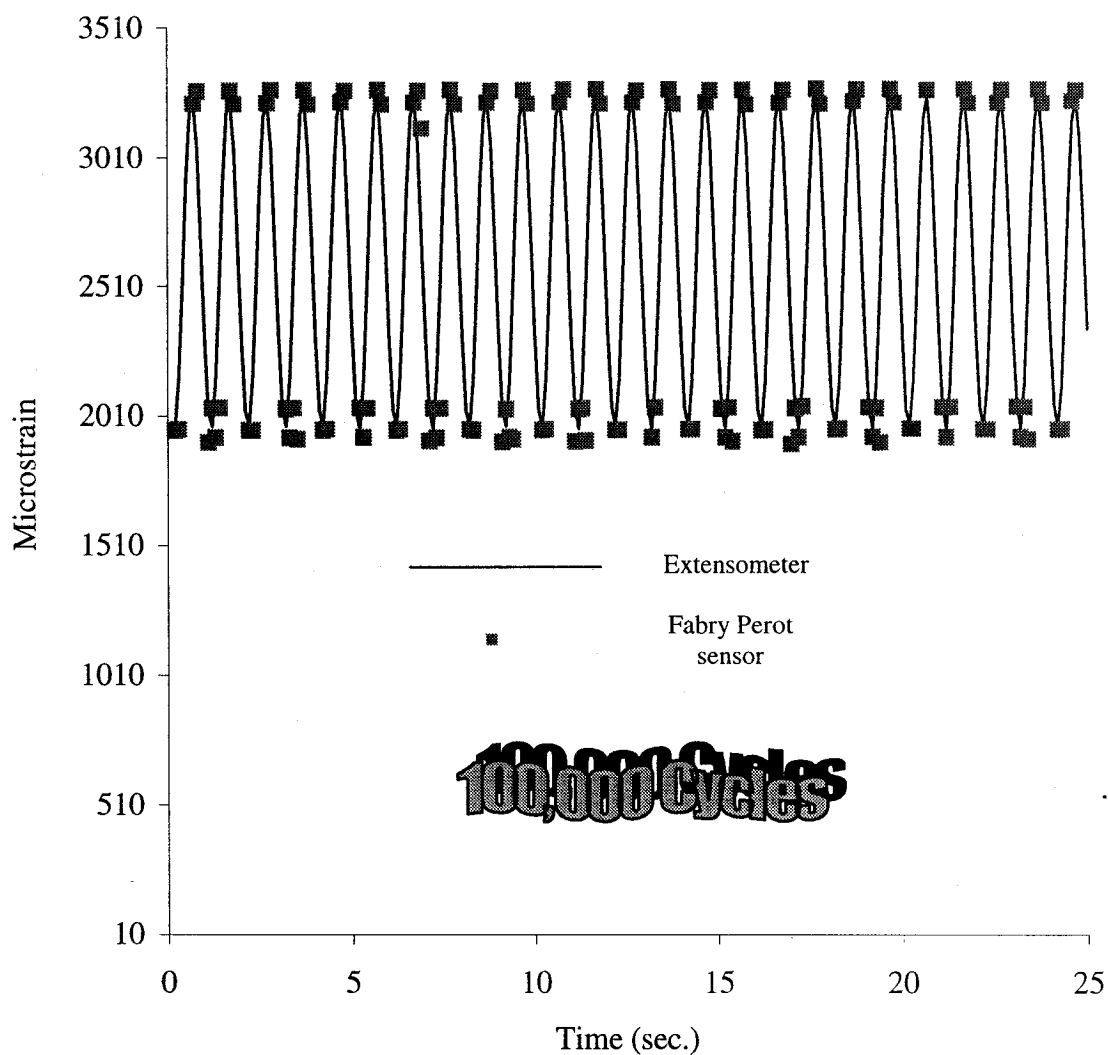
**Figure 5-109:** Strain from extensometer and Fabry Perot sensor in a GFRP tendon subjected to a fatigue load for 100,000 cycles

It is clear from Figures 5-107 and 5-109 that the strain output from the Fabry Perot sensor (as well as the extensometer) is essentially the same at 200 cycles as it is at 100,000 cycles. Consequently, and based on the results of these tests, one may conclude that Fabry Perot sensors remain accurate and reliable when the GFRP tendons in which they are embedded are subjected to 100,000 cycles of tension-tension fatigue.

Subsequently to the GFRP tendon, a CFRP tendon with an embedded Fabry Perot sensor was tested in much the same way.
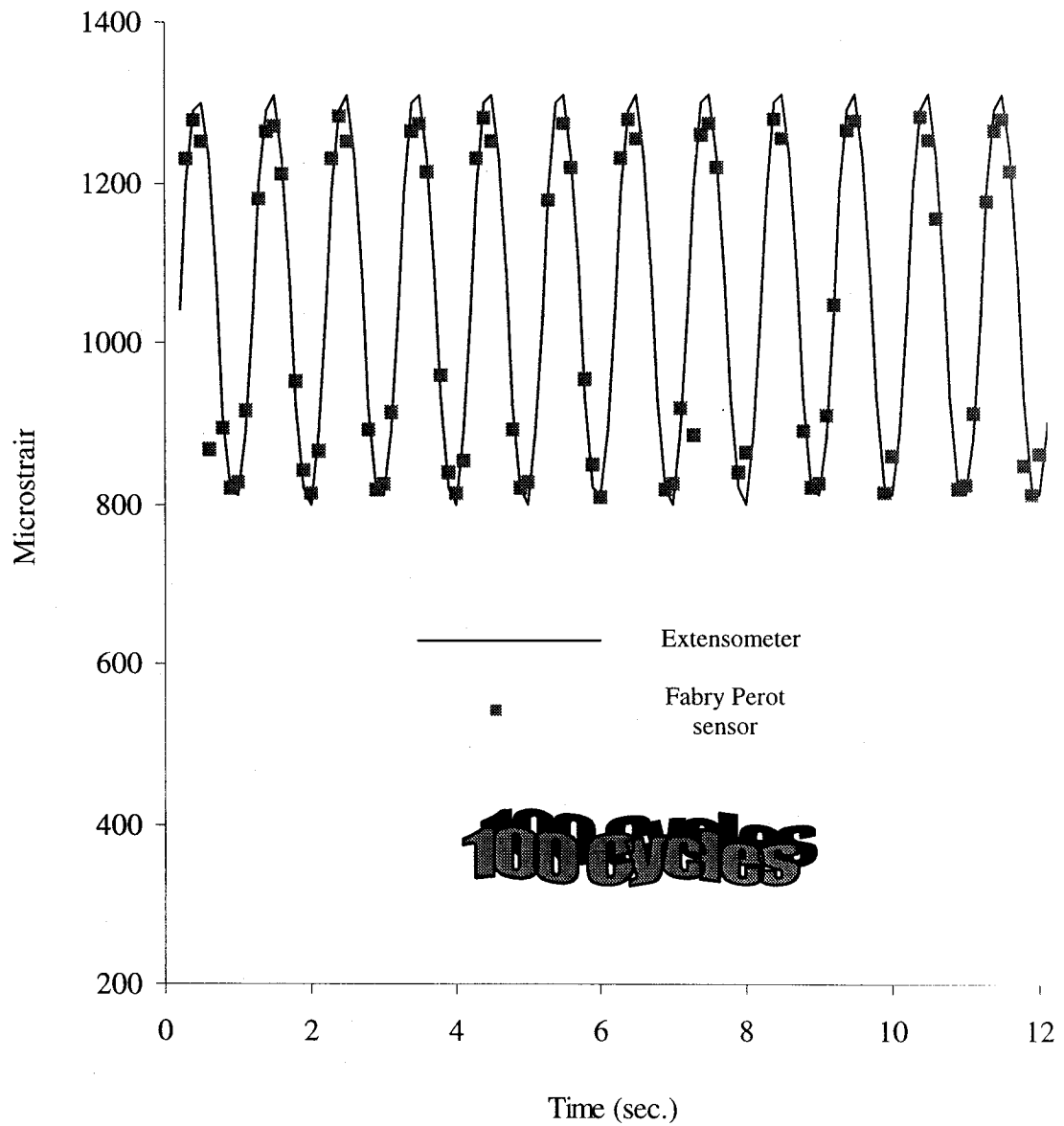


**Figure 5-110:** Strain from extensometer and Fabry Perot sensor in a CFRP tendon subjected to a fatigue load for 100 cycles

The results after the lapse of 100 cycles are shown in Figure 5-110. As for the case of its counterpart in the GFRP tendon, the Fabry Perot sensor embedded in the CFRP tendon agreed very well with the extensometer at the beginning of the test. However, there were again a lot of "no signal" readings in the data sheet, confirming one more time that the FIZ 10, contrary to the accompanying documentation, can not be relied upon to sample at 10 Hz.
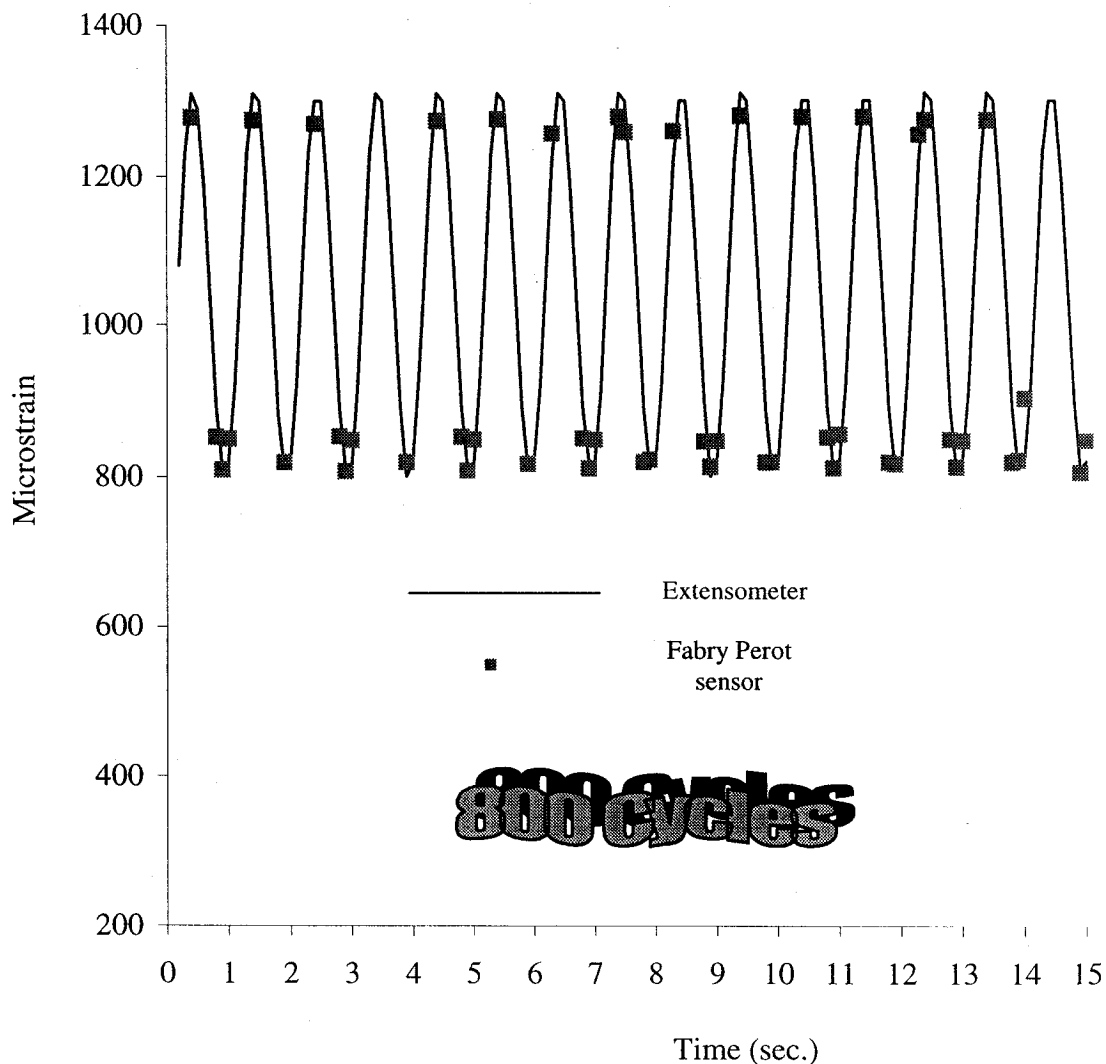


**Figure 5-111:** Strain from extensometer and Fabry Perot sensor in a CFRP tendon subjected to a fatigue load for 800 cycles

Figure 5-111 shows the results after 800 cycles. Once again, the Fabry Perot sensor and the extensometer agree very well with one another. Testing was continued until the next day, and the results after 70, 000 cycles are shown in Figure 5-112.
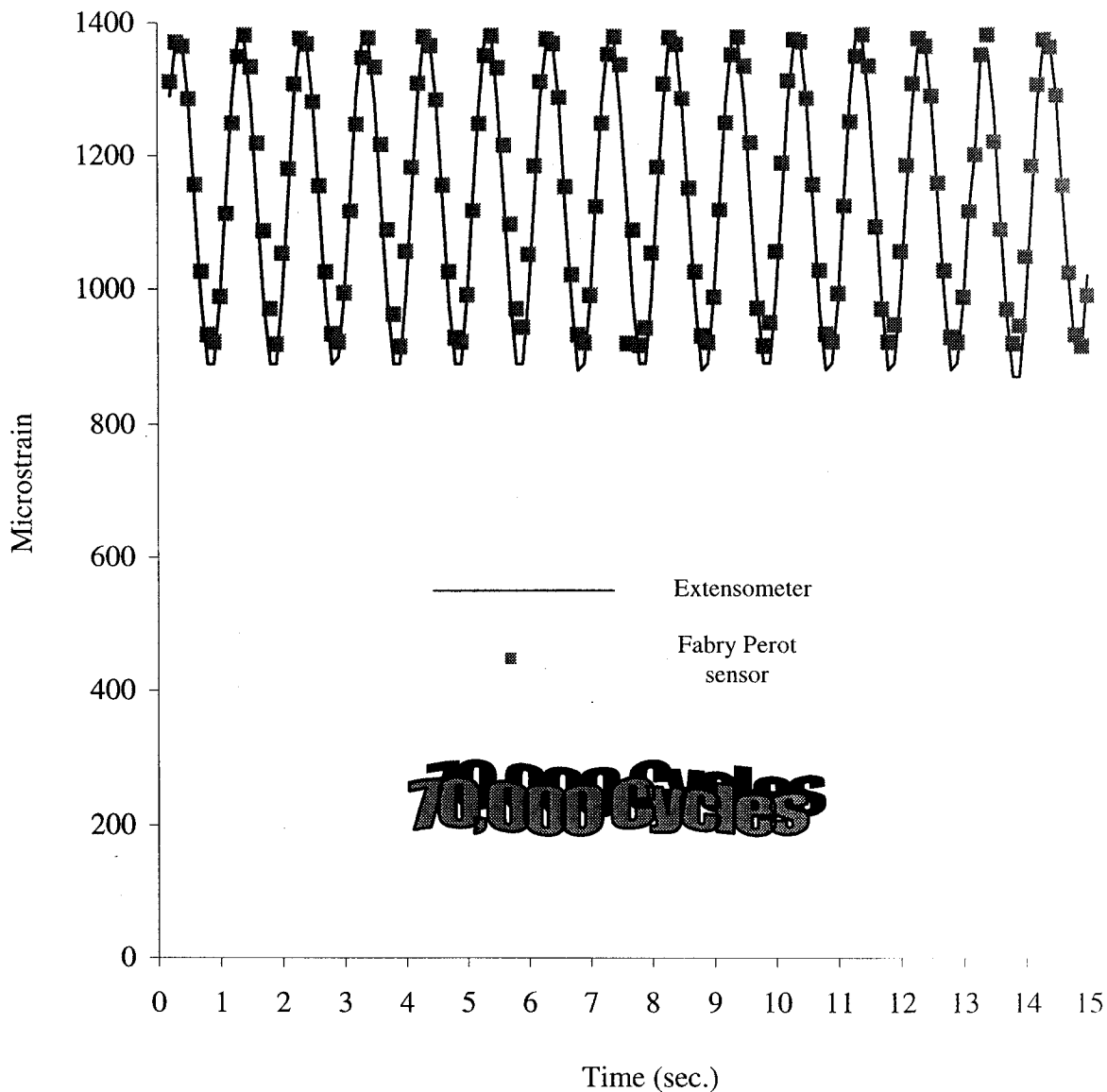


**Figure 5-112:** Strain from extensometer and Fabry Perot sensor in a CFRP tendon subjected to a fatigue load for 70,000 cycles

It is apparent in Figure 5-112 that the FIZ 10 demodulator worked properly for the first time and no "no signal" indications were recorded in the data sheet. It was decided to continue testing for another day and the results after about 138,000 cycles (38 hours) are shown in Figure 5-113.
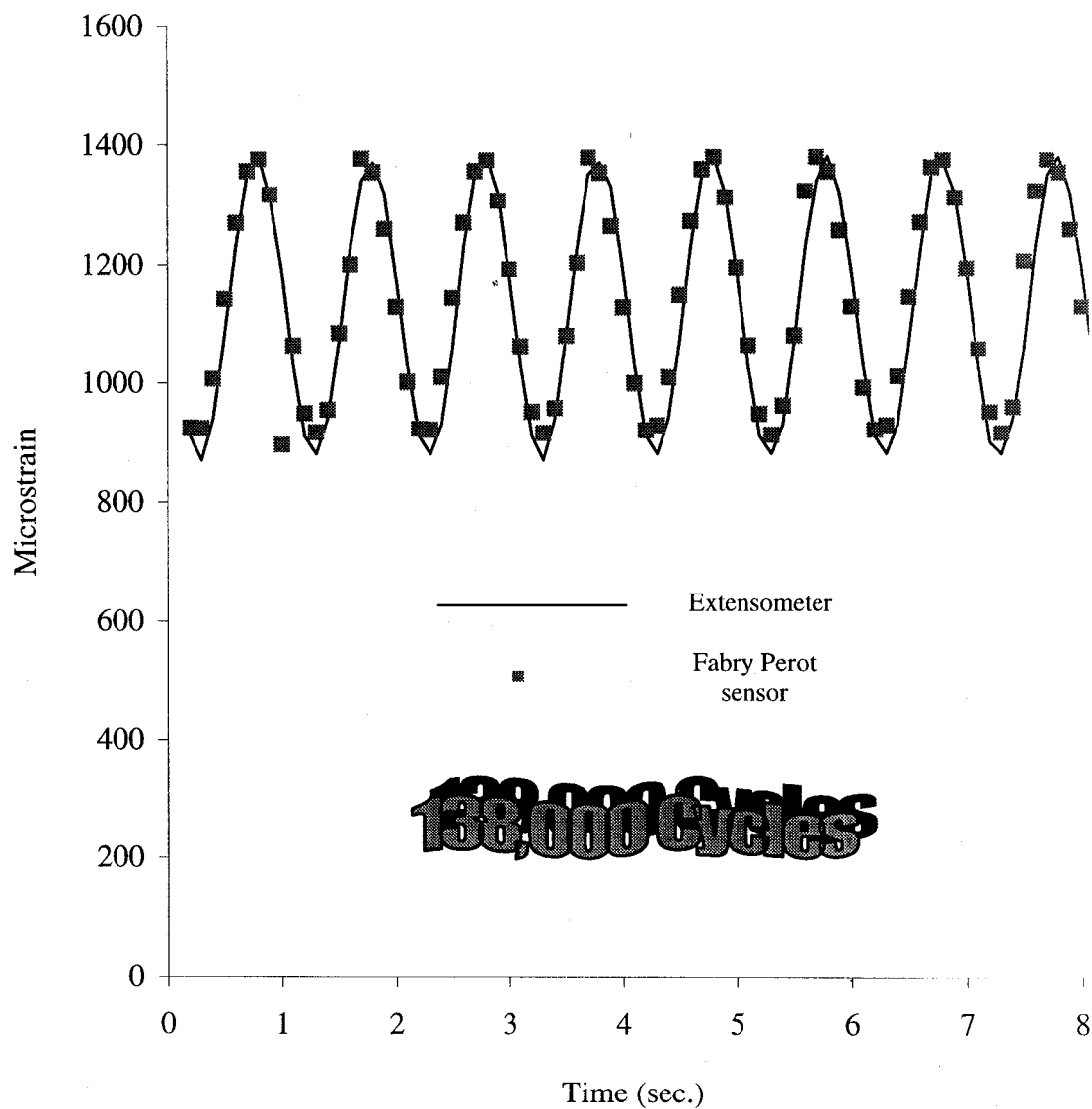
**Figure 5-113:** Strain from extensometer and Fabry Perot sensor in a CFRP tendon subjected to a fatigue load for 138,000 cycles

Figure 5-113 is very similar to Figure 5-112. Thus, one may conclude from Figures 5-107 to 5-113 that Fabry Perot sensors embedded in GFRP and CFRP tendons are not affected by up to 140,000 cycles of applied load, and they retain their accuracy and reliability.
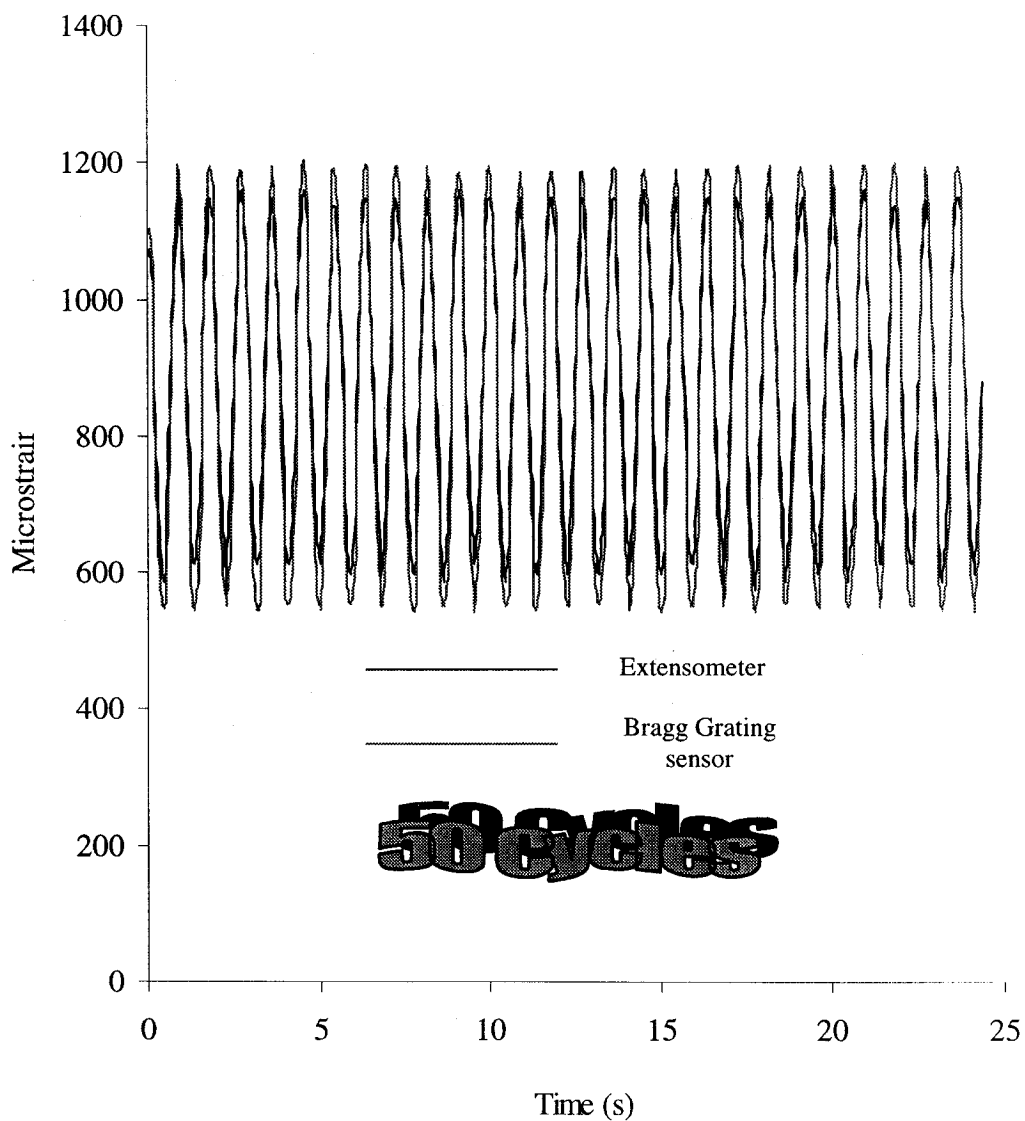


**Figure 5-114:** Strain from extensometer and Bragg Grating sensor in a CFRP tendon subjected to a fatigue load for 50 cycles

The testing program was then continued with Bragg Grating sensors embedded in GFRP and CFRP tendons. The FLS 3100 demodulation unit was used for these tests. It allows for a higher sampling rate than the FIZ 10, and so a frequency of 20 sample points per second was selected. The load was applied at 1 Hz as for the previous tests, and thus it was felt that 20 sample points per cycle would be more than sufficient to plot a smooth curve.
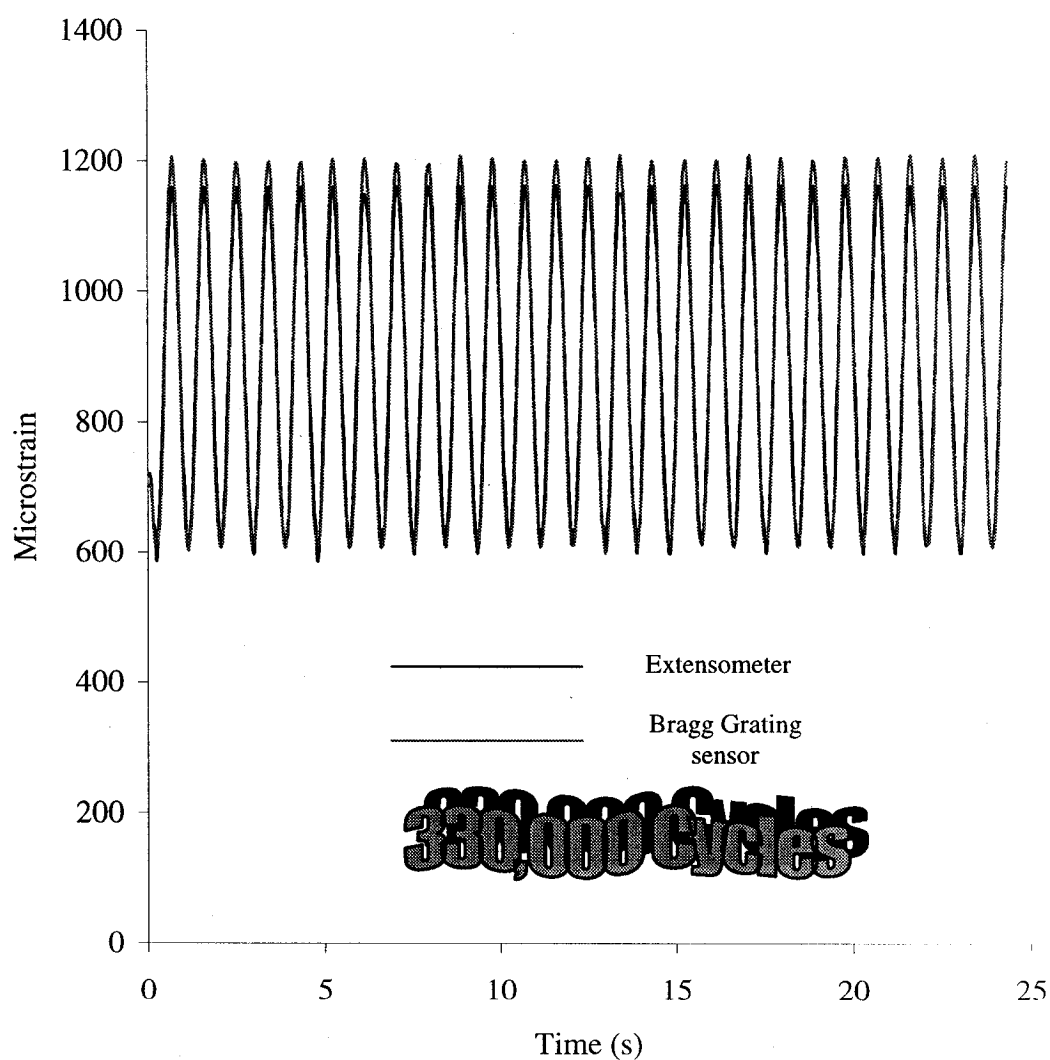
Figure 5-115: Strain from extensometer and Bragg Grating sensor in a CFRP tendon subjected to a fatigue load for 330,000 cycles

The first fatigue test involving Bragg Grating sensors was conducted on a CFRP tendon. Figure 5-114 shows the strain readings from the embedded sensor and the externally affixed extensometer at the beginning of testing (after 50 cycles). One may observe that the FLS 3100 demodulation unit can sample much more frequently and reliably than the corresponding FIZ 10 unit. Also, at the beginning of the test the two strain-monitoring devices agree very well with one another.
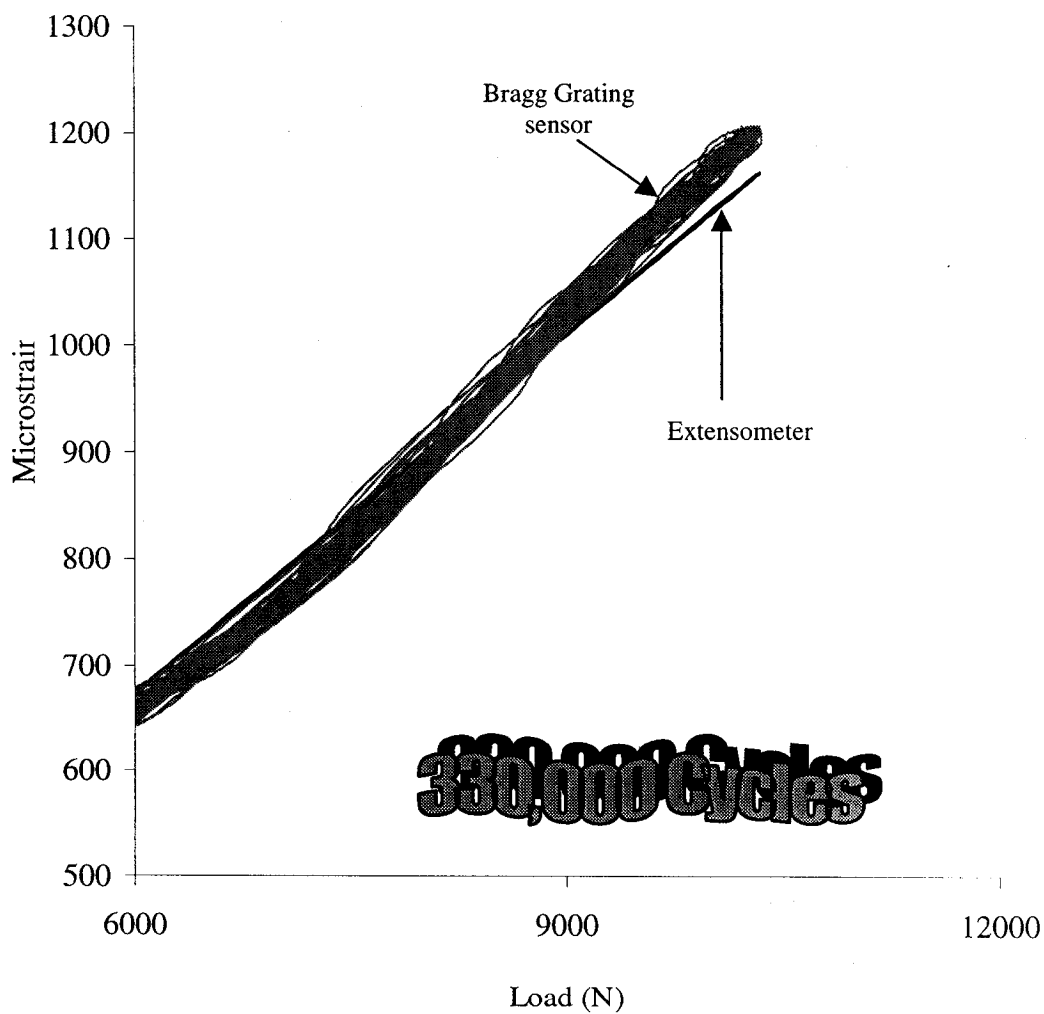


**Figure 5-116:** Strain vs. load for extensometer and Bragg Grating sensor in a CFRP tendon subjected to a fatigue load for 330,000 cycles

This tendon was tested for 4 days (330,000 cycles) at the end of which the data was collected and plotted. The results are shown in Figure 5-115. Comparing this plot with the corresponding one in Figure 5-114 reveals that the two are essentially the same. The data from Figure 5-115 are plotted as microstrain vs. load in Figure 5-116. Thus, one may conclude that Bragg Grating sensors embedded in CFRP tendons are not affected by more than 300,000 cycles of applied load, retaining their accuracy and reliability.
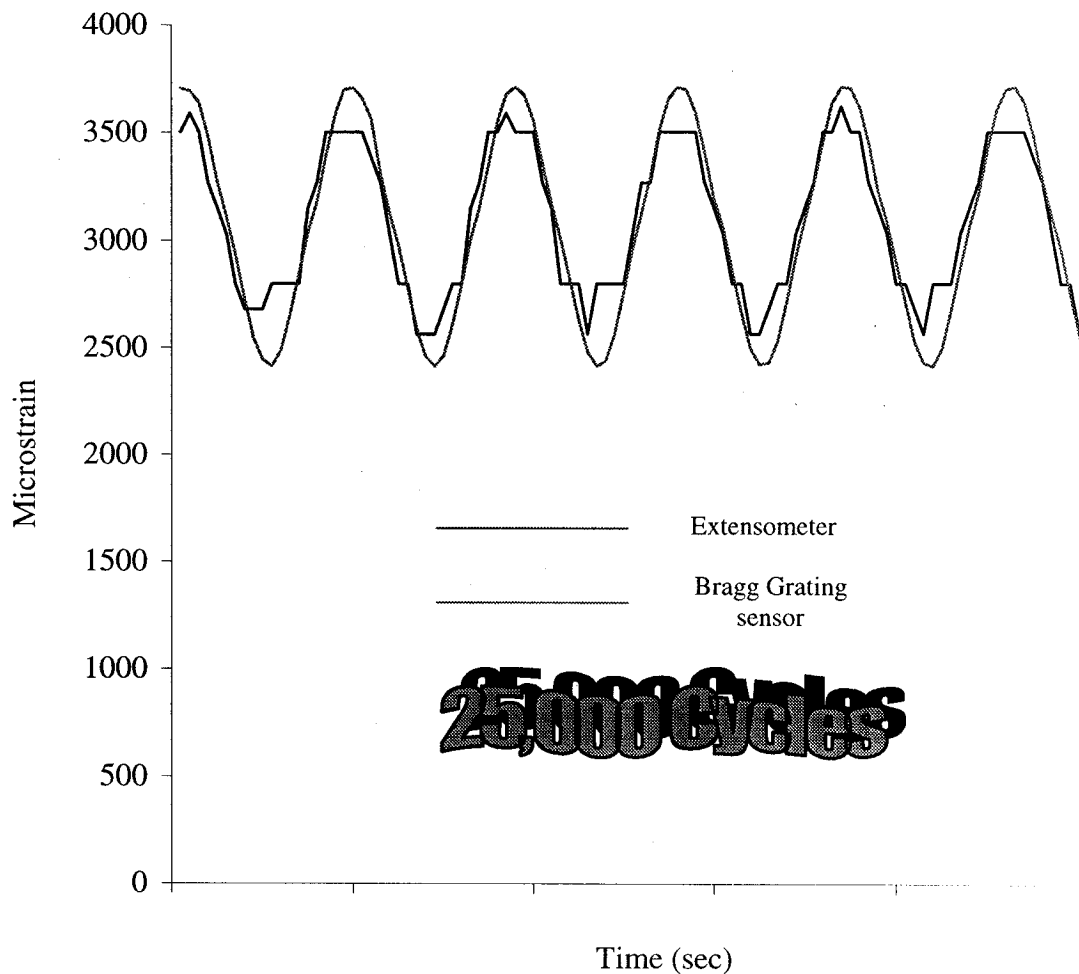


**Figure 5-117:** Strain from extensometer and Bragg Grating sensor in a GFRP tendon subjected to a fatigue load for 25,000 cycles

Finally, a pultruded GFRP tendon with an embedded Bragg Grating sensor was tested. The results after 25,000 cycles are shown in Figure 5-117. It is seen that the extensometer data are not as smooth as in previous tests, particularly at the peaks. The most probable reason for this behavior is the device was not firmly affixed to the tendon. On the contrary, the sensor data produced a well-defined plot. That aside, the two strain-monitoring devices conformed very well to one another. The data from Figure 5-117 are plotted as microstrain vs. load in Figure 5-118.
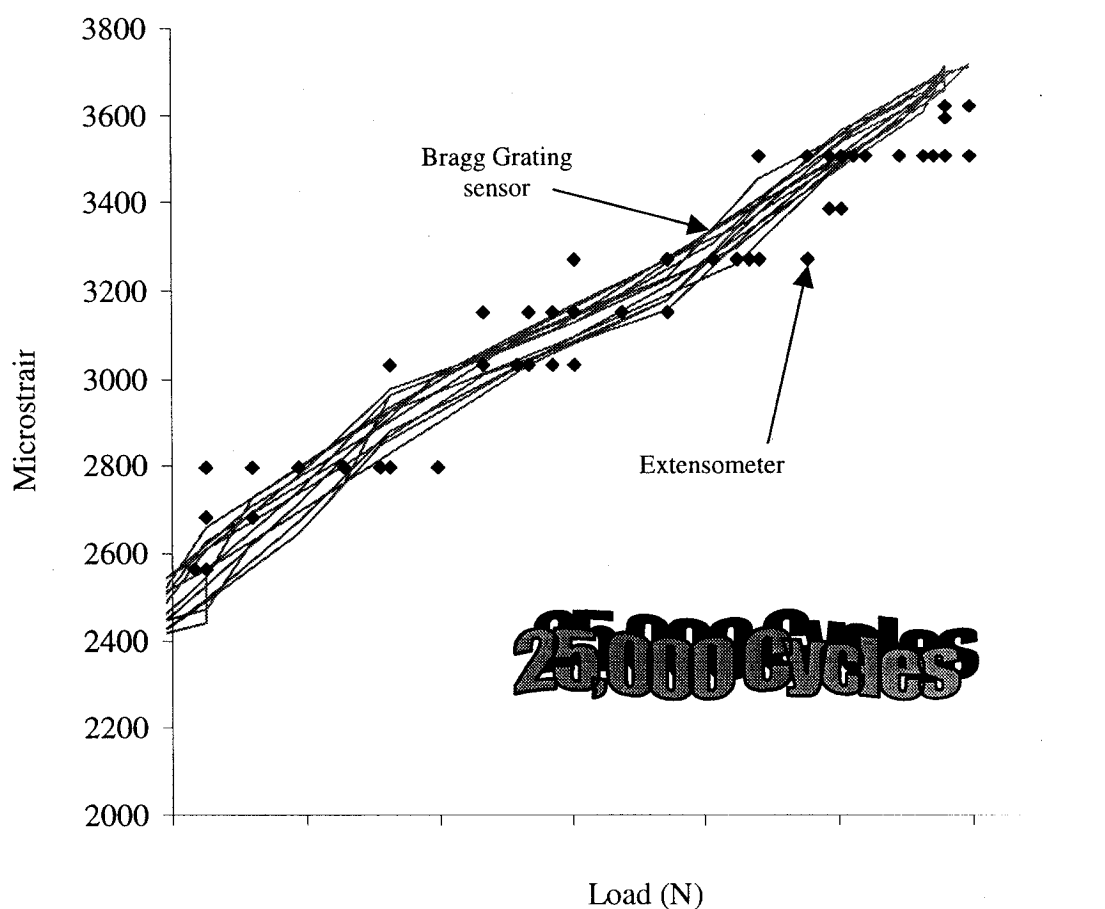


**Figure 5-118:** Strain vs. load for extensometer and Bragg Grating sensor in a GFRP tendon subjected to a fatigue load for 25,000 cycles

Unfortunately, after about 25,000 load cycles had elapsed, one spelter socket slipped from its grip and the loading stopped. As well, it was the socket on the side of the sensor lead that slipped, and in doing so it broke the lead off. Consequently, the GFRP tendon was of no further use.

## 5.6.5 Conclusions

It may be inferred from the tests of Section 5.6.3 that Fabry Perot sensors embedded in GFRP and CFRP tendons are not affected by many thousands of load cycles applied at a frequency of up to 1 Hz, and they maintain their accuracy and repeatability.

## 5.7 Short-Term Creep Behavior of Smart Pultruded GFRP & CFRP tendons

### 5.7.1 Introduction

When materials are subjected to a load for prolonged periods of time, they continue to experience strain even if the applied load level remains constant. This deformation is a combination of elastic and viscoelastic effects and is consequently non-linear in nature. It is called creep deformation and it depends primarily upon the stress level and the temperature.
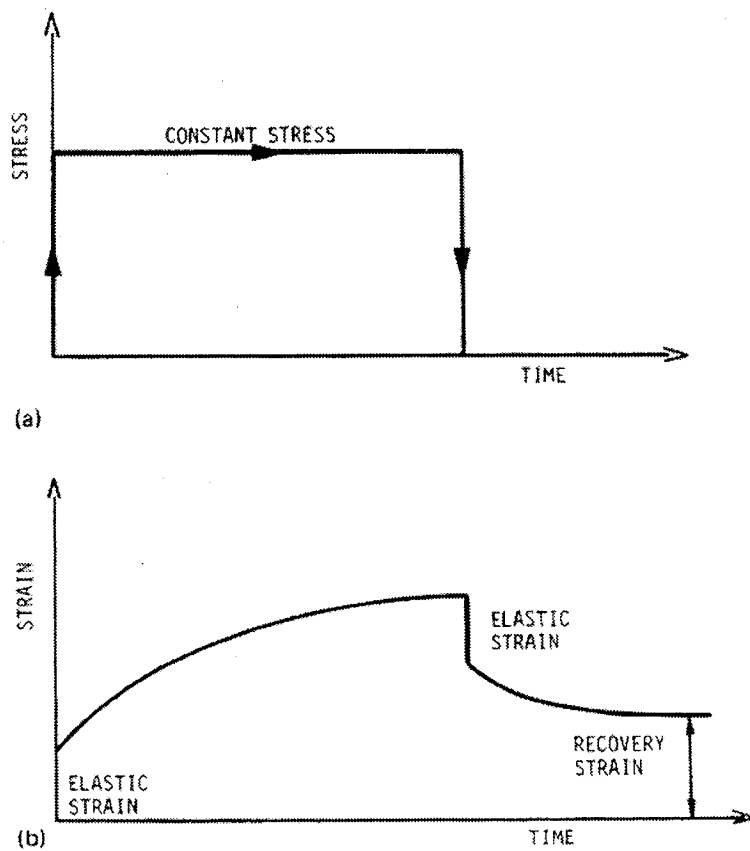


**Figure 5-119:** Schematic representation of creep strain and recovery strain in a polymer [Mallick, 1988]

As Figure 5-119 shows, the total strain experienced is the sum of the elastic mechanical strain that develops very quickly, and the creep strain that develops gradually over time. When the load is removed the elastic strain is recovered, but the creep strain recovers asymptotically to the recovery strain [Mallick, 1988].

In general, creep deformations become more important at elevated temperatures and are characterized by three phases as shown in Figure 5-120 [Evans and Wilshire, 1993]. The primary phase, during which the creep rate decreases with time, leads to the secondary phase of more or less constant strain rate, and this in turn leads to the tertiary phase whereby the creep rate increases steadily, eventually causing what is called creep rupture.
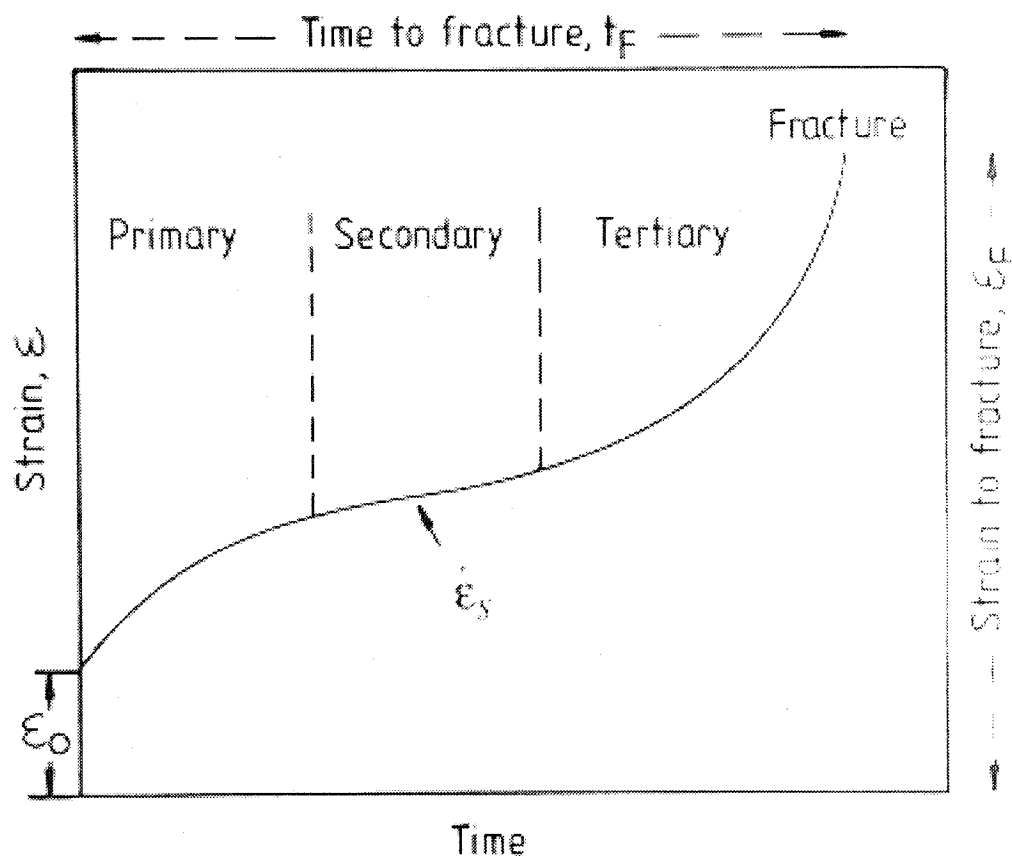


Figure 5-120: Schematic representation of a high temperature creep curve [Evans and Wilshire, 1993]

In spite of the dependence of creep on temperature, many unreinforced polymers do exhibit significant creep at low stress levels and ordinary temperatures. In general, thermoplastic polymers are characterized by larger creep strains than thermosetting polymers. As well, commercial fibers (glass, carbon, boron) with the exception of Kevlar 49 do not creep [Mallick, 1988].
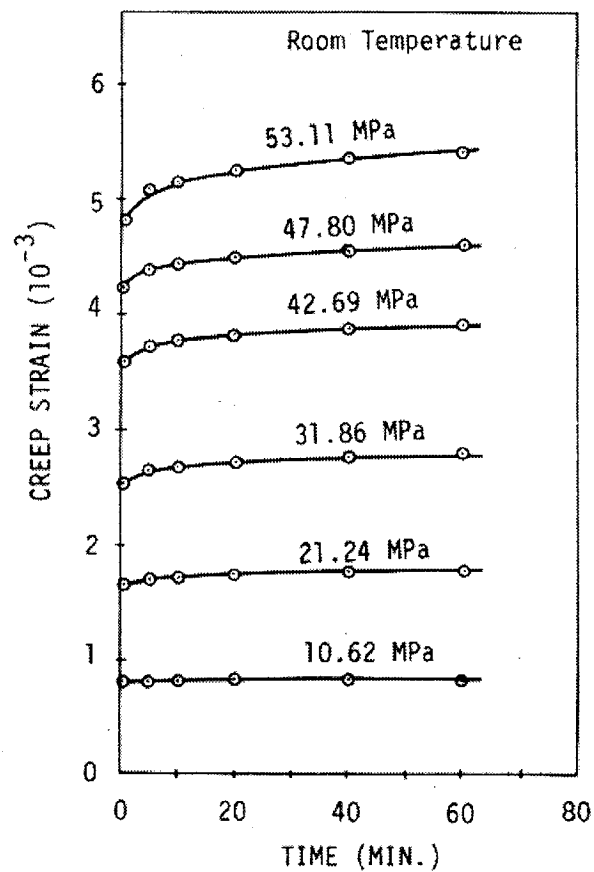


**Figure 5-121:** Tensile creep curves for SMC-R25 polyester laminates [Mallick, 1988]

An important parameter that characterizes the creep behavior of a polymer-matrix composite is the creep compliance, which is defined as the ratio of the time-dependent creep strain to the applied stress (a constant). Figure 5-121 [Mallick, 1988] shows typical creep curves for an SMC-R25 polyester laminate at different stress levels. As shown in

this figure, creep strains increase with time and applied stress level. As well, the higher the temperature, the larger the compliance. It was mentioned above that most of the commercially-available reinforcing fibers do not creep, but many unreinforced polymers exhibit substantial creep strains even at ordinary temperatures and low stress levels. Thus, for unidirectional composites, creep in the longitudinal direction is negligible because deformation in that direction is primarily fiber-dependent. For off-axis laminates however, longitudinal creep can be very high due to the significant matrix involvement in the deformation.
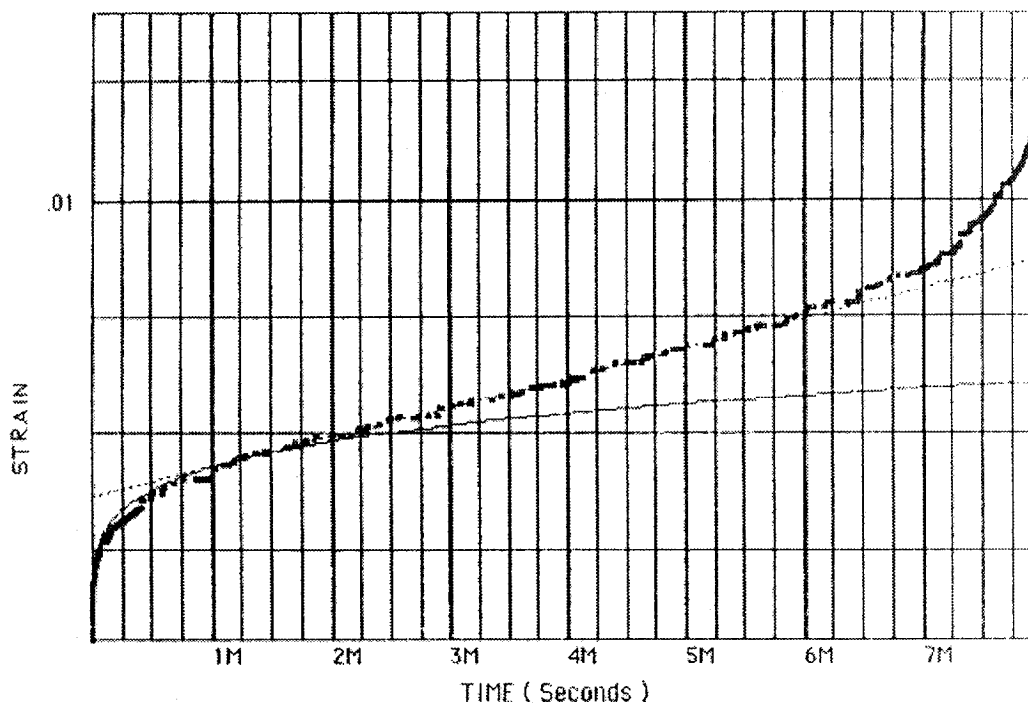


**Figure 5-122:** Strain-time plot obtained in a tensile creep test [Little et al., 1995]

Little et al., [1995] describe an experimental investigation of the tensile creep behavior of a random continuous fiber mat reinforced polypropylene composite commercially available under the name "Azdel". The authors used a specialized fixture for their testing. It consists of a tension rod placed inside a cylindrical tube. The upper end of the

specimen (which is located underneath the tension rod) is connected to the lower end of the tension rod by means of a grip. The specimen is attached to the outer tube by means of a lower grip and a pin. Tension is applied by turning a wheel at the top, which pulls the rod against a spring. Self-aligning bearings eliminate any flexural loads and an LVDT measures the changes of distance between the grips, from which the strain in the sample can be determined. The overall setup was placed inside a temperature chamber, and testing was performed at 75°C and 100°C. The samples were left in the temperature chamber for 48 hours prior to the commencement of the testing. Typical results are shown in the plot of Figure 5-122, that clearly shows the three different phases, namely primary, secondary, and tertiary creep.
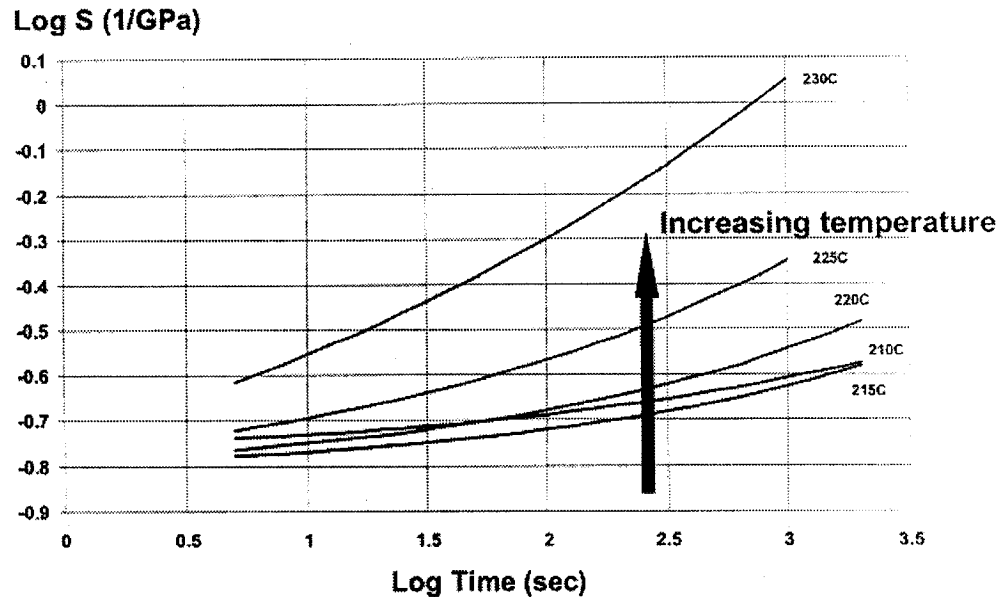


**Figure 5-123:** Creep compliance curves from flexure tests [Abdel-Magit and Gates, 2001]

Abdel-Magit and Gates [2001] used three accelerated (at high temperatures) experimental methods, flexural, tensile, and compression creep tests to obtain the creep properties of a unidirectional carbon/polyimide composite available in the commercial name IM7/K3B. The results from the three methods conformed well to one another. Figure 5-123 shows

creep compliance curves obtained from tests at 210°C, 215°C, 220°C, 225°C, and 230°C with a 30-minute duration for each test. The results clearly show that both creep rate and compliance are strong functions of temperature, and increase as the temperature is raised from 210°C to 235°C. Similar results were obtained from the tensile and compression creep tests.

Franke and Meyer [1992] derived and validated a model that predicted the creep-rupture behavior of pultruded GFRP rods. Their model encompasses some statistical techniques.

In addition to the experimental and analytical techniques used to study creep-related properties of composite materials, it is useful to examine the potential of fiber optic and other sensors to measure and assess creep strain. This is particularly important for long-term monitoring applications of large civil engineering structures such as bridges and overpasses. In an extensive report, Busel and Lindsay [1997] examine the incorporation of composite materials in 30 bridges in Europe, Japan and the United States. One of the important conclusions drawn by Busel was that "many of the British engineers complained that there is not enough known about composites in design and durability. They added that the lack of specifications and standards does not allow widespread use of composites in constructed facilities unless it is designated as a demonstration." The use of fiber optic sensors to continuously monitor long-term creep deformations in structures presumably eventually will arm engineers with the confidence they need to expand the volume of applications of composite materials. Unfortunately, a literature review did not reveal many publications dealing with the use of fiber optic sensors in monitoring creep deformations. Busel and Lindsay [1997] mention that fiber optic and chemical sensors are used for monitoring purposes in the Ulenborgstrasse and Schiessborgstrasse Bridges in Germany. Monitoring confirms that no creep has occurred.

A very interesting field application is described by Slowik et al. [1998]. In their work, four Bragg Grating sensors were embedded in a prestressed concrete bridge near

Dresden, Germany. The sensors were located in the midspan section of the bridge parallel to the prestressing cables. The results of the strain measurement are shown in Figure 5-124.
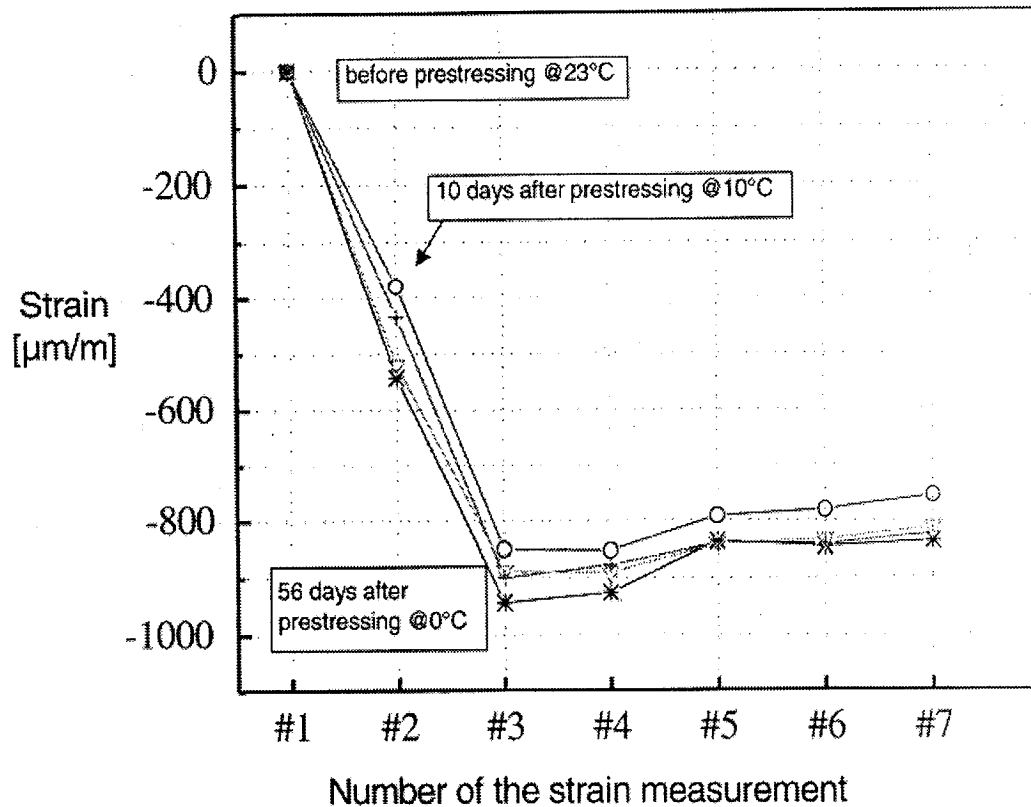


**Figure 5-124:** Results of the strain measurement [Slowik et al., 1998]

The compressive strain increase 10 to 56 days after prestressing is caused by temperature drop, shrinkage and creep. Although with the given arrangement the various effects (temperature, creep, shrinkage) cannot be separated, a more strategic sensor- system installation (including for example sensors for temperature compensation) could be used to decouple creep strain from other strain components. It is also worth noting that at the time of publication, the Bragg Grating sensors were still operational (1.5 years after casting), thus reiterating their potential for long-term monitoring. Finally, it should be remarked that in order to protect the sensors from accidental damage and damage due to

contact with the cement (alkaline environment), some sophisticated steel sensor-holders were fabricated. These worries would have been avoided if the sensors had been embedded in CFRP or GFRP rods, which would have provided protection against both accidental damage and a harsh alkaline environment. As well, as evidenced in the previous sections and as will be observed in the sequel, embedding fiber optic sensors in FRP tendons does not compromise their integrity or reliability even when the tendons are subjected to fatigue or creep loads, or experience low and high temperature extremes.

The combined effect of creep loads and high ambient temperatures on the reliability of fiber optic sensors was investigated by Barnes et al. [1995], who used Fabry Perot sensors bonded to the surface of stainless steel specimens, and subjected them to uniaxial strain. Testing was performed at temperatures up to 538°C, and the results indicated an excellent degree of conformance between the sensors and ceramic knife-edged extensometers.

## 5.7.2 Creep Tests

CFRP and GFRP tendons with embedded Fabry Perot sensors were used for short-term creep testing. One test was performed on a GFRP tendon, and it involved subjecting it to a sustained load of 9 kN for 150 hours at ordinary laboratory conditions. Two tests were performed on a CFRP tendon, one involving a 9 kN-load for 150 hours, and the other involving a 13 kN-load for 300 hours. Testing was conducted on an Instron Model 4507 electromechanical load frame at PSC Analytical. Special fixtures were used to anchor the tendons to the frame. As for the previous tests, the sensor readings were compared with extensometer readings.

The objectives of the testing regime were to investigate whether the FRP tendons would experience any creep strains, and more importantly to assess the behavior and reliability

of the embedded sensors when subjected to many hours of sustained load. Figure 5-125 shows the CFRP tendon that was used for the tests.
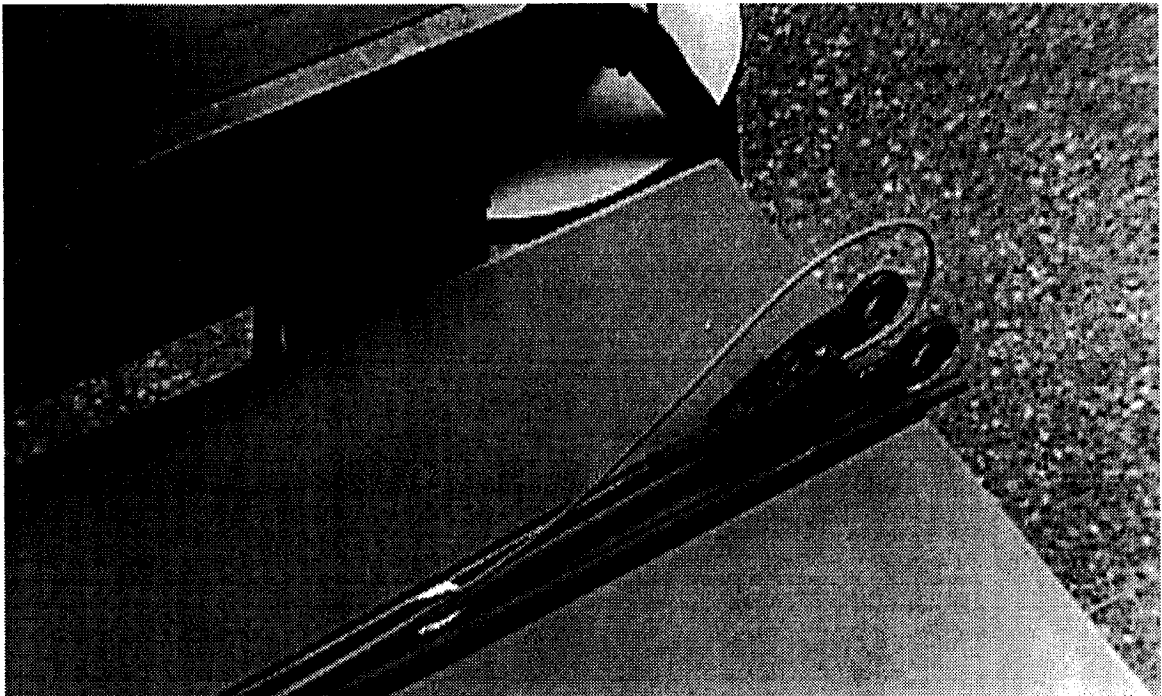


**Figure 5-125:** CFRP tendon (with embedded Fabry Perot sensor) used for creep testing

Figure 5-126 shows the results from the first test performed on the CFRP tendon. The strain readings of the Fabry Perot sensor remained almost perfectly constant, whereas the data from the extensometer showed a slight increase at first followed by a slight decrease later on. This behavior however, is attributable to the imperfect attachment of the extensometer to the tendon and not to any creep deformation. It is clear therefore that neither the sensor nor the tendon experience any creep strains. Since the load is applied in the direction of the reinforcing fibers, it is of no surprise that the tendon experiences no creep deformation at room temperature (see brief discussion on page 201).
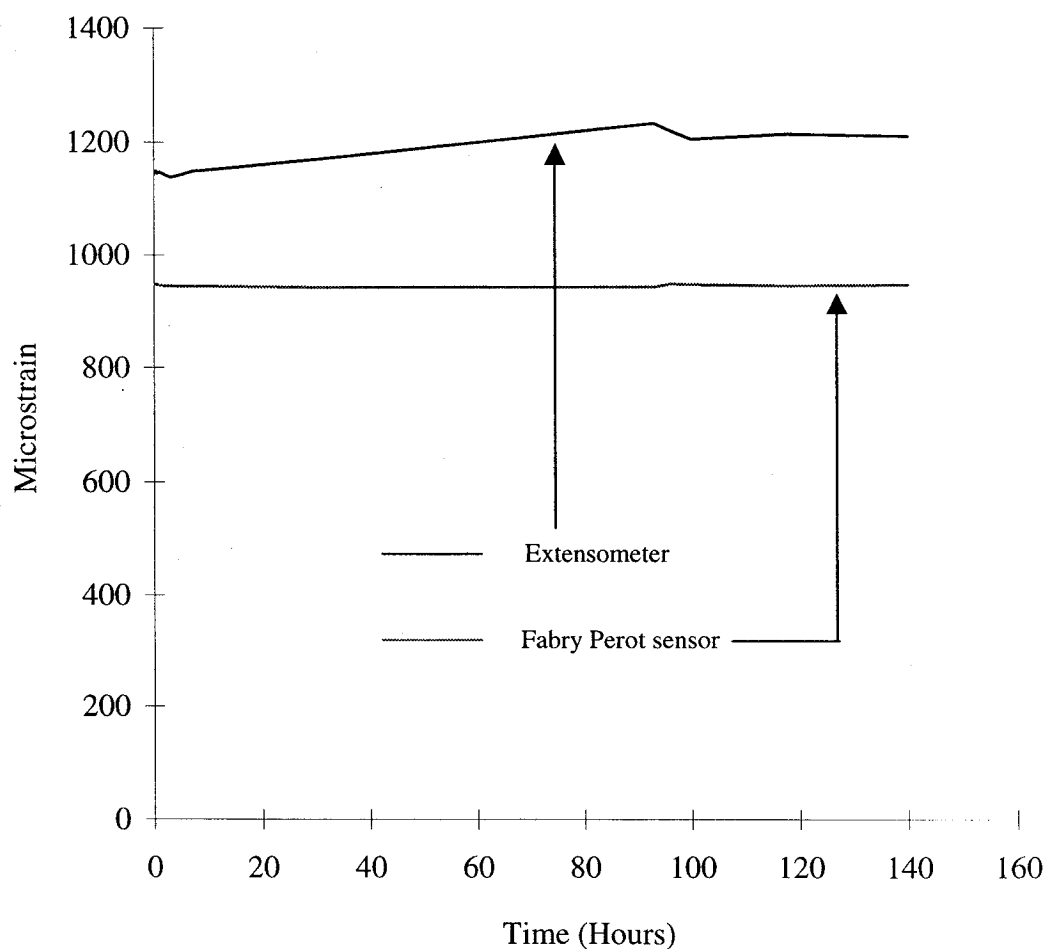


**Figure 5-126:** CFRP tendon (with embedded Fabry Perot sensor) subjected to a 9- kN load for 150 hours

The same CFRP tendon was subsequently subjected to a 13-kN load, but this time testing was conducted for twice long a period. The results are shown in Figure 5-127. Once again, neither the Fabry Perot sensor, nor the CFRP tendon experienced any creep strain.
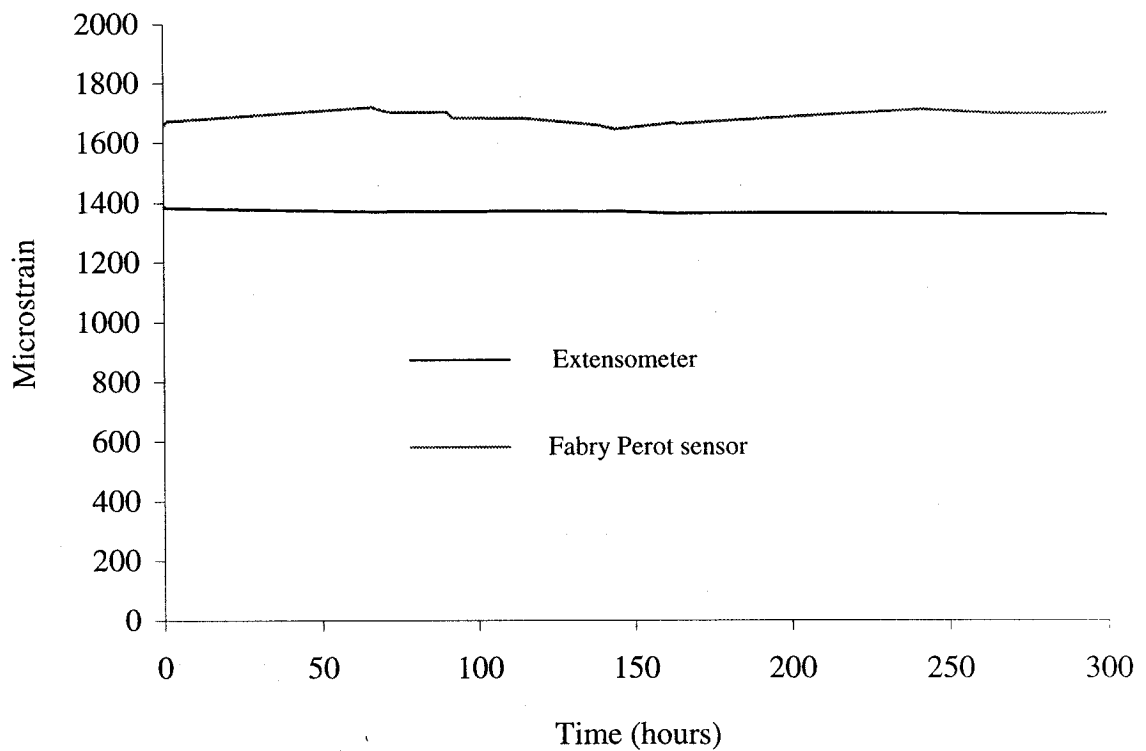


**Figure 5-127:** CFRP tendon (with embedded Fabry Perot sensor) subjected to a 13-kN load for 300 hours

The GFRP tendon was also subjected to a sustained 9-kN load, and the results after 150 hours are shown in Figure 5-128. Once again, it is evident that there is no creep in the sensor or the GFRP tendon. In fact, the output from the two strain-monitoring devices is essentially constant throughout the duration of the test.
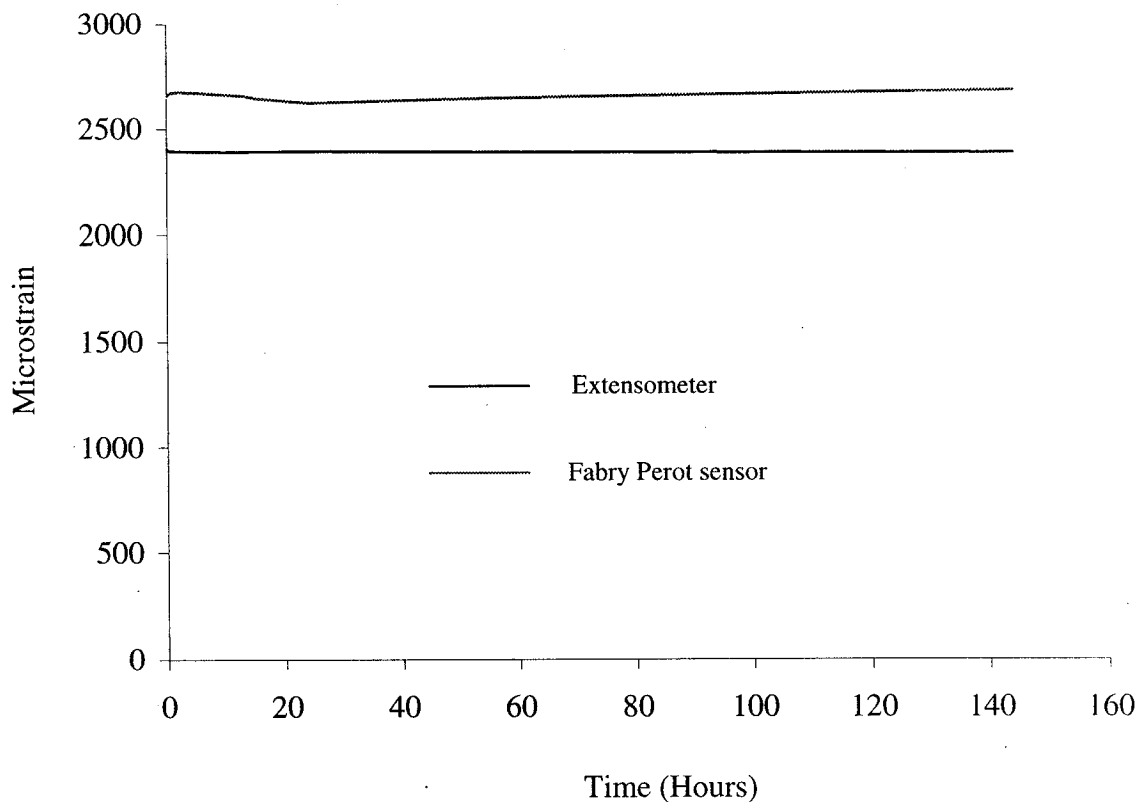
**Figure 5-128:** GFRP tendon (with embedded Fabry Perot sensor) subjected to a 9- kN load for 150 hours

## 5.7.3 Conclusions

It is concluded on the basis of these experiments that the embedded Fabry Perot sensors do not experience short-term creep strain, and that they maintain their reliability for up to at least 300 hours. As well, neither the GFRP nor the CFRP tendons experience any short-term creep if the applied load is in the direction of the reinforcements.

## 5.8 Long-Term Creep Behavior of Smart Pultruded GFRP & CFRP Tendons

### 5.8.1 Introduction

One of the major problems faced by engineers and designers in their quest for cost-effective rehabilitation of the infrastructure is the corrosion of steel. The immunity of fiber-reinforced polymer rebars and prestressing tendons to corrosion makes them the most attractive alternative to steel. The other advantages of composites, primarily their superior specific tensile characteristics, the ease with which their properties can be tailored to meet design criteria and specifications, and the ability to encompass other technologies such as fiber-optic sensors and piezoelectric and shape-memory-alloy actuators, simply makes their case stronger still. The only question lingering is whether their properties can remain durable during the lifetime of a structure. Naturally, the issues related to the durability of composites and smart reinforcements are interlinked with, and dependent on, the environment.

With regards to smart composite materials for infrastructure applications, one ought to consider the effects of the environment on the individual components (polymer matrix, reinforcing fibers, embedded or surface-attached sensor) as well as on the overall smart composites proper.

Duncan et al. [1985] investigated the fatigue-weakening of optical fibers by measuring their strength as a function of temperature, humidity, and other factors. Their results indicated that at constant relative humidity, the strength of silica and sodium borosilicate optical fibers decreased with an increase in temperature. The authors also measured the optical fiber breaking strain (at constant temperature) in environments with different moisture content. For both types of fiber, the breaking strain in vacuum or dry nitrogen were found to be considerably higher than in water or air with 50% relative humidity. In

conclusion, elevated temperatures and moisture have a degrading effect on the strength of optical fibers.
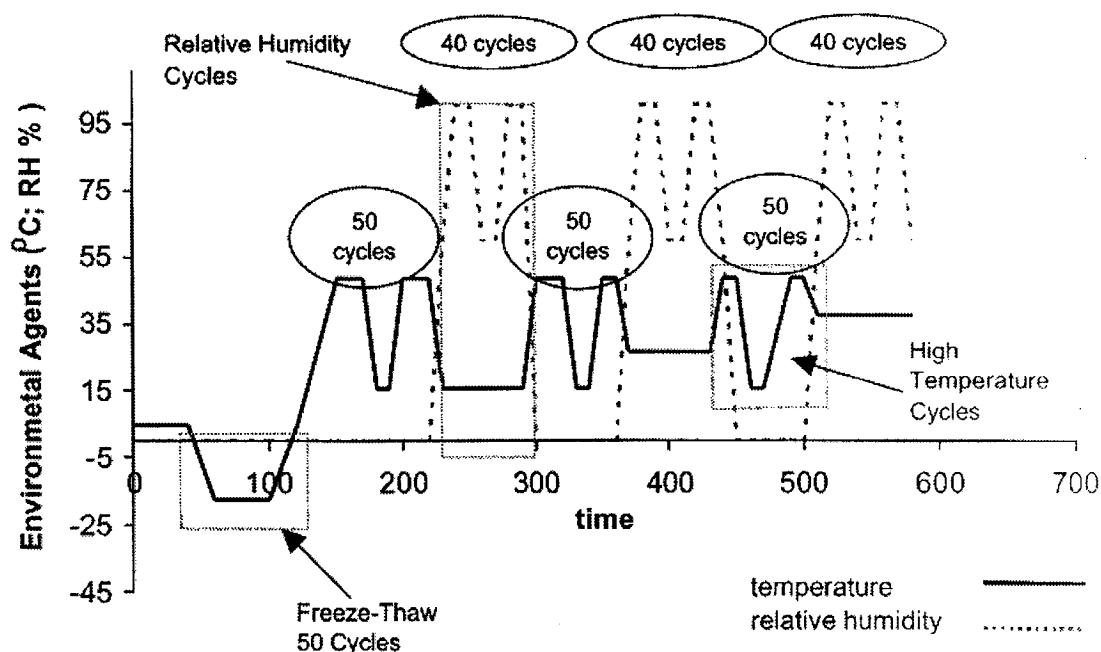


**Figure 5-129:** Environmental conditioning [Micelli et al., 2001]

An excellent paper by Micelli et al. [2001] reports the results of durability tests performed on GFRP composites. Two different types of specimens were used; "G1" bars (with a diameter of 12 mm) were E-glass-reinforced thermoplastic resin, and "G2" bars (with a diameter of 6 mm) were made of E-glass- reinforced polyester resin. Two test protocols were undertaken. The first protocol involved immersing the GFRP specimens in an alkaline solution consisting of 0.16 wt% $Ca(OH)_2$, 1 wt% $Na(OH)$, and 1.4 wt% $K(OH)$ in distilled water, giving a pH value of 12.6. The rods were simultaneously placed in an oven at 60°C in order to accelerate ageing. Under these conditions of alkalinity and temperature, a 42-day exposure is equivalent to 28 years in concrete. The second test protocol subjected the specimens to four combined environmental cycles. As Figure 5-129 shows, each exposure consisted of 50 freeze-thaw cycles, 120 relative humidity

cycles, and 150 high-temperature cycles. During the high-temperature cycles, the specimens were simultaneously subjected to UV radiation. It is known [Dutta et al., 1998] that prolonged exposure to UV rays may harden and discolor the matrix.

The main results from these protocols were that the G1 rods showed an excellent durability in the alkaline solution, but G2 rods were seriously degraded by alkali attack, and their tensile strength showed a marked decrease. Both types of rods were insensitive to the environmental exposure.

Another comprehensive testing program was conducted by Tannous and Saadtmanesh [1999] on pultruded glass/polyester and glass/vinylester rods. The specimens were immersed in eight different solutions simulating various ambient conditions. These solutions and their impact on the tensile properties of the specimen were as follows.

1. **Water at 25°C, simulating exposure to high humidity:** The amount of moisture content was higher for polyester than for vinylester bars. The tensile strength of the former was reduced by 7.3% and for the latter by 5.9%. The tensile modulus was not significantly degraded.

2. **Saturated $Ca(OH)_2$ solution (pH = 12) at 25°C, simulating exposure to hydrating cement:** Again, the amount of moisture content was lower for the vinylester specimens. The average loss of tensile strength was 13.3% for polyester bars and 9.9% for vinylester bars.

3. **Saturated $Ca(OH)_2$ solution (pH = 12) at 60°C, simulating exposure to hydrating cement at a higher temperature:** The amount of moisture content was higher under these conditions for both types of bars. As well, measured loss in strength ranged from 14.1% to 22.7% for vinylester specimens and 16.9% to 28% in polyester specimens. Hence, it is clear that elevated temperatures have an important impact on both diffusivity and strength.

4. **HCl solution (pH = 3) at 25°C, simulating exposure to acidic environment:** Moisture content was higher for polyester bars. However, no appreciable loss in strength was measured for either specimen type.

5. **NaCl 3.5 wt% solution at 25°C, simulating exposure to seawater:** As with all previous tests, it was observed that moisture content was higher for the polyester specimens. There was some loss in the tensile strength of both composite types.

6.  **NaCl + CaCl₂ (2:1) 7.5 wt% solution at 25°C, simulating exposure to sodium chloride and deicing salts:** The same general trend was observed in this case as for the case of the NaCl solution above. However, higher losses in tensile strength were reported, probably due to the higher chloride ion content.

7.  **NaCl + MgCl₂ (2:1) 7.5 wt% solution at 25°C, simulating exposure to sodium chloride and Ice-Stop deicing salts:** The conclusions drawn from this test are similar to the ones pertinent to the deicing-salts solution.

8.  **Ultraviolet Radiation:** After a six-month exposure in UV radiation, it was observed that the glass bars were not seriously affected. The average loss in tensile strength was 5.2% for polyester bars and 5.7% for their vinylester counterparts.

The results of this work indicate that environmental conditions may have a significant effect on the properties of smart composites, and should be given due consideration at the design stage.

Many other researchers performed accelerated reliability tests on composite materials. Strait et al. [1992] investigated the effects of seawater immersion on the impact resistance of GFRP composites. Two types of laminated specimens were used; type A consisted of E-glass fibers in an epoxy resin, and type B consisted of woven E-glass fibers in a rubber-toughened epoxy resin. The samples were soaked in synthetic seawater for a prolonged time. The samples were deemed saturated when their weight did not increase by more than 3% of the initial weight during the period of one week. To accelerate the effects of water absorption, the seawater was maintained at 60°C. Impact tests were subsequently performed on the specimens. The results showed that both A and B composites experienced significant reduction in peak load and energy absorbed at peak load due to degradation of the fibers and the fiber/matrix interface as a result moisture absorption. As well, the total energy absorbed was substantially reduced for both types. In conclusion, the authors remarked that moisture absorption significantly reduces the impact resistance of glass/epoxy composites.

Hamidah et al. [2001] investigated the absorption characteristics of aramid prestressing rods in aggressive solutions. The testing indicated that for rods immersed in water, the degradation occurs due to the volume changes and expansion of the matrix. For rods immersed in alkaline solutions, the solutions dissolve the surface and exposes the fibers, and for rods immersed in acid, the solution penetrates more deeply, dissolving the matrix and leaving the fibers unbound (see Figure 5-130).
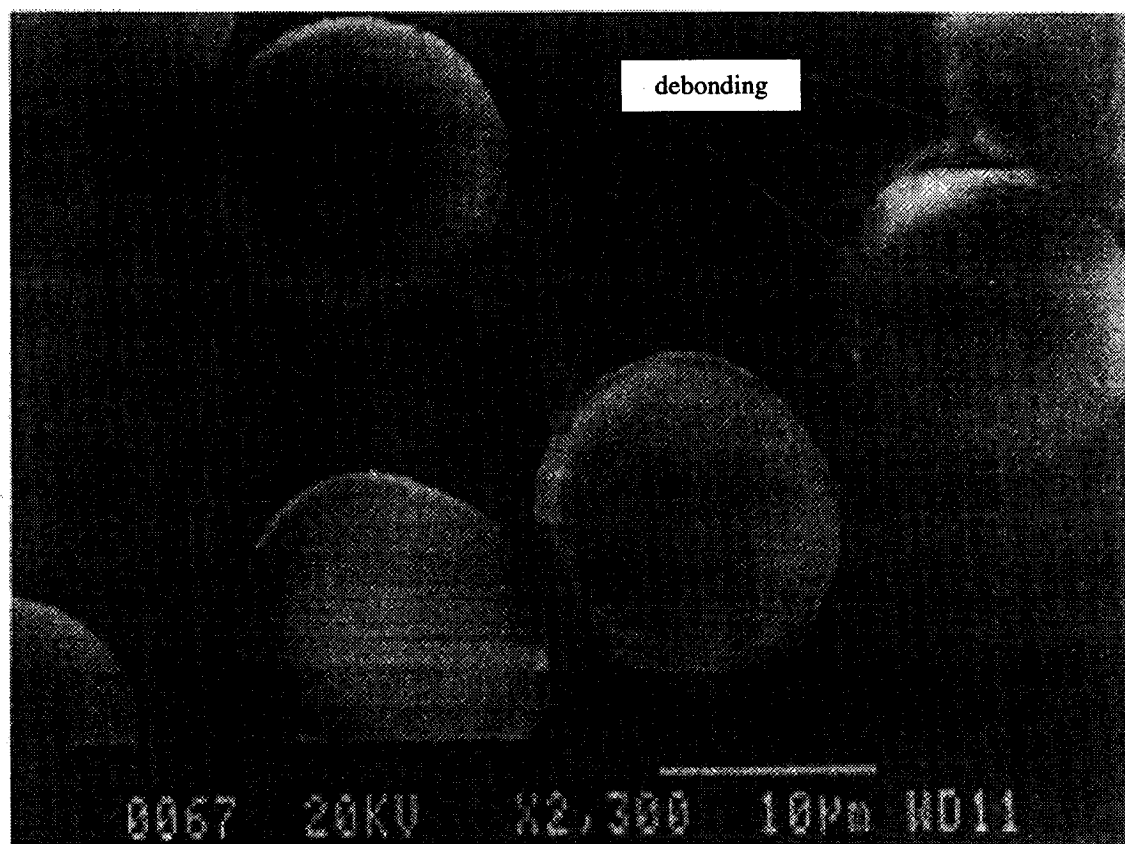


**Figure 5-130:** SEM micrograph shows debonding of aramid fibers after exposure to acidic solutions [Hamidah et al., 2001]

In conclusion, the effect of the environment will be perhaps the decisive factor that will determine the extent of integration of smart composite materials into the structural field. We have seen in previous sections that in order to protect surface-attached sensors from

the alkalinity of cement mixtures, researchers often resort to labor-intensive and potentially expensive casings to protect the sensors. It is clear that the issue of sensor protection can be resolved to a large extend by embedding the sensors in their respective GFRP or CFRP tendons. However, this section has evidenced that alkaline or acidic environments may cause degradation of the composite, and the aggressive solution may even penetrate enough into the composite to compromise the integrity of the sensor as well. Furthermore, the literature research revealed that researchers saturated the pertinent specimens in various stagnant solutions and only afterwards tested them. Bearing all these in mind, it is of interest to immerse the tendons in an alkaline solution which is continuously circulating, and at the same time subject them to sustained loads for prolonged periods of time. The readings from the embedded sensors will be compared once again with conventional strain-monitoring devices.

## 5.8.2 Experimental Details and Results

Long-term testing involved the combined effects of load and alkaline exposure. A schematic of the set-up is shown in Figure 5-131. The smart tendons were placed in a long-term fixture and loaded to 12 kN. The fixtures were made of square steel box tube with a base, two uprights and a single cross beam. Each fixture was approximately 2.13 m high and 0.91 m wide between the uprights. A smart tendon was then suspended from the cross beam of each fixture by using a chain and a turnbuckle. A shackle was used to attach the weights (solid steel bars welded together) to the tendon. The tendons were encased in a glass environmental chamber sealed at the two ends. A pump was used to circulate an alkaline solution from a reservoir nearby, in and out of the chamber. The solution was made of 0.32 mol/L KOH, 0.17 mol/L NaOH, and 0.07 mol/L $Ca(OH)_2$ dissolved in distilled water. The resulting pH value was 12.8 [Kalamkarov et al., 2000].
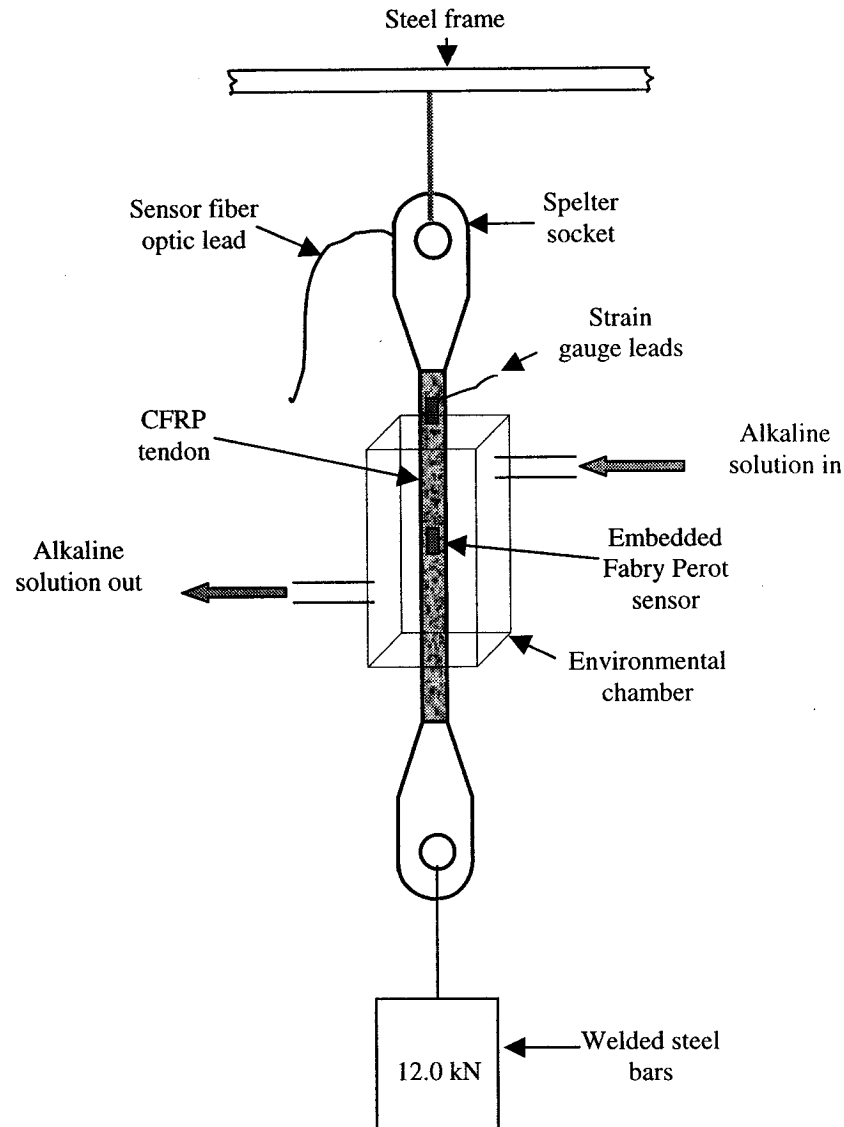
**Figure 5-131:** Experimental setup for long-term creep testing in alkaline environment

Testing was conducted for a period of 75 days. The readings from the embedded Fabry Perot sensors were compared with corresponding values from conventional foil gauges. Obviously, due to their vulnerability, the foil gauges were bonded to a small region of each tendon which was not inside the environmental chamber (near the top spelter socket). Figures 5-132 and 5-133 show the results from testing on the GFRP and CFRP tendons respectively. It is clear that there is a good agreement between the two strain monitoring

devices. As well, the output from the embedded sensor did not seem to be affected by either the sustained 12-kN load, or the alkaline solution.
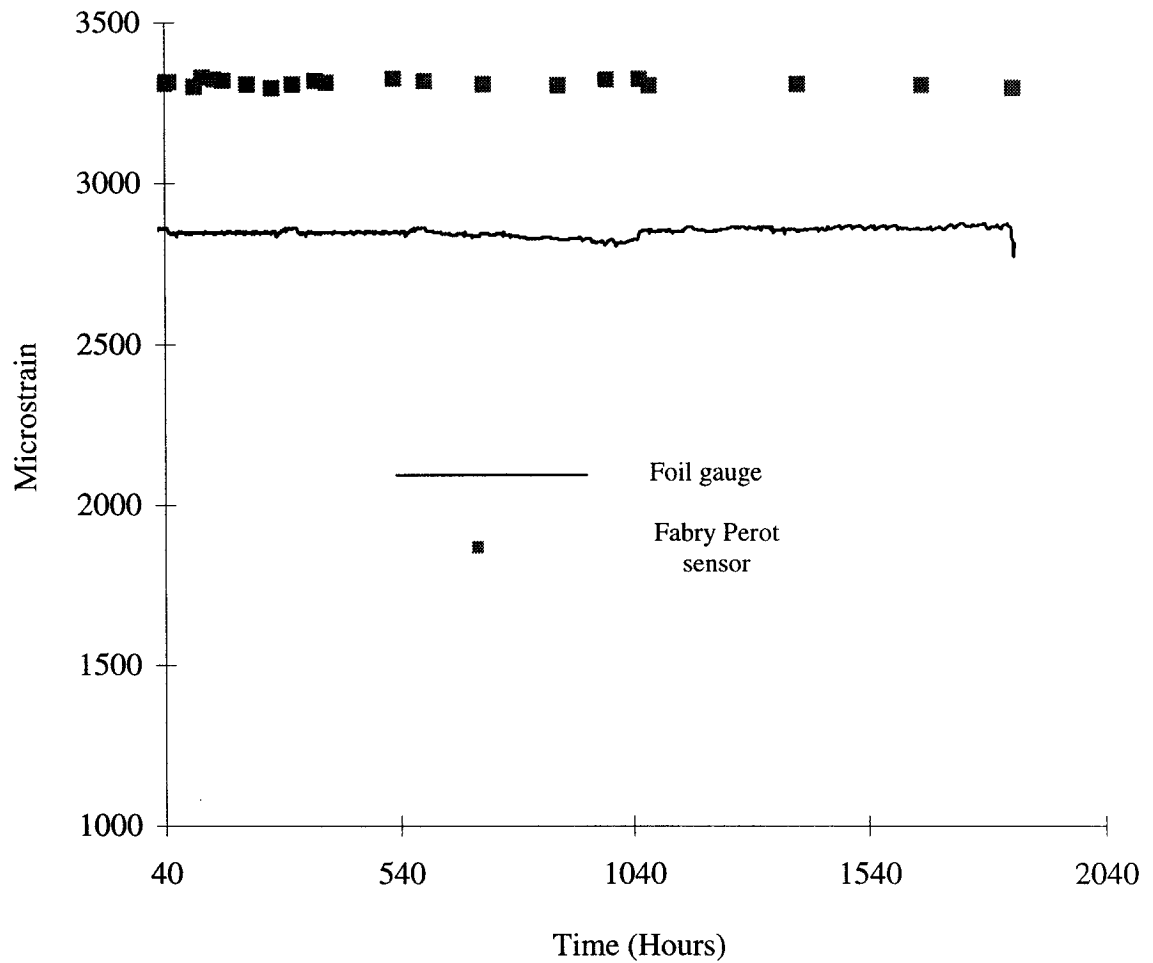


**Figure 5-132:** GFRP tendon with embedded Fabry-Perot sensor (in an alkaline solution) with a sustained load of 12 kN [Kalamkarov et al., 2000]
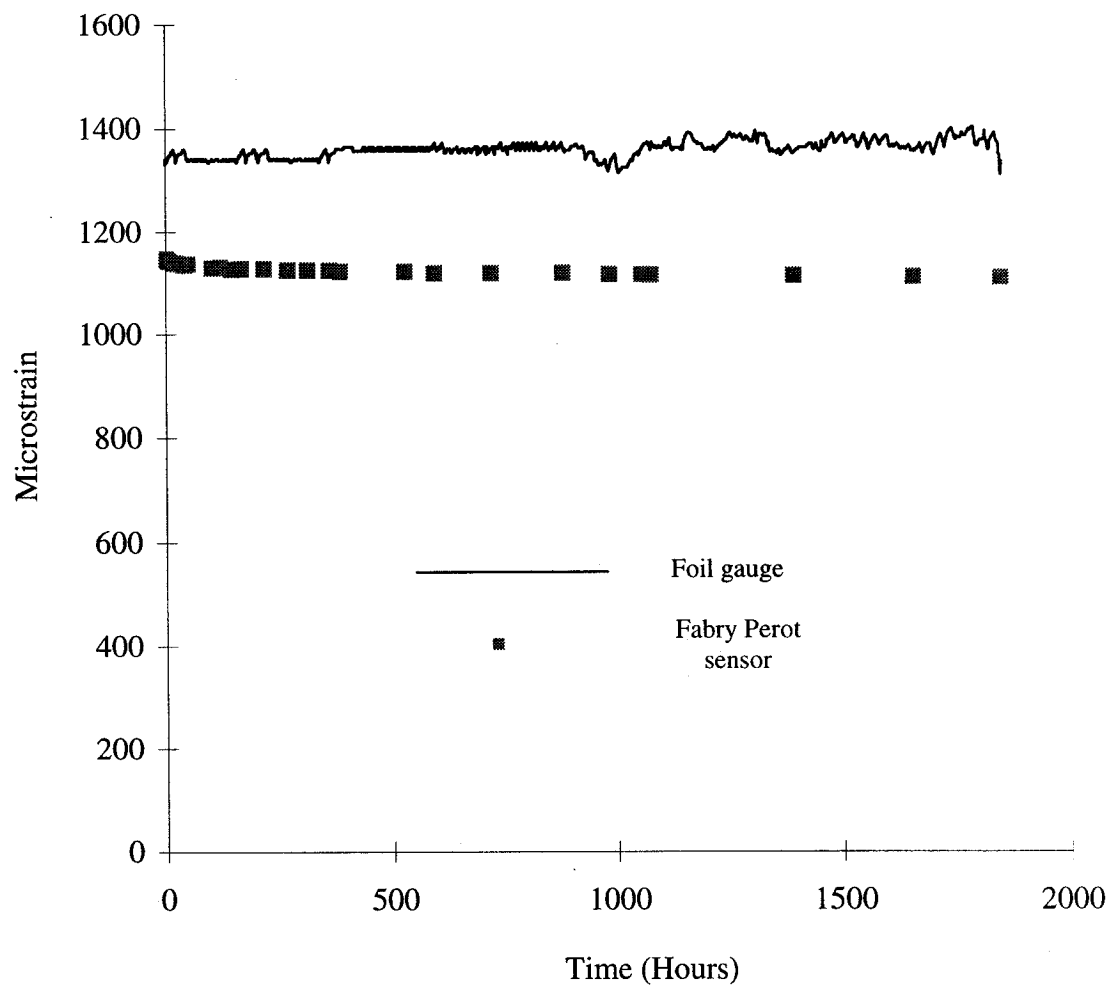
**Figure 5-133:** CFRP tendon with embedded Fabry-Perot sensor (in an alkaline solution) with a sustained load of 12 kN [Kalamkarov et al., 2000]

**5.8.3 Conclusions**

Based on the results of Sections 5.7 and 5.8, one may conclude that Fabry Perot sensors are not affected by sustained loads, exposure to alkaline solutions, or a combination of both. They retain their accuracy, repeatability and reliability, thus showing great potential for health–monitoring of civil engineering structures when embedded in composite prestressing tendons and rebars.

# 6.0 APPLICATIONS OF SMART COMPOSITE TENDONS

## 6.1 Introduction: ISIS Canada

The work described in the previous chapters of this thesis was conducted for the purposes of project T3.4, "Smart Reinforcements and Connectors", under the auspices of ISIS Canada (Intelligent Sensing for Innovative Structures). ISIS Canada is a federal Network of Centres of Excellence program combining the efforts of 15 universities throughout Canada. It was created in 1995, and the researchers involved are experts in their respective fields which include civil, mechanical, electrical, aerospace and materials engineering.

ISIS Canada was created with one goal in mind: to develop the means by which the problem of deteriorating steel-reinforced concrete in bridges, overpasses, dams and other structures could be combated, and to design integrated fiber-optic system technology that can be used for the remote strain sensing and field monitoring of such structures. It became clear that the most attractive and viable replacements for steel were fiber-reinforced polymers such as the ones described in this thesis. Under the guidance of ISIS Canada, GFRP U-shaped stirrups were used on the outside faces of beams to improve their shear strength, CFRP polymer sheets were wrapped around concrete columns for strengthening and rehabilitation, CFRP laminates were used to reinforce concrete beams, CFRP and GFRP rebars integrated with fiber optic sensors were used as concrete reinforcements and strain monitors in concrete bridge decks, etc.

This chapter will give a brief account of some of the applications of CFRP and GFRP rods with integrated fiber optic sensors. The applications to be described involved FRP tendons pultruded at Dalhousie University.

## 6.2 GFRP Rods with Pure Optical Fiber Embedded in Concrete Beams

The first application to be described involves the pultrusion of GFRP rods with embedded optical fibers. In other words, no Fabry Perot or Bragg Grating sensors were used, but rather a length of polyimide-coated optical fiber. It is known that regular optical fibers can act as strain and temperature sensors themselves, and one of the techniques that can be used to take advantage of this fact is the Brillouin scattering technique developed by Dr. Bao at the University of New Brunswick. Brillouin scattering uses optical time domain reflectometry (OTDR) techniques with pertinent signal processing to measure temperature and mechanical strain [Chhoa et al., 2001].
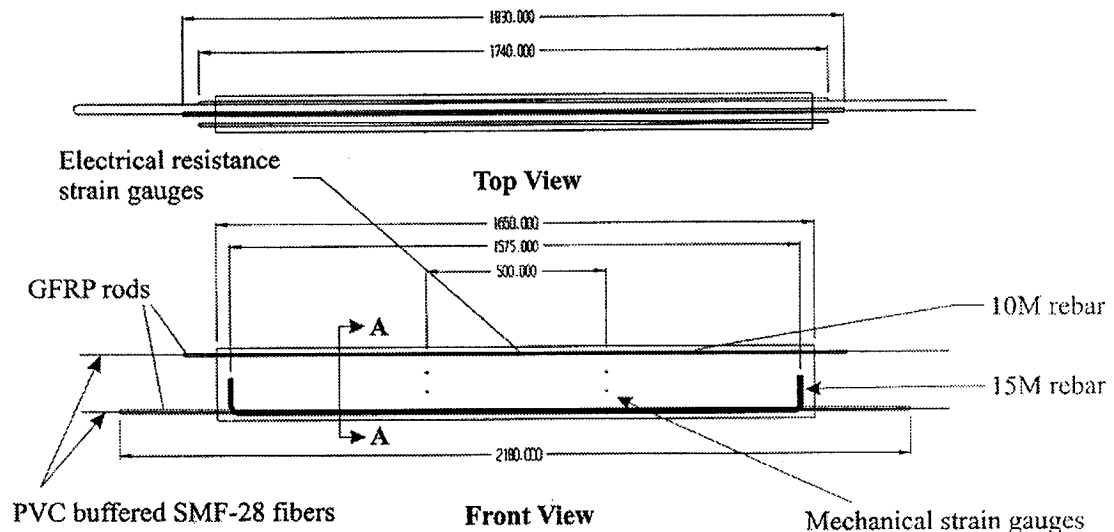


**Figure 6-1:** Concrete beam with embedded GFRP tendons [Chhoa et al., 2001]

For the purposes of this project, two GFRP tendons with embedded optical fibers were pultruded, sand-coated and embedded in concrete beams (Figure 6-1). The beams were then tested and the strain at mid span measured (see Figure 6-2). It was discovered that the strain readings from the optical fiber were not very accurate, probably because the rods slipped in the concrete. Before embedding the tendons, one must ensure that their

outside surface is rough enough so that a good bond with the surrounding concrete can be achieved. This entails the coating of the rods with silica sand. Unfortunately, in this case the GFRP tendons were only coated with regular "beach" sand that appeared to be inadequate for good bond strength.
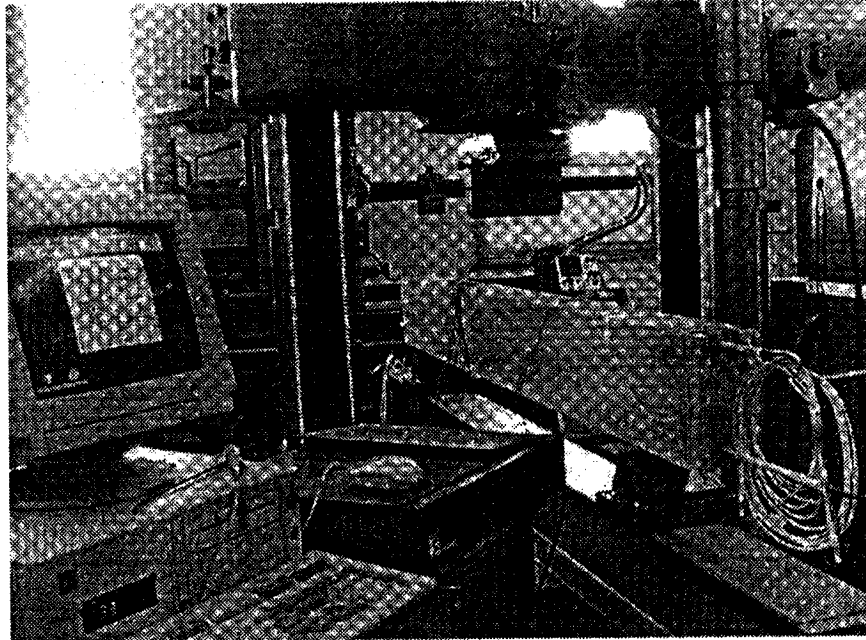


**Figure 6-2:** Concrete beam being tested. The ends of the GFRP tendons with the associated fiber-optic leads are shown on the RHS of the picture [Chhoa et al., 2001]

## 6.3 Waterloo Creek Bridge, British Columbia

The Waterloo Creek Bridge is one of a new series of bridges being constructed by the British Columbia Ministry of Transportation and Highways as part of the new Vancouver Island highway [ISIS Canada, 2000]. The bridge consists of two 25-m by 12-m single-span decks, one deck for the north-bound traffic and one deck for the south-bound traffic. Each deck is supported by five precast concrete girders. The south-bound deck is constructed of conventional steel-reinforced concrete, but its north-bound counterpart is steel-free and is reinforced with chopped polyethylene fibers and commercially manufactured GFRP rebars of diameter 25 mm.
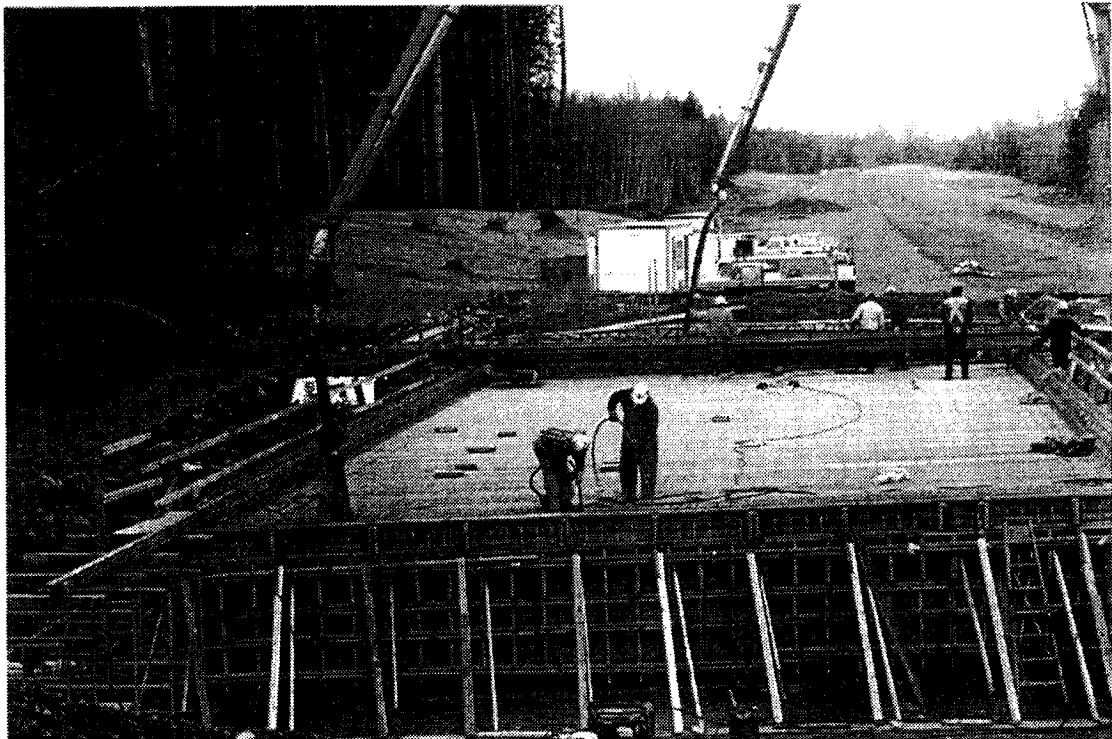


**Figure 6-3:** Construction of Waterloo Creek Bridge [Tsai and Ventura, 1998]

For the purposes of this project (Figure 6-3), three pultruded smart GFRP tendons with embedded Fabry Perot sensors were manufactured at Dalhousie University. These were

sand-coated and embedded in the deck girders together with the commercial GFRP rebars. The fiber optic leads from the sensors were 10 m long. The three embedded Fabry Perot sensors together with an additional array of 53 other sensors have been used for monitoring the deck. Figures 6-4 and 6-5 [Tsai and Ventura, 1998] show a close-up view of one of the commercial sand-coated GFRP rebars, and an instrumentation box respectively. The fiber optic leads protected with a rubber jacket are clearly visible in Figure 6-5.
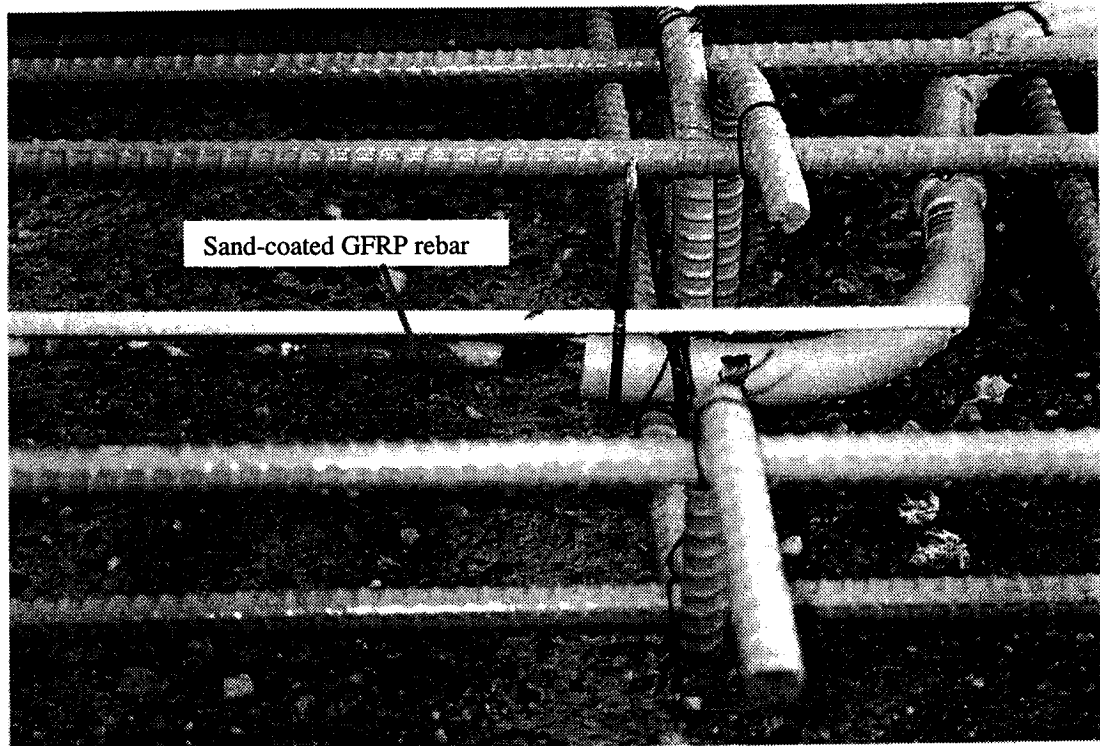


**Figure 6-4:** Close-up view of GFRP rebar in Waterloo Creek Bridge deck [Tsai and Ventura, 1998]
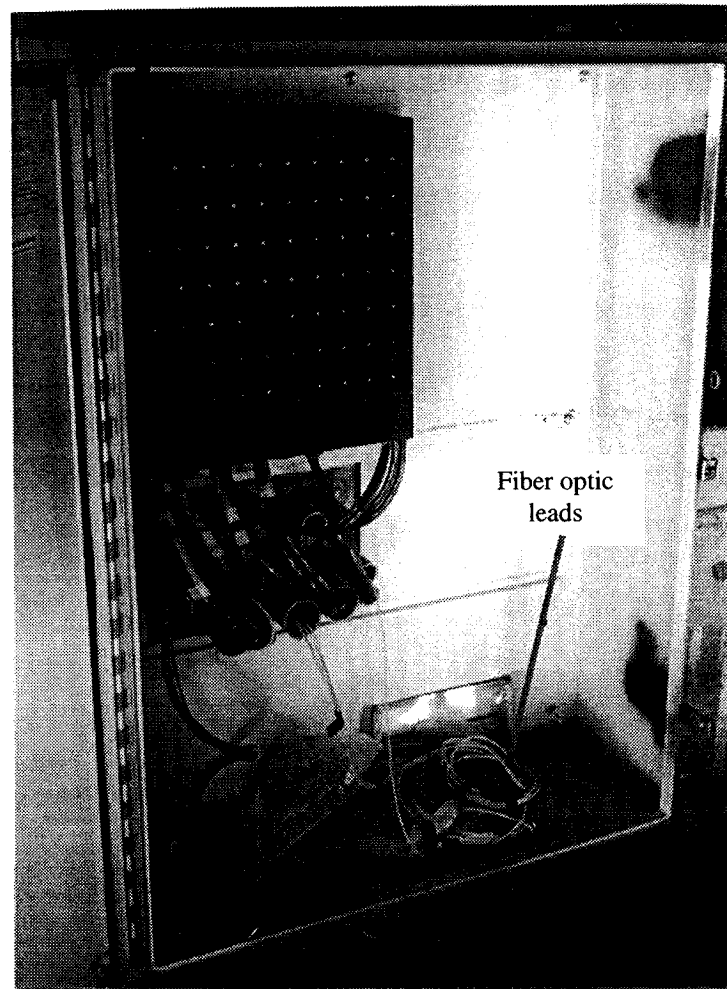
**Figure 6-5:** Instrumentation box at Waterloo Creek Bridge deck [Tsai and Ventura, 1998]

## 6.4 Crowchild Trail Bridge, Alberta

This is a 90-m long, 11-m wide bridge that carries two lanes of traffic over its three spans, see Figure 6-6. The deck is steel-free and is reinforced with chopped polyethylene fibers and commercially produced GFRP C-bars. GFRP bars were also used to reinforce the cantilever slabs of the bridge [ISIS Canada, 2000]. Three smart GFRP tendons with embedded Fabry Perot sensors were pultruded at Dalhousie University and embedded in the deck of the bridge. Unfortunately, these tendons were damaged during shipping or installation. In addition to these three Fabry Perot sensors, the bridge is instrumented with 81 strain gauges, 19 embedded gauges, and two other fiber optic sensors [ISIS Canada, 2000].
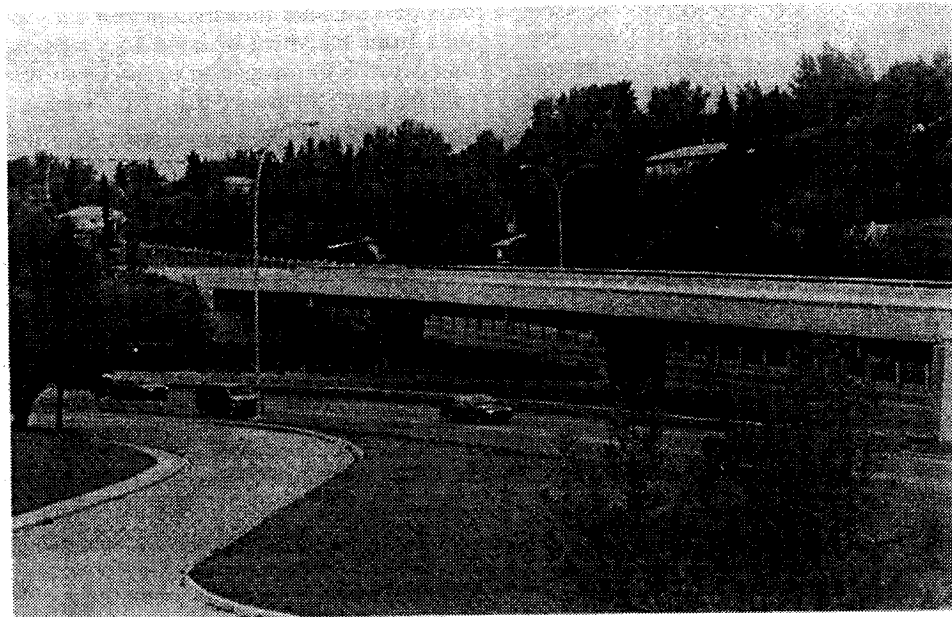


**Figure 6-6:** The Crowchild Trail Bridge in Alberta [Ventura et al., 2000]

## 6.5 Hall's Harbor Wharf, Nova Scotia

Hall's Harbor wharf (Figure 6-7) is a timber structure built in 1904 and Hall's Harbor is the only safe harbor on the Fundy Shore north of Digby, Nova Scotia that is open throughout the winter months. Hall's Harbor is a working fishing village involved with lobster exports and a thriving tourist industry.



**Figure 6-7:** Hall's Harbor wharf in Nova Scotia

On a cold February night in 1998, the people of the community woke up to a formidable sight. A 40-m section of the west breakwater of the wharf had collapsed overnight. For the rebuilding of the wharf, it was decided to construct a completely steel-free concrete deck reinforced with chopped polypropylene fibers and GFRP rebars. The deck is

supported by concrete beams 4 meters apart. The beams contain both GFRP and steel rebars (see Figure 6-8).
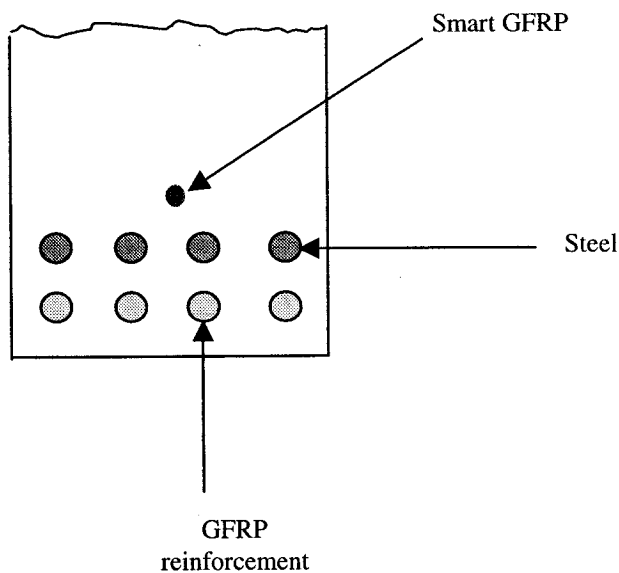


**Figure 6-8:** Concrete beam reinforced with GFRP rods and steel and instrumented with a pultruded smart GFRP rod with an embedded Bragg Grating sensor

For the purposes of this project, six smart GFRP rods with embedded Bragg Grating sensors were pultruded at Dalhousie University. A schematic showing one such tendon in a concrete beam is shown in Figure 6-8. Since the FRP rods produced in the pultrusion lab are much smaller than the 25-mm-diameter tendons required for the concrete reinforcement in this project, the smart tendons were used only as strain monitors and were not intended to carry any load. In addition to the embedded Bragg Grating sensors, the structure is instrumented with a large number of other sensors as well as strain gauges. Figure 6-9 shows one of the sand-coated GFRP smart tendons prior to installation in Hall's harbor wharf.
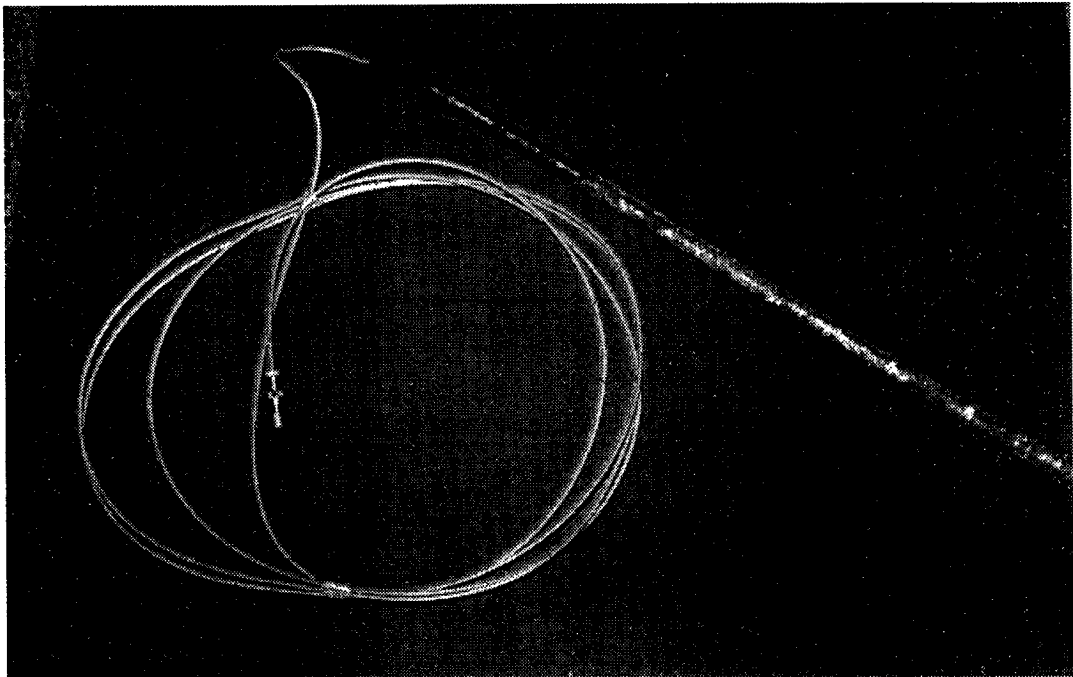
**Figure 6-9:** Sand-coated GFRP tendon with embedded Bragg Grating sensor prior to installation in Hall's Harbor wharf project

# 7.0 SURVEY OF ACTUATORS FOR ACTIVE SMART MATERIALS

## 7.1 Introduction

The previous chapters of this thesis dealt with manufacturing, processing, testing, and evaluation of passive smart composite reinforcements. The pultruded tendons were classified as "passive" because they were characterized by sensing capabilities alone. As demonstrated, the embedded Fabry Perot and Bragg Grating sensors provided very reliable strain information even under such adverse conditions as high- and low-temperature extremes, alkaline environments, creep loads, and fatigue loads. Thus, materials similar to these tendons are extremely useful in alerting technicians, engineers and other operators of changes or significant perturbations in the state (strain, thermal etc.) of the structure or part that they are monitoring. One would be even more interested, however, if the smart material could perform self-adjustment or self-repair as conditions change, because this could potentially prevent the aggravation of an unpleasant situation and consequently reduce downtime and maintenance costs and extend life e.g. of civil engineering structures. A material with combined sensory and response capabilities is called active or adaptive smart material and will incorporate both sensors and actuators. The integration of composites and sensors/actuators gave rise to the most promising material system known as active smart composites.

The use of smart composite structures will be greatly facilitated if the effective properties and coefficients such as elastic, actuation, thermal expansion, hygroscopic expansion etc. can be predicted at the design stage. The realization of this objective necessitates the development of mathematical models that characterize the behavior of the smart composite materials. It is understood that the microstructural makeup of a smart composite material is dependent upon the nature, distribution, orientation and interaction of both the reinforcements (long fibers, particles, whiskers etc.) and the sensors and

actuators. This microstructural composition will in turn govern the macroscopic behavior of the smart material. It is thus imperative that the mathematical models be neither too complicated for any practical implementation, nor too simple to reflect the real behavior and properties of the smart composite material.

Sensors, particularly fiber optic ones, have been discussed in sufficient detail in previous sections. This chapter will give a brief introduction to those material systems that are employed most commonly for their actuation characteristics in active smart materials. These are piezoelectrics, shape memory alloys, magnetostrictives, and electrorheological fluids.

## 7.2 Piezoelectrics

The term piezoelectric is derived from the Greek words "piesis" meaning pressure and "electronion" meaning electron. Thus piezoelectric materials will generate an electric voltage when a pressure is applied. The converse effect is also exhibited; the application of an electric field will lead to dimensional changes in a piezoelectric material.

A piezoelectric material has electric dipoles randomly oriented within its expanse. When it is heated above a characteristic temperature known as the Curie temperature, these dipoles can change their orientation, and under the influence of a strong electric field they become aligned in the direction of the field. If the material is cooled subsequently to a temperature below the Curie temperature, the dipoles are "locked in" and will maintain their existing orientation. This procedure is known as poling [Srinivasan and McFarland, 2001].

The most common piezoelectric material is lead-zirconate-titanate (PZT). Figure 7-1 [APC International, 1999] illustrates the piezoelectric effect in a cube of PZT material. Figure 7.1(a) shows the material before any load is applied. Figure 7-1(b) shows that

when a compressive force is applied, a resulting voltage develops across the electrodes and it has the same polarity as the poling voltage. If the applied force causes a tensile strain as shown in Figure 1(c), the resulting voltage is of opposite polarity to the poling voltage. The converse effect is illustrated in the remaining three figures. In Figure 1(d), an external voltage of opposite polarity to the poling voltage induces a compressive strain and in Figure 1(e), a voltage of like polarity as the poling voltage induces a tensile strain. Finally, in Figure 1(f), an alternating voltage causes the PZT cube to stretch and shrink at the same frequency as the applied voltage. Note also that in all of the figures, the dimensional changes in the longitudinal direction are accompanied by appropriate strains in the transverse direction in accordance with Poisson's effect.
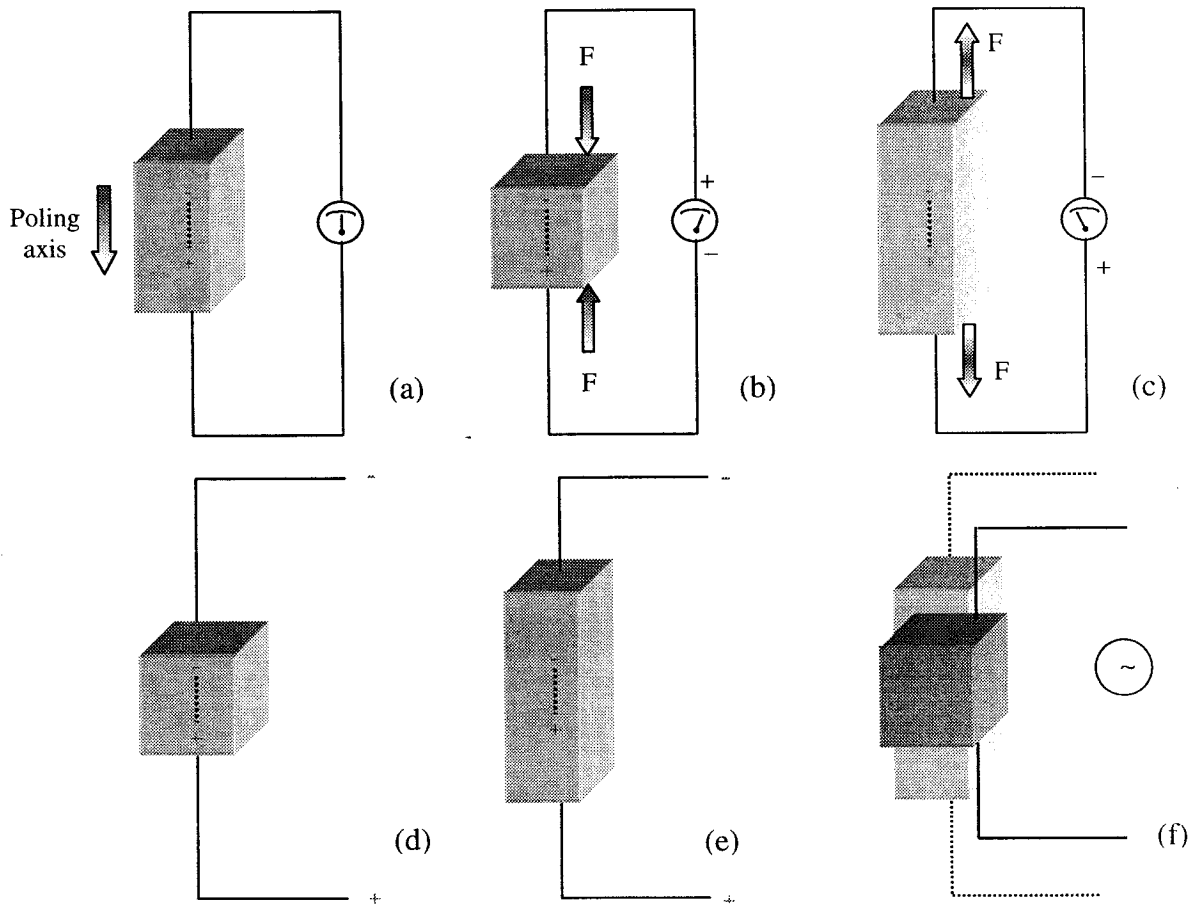


Figure 7-1: Piezoelectric effect in a cube of PZT material [APC International, 1999]

The relationship between the applied electric field and the resulting strain is defined by the piezoelectric strain coefficients $d_{ijk}$, where the subscripts i and j correspond to the mechanical strain in the tensorial sense, and the subscript k corresponds to the direction of the electric field.

The availability of piezoelectric materials in many forms such as thin films, patches and rods, and their light weight has made them ideal for active shape, vibration and control of structures. Their amenability to embeddement within composite materials and surface attachment to virtually all materials makes them attractive in structural control because all the moving parts encountered with conventional actuators are eliminated [Shakeri et al., 2001]. A number of applications involving piezoelectrically-driven actuation of structural components, such as axial motion of rods, bending of beams, and harmonic excitation of beams are discussed by Srinivasan and McFarland [2001]. Shakeri et al. [2001] discuss applications of piezoelectric actuators in vibration-isolation of the engines from the fuselage in aircraft, vibration control of a composite box beam, and others.

Mathematical modeling of piezoelectric composites has become very important in view of the widespread applications of such materials. Rajapakse [1997] developed closed-form plane-stress and plane-strain solutions for piezoelectric laminates. The use of piezoelectric actuators and sensors as elements of smart structures was investigated by Crawley and de Luis [1987], Tzou [1993], Tzou and Bao [1995], Sester and Poizat [2000], Wang and Quek [2000], Vel and Batra [2000a, 2001a, 2001b], Kalamkarov and Drosdov [1997], Reddy [1999] and others. A number of analytical results have been published concerning different aspects of piezoelectric problems, see for example Rose and Wang [2000], Yang et al. [2000], Tauchert et al. [1999] and others. Asymptotic approaches for thin piezoelectric plates were developed by Maughin and Attou [1990], Cheng et al. [2000], Kalamkarov and Kolpakov [2001], Kalamkarov and Georgiades [2001a, 2001b].

## 7.3 Shape Memory Alloys

Shape memory alloys (SMA) have the ability to "remember" a shape and revert to it at a characteristic temperature even if they have been extensively deformed. This shape memory effect was first observed in 1932 in samples of gold-cadmium, and in 1938 in samples of copper-zinc (brass). The most significant observation however did not occur until much later, in 1962, when William J. Buehler and his coworkers at the Naval Ordnance Laboratory (NOL) discovered that nickel-titanium alloys possessed this remarkable property [Srinivasan and McFarland, 2001]. Buehler named the nickel-titanium alloy NiTiNOL which includes the initials NOL of his laboratory. Typical SMA used today include Cu-Al-Ni, Cu-Zn-Al, Cu-Al-Ni, and of course Ni-Ti.
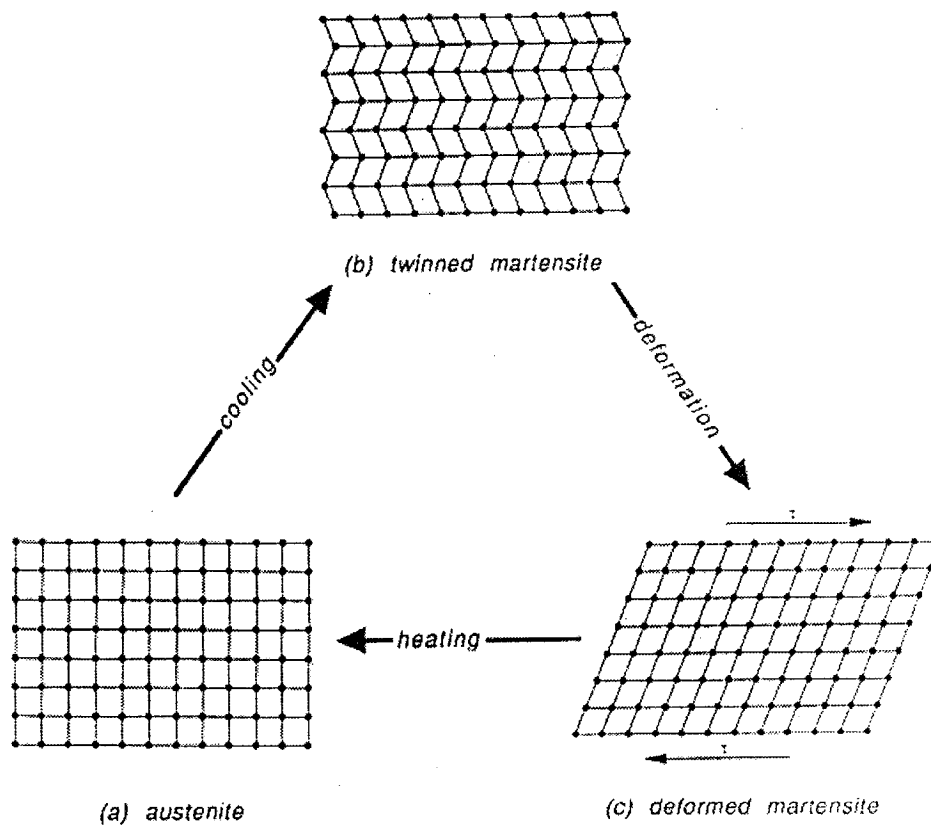
Figure 7-2: Shape memory effect [Wayman and Duerig, 1990]

SMA alloys are characterized by two distinct solid phases, a high-temperature phase and a low-temperature phase. The high-temperature phase is called austenite and the low-temperature phase is called martensite. Figure 7-2 shows the difference between the two phases and illustrates the salient features of the shape memory effect. The material in the austenite form is cooled to form twinned martensite. This phase transformation is not accompanied by a shape change. The martensite is then deformed by the application of stress. If the deformed material is now heated without physical constarint, it will revert to the austenite form and fully recover its original undeformed shape.
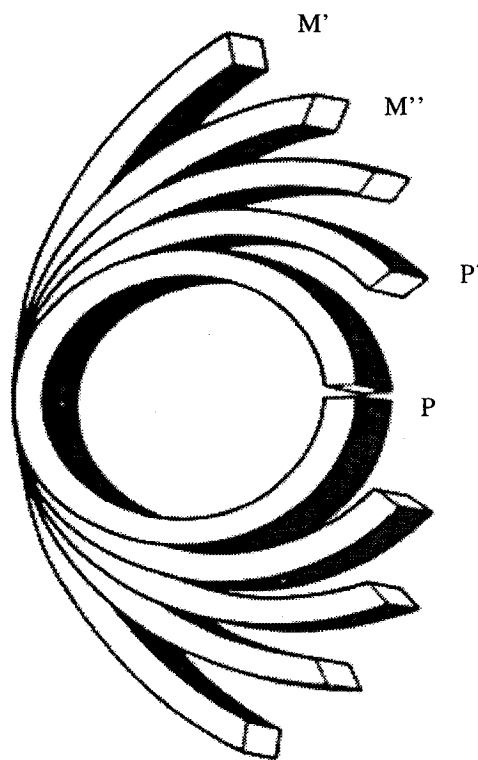


**Figure 7-3:** One-way and two-way shape memory effect [Perkins and Hodgson, 1990]

One should distinguish between one-way and two-way shape memory effects. Reference will be made to Figure 7-3 [Perkins and Hodgson, 1990]. In one-way effect, the sample P is cooled to the martensite form, deformed to shape M', and then heated to the austenite form to fully recover the original shape P. This high-temperature shape is retained on

subsequent cooling, and if it is desired to start another shape memory cycle, it must be deformed again. If the material is conditioned to display the two-way shape memory effect, it can be made to continuously revert from say M'' on cooling to P' on heating without the application of any force.

Shape memory alloys have been or have the potential to be used in a number of applications. Stöckel [1990] discusses a wide variety of potential automotive applications, Todoroki [1990] explains the advantages of SMA actuators as air-direction changing mechanisms in air-conditioning units, Runtsch [1990] investigates the performance of SMA actuators as circuit breakers, Furuya and Shimada [1990] discuss some very interesting robotics applications for SMA actuators.

One of the most popular areas of application of SMA actuators has been as elements of smart structures and smart composite structures for vibration excitation and vibration control. Some examples can be found in Lagoudas and Tadjbakhsh [1992], Rhee and Koval [1993], Madill and Wang [1998], Stalmans et al. [1998], Huang [1999], Brennan et al. [1999], Song et al. [2000], Adachi et al. [2000], Tawfik et al. [2000], Lammering and Schmidt [2001], Saadat et al. [2001].

Mathematical modeling of smart composite materials with integrated SMA actuators and other related issues have received a lot attention in recent years. Aboudi [1996] developed a microstructural model that encompasses both local and global effects, to analyze the behavior of resin-matrix and metal-matrix composites with embedded SMA fibers. Choi and Lee [1998] performed experimental and analytical studies on shape control of glass/epoxy composite beams with embedded SMA wire actuators. Vokoun and Kafka [1999] obtained a set of simple differential constitutive equations to model the shape memory effect in NiTiNOL alloys by hypothesizing that during transformation, the distances between the first atomic neighbors (Ni-Ti) remain unchanged, while the distances between second neighbors (Ni-Ni and Ti-Ti) change significantly.

It is certain that the volume of applications of SMA actuators as elements of smart composites will increase as engineers become familiar with their unusual behavior. The formulation of mathematical models which can relate internal stresses and strains with macroscopic behavior would be a step in the right direction.

## 7.4 Magnetostrictives and Electrorheological Fluids

Magnetostrictives are materials which experience strain under the influence of a magnetic field, and conversely generate a magnetic field when strained. The strength of the magnetic field is proportional to the rate of strain [Shakeri et al., 2001]. Early magnetostrictive materials were not studied extensively because the forces and strains they generated were much less than those for piezoelectric materials and shape memory alloys. This situation changed drastically with the development of Terfenol-D (an alloy of iron, terbium, and dysprosium) and other so-called giant magnetostrictors. These materials are capable of generating strains much larger than conventional piezoceramics with similar force outputs [Shakeri et al., 2001].

Kannan and Dasgupta [1994] performed finite element studies of the behavior of multi-functional composites with embedded magnetostrictive devices. Fenn and Gerver [1994] examined passive damping and velocity sensing using Terfenol-D transducers. Bi and Anjanappa [1994] examined the feasibility of implementing embedded magnetostrictive miniactuators for smart-structure applications, such as control of beam vibrations. Duenas et al. [1997] developed a composite magnetostrictive material by embedding Terfenol-D particles in a resin system and curing the composite under the influence of a strong magnetic field. The authors also developed a constitutive mathematical model for this material, which produced very accurate results when compared with experimental data.

Electrorheological fluids are suspensions of particles in a host liquid. These particles are typically 1 to 10 microns in size and are added to fluids such as mineral oils in weight fractions as high as 50% [Srinivasan and McFarland, 2001]. When an electrorheological fluid is subjected to an electric field, such properties as viscosity, and plasticity change dramatically, and these changes are reversible. Essentially, the electrorheological fluid changes from a liquid to solid-like gel when a field is applied [Shakeri et al., 2001]. It seems that these fluids have no potential for use with structural composite materials.

# 8.0 ASYMPTOTIC HOMOGENIZATION MODELS FOR SMART COMPOSITE MATERIALS

## 8.1 Introduction

Adaptive smart materials are expected to play an ever-increasing role in engineering applications, and consequently the mathematical formulation of such materials with a large number of actuators will be developed in this section. The general mathematical framework is that of asymptotic homogenization [Bensoussan et al., 1978; Sanchez-Palencia, 1980; Cioranescu and Donato, 1999]. The three essential features characterizing asymptotic homogenization are asymptotic or perturbation expansions, two-scale expansions and the homogenization process. These will be explained briefly in the following sections.

## 8.2 Asymptotic Expansions

The differential equations describing the behavior of real structures or systems are often characterized by the presence of a certain parameter, $\varepsilon$, which even though small in relation to the other parameters and variables, may have an effect too important to be ignored. However, the presence of this parameter more often than not, renders the pertinent differential equation extremely difficult to solve by making it for example weakly non-linear. One therefore looks to alternative methods of solution. Asymptotic expansions are simply infinite series representations of the solution of these differential equations, in terms of the small parameter $\varepsilon$. Typically, but certainly not always, these series are in the form of power terms of $\varepsilon$, i.e.

$$y_{solution} = y_o + \varepsilon y_1 + \varepsilon^2 y_2 + \varepsilon^3 y_3 + \dots \tag{8.1}$$

Here y may represent a scalar, vector or tensor. It is imperative of course that the series in Equation (8.1) converges, or at least converges before it starts diverging, so that one has control of the error incurred when the series is truncated after a certain number of terms.

As an illustration, standard asymptotic or perturbation techniques will be used to obtain the solution of the following differential equation with appropriate boundary condition:

$$\frac{dy}{dx} + y = \varepsilon y^2$$
$$y(0) = 1$$

(8.2)

The first step is to assume that the solution, y, may be expressed as:

$$y = y_o(x) + \varepsilon y_1(x) + \varepsilon^2 y_2(x) + O(\varepsilon^3)$$

(8.3)

The symbol "O" in Equation (8.3) is one of the two so-called Landau symbols, and it means "order of". Basically, a function $f(\varepsilon)$ is said to be of order $\varphi(\varepsilon)$ if the ratio $\left|\frac{f}{\varphi}\right|$ is bounded for $\varepsilon$ near $\varepsilon_o$ [Holmes, 1995]. In other words, if the limit

$$\lim_{\varepsilon \to \varepsilon_o} \frac{f(\varepsilon)}{\varphi(\varepsilon)}$$

(8.4)

exists, then $f = O(\varphi)$. Thus, in Equation (8.3), the error incurred by truncating the series after the $\varepsilon^2$ term is of order $\varepsilon^3$. It should also be noted in Equation (8.3) that the $y_i$ terms are all functions of the independent variable x, and do not depend on $\varepsilon$.

The next step in the process involves substitution of the expansion of Equation (8.3) into Equation (8.2), to obtain, after neglecting higher-order terms:

$$\frac{dy_o}{dx} + \varepsilon \frac{dy_1}{dx} + \varepsilon^2 \frac{dy_2}{dx} + y_o + \varepsilon y_1 + \varepsilon^2 y_2 = \varepsilon(y_o + \varepsilon y_1)^2$$

(8.5)

Collecting terms of like powers of $\varepsilon$, Equation (8.5) may be rewritten in the form:

$$\frac{dy_o}{dx} + y_o + \varepsilon\left(\frac{dy_1}{dx} + y_1\right) + \varepsilon^2\left(\frac{dy_2}{dx} + y_2\right) = \varepsilon y_o^2 + 2\varepsilon^2 y_o y_1$$

(8.6)

Since the $y_i$ functions in Equation (8.6) are independent of $\varepsilon$, the following three equations are implied:

$$\frac{dy_o}{dx} + y_o = 0 \qquad (8.7a)$$

$$\frac{dy_1}{dx} + y_1 = y_o^2 \qquad (8.7b)$$

$$\frac{dy_2}{dx} + y_2 = 2y_o y_1 \qquad (8.7c)$$

In order to have a well-formulated problem, one must also consider the boundary conditions. To this end, Equation (8.3) is substituted in the boundary condition in Equation (8.2) to give:

$$y_o(0) + \varepsilon y_1(0) + \varepsilon^2 y_2(0) = 1 \qquad (8.9)$$

Equating terms with like powers of $\varepsilon$ gives the following set of boundary conditions which must be satisfied in conjunction with Equations (8.7a) to (8.7c):

$$y_o(0) = 1 \qquad (8.10a)$$

$$y_1(0) = 0 \qquad (8.10b)$$

$$y_2(0) = 0 \qquad (8.10c)$$

From Equation (8.7a)

$$y_o(x) = Ae^{-x} \qquad (8.11a)$$

From Equation (8.10a) A = 1, so that

$$y_o(x) = e^{-x} \qquad (8.11b)$$

Substitution of Equation (8.11b) into Equation (8.7b) and solving gives:

$$y_1(x) = Be^{-x} - e^{-2x} \qquad (8.11c)$$

From Equation (8.10b) B = 1, so that

$$y_1(x) = e^{-x} - e^{-2x} \qquad (8.11d)$$

Finally, substitution of Equations (8.11b) and (8.11d) into Equation (8.7c) and solving gives the general expression for $y_2$ as:

$$y_2(x) = De^{-x} - 2e^{-2x} + e^{-3x} \qquad (8.11e)$$

The constant D = 1 is easily verified from Equation (8.10c), and thus:

$$y_2(x) = e^{-x} - 2e^{-2x} + e^{-3x} \qquad (8.11f)$$

Combining expressions (8.11b), (8.11d) and (8.11f) gives the total expression for the asymptotic solution of the problem at hand as follows:

$$y(x) = e^{-x} + \varepsilon\left(e^{-x} - e^{-2x}\right) + \varepsilon^2\left(e^{-x} - 2e^{-2x} + e^{-3x}\right) + O\left(\varepsilon^3\right) \qquad (8.12)$$

To assess the accuracy of this approximation, one must compare it with the exact solution. From Equation (8.2), a simple separation of variables gives the analytic solution as:

$$y(x) = \frac{1}{e^x(1+\varepsilon) - \varepsilon} \qquad (8.13)$$

Figure 8-1 compares the analytic and asymptotic solutions. It is seen that they conform so well to one another that they are virtually indistinguishable. For the purposes of this graph, a value of $\varepsilon = 0.1$ was selected.
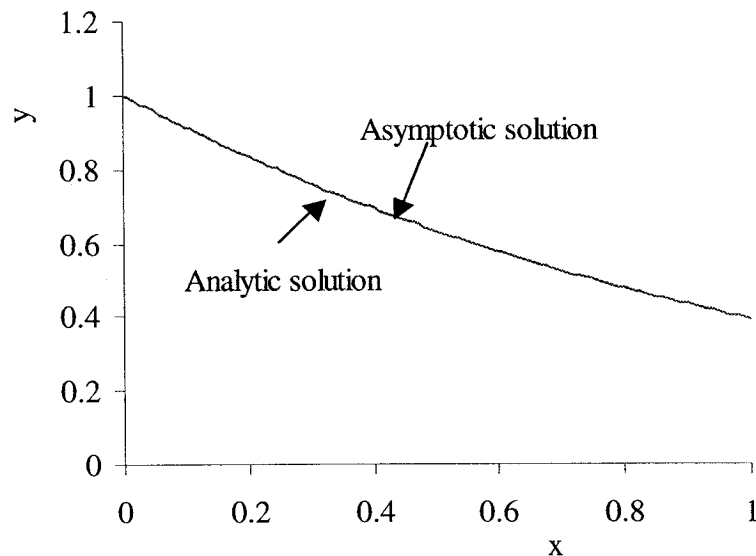


**Figure 8-1:** Comparison of analytic and asymptotic solutions for the example in Equation (8.2)

## 8.3 The Method of Two Scales

The second characteristic feature of the method of asymptotic homogenization is the two-scale expansion technique. The best way to illustrate this is by means of a very simple example. This example will also show why a "regular" asymptotic expansion like the one discussed in the previous section is not adequate to handle a problem of this nature.

Consider the following differential equation and pertinent initial conditions:

$$\ddot{x} + \varepsilon \dot{x} + x = 0 \tag{8.14a}$$

$$x(0) = 1, \quad \dot{x}(0) = 0 \tag{8.14b}$$

Equations (8.14a) and (8.14b) could represent a spring-mass-damper system with weak damping (since $\varepsilon$ is small in comparison to unity).

In an attempt to obtain a regular perturbation expansion, one writes:

$$x = x_0(t) + \varepsilon x_1(t) + \varepsilon^2 x_2(t) + O(\varepsilon^3) \tag{8.15}$$

Equation (8.15) is subsequently substituted in Equations (8.14a) and (8.14b) to obtain:

$$\ddot{x}_0(t) + \varepsilon \ddot{x}_1(t) + \varepsilon \dot{x}_0(t) + x_0 + \varepsilon x_1 = 0 \tag{8.16a}$$

$$x_0(0) + \varepsilon x_1(0) = 1 \tag{8.16b}$$

$$\dot{x}_0(0) + \varepsilon \dot{x}_1(0) = 0 \tag{8.16c}$$

The system of equations (8.16a) to (8.16c) splits into the following two groups:

$$\ddot{x}_0(t) + x_0 = 0 \tag{8.17a}$$

$$x_0(0) = 1 \tag{8.17b}$$

$$\dot{x}_0(0) = 0 \tag{8.17c}$$

and

$$\ddot{x}_1(t) + x_1 = -\dot{x}_0 \tag{8.17d}$$

$$x_1(0) = 0 \tag{8.17e}$$

$$\dot{x}_1(0) = 0 \qquad\qquad (8.17f)$$

The solution of Equation (8.17a) which satisfies the initial conditions (8.17b) and (8.17c) is readily obtained to be:

$$x_o = \cos(t) \qquad\qquad (8.18)$$

By substituting Equation (8.18) into Equation (8.17d) and solving in conjunction with the initial conditions (8.17e) and (8.17f) gives the solution of $x_1$ to be:

$$x_1 = \frac{1}{2}(\sin t - t\cos t) \qquad\qquad (8.19)$$

Thus, combining Equations (8.18) and (8.19) gives the total expression for x to be as follows:

$$x_o = \cos(t) + \frac{1}{2}\varepsilon(\sin t - t\cos t) \qquad\qquad (8.20)$$

To proceed further, the analytical solution must be obtained so that it can be compared with its asymptotic counterpart. Thus, from Equations (8.14a) and (8.14b), and after some algebraic manipulations, the exact solution for x is given by:

$$x(t) = e^{-\frac{\varepsilon}{2}t}\left( \frac{-\varepsilon/2}{\sqrt{1-\varepsilon^2/4}}\sin\sqrt{1-\frac{\varepsilon^2}{4}}t + \cos\sqrt{1-\frac{\varepsilon^2}{4}}t \right) \qquad\qquad (8.21)$$

Figure 8-2 is a plot of Equations (8.20) and (8.21) for $\varepsilon = 0.05$. It is clear that the solution is only accurate up to about 20 seconds and then the error becomes progressively larger. Thus the asymptotic solution is correct up to times $\approx O(1/\varepsilon) = 20$ seconds. The problem beyond t = 20 seconds is that the last term in Equation (8.20) becomes as large as the first term. In any valid expansion, it is required that each term be only a small correction to the previous term. In this case the term $\varepsilon t \cos t$ is small in comparison to cos t when the combination $\varepsilon t \ll 1$, i.e. when t = o(1/$\varepsilon$), where "o" is the small Landau symbol. Hence, for $\varepsilon = 1/20$, t must be less than 20 in order for the expansion to be valid.

To appreciate the source of the difficulty for the situation at hand, one ought to observe that the actual solution is characterized by two quite different scales. As shown in Figure

8-2, superimposed on a "rapid" oscillating scale, there exists a much slower (exponential) variation. Thus, the actual solution decays slowly, but the asymptotic solution can "capture" only the fast variation in this case. In its attempt to correct the first term, the second term in the asymptotic expansion becomes progressively larger and eventually even larger than the first term. The term $t \cos t$ is called a "secular" term.
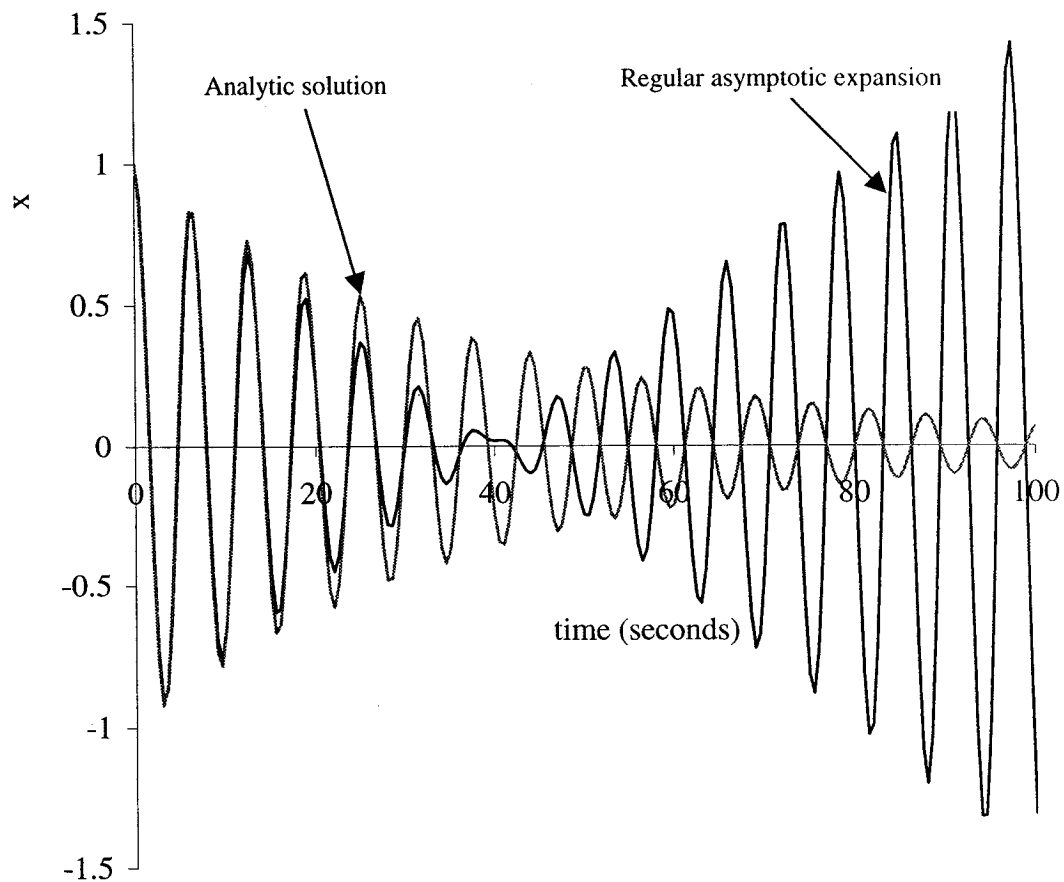


**Figure 8-2:** Comparison of analytic and regular asymptotic solutions for a weakly damped spring-mass-damper system

In an attempt to obtain a uniformly-valid asymptotic expansion, one recognizes that the problem arises because of the mismatch between the two time scales. The solution is to simply "speed up" the slow variation by introducing a new variable $t_2 = \varepsilon t$. Thus, the two time scales are:

$$t_1 = t$$
$$t_2 = \varepsilon t$$

(8.22)

In Equation (8.22) $t_1$ is commonly referred to as the fast variable and $t_2$ the slow variable. The procedure from here onward is straightforward and the two variables are treated as independent. The only problem associated with the introduction of a new variable, is that an o.d.e. (ordinary differential equation) becomes a p.d.e. (partial differential equation)! Thus,

$$\frac{d}{dt} \rightarrow \frac{\partial}{\partial t_1}\frac{\partial t_1}{\partial t} + \frac{\partial}{\partial t_2}\frac{\partial t_2}{\partial t}$$
$$\Rightarrow \frac{d}{dt} \rightarrow \frac{\partial}{\partial t_1} + \varepsilon\frac{\partial}{\partial t_2}$$

(8.23a)

and

$$\frac{d^2}{dt^2} = \frac{\partial}{\partial t}\left(\frac{\partial}{\partial t}\right) = \frac{\partial^2}{\partial t_1^2} + 2\varepsilon\frac{\partial^2}{\partial t_1\partial t_2} + \varepsilon^2\frac{\partial^2}{\partial t_2^2}$$

(8.23b)

The differential equation in (8.14a) and (8.14b) now becomes:

$$\frac{\partial^2 x}{\partial t_1^2} + 2\varepsilon\frac{\partial^2 x}{\partial t_1\partial t_2} + \varepsilon^2\frac{\partial^2 x}{\partial t_2^2} + \varepsilon\frac{\partial x}{\partial t_1} + \varepsilon^2\frac{\partial x}{\partial t_2} + x = 0$$

$$x\big|_{t_1=t_t=0} = 1 \text{ and}$$

$$\frac{\partial x}{\partial t_1} + \varepsilon\frac{\partial x}{\partial t_2}\bigg|_{t_1=t_t=0} = 0$$

(8.24)

It should be noted that even though Equation (8.24) is 2$^{nd}$ order with respect to $t_1$ and 2$^{nd}$ order with respect to $t_2$, only 2 initial conditions are given. These can be expanded to 4 in an infinite number of ways. To make the solution unique, one needs to impose certain restrictions so as to avoid secular terms [Holmes, 1995]. This will be demonstrated shortly.

Subsequently, one assumes an asymptotic expansion of the form:

$$x(t_1, t_2) = x_o(t_1, t_2) + \varepsilon x_1(t_1, t_2) + \ldots$$

(8.25)

This is then substituted in Equation (8.24) to give the following two problems:

$$\frac{\partial^2 x_o}{\partial t_1^2} + x_o = 0$$

$$x_o\big|_{t_1=t_2=0} = 1$$

$$\frac{\partial x_o}{\partial t_1}\bigg|_{t_1=t_2=0} = 0$$

(8.26a)

and

$$\frac{\partial^2 x_1}{\partial t_1^2} + x_1 = -2\frac{\partial^2 x_o}{\partial t_1 \partial t_2} - \frac{\partial x_o}{\partial t_1}$$

$$x_1\big|_{t_1=t_2=0} = 0$$

$$\frac{\partial x_1}{\partial t_1} + \frac{\partial x_o}{\partial t_2}\bigg|_{t_1=t_2=0} = 0$$

(8.26b)

The solution of Equation (8.26a) is readily obtained to be:

$$x_o = A(t_2)\sin t_1 + B(t_2)\cos t_1$$

(8.27a)

$$A(0) = 0, \quad B(0) = 1$$

(8.27b)

Substitution of Equation (8.27a) into Equation (8.26b) yields, after some manipulation:

$$x_1 = D(t_2)\sin t_1 + E(t_2)\cos t_1 - \frac{1}{2}\left(2\frac{dA}{dt_2} + A\right)t_1\sin t_1 - \frac{1}{2}\left(2\frac{dB}{dt_2} + B\right)t_1\cos t_1 \quad (8.28)$$

It is clear that to avoid secular terms, one must impose the following conditions on A and B:

$$2\frac{dA}{dt_2} + A = 0$$

$$2\frac{dB}{dt_2} + B = 0$$

(8.29)

The solution of Equation (8.29) in conjunction with Equation (8.27b) leads to:

$$A = 0 \quad \text{and} \quad B = e^{-\frac{t_2}{2}}$$

(8.30)

Thus, the solution of $x_o$ is:

$$x_o = e^{-\frac{t_1}{2}}\cos t_1 = e^{-\varepsilon\frac{t}{2}}\cos t$$

(8.31)

Finally, substituting the last expression into Equation (8.25) gives:

$$x = e^{-\varepsilon\frac{t}{2}}\cos t + O(\varepsilon^2) \qquad\qquad (8.32)$$

Note that the procedure outlined here simply amounts to letting $\varepsilon t = t_1$ be a new variable and substituting it into the model. The next term in the series will be of order $\varepsilon t_1 = O(\varepsilon^2)$, which explains the form of Equation (8.32). A plot of this asymptotic expansion alongside the analytical solution is shown in Figure 8-3.
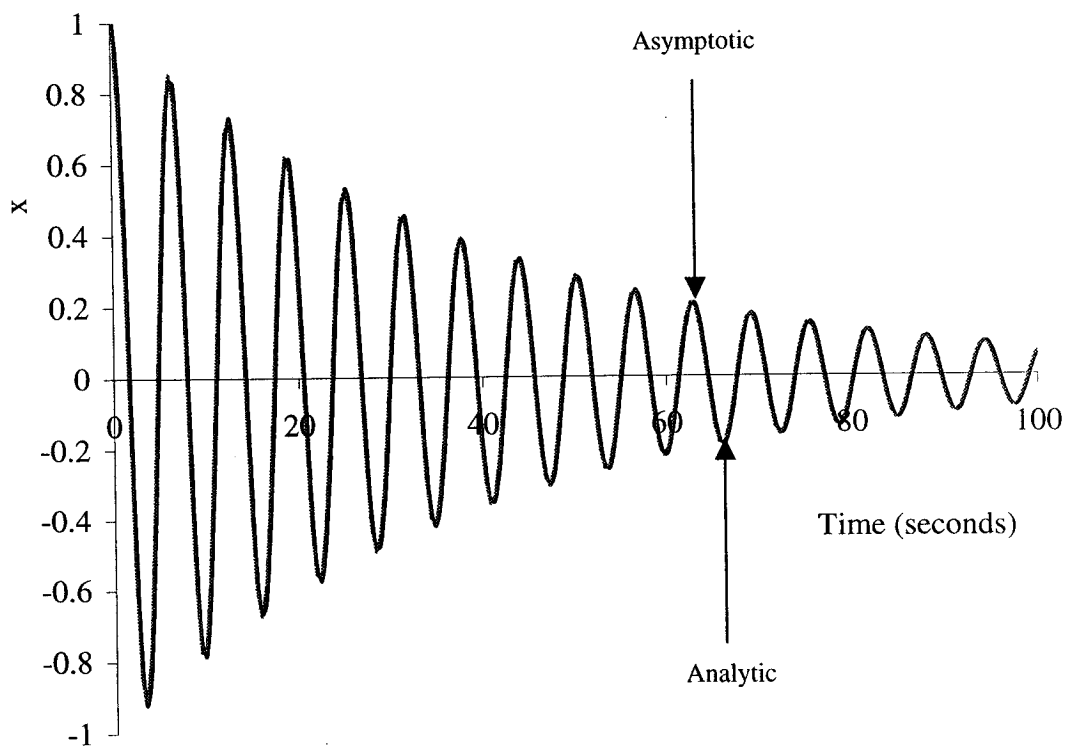


**Figure 8-3:** Comparison of analytic and two-scale asymptotic solutions for a weakly damped spring-mass-damper system

It is apparent that the two solutions are indistinguishable form one another.

## 8.4 Einstein's Summation Convention

It was mentioned previously that the method of homogenization will be used to develop a mathematical model describing the behavior of smart composite structures with a large number of actuators. It was also explained that the homogenization technique depends on (a) perturbation expansions, (b) the two-scale method, and (c) the homogenization process itself. A brief account of regular perturbation and two-scale expansions was given in the previous sections. The actual homogenization technique will become clear during the various stages of the model development. Before embarking on the task at hand, it is necessary to say a word about Einstein's summation convention, which will be used extensively in the sequel.

This convention was introduced by Einstein in his development of the theory of relativity [Kay, 1988]. According to this convention, an equation of the form

$$a_1 x_1 + a_2 x_2 + a_3 x_3 = \sum_{i=1}^{3} a_i x_i \tag{8.33}$$

will be represented as $a_i x_i$ with the understanding that the repeated index i is summed over its range 1 to 3. The index i is called a dummy index. Next consider the following equation:

$$u_i = c_{ij} b_j \tag{8.34}$$

Since j is repeated on the right hand side (RHS) of Equation (8.34), it is summed over its range. However, the index i is not repeated on the RHS and is therefore called a free index. Thus assuming that both i and j may attain values from 1 to 3, Equation (8.34) is equivalent to the following three equations:

$$u_1 = c_{11} b_1 + c_{12} b_2 + c_{13} b_3$$
$$u_2 = c_{21} b_1 + c_{22} b_2 + c_{23} b_3 \tag{8.35}$$
$$u_3 = c_{31} b_1 + c_{32} b_2 + c_{33} b_3$$

It is apparent that the notation in Equation (8.34) is much more concise than that of Equation (8.35) and is therefore a powerful time-saving tool.

## 8.5 Asymptotic Homogenization Model for Smart Structures

### 8.5.1 Introduction

As explained previously, smart structures consist of active and passive structural elements, actuators and sensors. In many cases, it is possible to assume that the sensors have no influence on the mechanical properties of the smart structure (see Chapter 4). Then, the mechanical properties and deformation of the smart structure are determined by the joint work of structural elements and actuators. In this context, the actuator is understood to be a structural element of arbitrary nature which can be activated in some way in order to produce residual strains and stresses. It can be an inclusion, or a device such as for example a piezoelectric element. If the characteristic dimensions of the structural elements are small in comparison to the overall dimensions of the structure, then the original inhomogeneous body can be replaced, in an asymptotic sense, by a homogeneous structure with similar mechanical behavior. The problem of calculating the effective characteristics of the homogenized structure is not a trivial matter. It requires application of rigorous mathematical methods. For inhomogeneous structures of a periodic nature, the asymptotic homogenization method has been applied in a number of cases [Duvaut, 1976; Bensoussan et al., 1978; Sanchez-Palencia, 1980].

Kalamkarov [1992] used the asymptotic homogenization technique for the case of a composite material containing a periodic array of reinforcements such as fibers. In this chapter, the same technique will be used to analyze a smart composite structure with a periodic arrangement of actuators. As well, due to the important effect of temperature and moisture on the mechanical properties of composites (see Chapter 5), the model developed will incorporate thermal expansion and moisture (hygroscopic) expansion effects.

## 8.5.2 Motivation and Methodology of Development of Mathematical Model

Consider a fiber-reinforced composite with a regular structure, such as the one depicted in Figure 8.4.
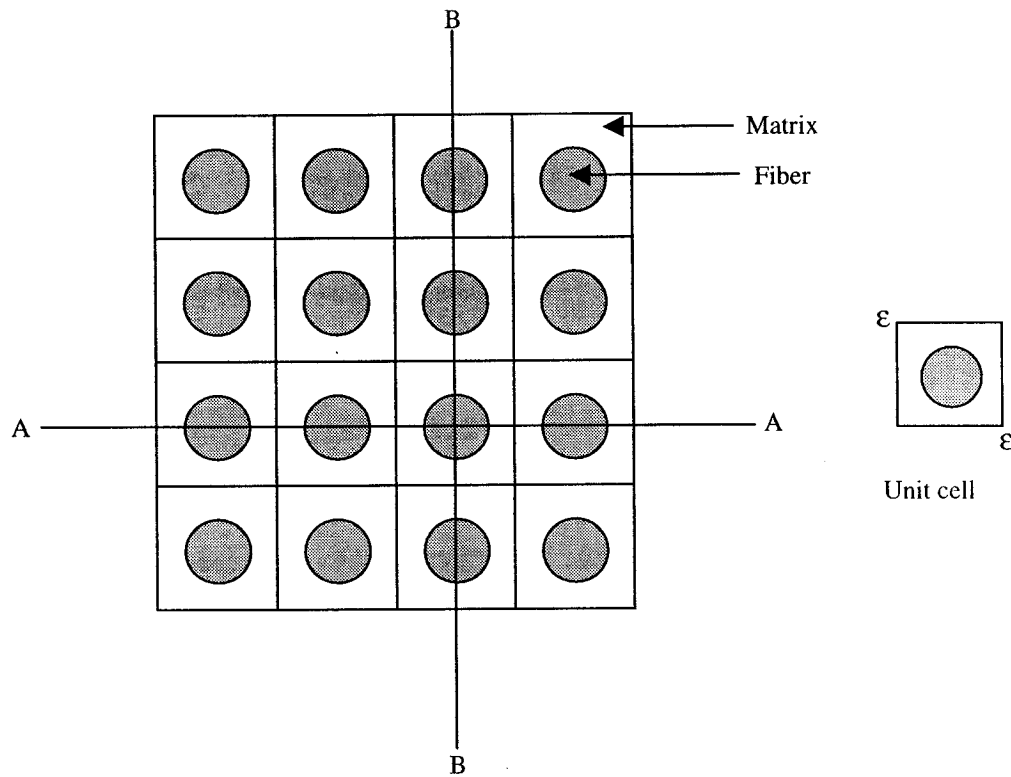


**Figure 8-4:** Cross-section of a periodic composite with a regular structure

It is evident from this figure that the composite medium can be thought of as a regular arrangement of what one might justifiably call unit cells. Suppose that the unit cell in this case has both length and width equal to $\varepsilon$, where $\varepsilon$ is clearly a very small number since its magnitude is of the same order as the diameter of the reinforcing fibers or the spacing between the fibers. For example, the glass and carbon fibers used in the pultrusion of the GFRP and CFRP tendons discussed in previous chapters of this thesis have a diameter of 23 microns and 7 microns respectively. Hence, comparing $\varepsilon$ to the overall macroscopic

dimensions of the composite, one will appreciate why the dimensions of the unit cell are specified as "small parameters".
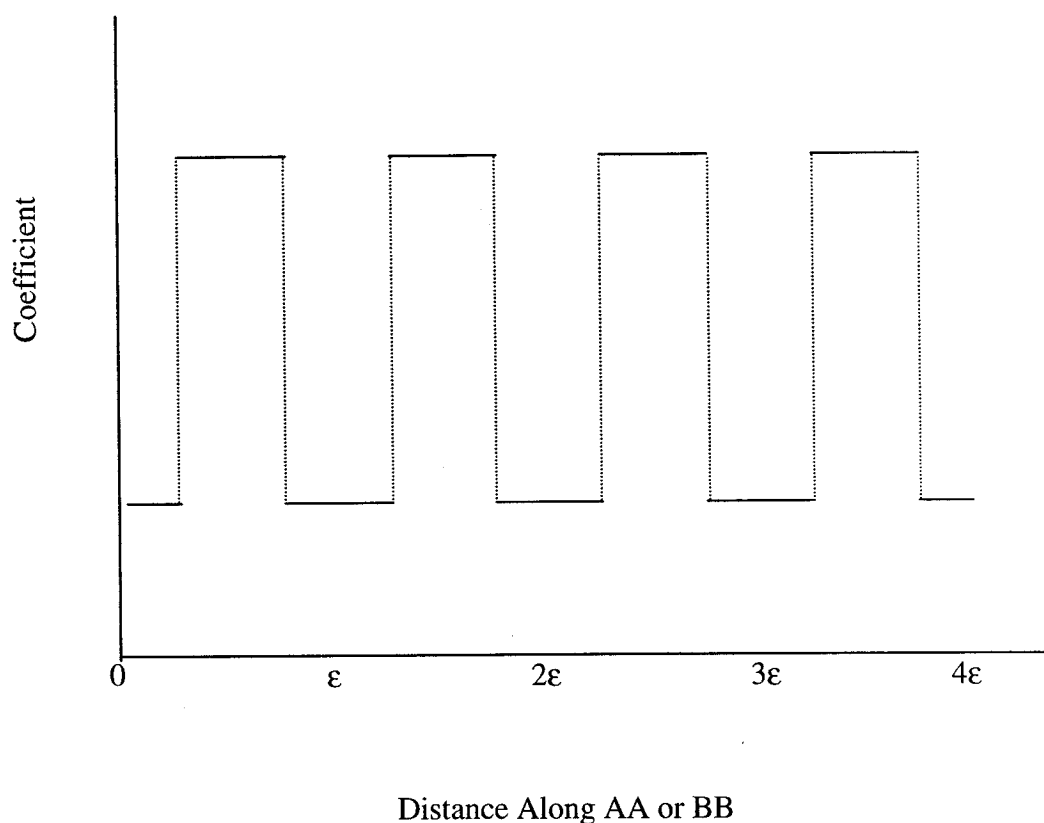


**Figure 8-5:** Cross-section of a periodic composite with a regular structure

Suppose now that one plots the variation along AA or BB, of a typical material parameter or coefficient such as the longitudinal stiffness. The result will resemble Figure 8-5. In other words, this coefficient will repeat itself regularly every $\varepsilon$ microns. Consequently, the differential equations characterizing heterogeneous media with a periodic structure have rapidly oscillating coefficients which depend upon the physical properties of the various constituents such as reinforcing fibers, actuators, sensors, and matrix. Said differently, these coefficients are periodic with extremely small period equal to $\varepsilon$. It further follows that the dependent variables that appear in these differential equations, for

example the stress or strain fields, temperature at steady state etc., will also be periodic with a period ε. In a general three-dimensional medium, these variables will be periodic in all three directions, $x_1$, $x_2$, $x_3$ (or x, y, z). In addition to being periodic, however, the dependent variables naturally will also depend upon the location in the composite. In other words, these variables will have periodic and non-periodic dependencies or components. For example, it is evident that the value of the stress field will be different at the location of a fiber at one end of a periodic composite than at a corresponding point in a fiber at the other end of the composite. Thus, from the discussion so far, it is apparent that the problem of a periodic structure is characterized by two vastly different scales, a microscopic scale which is a consequence of periodicity and, superimposed upon it, a macroscopic scale. Figure 8-6 shows a typical variation of a dependent variable along a certain direction in a periodic medium [Holmes, 1995].
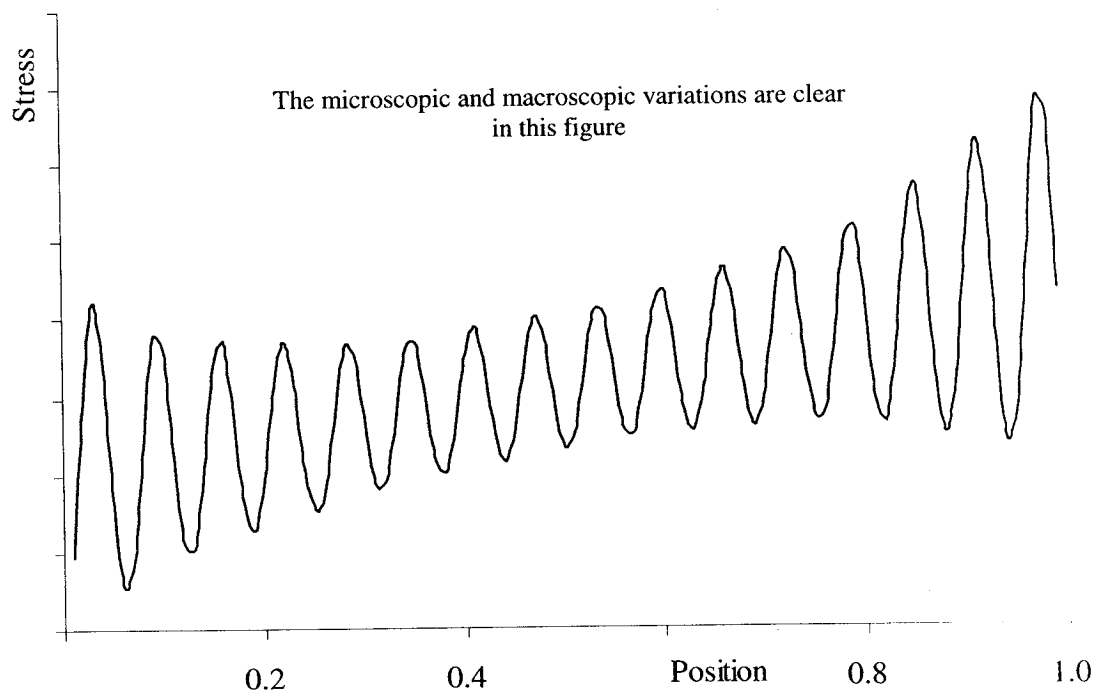


**Figure 8-6:** Variation of stress in a periodic medium shows microscopic and macroscopic scales [Holmes, 1995]

In Figure 8-6, one can observe a microscale which is of order 0.1 superimposed on a macroscale which is of order 1.

To put the notions of this section in a better perspective, reference will be made to Figure 8-7 [Sanchez-Palencia, 1980].
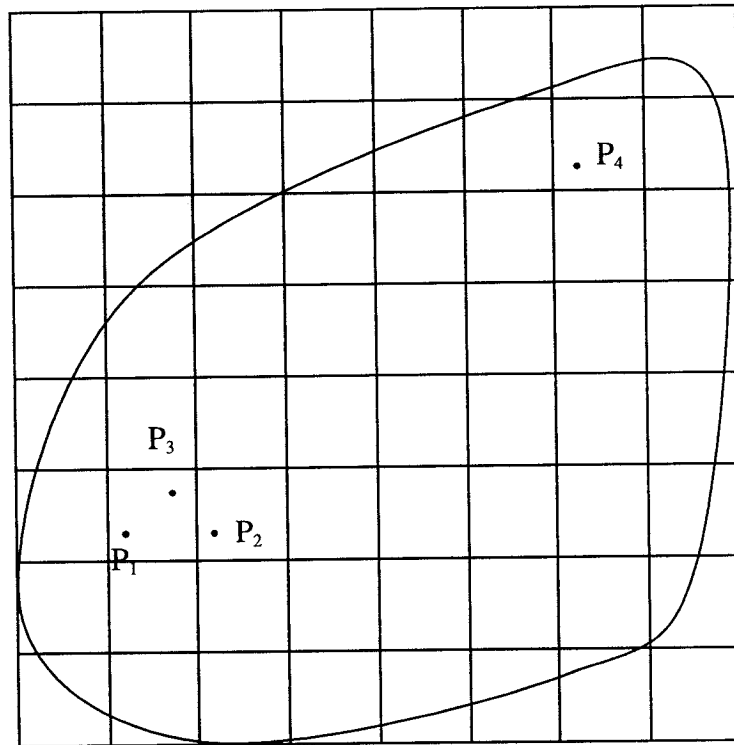


**Figure 8-7:** A periodic medium [Sanchez-Palencia, 1980]

Suppose one is interested in determining the temperature distribution, T, in the periodic composite of Figure 8.7. In a problem of this nature, the thermal conductivity, K, will inevitably show up in the pertinent differential equations. Because of the physical periodicity, and because points $P_1$, $P_2$, and $P_4$ represent corresponding points in different unit cells, the thermal conductivity at these points will be the same. However, the thermal conductivity at point $P_3$ will be different. Now suppose that one is looking at the temperature field at steady state. The periodic component of the temperature at points $P_1$

and $P_4$ will be the same, but the non-periodic component will be different because $P_1$ and $P_4$ are rather far apart. Consequently, the steady state temperature at these points will be different. For points $P_1$ and $P_2$ however, the situation is different. The periodic component of the temperature is again the same (corresponding points), but this time the non-periodic component is also essentially the same because the two unit cells are adjacent, and macroscopically their separation represents a small distance. We conclude by asserting that the thermal conductivity and other material parameters are strictly periodic in a medium of this nature, whereas, temperature and other dependent variables are characterized by both periodic and non-periodic dependencies.
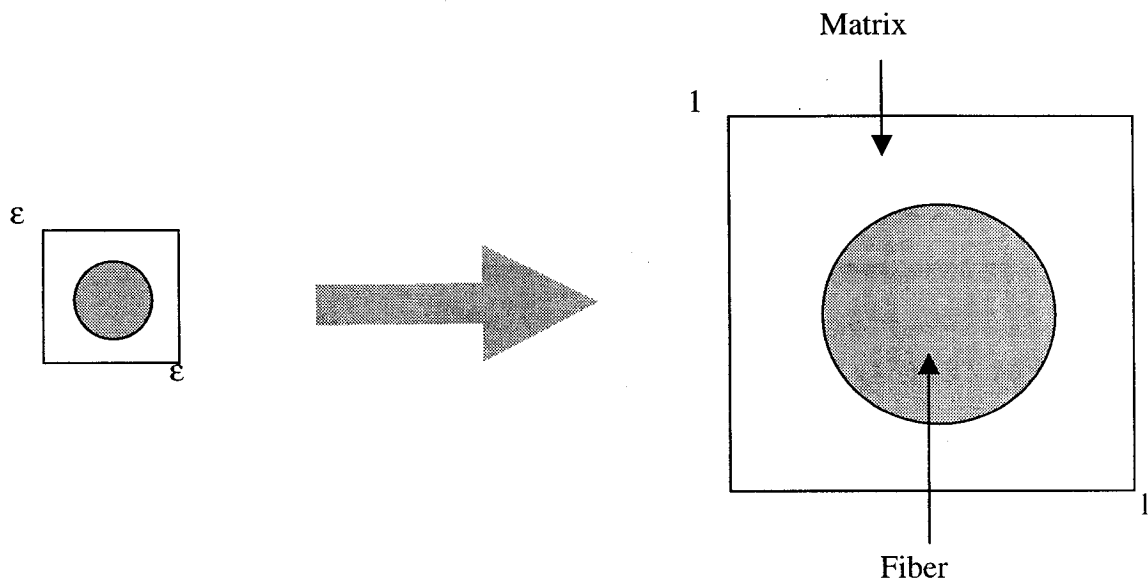


**Figure 8-8:** Introduction of fast variables

The presence of these two scales means that one will not be able to obtain a regular perturbation expansion for the problem of a periodic medium, much as it was not possible to obtain a regular uniformly-valid expansion for the weakly damped oscillator of Section 8.3. In that case, the difficulty was the mismatch between a rapid oscillating scale and slow exponential scale. This difficulty was overcome by "speeding up" the slow scale. The same technique will be employed for the case of a periodic medium. Here the

difficulty arises because the microscale is very small (order ε), while the macroscale is very large (order 1). The solution is to simply expand the domain of the unit cell! This is shown in Figure 8-8. Thus, in addition to the regular macroscopic variables, the periodic smart structure will be characterized by a new set of variables, the microscopic variables $y_1, y_2, y_3$ defined by:

$$y_i = \frac{x_i}{\varepsilon}, \quad i = 1, 2, 3 \qquad [8.36]$$

It was mentioned at the beginning of Section 8.5.2 that a differential equation which attempts to describe the physical behavior of a heterogeneous medium with a periodic structure is characterized by rapidly oscillating coefficients with period ε. In view of the introduction of the microscopic scale, these coefficients will now be periodic in $y_i$ with a period 1, the size of the enlarged unit cell. The introduction of the unit cell will eventually lead to the determination of averaged or homogenized coefficients which are independent of the fast scale. The combination of multiple scales and the determination of these homogenized coefficients is called the method of homogenization [Bensoussan et al., 1978; Sanchez-Palencia, 1980; Bakhvalov and Panasenko, 1984; Cioranescu and Donato, 1999]

### 8.5.3 Problem Formulation

Consider a smart structure representing an inhomogeneous solid occupying domain G with boundary ∂G that contains a large number of periodically arranged actuators as shown in Figure 8-9.

The elastic deformation of this smart structure can be described by means of the following boundary value problem:

$$\frac{\partial \sigma_{ij}^\varepsilon}{\partial x_j} = f_i \text{ on } G \qquad (8.37)$$

$$\mathbf{u}^\varepsilon = 0 \quad \text{on } \partial G \qquad (8.38)$$
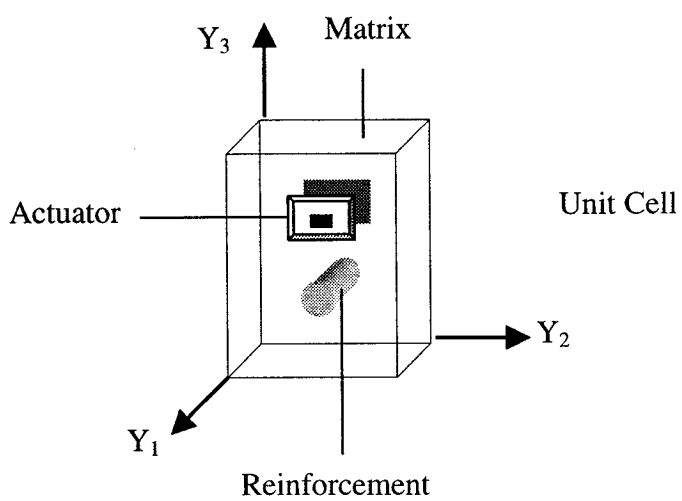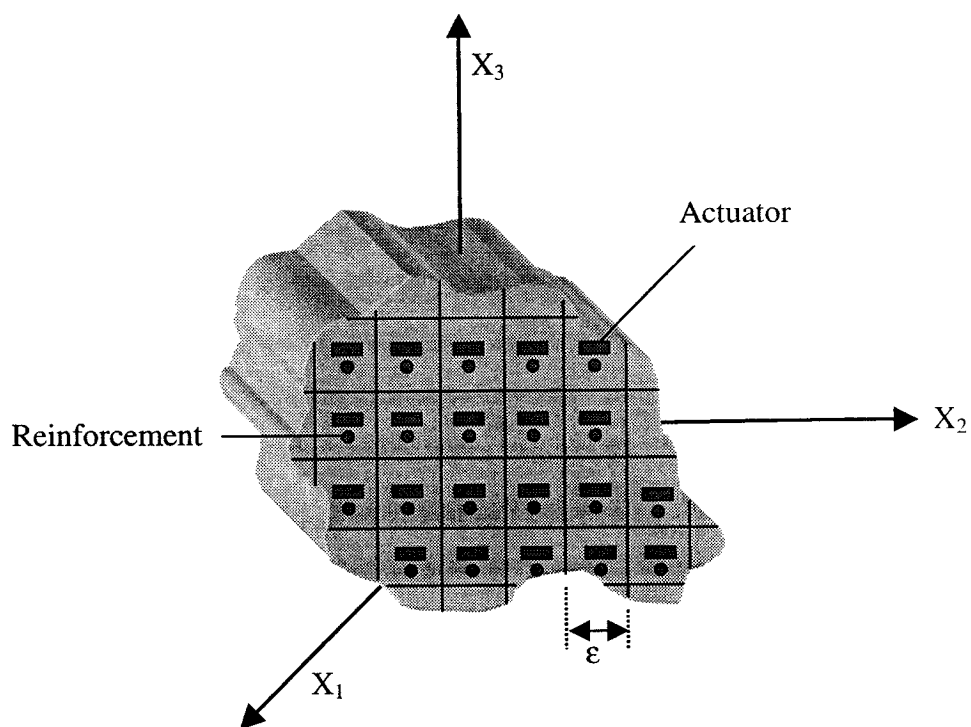
**Figure 8-9:** Composite containing a large number of periodically arranged actuators and its periodicity cell Y in the "fast" variables y

Equation (8.37) represents the equations of static equilibrium. A complete derivation can be found in Appendix A. In this equation and its accompanying boundary conditions, $\sigma_{ij}$ represents the stress field, and $\mathbf{u}$ is the displacement field. As well, $\mathbf{x}$, with components $x_i$ ($i = 1, 2, 3$) is the macroscopic position vector of any point in the smart structure.

As previously explained, a problem of such periodic nature is characterized by two very different scales. One scale, the macroscopic or slow scale accounts for the variation of the dependent variables such as the displacement and stress fields from one cell to another. This scale is of order 1. The other scale, referred to as the microscopic or fast scale, accounts for the periodicity of the problem at hand. The fast scale is of order $1/\varepsilon$. Thus, to account for these observations, Equations (8.37) and (8.38) may be rewritten as follows:

$$\frac{\partial \sigma_{ij}^{\varepsilon}\left(\mathbf{x}, \dfrac{\mathbf{x}}{\varepsilon}\right)}{\partial x_j} = f_i \quad \text{on } G \tag{8.39}$$

$$\mathbf{u}^{\varepsilon}\left(\mathbf{x}, \frac{\mathbf{x}}{\varepsilon}\right) = 0 \quad \text{on } \partial G \tag{8.40}$$

The strain field, $e_{ij}$, is given in terms of the displacement field by the following well-known expressions [Lai et al., 1993]:

$$e_{ij}^{\varepsilon}\left(\mathbf{x}, \frac{\mathbf{x}}{\varepsilon}\right) = \frac{1}{2}\left[\frac{\partial u_i}{\partial x_j}\left(\mathbf{x}, \frac{\mathbf{x}}{\varepsilon}\right) + \frac{\partial u_j}{\partial x_i}\left(\mathbf{x}, \frac{\mathbf{x}}{\varepsilon}\right)\right] \tag{8.41}$$

The stress-strain relationships for this structure will be given by Hooke's Law which is modified to include actuation, thermal expansion and hygroscopic absorption effects and has the following form:

$$\sigma_{ij}^{\varepsilon}\left(\mathbf{x}, \frac{\mathbf{x}}{\varepsilon}\right) = C_{ijkl}\left(\frac{\mathbf{x}}{\varepsilon}\right)e_{kl}^{\varepsilon}\left(\mathbf{x}, \frac{\mathbf{x}}{\varepsilon}\right) - P_{ijk}\left(\frac{\mathbf{x}}{\varepsilon}\right)R_k(\mathbf{x}) - K_{ij}\left(\frac{\mathbf{x}}{\varepsilon}\right)\Theta(\mathbf{x}) - B_{ij}\left(\frac{\mathbf{x}}{\varepsilon}\right)C(\mathbf{x}) \tag{8.42}$$

Here $C_{ijkl}$ is the tensor of elastic coefficients, $P_{ijk}$ is a tensor describing the effect of a control signal $R$ on the stress field $\sigma$, $K_{ij}$ is the thermal expansion tensor, and $B_{ij}$ the hygroscopic (moisture) expansion tensor. Finally, $\Theta$ and $C$ represent changes in temperature and moisture content (with respect to a reference hygrothermal state)

respectively. It is assumed in Equation (8.42) that $C_{ijkl}$, $P_{ijk}$, $K_{ij}$ and $B_{ij}$ are all periodic with a unit cell Y of characteristic dimension $\epsilon$, the characteristic distance between the actuators, as shown in Figure 8-9. Substituting Equation (8.41) in Equation (8.42) gives:

$$\sigma_{ij}^{\epsilon}\left(x,\frac{x}{\epsilon}\right) = \frac{1}{2}C_{ijkl}\left(\frac{x}{\epsilon}\right)\left(\frac{\partial u_k}{\partial x_l}+\frac{\partial u_l}{\partial x_k}\right) - P_{ijk}\left(\frac{x}{\epsilon}\right)R_k(x) - K_{ij}\left(\frac{x}{\epsilon}\right)\Theta(x) - B_{ij}\left(\frac{x}{\epsilon}\right)C(x) \quad (8.43)$$

Consider now the term

$$C_{ijkl}\frac{\partial u_k}{\partial x_l} \quad (8.44)$$

By interchanging the dummy variables k and l, the following equality is true:

$$C_{ijkl}\frac{\partial u_k}{\partial x_l} \equiv C_{ijlk}\frac{\partial u_l}{\partial x_k} \quad (8.45)$$

Symmetry of the elastic coefficients [Lai et al., 1993] stipulates that $C_{ijkl} \equiv C_{ijlk}$. Thus

$$C_{ijkl}\frac{\partial u_k}{\partial x_l} \equiv C_{ijkl}\frac{\partial u_l}{\partial x_k} \quad (8.46)$$

Consequently, Equation (8.43) may be written as follows:

$$\sigma_{ij}^{\epsilon}\left(x,\frac{x}{\epsilon}\right) = C_{ijkl}\left(\frac{x}{\epsilon}\right)\left(\frac{\partial u_k}{\partial x_l}\right) - P_{ijk}\left(\frac{x}{\epsilon}\right)R_k(x) - K_{ij}\left(\frac{x}{\epsilon}\right)\Theta(x) - B_{ij}\left(\frac{x}{\epsilon}\right)C(x) \quad (8.47)$$

The first step in the homogenization process is to define the fast variable $y = x / \epsilon$ as was explained in the previous section. With this new variable, the equations characterizing the smart structure now become:

$$\frac{\partial\sigma_{ij}^{\epsilon}(x,y)}{\partial x_j} = f_i \quad (8.48)$$

$$u^{\epsilon}(x,y) = 0 \quad \text{on } \partial G \quad (8.49)$$

$$\sigma_{ij}^{\epsilon}(x,y) = C_{ijkl}(y)\left(\frac{\partial u_k}{\partial x_l}\right) - P_{ijk}(y)R_k(x) - K_{ij}(y)\Theta(x) - B_{ij}(y)C(x) \quad (8.50)$$

At this point a quick note on the ensuing terminology is warranted. Suppose that the physical dimensions of the unit cell in Figure 8-9 are $2\epsilon$ microns in the $x_1$ direction, $\epsilon$ microns in the $x_2$ direction, and $3\epsilon$ microns in the $x_3$ direction. Upon introduction of the

fast variable **y**, the dimensions of the unit cell become 2 in the $y_1$ direction, 1 in the $y_2$ direction, and 3 in the $y_3$ direction. Thus, in Figure 8-9, $Y_1 = 2$, $Y_2 = 1$, and $Y_3 = 3$. One may refer to the problem as being 2-periodic in $y_1$, 1-periodic in $y_2$, and 3-periodic in $y_3$, or collectively **Y**-periodic in **y** where it is understood that **Y** may have unequal components (and in general will have) in the 3 directions.

## 8.5.4 Two-Scale Asymptotic expansions

Based on the method of two scales explained in Section 8.3, the displacement and stress fields may be expanded asymptotically as follows:

*(a) Asymptotic expansion for displacement:*

$$\mathbf{u}^\varepsilon(\mathbf{x},\mathbf{y}) = \mathbf{u}^{(0)}(\mathbf{x},\mathbf{y}) + \varepsilon\mathbf{u}^{(1)}(\mathbf{x},\mathbf{y}) + \varepsilon^2\mathbf{u}^{(1)}(\mathbf{x},\mathbf{y}) + \cdots \tag{8.51}$$

*(b) Asymptotic expansion for stress:*

$$\sigma_{ij}^\varepsilon(\mathbf{x},\mathbf{y}) = \sigma_{ij}^{(0)}(\mathbf{x},\mathbf{y}) + \varepsilon\sigma_{ij}^{(1)}(\mathbf{x},\mathbf{y}) + \varepsilon^2\sigma_{ij}^{(2)}(\mathbf{x},\mathbf{y}) + \cdots \tag{8.52}$$

The introduction of the fast variable **y** necessitates the transformation of the derivatives (through the application of the chain rule) as follows:

$$\frac{\partial}{\partial x_i} \to \frac{\partial}{\partial x_i} + \frac{\partial}{\partial y_i}\frac{\partial y_i}{\partial x_i} \quad \text{(no summation over i)} \tag{8.53a}$$

$$\text{Since } y_i = \frac{x_i}{\varepsilon} \Rightarrow \frac{\partial y_i}{\partial x_i} = \frac{1}{\varepsilon} \tag{8.53b}$$

$$\text{then } \frac{\partial}{\partial x_i} \to \frac{\partial}{\partial x_i} + \frac{1}{\varepsilon}\frac{\partial}{\partial y_i} \tag{8.53c}$$

Thus

$$\frac{\partial\sigma_{ij}^\varepsilon}{\partial x_j} \to \frac{\partial\sigma_{ij}^\varepsilon}{\partial x_j} + \frac{1}{\varepsilon}\frac{\partial\sigma_{ij}^\varepsilon}{\partial y_j}$$

$$\frac{\partial u_k^\varepsilon}{\partial x_l} \to \frac{\partial u_k^\varepsilon}{\partial x_l} + \frac{1}{\varepsilon}\frac{\partial u_k^\varepsilon}{\partial y_l} \tag{8.53d}$$

Thus, the problem in Equations (8.48) to (8.50) becomes:

$$\frac{\partial \sigma_{ij}^{\varepsilon}}{\partial x_j} + \frac{1}{\varepsilon}\frac{\partial \sigma_{ij}^{\varepsilon}}{\partial y_j} = f_i \quad \text{in } G \tag{8.54}$$

$$\mathbf{u}^{\varepsilon} = \mathbf{0} \quad \text{on } \partial G \tag{8.55}$$

$$\sigma_{ij}^{\varepsilon}(\mathbf{x},\mathbf{y}) = C_{ijkl}(\mathbf{y})\left(\frac{\partial u_k}{\partial x_l} + \frac{1}{\varepsilon}\frac{\partial u_k}{\partial y_l}\right) - P_{ijk}(\mathbf{y})R_k(\mathbf{x}) - K_{ij}(\mathbf{y})\Theta(\mathbf{x}) - B_{ij}(\mathbf{y})C(\mathbf{x}) \tag{8.56}$$

## 8.5.5 Elimination of the Fast Variables from $\mathbf{u}^{(0)}$

This section will show that the first term in the asymptotic expansion for the displacement field is independent of the fast variable. To this end, one proceeds to eliminate $\sigma$ by substituting Equation (8.56) into Equation (8.54) to get:

$$C_{ijkl}(\mathbf{y})\left\{\frac{\partial^2 u_k}{\partial x_j \partial x_l} + \frac{1}{\varepsilon}\frac{\partial^2 u_k}{\partial x_j \partial y_l}\right\} - P_{ijk}(\mathbf{y})\frac{\partial R_k}{\partial x_j} - K_{ij}(\mathbf{y})\frac{\partial \Theta}{\partial x_j} - B_{ij}(\mathbf{y})\frac{\partial C}{\partial x_j} +$$

$$\frac{1}{\varepsilon}\left\{\frac{\partial C_{ijkl}}{\partial y_j}\left[\frac{\partial u_k}{\partial x_l} + \frac{1}{\varepsilon}\frac{\partial u_k}{\partial y_l}\right] + C_{ijkl}\left[\frac{\partial^2 u_k}{\partial x_l \partial y_j} + \frac{1}{\varepsilon}\frac{\partial^2 u_k}{\partial y_j \partial y_l}\right]\right\} + \tag{8.57}$$

$$-\frac{1}{\varepsilon}\left\{\frac{\partial P_{ijk}}{\partial y_j}R_k + \frac{\partial K_{ij}}{\partial y_j}\Theta + \frac{\partial B_{ij}}{\partial y_j}C\right\} = f_i$$

In arriving at Equation (8.57) one takes advantage of the fact that $C_{ijkl}$, $P_{ijk}$, $K_{ij}$ and $B_{ij}$ are strictly functions of $\mathbf{y}$. The next step is to substitute expansion (8.51) into Equation (8.57) to get:

$$C_{ijkl}\left\{\varepsilon^2 \frac{\partial^2 u_k^{(0)}}{\partial x_j \partial x_l} + \varepsilon^3 \frac{\partial^2 u_k^{(1)}}{\partial x_j \partial x_l} + \varepsilon\frac{\partial^2 u_k^{(0)}}{\partial x_j \partial y_l} + \varepsilon^2 \frac{\partial^2 u_k^{(1)}}{\partial x_j \partial y_l}\right\} - \varepsilon^2 P_{ijk}\frac{\partial R_k}{\partial x_j} - \varepsilon^2 K_{ij}\frac{\partial \Theta}{\partial x_j} - \varepsilon^2 B_{ij}\frac{\partial C}{\partial x_j}$$

$$+ \frac{\partial C_{ijkl}}{\partial y_j}\left[\varepsilon\frac{\partial u_k^{(0)}}{\partial x_l} + \varepsilon^2 \frac{\partial u_k^{(1)}}{\partial x_l} + \frac{\partial u_k^{(0)}}{\partial y_l} + \varepsilon\frac{\partial u_k^{(1)}}{\partial y_l}\right] + \tag{8.58}$$

$$C_{ijkl}\left[\varepsilon\frac{\partial^2 u_k^{(0)}}{\partial x_l \partial y_j} + \varepsilon^2 \frac{\partial^2 u_k^{(1)}}{\partial x_l \partial y_j} + \frac{\partial^2 u_k^{(0)}}{\partial y_j \partial y_l} + \varepsilon\frac{\partial^2 u_k^{(1)}}{\partial y_j \partial y_l}\right] - \left[\varepsilon\frac{\partial P_{ijk}}{\partial y_j}R_k + \varepsilon\frac{\partial K_{ij}}{\partial y_j}\Theta + \varepsilon\frac{\partial B_{ij}}{\partial y_j}C\right] = \varepsilon^2 f_i$$

Since $u_m^{(n)}$ are all independent of $\varepsilon$, then one may equate terms with equal powers of $\varepsilon$ in Equation (8.58). Equating terms multiplied by $\varepsilon^0$ coefficients gives the following:

$$\frac{\partial C_{ijkl}}{\partial y_j}\frac{\partial u_k^{(0)}}{\partial y_l} + C_{ijkl}\frac{\partial^2 u_k^{(0)}}{\partial y_j \partial y_l} = 0 \tag{8.59}$$

Thus,

$$\frac{\partial}{\partial y_j}\left(C_{ijkl}(\mathbf{y})\frac{\partial u_k^{(0)}(\mathbf{x},\mathbf{y})}{\partial y_l}\right) = 0 \tag{8.60a}$$

Integrating both sides gives:

$$C_{ijkl}(\mathbf{y})\frac{\partial u_k^{(0)}(\mathbf{x},\mathbf{y})}{\partial y_l} = g_{ij}(\mathbf{x})$$

$$\therefore \frac{\partial u_k^{(0)}(\mathbf{x},\mathbf{y})}{\partial y_l} = C_{ijkl}^{-1}(\mathbf{y})g_{ij}(\mathbf{x}) \tag{8.60b}$$

Here $C_{ijkl}^{-1}$ is the inverse of $C_{ijkl}$. The next step is to integrate the last expression between 0 and $Y_l$, where $Y_l$ is the value of the period of the unit cell in the $y_l$ direction (see Figure 8-9). Thus

$$\int_0^{Y_l}\frac{\partial u_k^{(0)}(\mathbf{x},\mathbf{y})}{\partial y_l}dy_l = \int_0^{Y_l}C_{klij}^{-1}(\mathbf{y})g_{ij}(\mathbf{x})dy_l \tag{8.61}$$

Treating $\mathbf{x}$ as a parameter as far as integration with respect to $y_l$ is concerned, allows one to move $g_{ij}$ outside the integral sign. Thus

$$\left[u_k^{(0)}(\mathbf{x},\mathbf{y})\right]_0^{Y_L} = \int_0^{Y_L}C_{ijkl}^{-1}dy_l\, g_{ij}(\mathbf{x}) \tag{8.62}$$

From periodicity, the LHS of Equation (8.62) vanishes and therefore $g_{ij}(\mathbf{x}) = 0$. Hence, from Equation (8.60b) one arrives at:

$$\frac{\partial u_k^{(0)}(\mathbf{x},\mathbf{y})}{\partial y_l} = 0$$

$$\Rightarrow u_k^{(0)}(\mathbf{x},\mathbf{y}) = u_k^{(0)}(\mathbf{x}) \tag{8.63}$$

One concludes that the first term in the asymptotic expansion for the displacement field depends strictly on the slow variables.

## 8.5.6 Determination of Stress Terms

Based on the results of Section 8.5.5 the asymptotic expansions for the stress and displacement fields are:

$$u^{\varepsilon}(x,y) = u^{(0)}(x) + \varepsilon u^{(1)}(x,y) + \varepsilon^2 u^{(1)}(x,y) + \cdots \tag{8.64}$$

$$\sigma_{ij}^{\varepsilon}(x,y) = \sigma_{ij}^{(0)}(x,y) + \varepsilon \sigma_{ij}^{(1)}(x,y) + \varepsilon^2 \sigma_{ij}^{(2)}(x,y) + \cdots \tag{8.65}$$

Substitution of Equation (8.65) into the equilibrium expression (8.54) gives:

$$\varepsilon \frac{\partial \sigma_{ij}^{(0)}}{\partial x_j} + \varepsilon^2 \frac{\partial \sigma_{ij}^{(1)}}{\partial x_j} + \frac{\partial \sigma_{ij}^{(0)}}{\partial y_j} + \varepsilon \frac{\partial \sigma_{ij}^{(1)}}{\partial y_j} = \varepsilon f_i \tag{8.66}$$

Considering only terms multiplied by $\varepsilon^0$ and $\varepsilon^1$ one obtains the following two expressions from Equation (8.66):

$$\frac{\partial \sigma_{ij}^{(0)}}{\partial y_j} = 0 \tag{8.67a}$$

$$\frac{\partial \sigma_{ij}^{(1)}}{\partial y_j} + \frac{\partial \sigma_{ij}^{(0)}}{\partial x_j} = f_i \tag{8.67b}$$

These equations will be used in the sequel. Finally, substituting Equations (8.64) and (8.65) into Equation (8.56) and separating terms with like powers of $\varepsilon$ results in the following expressions for the first terms of the asymptotic expansion of the stress field:

$$\sigma_{ij}^{(0)} = C_{ijkl} \left( \frac{\partial u_k^{(0)}}{\partial x_1} + \frac{\partial u_k^{(1)}}{\partial y_1} \right) - P_{ijk} R_k - K_{ij}\Theta - B_{ij}C \tag{8.68a}$$

$$\frac{\partial \sigma_{ij}^{(0)}}{\partial y_j} = 0 \tag{8.68b}$$

## 8.5.7 Determination of the Unit Cell Problems

Combining Equations (8.67a) and (8.68a) leads to the following Equation:

$$\frac{\partial}{\partial y_j}\left\{C_{ijkl}\left[\frac{\partial u_k^{(0)}}{\partial x_l} + \frac{\partial u_k^{(1)}}{\partial y_l}\right] - P_{ijk}R_k - K_{ij}\Theta - B_{ij}C\right\} = 0$$

$$\therefore \frac{\partial}{\partial y_j}\left[C_{ijkl}\frac{\partial u_k^{(1)}(\mathbf{x},\mathbf{y})}{\partial y_l}\right] = \frac{\partial P_{ijk}}{\partial y_j}R_k + \frac{\partial K_{ij}}{\partial y_j}\Theta + \frac{\partial B_{ij}}{\partial y_j}C - \frac{\partial C_{ijkl}}{\partial y_j}\frac{\partial u_k^{(0)}}{\partial x_l} \tag{8.69}$$

The separation of the variables in each term on the RHS of Equation (8.69) permits one to write down the solution as follows:

$$u_n^{(1)}(\mathbf{x},\mathbf{y}) = V_n(\mathbf{x}) + R_k(\mathbf{x})N_n^k(\mathbf{y}) + \Theta(\mathbf{x})M_n(\mathbf{y}) + C(\mathbf{x})S_n(\mathbf{y}) + \frac{\partial u_k^{(0)}(\mathbf{x})}{\partial x_l}N_n^{kl}(\mathbf{y}) \tag{8.70}$$

In Equation (8.70) the various functions satisfy the following equations:

$$\frac{\partial}{\partial y_j}\left(C_{ijml}(\mathbf{y})\frac{\partial N_m^k(\mathbf{y})}{\partial y_l}\right) = \frac{\partial P_{ijk}}{\partial y_j} \tag{8.71a}$$

$$\frac{\partial}{\partial y_j}\left(C_{ijml}(\mathbf{y})\frac{\partial M_m(\mathbf{y})}{\partial y_l}\right) = \frac{\partial K_{ij}}{\partial y_j} \tag{8.71b}$$

$$\frac{\partial}{\partial y_j}\left(C_{ijml}(\mathbf{y})\frac{\partial S_m(\mathbf{y})}{\partial y_l}\right) = \frac{\partial B_{ij}}{\partial y_j} \tag{8.71c}$$

$$\frac{\partial}{\partial y_j}\left(C_{ijmn}(\mathbf{y})\frac{\partial N_m^{kl}(\mathbf{y})}{\partial y_n}\right) = -\frac{\partial C_{ijkl}}{\partial y_j} \tag{8.71d}$$

The function $V_m(\mathbf{x})$ is the homogeneous solution of Equation (8.70) and satisfies the following expression:

$$\frac{\partial}{\partial y_j}\left(C_{ijml}(\mathbf{y})\frac{\partial V_m(\mathbf{x})}{\partial y_l}\right) = 0 \tag{8.71e}$$

Notice that $V_m(\mathbf{x})$ is independent of the fast variables and this can be easily shown by integrating both sides of Equation (8.71e) to obtain:

$$C_{ijml}(\mathbf{y})\frac{\partial V_m}{\partial y_l} = g_{ij}(\mathbf{x}) \tag{8.72a}$$

$$\frac{\partial V_m}{\partial y_l} = C_{mlij}^{-1}(\mathbf{y})g_{ij}(\mathbf{x}) \tag{8.72b}$$

Integrating Equation (8.72) leads, on account of the periodicity of the pertinent functions, to:

$$g_{ij}(\mathbf{x}) = 0 \qquad (8.72c)$$

Substituting Equation (8.72c) into Equation (8.72a) finally leads to:

$$\frac{\partial V_m}{\partial y_1} = 0$$

$$\therefore V_m = V_m(\mathbf{x}) \qquad (8.72d)$$

One observes that Equations (8.71a) to (8.71d) depend entirely on the fast variable $\mathbf{y}$ and are thus solved in the domain $Y$ of the unit cell, remembering at the same time that $C_{ijkl}$, $N_m^{kl}$, $N_m^k$, $M_m$, $S_m$ are $Y_i$-periodic in $y_i$. Thus, the differential equations in (8.71a) to (8.71d) are appropriately referred to as "unit cell" problems.

Having determined $u_k^{(0)}(\mathbf{x})$ and $u_k^{(1)}(\mathbf{x},\mathbf{y})$, one naturally proceeds to the determination of the stress field. To this end, Equation (8.70) is substituted in Equation (8.68a) to get the following expression:

$$\sigma_{ij}^{(0)}(\mathbf{x},\mathbf{y}) = C_{ijkl}(\mathbf{y})\frac{\partial u_k^{(0)}(\mathbf{x})}{\partial x_1} + C_{ijmn}(\mathbf{y})\left\{\frac{\partial N_m^k(\mathbf{y})}{\partial y_n}R_k(\mathbf{x}) + \frac{\partial M_m(\mathbf{y})}{\partial y_n}\Theta(\mathbf{x}) + \frac{\partial S_m(\mathbf{y})}{\partial y_n}C(\mathbf{x})\right.$$
$$\left. + \frac{\partial N_m^{kl}(\mathbf{y})}{\partial y_n}\frac{\partial u_k^{(0)}(\mathbf{x})}{\partial x_1}\right\} - P_{ijk}R_k - K_{ij}\Theta - B_{ij}C. \qquad (8.73)$$

This equation is subsequently substituted in Equation (8.67b) to get:

$$\frac{\partial \sigma_{ij}^{(1)}(\mathbf{x},\mathbf{y})}{\partial y_j} + \frac{\partial}{\partial x_j}\left\{C_{ijkl}(\mathbf{y})\frac{\partial u_k^{(0)}(\mathbf{x})}{\partial x_1} + C_{ijmn}(\mathbf{y})\begin{bmatrix}\dfrac{\partial N_m^k(\mathbf{y})}{\partial y_n}R_k(\mathbf{x}) + \dfrac{\partial M_m(\mathbf{y})}{\partial y_n}\Theta(\mathbf{x}) + \dfrac{\partial S_m(\mathbf{y})}{\partial y_n}C(\mathbf{x}) + \\ \dfrac{\partial N_m^{kl}(\mathbf{y})}{\partial y_n}\dfrac{\partial u_k^{(0)}(\mathbf{x})}{\partial x_1}\end{bmatrix}\right\} +$$

$$-\frac{\partial}{\partial x_j}\left\{P_{ijk}R_k - K_{ij}T - B_{ij}C\right\} = f_i \qquad (8.74a)$$

After some simplification one finally arrives at the following expression:

$$\frac{\partial \sigma_{ij}^{(1)}(\mathbf{x},\mathbf{y})}{\partial y_j} + C_{ijkl}(\mathbf{y})\frac{\partial^2 u_k^{(0)}(\mathbf{x})}{\partial x_j \partial x_l} + C_{ijmn}(\mathbf{y})\left[\frac{\partial N_m^k(\mathbf{y})}{\partial y_n}\frac{\partial R_k(\mathbf{x})}{\partial x_j} + \frac{\partial M_m(\mathbf{y})}{\partial y_n}\frac{\partial \Theta(\mathbf{x})}{\partial x_j} + \frac{\partial S_m(\mathbf{y})}{\partial y_n}\frac{\partial C(\mathbf{x})}{\partial x_j}\right.$$

$$\left. + \frac{\partial N_m^{kl}(\mathbf{y})}{\partial y_n}\frac{\partial^2 u_k^{(0)}(\mathbf{x})}{\partial x_j \partial x_l}\right] - P_{ijk}\frac{\partial R_k}{\partial x_j} - K_{ij}\frac{\partial \Theta}{\partial x_j} - B_{ij}\frac{\partial C}{\partial x_j} = f_i \tag{8.74b}$$

The last expression will be used to obtain the governing equations of the problem by averaging over the domain of the unit cell.

## 8.5.8 Homogenization Procedure and Governing Equations

The next important step in the homogenization process is to average Equation (8.74b) over the domain of the unit cell (with volume $|\,Y\,|$) remembering to treat $x_i$ as a parameter as far as integration with respect to $\mathbf{y}$ is concerned. This gives the following expression:

$$\frac{1}{|Y|}\int_Y \frac{\partial \sigma_{ij}^{(1)}(\mathbf{x},\mathbf{y})}{\partial y_j}dv + \frac{1}{|Y|}\int_Y\left(C_{ijkl}(\mathbf{y}) + C_{ijmn}(\mathbf{y})\frac{\partial N_m^{kl}}{\partial y_n}\right)dv\frac{\partial^2 u_k^{(0)}(\mathbf{x})}{\partial x_j \partial x_l}$$

$$-\frac{1}{|Y|}\int_Y\left(P_{ijk}(\mathbf{y}) - C_{ijmn}(\mathbf{y})\frac{\partial N_m^k}{\partial y_n}\right)dv\frac{\partial R_k(\mathbf{x})}{\partial x_j} - \frac{1}{|Y|}\int_Y\left(K_{ij}(\mathbf{y}) - C_{ijmn}(\mathbf{y})\frac{\partial M_m}{\partial y_n}\right)dv\frac{\partial \Theta(\mathbf{x})}{\partial x_j} +$$

$$-\frac{1}{|Y|}\int_Y\left(B_{ij}(\mathbf{y}) - C_{ijmn}(\mathbf{y})\frac{\partial S_m}{\partial y_n}\right)dv\frac{\partial C(\mathbf{x})}{\partial x_j} = f_i \tag{8.75}$$

To simplify this expression the following definitions will be made:

$$\tilde{C}_{ijkl} = \frac{1}{|Y|}\int_Y\left(C_{ijkl}(\mathbf{y}) + C_{ijmn}(\mathbf{y})\frac{\partial N_m^{kl}}{\partial y_n}\right)dv \tag{8.76a}$$

$$\tilde{P}_{ijk} = \frac{1}{|Y|}\int_Y\left(P_{ijk}(\mathbf{y}) - C_{ijmn}(\mathbf{y})\frac{\partial N_m^k}{\partial y_n}\right)dv \tag{8.76b}$$

$$\tilde{K}_{ij} = \frac{1}{|Y|}\int_Y\left(K_{ij}(\mathbf{y}) - C_{ijmn}(\mathbf{y})\frac{\partial M_m}{\partial y_n}\right)dv \tag{8.76c}$$

$$\tilde{B}_{ij} = \frac{1}{|Y|}\int_Y\left(B_{ij}(\mathbf{y}) - C_{ijmn}(\mathbf{y})\frac{\partial S_m}{\partial y_n}\right)dv \tag{8.76d}$$

In Equations (8.76a) to (8.76d), quantities with the tilde denote averaged or homogenized coefficients. With these definitions, Equation (8.75) becomes:

$$\frac{1}{|Y|}\int_Y \frac{\partial \sigma_{ij}^{(1)}(\mathbf{x},\mathbf{y})}{\partial y_j}dv + \tilde{C}_{ijkl}\frac{\partial^2 u_k^{(0)}(\mathbf{x})}{\partial x_j \partial x_l} - \tilde{P}_{ijk}\frac{\partial R_k(\mathbf{x})}{\partial x_j} - \tilde{K}_{ij}\frac{\partial \Theta(\mathbf{x})}{\partial x_j} - \tilde{B}_{ij}\frac{\partial C(\mathbf{x})}{\partial x_j} = f_i \qquad (8.77)$$

Consider now the integral in Equation (8.77). It may be written as:

$$\int_Y \frac{\partial \sigma_{ij}^{(1)}(\mathbf{x},\mathbf{y})}{\partial y_j}dv = \int_Y \mathrm{div}\sigma^{(1)}dv \qquad (8.78)$$

Here use was made of the fact that the divergence of a second order tensor in index notation is given by [Holzapfel, 2000]:

$$\mathrm{div}A = \frac{\partial A_{ij}}{\partial y_j} \qquad (8.79)$$

Application of the divergence theorem to Equation (8.78) gives:

$$\int_Y \frac{\partial \sigma_{ij}^{(1)}(\mathbf{x},\mathbf{y})}{\partial y_j}dv = \int_Y \mathrm{div}\sigma^{(1)}dv = \int_{\partial Y} \sigma^{(1)}(\mathbf{x},\mathbf{y})\mathbf{n}\,dA \qquad (8.80)$$

In the last expression, n is the unit vector normal to the boundary surface $\partial Y$ of the unit cell. Owing to the periodicity of $\sigma^{(1)}(\mathbf{x},\mathbf{y})$, its values at corresponding points on opposite sides of the unit cell are the same. However, the unit normal vectors have opposite signs at these points as shown in Figure (8-10). Consequently, the integral in Equation (8.80) vanishes and the "homogenized" equation for the displacement field becomes:

$$\tilde{C}_{ijkl}\frac{\partial^2 u_k^{(0)}(\mathbf{x})}{\partial x_j \partial x_l} - \tilde{P}_{ijk}\frac{\partial R_k(\mathbf{x})}{\partial x_j} - \tilde{K}_{ij}\frac{\partial \Theta(\mathbf{x})}{\partial x_j} - \tilde{B}_{ij}\frac{\partial C(\mathbf{x})}{\partial x_j} = f_i \qquad (8.81a)$$

As well, from the boundary condition in Equation (8.55) and the asymptotic expansion (8.51) the following boundary condition is obtained:

$$\mathbf{u}^{(0)}(\mathbf{x}) = 0 \qquad (8.81b)$$

It is noteworthy to mention that any dependency on the fast variable y is removed after the effective coefficients in Equations (8.76a) to (8.76d) are calculated. Consequently, all functions in Equation (8.81a) are functions solely of the slow variables x.
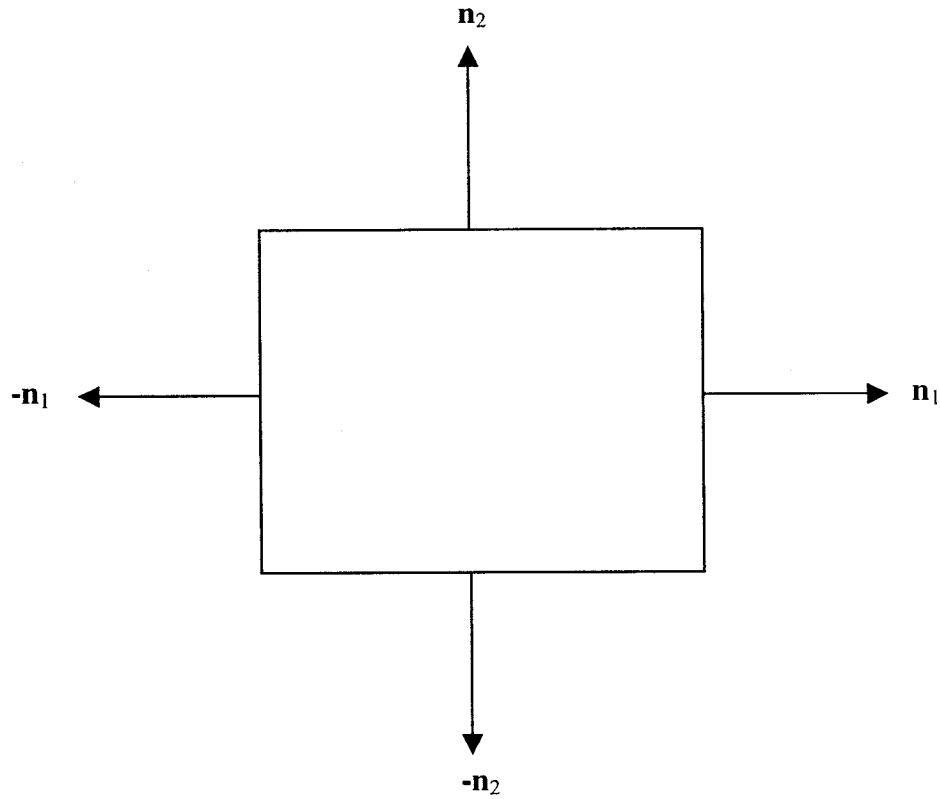
**Figure 8-10:** Unit normal vectors acting on opposite sides of the unit cell

Similarly to the procedure that was used to obtain the homogenized equation for the displacement field in (8.81a), one may obtain the homogenized equation for the stress field by averaging Equation (8.73) over the domain of the unit cell. Thus:

$$
\frac{1}{|Y|}\int_Y \sigma_{ij}^{(0)}(\mathbf{x},\mathbf{y})dv = \frac{1}{|Y|}\left\{\int_Y C_{ijkl}(\mathbf{y})+C_{ijmn}(\mathbf{y})\frac{\partial N_m^{kl}(\mathbf{y})}{\partial y_n}\right\}dv\,\frac{\partial u_k^{(0)}(\mathbf{x})}{\partial x_l}+
$$

$$
-\frac{1}{|Y|}\left\{\int_Y P_{ijk}(\mathbf{y})-C_{ijmn}(\mathbf{y})\frac{\partial N_m^k(\mathbf{y})}{\partial y_n}\right\}dv\,R_k(\mathbf{x})-\frac{1}{|Y|}\left\{\int_Y K_{ij}(\mathbf{y})-C_{ijmn}(\mathbf{y})\frac{\partial M_m(\mathbf{y})}{\partial y_n}\right\}dv\,\Theta(\mathbf{x})+
$$

$$
-\frac{1}{|Y|}\left\{\int_Y B_{ij}(\mathbf{y})-C_{ijmn}(\mathbf{y})\frac{\partial S_m(\mathbf{y})}{\partial y_n}\right\}dv\,C(\mathbf{x}) \tag{8.82a}
$$

Substituting definitions (8.76a) to (8.76d) into Equation (8.82a) results in the following expression:

$$\tilde{\sigma}_{ij}^{(0)} = \tilde{C}_{ijkl} \frac{\partial u_k^{(0)}}{\partial x_l} - \tilde{P}_{ijk} R_k - \tilde{K}_{ij} \Theta - \tilde{B}_{ij} C \qquad (8.82b)$$

Substituting Equation (8.82b) into Equation (8.81a) results in:

$$\frac{\partial \tilde{\sigma}_{ij}^{(0)}}{\partial x_j} = f_i(\mathbf{x}) \qquad (8.83a)$$

The similarity between this expression and the original differential equation

$$\frac{\partial \sigma_{ij}}{\partial x_j} = f_i \qquad (8.83b)$$

is evident.

## 8.5.9 Synopsis and Important Results

The main results arrived at during the development of the mathematical model are the following:

(a) *Unit cell problems*:

$$\frac{\partial}{\partial y_j} \left( C_{ijmn}(\mathbf{y}) \frac{\partial N_m^{kl}(\mathbf{y})}{\partial y_n} + C_{ijkl} \right) = 0$$

$$\frac{\partial}{\partial y_j} \left( C_{ijml}(\mathbf{y}) \frac{\partial N_m^k(\mathbf{y})}{\partial y_l} - P_{ijk} \right) = 0$$

$$\frac{\partial}{\partial y_j} \left( C_{ijml}(\mathbf{y}) \frac{\partial M_m(\mathbf{y})}{\partial y_l} - K_{ij} \right) = 0 \qquad (8.84)$$

$$\frac{\partial}{\partial y_j} \left( C_{ijml}(\mathbf{y}) \frac{\partial S_m(\mathbf{y})}{\partial y_l} - B_{ij} \right) = 0$$

(b) *Effective (homogenized) coefficients*:

$$\tilde{C}_{ijkl} = \frac{1}{|Y|} \int_Y \left( C_{ijkl}(\mathbf{y}) + C_{ijmn}(\mathbf{y}) \frac{\partial N_m^{kl}}{\partial y_n} \right) dv$$

$$\tilde{P}_{ijk} = \frac{1}{|Y|} \int_Y \left( P_{ijk}(\mathbf{y}) - C_{ijmn}(\mathbf{y}) \frac{\partial N_m^k}{\partial y_n} \right) dv \qquad (8.85a)$$

$$\widetilde{K}_{ij} = \frac{1}{|Y|} \int_Y \left( K_{ij}(\mathbf{y}) - C_{ijmn}(\mathbf{y}) \frac{\partial M_m}{\partial y_n} \right) dv$$

$$\widetilde{B}_{ij} = \frac{1}{|Y|} \int_Y \left( B_{ij}(\mathbf{y}) - C_{ijmn}(\mathbf{y}) \frac{\partial S_m}{\partial y_n} \right) dv$$

(8.85b)

(c) *Homogenized Problem*:

$$\widetilde{C}_{ijkl} \frac{\partial^2 u_k^{(0)}(\mathbf{x})}{\partial x_j \partial x_l} - \widetilde{P}_{ijk} \frac{\partial R_k(\mathbf{x})}{\partial x_j} - \widetilde{K}_{ij} \frac{\partial \Theta(\mathbf{x})}{\partial x_j} - \widetilde{B}_{ij} \frac{\partial C(\mathbf{x})}{\partial x_j} = f_i$$

(8.86)

$$\mathbf{u}^{(0)}(\mathbf{x}) = \mathbf{0}$$

(d) *Stress Field*:

$$\sigma_{ij}^{(0)} = \left\{ C_{ijmn}(\mathbf{y}) \frac{\partial N_m^{kl}(\mathbf{y})}{\partial y_n} + C_{ijkl}(\mathbf{y}) \right\} \frac{\partial u_k^{(0)}}{\partial x_l} - \left\{ P_{ijk}(\mathbf{y}) - C_{ijmn}(\mathbf{y}) \frac{\partial N_m^k(\mathbf{y})}{\partial y_n} \right\} R_k +$$

$$- \left\{ K_{ij}(\mathbf{y}) - C_{ijmn}(\mathbf{y}) \frac{\partial M_m(\mathbf{y})}{\partial y_n} \right\} \Theta - \left\{ B_{ij}(\mathbf{y}) - C_{ijmn}(\mathbf{y}) \frac{\partial S_m(\mathbf{y})}{\partial y_n} \right\} C$$

(8.87)

Equations (8.85a), (8.85b) and (8.86) represent the governing equations of the homogenized model of a smart composite structure with periodically arranged actuators. Equations (8.84) represent the unit cell problems which determine the $N_m^{kl}$, $N_m^k$, $M_m$, $S_m$ functions. These in turn lead to the calculation of the effective coefficients from Equations (8.85a) and (8.85b). These coefficients then enter the homogenized equation in (8.86) which is totally independent of the fast variable. The homogenized problem therefore is much more amenable to analytic or numerical solutions than the original problem in Equations (8.37) and (8.38). The determination of the displacement field $\mathbf{u}$ can be followed, if desired, by the determination of the stress field through Equation (8.87). The solution of the unit cell problems and the determination and use of the effective coefficients will be illustrated in Chapter 10.

# 9.0 HOMOGENIZATION MODELS FOR SMART COMPOSITE MATERIALS WITH NON-ZERO BOUNDARY CONDITIONS

## 9.1 Introduction: Boundary Layers

The problem discussed in Chapter 8 was characterized by homogeneous boundary conditions. In this chapter, a different model will be developed whereby mechanical stresses will be prescribed on the boundary. Before proceeding with the formulation of the problem at hand, a simple "boundary layer" example will be discussed here. It will be seen in the sequel that the essential difference between the mathematical model of this chapter and its counterpart in the previous chapter is the existence of "boundary layer" type solutions. It is therefore noteworthy to examine the underlying principles pertaining to boundary layers.

Consider the simple differential equation and accompanying boundary conditions shown in Equations (9.1a) and (9.1b).

$$\varepsilon \frac{d^2 y}{dx^2} + 2\frac{dy}{dx} + 3y = 0 \qquad 0 < x < 1 \tag{9.1a}$$

$$y(0) = 0 \quad \text{and} \quad y(1) = 2 \tag{9.1b}$$

In this equation $\varepsilon$ is a small parameter, much smaller than unity. The analytical solution of this problem is fairly straightforward and is:

$$y = \frac{2}{e^{\lambda_1} - e^{\lambda_2}} \left\{ e^{\lambda_1 x} - e^{\lambda_2 x} \right\} \qquad \text{where}$$

$$\lambda_1 = \frac{-1 - \sqrt{1 - 3\varepsilon}}{\varepsilon}, \quad \lambda_2 = \frac{-1 + \sqrt{1 - 3\varepsilon}}{\varepsilon} \tag{9.2}$$

For $\varepsilon = 0.01$ the plot of the solution over the domain of the problem is given in Figure 9-1. The source of difficulty is immediately apparent! The solution which is very smooth

over almost the entire range, changes abruptly at a region near x = 0 in order to satisfy the boundary condition there. This narrow region is called "boundary layer".
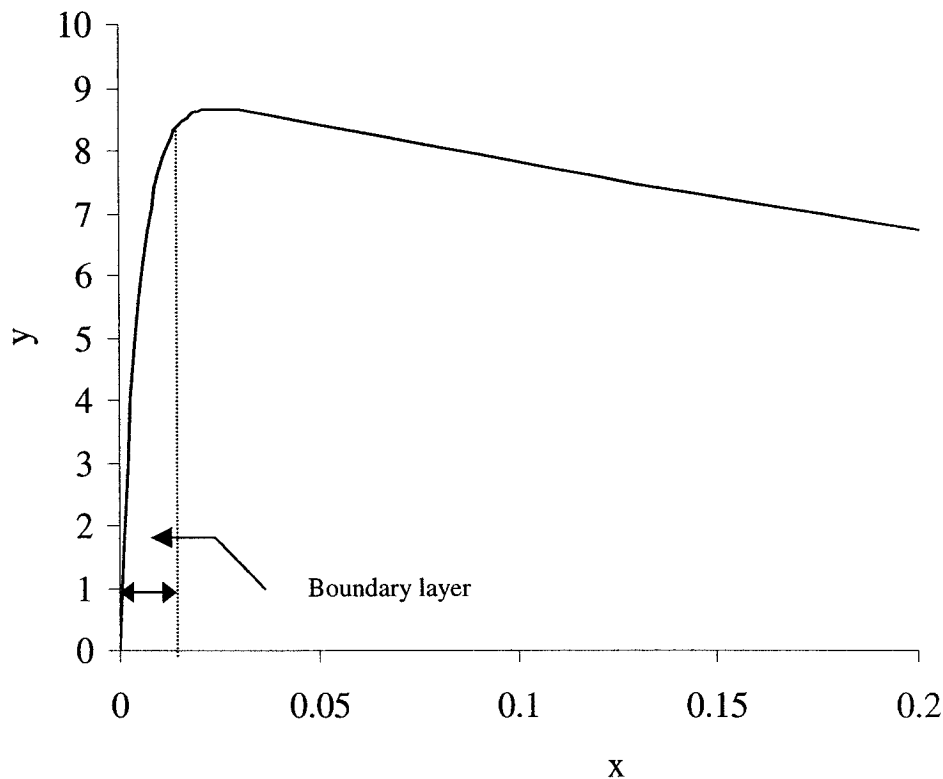


**Figure 9-1:** Analytic solution

It is therefore clear that a standard perturbation expansion (Section 8.2) will be able to follow y outside the boundary layer, but inevitably will not be able to capture the boundary condition at x = 0. In other words, a regular perturbation expansion will not approximate the solution within the boundary layer. This is also evident from another perspective. Consider an asymptotic solution for y, of the form:

$$y = y_0(x) + \varepsilon y_1(x) + \varepsilon^2 y_2(x) + O(\varepsilon^3)$$  (9.3)

It follows from Equation (9.3) that the first term in the expansion, $y_0(x)$, is the solution to the problem for $\varepsilon = 0$. But making $\varepsilon = 0$ in Equation (9.1a) changes the $2^{nd}$-order differential equation into a $1^{st}$-order one, namely:

$$2\frac{dy}{dx} + 3y = 0 \qquad 0 < x < 1 \qquad\qquad (9.4)$$

Since a $1^{st}$-order equation with a unique solution can only satisfy one boundary condition, then one of the two boundary conditions in Equation (9.1b) must be dropped. As Figure 9-1 shows, the boundary condition at $x = 0$ must be dropped, which means that the asymptotic expansion (9.3) will only satisfy the boundary condition at $x = 1$ and will only approximate y outside the boundary layer. To verify this, the first term of Equation (9.3) is determined as follows:

$$y_0(x) = 2e^{1.5}e^{-1.5x}$$
$$\therefore y = 2e^{1.5}e^{-1.5x} + O(\varepsilon) \qquad\qquad (9.5)$$

A plot of Equation (9.5) alongside the analytic solution is shown in Figure 9-2.
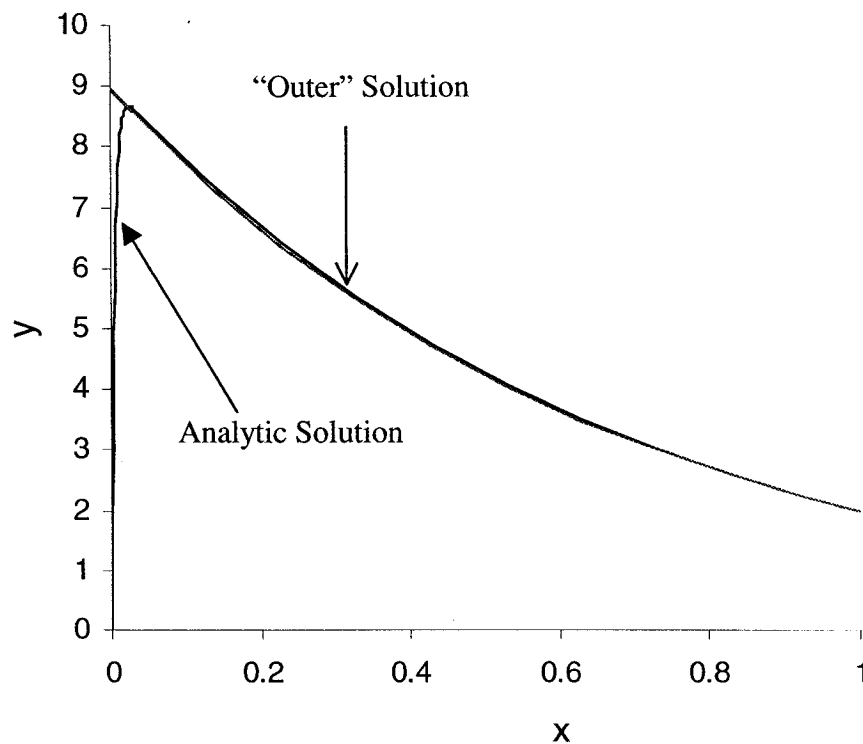


**Figure 9-2:** Analytic vs. "outer" solution

It is evident from the figure that even the first term of the asymptotic expansion (9.5b) matches the analytic solution extremely well, except in the narrow region of the boundary layer.

Since the singularity of this problem arises from the existence of the boundary layer and in particular from the fact that the solution changes rapidly in the boundary layer, the remedy is to introduce a new variable $\xi$ such that:

$$\xi = \frac{x}{\varepsilon} \qquad (9.6)$$

This has the effect of "stretching out" the boundary layer. Said differently, the new variable $\xi$ is now of order 1 and can be used to construct an asymptotic solution which is accurate within the boundary layer. One will observe that this is essentially the same technique as the one used in the two-scale expansion method of the previous chapter, whereby the region of the unit cell was "stretched out" and rendered of the same order as the macroscopic smart composite structure. With this new variable, the differential equation (9.1a) becomes:

$$\frac{d^2y}{d\xi^2} + 2\frac{dy}{d\xi} + 3\varepsilon y = 0 \qquad (9.7)$$

An asymptotic expansion of Equation (9.7) is of the form:

$$y = y_0(\xi) + \varepsilon y_1(\xi) + \varepsilon^2 y_2(\xi) + O(\varepsilon^3) \qquad (9.8)$$

The general solution of $y_0$ is readily determined to be:

$$y_0(\xi) = A + Be^{-2\xi} \qquad (9.9)$$

Since this is an "inner" solution, it must satisfy the boundary condition at $x = \xi = 0$. This means that:

$$A + B = 0 \Rightarrow A = -B$$
$$\therefore y_0(\xi) = A(1 - e^{-2\xi}) \qquad (9.10)$$

Equation (9.10) still has an extra constant remaining. To determine this constant, one refers to the "outer" expansion, Equation (9.5) and notes that:

$$\lim_{x \to 0} 2e^{1.5} e^{-1.5x} = 2e^{1.5} \qquad (9.11)$$

To calculate the constant A, one may then impose the following condition:

$$\lim_{\xi \to \infty} A\left(1 - e^{-2\xi}\right) = 2e^{1.5} \implies A = 2e^{1.5}$$

$$\therefore y_{inner} = 2e^{1.5}\left(1 - e^{-2\xi}\right) \qquad (9.12)$$

What was done in Equation (9.12) is usually referred to in literature [Nayfeh, 1973; Holmes, 1995] as "matching". The logic behind this technique is that if there is an "inner" expansion valid within the boundary layer, and an "outer" expansion valid outside the boundary layer, then there must be a small region just outside the boundary layer (but still close to it) where both expansions are equally valid. Since this region is outside the boundary layer, $\xi = x / \varepsilon$ takes on large values, but since it is still close to the boundary layer, x is still close to 0. Thus, one requires that:

$$\lim_{x \to 0} y_{inner} = \lim_{\xi \to \infty} y_{outer} \qquad (9.13)$$
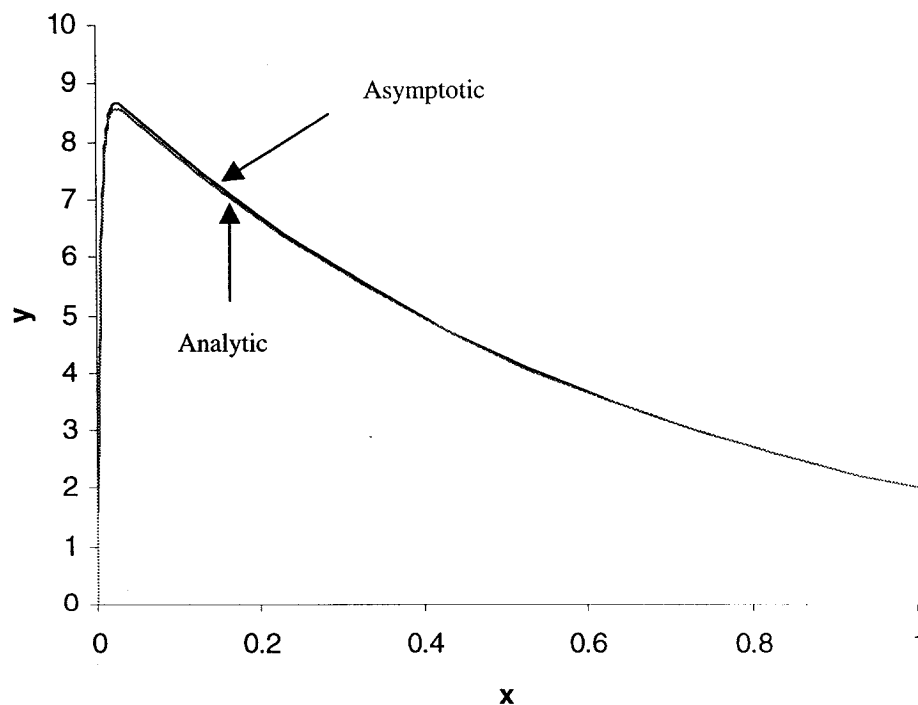


**Figure 9-3:** Analytic vs. uniformly valid asymptotic solution

Combining the "inner" and "outer" solutions from Equations (9.5) and (9.12) results in the final uniformly valid asymptotic solution plotted in Figure 9-3. It is apparent that the two solutions match one another extremely well throughout the entire domain. Thus, to summarize, the main result here was that the "outer" asymptotic solution was very accurate in most of the domain of the problem except near the boundary layer where the actual solution changed abruptly to capture the boundary condition. To "capture" this boundary condition, the "outer" solution had to be modified by adding an "inner" solution.

A similar boundary-layer situation will arise for the case of the smart composite structure with specified stress boundary conditions. The mathematical model for this structure will be derived in subsequent sections of this chapter.

## 9.2 Problem Formulation

The problem discussed in the previous chapter had homogeneous boundary conditions. When the boundary conditions are non-zero, one has to consider certain modifications. Kalamkarov [1992] used the homogenization technique for a 2-d problem of a regular periodic composite with non-zero boundary conditions. In this section, the same method will be applied to a more general 3-d problem that also includes (in addition to the composite reinforcements) a periodic array of embedded actuators. As well, the mathematical model derived here will incorporate hygroscopic and thermal expansion effects so that it can be compared directly with the corresponding model of the previous chapter. In particular, it will be interesting to see whether the same expressions for the effective coefficients are obtained, and how different the new homogenized equation will be.

Consider a smart structure representing an inhomogeneous solid occupying domain G with boundary $\partial G$ that contains a large number of periodically-arranged actuators as shown in Figure 9-4.

The elastic deformation of this smart structure can be described by means of the following boundary-value problem with prescribed stress boundary conditions imposed on $x_3 = 0$:

$$\frac{\partial \sigma_{ij}^{\varepsilon}}{\partial x_j} = f_i, \quad |x_1, x_2| < \infty, \quad x_3 \geq 0 \tag{9.14a}$$

$$\sigma_{i3}(x_1, x_2, 0) = P_i(x_1, x_2) \tag{9.14b}$$

$$e_{ij}^{\varepsilon}\left(x, \frac{x}{\varepsilon}\right) = \frac{1}{2}\left[\frac{\partial u_i}{\partial x_j}\left(x, \frac{x}{\varepsilon}\right) + \frac{\partial u_j}{\partial x_i}\left(x, \frac{x}{\varepsilon}\right)\right] \tag{9.14c}$$

$$\sigma_{ij}^{\varepsilon}\left(x, \frac{x}{\varepsilon}\right) = C_{ijkl}\left(\frac{x}{\varepsilon}\right)\frac{\partial u_k}{\partial x_l}\left(x, \frac{x}{\varepsilon}\right) - P_{ijk}\left(\frac{x}{\varepsilon}\right)R_k(x) - K_{ij}\left(\frac{x}{\varepsilon}\right)\Theta(x) - B_{ij}\left(\frac{x}{\varepsilon}\right)C(x)$$

where $i, j, k, l = 1,2,3$ \hfill (9.14d)
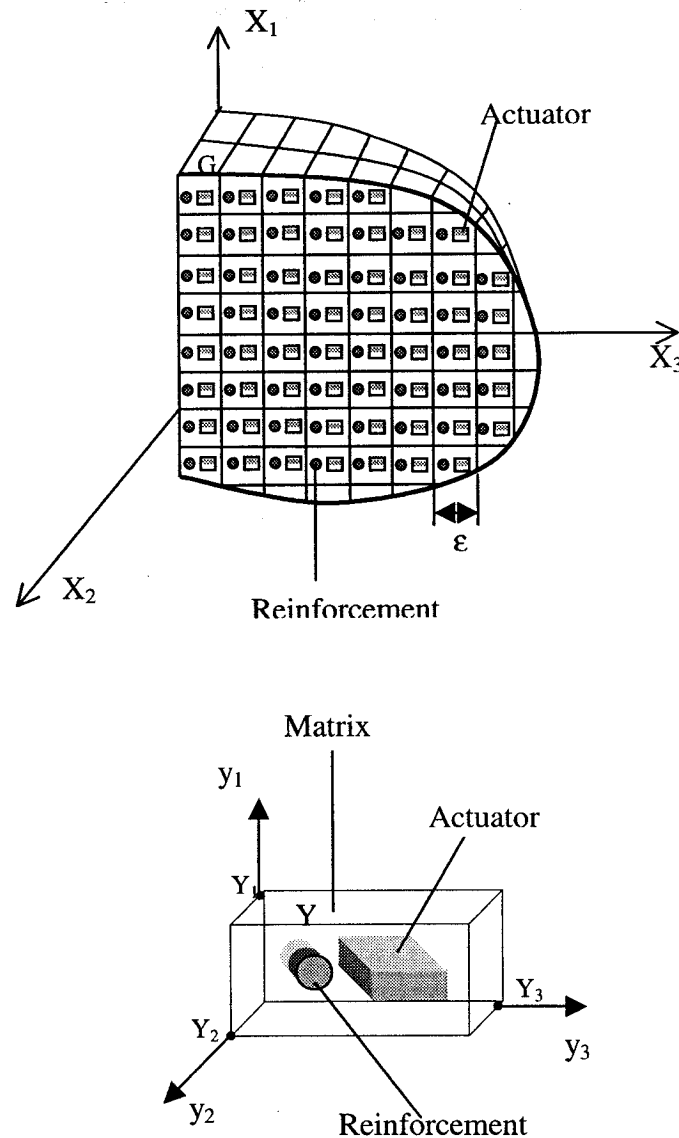
**Figure 9-4:** Composite containing a large number of periodically arranged actuators and its periodicity cell Y in the "fast" variables **y**

As before, $C_{ijkl}$ is the tensor of elastic coefficients, $e_{kl}$ is the strain tensor, $P_{ijk}$ a tensor describing the effect of a control signal R on the stress field $\sigma$, $K_{ij}$ is the thermal expansion tensor, and $B_{ij}$ the hygroscopic expansion tensor. Finally, $\Theta$ and C represent changes in the temperature and moisture content (with respect to a reference hygrothermal state) respectively. Also as explained in the previous chapter, $C_{ijkl}$, $P_{ijk}$, $K_{ij}$

and $B_{ij}$ are all periodic with a unit cell Y of characteristic dimension $\varepsilon$, the characteristic distance between the actuators, as in Figure 9-1. Consequently, the smart structure is seen to be made up of a large number of unit-cells periodically arranged within the domain G. It is evident that the condition "the number of actuators is large" is equivalent to the condition "$\varepsilon$ is small".

## 9.3 Two Scale Asymptotic expansions

The asymptotic expansions for the displacement and stress fields are the same as before (Chapter 8) and are given by:

*(a) Asymptotic expansion for displacement:*

$$\mathbf{u}^{\varepsilon}(\mathbf{x},\mathbf{y}) = \mathbf{u}^{(0)}(\mathbf{x}) + \varepsilon\mathbf{u}^{(1)}(\mathbf{x},\mathbf{y}) + \varepsilon^{2}\mathbf{u}^{(2)}(\mathbf{x},\mathbf{y}) + \cdots \qquad (9.15a)$$

*(b) Asymptotic expansion for stress:*

$$\sigma_{ij}^{\varepsilon}(\mathbf{x},\mathbf{y}) = \sigma_{ij}^{(0)}(\mathbf{x},\mathbf{y}) + \varepsilon\sigma_{ij}^{(1)}(\mathbf{x},\mathbf{y}) + \varepsilon^{2}\sigma_{ij}^{(2)}(\mathbf{x},\mathbf{y}) + \cdots \qquad (9.15b)$$

The introduction of the new variables, $\mathbf{y}$, necessitates the transformation of the derivatives, so that the boundary value problem in Equations (9.14a) and (9.15) becomes:

$$\frac{\partial\sigma_{ij}^{\varepsilon}}{\partial x_{j}} + \frac{1}{\varepsilon}\frac{\partial\sigma_{ij}^{\varepsilon}}{\partial y_{j}} = f_{i} \quad \text{in G}$$

$$\sigma_{i3}(x_{1},x_{2},0) = P_{i}(x_{1},x_{2}) \qquad (9.16)$$

It will be observed that the first term in the asymptotic expansion for the displacement field in Equation (9.15a) is independent of the fast variables $\mathbf{y}$. This can be readily seen by substituting Equations (9.14d) and (9.15a) into Equation (9.16) and considering the periodicity of $\mathbf{u}$.

Substitution of Equation (9.15b) into Equation (9.16) results in:

$$\frac{\partial\sigma_{ij}^{(0)}}{\partial x_{j}} + \frac{1}{\varepsilon}\frac{\partial\sigma_{ij}^{(0)}}{\partial y_{j}} + \varepsilon\frac{\partial\sigma_{ij}^{(1)}}{\partial x_{j}} + \frac{\partial\sigma_{ij}^{(1)}}{\partial y_{j}} + \ldots = F_{i} \qquad (9.17a)$$

$$\sigma_{i3}^{(0)}\Big|_{x_{3}=0} + \varepsilon\sigma_{i3}^{(1)}\Big|_{x_{3}=0} + \varepsilon^{2}\sigma_{i3}^{(0)}\Big|_{x_{3}=0} + \ldots = P_{i}(x_{1},x_{3}) \qquad (9.17b)$$

Equating like powers of $\varepsilon$ results in a series of differential equations (with pertinent boundary conditions) the first two of which are:

$$\frac{\partial \sigma_{ij}^{(0)}}{\partial y_j} = 0$$

$$\sigma_{i3}^{(0)}\Big|_{x_3=0} = P_i(x_2, x_3) \tag{9.18a}$$

$$\frac{\partial \sigma_{ij}^{(i)}}{\partial y_j} + \frac{\partial \sigma_{ij}^{(0)}}{\partial x_j} = F_i$$

$$\sigma_{i3}^{(0)}\Big|_{x_3=0} = 0 \tag{9.18b}$$

## 9.4 Determination of $u^{(1)}$

Substitution of Equations (9.15a) and (9.15b) into Equation (9.14d), equating like powers of $\varepsilon$, and combining the resulting expressions with those in Equations (9.18a) and (9.18b), results in the following expressions:

$$\frac{\partial}{\partial y_j}\left[C_{ijkl}(y)\frac{\partial u_k^{(1)}(x,y)}{\partial y_l}\right] = -\frac{\partial u_k^{(0)}(x)}{\partial x_l}\frac{\partial C_{ijkl}(y)}{\partial y_j} + P_{ijk}(y)R_k(x)$$
$$+ K_{ij}(y)T(x) + B_{ij}(y)C(x) \tag{9.19a}$$

$$C_{i3kl}\Big|_{y_3=0}\frac{\partial u_k^{(1)}}{\partial y_l}\Big|_{y_3=0} = -C_{i3kl}\Big|_{y_3=0}\frac{\partial u_k^{(0)}}{\partial x_l}\Big|_{y_3=0} + P_{i3k}\Big|_{y_3=0}R_k\Big|_{x_3=0} + K_{i3}\Big|_{y_3=0}T\Big|_{x_3=0} +$$
$$B_{i3}\Big|_{y_3=0}C\Big|_{x_3=0} + P_i(x_1, x_2) \tag{9.19b}$$

and

$$\frac{\partial}{\partial y_j}\left\{C_{ijkl}\frac{\partial u_k^{(2)}}{\partial y_l}\right\} = -\frac{\partial}{\partial y_j}\left\{C_{ijkl}\frac{\partial u_k^{(1)}}{\partial x_l}\right\} - C_{ijkl}\frac{\partial^2 u_k^{(0)}}{\partial x_j\partial x_l} - C_{ijkl}\frac{\partial^2 u_k^{(1)}}{\partial x_j\partial y_l} + P_{ijk}\frac{\partial R_k}{\partial x_k} +$$
$$K_{ij}\frac{\partial T}{\partial x} + B_{ij}\frac{\partial C}{\partial x} + F_i \tag{9.20a}$$

$$C_{i3kl}\Big|_{y_3=0}\frac{\partial u_k^{(2)}}{\partial y_l}\Big|_{y_3=0} = -C_{i3kl}\Big|_{y_3=0}\frac{\partial u_k^{(1)}}{\partial x_l}\Big|_{x_3,y_3=0} \tag{9.20b}$$

The separation on the RHS of Equation (9.19a) prompts one to write down the general solution as:

$$u_m^{(1)} = u_m^{(1,2)}(\mathbf{x},\mathbf{y}) + N_m^{kl}(\mathbf{y})\frac{\partial u_k^{(0)}(\mathbf{x})}{\partial x_1} + N_m^k(\mathbf{y})R_k(\mathbf{x}) + M_m(\mathbf{y})T(\mathbf{x}) + S_m(\mathbf{y})T(\mathbf{x}) \quad (9.21)$$

The various functions in Equation (9.21) satisfy the following equations:

$$\frac{\partial}{\partial y_j}\left[C_{ijml}\frac{\partial u_m^{(1,2)}(\mathbf{x},\mathbf{y})}{\partial y_1}\right] = 0 \quad (9.22a)$$

$$\frac{\partial}{\partial y_j}\left[C_{ijml}(\mathbf{y})\frac{\partial N_m^{kl}(\mathbf{y})}{\partial y_1}\right] = -\frac{\partial C_{ijkl}(\mathbf{y})}{\partial y_j} \quad (9.22b)$$

$$\frac{\partial}{\partial y_j}\left[C_{ijml}(\mathbf{y})\frac{\partial N_m^k(\mathbf{y})}{\partial y_1}\right] = \frac{\partial P_{ijk}(\mathbf{y})}{\partial y_j} \quad (9.22c)$$

$$\frac{\partial}{\partial y_j}\left[C_{ijml}(\mathbf{y})\frac{\partial M_m(\mathbf{y})}{\partial y_1}\right] = \frac{\partial K_{ij}(\mathbf{y})}{\partial y_j} \quad (9.22d)$$

$$\frac{\partial}{\partial y_j}\left[C_{ijml}(\mathbf{y})\frac{\partial S_m(\mathbf{y})}{\partial y_1}\right] = \frac{\partial B_{ij}(\mathbf{y})}{\partial y_j} \quad (9.22e)$$

Equation (9.51) satisfies the boundary condition at $x_3 = 0$. Thus substitution of Equation (9.21) into Equation (9.19b) leads to:

$$C_{i3ml}\Big|_{y_3=0}\frac{\partial u_m^{(1,2)}}{\partial y_1}\Big|_{x_3=0} = -\left(C_{i3ml}\frac{\partial N_m^k}{\partial y_1} - P_{i3k}\right)\Big|_{y_3=0} R_k\Big|_{x_3=0} - \left(C_{i3ml}\frac{\partial M_m}{\partial y_1} - K_{i3}\right)\Big|_{y_3=0} T\Big|_{x_3=0}$$

$$-\left(C_{i3ml}\frac{\partial S_m}{\partial y_1} - B_{i3}\right)\Big|_{y_3=0} C\Big|_{x_3=0} - \left(C_{i3ml}\frac{\partial N_m^{kl}}{\partial y_1} + C_{i3kl}\right)\Big|_{x_3=0}\frac{\partial u_k^{(0)}}{\partial x_1}\Big|_{x_3=0} + P_i(x_1,x_3) \quad (9.23)$$

As well, the following condition must be satisfied:

$$u_m^{(1,2)}(\mathbf{x},\mathbf{y}) \to 0 \qquad \text{as } y_3 \to \infty \quad (9.24)$$

Perhaps the most interesting feature of the solution (9.21) is the presence of the homogeneous portion $\mathbf{u}^{(1,2)}$ which is the only function that is not entirely dependent on $\mathbf{y}$. As well, $\mathbf{u}^{(1,2)}$ is periodic in $y_1$ and $y_2$ only (not $y_3$) as evidenced by Equation (9.24). To

appreciate this, one has to look at Equation (9.23) and in particular the term $P_i(x_1, x_3)$ which defines the prescribed stress boundary condition. It is evident that if this term were zero, then Equation (9.23) would have been satisfied only if $\partial u^{(1,2)}/ \partial y_1$ were also zero. This would imply further that $\mathbf{u}^{(1,2)}$ was solely a function of $\mathbf{x}$, a conclusion which could have also been established directly from Equation (9.22a) by insisting that $\mathbf{u}^{(1,2)}$ was periodic in *all* of $y_1$, $y_2$, and $y_3$ and not just $y_1$ and $y_2$. Thus, the presence of non-zero boundary conditions necessarily means that $\mathbf{u}^{(1,2)}$ is a function of both $\mathbf{x}$ and $\mathbf{y}$, and is periodic in $y_1$ and $y_2$ only. Alternatively, one can say that we have a boundary-layer type solution at $x_3 = 0$ (see Section 9.1 and also Kalamkarov, 1992; Nayfeh, 1973; Holmes, 1995) and $\mathbf{u}^{(1,2)}$ is the "inner" solution whereas the remaining terms in Equation (9.21) collectively represent the "outer" solution.

In an attempt to solve for $\mathbf{u}^{(1,2)}$, Equation (9.22a) will be integrated over the semi-infinite volume defined by $0 < y_1, y_2 < 1$, $y_3 > 0$. After some manipulation, the resulting expression is given by:

$$\int_0^1 \int_0^1 C_{i3kl} \frac{\partial u_k^{(1,2)}}{\partial y_1}\Bigg|_{y_3=0} dy_1 dy_2 = 0. \tag{9.25}$$

Equation (9.23) is subsequently integrated with respect to $y_1$ and $y_2$ taking at the same time Equation (9.25) into consideration. The resulting expression is of the form:

$$\int_0^1 \int_0^1 P_{i3k}(y_1, y_2, 0) R_k dy_1 dy_2 + \int_0^1 \int_0^1 K_{i3}(y_1, y_2, 0) T dy_1 dy_2 + \int_0^1 \int_0^1 B_{i3}(y_1, y_2, 0) C dy_1 dy_2$$
$$+ \int_0^1 \int_0^1 C_{i3kl}(y_1, y_2, 0) \frac{\partial u_k^{(0)}}{\partial x_1} dy_1 dy_2 - P_i = 0 \tag{9.26}$$

Here the following definitions are used:

$$\left( C_{i3ml} \frac{\partial N_m^{kl}}{\partial y_1} + C_{i3kl} \right)\Bigg|_{y_3=0} = C_{i3kl}(y_1, y_2, 0) \tag{9.27a}$$

$$\left( C_{i3ml} \frac{\partial N_m^k}{\partial y_1} - P_{i3k} \right)\Bigg|_{y_3=0} = P_{i3k}(y_1, y_2, 0) \tag{9.27b}$$

$$\left(C_{i3ml}\frac{\partial M_m}{\partial y_l} - K_{i3}\right)\Bigg|_{y_3=0} = K_{i3}(y_1,y_2,0) \qquad (9.27c)$$

$$\left(C_{i3ml}\frac{\partial S_m}{\partial y_l} - B_{i3}\right)\Bigg|_{y_3=0} = B_{i3}(y_1,y_2,0) \qquad (9.27d)$$

If further, the following definitions are made,

$$\int_0^1\int_0^1 P_{i3k}(y_1,y_2,0)dy_1dy_2 = P_{i3k}^* \qquad (9.28a)$$

$$\int_0^1\int_0^1 C_{i3kl}(y_1,y_2,0)dy_1dy_2 = C_{i3kl}^* \qquad (9.28b)$$

$$\int_0^1\int_0^1 K_{i3}(y_1,y_2,0)dy_1dy_2 = K_{i3}^* \qquad (9.28c)$$

$$\int_0^1\int_0^1 B_{i3}(y_1,y_2,0)dy_1dy_2 = B_{i3}^* \qquad (9.28d)$$

then Equation (9.26) becomes:

$$C_{i3kl}^*\frac{\partial u_k^{(0)}}{\partial x_l}\Bigg|_{x_3=0} + P_{i3k}^*R_k\Big|_{x_3=0} + K_{i3}^*T\Big|_{x_3=0} + B_{i3}^*C\Big|_{x_3=0} = P_i(x_1,x_2) \qquad (9.29)$$

This is now substituted back in Equation (9.23) in order to eliminate $P_i$. The resulting expression,

$$C_{i3ml}\frac{\partial u_m^{(1,2)}}{\partial y_l}\Bigg|_{y_3=0} = \left[C_{i3kl}^* - C_{i3kl}(y_1,y_2,0)\right]\frac{\partial u_k^{(0)}}{\partial x_l}\Bigg|_{x_3=0} + \left[P_{i3k}^* - P_{i3k}(y_1,y_2,0)\right]R_k\Big|_{x_3=0}$$
$$+ \left[K_{i3}^* - K_{i3}(y_1,y_2,0)\right]T\Big|_{x_3=0} + \left[B_{i3}^* - B_{i3}(y_1,y_2,0)\right]C\Big|_{x_3=0} \qquad (9.30)$$

together with Equation (9.22a) are satisfied by $u^{(1,2)}$. The solution of $u^{(1,2)}$ can be written in the form:

$$u_m^{(1,2)}(x,y) = N_m^{(1)kl}\frac{\partial u_k^{(0)}}{\partial x_l} + N_m^{(1)k}R_k + M_m^{(1)}T + S_m^{(1)}C \qquad (9.31)$$

Here $N_m^{(1)kl}, N_m^{(1)k}, M_m^{(1)}, S_m^{(1)}$ are all periodic in $y_1$ and $y_2$ but not $y_3$ and satisfy the following differential equations:

$$\frac{\partial}{\partial y_j}\left\{C_{ijml}(\mathbf{y})\frac{\partial N_m^{(1)kl}(\mathbf{y})}{\partial y_l}\right\} = 0, \quad 0 < y_1, y_2 < 1, \quad y_3 > 0 \tag{9.32a}$$

$$\frac{\partial}{\partial y_j}\left\{C_{ijml}(\mathbf{y})\frac{\partial N_m^{(1)k}(\mathbf{y})}{\partial y_l}\right\} = 0, \quad 0 < y_1, y_2 < 1, \quad y_3 > 0 \tag{9.32b}$$

$$\frac{\partial}{\partial y_j}\left\{C_{ijml}(\mathbf{y})\frac{\partial M_m^{(1)}(\mathbf{y})}{\partial y_l}\right\} = 0, \quad 0 < y_1, y_2 < 1, \quad y_3 > 0 \tag{9.32c}$$

$$\frac{\partial}{\partial y_j}\left\{C_{ijml}(\mathbf{y})\frac{\partial S_m^{(1)}(\mathbf{y})}{\partial y_l}\right\} = 0, \quad 0 < y_1, y_2 < 1, \quad y_3 > 0 \tag{9.32d}$$

As well, functions $N_m^{(1)kl}, N_m^{(1)k}, M_m^{(1)}, S_m^{(1)}$ satisfy the following boundary conditions:

$$C_{i3mr}\frac{\partial N_m^{(1)kl}}{\partial y_r}\bigg|_{y_3=0} = C_{i3kl}^* - C_{i3kl}(y_1, y_2, 0) \tag{9.33a}$$

$$C_{i3ml}\frac{\partial N_m^{(1)k}}{\partial y_l}\bigg|_{y_3=0} = P_{i3k}^* - P_{i3k}(y_1, y_2, 0) \tag{9.33b}$$

$$C_{i3ml}\frac{\partial M_m^{(1)}}{\partial y_l}\bigg|_{y_3=0} = K_{i3}^* - K_{i3}(y_1, y_2, 0) \tag{9.33c}$$

$$C_{i3ml}\frac{\partial S_m^{(1)}}{\partial y_l}\bigg|_{y_3=0} = B_{i3}^* - B_{i3}(y_1, y_2, 0) \tag{9.33d}$$

$$\text{and} \quad N_m^{(1)kl}, N_m^{(1)k}, M_m^{(1)}, S_m^{(1)} \to 0 \quad \text{as } y_3 \to \infty \tag{9.33e}$$

## 9.5 Determination of Effective Coefficients

One now returns to $\mathbf{u}^{(2)}$ defined by Equations (9.20a) and (9.20b). In particular, one substitutes Equations (9.21) and (9.31) into Equation (9.20a) to obtain the following differential equation:

$$\frac{\partial}{\partial y_j}\left[C_{ijkl}\frac{\partial u_k^{(2)}(\mathbf{x}, \mathbf{y})}{\partial y_l}\right] = \text{Part I} + \text{Part II} \tag{9.34}$$

where

$$\text{Part I} = -\frac{\partial}{\partial y_j}\left\{C_{ijmn}\left[N_m^{kl}\frac{\partial^2 u_k^{(0)}}{\partial x_l \partial x_n} + N_m^k\frac{\partial R_k}{\partial x_n} + M_m\frac{\partial T}{\partial x_n} + S_m\frac{\partial C}{\partial x_n}\right]\right\}$$

$$-C_{ijmn}\left\{\frac{\partial N_m^{kl}}{\partial y_n}\frac{\partial^2 u_k^{(0)}}{\partial x_j \partial x_l} + \frac{\partial N_m^k}{\partial y_n}\frac{\partial R_k}{\partial x_j} + \frac{\partial M_m}{\partial y_n}\frac{\partial T}{\partial x_j} + \frac{\partial S_m}{\partial y_n}\frac{\partial C}{\partial x_j}\right\} \qquad (9.35a)$$

$$-C_{ijkl}\frac{\partial^2 u_k^{(0)}}{\partial x_j \partial x_l} + P_{ijk}\frac{\partial R_k}{\partial x_j} + K_{ij}\frac{\partial T}{\partial x_j} + B_{ij}\frac{\partial C}{\partial x_j} + F_i$$

and,

$$\text{Part II} = -\frac{\partial}{\partial y_j}\left\{C_{ijmn}\left[N_m^{(1)kl}\frac{\partial^2 u_k^{(0)}}{\partial x_l \partial x_n} + N_m^{(1)k}\frac{\partial R_k}{\partial x_n} + M_m^{(1)}\frac{\partial T}{\partial x_n} + S_m^{(1)}\frac{\partial C}{\partial x_n}\right]\right\}$$

$$-C_{ijmn}\left\{\frac{\partial N_m^{(1)kl}}{\partial y_n}\frac{\partial^2 u_k^{(0)}}{\partial x_j \partial x_l} + \frac{\partial N_m^{(1)k}}{\partial y_n}\frac{\partial R_k}{\partial x_j} + \frac{\partial M_m^{(1)}}{\partial y_n}\frac{\partial T}{\partial x_j} + \frac{\partial S_m^{(1)}}{\partial y_n}\frac{\partial C}{\partial x_j}\right\} \qquad (9.35b)$$

Similarly, the pertinent boundary condition is given by the following expression:

$$C_{i3kl}\frac{\partial u_k^{(2)}}{\partial y_l}\bigg|_{y_3=0} = -C_{i3mn}\big|_{y_3=0}\frac{\partial}{\partial x_n}\left[N_m^{kl}\frac{\partial u_k^{(0)}}{\partial x_l} + N_m^k R_k + M_m T + S_m C\right]\bigg|_{y_3=x_3=0}$$

$$-C_{i3mn}\big|_{y_3=0}\frac{\partial}{\partial x_n}\left[N_m^{(1)kl}\frac{\partial u_k^{(0)}}{\partial x_l} + N_m^{(1)k}R_k + M_m^{(1)}T + S_m^{(1)}C\right]\bigg|_{y_3=x_3=0} \qquad (9.36)$$

It will be observed that functions $N_m^{kl}, N_m^k, M_m, S_m$ in Part I are periodic in all of $y_1$, $y_2$, $y_3$ whereas functions $N_m^{(1)kl}, N_m^{(1)k}, M_m^{(1)}, S_m^{(1)}$ in Part II are periodic in $y_1$ and $y_2$ only. The solution of $\mathbf{u}^{(2)}$ from Equation (9.34) can be written as:

$$u_k^{(2)}(\mathbf{x},\mathbf{y}) = u_k^{(2,1)}(\mathbf{x},\mathbf{y}) + u_k^{(2,2)}(\mathbf{x},\mathbf{y}) \qquad (9.37)$$

In Equation (9.37) $u_k^{(2,1)}$ satisfies Part I and $u_k^{(2,2)}$ satisfies Part II. Clearly, the former is periodic in $y_1$, $y_2$ and $y_3$, whereas the latter is only periodic in $y_1$ and $y_2$.

We will now average the differential equation satisfied by $\mathbf{u}^{(2,1)}$, i.e. Part I, by integrating it over the volume Y of the unit cell. This results in the following expression:

$$\tilde{C}_{ijkl}\frac{\partial u_k^{(0)}}{\partial x_j \partial x_l} - \tilde{P}_{ijk}\frac{\partial R_k}{\partial x_j} - \tilde{K}_{ij}\frac{\partial T}{\partial x_j} - \tilde{B}_{ij}\frac{\partial C}{\partial x_j} = F_i \qquad (9.38)$$

In arriving at Equation (9.38), use was made on a number of occasions of the well-known divergence theorem. For example:

$$\frac{1}{|Y|}\int_Y \frac{\partial}{\partial y_j}\left\{C_{ijkl}(y)\frac{\partial u_k^{(2,1)}(x,y)}{\partial y_l}\right\}dV = \frac{1}{|Y|}\int_Y \frac{\partial L_{ij}}{\partial y_j}dV$$

$$\text{where } L_{ij} = C_{ijkl}(y)\frac{\partial u_k^{(2,1)}(x,y)}{\partial y_l} \tag{9.39}$$

$$\therefore \frac{1}{|Y|}\int_Y \frac{\partial L_{ij}}{\partial y_j}dV = \frac{1}{|Y|}\int_Y divLdV = \frac{1}{|Y|}\int_{\partial Y} L_{ij}n_jdV = 0$$

In Equations (9.39), $n_i$ are the components of the unit vector normal to the boundary surface $\partial Y$ of the unit cell. Owing to the periodicity of $L_{ij}$ (a consequence of the periodicity of $u^{(2,1)}$ and $C_{ijkl}$), its values at corresponding points on opposite sides of the unit cell are the same. However, the unit normal vectors have opposite signs at these points and consequently the integral vanishes identically.

As well, the following definitions were made in Equation (9.39):

$$\tilde{C}_{ijkl} = \frac{1}{|Y|}\int_Y \left[C_{ijkl} + C_{ijmn}\frac{\partial N_m^{kl}}{\partial y_n}\right]dv \tag{9.40a}$$

$$\tilde{P}_{ijk} = \frac{1}{|Y|}\int_Y \left[P_{ijk} - C_{ijmn}\frac{\partial N_m^k}{\partial y_n}\right]dv \tag{9.40b}$$

$$\tilde{K}_{ij} = \frac{1}{|Y|}\int_Y \left[K_{ij} - C_{ijmn}\frac{\partial M_m}{\partial y_n}\right]dv \tag{9.40c}$$

$$\tilde{B}_{ij} = \frac{1}{|Y|}\int_Y \left[B_{ij} - C_{ijmn}\frac{\partial S_m}{\partial y_n}\right]dv \tag{9.40d}$$

Here $\tilde{C}_{ijkl}, \tilde{P}_{ijk}, \tilde{K}_{ij}, \tilde{B}_{ij}$ are the homogenized or effective elastic, actuation (such as piezoelectric), thermal expansion, and hygroscopic expansion coefficients respectively. In terms of these coefficients, Equation (9.38) may be termed the "homogenized" equation for the displacement field.

## 9.6 Synopsis and Important Results

(a) *Unit cell problems*:

$$\frac{\partial}{\partial y_j}\left(C_{ijmn}(\mathbf{y})\frac{\partial N_m^{kl}(\mathbf{y})}{\partial y_n}+C_{ijkl}\right)=0$$

$$\frac{\partial}{\partial y_j}\left(C_{ijml}(\mathbf{y})\frac{\partial N_m^k(\mathbf{y})}{\partial y_l}-P_{ijk}\right)=0$$

$$\frac{\partial}{\partial y_j}\left(C_{ijml}(\mathbf{y})\frac{\partial M_m(\mathbf{y})}{\partial y_l}-K_{ij}\right)=0 \tag{9.41}$$

$$\frac{\partial}{\partial y_j}\left(C_{ijml}(\mathbf{y})\frac{\partial S_m(\mathbf{y})}{\partial y_l}-B_{ij}\right)=0$$

(b) *Effective (homogenized) coefficients*:

$$\widetilde{C}_{ijkl}=\frac{1}{|Y|}\int_Y\left(C_{ijkl}(\mathbf{y})+C_{ijmn}(\mathbf{y})\frac{\partial N_m^{kl}}{\partial y_n}\right)dv$$

$$\widetilde{P}_{ijk}=\frac{1}{|Y|}\int_Y\left(P_{ijk}(\mathbf{y})-C_{ijmn}(\mathbf{y})\frac{\partial N_m^k}{\partial y_n}\right)dv$$

$$\widetilde{K}_{ij}=\frac{1}{|Y|}\int_Y\left(K_{ij}(\mathbf{y})-C_{ijmn}(\mathbf{y})\frac{\partial M_m}{\partial y_n}\right)dv \tag{9.42}$$

$$\widetilde{B}_{ij}=\frac{1}{|Y|}\int_Y\left(B_{ij}(\mathbf{y})-C_{ijmn}(\mathbf{y})\frac{\partial S_m}{\partial y_n}\right)dv$$

(c) *Homogenized Problem*:

$$\widetilde{C}_{ijkl}\frac{\partial^2 u_k^{(0)}(\mathbf{x})}{\partial x_j \partial x_l}-\widetilde{P}_{ijk}\frac{\partial R_k(\mathbf{x})}{\partial x_j}-\widetilde{K}_{ij}\frac{\partial\Theta(\mathbf{x})}{\partial x_j}-\widetilde{B}_{ij}\frac{\partial C(\mathbf{x})}{\partial x_j}=F_i$$

$$C_{i3kl}^*\frac{\partial u_k^{(0)}}{\partial x_l}\bigg|_{x_3=0}+P_{i3k}^*R_k\big|_{x_3=0}+K_{i3}^*T\big|_{x_3=0}+B_{i3}^*C\big|_{x_3=0}=P_i(x_1,x_2) \tag{9.43}$$

It is thus concluded that the original boundary-value problem defined by Equations (9.14a) and (9.14b) reduces to that of solving (9.43). To perform this solution one needs to only detrmine the effective coefficients from Equation (9.42) by calculating the local

functions $N_m^{kl}, N_m^k, M_m, S_m$ from Equation (9.41). It will be observed that these problems depend entirely on the fast variable $y$ and are thus solved on the domain Y of the unit cell remembering at the same time that all of $N_m^{kl}, N_m^k, M_m, S_m$ are periodic in $y_i$. These are the "unit-cell" problems. Comparing these equations with the corresponding equations (8.84), (8.85) and (8.86) of the previous chapter, one will observe that they are the same. Where the two models differ is in the determination of the next term in the displacement field (i.e. $u^{(1)}$) and the first term in the stress field. To calculate these, one needs to also find the auxiliary local functions $N_m^{(1)kl}, N_m^{(1)k}, M_m^{(1)}, S_m^{(1)}$ from Equations (9.32a) to (9.32d) and (9.33a) to (9.33e). The results are:

$$u_m = u_m^{(0)}(x) + \varepsilon \left\{ \begin{array}{l} \left[N_m^{kl}(y) + N_m^{(1)kl}(y)\right]\dfrac{\partial u_k^{(0)}(x)}{\partial x_1} + \left[N_m^k(y) + N_m^{(1)k}(y)\right]R_k(x) + \\[2mm] \left[M_m(y) + M_m^{(1)}(y)\right]T(x) + \left[S_m(y) + S_m^{(1)}(y)\right]C(x) \end{array} \right\} + O(\varepsilon^2) \quad (9.44)$$

and

$$\sigma_{ij} = C_{ijml}(y) \left\{ \begin{array}{l} \left[\dfrac{\partial u_m^{(0)}}{\partial x_1} + \left[\dfrac{\partial N_m^{kl}(y)}{\partial y_1} + \dfrac{\partial N_m^{(1)kl}(y)}{\partial y_1}\right]\right]\dfrac{\partial u_k^{(0)}(x)}{\partial x_1} + \left[\dfrac{\partial N_m^k(y)}{\partial y_1} + \dfrac{\partial N_m^{(1)k}(y)}{\partial y_1}\right]R_k(x) + \\[4mm] \left[\dfrac{\partial M_m(y)}{\partial y_1} + \dfrac{\partial M_m^{(1)}(y)}{\partial y_1}\right]T_k(x) + \left[\dfrac{\partial S_m(y)}{\partial y_1} + \dfrac{\partial S_m^{(1)}(y)}{\partial y_1}\right]C_k(x) \end{array} \right\}$$

$$- P_{ijk}(y)R_k(x) - K_{ij}(y)T(x) - B_{ij}(y)C(x) + O(\varepsilon) \quad (9.45)$$

Comaparing Equations (8.87) and (9.45), one observes that they differ only by the auxiliary local functions $N_m^{(1)kl}, N_m^{(1)k}, M_m^{(1)}, S_m^{(1)}$.

The most important parameters are the effective coefficients given in Equations (8.85) and (9.42). With the help of these coefficients, one is able to examine a variety of problems by studying only the unit cells specific to the smart composites in question. This will be illustrated in the next chapter.

# 10.0 APPLICATION OF UNIT CELL PROBLEMS FOR LAMINATED STRUCTURES

## 10.1 Introduction

In order to calculate the effective characteristics of the homogenized model, the unit-cell problems of Equations (8.84) or (9.41) must be solved and the formulae (8.85) or (9.42) must be applied. The unit-cell problems can be solved by means of different methods depending on the specific structure of the periodicity cell.

Let us consider a laminated composite structure made of layers of different materials that can be isotropic, transversely isotropic, orthotropic or generally anisotropic. The laminae may also exhibit piezoelectric or magnetostrictive effects, or in general be associated with some transduction characteristics that can be used to induce residual strains and stresses. All the characteristics of such a laminated solid will depend only on one spatial coordinate perpendicular to the laminae. Consequently, all the relevant unit cell problems will be reduced to ordinary differential equations and can be solved analytically. The effective characteristics can then be obtained.

In subsequent sections, the effective elastic, piezoelectric, thermal expansion and hygroscopic expansion coefficients will be determined and illustrated. Kalamkarov [1992] also calculated the effective elastic coefficients for laminated structures. However, it would be rather unreasonable to present the effective piezoelectric, thermal expansion, and hygroscopic expansion coefficients alone without mentioning anything about the elastic coefficients. Consequently, for the sake of continuity the effective elastic coefficients will be presented as well.

## 10.2 Effective Elastic Coefficients for Laminated Structures

Consider a laminated structure such as the one in Figure 10-1. Without loss of generality, it will be assumed that the laminate consists of only two different anisotropic materials, material A and material B.
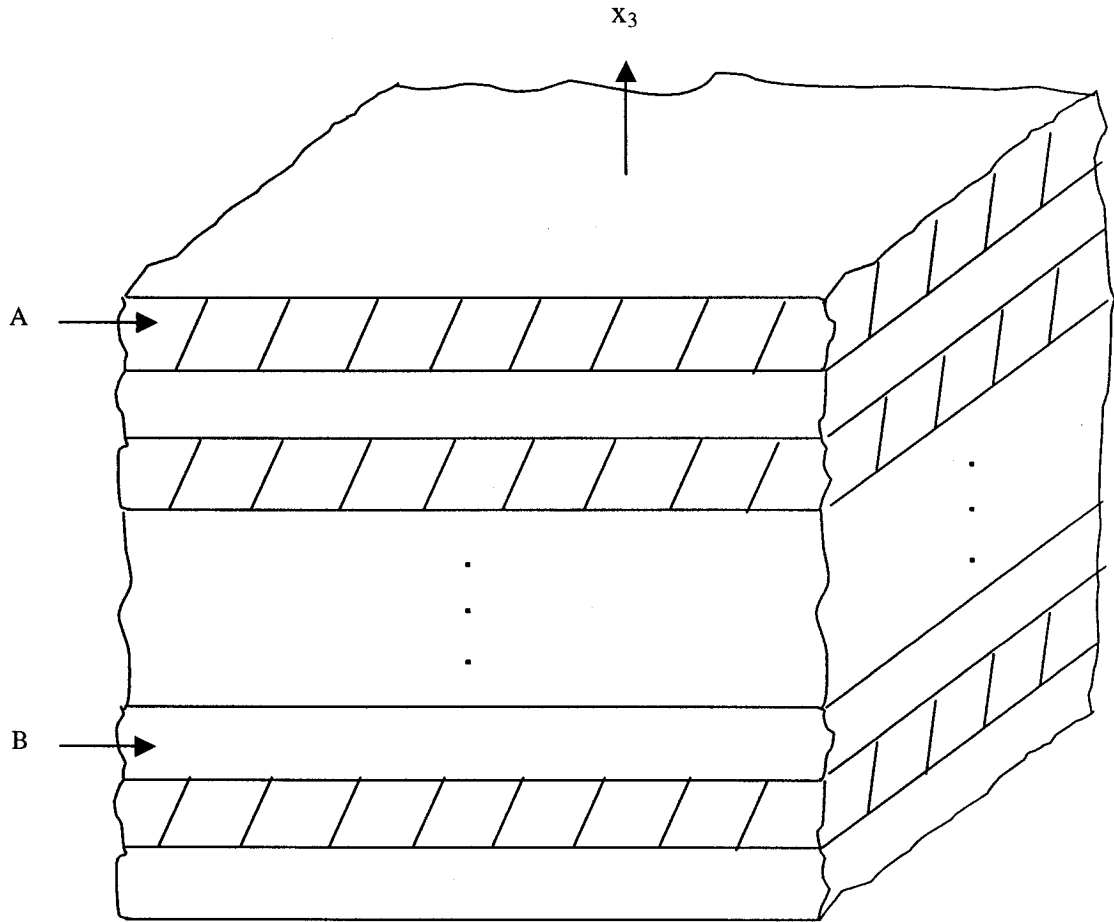
Figure 10-1: Laminated Structure

If all A layers have the same thickness, and all B layers have the same thickness (which may be different from that of A layers) the pertinent unit cell would be of the form shown in Figure 10-2.
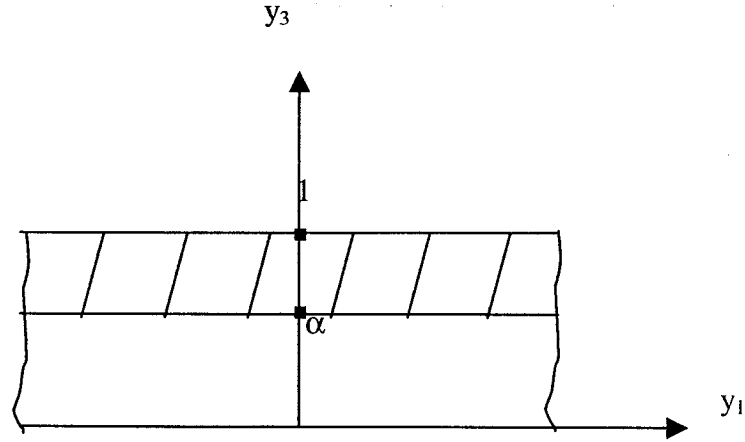
**Figure 10-2:** Unit cell of laminated structure

The first unit cell problem in Equation (9.41) is:

$$\frac{\partial}{\partial y_j}\left(C_{ijmn}(y)\frac{\partial N_m^{kl}(y)}{\partial y_n}\right) = -\frac{\partial C_{ijkl}}{\partial y_j} \tag{10.1}$$

Due to the nature of the unit cell, the partial derivatives in Equation (10.1) become total derivatives resulting in:

$$\frac{d}{dy_3}\left(C_{i3m3}(y_3)\frac{dN_m^{kl}(y_3)}{dy_3}\right) = -\frac{dC_{i3kl}}{dy_3} \qquad 0 \le y_3 \le 1 \tag{10.2a}$$

where,

$$C_{ijkl} = \begin{cases} C_{ijkl}^{(1)} & 0 \le y_3 \le \alpha \\ C_{ijkl}^{(2)} & \alpha \le y_3 \le 1 \end{cases} \tag{10.2b}$$

Integrating Equation (10.2a) results in:

$$C_{i3m3}(y_3)\frac{dN_m^{kl}(y_3)}{dy_3} = -C_{i3kl} + A_{ikl}$$

$$\therefore \frac{dN_m^{kl}(y_3)}{dy_3} = -C_{m3i3}^{-1}C_{i3kl} + C_{m3i3}^{-1}A_{ikl} \tag{10.2c}$$

In equation (10.2c) $A_{ijk}$ are arbitrary constants and $C_{ijkl}^{-1}$ is the inverse of $C_{ijkl}$ so that:

$$C_{i3m3}^{-1}C_{m3j3} = \delta_{ij} \tag{10.3}$$

Here, $\delta_{ij}$ is the Kronecker Delta [Holzapfel, 2000; Başar, Y., and Weichert, D., 1999]. Integrating Equation (10.2c) one more time with respect to $y_3$, while considering at the same time the periodicity of the pertinent functions gives:

$$\left\langle C^{-1}_{m3i3} C_{i3kl} \right\rangle = \left\langle C^{-1}_{m3i3} \right\rangle A_{ikl}$$

$$\therefore A_{ikl} = \left\langle C^{-1}_{i3m3} \right\rangle^{-1} \left\langle C^{-1}_{m3n3} C_{n3kl} \right\rangle$$

(10.4)

In Equation (10.4) quantities in angled brackets represent averaged quantities, which are obtained by integration through the volume of the unit cell. Constants $A_{ikl}$ from Equation (10.4) are then substituted into Equation (10.2c) the resulting expression is substituted into Equation (9.42),

$$\tilde{C}_{ijkl} = \frac{1}{|Y|} \int_Y \left( C_{ijkl}(y) + C_{ijmn}(y) \frac{\partial N^{kl}_m}{\partial y_n} \right) dv$$

(10.5)

to determine the effective elastic coefficients. The resulting expression is given by Equation (10.6):

$$\tilde{C}_{ijkl} = \left\langle C_{ijkl} \right\rangle - \left\langle C_{ijm3} C^{-1}_{m3q3} C_{q3kl} \right\rangle + \left\langle C_{ijm3} C^{-1}_{m3q3} \right\rangle \left\langle C^{-1}_{q3p3} \right\rangle^{-1} \left\langle C^{-1}_{p3n3} C_{n3kl} \right\rangle$$

(10.6)

To proceed further one needs to specify the symmetry of the anisotropic media within the unit cell. Suppose for illustration purposes that the unit cell consists of laminae which exhibit hexagonal symmetry about the $x_3$ axis. Examples of materials with hexagonal symmetry (6 mm) are many common piezoelectric materials such as $BaTiO_3$, PZT-4 and PZT-6B [Rajapakse, 1997]. In that case the effective elastic moduli are readily determined from Equation (10.6) and are given by expressions (10.7). It will be observed that the contracted notation for the elastic coefficients is used in Equation (10.7).

$$\tilde{C}_{11} = \left\langle C_{11} \right\rangle - \left\langle C^2_{13} C^{-1}_{33} \right\rangle + \left\langle C_{13} C^{-1}_{33} \right\rangle^2 \left\langle C^{-1}_{33} \right\rangle^{-1}, \qquad \tilde{C}_{12} = \left\langle C_{12} \right\rangle - \left\langle C^2_{13} C_{33} \right\rangle + \left\langle C_{13} C^{-1}_{33} \right\rangle^2 \left\langle C^{-1}_{33} \right\rangle^{-1}$$

$$\tilde{C}_{13} = \left\langle C_{13} C^{-1}_{33} \right\rangle \left\langle C^{-1}_{33} \right\rangle^{-1}, \qquad \tilde{C}_{33} = \left\langle C^{-1}_{33} \right\rangle^{-1}, \qquad \tilde{C}_{44} = \left\langle C^{-1}_{44} \right\rangle^{-1}$$

$$\tilde{C}_{22} = \tilde{C}_{11}, \qquad \tilde{C}_{23} = \tilde{C}_{13}, \qquad \tilde{C}_{55} = \tilde{C}_{44}, \qquad \tilde{C}_{66} = \frac{1}{2} \left( \tilde{C}_{11} - \tilde{C}_{12} \right)$$

(10.7)

It is seen from Equation (10.7) that the homogenized laminate behaves like a single material with hexagonal 6mm symmetry about the $x_3$ axis.

The use of expressions (10.7) will be demonstrated by means of a plane-stress example. In particular, consider a 21-ply laminate made of $BaTiO_3$ and PZT-6B piezoelectric layers with electroelastic properties shown in Table 10-1 [Rajapakse, 1997]. Here, $C_{ij}$ denote elastic coefficients, $e_{ij}$ denote piezoelectric constants, and $\varepsilon_{ij}$ denote dielectric permittivities. The piezoelectric and dielectric coefficients will be used in the next example. The top and bottom laminae have a thickness of 0.125 mm while the remaining laminae have a thickness of 0.25 mm. It is assumed that the in-plane dimensions of the laminate are such in order to justify the plane-stress assumption. The unit cell for this laminate is shown in Figure 10-3.

**Table 10-1:** Material Properties [Rajapakse, 1997]

| Material | $BaTiO_3$ | PZT-4 | PZT-6B |
|---|---|---|---|
| $C_{11}(\times 10^{10}\ Nm^{-2})$ | 15.0 | 13.9 | 16.8 |
| $C_{12}(\times 10^{10}\ Nm^{-2})$ | 6.6 | 7.78 | 6.0 |
| $C_{13}(\times 10^{10}\ Nm^{-2})$ | 6.6 | 7.43 | 6.0 |
| $C_{33}(\times 10^{10}\ Nm^{-2})$ | 14.6 | 11.5 | 16.3 |
| $C_{44}(\times 10^{10}\ Nm^{-2})$ | 4.4 | 2.56 | 2.71 |
| $e_{31}(Cm^{-2})$ | -4.35 | -5.2 | -0.9 |
| $e_{33}(Cm^{-2})$ | 17.5 | 15.1 | 7.1 |
| $e_{15}(Cm^{-2})$ | 11.4 | 12.7 | 4.6 |
| $\varepsilon_{11}(\times 10^{-9}\ Nm^{-2})$ | 9.87 | 6.45 | 3.6 |
| $\varepsilon_{33}(\times 10^{10}\ Nm^{-2})$ | 11.15 | 5.62 | 3.4 |

Figures (10-4) and (10-5) show through-the-thickness variation of the $C_{11}$ and $C_{44}$ elastic coefficients for the laminate in question, obtained through the application of Equation (10.7). Suppose now that the laminate is subjected to in-plane forces per unit length $N_x =$ 150 KPa m and $N_y = 50$ KPa m as well as to moments per unit length $M_x = 1.0$ KPa m$^2$ and $M_y = 0.5$ KPa m$^2$. Figure (10-6) shows that the mechanical strain in the x-direction $\varepsilon_x$ is virtually the same for the original laminate (calculated from the classical laminate theory) as for the homogenized one. Similar results pertain to the y-directed strain $\varepsilon_y$.

Figure (10-7) shows variation of the stress $\sigma_x$ through the thickness of the laminate which as expected is piecewise continuous, alongside corresponding values for the homogenized laminate. It is seen that the agreement between the two models is best at the inner plies where the actual stress variation from a PZT-6B layer to an adjacent BaTiO$_3$ layer is not very pronounced, and the maximum discrepancy occurs at the top and bottom plies. Similar considerations apply for $\sigma_y$ as is shown in Figure (10-8). It should be noted that for the all results pertinent to the actual laminate (Figures 10-6 to 10-8), the classical composite plate theory was used [Gibson, 1994; Reddy, 1997].
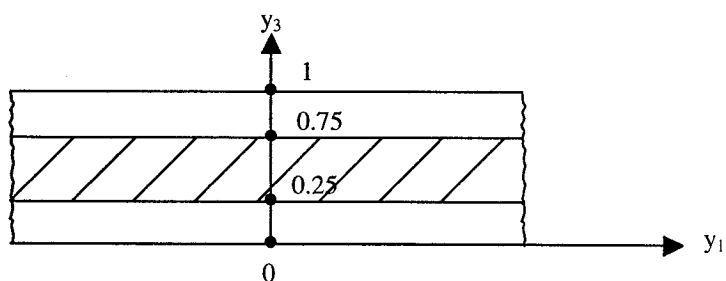
**Figure 10-3:** Unit cell for piezoelectric laminate
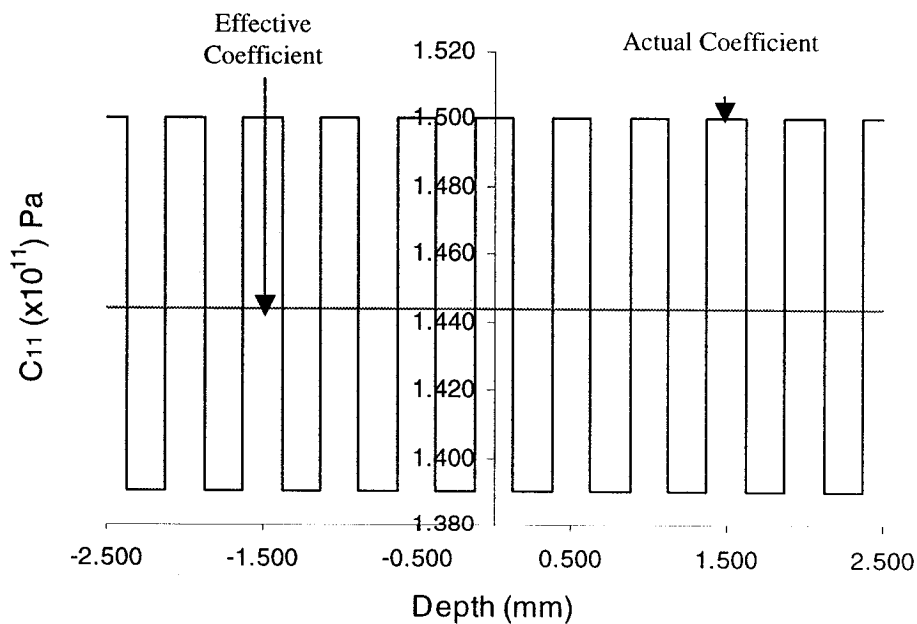
**Figure 10-4:** Variation of $C_{11}$ through thickness of laminate
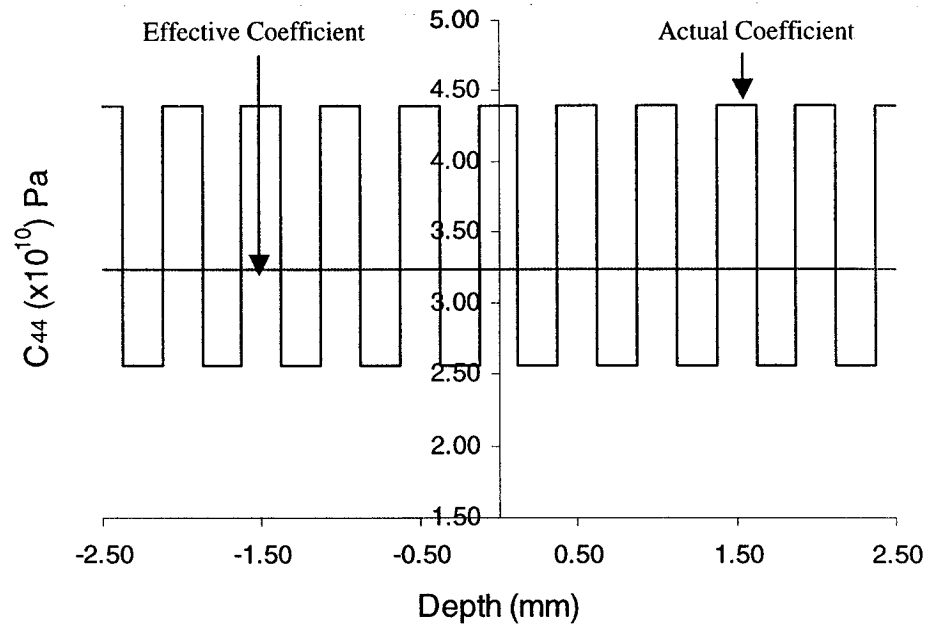
**Figure 10-5:** Variation of $C_{44}$ through thickness of laminate
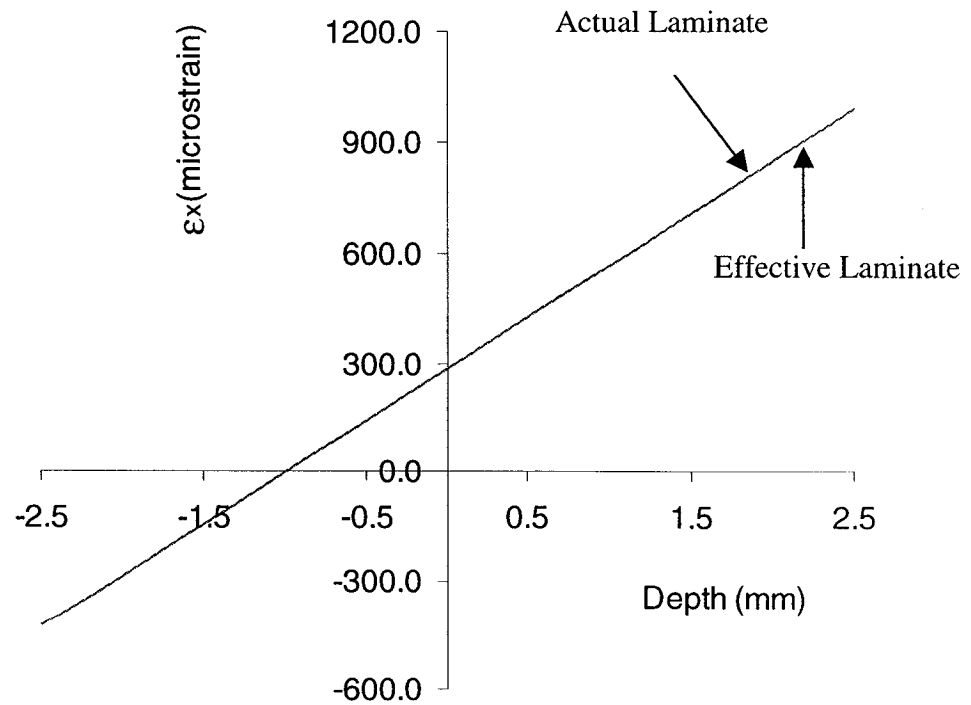


**Figure 10-6:** Variation of $\varepsilon_x$ through the thickness of laminate subjected to in-plane forces and moments
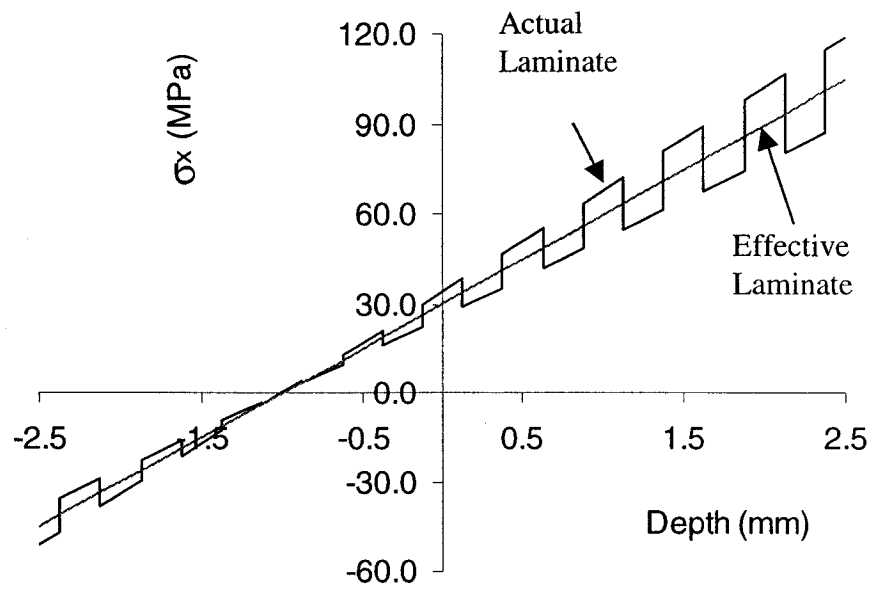
**Figure 10-7:** Variation of $\sigma_x$ through the thickness of laminate subjected to in-plane forces and moments
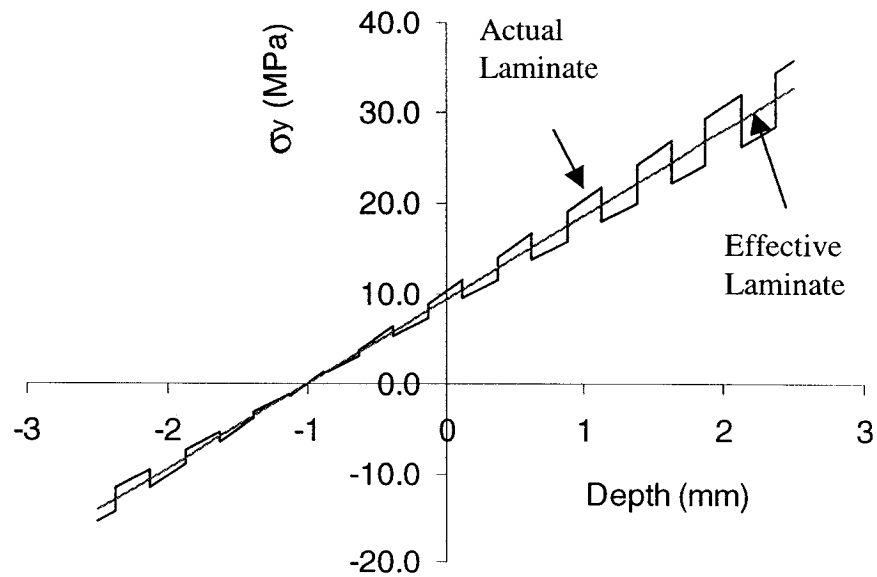


**Figure 10-8:** Variation of $\sigma_y$ through the thickness of laminate subjected to in-plane forces and moments

## 10.3 Effective Piezoelectric Coefficients for Laminated Structure

The next example to be considered is another laminate similar to the one discussed in the previous section, but consisting of alternate PZT-4 and BaTiO$_3$ laminae. The appropriate unit cell problem from Equation (9.41) is given by:

$$\frac{\partial}{\partial y_j}\left(C_{ijml}(\mathbf{y})\frac{\partial N_m^k(\mathbf{y})}{\partial y_l}\right) = \frac{\partial P_{ijk}}{\partial y_j} \tag{10.8}$$

The nature of the problem means that Equation (10.8) simplifies to:

$$\frac{d}{dy_3}\left(C_{i3m3}(y_3)\frac{dN_m^k(y_3)}{dy_3}\right) = \frac{dP_{i3k}}{dy_3} \tag{10.9}$$

Integrating Equation (10.9) results in the following expression:

$$C_{i3m3}\frac{dN_m^k}{dy_3} = P_{i3k} + B_{ik} \tag{10.10}$$

Here $B_{ik}$ are arbitrary constants. Integrating Equation (10.10) one more time with respect to $y_3$ results in:

$$\frac{dN_m^k}{dy_3} = C_{m3i3}^{-1}P_{i3k} + C_{m3i3}^{-1}B_{ik} \tag{10.11}$$

Before proceeding, and since the laminate under consideration in this section consists of plies with hexagonal symmetry, it is noteworthy to show how the structure of the piezoelectricity tensor (or any third order tensor for that matter) of a material with hexagonal symmetry compares to that of a completely anisotropic material.

$$\begin{bmatrix} P_{111} & P_{112} & P_{113} \\ P_{221} & P_{222} & P_{223} \\ P_{331} & P_{332} & P_{333} \\ P_{231} & P_{232} & P_{233} \\ P_{311} & P_{312} & P_{313} \\ P_{121} & P_{122} & P_{123} \end{bmatrix} = \begin{bmatrix} P_{11} & P_{21} & P_{31} \\ P_{12} & P_{22} & P_{32} \\ P_{13} & P_{23} & P_{33} \\ P_{14} & P_{24} & P_{34} \\ P_{15} & P_{25} & P_{35} \\ P_{16} & P_{26} & P_{36} \end{bmatrix} \tag{10.12a}$$

Equation (10.12a) shows the relationship between the actual tensorial coefficients of a third order tensor (such as the piezoelectric tensor) and the contracted coefficients

pertaining to an anisotropic material. The contracted notation is adopted in order to reduce computational effort. It must also be mentioned that many authors represent the contracted matrix in the following format instead:

$$
\begin{bmatrix}
P_{11} & P_{12} & P_{13} \\
P_{21} & P_{22} & P_{23} \\
P_{31} & P_{32} & P_{33} \\
P_{41} & P_{42} & P_{43} \\
P_{51} & P_{52} & P_{53} \\
P_{61} & P_{62} & P_{63}
\end{bmatrix}
\tag{10.12b}
$$

Irrespective of what format is adopted, the subscript which ranges from 1 to 3 represents the electric field strength, and the subscript with a range of values from 1 to 6 represents the strain field.

A material that exhibits hexagonal symmetry (6mm) has most of the terms in the piezoelectric matrix vanishing. In particular, for such a material, the matrix has the following format:

$$
\begin{bmatrix}
0 & 0 & P_{31} \\
0 & 0 & P_{31} \\
0 & 0 & P_{33} \\
0 & P_{15} & 0 \\
P_{15} & 0 & 0 \\
0 & 0 & 0
\end{bmatrix}
\tag{10.12c}
$$

Consequently, most of the $N_i^j$ functions will vanish. Returning to Equation (10.11), considering at the same time the matrix of Equation (10.12c), and bearing in mind the structure of the elasticity tensor of a material with hexagonal symmetry [Reddy, 1997], the following expressions are readily obtained:

$$
\frac{dN_1^1}{dy_3} = C_{13i3}^{-1} P_{i31} + C_{13i3}^{-1} B_{i1}
$$

$$
\therefore \frac{dN_1^1}{dy_3} = C_{1313}^{-1} P_{131} + C_{1313}^{-1} B_{11}
\tag{10.12d}
$$

Thus, from (10.12d), the final expression for $\dfrac{dN_1^1}{dy_3}$ is given by:

$$\frac{dN_1^1}{dy_3} = \frac{P_{131}}{C_{1313}} + \frac{B_{11}}{C_{1313}} \tag{10.12e}$$

Similarly,

$$\frac{dN_2^2}{dy_3} = C_{23i3}^{-1} P_{i32} + C_{23i3}^{-1} B_{i2}$$

$$\therefore \frac{dN_2^2}{dy_3} = C_{2323}^{-1} P_{232} + C_{2323}^{-1} B_{22} \tag{10.12f}$$

$$\therefore \frac{dN_2^2}{dy_3} = \frac{P_{232}}{C_{2323}} + \frac{B_{22}}{C_{2323}}$$

and

$$\frac{dN_3^3}{dy_3} = C_{33i3}^{-1} P_{i33} + C_{33i3}^{-1} B_{i3}$$

$$\therefore \frac{dN_3^3}{dy_3} = C_{3333}^{-1} P_{333} + C_{3333}^{-1} B_{33} \tag{10.12g}$$

$$\therefore \frac{dN_3^3}{dy_3} = \frac{P_{333}}{C_{3333}} + \frac{B_{33}}{C_{3333}}$$

The derivatives of the remaining functions all vanish. For example consider the following:

$$\frac{dN_1^2}{dy_3} = C_{13i3}^{-1} P_{i32} + C_{13i3}^{-1} B_{i2}$$

$$\therefore \frac{dN_1^2}{dy_3} = C_{1313}^{-1} B_{12} \tag{10.12h}$$

Integrating the latter expression with respect to $y_3$, gives on account of the periodicity of the $N_1^2$ function the following result:

$$C_{1313}^{-1} B_{12} = 0 \quad \Rightarrow B_{12} = 0$$

$$\therefore \frac{dN_1^2}{dy_3} = 0 \tag{10.12i}$$

Similar considerations lead to the following result:

$$\frac{dN_1^3}{dy_3} = \frac{dN_2^1}{dy_3} = \frac{dN_2^3}{dy_3} = \frac{dN_3^1}{dy_3} = \frac{dN_3^2}{dy_3} = 0 \qquad (10.12j)$$

The non-vanishing constants $B_{jj}$ (no summation on j) can now be determined readily. Firstly, from Equation (10.12e) one gets:

$$0 = \int \frac{P_{131}}{C_{1313}} dy_3 + \int \frac{B_{11}}{C_{1313}} dy_3$$

$$\therefore -\left\langle P_{131} C_{1313}^{-1} \right\rangle = B_{11} \left\langle C_{1313}^{-1} \right\rangle \qquad (10.13a)$$

$$\therefore B_{11} = \frac{-\left\langle P_{131} C_{1313}^{-1} \right\rangle}{\left\langle C_{1313}^{-1} \right\rangle}$$

Similarly, from Equations (10.12f) and (10.12g) the remaining non-vanishing constants are:

$$B_{22} = \frac{-\left\langle P_{232} C_{2323}^{-1} \right\rangle}{\left\langle C_{2323}^{-1} \right\rangle}$$

$$\qquad\qquad (10.13b)$$

$$B_{33} = \frac{-\left\langle P_{333} C_{3333}^{-1} \right\rangle}{\left\langle C_{3333}^{-1} \right\rangle}$$

These expressions then may be substituted back into Equations (10.12e), (10.12f), and (10.12g) to determine the $N_i^j$ functions. However, the objective here is to determine the effective piezoelectric coefficients, and for those, one does not need the $N_i^j$ functions, but rather their derivatives. From Equation (9.42), the effective piezoelectric coefficients are given by:

$$\tilde{P}_{ijk} = \frac{1}{|Y|} \int_Y \left( P_{ijk}(y) - C_{ijmn}(y) \frac{\partial N_m^k}{\partial y_n} \right) dv \qquad (10.14a)$$

For the problem at hand, Equation (10.14a) reduces to:

$$\tilde{P}_{ijk} = \int_0^1 \left( P_{ijk}(y_3) - C_{ijmn}(y_3) \frac{dN_m^k}{dy_3} \right) dy_3 \qquad (10.14b)$$

The effective moduli are therefore determined from Equation (10.14b).Thus, from Equations (10.12g), (10.13b), and (10.14b) the following result is obtained:

$$\tilde{P}_{113} = \int_0^1 \left( P_{113} - C_{11m3} \frac{dN_m^3}{dy_3} \right) dy_3$$

$$= \int_0^1 \left( P_{113} - C_{1133} \frac{dN_3^3}{dy_3} \right) dy_3$$

$$= \int_0^1 \left( P_{113} - C_{1133} \left\{ \frac{P_{333}}{C_{3333}} - \frac{\langle P_{333} C_{3333}^{-1} \rangle}{\langle C_{3333}^{-1} \rangle C_{3333}} \right\} \right) dy_3 \qquad (10.15a)$$

$$\tilde{P}_{113} = \langle P_{113} \rangle - \langle C_{1133} C_{3333}^{-1} P_{333} \rangle + \frac{\langle C_{1133} C_{3333}^{-1} \rangle \langle C_{3333}^{-1} P_{333} \rangle}{\langle C_{3333}^{-1} \rangle}$$

Similarly, from Equations (10.12g), (10.13b) and (10.14b) one obtains:

$$\tilde{P}_{333} = \int_0^1 \left( P_{333} - C_{33m3} \frac{dN_m^3}{dy_3} \right) dy_3$$

$$= \int_0^1 \left( P_{333} - C_{3333} \frac{dN_3^3}{dy_3} \right) dy_3$$

$$= \int_0^1 \left( P_{333} - C_{3333} \left\{ \frac{P_{333}}{C_{3333}} - \frac{\langle P_{333} C_{3333}^{-1} \rangle}{\langle C_{3333}^{-1} \rangle C_{3333}} \right\} \right) dy_3 \qquad (10.15b)$$

$$\tilde{P}_{333} = \frac{\langle C_{3333}^{-1} P_{333} \rangle}{\langle C_{3333}^{-1} \rangle}$$

From Equations (10.12f), (10.13b) and (10.14b), one obtains:

$$\tilde{P}_{232} = \int_0^1 \left( P_{232} - C_{23m3} \frac{dN_m^2}{dy_3} \right) dy_3$$

$$= \int_0^1 \left( P_{232} - C_{2323} \frac{dN_2^2}{dy_3} \right) dy_3$$

$$= \int_0^1 \left( P_{232} - C_{2323} \left\{ \frac{P_{232}}{C_{2323}} - \frac{\langle P_{232} C_{2323}^{-1} \rangle}{\langle C_{2323}^{-1} \rangle C_{2323}} \right\} \right) dy_3 \qquad (10.15c)$$

$$\tilde{P}_{232} = \frac{\langle C_{2323}^{-1} P_{232} \rangle}{\langle C_{2323}^{-1} \rangle}$$

Finally, it may be shown easily that:

$$\tilde{P}_{223} = \tilde{P}_{113}$$
$$\tilde{P}_{131} = \tilde{P}_{232}$$

(10.15d)

Collectively, the effective piezoelectric coefficients (in contracted notation) for such a laminate consisting of laminae with hexagonal symmetry are given by:

$$\tilde{P}_{31} = \langle P_{31} \rangle - \langle C_{13} C_{33}^{-1} P_{33} \rangle + \langle C_{13} C_{33}^{-1} \rangle \langle P_{33} C_{33}^{-1} \rangle \langle C_{33}^{-1} \rangle^{-1}, \quad \tilde{P}_{32} = \tilde{P}_{31}$$

$$\tilde{P}_{33} = \langle P_{33} C_{33}^{-1} \rangle \langle C_{33}^{-1} \rangle^{-1}, \quad \tilde{P}_{42} = \langle P_{42} C_{44}^{-1} \rangle \langle C_{33}^{-1} \rangle^{-1}, \quad \tilde{P}_{51} = \tilde{P}_{42}$$

(10.16)

Thus, the homogenized laminate behaves like a single material with hexagonal 6mm symmetry about the $x_3$ axis. The pertinent matrix is of the form shown in Equation (10.17).

$$\begin{bmatrix} 0 & 0 & \tilde{P}_{31} \\ 0 & 0 & \tilde{P}_{31} \\ 0 & 0 & \tilde{P}_{33} \\ 0 & \tilde{P}_{15} & 0 \\ \tilde{P}_{15} & 0 & 0 \\ 0 & 0 & 0 \end{bmatrix}$$

(10.17)

The use of Equation (10.16) will be demonstrated by determining the natural frequencies of a piezoelectric transducer in the form of a thick laminate with alternating PZT-4 and BaTiO$_3$ laminae. The transducer has 20 layers of 1 mm thickness each, with the width and depth of the transducer both equal to 8 cm. An electrode attached to the top surface of the laminate is grounded. With the help of finite element techniques, the first few natural frequencies of this laminated transducer are compared with the corresponding frequencies of a homogenized transducer with elastic coefficients determined by means of Equation (10.7) and piezoelectric coefficients determined by means of Equation (10.16). In other words two different numerical models are employed. The first (laminated model) is a model of the laminate in its actual form with the alternate PZT-4 and BaTiO$_3$ laminae. As expected, the material has step-wise continuous properties given in Table 10-1. The second (homogenized model) is a model of a structure with the same macroscopic dimensions but with uniform elastic and piezoelectric properties as

determined by Equations (10.7) and (10.16). The dielectric permittivity of the homogenized laminate was calculated in the same manner as the homogenized $2^{nd}$ order thermal expansion tensor explained in the next section. The unit cell for this laminate is given in Figure 10-9. The variation of the $P_{31}$ and $P_{42}$ piezoelectric coefficients through the thickness of the lamina is shown in Figures 10-10 and 10-11.

The geometry of both models allows us to take advantage of their quarter symmetry in order to reduce the number of elements and hence the computational effort involved. As well, consistency considerations necessitate the use of the same overall number of elements for both the actual laminate and the homogenized structure. Table 10-2 compares the first 5 natural frequencies from the laminated and homogenized models obtained by a finite element program. It can be seen that the two models predict similar results differing by at most 1%. Figures 10-12 and 10-13 show the mode shape for the $2^{nd}$ and $5^{th}$ modes. The mode shapes are the same for both the laminated and the homogenized models.
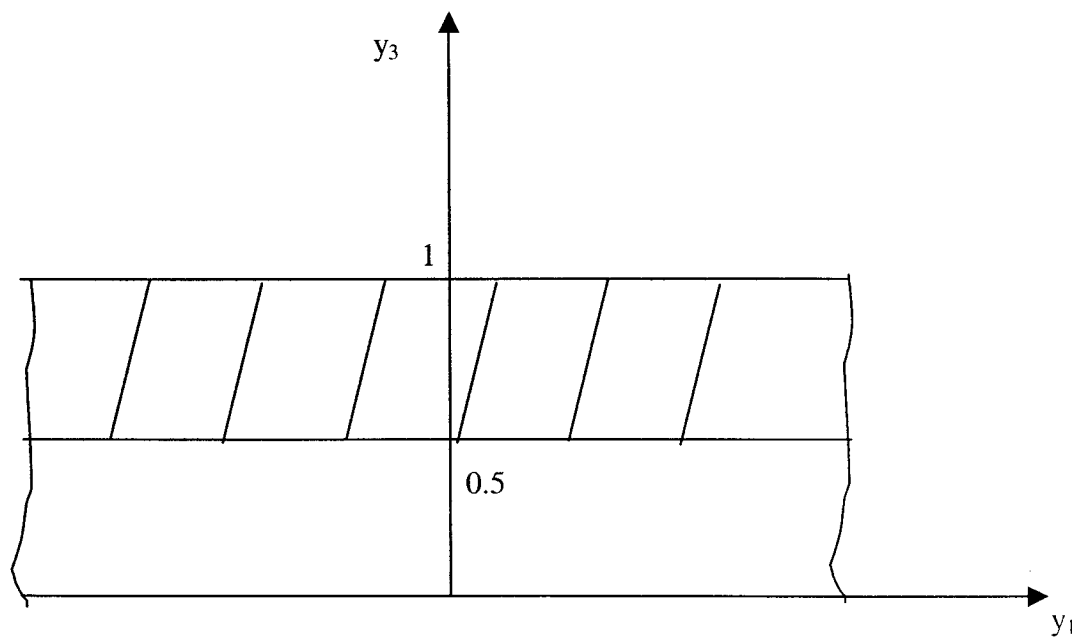


**Figure 10-9:** Unit cell for piezoelectric laminate
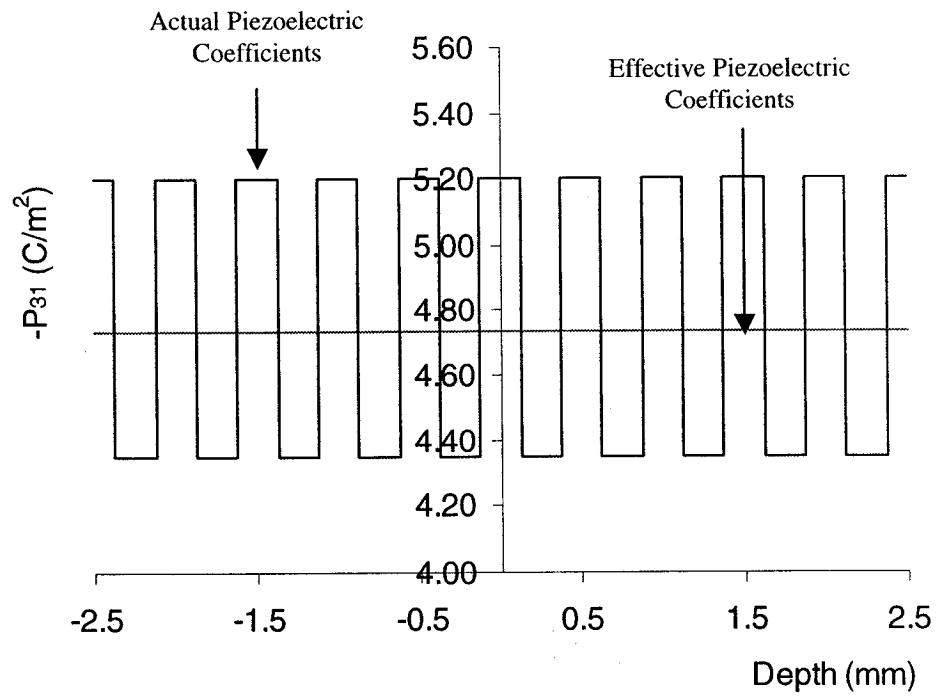
**Figure 10-10:** Variation of $-P_{31}$ through thickness of laminate
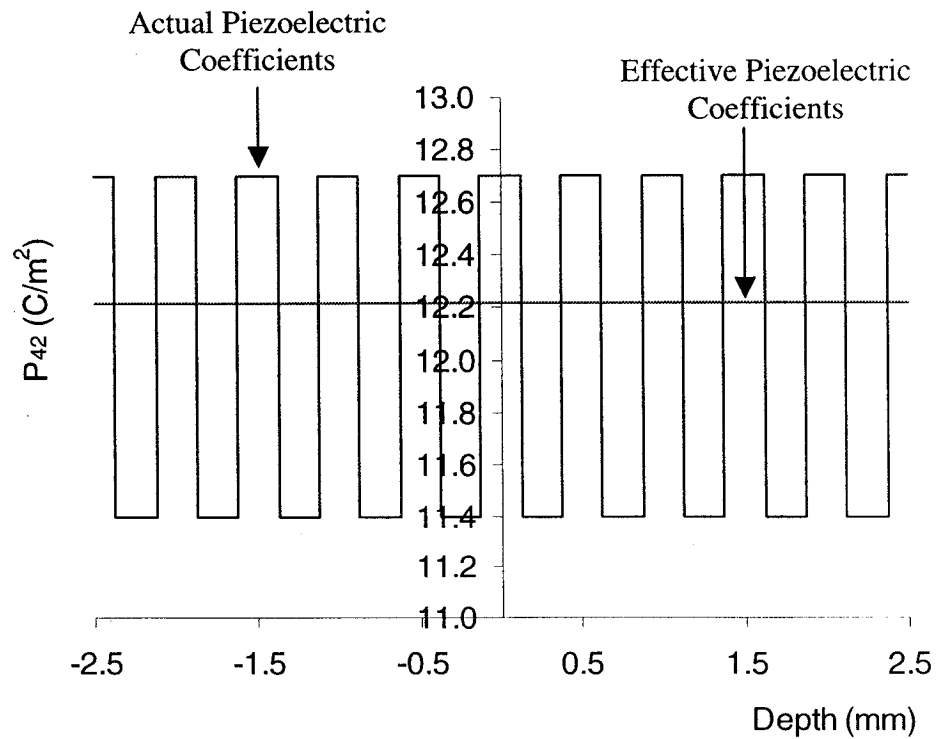


**Figure 10-11:** Variation of $P_{42}$ through thickness of laminate

**Table 10-2:** Natural Frequencies pertaining to the laminated and homogenized models

| Natural Frequency Laminate (kHz) | Natural Frequency Homogenized (kHz) |
|---|---|
| 9.74 | 9.71 |
| 12.98 | 12.85 |
| 20.94 | 20.88 |
| 24.32 | 24.25 |
| 24.65 | 24.58 |
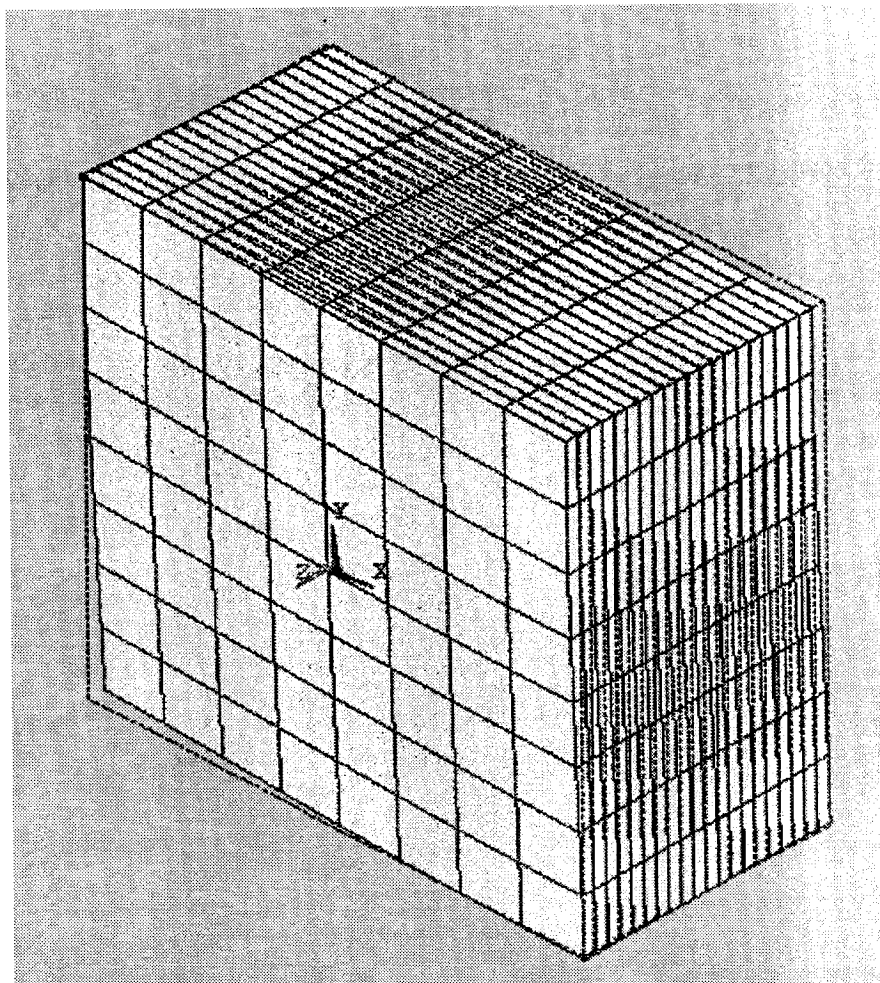
**Figure 10-12:** $2^{nd}$ mode of free vibration (original laminate or homogenized model)
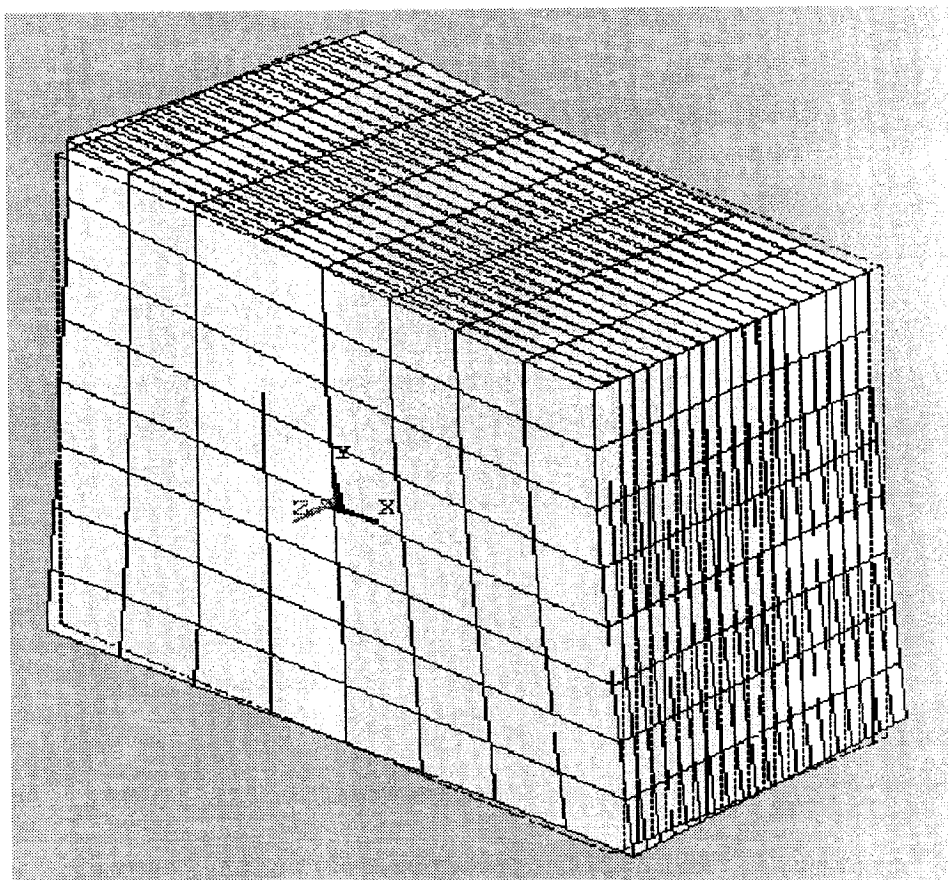
**Figure 10-13:** 5th mode of free vibration (original laminate or homogenized model)

## 10.4 Effective Thermal Expansion Coefficients for Laminated Structure

In this section the effective thermal expansion coefficients will be determined. The pertinent unit cell problem as given by Equation (9.41) is:

$$\frac{\partial}{\partial y_j}\left(C_{ijkl}(y)\frac{\partial M_k(y)}{\partial y_l}\right) = \frac{\partial K_{ij}}{\partial y_j} \tag{10.18}$$

Because of the nature of the unit cell, this equation simplifies to:

$$\frac{d}{dy_3}\left(C_{i3k3}(y_3)\frac{dM_k(y_3)}{dy_3}\right) = \frac{dK_{i3}}{dy_3} \tag{10.19}$$

Integrating Equation (10.19) results in the following expression:

$$C_{i3k3}(y_3)\frac{dM_k(y_3)}{dy_3} = K_{i3} + D_i \tag{10.20}$$

Here $D_i$ are arbitrary constants. Integrating Equation (10.20) one more time with respect to $y_3$ results in:

$$\frac{dM_k}{dy_3} = C_{k3i3}^{-1}K_{i3} + C_{k3i3}^{-1}D_i \tag{10.21}$$

In this section, the example that will be considered will involve composites with transversely isotropic laminae. As such, it will be important for subsequent work to show the nature of the thermal expansion tensor for such a material.

$$\begin{bmatrix} K_{11} & K_{12} & K_{13} \\ K_{12} & K_{22} & K_{23} \\ K_{13} & K_{23} & K_{33} \end{bmatrix} = \begin{bmatrix} K_{11} \\ K_{22} \\ K_{33} \\ K_{23} \\ K_{31} \\ K_{12} \end{bmatrix} = \begin{bmatrix} K_1 \\ K_2 \\ K_3 \\ K_4 \\ K_5 \\ K_6 \end{bmatrix} \tag{10.22}$$

Equation (10.22) shows the thermal expansion tensor for a general material with no symmetry. For transversely isotropic materials, such as for example fiber-reinforced laminae, the thermal expansion tensor ( and any second-order tensor) has the following format when referred to its principal coordinate system:

$$
\begin{bmatrix} K_{11} & 0 & 0 \\ 0 & K_{22} & 0 \\ 0 & 0 & K_{22} \end{bmatrix} = \begin{bmatrix} K_{11} \\ K_{22} \\ K_{22} \\ 0 \\ 0 \\ 0 \end{bmatrix} = \begin{bmatrix} K_1 \\ K_2 \\ K_2 \\ 0 \\ 0 \\ 0 \end{bmatrix}
\tag{10.23}
$$

However, most composite laminates, have laminae that are not all oriented in the same direction. For such a laminate, relevant parameters are expressed with respect to a coordinate system that does not coincide with the principal coordinate system of the laminae. The thermal expansion tensor for such a material has the same non-zero terms as a monoclinic material and has the following format:

$$
\begin{bmatrix} K_{xx} & K_{xy} & 0 \\ K_{xy} & K_{yy} & 0 \\ 0 & 0 & K_{zz} \end{bmatrix} = \begin{bmatrix} K_{xx} \\ K_{yy} \\ K_{zz} \\ 0 \\ 0 \\ K_{xy} \end{bmatrix} = \begin{bmatrix} K_x \\ K_y \\ K_z \\ 0 \\ 0 \\ K_{xy} \end{bmatrix}
\tag{10.24}
$$

Returning to Equation (10.21) and proceeding in a similar manner to the previous two unit cell problems, one obtains:

$$
\int_0^1 C_{k3i3}^{-1} K_{i3} dy_3 = -\int_0^1 C_{k3i3}^{-1} D_i dy_3
$$

$$
\therefore \left\langle C_{k3i3}^{-1} K_{i3} \right\rangle = -\left\langle C_{i3k3}^{-1} \right\rangle D_i
\tag{10.25}
$$

$$
\Rightarrow D_i = -\left\langle C_{i3k3}^{-1} \right\rangle^{-1} \left\langle C_{k3i3}^{-1} K_{i3} \right\rangle.
$$

The expression for $D_i$ from Equation (10.25) is then substituted into Equation (10.21) to obtain:

$$
\frac{dM_k}{dy_3} = C_{k3i3}^{-1} K_{i3} - C_{k3n3}^{-1} \left\langle C_{n3m3}^{-1} \right\rangle^{-1} \left\langle C_{m3s3}^{-1} K_{s3} \right\rangle
\tag{10.26}
$$

Having obtained the $M_i$ functions, one subsequently resorts to the general expression for the effective thermal expansion coefficients from Equation (9.42):

$$\tilde{K}_{ij} = \frac{1}{|Y|} \int_Y \left( K_{ij}(\mathbf{y}) - C_{ijmn}(\mathbf{y}) \frac{\partial M_m}{\partial y_n} \right) dv \qquad (10.27)$$

The first order of business is to transform Equation (10.27) according to:

$$\tilde{K}_{ij} = \int_0^1 \left( K_{ij}(y_3) - C_{ijm3}(y_3) \frac{dM_m}{dy_3} \right) dy_3 \qquad (10.28)$$

Substitution of Equation (10.26) into Equation (10.28) results in the following expression for the effective thermal expansion coefficients:

$$\tilde{K}_{ij} = \left\langle K_{ij} \right\rangle - \left\langle C_{ijm3} C_{m3n3}^{-1} K_{n3} \right\rangle + \left\langle C_{ijm3} C_{m3n3}^{-1} \right\rangle \left\langle C_{n3p3}^{-1} \right\rangle^{-1} \left\langle C_{p3q3}^{-1} K_{q3} \right\rangle \qquad (10.29)$$

For a laminate consisting of transversely isotropic laminae with the reinforcing fibers oriented along arbitrary directions, the effective thermal expansion coefficients (in condensed format) are readily determined from Equation (10.29) to be as follows:

$$\tilde{K}_1' = \left\langle K_1' \right\rangle - \left\langle C_{13}' \left(C_{33}'\right)^{-1} K_3' \right\rangle + \left\langle C_{13}' \left(C_{33}'\right)^{-1} \right\rangle \left\langle K_3' \left(C_{33}'\right)^{-1} \right\rangle \left\langle \left(C_{33}'\right)^{-1} \right\rangle^{-1}$$

$$\tilde{K}_2' = \left\langle K_2' \right\rangle - \left\langle C_{23}' \left(C_{33}'\right)^{-1} K_3' \right\rangle + \left\langle C_{23}' \left(C_{33}'\right)^{-1} \right\rangle \left\langle K_3' \left(C_{33}'\right)^{-1} \right\rangle \left\langle \left(C_{33}'\right)^{-1} \right\rangle^{-1}$$

$$\tilde{K}_6' = \left\langle K_6' \right\rangle - \left\langle C_{36}' \left(C_{33}'\right)^{-1} K_3' \right\rangle + \left\langle C_{36}' \left(C_{33}'\right)^{-1} \right\rangle \left\langle K_3' \left(C_{33}'\right)^{-1} \right\rangle \left\langle \left(C_{33}'\right)^{-1} \right\rangle^{-1}$$

$$\tilde{K}_3' = \left\langle K_3' \left(C_{33}'\right)^{-1} \right\rangle \left\langle \left(C_{33}'\right)^{-1} \right\rangle^{-1}$$

(10.30)

In Equation (10.30) primed coefficients denote quantities that are referenced with respect to an arbitrary coordinate system i.e.

$$\tilde{K}_1' = \tilde{K}_{xx}, \quad \tilde{K}_2' = \tilde{K}_{yy}, \quad \tilde{K}_3' = \tilde{K}_{zz}, \quad \tilde{K}_6' = \tilde{K}_{xy}, \qquad (10.31)$$

etc. It should also be reiterated at this point that the $K_{ij}$ coefficients referred to here relate stress and temperature as shown in Equation (8.42) or Equation (9.14d) and can be determined from the double contraction of the elastic coefficients $C_{ijkl}$ and the perhaps more familiar $\alpha_{ij}$ expansion coefficients (which relate strain with temperature). Thus $K_{ij} = C_{ijkl}\alpha_{kl}$.

For illustrative purposes, we will consider a 21-ply laminate consisting of alternating $0°$ and $90°$ AS/3501 graphite/epoxy plies with material properties given in Tables 10-3 and 10-4 [Gibson, 1994].

**Table 10-3:** Mechanical properties [Gibson, 1994]

| Material | $E_1$ (GPa) | $E_2$ (GPa) | $G_{12}$ (GPa) | $\nu_{12}$ |
|---|---|---|---|---|
| AS/3501 graphite/epoxy | 138 | 9.0 | 6.9 | 0.3 |
| Scotchply® E-glass/epoxy | 38.6 | 8.27 | 4.14 | 0.26 |

**Table 10-4:** Hygrothermal coefficients [Gibson, 1994]

| Material | Thermal Expansion Coefficients ($10^{-6}$ m/m)/°C | | Hygroscopic Expansion Coefficients(m/m) | |
|---|---|---|---|---|
| Property | $\alpha_1$ | $\alpha_2$ | $\beta_1$ | $\beta_2$ |
| AS/3501 graphite/epoxy | 0.88 | 31 | 0.09 | 0.30 |
| Scotchply® E-glass/epoxy | 6.3 | 20.0 | 0.014 | 0.29 |

As mentioned at the beginning of this section, when a transversely isotropic lamina is not referred to its principal material coordinate system, the number and location of the non-zero terms of the matrix of elastic coefficients coincide with those of a monoclinic material. This matrix has the following form [Reddy, 1997]:

$$\begin{bmatrix} C_{11} & C_{12} & C_{13} & 0 & 0 & C_{16} \\ C_{12} & C_{22} & C_{23} & 0 & 0 & C_{26} \\ C_{13} & C_{23} & C_{33} & 0 & 0 & C_{36} \\ 0 & 0 & 0 & C_{44} & C_{45} & 0 \\ 0 & 0 & 0 & C_{45} & C_{55} & 0 \\ C_{16} & C_{26} & C_{36} & 0 & 0 & C_{66} \end{bmatrix}$$

(10.32)

Consequently, the expressions in Equation (10.7) are not valid in this case, and in order to calculate the effective elastic coefficients, one has to resort to the general equation in (10.6) which of course is valid for all types of symmetry. The results obtained and shown in Equation (10.33) are the same as those determined for the case of layered media by Chou et al. [1972] (see also Bogdanovich, 1997) who used a completely different technique based on a combination of Voigt's hypothesis, that assumes that all the strain components for an anisotropic medium are uniform, and Reuss's hypothesis which assumes that all the stress components are uniform.

$$\tilde{C}_{ij} = \left\langle C_{ij} \right\rangle - \left\langle C_{i3}C_{j3}C_{33}^{-1} \right\rangle + \left\langle C_{i3}C_{33}^{-1} \right\rangle \left\langle C_{j3}C_{33}^{-1} \right\rangle \left\langle C_{33}^{-1} \right\rangle^{-1} \quad \text{for } i,j = 1,2,3,6$$

$$\tilde{C}_{ij} = \frac{\left\langle C_{ij}\mathfrak{R}^{-1} \right\rangle}{\left\langle C_{44}\mathfrak{R}^{-1} \right\rangle \left\langle C_{55}\mathfrak{R}^{-1} \right\rangle - \left\langle C_{45}\mathfrak{R}^{-1} \right\rangle^2} \quad \text{for } i,j = 4,5 \qquad (10.33)$$

$$\text{where } \mathfrak{R} = C_{44}C_{55} - C_{45}^2$$

Thus the effective elastic properties for the graphite/epoxy laminate are given by Equation (10.33) and the effective thermal expansion coefficients are given by Equation (10.30). The variation of typical thermal expansion coefficients through the thickness of the laminate is given in Figures 10-14 and 10-15

Comparing now the thermal strain induced in the original laminate caused by a temperature increase of 100°C with the corresponding strain from the homogenized laminate, one finds out that the x-directed strain, $\varepsilon_x$ for both models is the same and equals 319 microstrain. The same conclusion pertains to $\varepsilon_y$ which equals $\varepsilon_x$ (see Figure 10-16). Thus strains are predicted very accurately by the model.
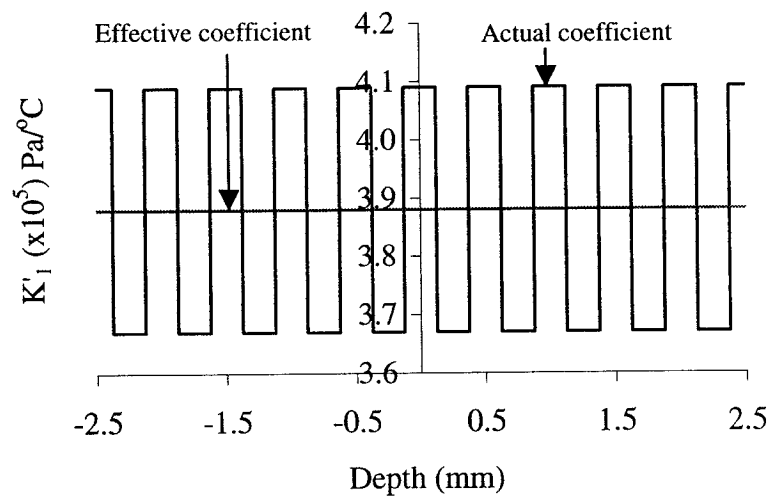
**Figure 10-14:** Variation of thermal expansion coefficient $K_1'$ ($K_{xx}$) through the thickness of laminate composed of graphite/epoxy layers, alongside effective value $\tilde{K}_1'$
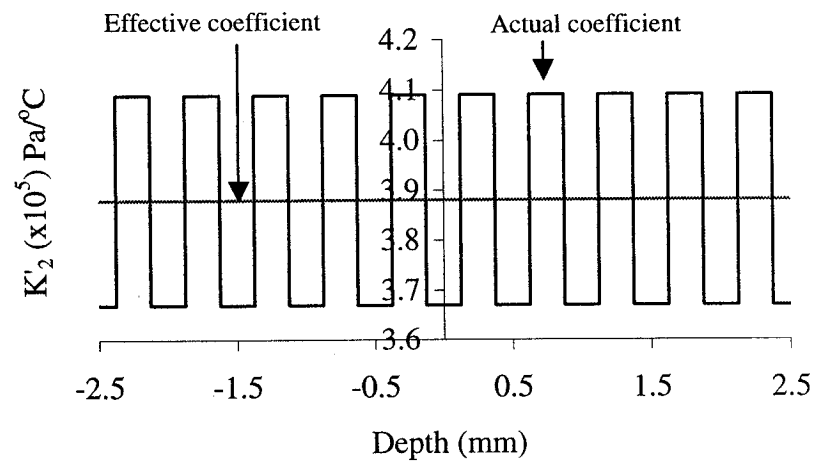


**Figure 10-15:** Variation of thermal expansion coefficient $K_2'$ ($K_{yy}$) through the thickness of laminate composed of graphite/epoxy layers, alongside effective value $\tilde{K}_2'$
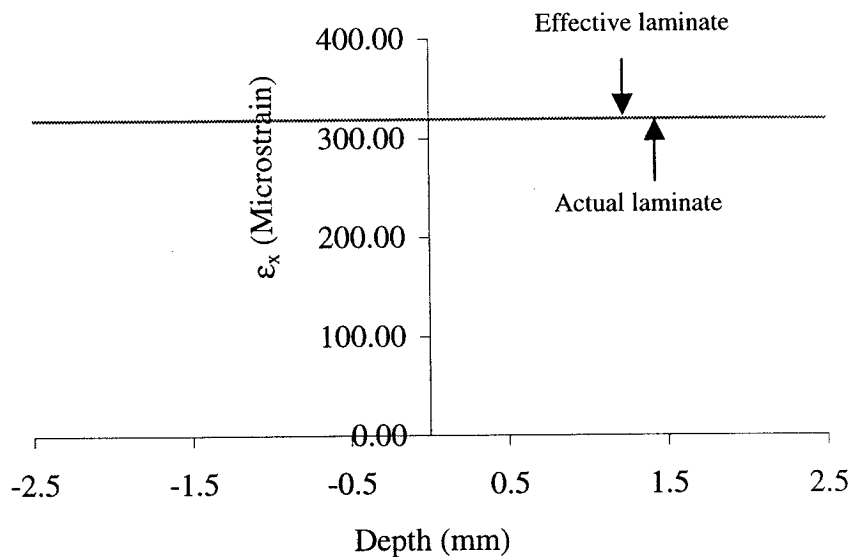
**Figure 10-16:** Variation of thermal strain induced in a laminate due to a temperature increase of $100^\circ$ C

## 10.5 Effective Hygroscopic Expansion Coefficients for Laminated Structure

From the unit cell problem in Equation (9.41) one notices that the effective hygroscopic expansion coefficients are obtained in the same way as the thermal expansion coefficients. Thus,

$$\tilde{B}_{ij} = \left\langle B_{ij} \right\rangle - \left\langle C_{ijm3}C_{m3n3}^{-1}B_{n3} \right\rangle + \left\langle C_{ijm3}C_{m3n3}^{-1} \right\rangle \left\langle C_{n3p3}^{-1} \right\rangle^{-1} \left\langle C_{p3q3}^{-1}B_{q3} \right\rangle \tag{10.34}$$

which is similar to Equation (10.29). For a laminate consisting of transversely isotropic laminae with the reinforcing fibers oriented along arbitrary directions, the homogenized hygroscopic expansion coefficients (in condensed format) are readily determined (39b) to be as follows:

$$\tilde{B}_1' = \left\langle B_1' \right\rangle - \left\langle C_{13}'\left(C_{33}'\right)^{-1}B_3' \right\rangle + \left\langle C_{13}'\left(C_{33}'\right)^{-1} \right\rangle\left\langle B_3'\left(C_{33}'\right)^{-1} \right\rangle\left\langle \left(C_{33}'\right)^{-1} \right\rangle^{-1}$$

$$\tilde{B}_2' = \left\langle B_2' \right\rangle - \left\langle C_{23}'\left(C_{33}'\right)^{-1}B_3' \right\rangle + \left\langle C_{23}'\left(C_{33}'\right)^{-1} \right\rangle\left\langle B_3'\left(C_{33}'\right)^{-1} \right\rangle\left\langle \left(C_{33}'\right)^{-1} \right\rangle^{-1}$$

$$\tilde{B}_6' = \left\langle B_6' \right\rangle - \left\langle C_{36}'\left(C_{33}'\right)^{-1}B_3' \right\rangle + \left\langle C_{36}'\left(C_{33}'\right)^{-1} \right\rangle\left\langle B_3'\left(C_{33}'\right)^{-1} \right\rangle\left\langle \left(C_{33}'\right)^{-1} \right\rangle^{-1}$$

$$\tilde{B}_3' = \left\langle B_3'\left(C_{33}'\right)^{-1} \right\rangle\left\langle \left(C_{33}'\right)^{-1} \right\rangle^{-1}$$

$$(10.35)$$

As for the thermal expansion coefficients, the $B_{ij}$ (which relate stress with moisture percent content) are given by the double contraction of the elastic coefficients $C_{ijkl}$ and the $\beta_{ij}$ coefficients (which relate strain with moisture percent content). Thus $B_{ij} = C_{ijkl}\beta_{kl}$.

Consider now a 21-ply laminate consisting of alternating $+45°$ and $-45°$ Scotchply® E-glass/epoxy plies with material properties given in Tables 10-3 and 10-4. The homogenized laminate has elastic coefficients given by Equation (10-33) and moisture expansion coefficients readily determined from (10-35). The variation of the moisture expansion coefficients through the thickness of the laminate is similar to that pertaining to the thermal expansion coefficients. A typical example is given in Figure 10-17. If now one compares the strain induced in the original laminate due to an increase in moisture content by 1% with the corresponding strain from the homogenized laminate, one observes that the two models predict the same value of 700 $\mu\varepsilon$ for both $\varepsilon_x$ and $\varepsilon_y$ (Figure 10-18).
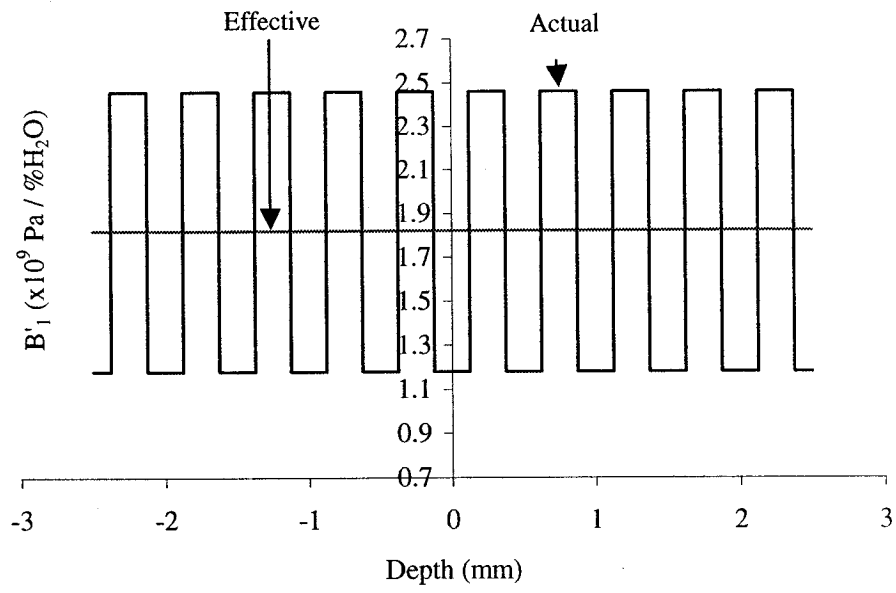
**Figure 10-17:** Variation of hygroscopic expansion coefficient $B_1'$ ($B_{xx}$) through the thickness of laminate composed of E-glass/epoxy layers, alongside effective value $\widetilde{B}_1'$
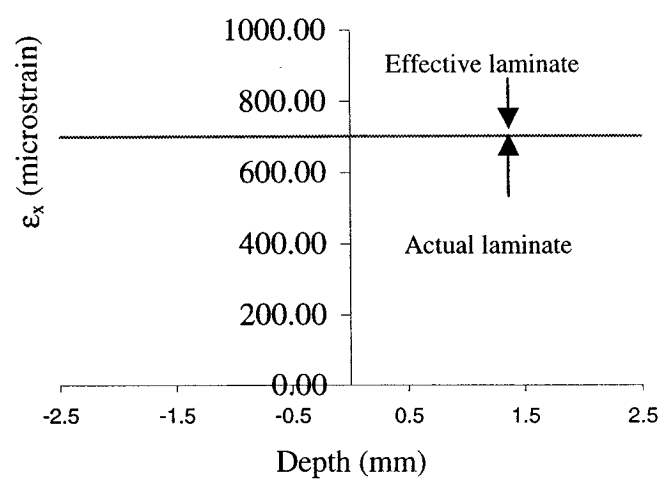


**Figure 10-18:** Variation of strain induced in a laminate due to a 1% increase in moisture concentration

# 11.0 MATHEMATICAL MODELS FOR SMART COMPOSITE PLATES WITH RAPIDLY VARYING THICKNESS

## 11.1 Introduction

In this chapter asymptotic homogenization models for smart composite plates with rapidly varying thickness and periodically arranged actuators are derived, and effective elastic, actuation, thermal expansion and hygroscopic expansion coefficients are obtained. The general symmetry properties of the effective actuation coefficients are obtained, with the implication that it suffices to find the solutions of the purely elastic local problem in conjunction with the constituent properties, in order to derive the effective actuation coefficients. It is shown that the original problem for the regularly non-homogeneous smart composite plate with rapidly oscillating thickness reduces to a system of eight simpler types of problem. It is precisely these "unit-cell" problems that enable the determination of the aforementioned effective coefficients and subsequently the strain and stress fields. In the limiting case of a thin elastic plate of uniform thickness, the derived model is shown to converge to the familiar classical plate model. In Chapter 12, the theory is illustrated by means of examples pertaining to a thin smart plate of uniform thickness and a wafer-type smart composite plate reinforced with smart ribs oriented along one or both of the tangential directions of the plate.

The mathematical model of a composite plate with rapidly varying thickness (including thermal effects) was developed by Kalamkarov [1992]. In this chapter the same technique is applied to a smart composite plate that also has a large number of embedded actuators. This problem has not yet been analyzed. As well, moisture absorption effects are also considered in order to make the model more comprehensive.

## 11.2 Problem Formulation

Consider a thin smart layer representing an inhomogeneous solid with wavy surfaces and containing a large number of periodically-arranged actuators as shown in Figure 11-1. This periodic structure is obtained by repeating a certain small unit cell $\Omega_\delta$ in the $x_1$-$x_2$ plane. All three pertinent coordinates are assumed to have been made dimensionless by dividing by a certain characteristic dimension of the body, L. Note that the shape of the lateral surface of the layer is determined by the type of the surface reinforcement, for example by shape of stiffeners or reinforcing ribs. In particular, this surface can be planar if surface reinforcements are not used.

The unit cell of the problem is defined by the following inequalities (see Figure 11-1),

$$\left\{ -\frac{\delta h_1}{2} < x_1 < \frac{\delta h_1}{2}, \quad -\frac{\delta h_2}{2} < x_2 < \frac{\delta h_2}{2}, \quad S^- < x_3 < S^+ \right\}, \quad \text{where}$$

$$S^\pm = \pm\frac{\delta}{2} \pm \delta F^\pm\left(\frac{x_1}{\delta h_1}, \frac{x_2}{\delta h_2}\right)$$

(11.1)

and the elastic deformation of this smart structure is characterized by the following system:

$$\frac{\partial \sigma_{ij}}{\partial x_j} - P_i = 0 \quad \text{where,}$$

$$\sigma_{ij} = C_{ijkl}\left\{ e_{kl} - d_{klm}^{(r)}R_m - \alpha_{kl}^{(\theta)}T - \beta_{kl}^{(c)}C \right\} \quad \text{and}$$

(11.2)

$$e_{ij} = \frac{1}{2}\left( \frac{\partial u_i}{\partial x_j} + \frac{\partial u_j}{\partial x_i} \right)$$

Here, $C_{ijkl}$ is the tensor of elastic coefficients, $e_{kl}$ is the strain tensor which is a function of the displacement field **u**, $d_{ijk}$ is a tensor of actuation (such as piezoelectric) strain coefficients describing the effect of a control signal **R** on the stress field $\sigma_{ij}$, $\alpha_{ij}^{(\theta)}$ is the thermal expansion strain tensor, and $\beta_{ij}^{(c)}$ is the hygroscopic expansion strain tensor. Finally, T and C represent changes in the temperature and moisture content (with respect to a reference hygrothermal state) respectively. It is assumed in Equation (11.2) that

$C_{ijkl}, d_{ijk}^{(r)}, \alpha_{kl}^{(\theta)}$ and $\beta_{kl}^{(c)}$ are all periodic in $x_1$ and $x_2$ with respective periods $\delta h_1$ and $\delta h_2$ but are not periodic in the transverse coordinate $x_3$.
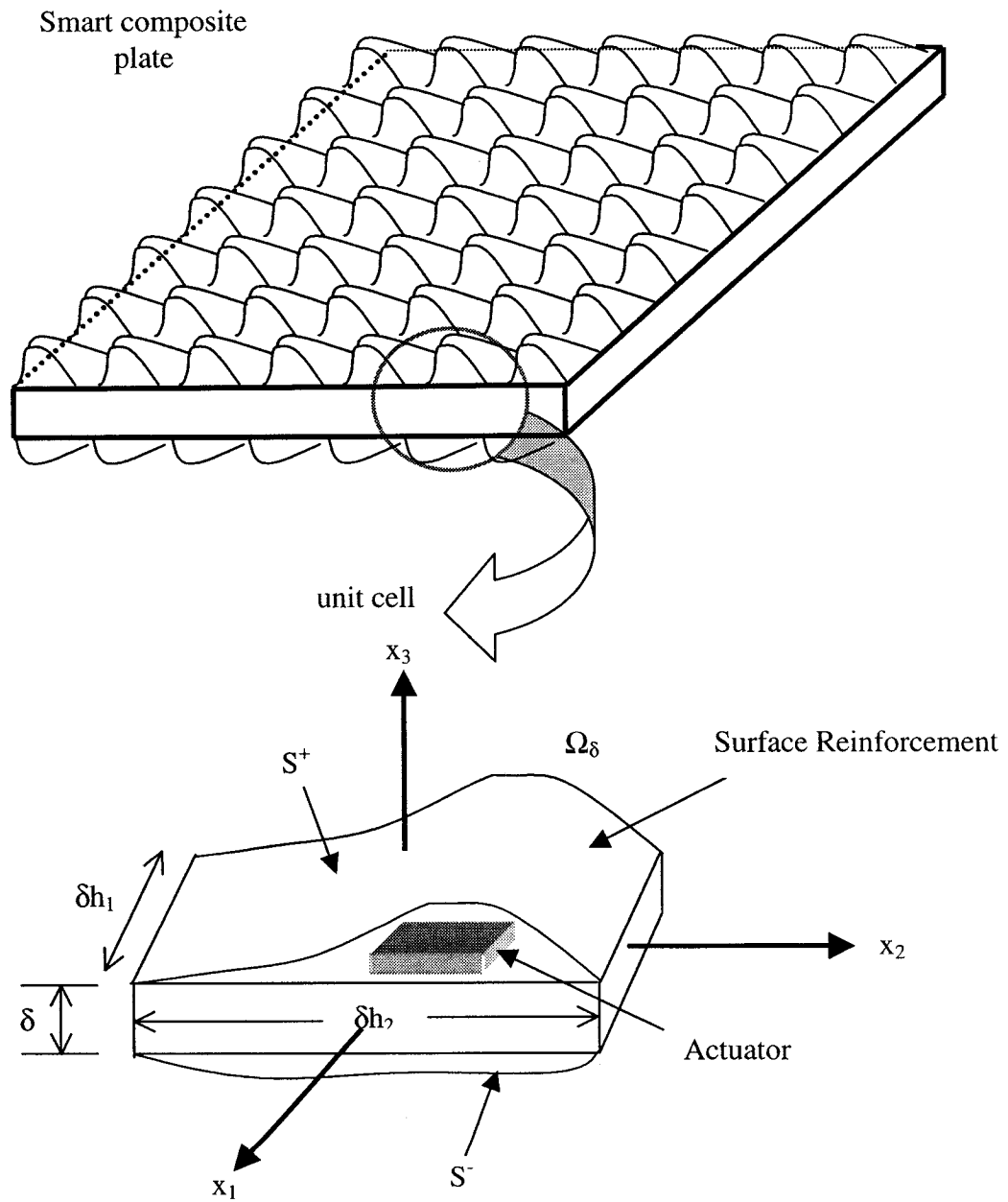


**Figure 11-1:** Thin smart composite solid of a periodic structure and its unit cell

Assume that the top and bottom surfaces of the plate $S^{\pm}$ are subjected to surface tractions $p_i$ (not to be confused with the body forces $P_i$) which are related to stresses by:

$$\sigma_{ij} n_j = p_i \tag{11.3}$$

Equation (11.3) is of course a statement of the well-known Cauchy's stress theorem. The unit normal vector for the surfaces $x_3 = S^{\pm}(x_1, x_2)$ is:

$$\mathbf{n}^{\pm} = \left( \mp \frac{\partial S^{\pm}}{\partial x_1}, \mp \frac{\partial S^{\pm}}{\partial x_2}, 1 \right) \left[ \left( \frac{\partial S^{\pm}}{\partial x_1} \right)^2 + \left( \frac{\partial S^{\pm}}{\partial x_2} \right)^2 + 1 \right]^{-1/2} \tag{11.4}$$

## 11.3 Asymptotic Analysis and Basic Assumptions

The analysis begins with the introduction of the "fast" variables as follows:

$$y_1 = \frac{x_1}{\delta h_1}, \quad y_2 = \frac{x_2}{\delta h_2}, \quad z = \frac{x_3}{\delta} \tag{11.5}$$

Remember that $\delta$ is the thickness of the smart layer. Hence, in terms of these variables, the unit-cell $\Omega_\delta$ is defined by:

$$\left\{ -\frac{1}{2} < y_1 < \frac{1}{2}, \quad -\frac{1}{2} < y_2 < \frac{1}{2}, \quad Z^- < z < Z^+ \right\}, \quad \text{where}$$

$$Z^{\pm} = \pm\frac{1}{2} \pm F^{\pm}(\mathbf{y}) \quad \text{and} \tag{11.6}$$

$$\mathbf{y} = (y_1, y_2), \quad \mathbf{x} = (x_1, x_2),$$

Then, the unit normal vector from Equation (11.4) becomes:

$$\mathbf{n}^{\pm} = \left( \mp \frac{1}{h_1} \frac{\partial F^{\pm}}{\partial y_1}, \mp \frac{1}{h_2} \frac{\partial F^{\pm}}{\partial y_2}, 1 \right) \left[ 1 + \frac{1}{h_1^2} \left( \frac{\partial F^{\pm}}{\partial y_1} \right)^2 + \frac{1}{h_2^2} \left( \frac{\partial F^{\pm}}{\partial y_2} \right)^2 \right]^{-1/2} \tag{11.7}$$

The next step is to make the following asymptotic assumptions

$$p_\alpha^{\pm} = \delta^2 r_\alpha(\mathbf{x}, \mathbf{y}), \quad p_3^{\pm} = \delta^3 q_3^{\pm}(\mathbf{x}, \mathbf{y})$$
$$P_\alpha = \delta f_\alpha(\mathbf{x}, \mathbf{y}, z), \quad P_3 = \delta^2 g_3(\mathbf{x}, \mathbf{y}, z) \tag{11.8a}$$

and

$$\alpha_{ij}^{(\theta)} = \delta\alpha_{ij}(y,z)$$

$$\beta_{ij}^{(c)} = \delta\beta_{ij}(y,z) \tag{11.8b}$$

$$d_{ijk}^{(r)} = \delta d_{ijk}(y,z)$$

As well, assume the following through-the-thickness linear relationships for T, C, $R_i$.

$$T = T^{(o)}(\mathbf{x}) + zT^{(1)}(\mathbf{x})$$

$$C = C^{(o)}(\mathbf{x}) + zC^{(1)}(\mathbf{x}) \tag{11.8c}$$

$$R_i = R_i^{(o)}(\mathbf{x}) + zR_i^{(1)}(\mathbf{x})$$

It should be noted that in Equation (11.8a) and in the sequel Greek indices will be assumed to take on the values of 1 and 2, and Latin indices will vary from 1 to 3.

The introduction of the fast variables necessitates the transformation of the derivatives according to,

$$\frac{\partial}{\partial x_\alpha} \rightarrow \frac{\partial}{\partial x_\alpha} + \frac{1}{\delta h_\alpha}\frac{\partial}{\partial y_\alpha} \quad \text{and} \quad \frac{\partial}{\partial x_3} = \frac{1}{\delta}\frac{\partial}{\partial z} \tag{11.9}$$

so that the equilibrium equations and the strain-displacement relationships in Equation (11.2) become:

$$\frac{\partial \sigma_{i\alpha}}{\partial x_\alpha} + \frac{1}{\delta h_\alpha}\frac{\partial \sigma_{i\alpha}}{\partial y\alpha} + \frac{1}{\delta}\frac{\partial \sigma_{i3}}{\partial z} = P_i \tag{11.10}$$

$$e_{\alpha\beta} = \frac{1}{2}\left(\frac{\partial u_\alpha}{\partial x_\beta} + \frac{1}{\delta h_\beta}\frac{\partial u_\alpha}{\partial y_\beta} + \frac{\partial u_\beta}{\partial x_\alpha} + \frac{1}{\delta h_\alpha}\frac{\partial u_\beta}{\partial y_\alpha}\right)$$

$$e_{3\beta} = \frac{1}{2}\left(\frac{\partial u_3}{\partial x_\beta} + \frac{1}{\delta h_\beta}\frac{\partial u_3}{\partial y_\beta} + \frac{1}{\delta}\frac{\partial u_\beta}{\partial z}\right) \tag{11.11}$$

$$e_{33} = \frac{1}{\delta}\frac{\partial u_3}{\partial z}$$

As in the previous chapters, one next assumes asymptotic expansions for the displacement and stress fields in the form of:

$$u_i = u_i^{(0)}(\mathbf{x}) + \delta u_i^{(1)}(x,y,z) + \delta^2 u_i^{(2)}(x,y,z) + \dots \tag{11.12a}$$

$$\sigma_{ij} = \sigma_{ij}^{(0)}(x,y,z) + \delta\sigma_{ij}^{(1)}(x,y,z) + \delta^2\sigma_{ij}^{(2)}(x,y,z) + \dots \tag{11.12b}$$

Subsequent substitution of Equation (11.12a) into (11.11) and equation of like powers of $\delta$, leads to the following asymptotic expansion for the strain field:

$$e_{ij} = e_{ij}^{(0)} + \delta e_{ij}^{(1)} + \delta^2 e_{ij}^{(2)} + ...$$

(11.13a)

where,

$$e_{\alpha\beta}^{(m)} = \frac{1}{2}\left( \frac{\partial u_\alpha^{(m)}}{\partial x_\beta} + \frac{\partial u_\beta^{(m)}}{\partial x_\alpha} + \frac{1}{h_\beta}\frac{\partial u_\alpha^{(m+1)}}{\partial y_\beta} + \frac{1}{h_\alpha}\frac{\partial u_\beta^{(m+1)}}{\partial y_\alpha} \right)$$

$$e_{3\beta}^{(m)} = \frac{1}{2}\left( \frac{\partial u_3^{(m)}}{\partial x_\beta} + \frac{1}{h_\beta}\frac{\partial u_3^{(m+1)}}{\partial y_\beta} + \frac{\partial u_\beta^{(m+1)}}{\partial z} \right)$$

(11.13b)

$$e_{33}^{(m)} = \frac{\partial u_3^{(m+1)}}{\partial z}$$

$$m = 0,1,2....$$

It is worth noting that unless the $u_i^{(0)}$ term in eq. (11.12a) is independent of the fast variables $y$ and $z$, the strain expressions in Equation (11.13b) become unbounded as $\delta$ becomes infinitesimally small.

## 11.4 Equilibrium Equations and Boundary Conditions

The next step in the homogenization procedure is to substitute the asymptotic expansion for the stress field, Equation (11.12b), into the modified equilibrium equation (11.10). This results in the following expression:

$$\frac{\partial \sigma_{i\alpha}^{(0)}}{\partial x_\alpha} + \delta\frac{\partial \sigma_{i\alpha}^{(1)}}{\partial x_\alpha} + \delta^2\frac{\partial \sigma_{i\alpha}^{(2)}}{\partial x_\alpha} + \frac{1}{\delta h_\alpha}\frac{\partial \sigma_{i\alpha}^{(0)}}{\partial y_\alpha} +$$

$$+ \frac{1}{h_\alpha}\frac{\partial \sigma_{i\alpha}^{(1)}}{\partial y_\alpha} + \frac{\delta}{h_\alpha}\frac{\partial \sigma_{i\alpha}^{(2)}}{\partial y_\alpha} + \frac{1}{\delta}\frac{\partial \sigma_{i3}^{(0)}}{\partial z} + \frac{\partial \sigma_{i3}^{(1)}}{\partial z} + \delta\frac{\partial \sigma_{\alpha i3}^{(2)}}{\partial z} = P_i$$

(11.14)

Equation (11.2a) necessitates the splitting of Equation (11.14) into two parts:

$$\frac{\partial \sigma_{\alpha\beta}^{(0)}}{\partial x_\beta} + \delta\frac{\partial \sigma_{\alpha\beta}^{(1)}}{\partial x_\beta} + \delta^2\frac{\partial \sigma_{\alpha\beta}^{(2)}}{\partial x_\beta} + \frac{1}{\delta h_\beta}\frac{\partial \sigma_{\alpha\beta}^{(0)}}{\partial y_\beta} + \frac{1}{h_\beta}\frac{\partial \sigma_{\alpha\beta}^{(1)}}{\partial y_\beta} +$$

$$\frac{\delta}{h_\beta}\frac{\partial \sigma_{\alpha\beta}^{(2)}}{\partial y_\beta} + \frac{1}{\delta}\frac{\partial \sigma_{\alpha3}^{(0)}}{\partial z} + \frac{\partial \sigma_{\alpha3}^{(1)}}{\partial z} + \delta\frac{\partial \sigma_{\alpha3}^{(2)}}{\partial z} = \delta f_\alpha$$

(11.15a)

and

$$\frac{\partial \sigma_{3\beta}^{(0)}}{\partial x_\beta} + \delta \frac{\partial \sigma_{3\beta}^{(1)}}{\partial x_\beta} + \delta^2 \frac{\partial \sigma_{3\beta}^{(2)}}{\partial x_\beta} + \frac{1}{\delta h_\beta} \frac{\partial \sigma_{3\beta}^{(0)}}{\partial y_\beta} + \frac{1}{h_\beta} \frac{\partial \sigma_{3\beta}^{(1)}}{\partial y_\beta} +$$

$$\frac{\delta}{h_\beta} \frac{\partial \sigma_{3\beta}^{(2)}}{\partial y_\beta} + \frac{1}{\delta} \frac{\partial \sigma_{33}^{(0)}}{\partial z} + \frac{\partial \sigma_{33}^{(1)}}{\partial z} + \delta \frac{\partial \sigma_{33}^{(2)}}{\partial z} = \delta^2 g_3$$

(11.15b)

Equating like powers of $\delta$ results in the following expressions:

$$\frac{1}{h_\beta} \frac{\partial \sigma_{i\beta}^{(0)}}{\partial y_\beta} + \frac{\partial \sigma_{i3}^{(0)}}{\partial z} = 0$$

$$\frac{\partial \sigma_{i\beta}^{(0)}}{\partial x_\beta} + \frac{1}{h_\beta} \frac{\partial \sigma_{i\beta}^{(1)}}{\partial y_\beta} + \frac{\partial \sigma_{i3}^{(1)}}{\partial z} = 0$$

$$\frac{\partial \sigma_{i\beta}^{(i)}}{\partial x_\beta} + \frac{1}{h_\beta} \frac{\partial \sigma_{i\beta}^{(2)}}{\partial y_\beta} + \frac{\partial \sigma_{i3}^{(2)}}{\partial z} = f_i \quad \text{and}$$

$$\frac{\partial \sigma_{i\beta}^{(2)}}{\partial x_\beta} + \frac{1}{h_\beta} \frac{\partial \sigma_{i\beta}^{(3)}}{\partial y_\beta} + \frac{\partial \sigma_{i3}^{(3)}}{\partial z} = g_i$$

(11.16)

Here the following definitions were made:

$$f_3 = g_1 = g_2 = 0$$

(11.17)

Attention is subsequently turned to the boundary conditions in (11.3) that may be rewritten as follows:

$$\sigma_{ij} n_j^\pm = \pm p_i$$

(11.18)

Here the negative sign on the right-hand-side of Cauchy's expression is necessary if one uses an inward, $\mathbf{n}^-$, instead of an outward, $\mathbf{n}^+$, unit normal vector (for the sake of computational convenience, an inward normal will be used for the lower surface $S^-$ of the plate). The stress field expansion in Equation (11.2b) is then substituted into Equation (11.18) to yield the following two equations that must be satisfied on the boundary of the plate:

$$\sigma_{\alpha j}^{(0)} N_j^\pm + \delta \sigma_{\alpha j}^{(1)} N_j^\pm + \delta^2 \sigma_{\alpha j}^{(1)} N_j^\pm + \delta^3 \sigma_{\alpha j}^{(2)} N_j^\pm + ... = \pm \omega^\pm \delta^2 r_\alpha^\pm$$

$$\sigma_{3j}^{(0)} N_j^\pm + \delta \sigma_{3j}^{(1)} N_j^\pm + \delta^2 \sigma_{3j}^{(1)} N_j^\pm + \delta^3 \sigma_{3j}^{(2)} N_j^\pm + ... = \pm \omega^\pm \delta^3 q_3^\pm$$

(11.19)

Here, use was again made of expressions (11.8a) and at the same time the following quantities were defined:

$$\mathbf{N}^{\pm} = \left( \mp \frac{1}{h_1} \frac{\partial F^{\pm}}{\partial y_1}, \frac{1}{h_2} \frac{\partial F^{\pm}}{\partial y_2}, 1 \right) \quad \text{and}$$

$$\omega^{\pm} = \sqrt{1 + \frac{1}{h_1^2} \left( \frac{\partial F^{\pm}}{\partial y_1} \right)^2 + \frac{1}{h_2^2} \left( \frac{\partial F^{\pm}}{\partial y_2} \right)^2} \qquad (11.20)$$

Equating equal powers of $\delta$ one finally obtain for the boundary conditions pertinent to surfaces $Z^{\pm}$,

$$\sigma_{ij}^{(m)} N_j^{\pm} = 0 \quad m = 0,1$$

$$\sigma_{ij}^{(2)} N_j^{\pm} = \pm \omega^{\pm} r_i^{\pm} \quad \text{and} \qquad (11.21a)$$

$$\sigma_{ij}^{(3)} N_j^{\pm} = \pm \omega^{\pm} q_i^{\pm}$$

where the following definitions were used:

$$r_3^{\pm} = q_1^{\pm} = q_2^{\pm} = 0 \qquad (11.21b)$$

The next step is to introduce the averaging procedure

$$\langle \psi \rangle = \int_{\Omega_\delta} \psi \, dy_1 dy_2 dz \qquad (11.22)$$

defined over the volume of the unit $\Omega_\delta$ with boundary surface $\partial\Omega_\delta$, and proceed to show the following relationship

$$\left\langle \frac{1}{h_\alpha} \frac{\partial Q_\alpha}{\partial y_\alpha} + \frac{\partial Q_3}{\partial z} \right\rangle = \int_{-\frac{1}{2}}^{\frac{1}{2}} \int_{-\frac{1}{2}}^{\frac{1}{2}} \left( Q_i^+ N_i^+ - Q_i^- N_i^- \right) dy_1 dy_2 \qquad (11.23)$$

where $\mathbf{N}^{\pm}$ is defined in Equation (11.20) and $Q_i^{\pm}$ are the values $Q_i$ takes on the surfaces $Z^{\pm}$. Starting with the divergence theorem one writes

$$\left\langle \frac{1}{h_\alpha} \frac{\partial Q_\alpha}{\partial y_\alpha} + \frac{\partial Q_3}{\partial z} \right\rangle = \int_{\Omega_\delta} \left( \frac{1}{h_\alpha} \frac{\partial Q_\alpha}{\partial y_\alpha} + \frac{\partial Q_3}{\partial z} \right) dv = \int_{\partial\Omega_\delta} \left( \frac{1}{h_\alpha} Q_\alpha n_{y\alpha} + Q_3 n_{y3} \right) dA , \qquad (11.24a)$$

where $n_y^+$ ($n_y^-$) is the outward (inward) unit normal vector defined with respect to the ($y_1$, $y_2$, z) coordinate system of the unit cell and is given by:

$$\mathbf{n}_y^{\pm} = \left( \mp \frac{\partial F^{\pm}}{\partial y_1}, \mp \frac{\partial F^{\pm}}{\partial y_1}, 1 \right) \Bigg/ \sqrt{\left(\frac{\partial F^{\pm}}{\partial y_1}\right)^2 + \left(\frac{\partial F^{\pm}}{\partial y_2}\right)^2 + 1} \qquad (11.24b)$$

Here dA is a surface area element. Now, the function $Q_i$ has the same values at corresponding points on opposite boundaries on the *lateral* surface of the unit cell on account of its periodicity, but the normal vector has opposite signs at these points. Consequently, the integrals vanish over the lateral surfaces of the unit cell and the integral in (11.24b) reduces to [Kalamkarov, 1992]:

$$\int_{S^+} \left( \frac{1}{h_\alpha} Q_\alpha^+ n_{y\alpha}^+ + Q_3^+ n_{y3}^+ \right) ds_\Omega^+ - \left( \frac{1}{h_\alpha} Q_\alpha^- n_{y\alpha}^- + Q_3^- n_{y3}^- \right) ds_\Omega^- \qquad (11.25)$$

Here, $\mathbf{n}_y^+$ $(\mathbf{n}_y^-)$ is the outer (inner) unit normal vector defined with respect to the $(y_1, y_2, z)$ coordinate system, and $ds_\Omega^+ (ds_\Omega^-)$ is a differential area element defined on the top (bottom) surfaces of the unit cell and is given by:

$$ds_\Omega^{\pm} = \sqrt{\left(\frac{\partial F^{\pm}}{\partial y_1}\right)^2 + \left(\frac{\partial F^{\pm}}{\partial y_2}\right)^2 + 1} \; dy_1 dy_2 \qquad (11.26)$$

Finally, substitution of Equation (11.26) into Equation (11.25) proves the result in Equation (11.23) on account of Equation (11.20).

## 11.5 Derivation of Unit Cell Problems

Substitution of Equations (11.4b), (11.13a) and (11.13b) into the second expression in Equation (11.2) and group terms multiplied by the same power of $\delta$, yields the following expressions for the terms $\sigma_{ij}^{(0)}$ and $\sigma_{ij}^{(1)}$ defined in expansion (11.12b):

$$\sigma_{ij}^{(0)} = C_{ijk\beta}\left( \frac{1}{h_\beta} \frac{\partial u_k^{(1)}}{\partial y_\beta} \right) + C_{ijk3}\left( \frac{\partial u_k^{(1)}}{\partial z} \right) + C_{ijk\beta}\varepsilon_{k\beta}^{(0)},$$

$$\varepsilon_{ij}^{(0)} = \frac{1}{2}C_{ijk\beta}\left( \frac{\partial u_k^{(0)}}{\partial x_\beta} + \frac{\partial u_\beta^{(0)}}{\partial x_k} \right) \qquad (11.27a)$$

and

$$\sigma_{ij}^{(1)} = C_{ijk\beta}\left(\frac{1}{h_\beta}\frac{\partial u_k^{(2)}}{\partial y_\beta}\right) + C_{ijk3}\left(\frac{\partial u_k^{(2)}}{\partial z}\right) + C_{ijk\beta}\left(\frac{1}{h_\beta}\frac{\partial u_k^{(1)}}{\partial x_\beta}\right) + \tag{11.27b}$$

$$- C_{ijkl}d_{klm}R_m^{(0)} - C_{ijkl}d_{klm}zR_m^{(1)} - C_{ijkl}\alpha_{kl}T^{(0)} - C_{ijkl}\alpha_{kl}zT^{(1)} - C_{ijkl}\beta_{kl}C^{(0)} - C_{ijkl}\beta_{kl}zC^{(1)}$$

Although the problem defined by Equation (11.27a) has been solved by Kalamkarov [1992], the solution will be repeated here because it (together with some ensuing definitions) will be used for the solution of problem (11.27b). Substitution of Equation (11.27a) into the first of the equilibrium equations (11.16) and the corresponding boundary condition (11.21a) gives the following two equations:

$$D_{ik}u_k^{(1)} = -c_{ik\alpha}(y,z)\varepsilon_{k\alpha}^{(0)}(x) \quad \text{and}$$
$$\left(L_{ijk}u_k^{(1)} + c_{ijk\beta}\varepsilon_{k\beta}^{(0)}\right)N_j^{\pm} = 0 \quad \text{on } Z^{\pm} \tag{11.28a}$$

Here, the following operators [Kalamkarov, 1992] are defined:

$$L_{ijk} = C_{ijk\alpha}\frac{1}{h_\alpha}\frac{\partial}{\partial y_\alpha} + C_{ijk3}\frac{\partial}{\partial z},$$

$$D_{ij} = \frac{1}{h_\alpha}\frac{\partial}{\partial y_\alpha}L_{i\alpha j} + \frac{\partial}{\partial z}L_{i3j}, \text{ and} \tag{11.28b}$$

$$c_{i\alpha j} = \frac{1}{h_\beta}\frac{\partial C_{i\beta\alpha j}}{\partial y_\beta} + \frac{\partial C_{i3\alpha j}}{\partial z}$$

The separation of variables on the right-hand-side of the equilibrium equation (11.28a) prompts one to write down the solution of $u^{(1)}$ in the form of:

$$u_m^{(1)} = U_m^{k\alpha}(y,z)\varepsilon_{k\alpha}^{(0)}(x) + v_m^{(1)}(x) \tag{11.29}$$

In Equation (11.29) $v_m^{(1)}$ is the homogeneous solution, which satisfies

$$D_{ik}v_k^{(1)} = 0 \tag{11.30a}$$

and $U_m^{k\alpha}$ the particular solution, which satisfies:

$$D_{ik}U_k^{m\alpha} = -c_{im\alpha} \quad \text{and}$$
$$\left(L_{ijk}U_k^{m\alpha} + C_{ijm\alpha}\right)N_j^{\pm} = 0 \quad \text{on } Z^{\pm} \tag{11.30b}$$

One can easily show the independency of $v_k^{(1)}$ on the fast variables by first writing out Equation (11.30a) in full using the operator definitions in Equation (11.28b).

$$\frac{1}{h_\beta}\frac{\partial}{\partial y_\beta}\left\{C_{i\beta k\alpha}\frac{1}{h_\alpha}\frac{\partial}{\partial y_\alpha}v_k^{(1)}+C_{i\beta k3}\frac{\partial}{\partial z}v_k^{(1)}\right\}+\frac{\partial}{\partial z}\left\{C_{i3k\alpha}\frac{1}{h_\alpha}\frac{\partial}{\partial y_\alpha}v_k^{(1)}+C_{i3k3}\frac{\partial}{\partial z}v_k^{(1)}\right\}=0 \quad (11.31)$$

Subsequent integration of the latter equation over the volume of the unit cell with a simultaneous consideration of the general result in Equation (11.23), finally leads to:

$$\frac{\partial v_k^{(1)}}{\partial y_\alpha}=\frac{\partial v_k^{(1)}}{\partial z}=0 \quad (11.32)$$

This shows that $v_k^{(1)}$ only depends on the slow variables.

Problem (11.30b) is solved easily for the case when m=3 giving the following results:

$$U_1^{31}=U_2^{32}=-z \quad\text{and}\quad U_2^{31}=U_3^{31}=U_1^{32}=U_3^{32}=0 \quad (11.33)$$

This can be seen immediately by writing the differential equation and boundary conditions in Equation (11.30b) explicitly and substituting solution (11.33) in the resulting expressions [Kalamkarov, 1992].

On defining [Kalamkarov, 1992],

$$b_{ij}^{m\alpha}=L_{ijk}U_k^{m\alpha}+C_{ijm\alpha} \quad (11.34)$$

and noting that $b_{ij}^{3\alpha}=0$ on account of Equation (11.33), then expression (11.27a) becomes:

$$\sigma_{ij}^{(0)}=b_{ij}^{\alpha\beta}\varepsilon_{\alpha\beta}^{(0)} \quad (11.35)$$

One subsequently averages the second equilibrium expression in Equation (11.16) while considering at the same time the boundary conditions (11.21a) and the general result (11.22), to arrive at:

$$\frac{\partial}{\partial x_\beta}\int_{\Omega_\delta}b_{i\beta}^{v\alpha}dv\ \varepsilon_{v\alpha}^{(0)}=0 \quad\Rightarrow\quad \varepsilon_{v\alpha}^{(0)}=0 \quad (11.36)$$

Finally, from Equations (11.27a) and (11.29) it is found that [Kalamkarov, 1992]:

$$u_1^{(0)} = u_2^{(0)} = 0, \quad u_3^{(0)} = w(\mathbf{x})$$

$$u_\nu^{(1)} = v_\nu^{(1)}(\mathbf{x}) - z\frac{\partial w}{\partial x_\nu}, \quad u_3^{(1)} = v_3^{(1)}(\mathbf{x}) \tag{11.37}$$

As well, Equation (11.35) leads to:

$$\sigma_{ij}^{(0)} = 0 \tag{11.38}$$

One is now in a position to solve for the second term of the asymptotic expansion of the stress field. To this end, substitution of solution (11.37) into Equation (11.27b) leads to the following result:

$$\sigma_{ij}^{(1)} = L_{ijk}u_k^{(2)} + C_{ijk\beta}\varepsilon_{k\beta}^{(1)} + zC_{ij\alpha\beta}\tau_{\alpha\beta} - P_{ijk}R_k^{(0)} - ZP_{ijk}R_k^{(1)} +$$
$$- K_{ij}T^{(0)} - zK_{ij}T^{(1)} - B_{ij}C^{(0)} - zB_{ij}C^{(1)} \tag{11.39}$$

Here the following definitions are made:

$$\varepsilon_{\alpha\beta}^{(1)} = \frac{1}{2}\left(\frac{\partial v_\alpha^{(1)}}{\partial x_\beta} + \frac{\partial v_\beta^{(1)}}{\partial x_\alpha}\right), \quad \tau_{\alpha\beta} = \frac{-\partial^2 w}{\partial x_\alpha \partial x_\beta} \tag{11.40a}$$

$$P_{ijm} = C_{ijkl}d_{klm}, \quad K_{ij} = C_{ijkl}\alpha_{kl}, \quad B_{ij} = C_{ijkl}\beta_{kl} \tag{11.40b}$$

Now, on account of Equation (11.38), the second equilibrium expression (11.16) and appropriate boundary conditions (11.21a) become:

$$\frac{1}{h_\beta}\frac{\partial \sigma_{i\beta}^{(1)}}{\partial y_\beta} + \frac{\partial \sigma_{i3}^{(1)}}{\partial z} = 0 \tag{11.41a}$$

$$\sigma_{ij}^{(1)}N_j^\pm = 0 \quad \left(\text{on } Z^\pm\right) \tag{11.41b}$$

Substitution of Equation (11.39) into Equation (11.41a) leads to:

$$D_{ik}u_k^{(2)} + \frac{1}{h_\beta}\frac{\partial}{\partial y_\beta}\left\{C_{i\beta k\alpha}\varepsilon_{k\alpha}^{(1)} + zC_{i\beta\alpha\mu}\tau_{\alpha\mu} - P_{i\beta k}R_k^{(0)} - zP_{i\beta k}R_k^{(1)} +\right.$$
$$- K_{i\beta}T^{(0)} - zK_{i\beta}T^{(1)} - B_{i\beta}C^{(0)} - zB_{i\beta}C^{(1)}\right\} + \frac{\partial}{\partial z}\left\{C_{i3k\alpha}\varepsilon_{k\alpha}^{(1)} + zC_{i3\alpha\mu}\tau_{\alpha\mu} +\right. \tag{11.41c}$$
$$\left. - P_{i3k}R_k^{(0)} - zP_{i3k}R_k^{(1)} - K_{i3}T^{(0)} - zK_{i3}T^{(1)} - B_{i3}C^{(0)} - zB_{i3}C^{(1)}\right\} = 0$$

Rewriting this equation as

$$D_{ik}u_k^{(2)} + \frac{1}{h_\beta}\frac{\partial C_{i\beta k\alpha}}{\partial y_\beta}\varepsilon_{k\alpha}^{(1)} + \frac{\partial C_{i3k\alpha}}{\partial z}\varepsilon_{k\alpha}^{(1)} + \frac{1}{h_\beta}\frac{\partial C_{i\beta\alpha\mu}}{\partial y_\beta}z\tau_{\alpha\mu} + \frac{\partial C_{i3\alpha\mu}}{\partial z}z\tau_{\alpha\mu} + C_{i3\alpha\mu}\tau_{\alpha\mu}$$

$$-\frac{1}{h_\beta}\frac{\partial P_{i\beta k}}{\partial y_\beta}R_k^{(0)} - \frac{\partial P_{i3k}}{\partial z}R_k^{(0)} - \frac{1}{h_\beta}\frac{\partial P_{i\beta k}}{\partial y_\beta}zR_k^{(1)} - P_{i3k}R_k^{(1)} +$$

$$-\frac{1}{h_\beta}\frac{\partial K_{i\beta}}{\partial y_\beta}T^{(0)} - \frac{\partial K_{i3}}{\partial z}T^{(0)} - \frac{1}{h_\beta}\frac{\partial K_{i\beta}}{\partial y_\beta}zT^{(1)} - K_{i3}T^{(1)} + \qquad (11.41d)$$

$$\frac{1}{h_\beta}\frac{\partial B_{i\beta}}{\partial y_\beta}C^{(0)} - \frac{\partial B_{i3}}{\partial z}C^{(0)} - \frac{1}{h_\beta}\frac{\partial B_{i\beta}}{\partial y_\beta}zC^{(1)} - B_{i3}C^{(1)} = 0$$

and making the following definitions

$$P_{ik}^* = \frac{1}{h_\beta}\frac{\partial P_{i\beta k}}{\partial y_\beta} + \frac{\partial P_{i3k}}{\partial z}$$

$$K_i^* = \frac{1}{h_\beta}\frac{\partial K_{i\beta}}{\partial y_\beta} + \frac{\partial K_{i3}}{\partial z} \qquad (11.41e)$$

$$B_i^* = \frac{1}{h_\beta}\frac{\partial B_{i\beta}}{\partial y_\beta} + \frac{\partial B_{i3}}{\partial z}$$

finally leads to the following expression for $u_k^{(2)}$:

$$D_{ik}u_k^{(2)} = -c_{ik\alpha}\varepsilon_{k\alpha}^{(1)} - \left(C_{i3\alpha\mu} + zc_{i\alpha\mu}\right)\tau_{\alpha\mu} + P_{ik}^*R_k^{(0)} + \left(P_{i3k} + zP_{ik}^*\right)R_k^{(1)} +$$

$$+ K_i^*T^{(0)} + \left(K_{i3} + zK_i^*\right)T^{(1)} + B_i^*C^{(0)} + \left(B_{i3} + zB_i^*\right)C^{(1)} \qquad (11.42)$$

Subsequently, one substitutes Equation (11.39) into Equation (11.41b) to get:

$$\left(L_{ijk}u_k^{(2)} + C_{ijk\beta}\varepsilon_{k\beta}^{(1)} + Z^\pm C_{ij\alpha\beta}\tau_{\alpha\beta} - P_{ijk}R_k^{(0)} - Z^\pm P_{ijk}R_k^{(1)} +\right.$$

$$\left. - K_{ij}T^{(0)} - Z^\pm K_{ij}T^{(1)} - B_{ij}C^{(0)} - Z^\pm B_{ij}C^{(1)}\right)N_j^\pm = 0 \quad \left(z = Z^\pm\right) \qquad (11.43)$$

The separation of variables in each term on the right-hand-side of Equation (11.42) prompts the solution for $u_k^{(2)}$ in the form of:

$$u_m^{(2)} = U_m^{k\alpha}\varepsilon_{k\alpha}^{(1)} + V_m^{\beta\alpha}\tau_{\beta\alpha} + U_m^K R_k^{(0)} + V_m^k R_k^{(1)} + W_m T^{(0)} + X_m T^{(1)} + Y_m C^{(0)} + A_m C^{(1)} \qquad (11.44)$$

Here use was also made of Equation (11.30b). Substitution of solution (11.44) into Equations (11.42) and (11.43), leads, on account of (11.34) and the following definitions

$$b_{ij}^{*\alpha\beta} = L_{ijk} V_k^{\alpha\beta} + zC_{ij\alpha\beta}$$

$$d_{ij}^k = P_{ijk} - L_{ijm} U_m^k$$

$$d_{ij}^{*k} = zP_{ijk} - L_{ijm} V_m^k$$

$$\Theta_{ij} = K_{ij} - L_{ijm} W_m \qquad\qquad (11.45)$$

$$\Theta_{ij}^* = zK_{ij} - L_{ijm} X_m$$

$$\Lambda_{ij} = B_{ij} - L_{ijm} Y_m$$

$$\Lambda_{ij}^* = zB_{ij} - L_{ijm} A_m$$

to a group of eight problems to be referred to in the sequel as unit-cell problems. They are

$$\frac{1}{h_\beta} \frac{\partial b_{i\beta}^{\mu\alpha}}{\partial y_\beta} + \frac{\partial b_{i3}^{\mu\alpha}}{\partial z} = 0,$$

$$b_{ij}^{\mu\alpha} N_j^\pm = 0 \quad \left(\text{on } Z^\pm\right) \qquad\qquad (11.46a)$$

$$\frac{1}{h_\beta} \frac{\partial b_{i\beta}^{*\mu\alpha}}{\partial y_\beta} + \frac{\partial b_{i3}^{*\mu\alpha}}{\partial z} = 0,$$

$$b_{ij}^{*\mu\alpha} N_j^\pm = 0 \quad \left(\text{on } Z^\pm\right) \qquad\qquad (11.46b)$$

$$\frac{1}{h_\beta} \frac{\partial d_{i\beta}^k}{\partial y_\beta} + \frac{\partial d_{i3}^k}{\partial z} = 0,$$

$$d_{ij}^k N_j^\pm = 0 \quad \left(\text{on } Z^\pm\right) \qquad\qquad (11.46c)$$

$$\frac{1}{h_\beta} \frac{\partial d_{i\beta}^{*k}}{\partial y_\beta} + \frac{\partial d_{i3}^{*k}}{\partial z} = 0,$$

$$d_{ij}^{*k} N_j^\pm = 0 \quad \left(\text{on } Z^\pm\right) \qquad\qquad (11.46d)$$

$$\frac{1}{h_\beta} \frac{\partial \Theta_{i\beta}}{\partial y_\beta} + \frac{\partial \Theta_{i3}}{\partial z} = 0,$$

$$\Theta_{ij} N_j^\pm = 0 \quad \left(\text{on } Z^\pm\right) \qquad\qquad (11.46e)$$

$$\frac{1}{h_\beta} \frac{\partial \Theta_{i\beta}^*}{\partial y_\beta} + \frac{\partial \Theta_{i3}^*}{\partial z} = 0,$$

$$\Theta_{ij}^* N_j^\pm = 0 \quad \left(\text{on } Z^\pm\right) \qquad\qquad (11.46f)$$

$$\frac{1}{h_\beta}\frac{\partial \Lambda_{i\beta}}{\partial y_\beta} + \frac{\partial \Lambda_{i3}}{\partial z} = 0, \tag{11.46g}$$

$$\Lambda_{ij}N_j^\pm = 0 \quad \left(\text{on } Z^\pm\right)$$

$$\frac{1}{h_\beta}\frac{\partial \Lambda_{i\beta}^*}{\partial y_\beta} + \frac{\partial \Lambda_{i3}^*}{\partial z} = 0, \tag{11.46h}$$

$$\Lambda_{ij}^*N_j^\pm = 0 \quad \left(\text{on } Z^\pm\right)$$

It should be noted that four of these unit-cell problems, (11.46a), (11.46b), (11.46e), (11.46f) were derived by Kalamkarov [1992]. Here, the same technique was used to derive the remaining four unit cell problems, (11.46c), (11.46d), (11.46g) and (11.46h), that account for the effect of the embedded actuators and hygroscopic absorption.

The unit-cell problems provide the functions $U_k^{\alpha\beta}(y,z)$, $V_k^{\alpha\beta}(y,z)$, $U_k^m(y,z)$, $V_k^m(y,z)$, and $W_k(y,z)$, $X_k(y,z)$, $Y_k(y,z)$, $A_k(y,z)$ which are 1-periodic in $y_1$ and $y_2$ and determine in turn the functions $b_{ij}^{\alpha\beta}$, $b_{ij}^{*\alpha\beta}$, $d_{ij}^k$, $d_{ij}^{*k}$, $\Theta_{ij}$, $\Theta_{ij}^*$, $\Lambda_{ij}$, $\Lambda_{ij}^*$ needed to calculate the first non-vanishing term in the asymptotic expansion for the stress field, Equation (11.12b), given by:

$$\sigma_{ij}^{(1)} = b_{ij}^{\alpha\beta}\varepsilon_{\alpha\beta}^{(1)} + b_{ij}^{*\alpha\beta}\tau_{\alpha\beta} - d_{ij}^k R_k^{(0)} - d_{ij}^{*k} R_k^{(1)} - \Theta_{ij}T^{(0)} - \Theta_{ij}^*T^{(1)} - \Lambda_{ij}C^{(0)} - \Lambda_{ij}^*C^{(1)} \tag{11.47}$$

As a final note, it should be remarked that unlike the unit-cell problems of classical homogenization schemes (Sanchez-Palencia 1980, Bakvalov and Panasenko 1984), those set by eqs. (5.17a)-(5.17h) depend on the boundary conditions at $Z^\pm$ rather than on periodicity in the z direction.

## 11.6 Governing Equations of Homogenized Smart Plate

Before deriving the governing equations of the homogenized smart composite plate with rapidly varying thickness, consider a typical unit cell problem, say (11.46h).

$$\frac{1}{h_\beta}\frac{\partial \Lambda_{i\beta}^*}{\partial y_\beta} + \frac{\partial \Lambda_{i3}^*}{\partial z} = 0 \tag{11.48a}$$

$$\Lambda_{ij}^{*} N_j^{\pm} = 0 \quad \left(\text{on } Z^{\pm}\right) \tag{11.48b}$$

Multiplying Equation (11.48a) by z and integrating over the volume of the unit cell gives:

$$\int \left( z \frac{1}{h_\beta} \frac{\partial \Lambda_{i\beta}^{*}}{\partial y_\beta} + z \frac{\partial \Lambda_{i3}^{*}}{\partial z} \right) dv = 0 \tag{11.49}$$

Due to the fact that the fast variables are independent of one another, Equation (11.49) reduces to:

$$\int \left( \frac{1}{h_\beta} \frac{\partial}{\partial y_\beta} z\Lambda_{i\beta}^{*} + z \frac{\partial \Lambda_{i3}^{*}}{\partial z} \right) dv = 0$$

$$\therefore \int \left( \frac{1}{h_\beta} \frac{\partial}{\partial y_\beta} z\Lambda_{i\beta}^{*} + \frac{\partial}{\partial z} z\Lambda_{i3}^{*} \right) dv - \int \Lambda_{i3}^{*} dv = 0 \tag{11.50}$$

$$\therefore \int \left( \frac{1}{h_\beta} \frac{\partial}{\partial y_\beta} z\Lambda_{i\beta}^{*} + \frac{\partial}{\partial z} z\Lambda_{i3}^{*} \right) = \left\langle \Lambda_{i3}^{*} \right\rangle$$

Using the result in Equation (11.24a) means that the last expression in Equation (11.50) becomes:

$$\int_{-\frac{1}{2}}^{\frac{1}{2}} \int_{-\frac{1}{2}}^{\frac{1}{2}} z^+ \Lambda_{ij}^{*} N_j^+ dy_1 dy_2 - \int_{-\frac{1}{2}}^{\frac{1}{2}} \int_{-\frac{1}{2}}^{\frac{1}{2}} z^- \Lambda_{ij}^{*} N_j^- dy_1 dy_2 = \left\langle \Lambda_{i3}^{*} \right\rangle \tag{11.51a}$$

Finally, from Equations (11.48b) and (11.51a) one arrives at:

$$\left\langle \Lambda_{i3}^{*} \right\rangle = 0 \tag{11.51b}$$

Similarly, from unit cell problem (11.46d) one writes:

$$\int \left( \frac{1}{h_\beta} \frac{\partial}{\partial y_\beta} z d_{i\beta}^{*k} + z \frac{\partial d_{i3}^{*k}}{\partial z} \right) dv = 0$$

$$\therefore \int \left( \frac{1}{h_\beta} \frac{\partial}{\partial y_\beta} z d_{i\beta}^{*k} + \frac{\partial}{\partial z} z d_{i3}^{*k} \right) dv - \int d_{i3}^{*k} dv = 0 \tag{11.51c}$$

$$\therefore \int \left( \frac{1}{h_\beta} \frac{\partial}{\partial y_\beta} z d_{i\beta}^{k*} + \frac{\partial}{\partial z} z d_{i3}^{*k} \right) = \left\langle d_{i3}^{*k} \right\rangle$$

From Equation (11.24a) and the boundary conditions in Equation (11.46d), the last expression in Equation (11.51c) reduces to:

$$\left\langle d_{i3}^{*k} \right\rangle = 0 \qquad (11.51d)$$

Thus, collectively one finds that:

$$\left\langle b_{i3}^{\alpha\beta} \right\rangle = \left\langle b_{i3}^{*\alpha\beta} \right\rangle = \left\langle d_{i3}^{k} \right\rangle = \left\langle d_{i3}^{*k} \right\rangle = \left\langle \Theta_{i3} \right\rangle = \left\langle \Theta_{i3}^{*} \right\rangle = \left\langle \Lambda_{i3} \right\rangle = \left\langle \Lambda_{i3}^{*} \right\rangle = 0 \qquad (11.52)$$

Next, consider a typical unit-cell problem, say Equation (11.46c), multiply by $z^2$ and then integrate over the volume of the unit cell. This gives:

$$\int \left( \frac{1}{h_\beta} \frac{\partial}{\partial y_\beta} z^2 d_{i\beta}^k + z^2 \frac{\partial d_{i3}^k}{\partial z} \right) dv = 0$$

$$\therefore \int \left( \frac{1}{h_\beta} \frac{\partial}{\partial y_\beta} z^2 d_{i\beta}^k + \frac{\partial}{\partial z} z^2 d_{i3}^k \right) dv - \int 2z d_{i3}^k dv = 0 \qquad (11.53a)$$

$$\therefore \int \left( \frac{1}{h_\beta} \frac{\partial}{\partial y_\beta} z^2 d_{i\beta}^k + \frac{\partial}{\partial z} z^2 d_{i3}^k \right) dv = 2\left\langle z d_{i3}^k \right\rangle$$

From Equation (11.24a), the last expression becomes:

$$\int_{-\frac{1}{2}}^{\frac{1}{2}} \int_{-\frac{1}{2}}^{\frac{1}{2}} z^{2+} d_{ij}^k N_j^+ dy_1 dy_2 - \int_{-\frac{1}{2}}^{\frac{1}{2}} \int_{-\frac{1}{2}}^{\frac{1}{2}} z^{2-} d_{ij}^k N_j^- dy_1 dy_2 = 2\left\langle z d_{i3}^k \right\rangle \qquad (11.53b)$$

From the boundary condition in Equation (11.46d) the integrals in the expression above vanish, giving:

$$\left\langle z d_{i3}^k \right\rangle = 0 \qquad (11.53c)$$

Thus collectively, one finds that:

$$\left\langle z b_{i3}^{\alpha\beta} \right\rangle = \left\langle z b_{i3}^{*\alpha\beta} \right\rangle = \left\langle z d_{i3}^k \right\rangle = \left\langle z d_{i3}^{*k} \right\rangle = \left\langle z \Theta_{i3} \right\rangle = \left\langle z \Theta_{i3}^{*} \right\rangle = \left\langle z \Lambda_{i3} \right\rangle = \left\langle z \Lambda_{i3}^{*} \right\rangle = 0 \quad (11.54)$$

Letting i = 3 in Equation (16.47) gives:

$$\sigma_{i3}^{(1)} = b_{i3}^{\alpha\beta} \varepsilon_{\alpha\beta}^{(1)} + b_{i3}^{*\alpha\beta} \tau_{\alpha\beta} - d_{i3}^k R_k^{(0)} - d_{i3}^{*k} R_k^{(1)} - \Theta_{i3} T^{(0)} - \Theta_{i3}^{*} T^{(1)} - \Lambda_{i3} C^{(0)} - \Lambda_{i3}^{*} C^{(1)} \quad (11.55)$$

Averaging Equation (11.55) over the volume of the unit cell results in:

$$\left\langle \sigma_{i3}^{(1)} \right\rangle = \left\langle b_{i3}^{\alpha\beta} \right\rangle \varepsilon_{\alpha\beta}^{(1)} + \left\langle b_{i3}^{*\alpha\beta} \right\rangle \tau_{\alpha\beta} - \left\langle d_{i3}^k \right\rangle R_k^{(0)} - \left\langle d_{i3}^{*k} \right\rangle R_k^{(1)} +$$
$$- \left\langle \Theta_{i3} \right\rangle T^{(0)} - \left\langle \Theta_{i3}^{*} \right\rangle T^{(1)} - \left\langle \Lambda_{i3} \right\rangle C^{(0)} - \left\langle \Lambda_{i3}^{*} \right\rangle C^{(1)} \qquad (11.56a)$$

In view of Equations (11.52), Equation (11.56) reduces to:

$$\left\langle \sigma_{i3}^{(1)} \right\rangle = 0 \tag{11.56b}$$

Similarly, multiplying Equation (11.55) by z and averaging over the volume of the unit cell, gives on account of Equation (11.54) the following expression:

$$\left\langle z\sigma_{i3}^{(1)} \right\rangle = 0 \tag{11.56c}$$

The averaging procedure is then applied to the last two equations in (11.16) to give, on account of Equations (11.56b) and (11.56c), the following expressions:

$$\frac{\partial}{\partial x_\beta} \left\langle \sigma_{\alpha\beta}^{(1)} \right\rangle + \rho_\alpha + \left\langle f_\alpha \right\rangle = 0, \tag{11.57a}$$

$$\frac{\partial}{\partial x_\beta} \left\langle \sigma_{\alpha\beta}^{(2)} \right\rangle = 0, \quad \frac{\partial}{\partial x_\beta} \left\langle \sigma_{3\beta}^{(2)} \right\rangle + \lambda_3 + \left\langle g_3 \right\rangle = 0 \tag{11.57b}$$

Here the following definitions were made:

$$\rho_\alpha(x) = \int_{-1/2}^{1/2} \int_{-1/2}^{1/2} \left( \omega^+ r_\alpha^+ + \omega^- r_\alpha^- \right) dy_1 dy_2$$

$$\lambda_3(x) = \int_{-1/2}^{1/2} \int_{-1/2}^{1/2} \left( \omega^+ q_3^+ + \omega^- q_3^- \right) dy_1 dy_2 \tag{11.57c}$$

By multiplying the third equation in (11.16) by z and averaging over the volume of the unit cell, taking boundary conditions (11.21a) into account, one can eliminate $\left\langle \sigma_{3\beta}^{(2)} \right\rangle$ from Equation (11.57b) to give:

$$\frac{\partial}{\partial x_\alpha} \left( \frac{\partial}{\partial x_\beta} \left\langle z\sigma_{\alpha\beta}^{(1)} \right\rangle + \kappa_\alpha(x) + \left\langle zf_\alpha \right\rangle \right) + \lambda_3 + \left\langle g_3 \right\rangle = 0 \tag{11.58}$$

Here the following definition was made:

$$\kappa_\alpha(x) = \int_{-1/2}^{1/2} \int_{-1/2}^{1/2} \left( z\omega^+ r_\alpha^+ + z\omega^- r_\alpha^- \right) dy_1 dy_2 \tag{11.59}$$

It is noteworthy that as far as the stresses are concerned, Equations (11.57a) and (11.58) only contain the averaged quantities $\left\langle \sigma_{\alpha\beta}^{(1)} \right\rangle$ and $\left\langle z\sigma_{\alpha\beta}^{(1)} \right\rangle$ which may be written down from Equation (11.47) as:

$$\left\langle \sigma_{\alpha\beta}^{(1)} \right\rangle = \left\langle b_{\alpha\beta}^{\mu\nu} \right\rangle \varepsilon_{\mu\nu}^{(1)} + \left\langle b_{\alpha\beta}^{*\mu\nu} \right\rangle \tau_{\mu\nu} - \left\langle d_{\alpha\beta}^{k} \right\rangle R_{k}^{(0)} - \left\langle d_{\alpha\beta}^{*k} \right\rangle R_{k}^{(1)} +$$
$$- \left\langle \Theta_{\alpha\beta} \right\rangle T^{(0)} - \left\langle \Theta_{\alpha\beta}^{*} \right\rangle T^{(1)} - \left\langle \Lambda_{\alpha\beta} \right\rangle C^{(0)} - \left\langle \Lambda_{\alpha\beta}^{*} \right\rangle C^{(1)} \tag{11.60a}$$

$$\left\langle z\sigma_{\alpha\beta}^{(1)} \right\rangle = \left\langle zb_{\alpha\beta}^{\mu\nu} \right\rangle \varepsilon_{\mu\nu}^{(1)} + \left\langle zb_{\alpha\beta}^{*\mu\nu} \right\rangle \tau_{\mu\nu} - \left\langle zd_{\alpha\beta}^{k} \right\rangle R_{k}^{(0)} - \left\langle zd_{\alpha\beta}^{*k} \right\rangle R_{k}^{(1)} +$$
$$- \left\langle z\Theta_{\alpha\beta} \right\rangle T^{(0)} - \left\langle z\Theta_{\alpha\beta}^{*} \right\rangle T^{(1)} - \left\langle z\Lambda_{\alpha\beta} \right\rangle C^{(0)} - \left\langle z\Lambda_{\alpha\beta}^{*} \right\rangle C^{(1)} \tag{11.60b}$$

In conclusion, the original problem for the regularly non-homogeneous smart composite plate with rapidly varying thickness and an embedded array of actuators reduces to eight simpler unit-cell problems given by Equations (11.46a) to (11.46h). These problems yield functions $U_k^{\alpha\beta}(y,z)$, $V_k^{\alpha\beta}(y,z)$, $U_k^{m}(y,z)$, $V_k^{m}(y,z)$, $W_k(y,z)$, $X_k(y,z)$, $Y_k(y,z)$, and $A_k(y,z)$ from which functions $b_{ij}^{\alpha\beta}$, $b_{ij}^{*\alpha\beta}$, $d_{ij}^{k}$, $d_{ij}^{*k}$, $\Theta_{ij}$, $\Theta_{ij}^{*}$, $\Lambda_{ij}$, $\Lambda_{ij}^{*}$ can in turn be determined using definitions (11.45). These latter functions are then averaged to give the effective elastic, actuation, thermal expansion and hygroscopic expansion coefficients, $\left\langle b_{ij}^{\alpha\beta} \right\rangle$, $\left\langle b_{ij}^{*\alpha\beta} \right\rangle$, $\left\langle zb_{ij}^{\alpha\beta} \right\rangle$, $\left\langle zb_{ij}^{*\alpha\beta} \right\rangle$, $\left\langle d_{ij}^{k} \right\rangle$, $\left\langle zd_{ij}^{k} \right\rangle$ etc, which enter Equations (11.60a) and (11.60b). One then naturally proceeds to the boundary-value problem and substitutes Equations (11.60a) and (11.60b) into Equations (11.57a) and (11.58) from which $\varepsilon_{\alpha\beta}^{(1)}$ and $\tau_{\alpha\beta}$ are determined which in turn give the displacement functions $v_1^{(1)}(\mathbf{x})$, $v_2^{(1)}(\mathbf{x})$, and $w(\mathbf{x})$. The displacement and stress fields are then found from expansions (11.12a) and (11.12b) and are given by:

$$u_1 = \delta v_1^{(1)}(\mathbf{x}) - x_3 \frac{\partial w}{\partial x_1} + \delta^2 \left( U_1^{\alpha\beta} \varepsilon_{\alpha\beta}^{(1)} + V_1^{\alpha\beta} \tau_{\alpha\beta} \right) +$$
$$+ \delta^2 \left( U_1^{k} R_k^{(0)} + V_1^{k} R_k^{(1)} + W_1 T^{(0)} + X_1 T^{(1)} + Y_1 C^{(0)} + A_1 C^{(1)} \right) \tag{11.61a}$$

$$u_2 = \delta v_2^{(1)}(\mathbf{x}) - x_3 \frac{\partial w}{\partial x_1} + \delta^2 \left( U_2^{\alpha\beta} \varepsilon_{\alpha\beta}^{(1)} + V_2^{\alpha\beta} \tau_{\alpha\beta} \right) +$$

$$+ \delta^2 \left( U_2^k R_k^{(0)} + V_2^k R_k^{(1)} + W_2 T^{(0)} + X_2 T^{(1)} + Y_2 C^{(0)} + A_2 C^{(1)} \right) \qquad (11.61b)$$

$$u_3 = w(\mathbf{x}) + \delta v_3^{(1)} + \delta^2 \left( U_3^{\alpha\beta} \varepsilon_{\alpha\beta}^{(1)} + \delta^2 V_3^{\alpha\beta} \tau_{\alpha\beta}^{(1)} \right) +$$

$$+ \delta^2 \left( U_3^k R_k^{(0)} + V_3^k R_k^{(1)} + W_3 T^{(0)} + X_3 T^{(1)} + Y_3 C^{(0)} + A_3 C^{(1)} \right) \qquad (11.61c)$$

$$\sigma_{ij} = \delta \left( b_{ij}^{\alpha\beta} \varepsilon_{\alpha\beta}^{(1)} + b_{ij}^{*\alpha\beta} \tau_{\alpha\beta} - d_{ij}^k R_k^{(0)} - d_{ij}^{*k} R_k^{(1)} - \Theta_{ij} T^{(0)} - \Theta_{ij}^* T^{(1)} - \Lambda_{ij} C^{(0)} - \Lambda_{ij}^* C^{(1)} \right) \quad (11.61d)$$

Here one recalls that the Greek suffixes $\alpha$, $\beta$ vary from 1 to 2 and the Latin suffixes i, j, and k vary from 1 to 3.

It is worth noting that the local problems are completely determined by the structure of the unit cell and are totally independent of the formulation of the global boundary value problem.

## 11.7 Symmetry Properties of the Effective Coefficients

When the properties of a material are periodic in all three coordinates, it can be shown [Bakhvalov and Panasenko, 1984] that the symmetry properties of the coefficients involved remain the same after the homogenization process. For the current work, there is no periodicity in the transverse direction and so the question of symmetry of the effective coefficients is given special consideration. The symmetry properties of the effective elastic coefficients and thermal expansion coefficients as stated below

$$\left\langle b_{ij}^{mn} \right\rangle = \left\langle b_{mn}^{ij} \right\rangle, \quad \left\langle zb_{ij}^{mn} \right\rangle = \left\langle b_{mn}^{*ij} \right\rangle, \quad \left\langle zb_{ij}^{*mn} \right\rangle = \left\langle zb_{mn}^{*ij} \right\rangle \qquad (11.62a)$$

$$\delta \left\langle \theta_{mn} \right\rangle = \left\langle \alpha_{ij}^{(\theta)} b_{ij}^{mn} \right\rangle, \quad \delta \left\langle z\theta_{mn} \right\rangle = \left\langle \alpha_{ij}^{(\theta)} b_{ij}^{*mn} \right\rangle$$

$$\delta \left\langle \theta_{mn}^* \right\rangle = \left\langle z\alpha_{ij}^{(\theta)} b_{ij}^{mn} \right\rangle, \quad \delta \left\langle z\theta_{mn}^* \right\rangle = \left\langle z\alpha_{ij}^{(\theta)} b_{ij}^{*mn} \right\rangle \qquad (11.62b)$$

have been proved by Kalamkarov [1992]. Here, the same technique will be used to prove following relationships pertaining to the effective actuation coefficients and hygroscopic expansion coefficients:

$$\delta\langle d_{mn}^k \rangle = \langle d_{ijk}^{(r)} b_{ij}^{mn} \rangle, \quad \delta\langle zd_{mn}^k \rangle = \langle d_{ijk}^{(r)} b_{ij}^{*mn} \rangle,$$

$$\delta\langle d_{mn}^{*k} \rangle = \langle zd_{ijk}^{(r)} b_{ij}^{mn} \rangle, \quad \delta\langle zd_{mn}^{*k} \rangle = \langle zd_{ijk}^{(r)} b_{ij}^{*mn} \rangle \tag{11.63a}$$

and

$$\delta\langle \Lambda_{mn} \rangle = \langle \beta_{ij}^{(c)} b_{ij}^{mn} \rangle, \quad \delta\langle z\Lambda_{mn} \rangle = \langle \beta_{ij}^{(c)} b_{ij}^{*mn} \rangle$$

$$\delta\langle \Lambda_{mn}^* \rangle = \langle z\beta_{ij}^{(c)} b_{ij}^{mn} \rangle, \quad \delta\langle z\Lambda_{mn}^* \rangle = \langle z\beta_{ij}^{(c)} b_{ij}^{*mn} \rangle \tag{11.63b}$$

In proving Equations (11.63a) the first step is to introduce the following new variables:

$$\xi_1 = h_1 y_1, \quad \xi_2 = h_1 y_2, \quad \xi_3 = z \tag{11.64a}$$

In view of Equation (11.64a), definitions (11.28b) become:

$$L_{ijk} = C_{ijkl} \frac{1}{h_1} \frac{\partial}{\partial \xi_l}, \quad D_{ij} = \frac{\partial}{\partial \xi_m} C_{imnk} \frac{\partial}{\partial \xi_k}, \quad c_{ijk} = \frac{\partial C_{imjk}}{\partial \xi_m} \tag{11.64b}$$

Likewise, unit-cell problem (11.46c) becomes:

$$\frac{\partial d_{ij}^k}{\partial \xi_j} = 0,$$

$$d_{ij}^k N_j^{\pm} = 0 \quad (\text{on } Z^{\pm}) \tag{11.65}$$

Next, for a tensor $\varphi$ of arbitrary rank, one writes:

$$\frac{\partial}{\partial \xi_j}\left(\varphi d_{ij}^k\right) = \varphi \frac{\partial d_{ij}^k}{\partial \xi_j} + d_{ij}^k \frac{\partial \varphi}{\partial \xi_j} = d_{ij}^k \frac{\partial \varphi}{\partial \xi_j} \tag{11.66a}$$

Here use was made of Equation (11.65). If Equation (11.66a) is integrated over the volume of the unit cell, the following expression follows, in view of Equation (11.23):

$$\left\langle d_{ij}^k \frac{\partial \varphi}{\partial \xi_j} \right\rangle = 0 \tag{11.66b}$$

Similarly, the following relationships can be shown in a similar manner:

$$\left\langle d_{ij}^{*k} \frac{\partial \varphi}{\partial \xi_j} \right\rangle = 0$$

$$\left\langle b_{qp}^{mn} \frac{\partial \varphi}{\partial \xi_p} \right\rangle = \left\langle b_{qp}^{*mn} \frac{\partial \varphi}{\partial \xi_p} \right\rangle = 0 \tag{11.66c}$$

Now, replacing $\varphi$ with $U_i^{qr}$ in Equation (11.66b) results in:

$$\left\langle d_{ij}^k \frac{\partial U_i^{qr}}{\partial \xi_j} \right\rangle = 0 \qquad (11.67a)$$

From the relations in Equation (11.64b), the basic definition of $d_{ij}^k$ from Equation (11.45) becomes:

$$d_{ij}^k = P_{ijk} - C_{ijml} \frac{\partial U_m^k}{\partial \xi_l} \qquad (11.67b)$$

Thus:

$$\left\langle d_{ij}^k \frac{\partial U_i^{qr}}{\partial \xi_j} \right\rangle = \left\langle P_{ijk} \frac{\partial U_i^{qr}}{\partial \xi_j} - C_{ijml} \frac{\partial U_m^k}{\partial \xi_l} \frac{\partial U_i^{qr}}{\partial \xi_j} \right\rangle = 0$$

$$\therefore \left\langle P_{ijk} \frac{\partial U_i^{qr}}{\partial \xi_j} \right\rangle = \left\langle C_{ijml} \frac{\partial U_m^k}{\partial \xi_l} \frac{\partial U_i^{qr}}{\partial \xi_j} \right\rangle \qquad (11.67c)$$

Then, replacing $\varphi$ with $U_q^r$ in the second expression in Equation (11.66c) results in:

$$\left\langle b_{qp}^{mn} \frac{\partial U_q^r}{\partial \xi_p} \right\rangle = 0 \qquad (11.68a)$$

From the relations in Equation (11.64b), the basic definition of $b_{qp}^{mn}$ from Equation (11.34) becomes:

$$b_{qp}^{mn} = C_{qprl} \frac{\partial U_r^{mn}}{\partial \xi_l} + C_{qpmn} \qquad (11.68b)$$

Thus from Equations (11.68a) and (11.68b), one obtains:

$$\left\langle C_{mlij} \frac{\partial U_i^{rq}}{\partial \xi_j} \frac{\partial U_m^n}{\partial \xi_l} \right\rangle + \left\langle C_{mlrq} \frac{\partial U_m^n}{\partial \xi_l} \right\rangle = 0$$

$$\therefore \left\langle C_{mlij} \frac{\partial U_m^k}{\partial \xi_l} \frac{\partial U_i^{qr}}{\partial \xi_j} \right\rangle + \left\langle C_{mlqr} \frac{\partial U_m^k}{\partial \xi_l} \right\rangle = 0 \qquad (11.68c)$$

$$\therefore \left\langle C_{mlij} \frac{\partial U_m^k}{\partial \xi_l} \frac{\partial U_i^{qr}}{\partial \xi_j} \right\rangle = -\left\langle C_{mlqr} \frac{\partial U_m^k}{\partial \xi_l} \right\rangle$$

Comparing the last expressions in Equations (11.67c) and (11.68c) leads to:

$$\left\langle P_{ijk} \frac{\partial U_i^{qr}}{\partial \xi_j} \right\rangle = -\left\langle C_{mlqr} \frac{\partial U_m^k}{\partial \xi_l} \right\rangle \tag{11.69}$$

Next, from Equation (11.67b) one writes:

$$\left\langle d_{qr}^k \right\rangle = \left\langle P_{qrk} \right\rangle - \left\langle C_{qrml} \frac{\partial U_m^k}{\partial \xi_l} \right\rangle \tag{11.70}$$

From Equations (11.69) and (11.70):

$$\left\langle d_{qr}^k \right\rangle = \left\langle P_{qrk} \right\rangle + \left\langle P_{ijk} \frac{\partial U_i^{qr}}{\partial \xi_j} \right\rangle \tag{11.71}$$

On account of Equation (11.40b), Equation (11.71) becomes:

$$\left\langle d_{qr}^k \right\rangle = \left\langle C_{qrmn} d_{mnk} \right\rangle + \left\langle C_{ijmn} d_{mnk} \frac{\partial U_i^{qr}}{\partial \xi_j} \right\rangle \tag{11.72a}$$

$$\therefore \left\langle d_{qr}^k \right\rangle = \left\langle \left\{ C_{qrmn} + C_{ijmn} \frac{\partial U_i^{qr}}{\partial \xi_j} \right\} d_{mnk} \right\rangle$$

On account of Equation (11.68b), the last expression in Equation (11.72a) becomes:

$$\left\langle d_{qr}^k \right\rangle = \left\langle b_{mn}^{qr} d_{mnk} \right\rangle \tag{11.72b}$$

Finally, on account of Equations (11.8b), Equation (11.72b) becomes:

$$\delta \left\langle d_{qr}^k \right\rangle = \left\langle d_{mnk}^{(r)} b_{mn}^{qr} \right\rangle \tag{11.73}$$

This is the desired symmetry relationship as it appears in Equation (11.63a).

Although the proof of the third expression in Equation (11.63a) is similar to the one given above, there are nonetheless a few differences that must be explained. The proof begins with the following equation:

$$\left\langle d_{ij}^{*k} \frac{\partial V_i^{qr}}{\partial \xi_j} \right\rangle = 0 \tag{11.74}$$

The similarity of this equation to Equation (11.67a) is obvious, and its validity can be established easily in the same manner. From the definition of $d_{qr}^{*k}$ in Equation (11.45), the following expression is true on account of definition (11.64a):

$$d_{ij}^{*k} = zP_{ijk} - C_{ijml}\frac{\partial V_m^k}{\partial \xi_l} \tag{11.75}$$

Combining Equations (11.74) and (11.75) and using the averaging procedure of Equation (11.22) results in:

$$\left\langle zP_{ijk}\frac{\partial V_i^{qr}}{\partial \xi_j}\right\rangle - \left\langle C_{ijml}\frac{\partial V_m^k}{\partial \xi_l}\frac{\partial V_i^{qr}}{\partial \xi_j}\right\rangle = 0$$

$$\therefore \left\langle zP_{ijk}\frac{\partial V_i^{qr}}{\partial \xi_j}\right\rangle = \left\langle C_{ijml}\frac{\partial V_m^k}{\partial \xi_l}\frac{\partial V_i^{qr}}{\partial \xi_j}\right\rangle \tag{11.76}$$

Then, replacing $\varphi$ with $V_q^r$ in the third expression in Equation (11.66c) results in:

$$\left\langle b_{qp}^{*mn}\frac{\partial V_q^r}{\partial \xi_p}\right\rangle = 0 \tag{11.77}$$

From Equation (11.77) and the basic definition of $b_{qp}^{*mn}$ from Equation (11.45), the following expression can be derived:

$$\therefore \left\langle zC_{ijqr}\frac{\partial V_i^k}{\partial \xi_j}\right\rangle = -\left\langle C_{mlij}\frac{\partial V_m^k}{\partial \xi_l}\frac{\partial UV_i^{qr}}{\partial \xi_j}\right\rangle \tag{11.78}$$

Comparing the last expression in Equation (11.76) with Equation (11.78), and considering at the same time the symmetry of the elastic coefficients, results in:

$$\left\langle zP_{ijk}\frac{\partial V_i^{qr}}{\partial \xi_j}\right\rangle = -\left\langle zC_{ijqr}\frac{\partial V_i^k}{\partial \xi_{kj}}\right\rangle \tag{11.79}$$

Next, from Equation (11.75) one arrives at:

$$\left\langle zd_{qr}^{*k}\right\rangle = -\left\langle z^2P_{qrk}\right\rangle - \left\langle zC_{ijqr}\frac{\partial V_i^k}{\partial \xi_j}\right\rangle \tag{11.80}$$

Thus, from the last two Equations:

$$\left\langle zd_{qr}^{*k}\right\rangle = \left\langle z^2P_{qrk} + zP_{ijk}\frac{\partial V_i^{qr}}{\partial \xi_j}\right\rangle \tag{11.81}$$

On account of Equation (11.40b), Equation (11.81) becomes:

$$\left\langle zd_{qr}^{*k}\right\rangle = \left\langle z^2 C_{qrmn}d_{mnk} + zC_{ijmn}d_{mnk}\frac{\partial V_i^{qr}}{\partial \xi_j}\right\rangle$$

$$\therefore \left\langle zd_{qr}^{*k}\right\rangle = \left\langle \left\{ zC_{qrmn} + C_{ijmn}\frac{\partial V_i^{qr}}{\partial \xi_j}\right\} zd_{mnk}\right\rangle$$

(11.82)

On account of the first expression in Equation (11.45), the last expression in Equation (11. 82) becomes:

$$\left\langle zd_{qr}^{*k}\right\rangle = \left\langle zb_{mn}^{*qr}d_{mnk}\right\rangle$$

(11.83)

Finally, on account of Equations (11.8b), Equation (11.83) becomes:

$$\delta\left\langle zd_{qr}^{*k}\right\rangle = \left\langle zd_{mnk}^{(r)}b_{mn}^{*qr}\right\rangle$$

(11.84)

This is the desired symmetry relationship as it appears in Equation (11.63a). The remaining two expressions in Equation (11.63a) can be shown in a similar manner. Finally, the symmetry properties of the effective actuation coefficients as shown in Equation (11.63b), can be proved in a similar manner.

## 11.8 Homogenized Plate vs. Composite Laminate Theory

The model derived in this chapter is valid for a thin plate with a rapidly oscillating thickness. However, it is interesting to see what the model converges to for the case when the plate has a uniform thickness.

Consider the stress components acting on a differential plate element as shown in Figure 11-2. It follows from the notation introduced in this paper that the force and moment resultants as defined by Gibson [1994)] or Vinson ([1993] among others, are given by:

$$N_1 = \delta^2\left\langle \sigma_{11}^{(1)}\right\rangle, \quad N_2 = \delta^2\left\langle \sigma_{22}^{(1)}\right\rangle, \quad N_{12} = \delta^2\left\langle \sigma_{12}^{(1)}\right\rangle$$

$$Q_1 = \delta^3\left\langle \sigma_{13}^{(2)}\right\rangle, \quad Q_2 = \delta^3\left\langle \sigma_{23}^{(2)}\right\rangle$$

$$M_1 = \delta^3\left\langle z\sigma_{11}^{(1)}\right\rangle, \quad M_2 = \delta^3\left\langle z\sigma_{22}^{(1)}\right\rangle, \quad M_{12} = \delta^3\left\langle z\sigma_{12}^{(1)}\right\rangle$$

(11.85)

Here, the results in Equations (11.56b) and (11.56c) were also used.
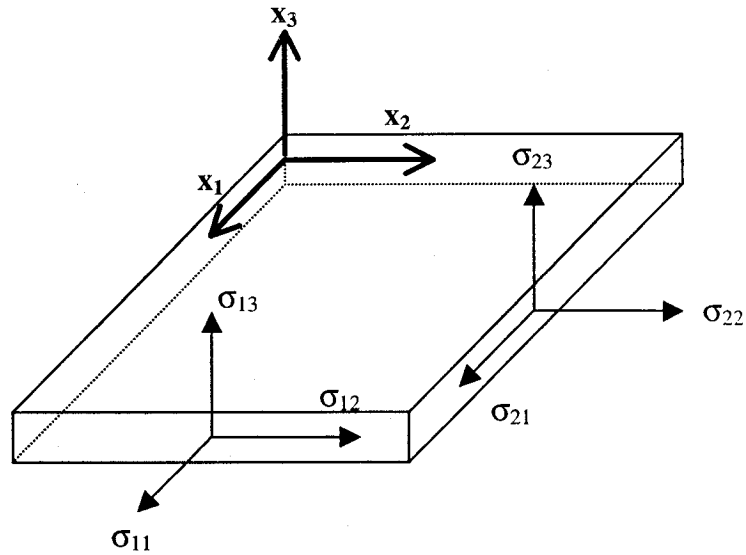
**Figure 11-2:** Differential plate element

Substitution of Equations (11.60a) and (11.60b) into Equation (11.85) with a simultaneous consideration of Equations (11. 61a), (11.61b) and (11.61c) leads to:

$$u_1 = v_1(\mathbf{x}) - x_3 \frac{\partial w}{\partial x_1} + \delta U_1^{\alpha\beta}\varepsilon_{\alpha\beta} + \delta^2 V_1^{\alpha\beta}\tau_{\alpha\beta} +$$
$$+ \delta^2 \left( U_1^k R_k^{(0)} + V_1^k R_k^{(1)} + W_1 T^{(0)} + X_1 T^{(1)} + Y_1 C^{(0)} + A_1 C^{(1)} \right) \tag{11.86a}$$

$$u_2 = v_2(\mathbf{x}) - x_3 \frac{\partial w}{\partial x_2} + \delta U_2^{\alpha\beta}\varepsilon_{\alpha\beta} + \delta^2 V_2^{\alpha\beta}\tau_{\alpha\beta} +$$
$$+ \delta^2 \left( U_2^k R_k^{(0)} + V_2^k R_k^{(1)} + W_2 T^{(0)} + X_2 T^{(1)} + Y_2 C^{(0)} + A_2 C^{(1)} \right) \tag{11.86b}$$

$$u_3 = w(\mathbf{x}) + \delta v_3^{(1)} + \delta U_3^{\alpha\beta}\varepsilon_{\alpha\beta} + \delta^2 V_3^{\alpha\beta}\tau_{\alpha\beta} +$$
$$+ \delta^2 \left( U_3^k R_k^{(0)} + V_3^k R_k^{(1)} + W_3 T^{(0)} + X_3 T^{(1)} + Y_3 C^{(0)} + A_3 C^{(1)} \right) \tag{11.86c}$$

$$N_1 = \delta\langle b_{11}^{\alpha\beta}\rangle\varepsilon_{\alpha\beta} + \delta^2\langle b_{11}^{*\alpha\beta}\rangle\tau_{\alpha\beta} - \delta^2\langle d_{11}^k\rangle R_k^{(0)} - \delta^2\langle d_{11}^{*k}\rangle R_k^{(1)} +$$
$$- \delta^2\langle\Theta_{11}\rangle T^{(0)} - \delta^2\langle\Theta_{11}^*\rangle T^{(1)} - \delta^2\langle\Lambda_{11}\rangle C^{(0)} - \delta^2\langle\Lambda_{11}^*\rangle C^{(1)} \tag{11.86d}$$

$$N_2 = \delta\langle b_{22}^{\alpha\beta}\rangle\varepsilon_{\alpha\beta} + \delta^2\langle b_{22}^{*\alpha\beta}\rangle\tau_{\alpha\beta} - \delta^2\langle d_{22}^k\rangle R_k^{(0)} - \delta^2\langle d_{22}^{*k}\rangle R_k^{(1)} +$$
$$- \delta^2\langle\Theta_{22}\rangle T^{(0)} - \delta^2\langle\Theta_{22}^*\rangle T^{(1)} - \delta^2\langle\Lambda_{22}\rangle C^{(0)} - \delta^2\langle\Lambda_{22}^*\rangle C^{(1)} \tag{11.86e}$$

$$N_{12} = \delta\langle b_{12}^{\alpha\beta}\rangle\varepsilon_{\alpha\beta} + \delta^2\langle b_{12}^{*\alpha\beta}\rangle\tau_{\alpha\beta} - \delta^2\langle d_{12}^{k}\rangle R_k^{(0)} - \delta^2\langle d_{12}^{*k}\rangle R_k^{(1)} +$$
$$-\delta^2\langle\Theta_{12}\rangle T^{(0)} - \delta^2\langle\Theta_{12}^{*}\rangle T^{(1)} - \delta^2\langle\Lambda_{12}\rangle C^{(0)} - \delta^2\langle\Lambda_{12}^{*}\rangle C^{(1)}$$

(11.86f)

$$Q_1 = \delta^3\langle\sigma_{13}^{(2)}\rangle$$

(11.86g)

$$Q_2 = \delta^3\langle\sigma_{23}^{(2)}\rangle$$

(11.86h)

$$M_1 = \delta\langle zb_{11}^{\alpha\beta}\rangle\varepsilon_{\alpha\beta} + \delta^2\langle zb_{11}^{*\alpha\beta}\rangle\tau_{\alpha\beta} - \delta^2\langle zd_{11}^{k}\rangle R_k^{(0)} - \delta^2\langle zd_{11}^{*k}\rangle R_k^{(1)} +$$
$$-\delta^2\langle z\Theta_{11}\rangle T^{(0)} - \delta^2\langle z\Theta_{11}^{*}\rangle T^{(1)} - \delta^2\langle z\Lambda_{11}\rangle C^{(0)} - \delta^2\langle z\Lambda_{11}^{*}\rangle C^{(1)}$$

(11.86i)

$$M_2 = \delta\langle zb_{22}^{\alpha\beta}\rangle\varepsilon_{\alpha\beta} + \delta^2\langle zb_{22}^{*\alpha\beta}\rangle\tau_{\alpha\beta} - \delta^2\langle zd_{22}^{k}\rangle R_k^{(0)} - \delta^2\langle zd_{22}^{*k}\rangle R_k^{(1)} +$$
$$-\delta^2\langle z\Theta_{22}\rangle T^{(0)} - \delta^2\langle z\Theta_{22}^{*}\rangle T^{(1)} - \delta^2\langle z\Lambda_{22}\rangle C^{(0)} - \delta^2\langle z\Lambda_{22}^{*}\rangle C^{(1)}$$

(11.86j)

$$M_{12} = \delta\langle zb_{12}^{\alpha\beta}\rangle\varepsilon_{\alpha\beta} + \delta^2\langle zb_{12}^{*\alpha\beta}\rangle\tau_{\alpha\beta} - \delta^2\langle zd_{12}^{k}\rangle R_k^{(0)} - \delta^2\langle zd_{12}^{*k}\rangle R_k^{(1)} +$$
$$-\delta^2\langle z\Theta_{12}\rangle T^{(0)} - \delta^2\langle z\Theta_{12}^{*}\rangle T^{(1)} - \delta^2\langle z\Lambda_{12}\rangle C^{(0)} - \delta^2\langle z\Lambda_{12}^{*}\rangle C^{(1)}$$

(11.87k)

In Equations (11.87a) to (11.87k) the following definitions were made:

$$v_1(x) = \delta v_1^{(1)}(x), \quad v_2(x) = \delta v_2^{(1)}(x), \quad \varepsilon_{\alpha\beta} = \delta\varepsilon_{\alpha\beta}^{(1)}$$

(11.88)

One therefore concludes that $v_1(x)$, $v_2(x)$ and $w(x)$ represent the displacements of the middle plane of the plate and consequently $\varepsilon_{11}$, $\varepsilon_{22}$ and $\varepsilon_{12}$ are the mid-surface strains. As well, $-\dfrac{\partial w^2}{\partial x_1^2} = \tau_{11} = \kappa_{x1}$ and $-\dfrac{\partial w^2}{\partial x_2^2} = \tau_{22} = \kappa_{x2}$ are the bending curvatures associated with bending of the middle surface in the $x_1$-$x_3$ and $x_2$-$x_3$ planes respectively, and $-2\dfrac{\partial w^2}{\partial x_1\partial x_2} = 2\tau_{12} = k_{xy}$ is the twisting curvature associated with torsion of the middle surface, see also Equation (11.49a). Other terms in Equations (11.86a), (11.86b) and (11.86c) account for the effect of hygrothermal expansion as well as that of the external control signal R on the displacement field. In addition, the following relationships are evident [Gibson, 1994]:

$$A_{11} = \delta\left\langle b_{11}^{11}\right\rangle, \quad A_{12} = \delta\left\langle b_{11}^{22}\right\rangle, \quad A_{16} = \delta\left\langle b_{11}^{12}\right\rangle, \quad A_{22} = \delta\left\langle b_{22}^{22}\right\rangle, \quad A_{26} = \delta\left\langle b_{22}^{12}\right\rangle, \quad A_{66} = \delta\left\langle b_{12}^{12}\right\rangle,$$

$$B_{11} = \delta^2\left\langle zb_{11}^{11}\right\rangle = \delta^2\left\langle b_{11}^{*11}\right\rangle, \quad B_{12} = \delta^2\left\langle zb_{11}^{22}\right\rangle = \delta^2\left\langle b_{11}^{*22}\right\rangle, \quad B_{16} = \delta^2\left\langle zb_{11}^{12}\right\rangle = \delta^2\left\langle b_{11}^{*12}\right\rangle,$$

$$B_{22} = \delta^2\left\langle zb_{22}^{22}\right\rangle = \delta^2\left\langle b_{22}^{*22}\right\rangle, \quad B_{26} = \delta^2\left\langle zb_{22}^{12}\right\rangle = \delta^2\left\langle b_{12}^{*22}\right\rangle, \quad B_{66} = \delta^2\left\langle zb_{12}^{12}\right\rangle = \delta^2\left\langle b_{12}^{*12}\right\rangle,$$

$$D_{11} = \delta^3\left\langle zb_{11}^{*11}\right\rangle, \quad D_{12} = \delta^3\left\langle zb_{11}^{*22}\right\rangle, \quad D_{16} = \delta^3\left\langle zb_{11}^{*12}\right\rangle,$$

$$D_{22} = \delta^3\left\langle zb_{22}^{*22}\right\rangle, \quad D_{26} = \delta^3\left\langle zb_{22}^{*12}\right\rangle, \quad D_{66} = \delta^3\left\langle zb_{12}^{*12}\right\rangle \tag{11.89}$$

To continue the comparison, it becomes necessary to consider the thermal, hygroscopic and actuation (e.g. piezoelectric) effects on the force and moment vectors. Gibson [1994], defines the force and moment vectors due to hygrothermal effects by the following relationships:

$$\left\{N^T\right\} = T^{(0)}\sum_{k=1}^{N}\left[\overline{Q}\right]_k\left\{\alpha^{(\theta)}\right\}_k\left(x_{3,k} - x_{3,k-1}\right) \quad \left\{M^T\right\} = \frac{T^{(0)}}{2}\sum_{k=1}^{N}\left[\overline{Q}\right]_k\left\{\alpha^{(\theta)}\right\}_k\left(x_{3,k}^2 - x_{3,k-1}^2\right)$$

$$\left\{N^M\right\} = C^{(0)}\sum_{k=1}^{N}\left[\overline{Q}\right]_k\left\{\beta^{(c)}\right\}_k\left(x_{3,k} - x_{3,k-1}\right) \quad \left\{M^M\right\} = \frac{C^{(0)}}{2}\sum_{k=1}^{N}\left[\overline{Q}\right]_k\left\{\beta^{(c)}\right\}_k\left(x_{3,k}^2 - x_{3,k-1}^2\right) \tag{11.90}$$

Here, $\left[\overline{Q}\right]_k$ is the matrix of the plane stress-reduced elastic coefficients for the $k^{th}$ ply, and $x_{3,k}$ $x_{3,k-1}$ denote the distance of that ply from the middle of the laminate. As well, the superscripts T and M refer to thermal and hygroscopic effects respectively. For the purposes of the work in this chapter, one has to modify Equation (11.90) to take into consideration the linear (rather than constant) variation in the change in temperature and moisture content, see Equation (11.8c). Thus the thermal and hygroscopic forces and moments become:

$$N_{\alpha\beta}^T = \delta^2\left\langle \Theta_{\alpha\beta}\right\rangle T^{(0)} + \delta^2\left\langle \Theta_{\alpha\beta}^*\right\rangle T^{(1)},$$

$$M_{\alpha\beta}^T = \delta^3\left\langle z\Theta_{\alpha\beta}\right\rangle T^{(0)} + \delta^3\left\langle z\Theta_{\alpha\beta}^*\right\rangle T^{(1)}$$

$$N_{\alpha\beta}^M = \delta^2\left\langle \Lambda_{\alpha\beta}\right\rangle C^{(0)} + \delta^2\left\langle \Lambda_{\alpha\beta}^*\right\rangle C^{(1)},$$

$$M_{\alpha\beta}^M = \delta^3\left\langle z\Lambda_{\alpha\beta}\right\rangle C^{(0)} + \delta^3\left\langle z\Lambda_{\alpha\beta}^*\right\rangle C^{(1)} \tag{11.91}$$

Similarly, one may define actuation forces and moments as follows:

$$N_{\alpha\beta}^{R} = \delta^{2}\langle d_{\alpha\beta}^{m}\rangle R_{m}^{(0)} + \delta^{2}\langle d_{\alpha\beta}^{*m}\rangle R_{m}^{(1)}$$

$$M_{\alpha\beta}^{R} = \delta^{3}\langle zd_{\alpha\beta}^{m}\rangle R_{m}^{(0)} + \delta^{3}\langle zd_{\alpha\beta}^{*m}\rangle R_{m}^{(1)}$$

(11.92)

In view of relations (11.86d)-(11.86k), (11.91), (11.92), the meaning of the effective properties as defined in Section 11.6 is clear.

## 11.9 Summary and Concluding Remarks

The method of asymptotic homogenization was used to analyze a periodic smart composite plate of rapidly varying thickness and a large number of embedded actuators. A set of eight three-dimensional local unit-cell problems was derived which, unlike classical homogenization schemes, were shown to depend on boundary conditions rather than periodicity in the transverse direction. The solution of the unit-cell problems yields a set of functions which, when averaged over the volume of the periodicity cell, determine the effective elastic, actuation, thermal expansion and hygroscopic expansion coefficients pertinent to the homogenized anisotropic smart plate. These effective coefficients then enter the governing equations of the system, which in turn yield a set of displacement functions. These functions having been determined enable one to make accurate predictions concerning the three-dimensional local structure of the displacement and stress fields.

It will be observed that the local problems are completely determined by the structure of the unit cell of the smart plate, and are totally independent of the global formulation of the problem. Hence, the effective coefficients determined from these problems are quite general and may be used to examine a variety of problems associated with a given smart structure. Finally, it is shown that in the limiting case of a thin elastic plate of uniform thickness the derived model converges to the familiar classical plate model.

Appropriately, Chapter 12 illustrates the theory developed here with some practically-important examples. In particular, two broad classes of examples are considered. One

pertains to various laminates composed of monoclinic or orthotropic materials, and the other deals with the determination of the effective properties of wafer-type piezoelectric plates reinforced with mutually perpendicular ribs or stiffeners.

# 12.0 APPLICATIONS OF MODEL ON SMART COMPOSITE PLATES WITH RAPIDLY VARYING THICKNESS

## 12.1 Introduction

In Chapter 11, the mathematical model for a thin smart composite plate with rapidly varying thickness and an embedded array of actuators (see Figure 12-1) was derived.
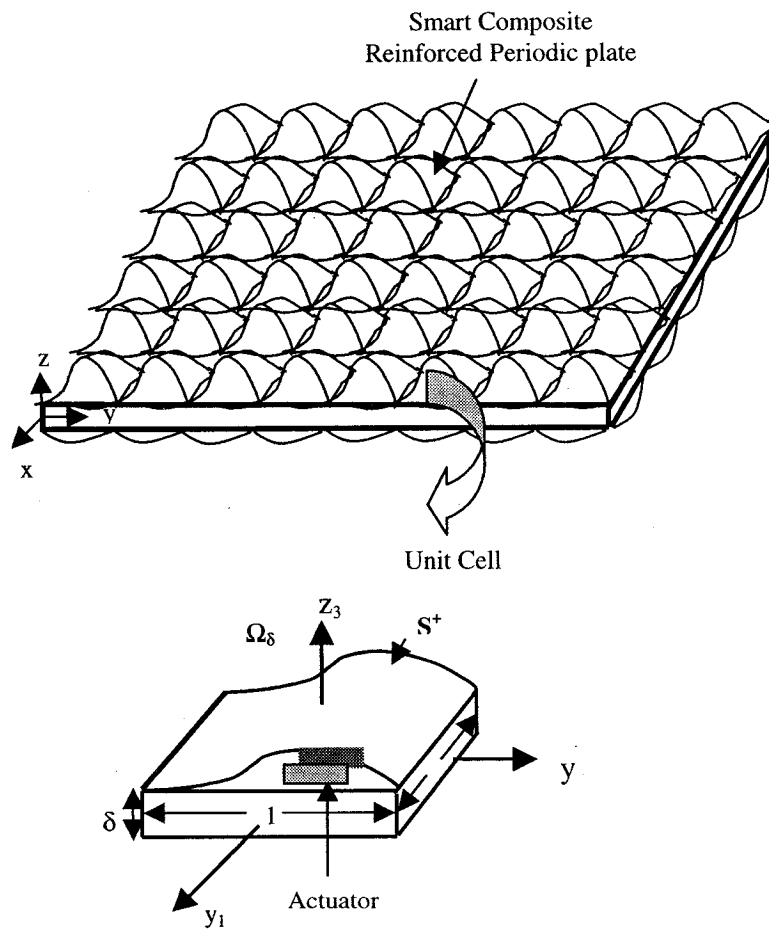


**Figure 12-1:** Thin smart composite periodic plate with rapidly varying thickness and its unit cell

In this Chapter, the theory developed will be illustrated by means of various examples. At first, the effective properties of constant thickness laminates comprised of monoclinic materials or orthotropic materials not referred to their principal coordinate system will be determined. These effective coefficients subsequently will be used to calculate strains and stresses induced in laminates by external loads, hygrothermal effects, or electric fields. Further examples illustrate the determination of the effective properties of wafer-type smart composite plates reinforced with smart ribs or stiffeners oriented along the tangential directions of the plate. For generality, it will be assumed that the ribs and the base plate are made of different orthotropic materials.

## 12.2 Constant-Thickness Laminates

The first examples pertain to laminates of constant thickness, as shown in Figure 12-2. It will be assumed that all layers are made of homogeneous materials and are perfectly bonded with one another. As shown in the unit cell of Figure 12-2, each layer is completely determined by the parameters $\delta_1$, $\delta_2$,... $\delta_M$ where M is the total number of layers. The thickness of the $m^{th}$ layer is therefore $\delta_m - \delta_{m-1}$ with $\delta_0 = 0$ and $\delta_M = 1$. The real thickness of the $m^{th}$ layer as measured in the original $(x_1, x_2, x_3)$ coordinate system is $\delta(\delta_m - \delta_{m-1})$ where $\delta$ is the thickness of the laminate (again with respect to the original coordinate system). Clearly, since material coefficients for this problem are independent of $y_1$ and $y_2$, then all partial derivatives in the unit cell problems of Equations (11.46a)-(11.46h) become ordinary derivatives with respect to z and the unit cell problems can be solved in a straightforward manner. As well, it is known that when an orthotropic or transversely isotropic material is not referred to its principal coordinate system, the number and location of the non-zero terms of the matrix of elastic, thermal expansion etc. coefficients conform to those of a monoclinic material, see Equation (12.1), [Reddy, 1997]. Consequently, the effective coefficients derived next will pertain to monoclinic materials.

$$
\begin{bmatrix}
C_{11} & C_{12} & C_{13} & 0 & 0 & C_{16} \\
C_{12} & C_{22} & C_{23} & 0 & 0 & C_{26} \\
C_{13} & C_{23} & C_{33} & 0 & 0 & C_{36} \\
0 & 0 & 0 & C_{44} & C_{45} & 0 \\
0 & 0 & 0 & C_{45} & C_{55} & 0 \\
C_{16} & C_{26} & C_{36} & 0 & 0 & C_{66}
\end{bmatrix}
\qquad
\begin{bmatrix}
0 & 0 & d_{31}^{(r)} \\
0 & 0 & d_{32}^{(r)} \\
0 & 0 & d_{33}^{(r)} \\
d_{14}^{(r)} & d_{24}^{(r)} & 0 \\
d_{15}^{(r)} & d_{25}^{(r)} & 0 \\
0 & 0 & d_{36}^{(r)}
\end{bmatrix}
\qquad (12.1a)
$$

(a) \qquad\qquad (b)

$$
\begin{bmatrix}
\alpha_{11}^{(\theta)} & \alpha_{12}^{(\theta)} & 0 \\
\alpha_{12}^{(\theta)} & \alpha_{22}^{(\theta)} & 0 \\
0 & 0 & \alpha_{33}^{(\theta)}
\end{bmatrix}
\qquad
\begin{bmatrix}
\beta_{11}^{(c)} & \beta_{12}^{(c)} & 0 \\
\beta_{12}^{(c)} & \beta_{22}^{(c)} & 0 \\
0 & 0 & \beta_{33}^{(c)}
\end{bmatrix}
\qquad (12.1b)
$$

(c) \qquad\qquad (d)
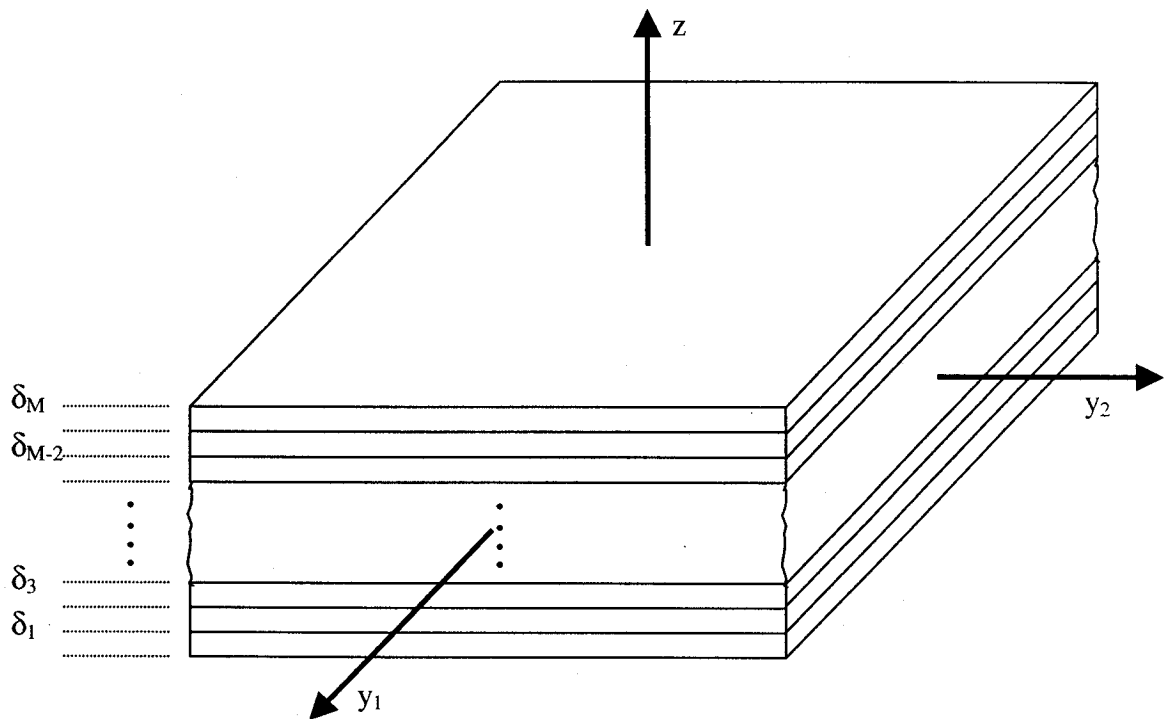


**Figure 12-2:** Unit cell of laminated plate

Before proceeding to the solution of the unit-cell problems observe that definitions (11.28b) now become:

$$L_{ijn} = C_{ijn3} \frac{d}{dz}, \quad D_{in} = \frac{d}{dz} L_{i3n}, \quad c_{i\alpha\beta} = \frac{dC_{i3\alpha\beta}}{dz} \tag{12.2}$$

As well, one observes from Figure 12-2 that:

$$Z^{\pm} = \pm \frac{1}{2}, \quad \mathbf{n} = \mathbf{N} = (0,0,1), \quad \delta_m = z + \frac{1}{2} \tag{12.3}$$

## 12.2.1 Effective Elastic Coefficients

In view of Equation (12.2), the unit-cell problem (11.46a) becomes:

$$\frac{d}{dz} b_{i3}^{\alpha\beta} = 0 \tag{12.4a}$$

$$b_{i3}^{\alpha\beta} = 0 \quad \text{on} \ z = z^{\pm}$$

The solution of Equation (12.4a) leads to

$$b_{i3}^{\alpha\beta} = 0 \tag{12.4b}$$

everywhere in the unit cell. On account of the pertinent definition in Equation (11.45) implies that

$$\frac{dU_k^{\alpha\beta}}{dz} = -C_{k3i3}^{-1} C_{i3\alpha\beta} \quad \text{where} \tag{12.4c}$$

$$C_{k3i3}^{-1} C_{i3n3} = \delta_{kn},$$

$\delta_{kn}$ being the Kronecker symbol. Hence, for a monoclinic material, see Equations (12.1a) and (12.1b),

$$\frac{dU_1^{\alpha\beta}}{dz} = \frac{dU_2^{\alpha\beta}}{dz} = 0, \quad \frac{dU_3^{\alpha\beta}}{dz} = -\frac{C_{33\alpha\beta}}{C_{3333}}$$

$$\text{and} \ \therefore b_{ij}^{\alpha\beta} = -C_{ij33} \frac{C_{33\alpha\beta}}{C_{3333}} + C_{ij\alpha\beta} \tag{12.5}$$

The elastic $b_{\alpha\beta}^{\lambda\mu}$ parameters for this material are thus given by:

$$b_{11}^{11} = -\frac{C_{13}^2}{C_{33}} + C_{11}, \quad b_{11}^{22} = -\frac{C_{13}C_{23}}{C_{33}} + C_{12}, \quad b_{11}^{12} = -\frac{C_{13}C_{36}}{C_{33}} + C_{16}, \quad b_{22}^{22} = -\frac{C_{23}^2}{C_{33}} + C_{22},$$

$$b_{22}^{12} = -\frac{C_{23}C_{36}}{C_{33}} + C_{26}, \quad b_{12}^{12} = -\frac{C_{36}^2}{C_{33}} + C_{66}, \quad b_{\lambda\mu}^{\alpha\beta} = b_{\mu\lambda}^{\beta\alpha} = b_{\alpha\beta}^{\lambda\mu} \tag{12.6}$$

Here the contracted notation for the elastic coefficients was used.

The solution of the second unit cell problem from Equation (11.46b) proceeds in a similar manner. Thus:

$$\frac{d}{dz} b_{i3}^{*\alpha\beta} = 0$$

$$b_{i3}^{*\alpha\beta} = 0 \quad \text{on} \quad z = z^{\pm}$$

(12.7a)

Therefore:

$$b_{i3}^{*\alpha\beta} = 0$$

$$\therefore \frac{dV_k^{\alpha\beta}}{dz} = -z C_{k3i3}^{-1} C_{i3\alpha\beta}$$

(12.7b)

Consequently, for a monoclinic material, one finds that:

$$\frac{dV_1^{\alpha\beta}}{dz} = \frac{dV_2^{\alpha\beta}}{dz} = 0, \quad \frac{dV_3^{\alpha\beta}}{dz} = -z \frac{C_{33\alpha\beta}}{C_{3333}}$$

$$\text{and} \quad \therefore b_{ij}^{*\alpha\beta} = -z C_{ij33} \frac{C_{33\alpha\beta}}{C_{3333}} + z C_{ij\alpha\beta}$$

(12.7c)

The elastic $b_{\alpha\beta}^{*\lambda\mu}$ parameters for this material are thus given by:

$$b_{11}^{*11} = -z \frac{C_{13}^2}{C_{33}} + z C_{11}, \quad b_{11}^{*22} = -z \frac{C_{13}C_{23}}{C_{33}} + z C_{12}, \quad b_{11}^{*12} = -z \frac{C_{13}C_{36}}{C_{33}} + z C_{16},$$

(12.7d)

$$b_{22}^{*22} = -z \frac{C_{23}^2}{C_{33}} + z C_{22}, \quad b_{22}^{*12} = -z \frac{C_{23}C_{36}}{C_{33}} + z C_{26}, \quad b_{12}^{*12} = -z \frac{C_{36}^2}{C_{33}} + z C_{66}, \quad b_{\lambda\mu}^{*\alpha\beta} = b_{\mu\lambda}^{*\beta\alpha} = b_{\alpha\beta}^{*\lambda\mu}$$

Comparing Equations (12.6) and (12.7d) one observes that:

$$b_{\alpha\beta}^{*\lambda\mu} = z b_{\alpha\beta}^{\lambda\mu}$$

(12.7e)

To calculate the effective elastic coefficients, one proceeds in accordance with definition (11.22) and integrates throughout the volume of the unit cell, considering at the same time Equation (12.3). The results are:

$$\left\langle b_{\alpha\beta}^{\lambda\mu} \right\rangle = \sum_{m=1}^{M} b_{\alpha\beta}^{\lambda\mu(m)} \left( \delta_m - \delta_{m-1} \right)$$

$$\left\langle z b_{\alpha\beta}^{\lambda\mu} \right\rangle = \frac{1}{2} \sum_{m=1}^{M} b_{\alpha\beta}^{\lambda\mu(m)} \left( \delta_m^2 - \delta_{m-1}^2 - \left( \delta_m - \delta_{m-1} \right) \right)$$

(12.8a)

$$\left\langle b_{\alpha\beta}^{*\lambda\mu} \right\rangle = \left\langle zb_{\alpha\beta}^{\lambda\mu} \right\rangle = \frac{1}{2}\sum_{m=1}^{M} b_{\alpha\beta}^{\lambda\mu(m)}\left(\delta_m^2 - \delta_{m-1}^2 - \left(\delta_m - \delta_{m-1}\right)\right) \tag{12.8b}$$

$$\left\langle zb_{\alpha\beta}^{*\lambda\mu} \right\rangle = \left\langle z^2 b_{\alpha\beta}^{\lambda\mu} \right\rangle = \frac{1}{3}\sum_{m=1}^{M} b_{\alpha\beta}^{\lambda\mu(m)}\left(\delta_m^3 - \delta_{m-1}^3 - \frac{3}{2}\left(\delta_m^2 - \delta_{m-1}^2\right) + \frac{3}{4}\left(\delta_m - \delta_{m-1}\right)\right)$$

The use of these coefficients will be illustrated by calculating the strains and stresses in an 8-layer [+45/-45]$_4$ antisymmetric angle-ply laminate consisting of 0.125-mm-thick AS/3501 graphite/epoxy laminae with material properties shown in Table 10-3 [Gibson, 1994], and subjected to forces $N_x$ = 10 kN/m, $N_y$ = -5 kN/m and moments $M_x$ = 4 Nm/m and $M_y$ = -3 Nm/m. Typical plots are shown in Figures 12-3 and 12-4. Figure 12-3 shows the variation of $\varepsilon_x$ and $\varepsilon_y$ through the thickness of the laminate and Figure 12-4 the variation of $\sigma_x$. The results are consistent with the classical plate theory to which the model converges.
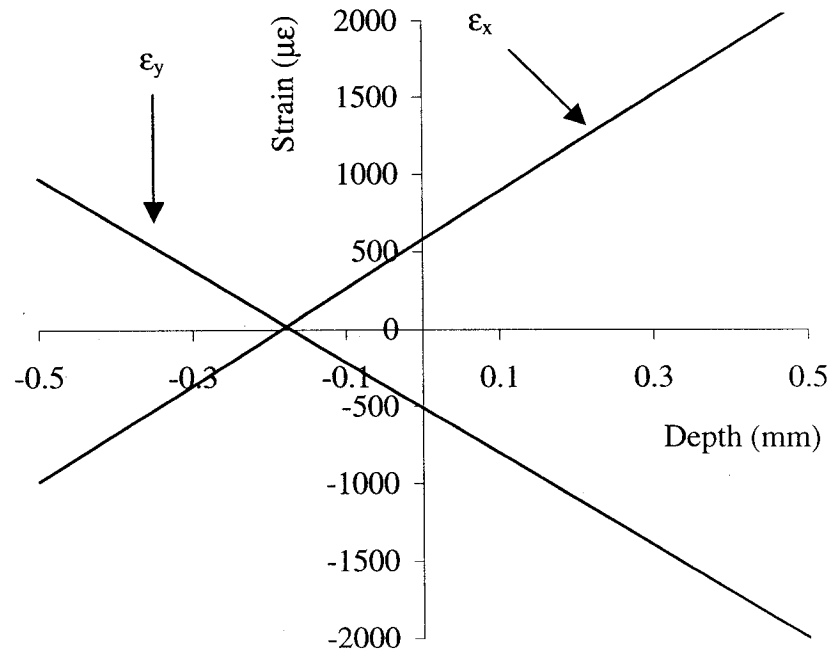


**Figure 12-3:** Variation of $\varepsilon_x$ and $\varepsilon_y$ through thickness of laminate
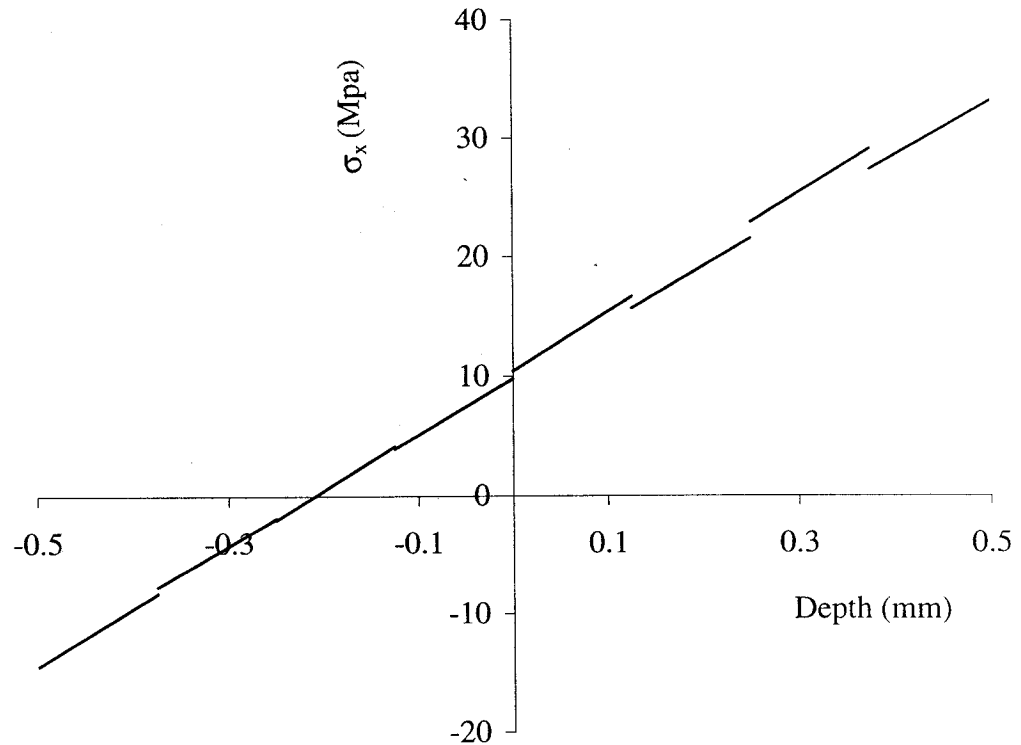
**Figure 12-4:** Variation of $\sigma_x$ through thickness of laminate

## 12.2.2 Effective Thermal Expansion Coefficients

In view of Equation (12.2), the unit cell problem (11.46e) becomes:

$$\frac{d}{dz}\Theta_{i3} = 0, \quad \text{subject to}$$

$$\Theta_{i3} = 0 \quad \text{on } Z^{\pm} \tag{12.9a}$$

The solution of Equation (12.9a) leads to:

$$\Theta_{i3} = 0 \quad \text{everywhere in the unit cell}$$

$$\Rightarrow \frac{dW_m}{dz} = C^{-1}_{m3i3}K_{i3} \tag{12.9b}$$

The latter expression follows directly from the appropriate definition in Equation (11.45).

It should be recalled that the $K_{ij}$ coefficients relate stress and temperature and are determined from the double contraction of the elastic coefficients $C_{ijkl}$ and the more familiar $\alpha_{ij}$ coefficients (which relate strain and temperature), see Equation (11.40b). Hence, for a monoclinic material, Equation (12.1b), the solution of Equation (12.9b) leads to:

$$\Theta_{ij} = K_{ij} - \frac{C_{ij33}K_{i3}}{C_{3333}}$$

$$\Rightarrow \Theta_{11} = K_{11} - \frac{C_{13}K_{33}}{C_{33}}, \quad \Theta_{22} = K_{22} - \frac{C_{23}K_{33}}{C_{33}}, \quad \Theta_{12} = K_{12} - \frac{C_{36}K_{33}}{C_{33}}$$

(12.10)

The unit cell problem from Equation (11.46f) proceeds in much the same way. Thus:

$$\frac{d}{dz}\Theta^*_{i3} = 0, \quad \text{subject to}$$

$$\Theta^*_{i3} = 0 \quad \text{on } Z^\pm$$

(12.11a)

The solution of Equation (12.9a) leads to:

$$\Theta^*_{i3} = 0 \quad \text{everywhere in the unit - cell}$$

$$\Rightarrow \frac{dX_m}{dz} = zC^{-1}_{m3i3}K_{i3}$$

(12.11b)

Hence, for a monoclinic material, the solution of Equation (12.11b) leads to:

$$\Theta^*_{ij} = zK_{ij} - \frac{zC_{ij33}K_{33}}{C_{3333}}$$

(12.12)

$$\Rightarrow \Theta^*_{11} = z\left(K_{11} - \frac{C_{13}K_{33}}{C_{33}}\right), \quad \Theta^*_{22} = z\left(K_{22} - \frac{C_{23}K_{33}}{C_{33}}\right), \quad \Theta^*_{12} = z\left(K_{12} - \frac{C_{36}K_{33}}{C_{33}}\right)$$

Integrating Equations (12.10) and (12.12) over the volume of the unit-cell gives the effective coefficients. They are:

$$\left\langle \Theta_{\alpha\beta} \right\rangle = \sum_{m=1}^{M} \Theta^{(m)}_{\alpha\beta}\left(\delta_m - \delta_{m-1}\right)$$

$$\left\langle \Theta^*_{\alpha\beta} \right\rangle = \left\langle z\Theta_{\alpha\beta} \right\rangle = \frac{1}{2}\sum_{m=1}^{M} \Theta^{(m)}_{\alpha\beta}\left[\delta^2_m - \delta^2_{m-1} - \left(\delta_m - \delta_{m-1}\right)\right]$$

(12.13)

$$\left\langle z\Theta^*_{\alpha\beta} \right\rangle = \left\langle z^2\Theta_{\alpha\beta} \right\rangle = \frac{1}{3}\sum_{m=1}^{M} \Theta^{(m)}_{\alpha\beta}\left[\delta^3_m - \delta^3_{m-1} - \frac{3}{2}\left(\delta^2_m - \delta^2_{m-1}\right) + \frac{3}{4}\left(\delta_m - \delta_{m-1}\right)\right]$$

The use of these effective coefficients will be illustrated by subjecting the same 8-layer [+45/-45]$_4$ antisymmetric angle-ply laminate considered in the previous example to a temperature change. In particular it will be assumed that $T^{(0)}$ and $T^{(1)}$ as defined in Equation (11.8c) are 40° C and 100° C respectively. One recalls that based on Equation (11.91) the expressions for the thermal force and moment vectors in terms of the effective coefficients were determined to be:

$$N_{\alpha\beta}^T = \delta^2 \left\langle \Theta_{\alpha\beta} \right\rangle T^{(0)} + \delta^2 \left\langle \Theta_{\alpha\beta}^* \right\rangle T^{(1)},$$

$$M_{\alpha\beta}^T = \delta^3 \left\langle z\Theta_{\alpha\beta} \right\rangle T^{(0)} + \delta^3 \left\langle z\Theta_{\alpha\beta}^* \right\rangle T^{(1)}$$

$$(12.14)$$
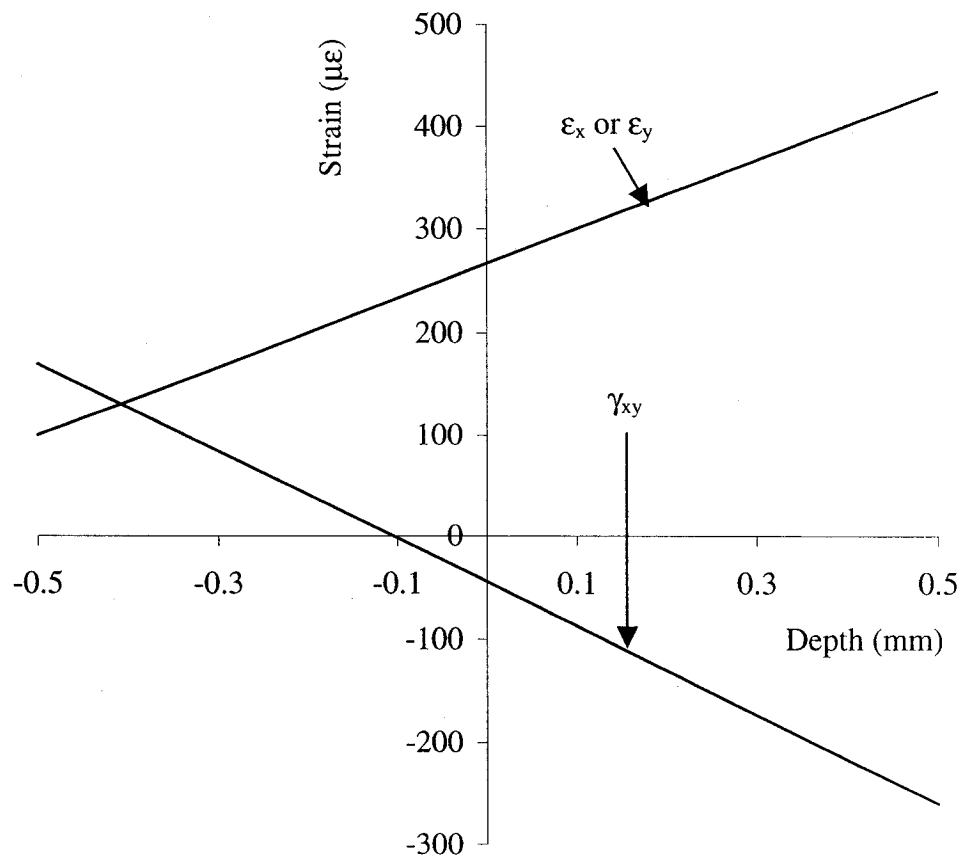


**Figure 12-5:** Strain variation through thickness of laminate subjected to temperature change

The thermal expansion coefficients for the graphite epoxy laminae in question are given in Table 10-4, [Gibson, 1994]. Figure 12-5 shows the normal and shear strain distribution in the laminate as a result of the given temperature increase. As expected, if $T^{(1)} = 0$ (or if the $\langle \Theta^*_{\alpha\beta} \rangle$ and $\langle z\Theta^*_{\alpha\beta} \rangle$ effective thermal expansion coefficients are neglected) the strain values obtained conform with those pertaining to the classical plate theory. Figures 12-6 and 12-7 show the variation of $\sigma_x$ (or $\sigma_y$) and $\tau_{xy}$ respectively. It is observed that the stress distribution is quite complex (due to coupling) and that the laminate experiences both bending about the $x_1$ and $x_2$ axes, as well as out-of-plane warping.
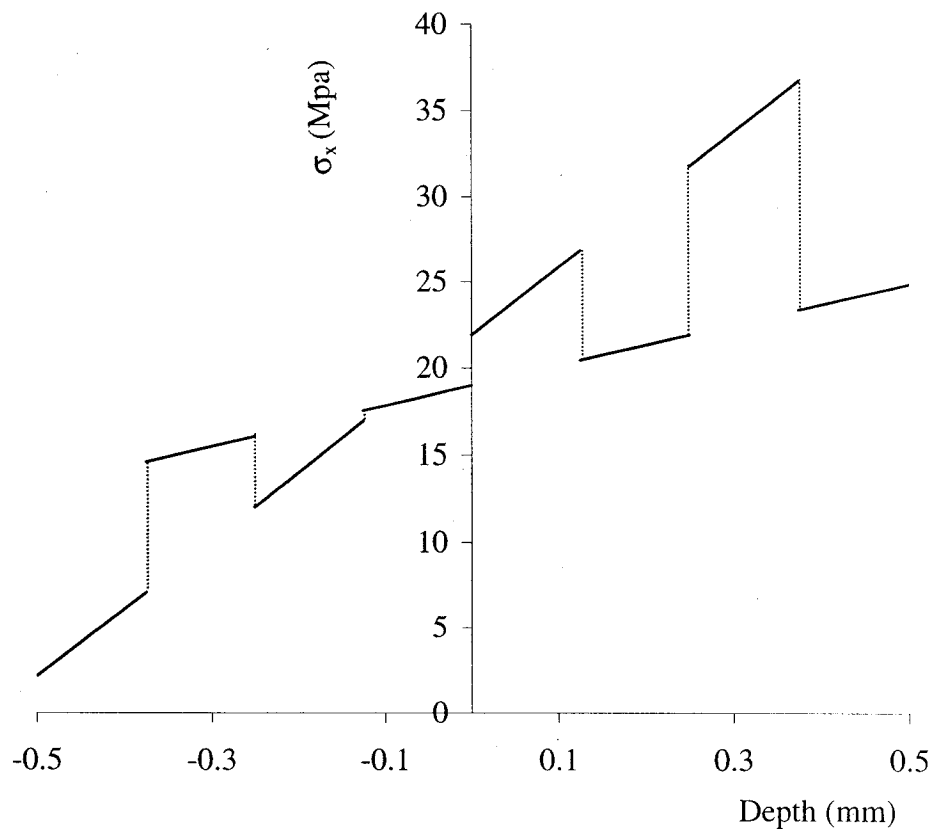


**Figure 12-6:** $\sigma_x$ (or $\sigma_y$) variation through thickness of laminate subjected to temperature change
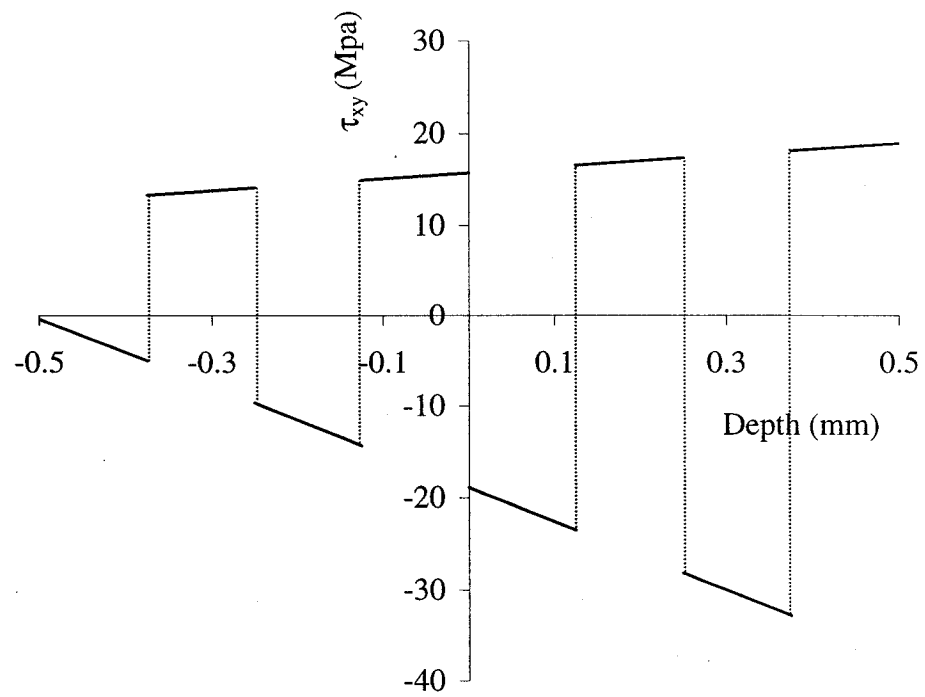
**Figure 12-7:** $\tau_{xy}$ variation through thickness of laminate subjected to temperature change

### 12.2.3 Effective Hygroscopic Expansion Coefficients

In view of Equation (12.2), the unit-cell problem (11.46g) becomes:

$$\frac{d}{dz}\Lambda_{i3} = 0, \quad \text{subject to}$$

$$\Lambda_{i3} = 0 \quad \text{on } Z^{\pm}$$

(12.15a)

The solution of Equation (12.15a) leads to:

$$\Lambda_{i3} = 0 \quad \text{everywhere in the unit cell}$$

$$\Rightarrow \frac{dY_m}{dz} = C_{m3i3}^{-1}B_{i3}$$

(12.15b)

Hence, for a monoclinic material, the solution of Equation (12.15b) leads to:

$$\Lambda_{ij} = B_{ij} - \frac{C_{ij33}B_{i3}}{C_{3333}}$$

$$\Rightarrow \Lambda_{11} = B_{11} - \frac{C_{13}B_{33}}{C_{33}}, \quad \Lambda_{22} = B_{22} - \frac{C_{23}B_{33}}{C_{33}}, \quad \Lambda_{12} = B_{12} - \frac{C_{36}B_{33}}{C_{33}}$$

(12.16)

Similarly, the unit-cell problem (11.46h) becomes:

$$\frac{d}{dz}\Lambda_{i3}^{*} = 0, \quad \text{subject to}$$

$$\Lambda_{i3}^{*} = 0 \quad \text{on } Z^{\pm}$$

(12.17a)

The solution of Equation (12.17a) leads to:

$$\Lambda_{i3}^{*} = 0 \quad \text{everywhere in the unit cell}$$

$$\Rightarrow \frac{dA_{m}}{dz} = zC_{m3i3}^{-1}K_{i3}$$

(12.17b)

Hence, for a monoclinic material, the solution of Equation (12.17b) leads to:

$$\Lambda_{ij}^{*} = zB_{ij} - \frac{zC_{ij33}B_{33}}{C_{3333}}$$

(12.18)

$$\Rightarrow \Lambda_{11}^{*} = z\left(B_{11} - \frac{C_{13}B_{33}}{C_{33}}\right), \quad \Lambda_{22}^{*} = z\left(B_{22} - \frac{C_{23}B_{33}}{C_{33}}\right), \quad \Lambda_{12}^{*} = z\left(B_{12} - \frac{C_{36}B_{33}}{C_{33}}\right)$$

It should be noted here that the $B_{ij}$ coefficients relate stress to change in moisture concentration, and are determined from the double contraction of the elastic coefficients $C_{ijkl}$ and the more familiar $\beta_{ij}$ coefficients (which relate strain and moisture concentration). The effective hygroscopic expansion coefficients pertaining to a monoclinic elastic solid are thus obtained from Equations (12.16) and (12.18) by integrating over the volume of the unit cell. The results are:

$$\langle \Lambda_{\alpha\beta} \rangle = \sum_{m=1}^{M} \Lambda_{\alpha\beta}^{(m)} (\delta_{m} - \delta_{m-1})$$

$$\langle \Lambda_{\alpha\beta}^{*} \rangle = \langle z\Lambda_{\alpha\beta} \rangle = \frac{1}{2}\sum_{m=1}^{M} \Lambda_{\alpha\beta}^{(m)} \left[\delta_{m}^{2} - \delta_{m-1}^{2} - (\delta_{m} - \delta_{m-1})\right]$$

(12.19)

$$\langle z\Lambda_{\alpha\beta}^{*} \rangle = \langle z^{2}\Lambda_{\alpha\beta} \rangle = \frac{1}{3}\sum_{m=1}^{M} \Lambda_{\alpha\beta}^{(m)} \left[\delta_{m}^{3} - \delta_{m-1}^{3} - \frac{3}{2}(\delta_{m}^{2} - \delta_{m-1}^{2}) + \frac{3}{4}(\delta_{m} - \delta_{m-1})\right]$$

As an illustration of the use of the effective hygroscopic coefficients, consider the same angle-ply laminate from the previous example and assume that both $C^{(0)}$ and $C^{(1)}$ defined

in Equation (11.8c) to be 0.5%. The variation of the normal and shear strains through the thickness of the laminate is determined and plotted in Figure 12-8. It is noted that the calculation of these induced strains was based on the expressions for the hygroscopic forces and moments determined from Equation (11.91) to be:

$$N_{\alpha\beta}^{M} = \delta^{2}\left\langle\Lambda_{\alpha\beta}\right\rangle C^{(0)} + \delta^{2}\left\langle\Lambda_{\alpha\beta}^{*}\right\rangle C^{(1)}$$
$$M_{\alpha\beta}^{T} = \delta^{3}\left\langle z\Lambda_{\alpha\beta}\right\rangle C^{(0)} + \delta^{3}\left\langle z\Lambda_{\alpha\beta}^{*}\right\rangle C^{(1)}$$

(12.20)

As well, Figures 12-9 and 12-10 show the variation of $\sigma_x$ (or $\sigma_y$) and $\tau_{xy}$ respectively. Similarly to the previous example, the laminate experiences both bending and out-of-plane warping. It should be noted that if $\left\langle\Lambda_{\alpha\beta}^{*}\right\rangle$ and $\left\langle z\Lambda_{\alpha\beta}^{*}\right\rangle$ are neglected, or equivalently if $C^{(1)} = 0$, then the resulting strains and stresses agree with their counterparts from the classical laminate theory.
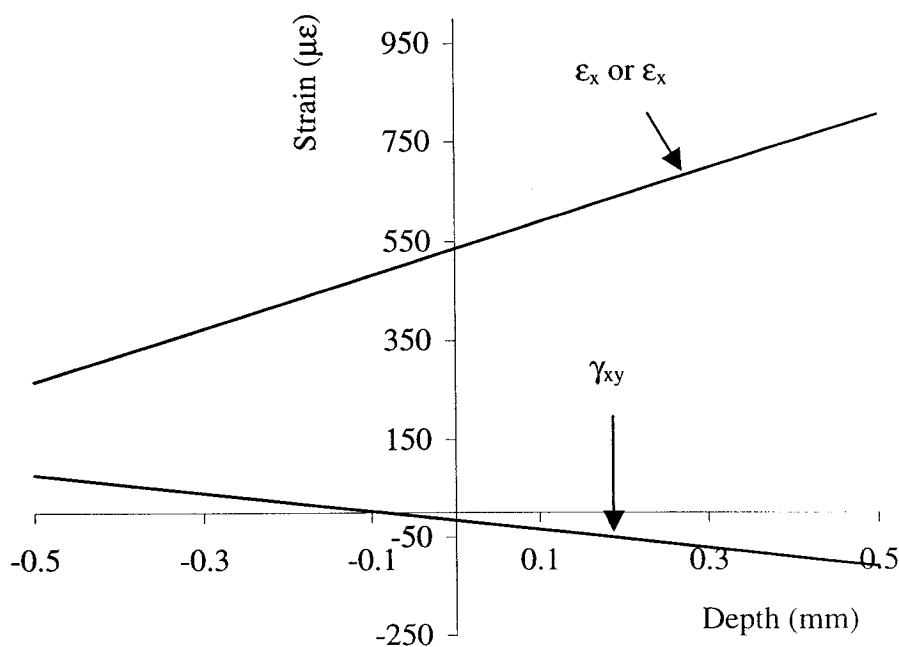


**Figure 12-8:** Strain variation through thickness of laminate subjected to a change in moisture content
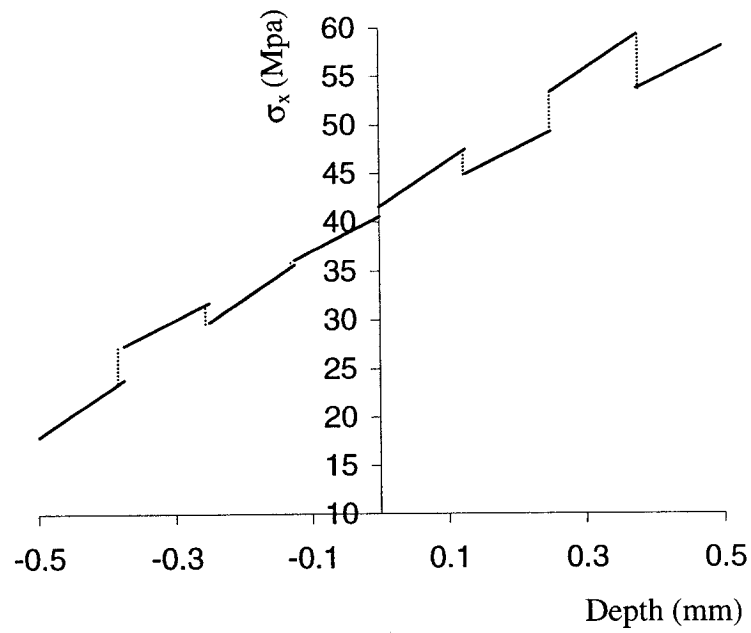
**Figure 12-9:** $\sigma_x$ (or $\sigma_y$) variation through thickness of laminate subjected to a change in moisture concentration
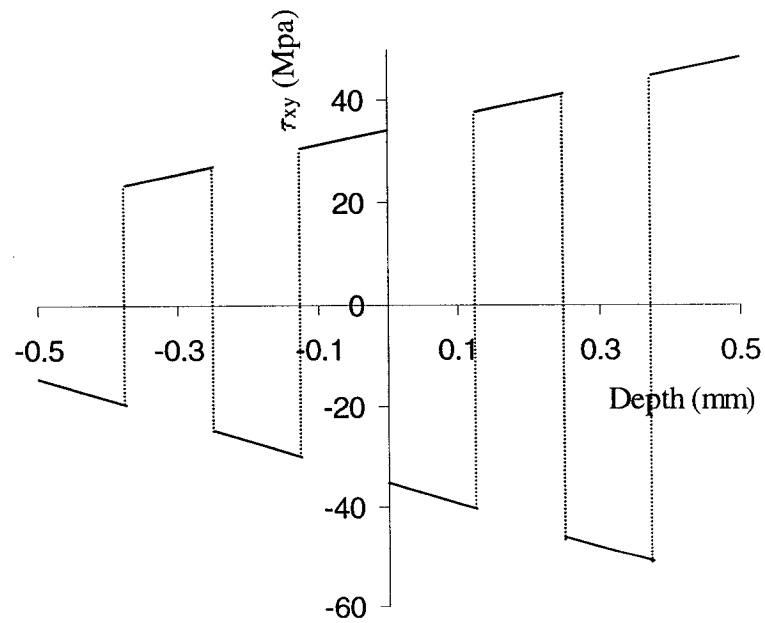


**Figure 12-10:** $\tau_{xy}$ variation through thickness of laminate subjected to a change in moisture concentration

### 12.2.4 Effective Piezoelectric Coefficients

Consider now the unit-cell problem (11.46c), which, for a laminate made of homogeneous layers, reduces to:

$$\frac{d}{dz}d_{i3}^k = 0, \quad \text{subject to}$$

$$d_{i3}^k = 0 \quad \text{on } Z^\pm \tag{12.21}$$

The solution of Equation (12.21) leads to

$$d_{i3}^k = 0 \quad \text{everywhere in the unit cell}$$

$$\Rightarrow \frac{dU_m^k}{dz} = C_{m3i3}^{-1}P_{i3k}, \tag{12.22}$$

the latter following from the appropriate definition in Equation (11.45).

Thus, for a monoclinic piezoelectric solid, one obtains:

$$\frac{dU_1^1}{dz} = C_{55}^{-1}P_{15} + C_{45}^{-1}P_{14}, \quad \frac{dU_1^2}{dz} = C_{55}^{-1}P_{25} + C_{45}^{-1}P_{24},$$

$$\frac{dU_2^1}{dz} = C_{45}^{-1}P_{25} + C_{44}^{-1}P_{14}, \quad \frac{dU_2^2}{dz} = C_{45}^{-1}P_{25} + C_{44}^{-1}P_{24},$$

$$\frac{dU_3^3}{dz} = \frac{P_{33}}{C_{33}}, \tag{12.23}$$

$$\frac{dU_1^3}{dz} = \frac{dU_2^3}{dz} = \frac{dU_3^1}{dz} = \frac{dU_3^2}{dz} = 0$$

The solution of Equation (12.23) leads to,

$$d_{11}^3 = P_{31} - \frac{C_{13}}{C_{33}}P_{33}, \quad d_{22}^3 = P_{32} - \frac{C_{23}}{C_{33}}P_{33}, \quad d_{12}^3 = P_{36} - \frac{C_{36}}{C_{33}}P_{33}$$

$$d_{\alpha\beta}^\mu = 0, \tag{12.24}$$

where, as before, Greek suffixes range from 1 to 2 as opposed to Latin indices, which range from 1 to 3.

Likewise, unit-cell problem (11.46d) becomes:

$$\frac{d}{dz}d_{i3}^{*k} = 0, \quad \text{subject to}$$

$$d_{i3}^{*k} = 0 \quad \text{on } Z^{\pm}$$

(12.25)

The solution of Equation (12.25) leads to:

$$d_{i3}^{*k} = 0 \quad \text{everywhere in the unit cell}$$

$$\Rightarrow \frac{dV_m^k}{dz} = zC_{m3i3}^{-1}P_{i3k}$$

(12.26)

It will be observed from the last expressions in Equations (12.22) and (12.26) that:

$$\frac{dV_m^k}{dz} = z\frac{dU_m^k}{dz}$$

(12.27)

Thus,

$$\frac{dV_1^1}{dz} = z\left(C_{55}^{-1}P_{15} + C_{45}^{-1}P_{14}\right), \quad \frac{dV_1^2}{dz} = z\left(C_{55}^{-1}P_{25} + C_{45}^{-1}P_{24}\right),$$

$$\frac{dV_2^1}{dz} = z\left(C_{45}^{-1}P_{25} + C_{44}^{-1}P_{14}\right), \quad \frac{dV_2^2}{dz} = z\left(C_{45}^{-1}P_{25} + C_{44}^{-1}P_{24}\right),$$

$$\frac{dV_3^3}{dz} = z\left(\frac{P_{33}}{C_{33}}\right),$$

$$\frac{dV_1^3}{dz} = \frac{dV_2^3}{dz} = \frac{dV_3^1}{dz} = \frac{dV_3^2}{dz} = 0$$

(12.28)

The solution of Equation (12.28) leads to:

$$d_{11}^{*3} = z\left(P_{31} - \frac{C_{13}}{C_{33}}P_{33}\right), \quad d_{22}^{*3} = z\left(P_{32} - \frac{C_{23}}{C_{33}}P_{33}\right), \quad d_{12}^{*3} = z\left(P_{36} - \frac{C_{36}}{C_{33}}P_{33}\right)$$

$$d_{\alpha\beta}^{*\mu} = 0$$

(12.29)

It is noted here that $P_{ijk}$ represent the piezoelectric stress coefficients which are obtained by the double contraction of the elastic coefficients and the piezoelectric strain coefficients $d_{ijk}$.

The effective piezoelectric constants pertinent to a monoclinic laminate are determined from Equations (12.24) and (12.29) and the averaging procedure, defined in this work as the integration over the volume of the unit cell. They are:

$$\left\langle d_{\alpha\beta}^3 \right\rangle = \sum_{m=1}^{M} d_{\alpha\beta}^{3(m)} \left( \delta_m - \delta_{m-1} \right),$$

$$\left\langle z d_{\alpha\beta}^3 \right\rangle = \left\langle d_{\alpha\beta}^{*3} \right\rangle = \frac{1}{2} \sum_{m=1}^{M} d_{\alpha\beta}^{3(m)} \left[ \left( \delta_m^2 - \delta_{m-1}^2 \right) - \left( \delta_m - \delta_{m-1} \right) \right],$$

$$\left\langle z d_{\alpha\beta}^{*3} \right\rangle = \left\langle z^2 d_{\alpha\beta}^3 \right\rangle = \frac{1}{3} \sum_{m=1}^{M} d_{\alpha\beta}^{3(m)} \left[ \left( \delta_m^3 - \delta_{m-1}^3 \right) - \frac{3}{2} \left( \delta_m^2 - \delta_{m-1}^2 \right) + \frac{3}{4} \left( \delta_m - \delta_{m-1} \right) \right]$$

(12.30)

**Table 12-1:** Material Properties [Vel and Batra, 2000b]

| Material Property | 0° PVDF |
| --- | --- |
| $C_{11}$ (GPa) | 238.24 |
| $C_{12}$ (GPa) | 3.98 |
| $C_{13}$ (GPa) | 2.19 |
| $C_{22}$ (GPa) | 14.6 |
| $C_{23}$ (GPa) | 4.4 |
| $C_{33}$ (GPa) | 10.64 |
| $C_{44}$ (GPa) | 2.15 |
| $C_{55}$ (GPa) | 2.15 |
| $C_{66}$ (GPa) | 6.43 |
| $e_{31}$(Cm$^{-2}$) | -0.130 |
| $e_{32}$(Cm$^{-2}$) | -0.145 |
| $e_{33}$(Cm$^{-2}$) | -0.276 |
| $e_{24}$(Cm$^{-2}$) | -0.009 |
| $e_{15}$(Cm$^{-2}$) | -0.135 |

The use of the effective piezoelectric coefficients will be illustrated by calculating the strains and stresses induced in a $[0/90]_4$ laminate composed of PVDF piezoelectric layers with elastic and piezoelectric properties shown in Table 12-1 [Vel and Batra, 2000b]. It will be assumed that $R_3^{(0)}$ and $R_3^{(1)}$ are both equal to 100V/mm. After calculating the effective elastic coefficients of this laminate from Equations (12.8a) and (12.8b), and using the derived expressions for the piezoelectric force and moment vectors from Equation (11.92), i.e.,

$$N_{\alpha\beta}^R = \delta^2 \left\langle d_{\alpha\beta}^m \right\rangle R_m^{(0)} + \delta^2 \left\langle d_{\alpha\beta}^{*m} \right\rangle R_m^{(1)}$$

$$M_{\alpha\beta}^R = \delta^3 \left\langle z d_{\alpha\beta}^m \right\rangle R_m^{(0)} + \delta^3 \left\langle z d_{\alpha\beta}^{*m} \right\rangle R_m^{(1)}$$

(12.31)

the strains due to the electric field are readily determined and are plotted in Figure 12-11. Figures 12-12 and 12-13 are plots of $\sigma_x$ and $\sigma_y$ respectively.
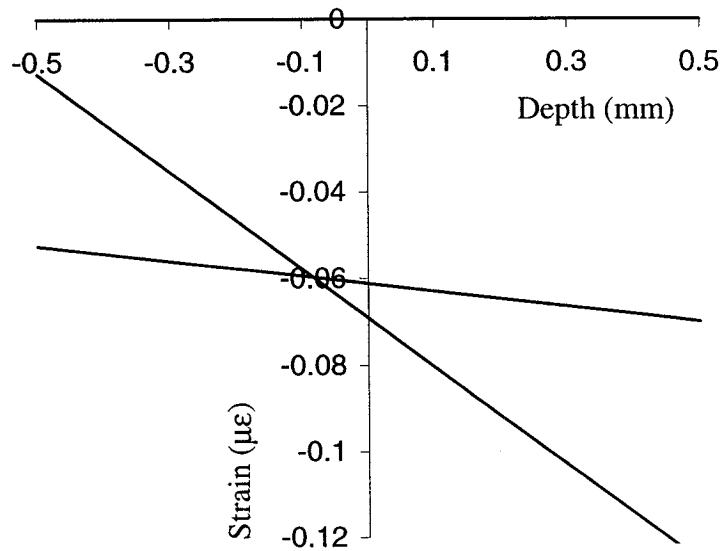


**Figure 12-11:** Strain variation through thickness of piezoelectric laminate due to an electric field
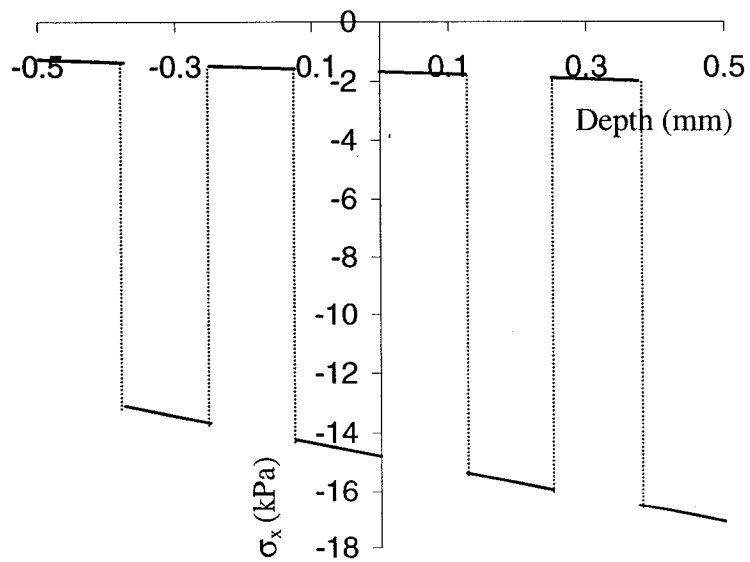


**Figure 12-12:** $\sigma_x$ variation through thickness of piezoelectric laminate due to an electric field
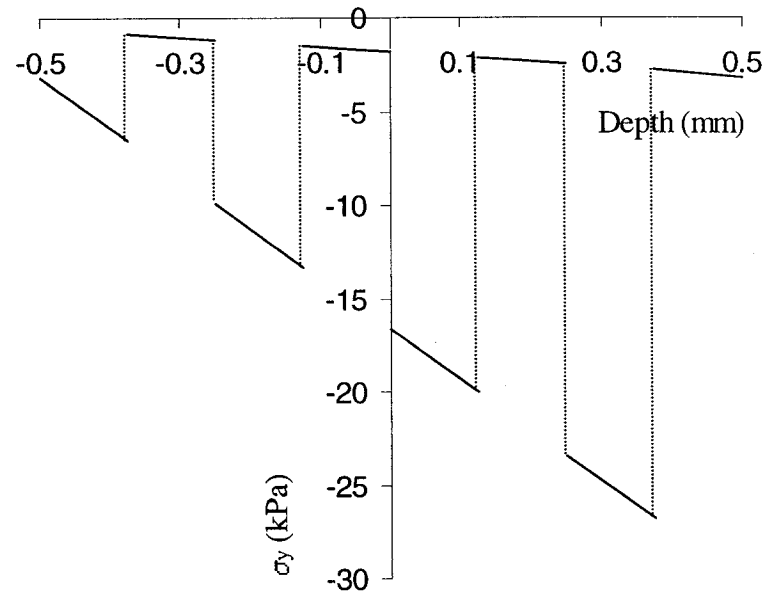
**Figure 12-13:** $\sigma_y$ variation through thickness of piezoelectric laminate due to an electric field

## 12.3 Wafer-type Reinforced Plates

In the subsequent examples a different type of structure will be considered, namely a wafer-reinforced piezoelectric plate, shown in Figure 12-14 [Kalamkarov, 1992]. For generality it will be assumed that the reinforcements also exhibit piezoelectric properties, which may be, if desired, set to zero. As well, each constituent of the unit cell will be made of a different orthotropic material. We are interested in calculating the effective piezoelectric, elastic, thermal expansion and hygroscopic coefficients for this structure.

The elastic and thermal expansion coefficients for wafer-reinforced composite plates were calculated by Kalamkarov [1992]. Neither the plate nor its reinforcements exhibited any actuation characteristics. In this section, the same technique will be applied to smart composite plates with smart wafers or ribs. In addition to the effective piezoelectric coefficients, the effective hygroscopic coefficients will also be determined. As well, Kalamkarov [1992] did not use the unit-cell problems defined by Equations (11.46e) and (11.46f) when calculating the effective thermal expansion coefficients. Instead, he used the symmetry relationships shown in Equation (11.62b). Hence, in this section, in addition to the piezoelectric and hygroscopic expansion coefficients, the thermal expansion coefficients will also be calculated directly from the unit-cell problems.

A solution of the local problems relevant to this kind of geometry may be found under the assumption that the thickness of each of the three elements of the unit cell is small in comparison with the other two dimensions, i.e.

$$t_1 \ll h_2, \quad t_2 \ll h_1, \quad H \sim h_1, h_2. \tag{12.31}$$

The local problems then can be solved approximately for each of the unit-cell elements, assuming that complications at the joints are highly localized and do not contribute significantly to the integrals over the unit cell. Consequently, the local problems can be solved independently for regions $\Omega_1$, $\Omega_2$ and $\Omega_3$ as shown in Figure 12-15 [Kalamkarov,

1992]. Figure 12-15 also shows the transformed unit cell under the introduction of the rapid coordinates $y_1$, $y_2$, and $z$.

Wafer reinforced plate
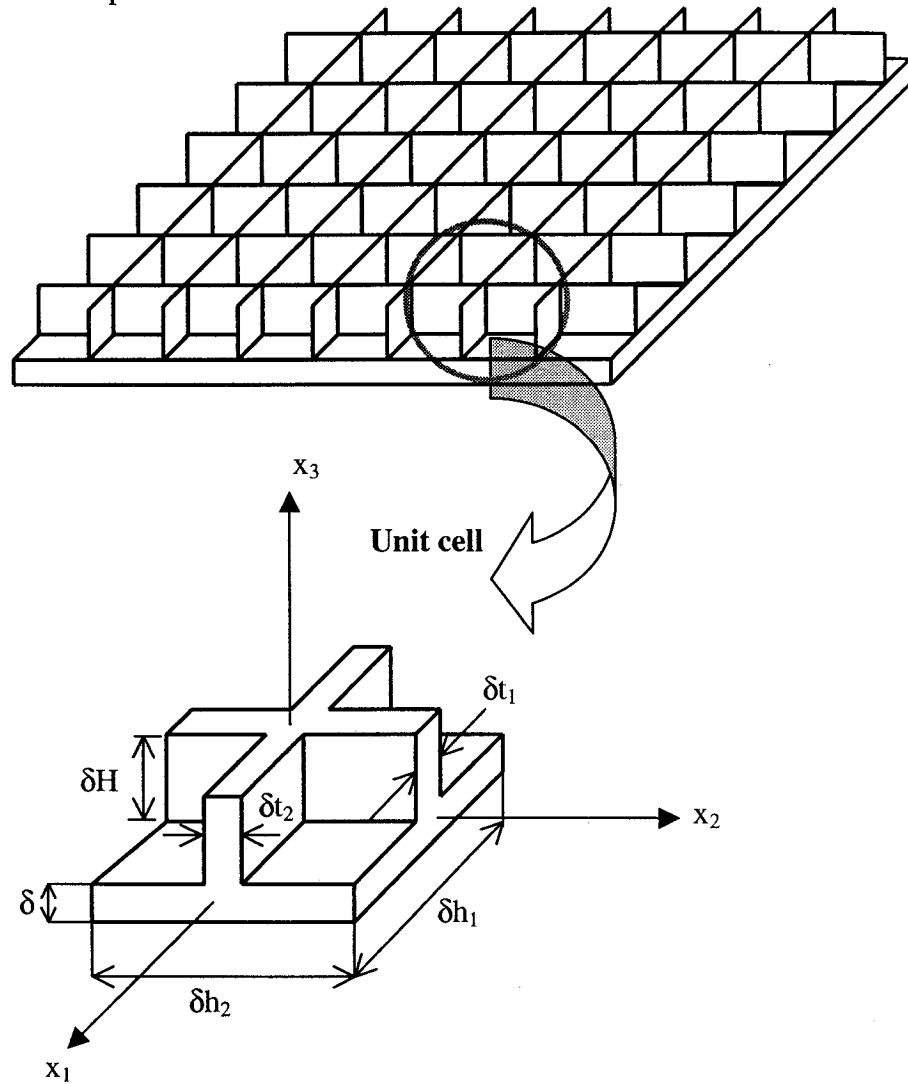


**Figure 12-14:** A wafer-reinforced plate and its unit cell [Kalamkarov, 1992]
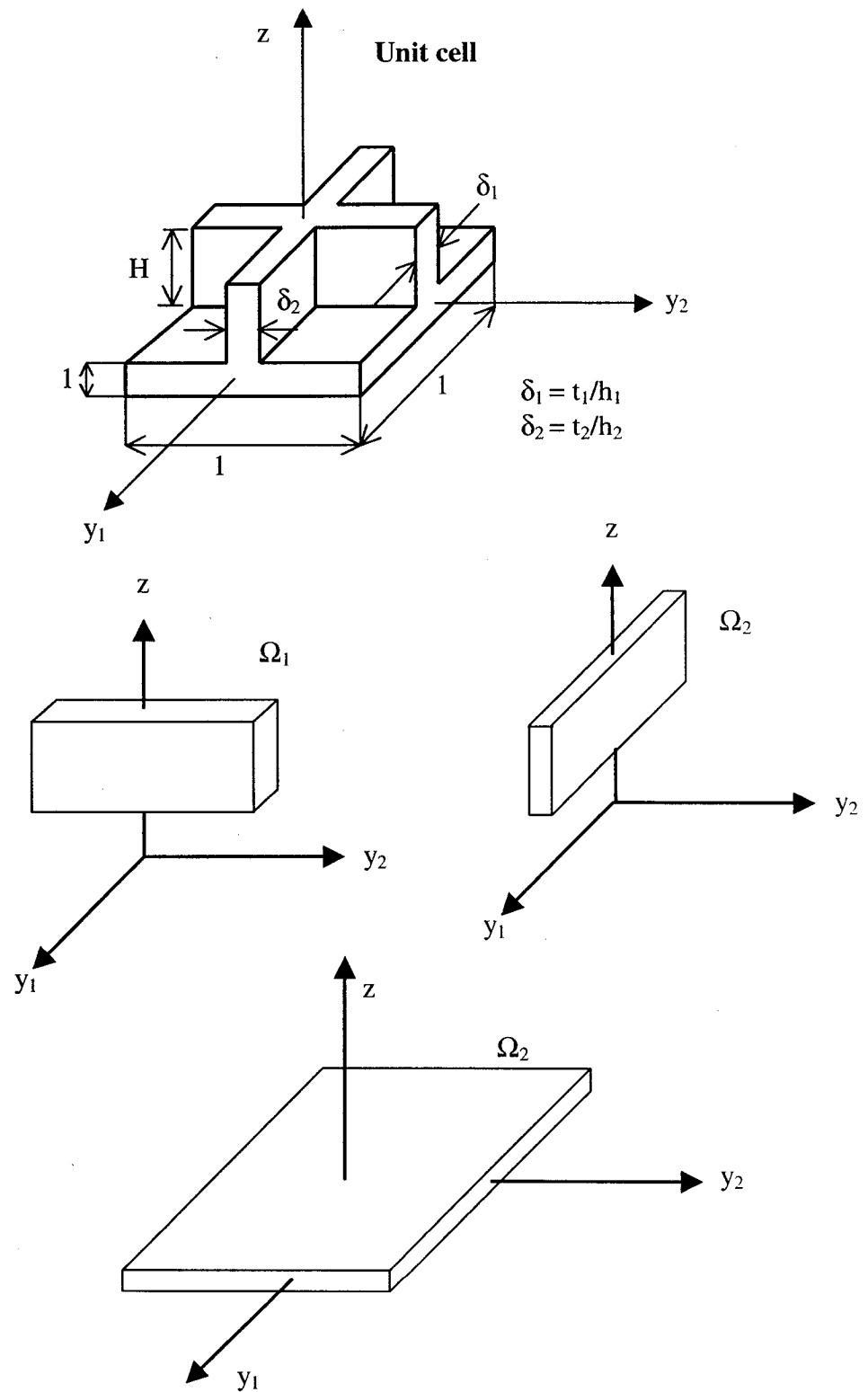
**Figure 12-15:** Unit cell of a wafer (with respect to fast coordinates) and the individual elements [Kalamkarov, 1992]

### 12.3.1 Effective Elastic Coefficients

The solution of the elasticity problem through unit-cell problems (11.46a) and (11.46b) has been obtained by Kalamkarov [1992]. The results only will be given below:

$$b_{11}^{11} = \begin{cases} 0 & \text{in } \Omega_1 \\ E_1 & \text{in } \Omega_2 \\ \dfrac{E_1}{1 - \nu_{12}\nu_{21}} & \text{in } \Omega_3 \end{cases} \qquad b_{22}^{11} = b_{11}^{22} = \begin{cases} 0 & \text{in } \Omega_1, \Omega_2 \\ \dfrac{\nu_{12}E_2}{1 - \nu_{12}\nu_{21}} & \text{in } \Omega_3 \end{cases} \quad , \qquad b_{12}^{11} = b_{12}^{22} = 0$$

$$b_{22}^{22} = \begin{cases} E_2 & \text{in } \Omega_1 \\ 0 & \text{in } \Omega_2 \\ \dfrac{E_2}{1 - \nu_{12}\nu_{21}} & \text{in } \Omega_3 \end{cases} \qquad b_{12}^{12} = \begin{cases} 0 & \text{in } \Omega_1, \Omega_2 \\ G_{12} & \text{in } \Omega_3 \end{cases} \qquad b_{11}^{12} = b_{22}^{12} = b_{3i}^{\alpha\beta} = 0,$$

$$b_{ij}^{*11} = z b_{ij}^{11}, \qquad b_{ij}^{*22} = z b_{ij}^{22},$$

$$b_{12}^{*12} = \begin{cases} G_{12}\left(z - \dfrac{H+1}{2}\right) + G_{12}\dfrac{2H}{\pi^2}\sum_{n=1}^{\infty} \dfrac{\left[1 - (-1)^n\right]\cosh\left(\dfrac{n\pi h_1}{H}\sqrt{\dfrac{G_{23}}{G_{12}}}\,y_1\right)}{\cosh\left(\dfrac{n\pi h_1\delta_1}{2H}\sqrt{\dfrac{G_{23}}{G_{12}}}\right)}\cos\dfrac{n\pi\left(z - \dfrac{1}{2}\right)}{H} & \text{in } \Omega_1 \\[3em] G_{12}\left(z - \dfrac{H+1}{2}\right) + G_{12}\dfrac{2H}{\pi^2}\sum_{n=1}^{\infty} \dfrac{\left[1 - (-1)^n\right]\cosh\left(\dfrac{n\pi h_2}{H}\sqrt{\dfrac{G_{13}}{G_{12}}}\,y_2\right)}{\cosh\left(\dfrac{n\pi h_2\delta_2}{2H}\sqrt{\dfrac{G_{13}}{G_{12}}}\right)}\cos\dfrac{n\pi\left(z - \dfrac{1}{2}\right)}{H} & \text{in } \Omega_2 \\[3em] z G_{12} & \text{in } \Omega_3 \end{cases}$$

$$(12.32)$$

$$b_{11}^{*12} = b_{22}^{*12} = b_{33}^{*12} = 0$$

The effective elastic coefficients are determined from Equation (11.22) and (12.32) and are:

$$\left\langle b_{11}^{11}\right\rangle = \frac{E_1^{(3)}}{1-v_{12}^{(3)}v_{21}^{(3)}}+E_1^{(2)}F_2^{(w)}, \quad \left\langle b_{22}^{22}\right\rangle = \frac{E_2^{(3)}}{1-v_{12}^{(3)}v_{21}^{(3)}}+E_2^{(1)}F_1^{(w)}, \quad \left\langle b_{22}^{11}\right\rangle = \frac{v_{21}^{(3)}E_1^{(3)}}{1-v_{12}^{(3)}v_{21}^{(3)}},$$

$$\left\langle b_{12}^{12}\right\rangle = G_{12}^{(3)}, \quad \left\langle zb_{11}^{11}\right\rangle = \left\langle b_{11}^{*11}\right\rangle = E_1^{(2)}S_2^{(w)}, \quad \left\langle zb_{22}^{22}\right\rangle = \left\langle b_{22}^{*22}\right\rangle = E_2^{(1)}S_1^{(w)},$$

$$\left\langle zb_{11}^{*11}\right\rangle = \frac{E_1^{(3)}}{12\left(1-v_{12}^{(3)}v_{21}^{(3)}\right)}+E_1^{(2)}J_2^{(w)}, \quad \left\langle zb_{22}^{*22}\right\rangle = \frac{E_2^{(3)}}{12\left(1-v_{12}^{(3)}v_{21}^{(3)}\right)}+E_2^{(1)}J_1^{(w)},$$

$$\left\langle zb_{22}^{*11}\right\rangle = \frac{v_{21}^{(3)}E_1^{(3)}}{12\left(1-v_{12}^{(3)}v_{21}^{(3)}\right)}, \quad \left\langle zb_{12}^{*12}\right\rangle = \frac{G_{12}^{(3)}}{12}+\frac{G_{12}^{(1)}}{12}\left(\frac{H^3t_1}{h_1}-K_1\right)+\frac{G_{12}^{(2)}}{12}\left(\frac{H^3t_2}{h_2}-K_2\right) \quad (12.33)$$

where $K_1 = \dfrac{96H^4}{\pi^5 h_1}\sqrt{\dfrac{G_{12}^{(1)}}{G_{23}^{(1)}}}\sum_{n=1}^{\infty}\dfrac{\left[1-(-1)^n\right]}{n^5}\tanh\left(\sqrt{\dfrac{G_{23}^{(1)}}{G_{12}^{(1)}}}\dfrac{n\pi t_1}{2H}\right)$,

and $K_2 = \dfrac{96H^4}{\pi^5 h_2}\sqrt{\dfrac{G_{12}^{(2)}}{G_{13}^{(2)}}}\sum_{n=1}^{\infty}\dfrac{\left[1-(-1)^n\right]}{n^5}\tanh\left(\sqrt{\dfrac{G_{13}^{(2)}}{G_{12}^{(2)}}}\dfrac{n\pi t_2}{2H}\right)$.

Here the superscripts (1), (2), and (3) refer to regions $\Omega_1$, $\Omega_2$, and $\Omega_3$ respectively and the quantities $F_1^{(w)}$, $S_1^{(w)}$, $J_1^{(w)}$ are defined as follows [Kalamkarov, 1992]:

$$\left\langle 1\right\rangle_{\Omega_\alpha} = \int_{\Omega_\alpha}1dy_1 dy_2 dz = \frac{Ht_\alpha}{h_\alpha}=F_\alpha^{(w)}, \qquad \left\langle 1\right\rangle_{\Omega_3}=1,$$

$$\left\langle z\right\rangle_{\Omega_\alpha} = \int_{\Omega_\alpha}zdy_1 dy_2 dz = \frac{\left(H^2+H\right)t_\alpha}{2h_\alpha}=S_\alpha^{(w)}, \qquad \left\langle z\right\rangle_{\Omega_3}=0, \qquad (12.34a)$$

$$\left\langle z^2\right\rangle_{\Omega_\alpha} = \int_{\Omega_\alpha}z^2 dy_1 dy_2 dz = \frac{\left(4H^3+6H^2+3H\right)t_\alpha}{12h_\alpha}=J_\alpha^{(w)}, \qquad \left\langle z\right\rangle_{\Omega_3}=1/12,$$

Thus $F_1^{(w)}, F_2^{(w)}$ are cross-sectional areas, $S_1^{(w)}, S_2^{(w)}$ are first moments, and $J_1^{(w)}, J_2^{(w)}$ are moments of inertia of the cross-sections of the reinforcing elements $\Omega_1$ and $\Omega_2$ relative to the middle surface of the plate $\Omega_3$. Reference to Figure 12-15 in conjunction with Equation (11.22) leads to Equations (12.34) in a straightforward manner.

As a final note, it is worthwhile to mention here the following relationships between the elastic coefficients and the engineering constants [Kalamkarov, 1992]:

$$\frac{v_{21}E_1}{1-v_{12}v_{21}} = C_{12} - \frac{C_{13}C_{23}}{C_{33}}, \qquad \frac{E_1}{1-v_{12}v_{21}} = C_{11} - \frac{C_{13}^2}{C_{33}}, \qquad \frac{E_2}{1-v_{12}v_{21}} = C_{22} - \frac{C_{23}^2}{C_{33}}$$

$$E_1 = C_{11} + \frac{2C_{12}C_{13}C_{23} - C_{12}^2C_{33} - C_{13}^2C_{22}}{C_{22}C_{33} - C_{23}^2}, \quad E_2 = C_{11} + \frac{2C_{12}C_{13}C_{23} - C_{12}^2C_{33} - C_{23}^2C_{11}}{C_{11}C_{33} - C_{13}^2},$$

$$E_3 = C_{33} + \frac{2C_{12}C_{13}C_{23} - C_{13}^2C_{22} - C_{23}^2C_{11}}{C_{11}C_{22} - C_{12}^2}, \quad v_{12} = \frac{C_{12}C_{33} - C_{13}C_{23}}{C_{22}C_{33} - C_{23}^2}, \qquad (12.34b)$$

$$v_{21} = \frac{C_{12}C_{33} - C_{13}C_{23}}{C_{11}C_{33} - C_{13}^2}, \quad v_{13} = \frac{C_{22}C_{13} - C_{12}C_{23}}{C_{22}C_{33} - C_{23}^2}, \quad v_{31} = \frac{C_{22}C_{13} - C_{12}C_{23}}{C_{11}C_{22} - C_{12}^2},$$

$$v_{23} = \frac{C_{11}C_{23} - C_{13}C_{12}}{C_{11}C_{33} - C_{13}^2}, \quad v_{32} = \frac{C_{11}C_{23} - C_{13}C_{12}}{C_{11}C_{22} - C_{12}^2}, \quad G_{23} = C_{44}, \ G_{13} = C_{55}, \ G_{12} = C_{66}$$

Here $v_{12}, v_{21}, v_{13}, v_{31}, v_{23}, v_{32}$ are Poisson's ratios, $E_1, E_2, E_3$ are Young's moduli, and $G_{12}, G_{13}, G_{23}$ are the shear moduli.

## 12.3.2 Effective Hygroscopic Expansion Coefficients

One starts with the unit-cell problem (11.46g), in an attempt to calculate the effective hygroscopic expansion coefficients. In the pertinent definition of Equation (11.45), define:

$$\tau_{ij} = L_{ijm} Y_m \qquad (12.35a)$$

One recalls that the operator $L_{ijk}$ is defined by:

$$L_{ijk} = C_{ijk\alpha} \frac{1}{h_\alpha} \frac{\partial}{\partial y_\alpha} + C_{ijk3} \frac{\partial}{\partial z} \qquad (12.35b)$$

Since each element of the periodicity cell is made of a homogeneous material, the differential equation of the unit-cell problem in Equation (11.46g) becomes:

$$\frac{1}{h_\beta} \frac{\partial \tau_{i\beta}}{\partial y_\beta} + \frac{\partial \tau_{i3}}{\partial z} = 0 \qquad (12.36)$$

Thus for an orthotropic material, the functions $\tau_{ij}$ pertinent to the hygroscopic problem become:

$$\tau_{11} = \frac{1}{h_1}C_{11}\frac{\partial Y_1}{\partial y_1} + \frac{1}{h_2}C_{12}\frac{\partial Y_2}{\partial y_2} + C_{13}\frac{\partial Y_3}{\partial z}$$

$$\tau_{22} = \frac{1}{h_1}C_{12}\frac{\partial Y_1}{\partial y_1} + \frac{1}{h_2}C_{22}\frac{\partial Y_2}{\partial y_2} + C_{23}\frac{\partial Y_3}{\partial z}$$

$$\tau_{33} = \frac{1}{h_1}C_{13}\frac{\partial Y_1}{\partial y_1} + \frac{1}{h_2}C_{23}\frac{\partial Y_2}{\partial y_2} + C_{33}\frac{\partial Y_3}{\partial z}$$

$$\tau_{23} = C_{44}\left(\frac{1}{h_2}\frac{\partial Y_3}{\partial y_2} + \frac{\partial Y_2}{\partial z}\right) \tag{12.37}$$

$$\tau_{13} = C_{55}\left(\frac{1}{h_1}\frac{\partial Y_3}{\partial y_1} + \frac{\partial Y_1}{\partial z}\right)$$

$$\tau_{12} = C_{66}\left(\frac{1}{h_2}\frac{\partial Y_1}{\partial y_2} + \frac{\partial Y_2}{\partial y_1}\right)$$

Next, the boundary conditions from Equation (11.46g) will be considered. These will firstly be rewritten as:

$$\frac{1}{h_\alpha}\Lambda_{i\alpha}n_\alpha + \Lambda_{i3}n_3 = 0 \tag{12.38}$$

Here, one recalls that **n** is the unit vector normal to the surface $Z^\pm$ of the unit cell, and

$$n_\alpha = \frac{1}{h_\alpha}N_\alpha, \quad n_3 = N_3 \tag{12.39}$$

Thus from Equation (12.38) one writes:

$$\frac{1}{h_1}\Lambda_{i1}n_1 + \frac{1}{h_2}\Lambda_{i2}n_2 + \Lambda_{i3}n_3 = 0$$

$$\therefore \frac{1}{h_1}(B_{i1} - \tau_{i1})n_1 + \frac{1}{h_2}(B_{i2} - \tau_{i2})n_2 + (B_{i3} - \tau_{i3})n_3 = 0 \tag{12.40a}$$

Define next the following quantities:

$$t_1 = \tau_{11}\frac{n_1}{h_1} + \tau_{12}\frac{n_2}{h_2} + \tau_{13}n_3$$

$$t_2 = \tau_{21}\frac{n_1}{h_1} + \tau_{22}\frac{n_2}{h_2} + \tau_{23}n_3 \tag{12.40b}$$

$$t_3 = \tau_{31}\frac{n_1}{h_1} + \tau_{32}\frac{n_2}{h_2} + \tau_{33}n_3$$

Thus, from the last expression in Equation (12.40a) one writes:

$$B_{i\alpha}\frac{n_\alpha}{h_\alpha} + B_{i3}n_3 - t_i = 0 \qquad (12.40c)$$

Finally, for an orthotropic material the boundary conditions become:

$$t_1 = B_{11}\frac{n_1}{h_1}, \quad t_2 = B_{22}\frac{n_2}{h_2}, \quad t_3 = B_{33}\frac{n_3}{h_3} \qquad \text{on } Z^\pm \qquad (12.41)$$

The $\Lambda_{ij}$ functions (for an orthotropic material) are obtained as follows:

$$\begin{aligned}
\Lambda_{11} &= B_{11} - \tau_{11} \\
\Lambda_{22} &= B_{22} - \tau_{22} \\
\Lambda_{33} &= B_{33} - \tau_{33} \\
\Lambda_{12} &= -\tau_{12} \\
\Lambda_{13} &= -\tau_{13} \\
\Lambda_{23} &= -\tau_{23}
\end{aligned} \qquad (12.42)$$

As explained above, the $\Lambda_{ij}$ functions will be solved by considering each element of the unit cell separately, see Figure 12-15.

## (a) Region $\Omega_1$:

This is defined by:

$$-\delta_1/2 < y_1 < \delta_1/2, \quad -1/2 < y_2 < 1/2, \quad 1/2 < z < 1/2 + H \qquad (12.43a)$$

Boundary conditions must be supplied on $z = \frac{1}{2}$, $z = \frac{1}{2}+H$, where $n_1 = n_2 = 0$, $n_3 = 1$ and on $y_1 = \pm\delta_1/2$ where $n_1 = n_3 = 0$, $n_2 = 1$. Thus, from Equations (12.40b) and (12.41) the boundary conditions become:

$$t_2 = t_3 = 0, \quad t_1 = \frac{B_{11}}{h_1}$$
$$\Rightarrow \tau_{12} = \tau_{13} = 0, \quad \tau_{11} = B_{11} \qquad (\text{on } y_1 = \pm\delta_1/2) \qquad (12.43b)$$

and

$$t_1 = t_2 = 0, \quad t_3 = B_{33}$$
$$\Rightarrow \tau_{13} = \tau_{23} = 0, \quad \tau_{33} = B_{33} \qquad (\text{on } z = 1/2, z = 1/2 + H) \qquad (12.43c)$$

Keeping in mind that in region $\Omega_1$ there is periodicity in $y_2$, the $Y_i$ functions are readily determined to be:

$$Y_1 = \frac{h_1(C_{13}B_{33} - C_{33}B_{11})}{C_{13}^2 - C_{11}C_{33}} y_1$$

$$Y_2 = 0 \qquad (12.44a)$$

$$Y_3 = \frac{C_{13}B_{11} - C_{11}B_{33}}{C_{13}^2 - C_{11}C_{33}} z$$

These functions, yield, on account of Equations (12.37), (12.42) and (12.34b) the following expressions:

$$\Lambda_{11} = 0, \quad \Lambda_{22} = B_{22} - \nu_{23}B_{33} - \nu_{21}B_{11},$$

$$\Lambda_{33} = \Lambda_{12} = \Lambda_{13} = \Lambda_{23} = 0 \qquad (12.44b)$$

### (b) Region $\Omega_2$:

This is defined by:

$$-1/2 < y_1 < 1/2, \quad -\delta_2/2 < y_2 < \delta_2/2, \quad 1/2 < z < 1/2 + H \qquad (12.45a)$$

Boundary conditions must be supplied on $z = \frac{1}{2}$, $z = \frac{1}{2}+H$, where $n_1 = n_2 = 0$, $n_3 = 1$ and on $y_2 = \pm\delta_2/2$ where $n_1 = n_3 = 0$, $n_2 = 1$. Thus, from Equations (12.40b) and (12.41) the boundary conditions become:

$$t_1 = t_3 = 0, \quad t_2 = \frac{B_{22}}{h_2}$$

$$\Rightarrow \tau_{12} = \tau_{23} = 0, \quad \tau_{22} = B_{22} \qquad (\text{on } y_2 = \pm\delta_2/2) \qquad (12.45b)$$

and

$$t_1 = t_2 = 0, \quad t_3 = B_{33}$$

$$\Rightarrow \tau_{13} = \tau_{23} = 0, \quad \tau_{33} = B_{33} \qquad (\text{on } z = 1/2, z = 1/2 + H) \qquad (12.45c)$$

Keeping in mind that in region $\Omega_2$ there is periodicity in $y_1$, the $Y_i$ functions are readily determined to be:

$$Y_1 = 0 \qquad (12.46a)$$

and

$$Y_2 = \frac{h_2(C_{33}B_{22} - C_{23}B_{33})}{C_{22}C_{33} - C_{23}^2} y_2$$

$$Y_3 = \frac{C_{22}B_{33} - C_{23}B_{22}}{C_{22}C_{33} - C_{23}^2} z$$

(12.46b)

These functions, yield, on account of Equations (12.37), (12.42) and (12.34b) the following expressions:

$$\Lambda_{11} = B_{11} - \nu_{12}B_{22} - \nu_{13}B_{33}, \quad \Lambda_{22} = 0,$$

$$\Lambda_{33} = \Lambda_{12} = \Lambda_{13} = \Lambda_{23} = 0$$

(12.46c)

## (c) Region $\Omega_3$:

This is defined by:

$$-1/2 < y_1 < 1/2, \quad -1/2 < y_2 < 1/2, \quad -1/2 < z < 1/2$$

(12.47a)

Boundary conditions must be supplied on z = ½, z = ½+H, where $n_1 = n_2 = 0$, $n_3 = 1$. Thus, from Equations (12.40b) and (12.41) the boundary conditions become:

$$t_1 = t_2 = 0, \quad t_3 = B_{33}$$

$$\Rightarrow \tau_{13} = \tau_{23} = 0, \quad \tau_{33} = B_{33} \quad (\text{on } z = \pm 1/2)$$

(12.47b)

An account of periodicity in $y_1$ and $y_2$, and from differential equations (12.36) and boundary conditions (12.47b) one writes:

$$\tau_{13} = \tau_{23} = 0, \quad \tau_{33} = B_{33} \quad \text{everywhere in } \Omega_3$$

(12.48)

Hence, from Equations (12.48) and (12.37) the functions $Y_i$ are given by the following expressions:

$$Y_1 = Y_2 = 0$$

$$Y_3 = \frac{B_{33}}{C_{33}} z$$

(12.49a)

The latter expressions yield, on account of Equations (12.37) and (12.42), the following expressions for the $\Lambda_{ij}$ functions:

$$\Lambda_{11} = B_{11} - \frac{C_{13}B_{33}}{C_{33}}, \quad \Lambda_{22} = B_{22} - \frac{C_{23}B_{33}}{C_{33}}, \quad \Lambda_{33} = 0$$

$$\Lambda_{23} = \Lambda_{13} = \Lambda_{12} = 0$$

(12.49b)

The solution of the unit cell problem from Equation (11.46h) proceeds in much the same way. Starting from

$$\frac{1}{h_\beta}\frac{\partial \Lambda^*_{i\beta}}{\partial y_\beta} + \frac{\partial \Lambda^*_{i3}}{\partial z} = 0,$$

$$\Lambda^*_{ij}N^\pm_j = 0 \quad \left(\text{on } Z^\pm\right)$$

(12.50a)

and defining

$$\overline{\tau}_{ij} = L_{ijm}A_m$$

(12.50b)

leads to

$$\frac{1}{h_\beta}\frac{\partial \overline{\tau}_{i\beta}}{\partial y_\beta} + \frac{\partial \overline{\tau}_{i3}}{\partial z} = 0$$

(12.50c)

on account of the fact that each element of the periodicity cell is made of a homogeneous material.

Thus for an orthotropic material, the functions $\overline{\tau}_{ij}$ pertinent to the hygroscopic problem, become:

$$\overline{\tau}_{11} = \frac{1}{h_1}C_{11}\frac{\partial A_1}{\partial y_1} + \frac{1}{h_2}C_{12}\frac{\partial A_2}{\partial y_2} + C_{13}\frac{\partial A_3}{\partial z}$$

$$\overline{\tau}_{22} = \frac{1}{h_1}C_{12}\frac{\partial A_1}{\partial y_1} + \frac{1}{h_2}C_{22}\frac{\partial A_2}{\partial y_2} + C_{23}\frac{\partial A_3}{\partial z}$$

$$\overline{\tau}_{33} = \frac{1}{h_1}C_{13}\frac{\partial A_1}{\partial y_1} + \frac{1}{h_2}C_{23}\frac{\partial A_2}{\partial y_2} + C_{33}\frac{\partial A_3}{\partial z}$$

$$\overline{\tau}_{23} = C_{44}\left(\frac{1}{h_2}\frac{\partial A_3}{\partial y_2} + \frac{\partial A_2}{\partial z}\right)$$

$$\overline{\tau}_{13} = C_{55}\left(\frac{1}{h_1}\frac{\partial A_3}{\partial y_1} + \frac{\partial A_1}{\partial z}\right)$$

$$\overline{\tau}_{12} = C_{66}\left(\frac{1}{h_2}\frac{\partial A_1}{\partial y_2} + \frac{\partial A_2}{\partial y_1}\right)$$

(12.51)

Next, the boundary conditions from Equation (12.50A) will be considered. First define the following:

$$\bar{t}_1 = \bar{\tau}_{11} \frac{n_1}{h_1} + \bar{\tau}_{12} \frac{n_2}{h_2} + \bar{\tau}_{13} n_3$$

$$\bar{t}_2 = \bar{\tau}_{21} \frac{n_1}{h_1} + \bar{\tau}_{22} \frac{n_2}{h_2} + \bar{\tau}_{23} n_3 \qquad (12.52a)$$

$$\bar{t}_3 = \bar{\tau}_{31} \frac{n_1}{h_1} + \bar{\tau}_{32} \frac{n_2}{h_2} + \bar{\tau}_{33} n_3$$

Thus the boundary conditions become:

$$zB_{i\alpha} \frac{n_\alpha}{h_\alpha} + zB_{i3} n_3 - \bar{t}_i = 0$$

$$(12.52b)$$

$$\bar{t}_1 = B_{11} \frac{n_1}{h_1}, \quad \bar{t}_2 = B_{22} \frac{n_2}{h_2}, \quad \bar{t}_3 = B_{33} \frac{n_3}{h_3} \quad \text{on } Z^\pm$$

The $\Lambda^*_{ij}$ functions (for an orthotropic material) are obtained as follows:

$$\Lambda^*_{11} = zB_{11} - \bar{\tau}_{11}$$

$$\Lambda^*_{22} = zB_{22} - \bar{\tau}_{22}$$

$$\Lambda^*_{33} = zB_{33} - \bar{\tau}_{33}$$

$$\Lambda^*_{12} = -\bar{\tau}_{12} \qquad (12.52c)$$

$$\Lambda^*_{13} = -\bar{\tau}_{13}$$

$$\Lambda^*_{23} = -\bar{\tau}_{23}$$

The $\Lambda^*_{ij}$ functions will be solved by considering each element of the unit cell separately, as was done for the previous unit cell problem.

## (a) Region $\Omega_1$:

The boundary conditions are:

$$\bar{t}_2 = \bar{t}_3 = 0, \quad \bar{t}_1 = z \frac{B_{11}}{h_1}$$

$$(12.53a)$$

$$\Rightarrow \bar{\tau}_{12} = \bar{\tau}_{13} = 0, \quad \bar{\tau}_{11} = zB_{11} \qquad (\text{on } y_1 = \pm \delta_1/2)$$

and

$$\bar{t}_1 = \bar{t}_2 = 0, \quad \bar{t}_3 = zB_{33}$$

$$\Rightarrow \tau_{13} = \tau_{23} = 0, \quad \tau_{33} = B_{33} \qquad (\text{on } z = 1/2, z = 1/2 + H)$$

$$(12.53b)$$

Keeping in mind that in region $\Omega_1$ there is periodicity in $y_2$, the $A_i$ functions are readily determined to be:

$$A_1 = \frac{h_1(C_{33}B_{11} - C_{13}B_{33})}{C_{11}C_{33} - C_{13}^2} y_1 z$$

$$A_2 = 0 \qquad\qquad (12.54a)$$

$$A_3 = \frac{C_{11}B_{33} - C_{13}B_{11}}{C_{11}C_{33} - C_{13}^2} \frac{z^2}{2} + h_1^2 \frac{(C_{13}B_{33} - C_{33}B_{11})}{C_{11}C_{33} - C_{13}^2} \frac{y_1^2}{2}$$

These functions yield, on account of Equations (12.51), (12.52c) and (12.34b), the following expressions:

$$\Lambda_{11}^* = 0, \quad \Lambda_{22}^* = z(B_{22} - v_{23}B_{33} - v_{21}B_{11}),$$
$$\Lambda_{33}^* = \Lambda_{13}^* = \Lambda_{13}^* = \Lambda_{23}^* = 0 \qquad\qquad (12.54b)$$

## (b)  Region $\Omega_2$:

The boundary conditions are:

$$\bar{t}_1 = \bar{t}_3 = 0, \quad \bar{t}_2 = \frac{zB_{22}}{h_2}$$
$$\Rightarrow \bar{\tau}_{12} = \bar{\tau}_{23} = 0, \quad \bar{\tau}_{22} = zB_{22} \qquad (\text{on } y_2 = \pm\delta_2/2) \qquad (12.55a)$$

and

$$\bar{t}_1 = \bar{t}_2 = 0, \quad \bar{t}_3 = zB_{33}$$
$$\Rightarrow \bar{\tau}_{13} = \bar{\tau}_{23} = 0, \quad \bar{\tau}_{33} = zB_{33} \qquad (\text{on } z = 1/2, z = 1/2 + H) \qquad (12.55b)$$

Keeping in mind that in region $\Omega_2$ there is periodicity in $y_1$, the $A_i$ functions are readily determined to be:

$$A_1 = 0$$

$$A_2 = \frac{h_2(C_{33}B_{22} - C_{23}B_{33})}{C_{22}C_{33} - C_{23}^2} y_2 z \qquad\qquad (12.56a)$$

$$A_3 = \frac{C_{22}B_{33} - C_{23}B_{22}}{C_{22}C_{33} - C_{23}^2} \frac{z^2}{2} + h^2 \frac{C_{23}B_{33} - C_{33}B_{22}}{C_{22}C_{33} - C_{23}^2} \frac{y_2^2}{2}$$

These functions, yield, on account of Equations (12.51), (12.52c) and (12.34b) the following expressions:

$$\Lambda_{11}^* = z(B_{11} - \nu_{12}B_{22} - \nu_{13}B_{33}), \quad \Lambda_{22}^* = 0,$$
$$\Lambda_{33}^* = \Lambda_{12}^* = \Lambda_{13}^* = \Lambda_{23}^* = 0 \tag{12.56b}$$

## (c)  Region $\Omega_3$:

The boundary conditions are:

$$\bar{t}_1 = \bar{t}_2 = 0, \quad \bar{t}_3 = zB_{33}$$
$$\Rightarrow \bar{\tau}_{13} = \bar{\tau}_{23} = 0, \quad \bar{\tau}_{33} = zB_{33} \qquad (\text{on } z = \pm 1/2) \tag{12.57a}$$

An account of periodicity in $y_1$ and $y_2$, and from differential equations (12.50c) and boundary conditions (12.57a) one writes:

$$\bar{\tau}_{13} = \bar{\tau}_{23} = 0, \quad \bar{\tau}_{33} = zB_{33} \quad \text{everywhere in } \Omega_3 \tag{12.57b}$$

Hence, from Equations (12.57b) and (12.51) the functions $A_i$ are given by the following expressions:

$$A_1 = A_2 = 0$$
$$A_3 = \frac{B_{33}}{C_{33}} \frac{z^2}{2} \tag{12.58a}$$

The latter expressions, yield on account of Equations (12.51) and (12.52c) the following expressions for the $\Lambda_{ij}^*$ functions:

$$\Lambda_{11}^* = z\left(B_{11} - \frac{C_{13}B_{33}}{C_{33}}\right), \quad \Lambda_{22}^* = z\left(B_{22} - \frac{C_{23}B_{33}}{C_{33}}\right), \quad \Lambda_{33}^* = 0$$
$$\Lambda_{23}^* = \Lambda_{13}^* = \Lambda_{12}^* = 0 \tag{12.58b}$$

Having solved the unit-cell problems for the hygroscopic coefficients and remembering that

$$B_{ij} = C_{ijkl} \frac{\beta_{kl}^{(c)}}{\delta} \tag{12.59}$$

then on account of Equation (12.34b), the hygroscopic strain coefficients are given from Equations (12.44b), (12.46c), (12.49b), (12.54b), (12.56b), and (12.58b) by the following expressions:

$$\Lambda_{11} = 0, \quad \delta\Lambda_{22} = E_2\beta_2^{(c)} \quad \text{in } \Omega_1$$

$$\Lambda_{22} = 0, \quad \delta\Lambda_{11} = E_1\beta_1^{(c)} \quad \text{in } \Omega_2 \tag{12.60a}$$

$$\delta\Lambda_{11} = \frac{E_1\beta_1^{(c)}}{1-\nu_{12}\nu_{21}} + \frac{\nu_{21}E_1\beta_2^{(c)}}{1-\nu_{12}\nu_{21}}, \quad \delta\Lambda_{22} = \frac{E_2\beta_2^{(c)}}{1-\nu_{12}\nu_{21}} + \frac{\nu_{21}E_1\beta_1^{(c)}}{1-\nu_{12}\nu_{21}} \quad \text{in } \Omega_3$$

$$\Lambda_{33} = \Lambda_{12} = \Lambda_{13} = \Lambda_{23} = 0 \quad \text{in } \Omega_1, \Omega_2, \Omega_3$$

and

$$\Lambda_{11}^* = 0, \quad \delta\Lambda_{22}^* = zE_2\beta_2^{(c)} \quad \text{in } \Omega_1$$

$$\Lambda_{22}^* = 0, \quad \delta\Lambda_{11}^* = zE_1\beta_1^{(c)} \quad \text{in } \Omega_2 \tag{12.60b}$$

$$\delta\Lambda_{11}^* = z\left(\frac{E_1\beta_1^{(c)}}{1-\nu_{12}\nu_{21}} + \frac{\nu_{21}E_1\beta_2^{(c)}}{1-\nu_{12}\nu_{21}}\right), \quad \delta\Lambda_{22}^* = z\left(\frac{E_2\beta_2^{(c)}}{1-\nu_{12}\nu_{21}} + \frac{\nu_{21}E_1\beta_1^{(c)}}{1-\nu_{12}\nu_{21}}\right) \quad \text{in } \Omega_3$$

$$\Lambda_{33}^* = \Lambda_{12}^* = \Lambda_{13}^* = \Lambda_{23}^* = 0 \quad \text{in } \Omega_1, \Omega_2, \Omega_3.$$

Comparison of Equations (12.60a) and (12.60b) reveals that:

$$\Lambda_{ij}^* = z\Lambda_{ij} \tag{12.60c}$$

The effective hygroscopic expansion coefficients are determined from Equations (12.60a) and (12.60b), bearing Equations (11.22) and (12.34b) in mind. They are given by the following expressions:

$$\delta\langle\Lambda_{11}\rangle = E_1^{(2)}\beta_1^{(c)(2)}F_2^{(w)} + \frac{E_1^{(3)}\beta_1^{(c)(3)} + E_1^{(3)}\nu_{21}^{(3)}\beta_2^{(c)(3)}}{1-\nu_{12}^{(3)}\nu_{21}^{(3)}}$$

$$\delta\langle\Lambda_{22}\rangle = E_2^{(1)}\beta_2^{(c)(1)}F_1^{(w)} + \frac{E_2^{(3)}\beta_2^{(c)(3)} + E_2^{(3)}\nu_{12}^{(3)}\beta_1^{(c)(3)}}{1-\nu_{12}^{(3)}\nu_{21}^{(3)}}$$

$$\delta\langle z\Lambda_{11}\rangle = \delta\langle\Lambda_{11}^*\rangle = E_1^{(2)}\beta_1^{(c)(2)}S_2^{(w)}$$

$$\delta\langle z\Lambda_{22}\rangle = \delta\langle\Lambda_{22}^*\rangle = E_2^{(1)}\beta_2^{(c)(1)}S_1^{(w)} \tag{12.61}$$

$$\delta\langle z\Lambda_{11}^*\rangle = E_1^{(2)}\beta_1^{(c)(2)}J_2^{(w)} + \frac{E_1^{(3)}\beta_1^{(c)(3)} + E_1^{(3)}\nu_{21}^{(3)}\beta_2^{(c)(3)}}{12\left(1-\nu_{12}^{(3)}\nu_{21}^{(3)}\right)}$$

$$\delta\langle z\Lambda_{22}^*\rangle = E_2^{(1)}\beta_2^{(c)(1)}J_1^{(w)} + \frac{E_2^{(3)}\beta_2^{(c)(3)} + E_2^{(3)}\nu_{12}^{(3)}\beta_1^{(c)(3)}}{12\left(1-\nu_{12}^{(3)}\nu_{21}^{(3)}\right)}$$

### 12.3.3 Effective Piezoelectric Coefficients

It should be first noted that for an orthotropic material, the matrix of piezoelectric stress or strain coefficients is of the following form:

$$
\begin{bmatrix}
0 & 0 & d_{31}^{(r)} \\
0 & 0 & d_{32}^{(r)} \\
0 & 0 & d_{33}^{(r)} \\
0 & d_{24}^{(r)} & 0 \\
d_{15}^{(r)} & 0 & 0 \\
0 & 0 & 0
\end{bmatrix}
\tag{12.62}
$$

The first unit cell problem to be dealt with is Equation (11.46c) repeated here for convenience:

$$
\frac{1}{h_\beta} \frac{\partial d_{i\beta}^k}{\partial y_\beta} + \frac{\partial d_{i3}^k}{\partial z} = 0
\tag{12.63}
$$

$$
d_{ij}^k N_j^\pm = 0 \quad \left(\text{on } Z^\pm\right)
$$

One also recalls that:

$$
d_{ij}^k = P_{ijk} - L_{ijm} U_m^k
\tag{12.64}
$$

If next, one defines

$$
\tau_{ij}^k = L_{ijm} U_m^k
\tag{12.65}
$$

then the differential equation in(12.63) becomes:

$$
\frac{1}{h_\beta} \frac{\partial \tau_{i\beta}^k}{\partial y_\beta} + \frac{\partial \tau_{i3}^k}{\partial z} = 0
\tag{12.66}
$$

Here the $\tau_{ij}^k$ functions for an orthotropic material are given by the following expressions:

$$
\tau_{11}^k = \frac{1}{h_1} C_{11} \frac{\partial U_1^k}{\partial y_1} + \frac{1}{h_2} C_{12} \frac{\partial U_2^k}{\partial y_2} + C_{13} \frac{\partial U_3^k}{\partial z}
$$

$$
\tau_{22}^k = \frac{1}{h_1} C_{12} \frac{\partial U_1^k}{\partial y_1} + \frac{1}{h_2} C_{22} \frac{\partial U_2^k}{\partial y_2} + C_{23} \frac{\partial U_3^k}{\partial z}
\tag{12.67a}
$$

$$
\tau_{33}^k = \frac{1}{h_1} C_{13} \frac{\partial U_1^k}{\partial y_1} + \frac{1}{h_2} C_{23} \frac{\partial U_2^k}{\partial y_2} + C_{33} \frac{\partial U_3^k}{\partial z}
$$

$$\tau_{23}^k = C_{44}\left(\frac{1}{h_2}\frac{\partial U_3^k}{\partial y_2} + \frac{\partial U_2^k}{\partial z}\right)$$

$$\tau_{13}^k = C_{55}\left(\frac{1}{h_1}\frac{\partial U_3^k}{\partial y_2} + \frac{\partial U_1^k}{\partial z}\right) \qquad (12.67b)$$

$$\tau_{12}^k = C_{66}\left(\frac{1}{h_2}\frac{\partial U_1^k}{\partial y_2} + \frac{\partial U_2^k}{\partial y_1}\right)$$

One subsequently considers the boundary conditions in Equation (12.63). To this end, one defines:

$$t_i^k = \tau_{i\alpha}^k \frac{n_\alpha}{h_\alpha} + \tau_{i3}^k n_3 \qquad (12.68a)$$

Thus, from Equation (12.68a) the boundary conditions become:

$$t_1^1 = P_{15}n_3, \quad t_2^1 = 0, \quad t_3^1 = P_{15}\frac{n_1}{h_1},$$

$$t_1^2 = 0, \quad t_2^2 = P_{24}n_3, \quad t_3^2 = P_{24}\frac{n_2}{h_2}, \qquad \text{on } z^{\pm} \quad (12.68b)$$

$$t_1^3 = P_{31}\frac{n_1}{h_1}, \quad t_2^3 = P_{32}\frac{n_2}{h_2}, \quad t_3^3 = P_{33}n_3$$

The $d_{ij}^k$ functions are then obtained from the following expressions:

$$
\begin{array}{lll}
d_{11}^1 = -\tau_{11}^1 & d_{11}^2 = -\tau_{11}^2 & d_{11}^3 = P_{31} - \tau_{11}^3 \\
d_{12}^1 = -\tau_{12}^1 & d_{12}^2 = -\tau_{12}^2 & d_{12}^3 = -\tau_{12}^3 \\
d_{22}^1 = -\tau_{22}^1 & d_{22}^2 = -\tau_{22}^2 & d_{22}^3 = P_{32} - \tau_{22}^3 \\
d_{32}^1 = -\tau_{32}^1 & d_{32}^2 = P_{24} - \tau_{32}^2 & d_{32}^3 = -\tau_{22}^3 \\
d_{33}^1 = -\tau_{33}^1 & d_{33}^2 = -\tau_{33}^2 & d_{33}^3 = P_{33} - \tau_{33}^3 \\
d_{31}^1 = P_{15} - \tau_{33}^1 & d_{31}^2 = -\tau_{31}^2 & d_{31}^3 = -\tau_{33}^3
\end{array}
\qquad (12.69)
$$

As for the hygroscopic problem, the $d_{ij}^k$ functions will be solved by considering each element of the unit cell separately. The $\tau_{ij}^1$ problem will be dealt with first.

## (a) Region $\Omega_1$:

From Equations (12.68a) and (12.68b) the boundary conditions are:

$$t_1^1 = t_2^1 = 0 \qquad t_3^1 = \frac{P_{15}}{h_1}$$

$$\therefore \tau_{11}^1 = \tau_{12}^1 = 0 \qquad \tau_{13}^1 = P_{15} \quad \text{on } y_1 = \pm \delta_1/2$$

and $\qquad\qquad\qquad\qquad\qquad\qquad\qquad\qquad\qquad\qquad$ (12.70a)

$$t_2^1 = t_3^1 = 0 \qquad t_1^1 = P_{15}$$

$$\therefore \tau_{13}^1 = P_{15}, \quad \tau_{23}^1 = \tau_{33}^1 = 0 \quad \text{on } z = 1/2, \quad z = 1/2 + H$$

Thus, considering the periodicity in $y_2$, and using Equations (12.66), (12.67a), (12.67b) and (12.70a), the following functions are determined:

$$U_1^1 = \frac{P_{15}}{C_{55}} z,$$

$$U_2^1 = U_3^1 = 0 \qquad\qquad\qquad\qquad\qquad (12.70b)$$

$$\Rightarrow \tau_{11}^1 = \tau_{22}^1 = \tau_{33}^1 = \tau_{23}^1 = \tau_{12}^1 = 0, \quad \tau_{13}^1 = P_{15}$$

## (b) Region $\Omega_2$:

From Equations (12.68a) and (12.68b) the boundary conditions are:

$$t_1^1 = t_2^1 = t_3^1 = 0$$

$$\therefore \tau_{12}^1 = \tau_{22}^1 = \tau_{23}^1 = 0 \quad \text{on } y_2 = \pm \delta_2/2$$

and $\qquad\qquad\qquad\qquad\qquad\qquad\qquad\qquad\qquad\qquad$ (12.71a)

$$t_2^1 = t_3^1 = 0 \qquad t_1^1 = P_{15}$$

$$\therefore \tau_{13}^1 = P_{15}, \quad \tau_{23}^1 = \tau_{33}^1 = 0 \quad \text{on } z = 1/2, \quad z = 1/2 + H$$

Thus, considering the periodicity in $y_1$, and using Equations (12.66), (12.67a), (12.67b) and (12.71a), the following functions are determined:

$$U_1^1 = \frac{P_{15}}{C_{55}} z,$$

$$U_2^1 = U_3^1 = 0 \qquad\qquad\qquad\qquad\qquad (12.71b)$$

$$\Rightarrow \tau_{11}^1 = \tau_{22}^1 = \tau_{33}^1 = \tau_{23}^1 = \tau_{12}^1 = 0, \quad \tau_{13}^1 = P_{15}$$

## (c) Region $\Omega_3$:

The boundary conditions are:

$$t_1^1 = P_{15} \quad t_2^1 = t_3^1 = 0$$

$$\therefore \tau_{13}^1 = P_{15} \quad \tau_{23}^1 = \tau_{33}^1 = 0 \quad \text{on } z = \pm 1/2 \tag{12.72a}$$

Thus, considering the periodicity in $y_1$, $y_2$ and using Equations (12.66), (12.67a), (12.67b) and (12.72a), the following functions are determined:

$$U_1^1 = \frac{P_{15}}{C_{55}} z,$$

$$U_2^1 = U_3^1 = 0 \tag{12.72b}$$

$$\Rightarrow \tau_{11}^1 = \tau_{22}^1 = \tau_{33}^1 = \tau_{23}^1 = \tau_{12}^1 = 0, \quad \tau_{13}^1 = P_{15}$$

Thus, considering Equations (12.64), (12.65), (12.70b), (12.71b) and (12.72b) one obtains:

$$\left.\begin{array}{l} d_{11}^1 = d_{12}^1 = d_{22}^1 = d_{23}^1 = d_{33}^1 = 0, \\ d_{13}^1 = P_{15} - P_{15} = 0 \end{array}\right\} \text{in } \Omega_1, \Omega_2, \Omega_3 \tag{12.73}$$

The solution of the $\tau_{ij}^2$ problem is very similar to the $\tau_{ij}^1$ problem and is:

$$\left.\begin{array}{l} \tau_{11}^2 = \tau_{22}^2 = \tau_{33}^2 = \tau_{13}^2 = \tau_{12}^2 = 0 \\ \tau_{23}^2 = P_{24} \end{array}\right\} \text{in } \Omega_1, \Omega_2, \Omega_3 \tag{12.74a}$$

Thus:

$$\left.\begin{array}{l} d_{11}^2 = d_{12}^2 = d_{22}^2 = d_{13}^2 = d_{33}^2 = 0 \\ d_{23}^2 = P_{24} - P_{24} = 0 \end{array}\right\} \text{in } \Omega_1, \Omega_2, \Omega_3 \tag{12.74b}$$

The final problem to be solved pertains to the $\tau_{ij}^3$ functions. As usual, the solution will be obtained on region-by-region basis.

**(a) Region $\Omega_1$:**

In $\Omega_1$ the boundary conditions are:

$$t_2^3 = t_3^3 = 0 \qquad t_1^3 = \frac{P_{31}}{h_1}$$

$$\therefore \tau_{12}^3 = \tau_{13}^3 = 0 \qquad \tau_{11}^3 = P_{31} \quad \text{on } y_1 = \pm \delta_1/2 \tag{12.75a}$$

and

$$t_1^3 = t_2^3 = 0 \qquad t_3^3 = P_{33} \qquad (12.75b)$$

$$\therefore \tau_{33}^3 = P_{33}, \quad \tau_{13}^3 = \tau_{23}^3 = 0 \quad \text{on } z = 1/2, \quad z = 1/2 + H$$

Hence, from Equations (12.66), (12.67a), (12.75a) and (12.75b), and considering periodicity in $y_2$ the $U_i^3$ functions are:

$$U_1^3 = \frac{C_{33}P_{31} - C_{13}P_{33}}{C_{11}C_{33} - C_{13}^2} h_1 y_1$$

$$U_2^3 = 0 \qquad (12.76)$$

$$U_3^3 = \frac{C_{11}P_{33} - C_{13}P_{31}}{C_{11}C_{33} - C_{13}^2} z$$

Thus, the $d_{ij}^3$ piezoelectric coefficients are obtained through Equations (12.67b), (12.69), (12.34b) and (12.76) and are:

$$d_{22}^3 = P_{32} - \nu_{21}P_{31} - \nu_{23}P_{33}, \quad d_{11}^3 = d_{33}^3 = d_{12}^3 = d_{13}^3 = d_{23}^3 = 0 \qquad (12.77)$$

## (b) Region $\Omega_2$:

In $\Omega_2$ the boundary conditions are:

$$t_1^3 = t_3^3 = 0 \qquad t_2^3 = \frac{P_{32}}{h_2}$$

$$\therefore \tau_{12}^3 = \tau_{23}^3 = 0 \qquad \tau_{22}^3 = P_{32} \quad \text{on } y_2 = \pm \delta_2 / 2 \qquad (12.78a)$$

and

$$t_1^3 = t_2^3 = 0 \qquad t_3^3 = P_{33}$$

$$\therefore \tau_{33}^3 = P_{33}, \quad \tau_{13}^3 = \tau_{23}^3 = 0 \quad \text{on } z = 1/2, \quad z = 1/2 + H \qquad (12.78b)$$

Hence, from Equations (12.66), (12.67a), (12.78a) and (12.78b), and considering periodicity in $y_1$ the $U_i^3$ functions are:

$$U_1^3 = 0$$

$$U_2^3 = \frac{C_{33}P_{32} - C_{23}P_{33}}{C_{22}C_{33} - C_{23}^2} h_2 y_2 \qquad (12.79)$$

$$U_3^3 = \frac{C_{22}P_{33} - C_{23}P_{32}}{C_{22}C_{33} - C_{23}^2} z$$

Thus, the $d_{ij}^3$ piezoelectric coefficients are obtained through Equations (12.67a), (12.67b), (12.69), (12.34b) and (12.79) and are:

$$d_{11}^3 = P_{31} - v_{12}P_{32} - v_{13}P_{33}, \quad d_{22}^3 = d_{33}^3 = d_{12}^3 = d_{13}^3 = d_{23}^3 = 0 \qquad (12.80)$$

## (c) Region $\Omega_3$:

The appropriate boundary conditions are:

$$t_1^3 = t_2^3 = 0, \quad t_3^3 = P_{33}$$
$$\tau_{33}^3 = zP_{33}, \quad \tau_{13}^1 = \tau_{23}^1 = 0 \quad \text{on } z = \pm 1/2 \qquad (12.81a)$$

Thus from Equations (12.66), (12.67a), (12.67b) and (12.81a) and on account of periodicity in $y_1$ and $y_2$ one obtains:

$$U_3^3 = \frac{P_{33}}{C_{33}}z, \quad U_1^3 = U_2^3 = 0$$

$$\Rightarrow \tau_{11}^3 = \frac{C_{13}}{C_{33}}P_{33}, \quad \tau_{22}^3 = \frac{C_{23}}{C_{33}}P_{33}, \quad \tau_{33}^3 = P_{33} \qquad (12.81b)$$

$$\tau_{12}^3 = \tau_{13}^3 = \tau_{23}^3 = 0$$

Thus, from Equation (12.69) the $d_{ij}^3$ functions are obtained as follows:

$$d_{11}^3 = P_{31} - \frac{C_{13}}{C_{33}}P_{33}$$

$$d_{22}^3 = P_{32} - \frac{C_{23}}{C_{33}}P_{33} \qquad (12.81c)$$

$$d_{33}^3 = d_{12}^3 = d_{13}^3 = d_{23}^3 = 0$$

The solution of the unit-cell problem from Equation (11.46d) will now be presented. Starting from

$$\frac{1}{h_\beta}\frac{\partial d_{i\beta}^{*k}}{\partial y_\beta} + \frac{\partial d_{i3}^{*k}}{\partial z} = 0 \qquad (12.82a)$$

$$d_{ij}^{*k}N_j^{\pm} = 0 \quad \left(\text{on } Z^{\pm}\right)$$

and defining

$$\overline{\tau}_{ij}^k = L_{ijm}V_m^k \qquad (12.82b)$$

leads to:

$$\frac{1}{h_\beta}\frac{\partial \bar{\tau}_{i\beta}^k}{\partial y_\beta} + \frac{\partial \bar{\tau}_{i3}^k}{\partial z} = P_{i3k} \qquad (12.82c)$$

Thus, for an orthotropic material, the functions $\bar{\tau}_{ij}^k$ pertinent to the piezoelectric problem become:

$$\bar{\tau}_{11}^k = \frac{1}{h_1}C_{11}\frac{\partial V_1^k}{\partial y_1} + \frac{1}{h_2}C_{12}\frac{\partial V_2^k}{\partial y_2} + C_{13}\frac{\partial V_3^k}{\partial z}$$

$$\bar{\tau}_{22}^k = \frac{1}{h_1}C_{12}\frac{\partial V_1^k}{\partial y_1} + \frac{1}{h_2}C_{22}\frac{\partial V_2^k}{\partial y_2} + C_{23}\frac{\partial V_3^k}{\partial z}$$

$$\bar{\tau}_{33}^k = \frac{1}{h_1}C_{13}\frac{\partial V_1^k}{\partial y_1} + \frac{1}{h_2}C_{23}\frac{\partial V_2^k}{\partial y_2} + C_{33}\frac{\partial V_3^k}{\partial z}$$

$$\bar{\tau}_{23}^k = C_{44}\left(\frac{1}{h_2}\frac{\partial V_3^k}{\partial y_2} + \frac{\partial V_2^k}{\partial z}\right) \qquad (12.83)$$

$$\bar{\tau}_{13}^k = C_{55}\left(\frac{1}{h_1}\frac{\partial V_3^k}{\partial y_2} + \frac{\partial V_1^k}{\partial z}\right)$$

$$\bar{\tau}_{12}^k = C_{66}\left(\frac{1}{h_2}\frac{\partial V_1^k}{\partial y_2} + \frac{\partial V_2^k}{\partial y_1}\right)$$

Next, define the following:

$$\bar{t}_1^k = \bar{\tau}_{11}^k\frac{n_1}{h_1} + \bar{\tau}_{12}^k\frac{n_2}{h_2} + \bar{\tau}_{13}^k n_3$$

$$\bar{t}_2^k = \bar{\tau}_{12}^k\frac{n_1}{h_1} + \bar{\tau}_{22}^k\frac{n_2}{h_2} + \bar{\tau}_{23}^k n_3 \qquad (12.84)$$

$$\bar{t}_3^k = \bar{\tau}_{13}^k\frac{n_1}{h_1} + \bar{\tau}_{23}^k\frac{n_2}{h_2} + \bar{\tau}_{33}^k n_3$$

In view of Equation (12.84), the boundary conditions in Equation (12.82a) become:

$$\bar{t}_i^k = zP_{i\alpha k}\frac{n_\alpha}{h_\alpha} + zP_{i3k}n_3 \qquad (12.85a)$$

Thus:

$$\bar{t}_1^1 = zP_{15}n_3, \quad \bar{t}_2^1 = 0, \quad \bar{t}_3^1 = zP_{15}\frac{n_1}{h_1},$$

$$\bar{t}_1^2 = 0, \quad \bar{t}_2^2 = zP_{24}n_3, \quad \bar{t}_3^2 = zP_{24}\frac{n_2}{h_2}, \quad \left.\right\} \text{ on } z^\pm \qquad (12.85b)$$

$$\bar{t}_1^3 = zP_{31}\frac{n_1}{h_1}, \quad \bar{t}_2^3 = zP_{32}\frac{n_2}{h_2}, \quad \bar{t}_3^3 = zP_{33}n_3$$

The $d_{ij}^k$ functions for an orthotropic material are then obtained from the following expressions:

$$
\begin{array}{lll}
d_{11}^{*1} = -\bar{\tau}_{11}^1 & d_{11}^{*2} = -\bar{\tau}_{11}^2 & d_{11}^{*3} = zP_{31} - \bar{\tau}_{11}^3 \\[4pt]
d_{12}^{*1} = -\bar{\tau}_{12}^1 & d_{12}^{*2} = -\bar{\tau}_{12}^2 & d_{12}^{*3} = -\bar{\tau}_{12}^3 \\[4pt]
d_{22}^{*1} = -\bar{\tau}_{22}^1 & d_{22}^{*2} = -\bar{\tau}_{22}^2 & d_{22}^{*3} = zP_{32} - \bar{\tau}_{22}^3 \\[4pt]
d_{32}^{*1} = -\bar{\tau}_{32}^1 & d_{32}^{*2} = zP_{24} - \bar{\tau}_{32}^2 & d_{32}^{*3} = -\bar{\tau}_{22}^3 \\[4pt]
d_{33}^{*1} = -\bar{\tau}_{33}^1 & d_{33}^{*2} = -\bar{\tau}_{33}^2 & d_{33}^{*3} = zP_{33} - \bar{\tau}_{33}^3 \\[4pt]
d_{31}^{*1} = zP_{15} - \bar{\tau}_{33}^1 & d_{31}^{*2} = -\bar{\tau}_{31}^2 & d_{31}^{*3} = -\bar{\tau}_{33}^3
\end{array}
\qquad (12.86)
$$

As for the previous unit-cell problem, the $d_{ij}^{*k}$ functions will be solved by considering each element of the unit cell separately. The $\bar{\tau}_{ij}^1$ problem will be dealt with first.

## (a) Region $\Omega_1$:

From Equations (12.84) and (12.85b) the boundary conditions are:

$$\bar{t}_1^1 = \bar{t}_2^1 = 0 \qquad \bar{t}_3^1 = z\frac{P_{15}}{h_1}$$

$$\therefore \bar{\tau}_{11}^1 = \bar{\tau}_{12}^1 = 0 \qquad \bar{\tau}_{13}^1 = zP_{15} \quad \text{on } y_1 = \pm\delta_1/2$$

and $\qquad\qquad\qquad\qquad\qquad\qquad\qquad\qquad\qquad (12.87a)$

$$\bar{t}_2^1 = \bar{t}_3^1 = 0 \qquad \bar{t}_1^1 = zP_{15}$$

$$\therefore \bar{\tau}_{13}^1 = zP_{15}, \quad \bar{\tau}_{23}^1 = \bar{\tau}_{33}^1 = 0 \quad \text{on } z = 1/2, \quad z = 1/2 + H$$

Thus, considering the periodicity in $y_2$, and using Equations (12.82c), (12.83), and (12.87a), the following functions are determined:

$$V_1^1 = \frac{P_{15}}{C_{55}} \frac{z^2}{2}$$

$$V_2^1 = V_3^1 = 0 \tag{12.87b}$$

$$\Rightarrow \overline{\tau}_{11}^1 = \overline{\tau}_{22}^1 = \overline{\tau}_{33}^1 = \overline{\tau}_{23}^1 = \overline{\tau}_{12}^1 = 0, \quad \overline{\tau}_{13}^1 = zP_{15}$$

## (b) Region $\Omega_2$:

From Equations (12.84) and (12.85b) the boundary conditions are:

$$\overline{t}_1^1 = \overline{t}_2^1 = \overline{t}_3^1 = 0$$

$$\therefore \overline{\tau}_{12}^1 = \overline{\tau}_{22}^1 = \overline{\tau}_{23}^1 = 0 \quad \text{on } y_2 = \pm\delta_2/2$$

and $\tag{12.88a}$

$$\overline{t}_2^1 = \overline{t}_3^1 = 0 \qquad \overline{t}_1^1 = zP_{15}$$

$$\therefore \overline{\tau}_{13}^1 = zP_{15}, \quad \overline{\tau}_{23}^1 = \overline{\tau}_{33}^1 = 0 \quad \text{on } z = 1/2, \quad z = 1/2 + H$$

Thus, considering the periodicity in $y_1$, and using Equations (12.82c), (12.83), and (12.88a), the following functions are determined:

$$V_1^1 = \frac{P_{15}}{C_{55}} \frac{z^2}{2}$$

$$V_2^1 = V_3^1 = 0 \tag{12.88b}$$

$$\Rightarrow \overline{\tau}_{11}^1 = \overline{\tau}_{22}^1 = \overline{\tau}_{33}^1 = \overline{\tau}_{23}^1 = \overline{\tau}_{12}^1 = 0, \quad \overline{\tau}_{13}^1 = zP_{15}$$

## (c) Region $\Omega_3$:

The boundary conditions are:

$$\overline{t}_1^1 = zP_{15} \quad \overline{t}_2^1 = \overline{t}_3^1 = 0$$

$$\therefore \overline{\tau}_{13}^1 = zP_{15} \quad \overline{\tau}_{23}^1 = \overline{\tau}_{33}^1 = 0 \quad \text{on } z = \pm 1/2 \tag{12.89a}$$

Thus, considering the periodicity in $y_1$, $y_2$ and using Equations (12.82c), (12.83), and (12.89a), the following functions are determined:

$$V_1^1 = \frac{P_{15}}{C_{55}} \frac{z^2}{2},$$

$$V_2^1 = V_3^1 = 0 \tag{12.89b}$$

$$\Rightarrow \overline{\tau}_{11}^1 = \overline{\tau}_{22}^1 = \overline{\tau}_{33}^1 = \overline{\tau}_{23}^1 = \overline{\tau}_{12}^1 = 0, \quad \overline{\tau}_{13}^1 = zP_{15}$$

Thus, considering Equations (12.87b), (12.88b), (12.89b), and (12.86) one obtains:

$$\left.\begin{aligned} d_{11}^{*1} = d_{12}^{*1} = d_{22}^{*1} = d_{23}^{*1} = d_{33}^{*1} = 0, \\ d_{13}^{*1} = zP_{15} - zP_{15} = 0 \end{aligned}\right\} \text{ in } \Omega_1, \Omega_2, \Omega_3 \qquad (12.90)$$

The solution of the $\overline{\tau}_{ij}^2$ problem is very similar to the $\overline{\tau}_{ij}^1$ problem and is:

$$\left.\begin{aligned} \tau_{11}^2 = \tau_{22}^2 = \tau_{33}^2 = \tau_{13}^2 = \tau_{12}^2 = 0 \\ \overline{\tau}_{23}^2 = zP_{24} \end{aligned}\right\} \text{ in } \Omega_1, \Omega_2, \Omega_3 \qquad (12.91a)$$

Thus:

$$\left.\begin{aligned} d_{11}^{*2} = d_{12}^{*2} = d_{22}^{*2} = d_{13}^{*2} = d_{33}^{*2} = 0 \\ d_{23}^{*2} = zP_{24} - zP_{24} = 0 \end{aligned}\right\} \text{ in } \Omega_1, \Omega_2, \Omega_3 \qquad (12.91b)$$

Now the $\overline{\tau}_{ij}^3$ problem will be dealt with.

## (a) Region $\Omega_1$:

In $\Omega_1$ the boundary conditions are:

$$\overline{t}_2^3 = \overline{t}_3^3 = 0 \qquad \overline{t}_1^3 = z\frac{P_{31}}{h_1} \qquad (12.92a)$$

$$\therefore \overline{\tau}_{12}^3 = \overline{\tau}_{13}^3 = 0 \qquad \overline{\tau}_{11}^3 = zP_{31} \quad \text{on } y_1 = \pm \delta_1/2$$

and

$$\overline{t}_1^3 = \overline{t}_2^3 = 0 \qquad \overline{t}_3^3 = zP_{33} \qquad (12.92b)$$

$$\therefore \overline{\tau}_{33}^3 = zP_{33}, \quad \overline{\tau}_{13}^3 = \overline{\tau}_{23}^3 = 0 \quad \text{on } z = 1/2, \quad z = 1/2 + H$$

Hence, from Equations (12.82c), (12.83), (12.92a) and (12.92b), and considering periodicity in $y_2$ the $V_i^3$ functions are:

$$V_1^3 = \frac{C_{33}P_{31} - C_{13}P_{33}}{C_{11}C_{33} - C_{13}^2} h_1 y_1 z$$

$$V_2^3 = 0 \qquad (12.93)$$

$$V_3^3 = \frac{C_{11}P_{33} - C_{13}P_{31}}{C_{11}C_{33} - C_{13}^2} \frac{z^2}{2} - \frac{C_{33}P_{31} - C_{13}P_{33}}{C_{11}C_{33} - C_{13}^2} h_1^2 \frac{y_1^2}{2}$$

Thus, the $d_{ij}^{*3}$ piezoelectric coefficients are obtained through Equations (12.83), (12.86), (12.34b) and (12.93) and are:

$$d_{11}^{*3} = d_{33}^{*3} = d_{12}^{*3} = d_{13}^{*3} = d_{23}^{*3} = 0$$
$$d_{22}^{*3} = z(P_{32} - v_{21}P_{31} - v_{23}P_{33})$$

(12.94)

**(b) Region $\Omega_2$:**

In $\Omega_2$ the boundary conditions are:

$$\bar{t}_1^3 = \bar{t}_3^3 = 0 \qquad \bar{t}_2^3 = z\frac{P_{32}}{h_2}$$
$$\therefore \bar{\tau}_{12}^3 = \bar{\tau}_{23}^3 = 0 \qquad \bar{\tau}_{22}^3 = P_{32} \quad \text{on } y_2 = \pm\delta_2/2$$

(12.95a)

and

$$\bar{t}_1^3 = \bar{t}_2^3 = 0 \qquad \bar{t}_3^3 = zP_{33}$$
$$\therefore \bar{\tau}_{33}^3 = zP_{33}, \quad \bar{\tau}_{13}^3 = \bar{\tau}_{23}^3 = 0 \quad \text{on } z = 1/2, \quad z = 1/2 + H$$

(12.95b)

Hence, from Equations (12.82c), (12.83), (12.95a) and (12.95b), and considering periodicity in $y_1$, the $V_i^3$ functions are:

$$V_1^3 = 0$$
$$V_2^3 = \frac{C_{33}P_{32} - C_{23}P_{33}}{C_{22}C_{33} - C_{23}^2}h_2y_2z$$
$$V_3^3 = \frac{C_{22}P_{33} - C_{23}P_{32}}{C_{22}C_{33} - C_{23}^2}\frac{z^2}{2} - \frac{C_{33}P_{32} - C_{23}P_{33}}{C_{22}C_{33} - C_{23}^2}h_2^2\frac{y_2^2}{2}$$

(12.96)

Thus, the $d_{ij}^{*3}$ piezoelectric coefficients are obtained through Equations ((12.83), (12.86), (12.34b) and (12.96) and are:

$$d_{11}^{*3} = z(P_{31} - v_{12}P_{32} - v_{13}P_{33})$$
$$d_{22}^{*3} = d_{33}^{*3} = d_{12}^{*3} = d_{13}^{*3} = d_{23}^{*3} = 0$$

(12.97)

**(c) Region $\Omega_3$:**

The appropriate boundary conditions are:

$$\bar{t}_1^3 = \bar{t}_2^3 = 0, \quad \bar{t}_3^3 = zP_{33}$$
$$\bar{\tau}_{33}^3 = zP_{33}, \quad \bar{\tau}_{13}^1 = \bar{\tau}_{23}^1 = 0 \quad \text{on } z = \pm 1/2$$

(12.98a)

Thus from Equations (12.82c), (12.83), and (12.98a) and on account of periodicity in $y_1$ and $y_2$ one obtains:

$$V_3^3 = \frac{P_{33}}{C_{33}} \frac{z^2}{2}$$

$$V_1^3 = V_2^3 = 0$$

$$\Rightarrow \bar{\tau}_{11}^3 = \frac{C_{13}}{C_{33}} P_{33} z, \quad \bar{\tau}_{22}^3 = \frac{C_{23}}{C_{33}} P_{33} z, \quad \bar{\tau}_{33}^3 = P_{33} z$$

$$\bar{\tau}_{12}^3 = \bar{\tau}_{13}^3 = \bar{\tau}_{23}^3 = 0$$

(12.98b)

Thus, from Equation (12.69) the $d_{ij}^3$ functions are obtained as follows:

$$d_{11}^{*3} = z \left( P_{31} - \frac{C_{13}}{C_{33}} P_{33} \right)$$

$$d_{22}^{*3} = z \left( P_{32} - \frac{C_{23}}{C_{33}} P_{33} \right)$$

(12.98c)

$$d_{33}^{*3} = d_{12}^{*3} = d_{13}^{*3} = d_{23}^3 = 0$$

Having solved the unit-cell problems for the piezoelectric coefficients and remembering that

$$P_{ijm} = C_{ijkl} \frac{d_{klm}^{(r)}}{\delta}$$

(12.99)

then on account of Equation (12.34b), the piezoelectric strain coefficients are given from Equations (12.73), (12.74), (12.77), (12.80), (12.81c), (12.90), (12.91b), (12.94), (12.97) and (12.98c) by the following expressions:

$$d_{ij}^1 = d_{ij}^2 = d_{33}^3 = d_{12}^3 = d_{13}^3 = d_{23}^3 = 0 \quad \text{in } \Omega_1, \Omega_2, \Omega_3$$

$$\delta d_{11}^3 = \begin{cases} 0 & \text{in } \Omega_1 \\ d_{31}^{(r)} E_1 & \text{in } \Omega_2 \\ \dfrac{d_{31}^{(r)} E_1 + d_{32}^{(r)} \nu_{21} E_1}{1 - \nu_{12} \nu_{21}} & \text{in } \Omega_3 \end{cases}$$

(12.100a)

$$\delta d_{22}^{3} = \begin{cases} d_{32}^{(r)}E_{2} & \text{in } \Omega_{1} \\ 0 & \text{in } \Omega_{2} \\ \dfrac{d_{32}^{(r)}E_{2} + d_{31}^{(r)}v_{12}E_{2}}{1 - v_{12}v_{21}} & \text{in } \Omega_{3} \end{cases} \qquad (12.100b)$$

$$d_{ij}^{*1} = d_{ij}^{*2} = d_{33}^{*3} = d_{12}^{*3} = d_{13}^{*3} = d_{23}^{*3} = 0 \quad \text{in } \Omega_{1}, \Omega_{2}, \Omega_{3}$$

$$\delta d_{11}^{*3} = \begin{cases} 0 & \text{in } \Omega_{1} \\ z d_{31}^{(r)}E_{1} & \text{in } \Omega_{2} \\ \dfrac{d_{31}^{(r)}E_{1} + d_{32}^{(r)}v_{21}E_{1}}{1 - v_{12}v_{21}} z & \text{in } \Omega_{3} \end{cases} \qquad (12.100c)$$

$$d_{ij}^{*1} = d_{ij}^{*2} = d_{33}^{*3} = d_{12}^{*3} = d_{13}^{*3} = d_{23}^{*3} = 0 \quad \text{in } \Omega_{1}, \Omega_{2}, \Omega_{3}$$

$$\delta d_{22}^{*3} = \begin{cases} z d_{32}^{(r)}E_{2} & \text{in } \Omega_{1} \\ 0 & \text{in } \Omega_{2} \\ \dfrac{d_{32}^{(r)}E_{2} + d_{31}^{(r)}v_{12}E_{2}}{1 - v_{12}v_{21}} z & \text{in } \Omega_{3}. \end{cases} \qquad (12.100d)$$

Comparison of these Equations reveals that:

$$d_{ij}^{*k} = z d_{ij}^{k} \quad \text{in } \Omega_{1}, \Omega_{2}, \Omega_{3} \qquad (12.100e)$$

The effective piezoelectric coefficients are determined from Equations (12.100a), (12.100b), (12.100c), and (12.100d), bearing Equations (11.22) and (12.34b) in mind. They are given by the following expressions:

$$\delta \langle d_{11}^{3} \rangle = E_{1}^{(2)} d_{31}^{(r)(2)} F_{2}^{(w)} + \frac{E_{1}^{(3)} d_{31}^{(r)(3)} + E_{1}^{(3)} v_{21}^{(3)} d_{32}^{(r)(3)}}{1 - v_{12}^{(3)} v_{21}^{(3)}}$$

$$\delta \langle d_{22}^{3} \rangle = E_{2}^{(1)} d_{32}^{(r)(1)} F_{1}^{(w)} + \frac{E_{2}^{(3)} d_{32}^{(r)(3)} + E_{2}^{(3)} v_{12}^{(3)} d_{31}^{(r)(3)}}{1 - v_{12}^{(3)} v_{21}^{(3)}} \qquad (12.101a)$$

$$\delta \langle z d_{11}^{3} \rangle = \delta \langle d_{11}^{*3} \rangle = E_{1}^{(2)} d_{31}^{(r)(2)} S_{2}^{(w)}$$

$$\delta \langle z d_{22}^{3} \rangle = \delta \langle d_{22}^{*3} \rangle = E_{2}^{(1)} d_{32}^{(r)(1)} S_{1}^{(w)}$$

$$\delta\left\langle zd_{11}^{*3}\right\rangle = E_1^{(2)}d_{31}^{(r)(2)}J_2^{(w)} + \frac{E_1^{(3)}d_{31}^{(r)(3)} + E_1^{(3)}v_{21}^{(3)}d_{32}^{(r)(3)}}{12\left(1 - v_{12}^{(3)}v_{21}^{(3)}\right)}$$

$$\delta\left\langle zd_{22}^{*3}\right\rangle = E_2^{(1)}d_{32}^{(r)(1)}J_1^{(w)} + \frac{E_2^{(3)}d_{32}^{(r)(3)} + E_2^{(3)}v_{12}^{(3)}d_{31}^{(r)(3)}}{12\left(1 - v_{12}^{(3)}v_{21}^{(3)}\right)}$$

(12.101b)

### 12.3.4 Use of Symmetry Relationships for Effective Piezoelectric Coefficients

In Section 11.7 the symmetry properties of the effective piezoelectric coefficients were derived. The implication was that it suffices to find the solution of the purely elastic local problem in conjunction with the constituent properties, in order to derive the effective piezoelectric coefficients. In this section, these symmetry properties will be shown to produce the same results as the direct solution of the pertinent unit-cell problems.

One begins with the symmetry relationships from Equation (11.63a). They are repeated here for convenience:

$$\delta\left\langle d_{mn}^k\right\rangle = \left\langle d_{ijk}^{(r)}b_{ij}^{mn}\right\rangle, \quad \delta\left\langle zd_{mn}^k\right\rangle = \left\langle d_{ijk}^{(r)}b_{ij}^{*mn}\right\rangle,$$

$$\delta\left\langle d_{mn}^{*k}\right\rangle = \left\langle zd_{ijk}^{(r)}b_{ij}^{mn}\right\rangle, \quad \delta\left\langle zd_{mn}^{*k}\right\rangle = \left\langle zd_{ijk}^{(r)}b_{ij}^{*mn}\right\rangle$$

(12.102)

As an illustration of Equation (12.102) the following expression from Equation (12.101a) will be proved:

$$\delta\left\langle d_{11}^3\right\rangle = E_1^{(2)}d_{31}^{(r)(2)}F_2^{(w)} + \frac{E_1^{(3)}d_{31}^{(r)(3)} + E_1^{(3)}v_{21}^{(3)}d_{32}^{(r)(3)}}{1 - v_{12}^{(3)}v_{21}^{(3)}}$$

(12.103)

One begins with the first expression in Equation (12.102) and expands the appropriate indices to obtain for k = 3 and m = n = 1, the following expression:

$$\delta\left\langle d_{11}^3\right\rangle = \left\langle d_{113}^{(r)}b_{11}^{11} + 2d_{123}^{(r)}b_{12}^{11} + d_{223}^{(r)}b_{22}^{11} + d_{333}^{(r)}b_{33}^{11} + 2d_{313}^{(r)}b_{31}^{11} + 2d_{323}b_{32}^{11}\right\rangle$$ (12.104a)

Thus

$$\delta\left\langle d_{11}^3\right\rangle = \left\langle d_{31}^{(r)}b_{11}^{11} + 2d_{36}^{(r)}b_{12}^{11} + d_{32}^{(r)}b_{22}^{11} + d_{33}^{(r)}b_{33}^{11} + 2d_{53}^{(r)}b_{31}^{11} + 2d_{43}b_{32}^{11}\right\rangle$$ (12.104b)

In Equation (12.104b) the piezoelectric coefficients were written in the contracted (rather than the tensorial) format. Now, for an orthotropic material, see Equation (12.62), the piezoelectric coefficients $d_{36}^{(r)}, d_{53}^{(r)}, d_{43}^{(r)}$ all vanish. As well, the elastic coefficient $b_{33}^{11}$ also vanishes, see Equation (12.32). Consequently, Equation (12.104b) reduces to:

$$\delta\left\langle d_{11}^3 \right\rangle = \left\langle d_{31}^{(r)} b_{11}^{11} + d_{32}^{(r)} b_{22}^{11} \right\rangle \qquad (12.104c)$$

The RHS of Equation (12.104c) will be treated term by term bearing the averaging procedure of Equation (11.22) in mind. Thus:

$$\left\langle d_{31}^{(r)} b_{11}^{11} \right\rangle = \int d_{31}^{(r)} b_{11}^{11}\, dv = \sum_{i-1}^{3} \int_{\Omega_i} d_{31}^{(r)} b_{11}^{11}\, dv = \sum_{i-1}^{3} d_{31}^{(r)(i)} b_{11}^{11(i)} \left\langle 1 \right\rangle_{\Omega_i} \qquad (12.104d)$$

Substituting the first expressions of Equations (12.32) and (12.34a) into Equation (12.104d) results in the following:

$$\left\langle d_{31}^{(r)} b_{11}^{11} \right\rangle = d_{31}^{(r)(2)} E_1^{(2)} F_2^{(w)} + \frac{d_{31}^{(r)(3)} E_1^{(3)}}{1 - v_{12}^{(3)} v_{21}^{(3)}} \qquad (12.104e)$$

Likewise, the second term on the RHS of Equation (12.104c) is:

$$\left\langle d_{32}^{(r)} b_{22}^{11} \right\rangle = \int d_{32}^{(r)} b_{22}^{11}\, dv = \sum_{i-1}^{3} \int_{\Omega_i} d_{32}^{(r)} b_{22}^{11}\, dv = \sum_{i-1}^{3} d_{32}^{(r)(i)} b_{22}^{11(i)} \left\langle 1 \right\rangle_{\Omega_i} \qquad (12.104f)$$

Thus,

$$\left\langle d_{32}^{(r)} b_{22}^{11} \right\rangle = \frac{d_{32}^{(r)(3)} v_{21}^{(3)} E_1^{(3)}}{1 - v_{12}^{(3)} v_{21}^{(3)}} \qquad (12.104g)$$

Hence, from Equations (12.104e) and (12.104g) one writes:

$$\delta\left\langle d_{11}^3 \right\rangle = d_{31}^{(r)(2)} E_1^{(2)} F_2^{(w)} + \frac{d_{32}^{(r)(3)} E_1^{(3)} + d_{32}^{(r)(3)} v_{21}^{(3)} E_1^{(3)}}{1 - v_{12}^{(3)} v_{21}^{(3)}} \qquad (12.105)$$

This is then the desired expression. Likewise all the remaining expressions for the effective piezoelectric coefficients can be determined in this manner. Using the expressions in Equation (11.63b) that represent the symmetry properties of the hygroscopic expansion coefficients will give the same results as those shown in Equation (12.61) which were determined directly from the unit-cell problems.

### 12.3.5 Effective Thermal Expansion Coefficients

The last effective coefficients to be determined are the thermal expansion coefficients. The solution of the unit cell problems from Equations (11.46e) and (11.46f) results in the following expressions:

$$\Theta_{11} = 0, \quad \delta\Theta_{22} = E_2\alpha_2^{(\theta)} \quad \text{in } \Omega_1$$

$$\Theta_{22} = 0, \quad \delta\Theta_{11} = E_1\alpha_1^{(\theta)} \quad \text{in } \Omega_2$$

$$\left.\begin{array}{l} \delta\Theta_{11} = \dfrac{E_1\alpha_1^{(\theta)}}{1-\nu_{12}\nu_{21}} + \dfrac{\nu_{21}E_1\alpha_2^{(\theta)}}{1-\nu_{12}\nu_{21}} \\[4mm] \delta\Theta_{22} = \dfrac{E_2\alpha_2^{(\theta)}}{1-\nu_{12}\nu_{21}} + \dfrac{\nu_{21}E_1\alpha_1^{(\theta)}}{1-\nu_{12}\nu_{21}} \end{array}\right\} \text{in } \Omega_3 \tag{12.106}$$

$$\Theta_{33} = \Theta_{12} = \Theta_{13} = \Theta_{23} = 0 \quad \text{in } \Omega_1,\Omega_2,\Omega_3$$

$$\Theta_{11}^* = 0, \quad \delta\Theta_{22}^* = zE_2\alpha_2^{(\theta)} \quad \text{in } \Omega_1$$

$$\Theta_{22}^* = 0, \quad \delta\Theta_{11}^* = zE_1\alpha_1^{(\theta)} \quad \text{in } \Omega_2$$

$$\left.\begin{array}{l} \delta\Theta_{11}^* = z\left(\dfrac{E_1\alpha_1^{(\theta)}}{1-\nu_{12}\nu_{21}} + \dfrac{\nu_{21}E_1\alpha_2^{(\theta)}}{1-\nu_{12}\nu_{21}}\right) \\[4mm] \delta\Theta_{22}^* = z\left(\dfrac{E_2\alpha_2^{(\theta)}}{1-\nu_{12}\nu_{21}} + \dfrac{\nu_{21}E_1\alpha_1^{(\theta)}}{1-\nu_{12}\nu_{21}}\right) \end{array}\right\} \text{in } \Omega_3 \tag{12.107}$$

$$\Theta_{33}^* = \Theta_{12}^* = \Theta_{13}^* = \Theta_{23}^* = 0 \quad \text{in } \Omega_1,\Omega_2,\Omega_3$$

The effective thermal expansion coefficients are thus determined as follows:

$$\delta\langle\Theta_{11}\rangle = E_1^{(2)}\alpha_1^{(\theta)(2)}F_2^{(w)} + \frac{E_1^{(3)}\alpha_1^{(\theta)(3)} + E_1^{(3)}\nu_{21}^{(3)}\alpha_2^{(\theta)(3)}}{1-\nu_{12}^{(3)}\nu_{21}^{(3)}}$$

$$\delta\langle\Theta_{22}\rangle = E_2^{(1)}\alpha_2^{(\theta)(1)}F_1^{(w)} + \frac{E_2^{(3)}\alpha_2^{(\theta)(3)} + E_2^{(3)}\nu_{12}^{(3)}\alpha_1^{(\theta)(3)}}{1-\nu_{12}^{(3)}\nu_{21}^{(3)}}$$

$$\delta\langle z\Theta_{11}\rangle = \delta\langle\Theta_{11}^*\rangle = E_1^{(2)}\alpha_1^{(\theta)(2)}S_2^{(w)}$$

$$\delta\langle z\Theta_{22}\rangle = \delta\langle\Theta_{22}^*\rangle = E_2^{(1)}\alpha_2^{(\theta)(1)}S_1^{(w)} \tag{12.108}$$

$$\delta\langle z\Theta_{11}^*\rangle = E_1^{(2)}\alpha_1^{(\theta)(2)}J_2^{(w)} + \frac{E_1^{(3)}\alpha_1^{(\theta)(3)} + E_1^{(3)}\nu_{21}^{(3)}\alpha_2^{(\theta)(3)}}{12\left(1-\nu_{12}^{(3)}\nu_{21}^{(3)}\right)}$$

$$\delta\langle z\Theta_{22}^*\rangle = E_2^{(1)}\alpha_2^{(\theta)(1)}J_1^{(w)} + \frac{E_2^{(3)}\alpha_2^{(\theta)(3)} + E_2^{(3)}\nu_{12}^{(3)}\alpha_1^{(\theta)(3)}}{12\left(1-\nu_{12}^{(3)}\nu_{21}^{(3)}\right)}$$

### 12.3.6 Summary of Effective Coefficients

For the wafer-reinforced piezoelectric plates shown in Figure 12-14, the effective elastic, piezoelectric, thermal expansion and hygroscopic expansion coefficients are summarized below:

**(1) Elastic:**

$$\left\langle b_{11}^{11} \right\rangle = \frac{E_1^{(3)}}{1 - v_{12}^{(3)} v_{21}^{(3)}} + E_1^{(2)} F_2^{(w)}, \quad \left\langle b_{22}^{22} \right\rangle = \frac{E_2^{(3)}}{1 - v_{12}^{(3)} v_{21}^{(3)}} + E_2^{(1)} F_1^{(w)}, \quad \left\langle b_{22}^{11} \right\rangle = \frac{v_{21}^{(3)} E_1^{(3)}}{1 - v_{12}^{(3)} v_{21}^{(3)}},$$

$$\left\langle b_{12}^{12} \right\rangle = G_{12}^{(3)}, \quad \left\langle zb_{11}^{11} \right\rangle = \left\langle b_{11}^{*11} \right\rangle = E_1^{(2)} S_2^{(w)}, \quad \left\langle zb_{22}^{22} \right\rangle = \left\langle b_{22}^{*22} \right\rangle = E_2^{(1)} S_1^{(w)},$$

$$\left\langle zb_{11}^{*11} \right\rangle = \frac{E_1^{(3)}}{12\left(1 - v_{12}^{(3)} v_{21}^{(3)}\right)} + E_1^{(2)} J_2^{(w)}, \quad \left\langle zb_{22}^{*22} \right\rangle = \frac{E_2^{(3)}}{12\left(1 - v_{12}^{(3)} v_{21}^{(3)}\right)} + E_2^{(1)} J_1^{(w)},$$

$$\left\langle zb_{22}^{*11} \right\rangle = \frac{v_{21}^{(3)} E_1^{(3)}}{12\left(1 - v_{12}^{(3)} v_{21}^{(3)}\right)}, \quad \left\langle zb_{12}^{*12} \right\rangle = \frac{G_{12}^{(3)}}{12} + \frac{G_{12}^{(1)}}{12}\left( \frac{H^3 t_1}{h_1} - K_1 \right) + \frac{G_{12}^{(2)}}{12}\left( \frac{H^3 t_2}{h_2} - K_2 \right)$$

$$\text{where } K_1 = \frac{96 H^4}{\pi^5 h_1} \sqrt{\frac{G_{12}^{(1)}}{G_{23}^{(1)}}} \sum_{n=1}^{\infty} \frac{\left[1 - (-1)^n\right]}{n^5} \tanh\left( \sqrt{\frac{G_{23}^{(1)}}{G_{12}^{(1)}}} \frac{n\pi t_1}{2H} \right) \tag{12.109}$$

$$\text{and } K_2 = \frac{96 H^4}{\pi^5 h_2} \sqrt{\frac{G_{12}^{(2)}}{G_{13}^{(2)}}} \sum_{n=1}^{\infty} \frac{\left[1 - (-1)^n\right]}{n^5} \tanh\left( \sqrt{\frac{G_{13}^{(2)}}{G_{12}^{(2)}}} \frac{n\pi t_2}{2H} \right)$$

**(2) Piezoelectric:**

$$\delta\left\langle d_{11}^3 \right\rangle = E_1^{(2)} d_{31}^{(r)(2)} F_2^{(w)} + \frac{E_1^{(3)} d_{31}^{(r)(3)} + E_1^{(3)} v_{21}^{(3)} d_{32}^{(r)(3)}}{1 - v_{12}^{(3)} v_{21}^{(3)}}$$

$$\delta\left\langle d_{22}^3 \right\rangle = E_2^{(1)} d_{32}^{(r)(1)} F_1^{(w)} + \frac{E_2^{(3)} d_{32}^{(r)(3)} + E_2^{(3)} v_{12}^{(3)} d_{31}^{(r)(3)}}{1 - v_{12}^{(3)} v_{21}^{(3)}}$$

$$\delta\left\langle zd_{11}^3 \right\rangle = \delta\left\langle d_{11}^{*3} \right\rangle = E_1^{(2)} d_{31}^{(r)(2)} S_2^{(w)}$$

$$\delta\left\langle zd_{22}^3 \right\rangle = \delta\left\langle d_{22}^{*3} \right\rangle = E_2^{(1)} d_{32}^{(r)(1)} S_1^{(w)} \tag{12.110}$$

$$\delta\left\langle zd_{11}^{*3} \right\rangle = E_1^{(2)} d_{31}^{(r)(2)} J_2^{(w)} + \frac{E_1^{(3)} d_{31}^{(r)(3)} + E_1^{(3)} v_{21}^{(3)} d_{32}^{(r)(3)}}{12\left(1 - v_{12}^{(3)} v_{21}^{(3)}\right)}$$

$$\delta\left\langle zd_{22}^{*3} \right\rangle = E_2^{(1)} d_{32}^{(r)(1)} J_1^{(w)} + \frac{E_2^{(3)} d_{32}^{(r)(3)} + E_2^{(3)} v_{12}^{(3)} d_{31}^{(r)(3)}}{12\left(1 - v_{12}^{(3)} v_{21}^{(3)}\right)}$$

## (3) Hygroscopic:

$$\delta\langle\Lambda_{11}\rangle = E_1^{(2)}\beta_1^{(c)(2)}F_2^{(w)} + \frac{E_1^{(3)}\beta_1^{(c)(3)} + E_1^{(3)}\nu_{21}^{(3)}\beta_2^{(c)(3)}}{1-\nu_{12}^{(3)}\nu_{21}^{(3)}}$$

$$\delta\langle\Lambda_{22}\rangle = E_2^{(1)}\beta_2^{(\theta)(1)}F_1^{(w)} + \frac{E_2^{(3)}\beta_2^{(c)(3)} + E_2^{(3)}\nu_{12}^{(3)}\beta_1^{(c)(3)}}{1-\nu_{12}^{(3)}\nu_{21}^{(3)}}$$

$$\delta\langle z\Lambda_{11}\rangle = \delta\langle\Lambda_{11}^*\rangle = E_1^{(2)}\beta_1^{(c)(2)}S_2^{(w)}$$

$$\delta\langle z\Lambda_{22}\rangle = \delta\langle\Lambda_{22}^*\rangle = E_2^{(1)}\beta_2^{(c)(1)}S_1^{(w)}$$

$$\delta\langle z\Lambda_{11}^*\rangle = E_1^{(2)}\beta_1^{(c)(2)}J_2^{(w)} + \frac{E_1^{(3)}\beta_1^{(c)(3)} + E_1^{(3)}\nu_{21}^{(3)}\beta_2^{(c)(3)}}{12\left(1-\nu_{12}^{(3)}\nu_{21}^{(3)}\right)}$$

$$\delta\langle z\Lambda_{22}^*\rangle = E_2^{(1)}\beta_2^{(c)(1)}J_1^{(w)} + \frac{E_2^{(3)}\beta_2^{(c)(3)} + E_2^{(3)}\nu_{12}^{(3)}\beta_1^{(c)(3)}}{12\left(1-\nu_{12}^{(3)}\nu_{21}^{(3)}\right)}$$

$$(12.111)$$

## (4) Thermal:

$$\delta\langle\Theta_{11}\rangle = E_1^{(2)}\alpha_1^{(\theta)(2)}F_2^{(w)} + \frac{E_1^{(3)}\alpha_1^{(\theta)(3)} + E_1^{(3)}\nu_{21}^{(3)}\alpha_2^{(\theta)(3)}}{1-\nu_{12}^{(3)}\nu_{21}^{(3)}}$$

$$\delta\langle\Theta_{22}\rangle = E_2^{(1)}\alpha_2^{(\theta)(1)}F_1^{(w)} + \frac{E_2^{(3)}\alpha_2^{(\theta)(3)} + E_2^{(3)}\nu_{12}^{(3)}\alpha_1^{(\theta)(3)}}{1-\nu_{12}^{(3)}\nu_{21}^{(3)}}$$

$$\delta\langle z\Theta_{11}\rangle = \delta\langle\Theta_{11}^*\rangle = E_1^{(2)}\alpha_1^{(\theta)(2)}S_2^{(w)}$$

$$\delta\langle z\Theta_{22}\rangle = \delta\langle\Theta_{22}^*\rangle = E_2^{(1)}\alpha_2^{(\theta)(1)}S_1^{(w)}$$

$$\delta\langle z\Theta_{11}^*\rangle = E_1^{(2)}\alpha_1^{(\theta)(2)}J_2^{(w)} + \frac{E_1^{(3)}\alpha_1^{(\theta)(3)} + E_1^{(3)}\nu_{21}^{(3)}\alpha_2^{(\theta)(3)}}{12\left(1-\nu_{12}^{(3)}\nu_{21}^{(3)}\right)}$$

$$\delta\langle z\Theta_{22}^*\rangle = E_2^{(1)}\alpha_2^{(\theta)(1)}J_1^{(w)} + \frac{E_2^{(3)}\alpha_2^{(\theta)(3)} + E_2^{(3)}\nu_{12}^{(3)}\alpha_1^{(\theta)(3)}}{12\left(1-\nu_{12}^{(3)}\nu_{21}^{(3)}\right)}$$

$$(12.112)$$

## 12.4 Thin Plates Reinforced by Parallel Ribs

Thin reinforced
plate



unit cell

$x_3$

$\delta t_2$

$\delta H$

$x_2$

$\delta h_1$

$\delta$

$\delta h_2$

$x_1$
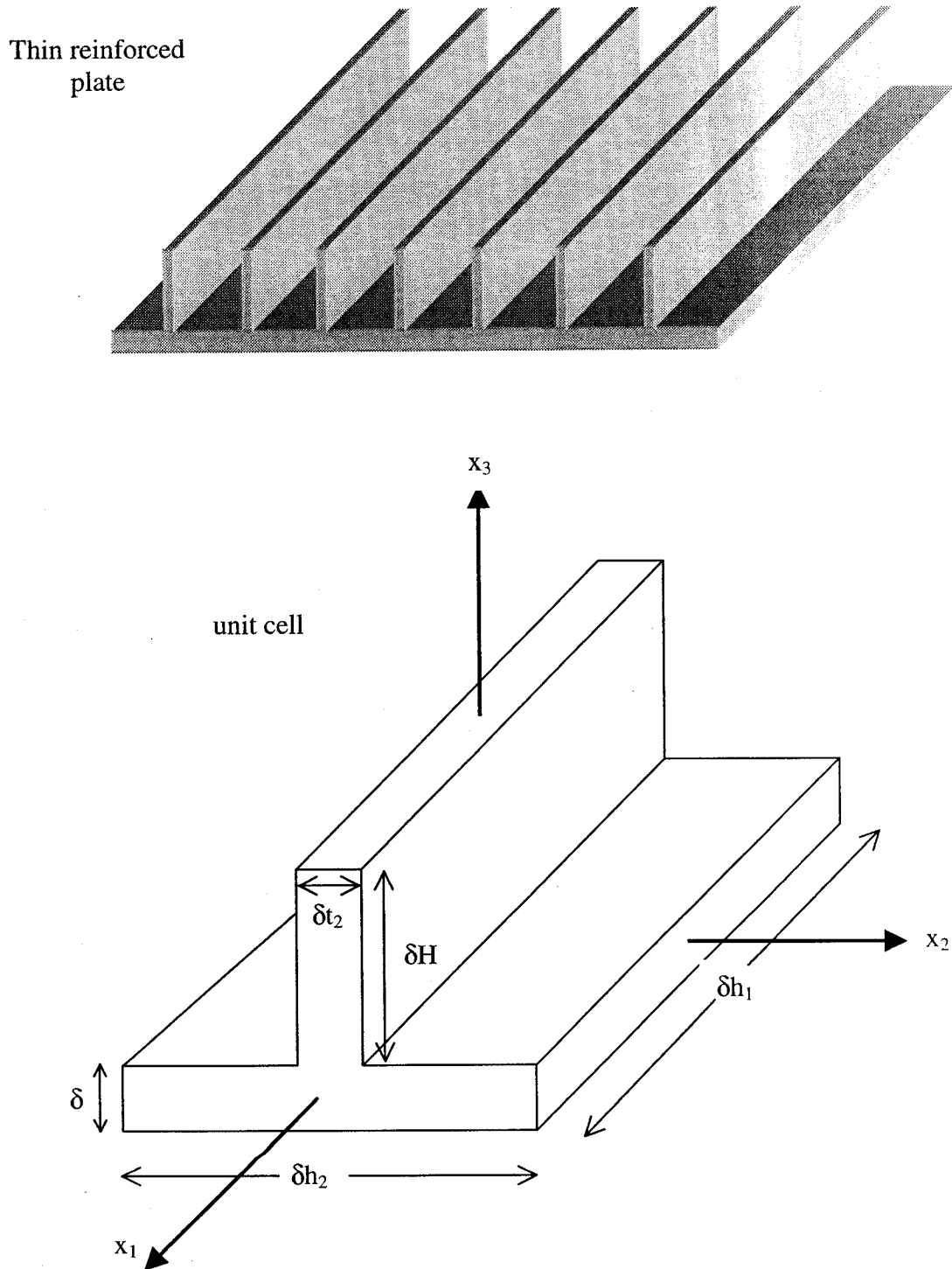
**Figure 12-16:** A thin plate reinforced with ribs and its unit cell
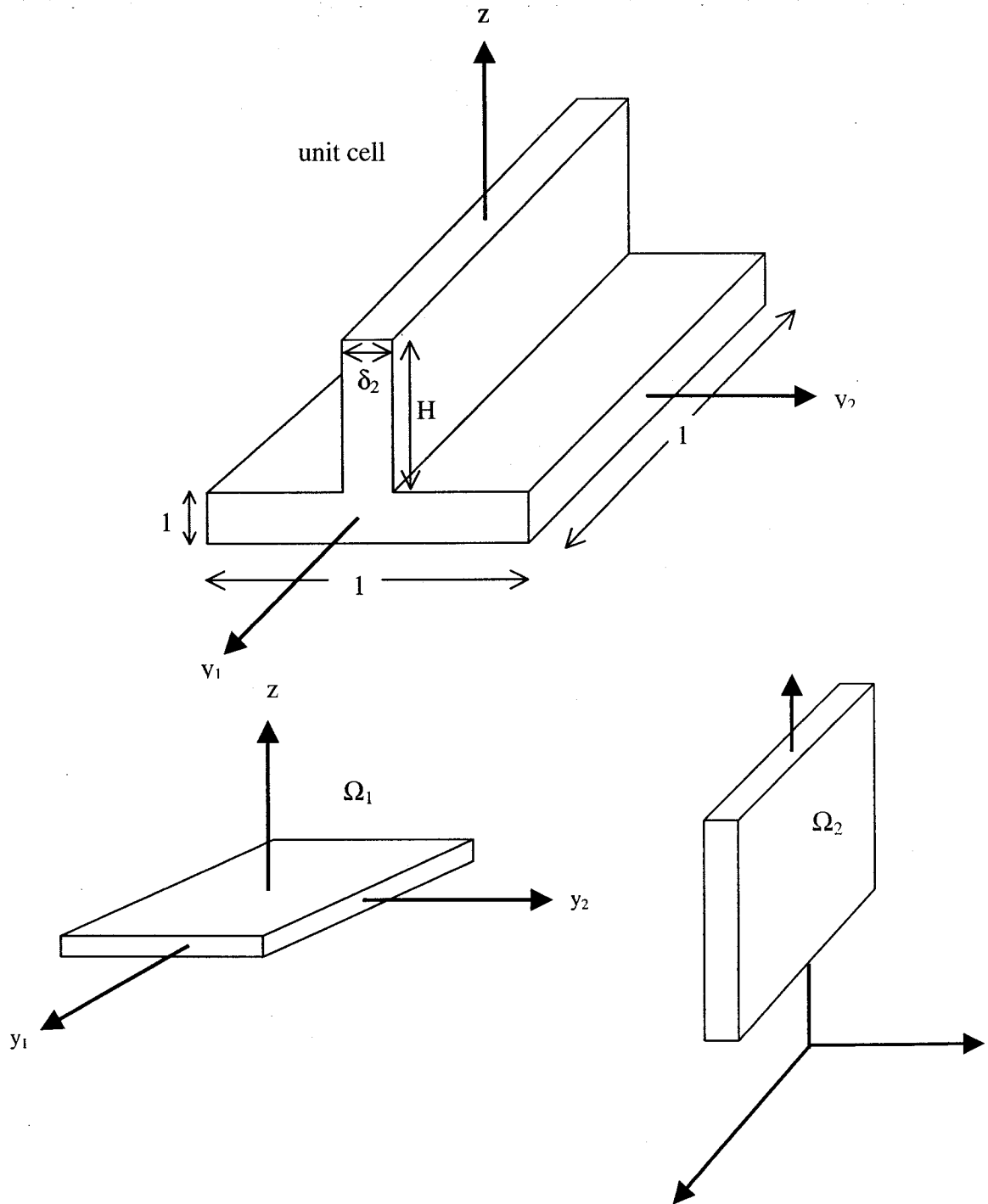
**Figure 12-17:** Unit cell of a reinforced plate (with respect to fast coordinates) and the individual elements

The results obtained for the wafer-reinforced plate in Section 12.3 can be extrapolated for the case of a piezoelectric plate reinforced by parallel ribs as shown in Figures 12-16 and 12-17. The average coefficients are simply stated below:

**(1) Elastic:**

$$\left\langle b_{11}^{11}\right\rangle = \frac{E_1^{(1)}}{1-v_{12}^{(1)}v_{21}^{(1)}}+E_1^{(2)}F_2^{(w)}, \quad \left\langle b_{22}^{22}\right\rangle = \frac{E_2^{(1)}}{1-v_{12}^{(1)}v_{21}^{(1)}}, \quad \left\langle b_{22}^{11}\right\rangle = \frac{v_{21}^{(1)}E_1^{(1)}}{1-v_{12}^{(1)}v_{21}^{(1)}}$$

$$\left\langle b_{12}^{12}\right\rangle = G_{12}^{(1)}, \quad \left\langle zb_{11}^{11}\right\rangle = \left\langle b_{11}^{*11}\right\rangle = E_1^{(2)}S_2^{(w)}, \quad \left\langle zb_{22}^{22}\right\rangle = \left\langle b_{22}^{*22}\right\rangle = 0$$

$$\left\langle zb_{11}^{*11}\right\rangle = \frac{E_1^{(1)}}{12\left(1-v_{12}^{(1)}v_{21}^{(1)}\right)}+E_1^{(2)}J_2^{(w)}, \quad \left\langle zb_{22}^{*22}\right\rangle = \frac{E_2^{(1)}}{12\left(1-v_{12}^{(1)}v_{21}^{(1)}\right)} \tag{12.113}$$

$$\left\langle zb_{22}^{*11}\right\rangle = \frac{v_{21}^{(1)}E_1^{(1)}}{12\left(1-v_{12}^{(1)}v_{21}^{(1)}\right)}, \quad \left\langle zb_{12}^{*12}\right\rangle = \frac{G_{12}^{(1)}}{12}+\frac{G_{12}^{(2)}}{12}\left(\frac{H^3t_2}{h_2}-K\right)$$

$$\text{where} \quad K = \frac{96H^4}{\pi^5 h_2}\sqrt{\frac{G_{12}^{(2)}}{G_{13}^{(2)}}}\sum_{n=1}^{\infty}\frac{\left[1-(-1)^n\right]}{n^5}\tanh\left(\sqrt{\frac{G_{13}^{(2)}}{G_{12}^{(2)}}}\frac{n\pi t_2}{2H}\right)$$

**(2) Piezoelectric:**

$$\delta\left\langle d_{11}^{3}\right\rangle = E_1^{(2)}d_{31}^{(r)(2)}F_2^{(w)} + \frac{E_1^{(1)}d_{31}^{(r)(1)}+E_1^{(1)}v_{21}^{(1)}d_{32}^{(r)(1)}}{1-v_{12}^{(1)}v_{21}^{(1)}}$$

$$\delta\left\langle d_{22}^{3}\right\rangle = \frac{E_2^{(1)}d_{32}^{(r)(1)}+E_2^{(1)}v_{12}^{(1)}d_{31}^{(r)(1)}}{1-v_{12}^{(1)}v_{21}^{(1)}}$$

$$\delta\left\langle zd_{11}^{3}\right\rangle = \delta\left\langle d_{11}^{*3}\right\rangle = E_1^{(2)}d_{31}^{(r)(2)}S_2^{(w)}$$

$$\delta\left\langle zd_{22}^{3}\right\rangle = \delta\left\langle d_{22}^{*3}\right\rangle = 0 \tag{12.114}$$

$$\delta\left\langle zd_{11}^{*3}\right\rangle = E_1^{(2)}d_{31}^{(r)(2)}J_2^{(w)} + \frac{E_1^{(1)}d_{31}^{(r)(1)}+E_1^{(1)}v_{21}^{(1)}d_{32}^{(r)(1)}}{12\left(1-v_{12}^{(1)}v_{21}^{(1)}\right)}$$

$$\delta\left\langle zd_{22}^{*3}\right\rangle = \frac{E_2^{(1)}d_{32}^{(r)(1)}+E_2^{(1)}v_{12}^{(1)}d_{31}^{(r)(1)}}{12\left(1-v_{12}^{(1)}v_{21}^{(1)}\right)}$$

**(3) Hygroscopic:**

$$\delta\langle\Lambda_{11}\rangle = E_1^{(2)}\beta_1^{(c)(2)}F_2^{(w)} + \frac{E_1^{(1)}\beta_1^{(c)(1)} + E_1^{(1)}v_{21}^{(1)}\beta_2^{(c)(1)}}{1-v_{12}^{(1)}v_{21}^{(1)}}$$

$$\delta\langle\Lambda_{22}\rangle = \frac{E_2^{(1)}\beta_2^{(c)(1)} + E_2^{(1)}v_{12}^{(1)}\beta_1^{(c)(1)}}{1-v_{12}^{(1)}v_{21}^{(1)}}$$

$$\delta\langle z\Lambda_{11}\rangle = \delta\langle\Lambda_{11}^*\rangle = E_1^{(2)}\beta_1^{(c)(2)}S_2^{(w)}$$

$$\delta\langle z\Lambda_{22}\rangle = \delta\langle\Lambda_{22}^*\rangle = 0$$

$$\delta\langle z\Lambda_{11}^*\rangle = E_1^{(2)}\beta_1^{(c)(2)}J_2^{(w)} + \frac{E_1^{(1)}\beta_1^{(c)(1)} + E_1^{(1)}v_{21}^{(1)}\beta_2^{(c)(1)}}{12\left(1-v_{12}^{(1)}v_{21}^{(1)}\right)}$$

$$\delta\langle z\Lambda_{22}^*\rangle = \frac{E_2^{(1)}\beta_2^{(c)(1)} + E_2^{(1)}v_{12}^{(1)}\beta_1^{(c)(1)}}{12\left(1-v_{12}^{(1)}v_{21}^{(1)}\right)}$$

(12.115)

**(4) Thermal:**

$$\delta\langle\Theta_{11}\rangle = E_1^{(2)}\alpha_1^{(\theta)(2)}F_2^{(w)} + \frac{E_1^{(1)}\alpha_1^{(\theta)(1)} + E_1^{(1)}v_{21}^{(1)}\alpha_2^{(\theta)(1)}}{1-v_{12}^{(1)}v_{21}^{(1)}}$$

$$\delta\langle\Theta_{22}\rangle = \frac{E_2^{(1)}\alpha_2^{(\theta)(1)} + E_2^{(1)}v_{12}^{(1)}\alpha_1^{(\theta)(1)}}{1-v_{12}^{(1)}v_{21}^{(1)}}$$

$$\delta\langle z\Theta_{11}\rangle = \delta\langle\Theta_{11}^*\rangle = E_1^{(2)}\alpha_1^{(\theta)(2)}S_2^{(w)}$$

$$\delta\langle z\Theta_{22}\rangle = \delta\langle\Theta_{22}^*\rangle = 0$$

$$\delta\langle z\Theta_{11}^*\rangle = E_1^{(2)}\alpha_1^{(\theta)(2)}J_2^{(w)} + \frac{E_1^{(1)}\alpha_1^{(\theta)(1)} + E_1^{(1)}v_{21}^{(1)}\alpha_2^{(\theta)(1)}}{12\left(1-v_{12}^{(1)}v_{21}^{(1)}\right)}$$

$$\delta\langle z\Theta_{22}^*\rangle = \frac{E_2^{(1)}\alpha_2^{(\theta)(1)} + E_2^{(1)}v_{12}^{(1)}\alpha_1^{(\theta)(1)}}{12\left(1-v_{12}^{(1)}v_{21}^{(1)}\right)}$$

(12.116)

## 12.5 Summary

The method of asymptotic homogenization was used to analyze a general periodic smart composite plate of rapidly varying thickness and a large number of embedded actuators. From a set of eight three-dimensional local unit cell problems the effective elastic, actuation, thermal expansion and hygroscopic expansion coefficients pertinent to the homogenized anisotropic smart plate were derived. These effective coefficients are very general in nature and may be utilized in studying different types of problems associated with a variety of smart structures.

To illustrate the use of the unit cells and the applicability of the effective coefficients, two broad classes of examples were considered. The first pertained to various laminates composed of monoclinic or orthotropic materials. In particular, an 8-layer [+45/-45]₄ angle-ply graphite/epoxy laminate was subjected to mechanical loads, electric fields, changes in temperature and changes in moisture concentration. In each case, the resulting strain and stress distribution was calculated and plotted. If some of the effective coefficients are neglected, the results obtained are consistent with the classical plate theory to which the model converges.

The other example dealt with wafer- or rib-reinforced piezoelectric plates. These are plates reinforced with ribs or stiffeners oriented in one or both of the tangential directions of the base plate. The most general case was examined whereby the ribs had different properties than the base plate and also exhibited piezoelectric characteristics. The unit cell problems were solved for this unique structure by considering each of the regions of the unit cell separately. In the solution, complications at the joints were ignored because they are highly localized and contribute very little to the integrals over the unit cell. The solution of the unit cell problems led to the determination of the effective elastic, piezoelectric, thermal expansion and hygroscopic expansion coefficients.

# 13.0 SYNOPSIS & CONCLUSIONS PERTAINING TO THESIS

This thesis dealt with experimental and analytical issues regarding smart composite materials. Smart materials in general may be divided into two broad classes, passive and active smart materials. Passive smart materials contain a built-in sensing device such as a fiber optic sensor, to continuously assess the current condition and serviceability of a structure. Active or adaptive smart materials have, in addition to sensors, integrated actuators such as piezoelectrics or magnetostrictives, and can perform self-adjustment or self-repair as conditions change.

The experimental aspects of this thesis were focused on the fabrication, processing, testing and assessment of pultruded smart GFRP and CFRP tendons with embedded Fabry Perot and Bragg Grating sensors. The long-term objective is to be able to use smart composite tendons of this nature in civil-engineering structures wherein they would replace steel as the primary concrete reinforcement, and at the same time act as strain gauges so as to permit continuous health-monitoring of these structures. This work was conducted for the purposes of ISIS Canada Project T3.4, on smart reinforcements and connectors. ISIS Canada is a National Network of Centers of Excellence that combines the collaborative efforts of researchers from fifteen universities across Canada. Its mandate is to develop advanced technologies for civil engineering infrastructure that incorporate integrated fiber-optic systems with advanced composite materials.

The analytical aspects of this work pertained to the mathematical modeling of active smart materials with a periodic array of embedded actuators. It is evident that the use of smart composite materials will be greatly facilitated if the effective properties and coefficients such as elastic, piezoelectric, etc. can be predicted at the design stage. One of the most useful means by which this goal can be achieved is the development of mathematical models that must on one hand be as realistic and consistent as possible,

while on the other hand not too complicated to implement. In this thesis, different mathematical models describing the behavior of smart composite materials have been developed and illustrated.

For the experimental work, GFRP and CFRP tendons were produced by the method of pultrusion. Fiber optic sensors were embedded in the smart tendons during pultrusion. However, the pultrusion process has the inherent potential to generate residual stresses within a composite component that may have a detrimental effect on its structural and mechanical integrity. It is therefore useful to investigate the ability of the embedded sensors to monitor the strains during the composite processing. For this purpose, Bragg Grating and Fabry Perot sensors were embedded successfully into carbon and glass tendons and the strain output was recorded as the sensors passed through the die and the pulling wheels. The information provided by these experiments yields valuable insight as to the specifics of the pultrusion process.

It was discovered also that Bragg Grating sensors exhibited good survivability in the pultrusion process and therefore could be embedded without any modification. Fabry Perot sensors however, did not survive during the pultrusion process, so that they had to be prereinforced. The prereinforcement procedure entailed encapsulating the Fabry Perot sensor inside a bundle of reinforcing glass or carbon fibers and then curing this bundle with a suitable epoxy. In effect, this creates a composite microtube with the optical sensor inside. In turn, this microtube was embedded in the glass or carbon tendon during pultrusion.

Pertinent microscopic analysis indicated that polyimide-coated optical fibers formed a good interface between the optical fiber and the host material. On the other hand, acrylate-coated optical fibers did not survive pultrusion and led to significant debonding between the fiber and the composite matrix. For this reason, acrylate coatings were excluded from further research. Standard tensile and shear tests performed on the

pultruded tendons indicated that a single embedded optical fiber did not affect the tensile properties, but had a slight deteriorating effect on the shear properties. This effect was more evident for the case of the glass tendons, and became more pronounced as the number of embedded optical fibers increased.

GFRP and CFRP tendons with embedded Bragg Grating and Fabry Perot sensors were subsequently subjected to trapezoidal and sinusoidal tests at room temperature. During the trapezoidal tests, the applied load was increased from a low preload level to a maximum value at a constant rate, held there for a few seconds and then ramped back down at the same rate as for the ramp-up. Sinusoidal tests involved subjecting the tendons to 5 or 6 load cycles at a frequency of 1 cycle per minute. In each case, the strain output from the embedded sensors was compared to that from externally affixed extensometers. It was observed that at ordinary laboratory conditions, the readings from Bragg Grating and Fabry Perot sensors embedded in both GFRP and CFRP tendons conformed very well to the corresponding extensometer values.

Since the long-term objective of this part of the research is to embed these smart tendons in concrete structures, it became necessary to assess the performance of the embedded sensors in low and high temperature environments. For this reason, the same trapezoidal and sinusoidal tests described above were also conducted in an environmental chamber wherein the temperature was controlled between $-40^{\circ}C$ and $+60^{\circ}C$ temperature extremes.

Fabry Perot sensors embedded in GFRP and CFRP tendons were first tested under these conditions. It was found that the sensors behaved very accurately and reliably in both cold and hot conditions, providing strain readings that agreed very well with corresponding extensometer readings.

Subsequently, Bragg Grating sensors embedded in GFRP tendons were tested. It was observed that high temperatures did not affect the performance of the Bragg Grating

sensors, which gave accurate readings closely matching extensometer readings even at temperatures as high as +80°C. At low temperatures however, the Bragg Grating sensors provided accurate readings only at the peak loads. At low load levels, the sensors failed to record the correct values, and this discrepancy seemed to worsen as the temperature was lowered even further.

Bragg Grating sensors embedded in CFRP tendons were also tested under conditions of high and low temperature extremes. At high load levels the extensometer readings were accurate and reliable, agreeing well with extensometer readings. At low load levels, however, the sensor did not record the correct strains. The situation was worse at low than at high temperatures. These results were believed not to be an indication of the performance of the sensor itself, but rather the demodulating unit. This conclusion was further reinforced by the fact that every time the Bragg Grating sensors were disconnected from the demodulator they did not retain their "zero" or reference value, and had to be constantly recalibrated. However, Bragg Grating sensors (as well as their Fabry Perot counterparts) are "absolute" sensors and should not require recalibration. Other researchers have been faced with similar problems, and after many complaints the manufacturer was forced to recall the demodulator units in order to make the necessary adjustments.

The behavior of the embedded sensors under the influence of fatigue loads was also investigated. The tendons were subjected to tension-tension fatigue whereby the load was cycled between 7 kN and 11 kN (stress ratio of about 0.64) at a frequency of 1 Hz. It was discovered that Fabry Perot sensors embedded in GFRP tendons performed very well through 100,000 load cycles and their strain output was the same as at the beginning of the test. The same results were observed for the CFRP tendons with embedded Fabry Perot sensors. The sensor behaved just as accurately and reliably after 140,000 cycles of applied load as it did at the early stages of testing. For Bragg Grating sensors, testing was conducted for more than 300,000 cycles. For these tests, it was concluded once again that

Bragg Grating sensors embedded in GFRP and CFRP tendons were not affected by fatigue loads.

Subsequently to the fatigue tests, CFRP and GFRP tendons with embedded Fabry Perot sensors were subjected to sustained loads for many hours in order to assess their creep behavior. The GFRP tendon was subjected to a 9-kN load for 150 hours, while the CFRP tendon was subjected to a 13-kN load for a duration of 300 hours. In all cases, it was observed that the sensor gave a nearly constant strain output that agreed well with the extensometer output. These results indicated that no creep deformation had occurred in either the sensor or the composite tendon.

Longer-term testing was finally conducted on GFRP and CFRP tendons with embedded Fabry Perot sensors. This testing included the combined effects of a sustained load and the action of a continuously circulating highly alkaline solution. This environment simulates conditions encountered in concrete structures wherein the rods may be used as prestressing tendons and rebars. The tendons were located inside an environmental chamber through which an alkaline solution (pH. of 12.8) was circulated by a pump. The solution was composed of 0.32 mol/L KOH, 0.17 mol/L NaOH, and 0.07 mol/L $Ca(OH)_2$ in distilled water. At the same time, the tendons were also subjected to a constant load of 12 kN, and testing was conducted for a period of more than two months. The strain output from the embedded Fabry Perot sensors was nearly constant for the duration of the tests and conformed well to that from externally bonded foil gauges. Thus, the combination of aggressive solution/sustained load did not have an effect on the behavior of the embedded Fabry Perot sensors.

The results of these tests indicate that the smart tendons have potential for significant benefit in the long-term monitoring of strain levels in civil engineering structures such as bridges, dams and overpasses. At the same time, the composites represent a viable

solution to the problem of replacing corroding steel as the primary concrete-reinforcement.

The analytical aspects of the work presented in this thesis dealt with active or adaptive smart materials which are expected to play an ever-increasing role in a great many engineering applications. In particular, mathematical models describing the behavior of broad classes of such structures were developed and applied.

The first mathematical model developed pertained to a general three-dimensional smart composite structure with a periodic arrangement of reinforcements and embedded actuators. It is known that the differential equations that govern the behavior of such structures are characterized by rapidly oscillating coefficients that render their solution extremely difficult even with the help of high-powered computers. Consequently, one looks at alternative methods of analysis. A mathematical technique that provides a suitable framework for the study of periodic smart structures is the method of asymptotic homogenization. Asymptotic homogenization permits the transformation of the original boundary value problem into a similar problem with so-called effective coefficients that make the problem much more amenable to both analytic and numerical treatment.

Thus, the asymptotic homogenization model pertinent to a smart structure was derived, and subsequently general expressions called unit cell problems were obtained. It is precisely these unit-cell problems that were used to determine the effective coefficients mentioned above. For the purposes of this first model, four different effective coefficients were determined. These were the elastic, actuation, thermal expansion and hygroscopic expansion coefficients. The actuation coefficients characterize the intrinsic transducer nature of active smart materials that can be used to induce strains and stresses in a controlled manner. The analysis presented was applied to piezoelectric materials, but the equations derived should be considered to hold equally well if the material in question exhibits for example magnetostrictive characteristics or is associated with some general

transduction characteristics that can be used to induce strains and stresses. The effective thermal expansion and hygroscopic expansion coefficients were introduced in order to make the mathematical model more comprehensive especially in light of the fact that temperature variations and moisture absorption are very important for composites because they lead to dimensional changes which in turn lead to residual stresses and a consequent degradation of their mechanical properties.

The use of the unit-cell problems was illustrated by means of two- and three-dimensional examples. In particular, a laminate composed of piezoelectric layers was subjected to in-plane forces and moments, and the resulting stress and strain fields were compared to those obtained with the homogenized model. The two models agree quite well. Next, the first few natural frequencies of a thick laminated piezoelectric transducer were determined and compared with corresponding values from the homogenized model. The results from the two models conformed very well with one another, differing by at most 1 %. Finally, the mechanical strains induced in laminated composites by temperature or moisture content changes were determined and again compared with the strains pertinent to the homogenized model. The two models gave results that conformed very well to one another.

The mathematical model just described was characterized by homogeneous boundary conditions. The second model that was developed was similar to the first one, but differed in the sense that part of its boundary had prescribed boundary stress conditions. Once again, the governing equations pertaining to a very general model that included elastic, actuation, thermal expansion and hygroscopic expansion effects were derived. These equations were shown to differ from those of the corresponding problem with homogeneous boundary conditions by what amounts to a so-called "boundary layer" solution. However, the effective coefficients obtained through this model were the same as the ones pertinent to the first model. Hence, it was concluded that these coefficients

are universal in nature, and once determined they can be used to study a wide variety of static and dynamic problems associated with composite smart structures.

The third and final mathematical model developed was used to analyze a periodic smart composite plate with rapidly varying thickness and a large number of periodically-arranged actuators. A set of eight three-dimensional local unit-cell problems was derived which, unlike the homogenization schemes pertinent to the first two models were shown to depend upon boundary conditions rather than periodicity in the transverse direction. In other words, this model was characterized by periodicity in only the two tangential directions.

The solution of the unit-cell problems yields a set of functions which when averaged over the volume of the periodicity cell determine the effective elastic, actuation, thermal expansion and hygroscopic expansion coefficients pertinent to the homogenized anisotropic smart plate. These effective coefficients then enter the governing equations of the system which in turn yield a set of displacement functions. These functions having been determined, enable one to make very accurate predictions concerning the three-dimensional local structure of the displacement and stress fields.

The general symmetry properties of the effective actuation, thermal expansion and hygroscopic expansion coefficients were obtained with the implication that it suffices to know the solution of the purely elastic problem in order to calculate the remaining effective coefficients. It was subsequently shown that in the limiting case of a thin homogeneous elastic plate of uniform thickness, the model converges to the familiar classical plate model.

To illustrate the use of the unit cells and the applicability of the effective coefficients, two broad classes of examples were considered. The first pertained to various laminates composed of monoclinic or orthotropic materials. In particular, an 8-layer $[+45/-45]_4$

angle-ply graphite/epoxy laminate was subjected to mechanical loads and the resulting strain and stress distribution was calculated and plotted. The results are consistent with the classical plate theory to which the model converges in this case. The same laminate was subsequently subjected to a temperature variation, and the normal and shear strain and stress distribution through the thickness of the laminate were determined. If some of the effective thermal expansion coefficients are neglected the strain and stress values obtained conform to those pertaining to the classical plate theory. Further examples examined the effect of a change in moisture content on this laminate. As with the case of temperature variations, it was observed that the moisture content of the laminate induces both bending and out-of-plane warping. Again, in the limiting case when some of the effective hygroscopic expansion coefficients are ignored, the stress and strain values agree quite well with the classical plate theory. Finally, the effect of an electric field on the strains and stresses in a $[0/90]_4$ piezoelectric PVDF laminate was examined. It was shown that the piezoelectric effect is similar to the hygrothermal effect.

The second example dealt with wafer-reinforced piezoelectric plates. These are plates reinforced with mutually perpendicular ribs or stiffeners. The most general case was examined whereby the ribs had different properties than the base plate and exhibited piezoelectric characteristics. The unit-cell problems were solved for this unique structure by considering each of the three regions of the unit cell separately. In the solution, complications at the joints were ignored because they are highly localized and contribute very little to the integrals over the unit cell. The solution of the unit cell problems led to the determination of the effective elastic, piezoelectric, thermal expansion and hygroscopic expansion coefficients. Finally, the results were extrapolated for a case of a plate reinforced with ribs in only one of the tangential directions.

# 14.0 REFERENCES

Abdel-Magid, B.M., Gates, T.S., (2002) Accelerated Testing of polymeric composites using the dynamic mechanical analyzer [online]
Available:
http://techreports.larc.nasa.gov/ltrs/PDF/2001/mtg/NASA-2001-16asc-bma.pdf [2002]

Aboudi, J., The response of shape memory alloy composites, Smart Materials and Structures, Vol. 6, 1997, pp. 1-9

Adachi, Y., Unjoh, S., Kondoh, M., Development of a shape memory alloy damper for intelligent bridge systems, Proceedings of the International Symposium on Shape Memory Materials, Kanazawa, Japan, 1999, pp. 31-34

Alavie, A.T., Maaskant, R., Ohn, M.M., Rizkalla, S., Measures, R.M., Application and characterization of intracore grating sensors in a CFRP prestressed concrete girder, SPIE, Vol. 2191, 1994, pp. 103-110

APC International Limited, (1999) Piezoelectric ceramics [online]
Available:
http://www.americanpiezo.com [2002]

ASTM D3039/D3039M: Standard test method for tensile properties of polymer matrix composite materials

ASTM D3479/D3479M: Standard test method for tension-tension fatigue of polymer matrix composite materials

Bakhvalov N., & Panasenko, G., Homogenisation: Averaging processes in periodic media, Kluwer Academic Publishers, Netherlands, 1984

Barnes, A., Pedrazzani, M.J., Murphy, K., Claus, R., Tran, T., Greene, J., Poland, S., Coate, J., Creep measurement of refractory material in high-temperature tensile loading tests, SPIE, Vol. 2444, 1995, pp. 432-437

Başar, Y., Weichert, D., Nonlinear continuum mechanics of solids, Springer, 1999

Bensoussan, A., Lions, J.L., Papanicolaou, G., Asymptotic analysis for periodic structures, North-Holland Publ. Comp., Amsterdam, 1978

Bi, J., Anjanappa, M.A., Active vibration damping using magnetostrictive miniactuators, SPIE, Vol. 2190, 1994, pp. 171-180

BIS1000PC and BIS SoftControls Operation Manual, Electrophotonics Corporation, Toronto, 1996

Bogdanovich, A.E., Deepak, B.P., Three-dimensional analysis of thick composite plates with multiple layers, Composites part B: Engineering, Vol. 28B(4), 1997, pp. 345-357

Brennan, M.J., Garcia-Bonito, J., Elliot, S.J., David, A., Pinnington, R.J., Experimental investigation of different actuator technologies for active vibration control, Smart Materials and Structures, Vol. 8, 1999, pp. 145-153

Busel, J.P., Lindsay, K., On the road with John Busel: A look at the world's bridges, Composites Design & Application, January/February 1997, pp. 14-23

Carman, G.P., Mitrovic, M., Health monitoring techniques for composite materials employing thermal parameters and fiber optic sensors, SPIE, Vol. 2191, 1994, pp. 244-256

Carman, G.P., Paul, C., Sendeckyj, G.P., Transverse strength of composites containing optical fibers, SPIE, Vol. 1917, 1993, pp. 307-316

Chawla, K.K., Ceramic matrix composites, Chapman & Hall, London, 1993

Cheng, Z.Q., Lim, C.W., Kitipornchai, S., Three-dimensional asymptotic approach to inhomogeneous and laminated plates, International Journal of Solids and Structures, Vol. 37, 2000, pp. 3153-3175

Chhoa, C.Y., Bao, X., Bremner, T.W., Brown, A.W., DeMerchant, M.D., Kalamkarov, A.L., Georgiades, A.V., Strain measurement in concrete structure using distributed fiber optic sensing based on Brillouin scattering with single mode fibers embedded in glass fiber reinforcing Vinyl ester rod and bonded to steel reinforcing bars, SPIE, Vol. 4337, 2001, pp. 466-476

Choi, S., Lee, J.J., The shape control of a composite beam with embedded shape memory alloy wire actuators, Smart Materials and Structures, Vol. 7, 1998, pp. 759-770

Chou, P.C., Carleone, J., Hsu, C.M., Elastic constants of layered media, Journal of Composite Materials, Vol. 6, 1972, pp. 80-93.

Cioranescu, D., Donato, P., An Introduction to homogenization, Oxford University Press, 1999

Crawley, E.F., de Luis, J., Use of piezoelectric actuators as elements of intelligent structures, AIAA J., Vol. 25, 1987, pp. 1373-1385.

Daniel, I.M., Ishai, O., Engineering mechanics of composite materials, Oxford University press, Inc., New York, 1994

Davidson, R., Bowen, D.H., Roberts, S.J., Composite materials monitoring through embedded fiber optics, 1997, SPIE, Vol. 1120, 1989

Davis, M.A., Kersey, A.D., Berkoff, T.A., Jones, R.T., Idriss, R.L., and Kodinduma, M., Dynamic strain monitoring of an in-use interstate bridge using fiber Bragg Grating sensors, SPIE, Vol. 3043, pp. 87-95

Duenas, T.A., Hsu, L., Carman, G.P., Magnetostrictive composite material systems: Analytical/Experimental, Symposium on Materials for Smart Systems II, Vol. 459, Ed. George, E.P., Gotthardt, R., Otsuka, K., Trolier-McKinstry, S., Wun-Fogle, M., 1997, pp. 527-543

Duncan, W.J., France, P.W., Craig, S.P., The effect of environment on the strength of optical fiber, Strength of organic glass, Ed. C.R. Kurkjan, Plenum Press, New York, 1995

Dutta, P.K., Bailey, D.M., Tsai, S.W., Jensen, D.W., Hayes, J.R., McDonald, W.E., Smart, C.W., Colwell, T., Earl, J.S., Chen, H.J., Composite grids for reinforcement of concrete structures, USACERL Technical Report 98/81, June 1988

Duvaut, G.,. Analyse fonctionnelle et méchanique des milieux continus, Proceeding of the 14th IUTAM Congress, Delft, 1976, pp. 119-132

Eaton, N.C., Drew, R.C., and Geiger, H., Finite element stress and strain analysis in composites with embedded optical fiber sensors, Smart Materials and Structures, Vol. 4, 1995, pp. 113-117

Engineered materials handbook, Volume 1: Composites, ASM International, Metals Park, Ohio, 1987

Erdogan, T., Mizrahi, V., Lemaire, P.J., and Monroe, D., Decay of ultraviolet-induced fiber Bragg Gratings, Journal of Applied Physics, Vol. 76(1), 1994, 73-80.
Evans

Fenn, R., Gerver, M.J., Passive damping and velocity sensing using magnetostrictive transduction, SPIE, Vol. 2190, 1994, pp. 216-227

FLS 3100 operation manual, Electrophotonics Corporation, Toronto, 1998

Franke, L., Meyer, H.J., Predicting the tensile strength and creep-rupture behavior of pultruded glass-reinforced polymer rods, Journal of Materials Science, Vol. 27, 1992, pp. 4899-4908

Furuya, Y., Shimada, H., Shape memory actuators for robotic applications, Engineering aspects of shape memory alloys, Edited by Duerig, T.W., Melton, K.N., Stöckel, D., Wayman, C.M., Butterworth-Heinemann, 1990

Georgiades, A.V., Fabrication, processing, testing and evaluation of pultruded smart composite tendons, MAsc. Thesis, Dalhousie University, Halifax, Nova Scotia, 1998

Gibson, R.F., Principles of composite material mechanics, McGraw-Hill, Inc., 1994
Guide to fiber optics system design, Belden Wire and Cable, 1996

Gu, X., Ansari, F., (2000) Distributed monitoring of structural cracks by interferometric fiber optic sensors [online]
Available:
www.ce.utexas.edu/em 2000/papers/XiangGu.pdf, 2002

Gunther, M.F., Zeakes, J.S., Leber, D.E., May, R.G., and Claus, R.O., Sputtered metallic coatings for optical fibers used in high temperature environments, SPIE, Vol. 2191, 1994, pp. 2-12

Habel, W.R., Hofmann, D., Strain measurements in reinforced concrete walls during the hydration reaction by means of embedded fiber interferometers, SPIE, Vol. 2361, 1994, pp. 180-183

Habel, W.R., Höpcke, M., Basedau, F., and Polster, H., The influence of concrete and alkaline solutions on different surfaces of optical fibers for sensors, SPIE, Vol. 2361, 1994, pp. 168-179

Hamidah, H.M., Gowripalan, N., Fadhil, N.M., Absorption of aramid prestressing rods in aggressive solutions, Journal of Composites for Construction, Vol. 5(4), 2001, pp. 254-257

Handbook for infrastructure applications of composite materials, SAMPE, 1998

Harvey, J.A., Polymeric-matrix composites for intermediate and high-temperature applications, Proceedings of the conference on processing, fabrication and application of advanced composites, Long Beach, California, 1993, pp. 199-202

Hecht, J., Understanding fiber optics, Sams Publishing, Indianapolis, 1993

Holmes, M.H., Introduction to Perturbation Methods, Springer-Verlag, New York, 1995.
Holzapfel, G.A., Nonlinear solid mechanics, John Wiley & Sons, 2000

Huang, W., Modified shape memory alloy (SMA) model for SMA wire based actuator design, Journal of intelligent material systems and structures, Vol. 10, 1999, pp. 221-231

ISIS Canada annual report, 1996

Jain, A.K., Sirkis, J.S., Continuum damage mechanics in piezoelectric ceramics, Adaptive Structures and Composite Materials: Analysis and Application, Eds. E. Garcia, H. Cudney, A. Dasgupta, 1994, pp. 47-58

Jensen, D.W., Pascual, J., Degradation of graphite/bismaleimide laminates with multiple embedded fiber-optic sensors, SPIE, Vol. 1370, 1990, pp. 228-237

Juvinall, R.C., and Marshek, K.M., Fundamentals of machine component design, John Wiley & Sons, 1991

Kalamkarov, A.L., Composite and reinforced elements of construction, Wiley, New York, 1992

Kalamkarov, A.L., Drosdov, A.D., Optimal design of intelligent composite structures, Journal of Intelligent Materials Systems and Structures, Vol. 8(9), 1997, pp. 757-766

Kalamkarov, A.L., Fitzgerald, S.B., MacDonald, D.O., The use of fiber optic sensors to monitor residual stresses during pultrusion of FRP composites, Composites B: Engineering, Vol. B30(2), 1998, pp. 167-175

Kalamkarov, A.L., Fitzgerald, S.B., MacDonald, D.O., and Georgiades, A.V., Smart pultruded composite reinforcements incorporating fiber optic sensors, SPIE, Vol. 3400, 1998, pp. 94-105

Kalamkarov, A.L., Georgiades A.V., Modeling of smart composites on account of actuation, thermal conductivity and hygroscopic absorption, Composites part B: Engineering, 2001a, in press

Kalamkarov, A.L., Georgiades, A.V., Micromechanical modeling of smart composite materials with a periodic structure, Proceedings of the SPIE's 9th Annual International Symposium on Smart Structures and Materials, 2001b, in press

Kalamkarov, A.L., Georgiades, A.V., MacDonald, D.O., Fitzgerald, S.B., Pultruded fiber reinforced polymer reinforcements with embedded fiber optic sensors, Canadian Journal of Civil Engineering, Vol. 27(5), 2000, pp. 972-984

Kalamkarov, A.L., Kolpakov A.G., Analysis, design and optimization of composite structures, Wiley, New York, 1997

Kalamkarov, A.L., Kolpakov, A.G., A new asymptotic model for a composite piezoelastic plate, International Journal of Solids and Structures, Vol. 38, 2001, pp. 6027-6044

Kalamkarov, A.L., MacDonald, D.O., Westhaver, P., On pultrusion of smart FRP composites, SPIE, Vol. 3042, 1997, pp. 400-409

Kannan, K. S., Dasgupta, A., Finite element modeling of multi-functional composites with embedded magnetostrictive devices, Adaptive Structures and Composite Materials: Analysis and Application, Editors Garcia, E., Cudney, H., Dasgupta, A., 1994, pp. 21-28

Kay, D.C., Theory and problems of tensor calculus, Schaum's Outlines, McGraw-Hill, 1988

Kim, K.S., Ryu, J.U., Lee, S.J., Choi, L., In-situ monitoring of Sungsan bridge in Han river with an optical fiber sensor system, SPIE, Vol. 3043, 1997, pp. 72-76

Kowsika, M., Raju, P.M., Optimal pultrusion process conditions for improving the dynamic properties of graphite-epoxy composite beams, Materials Evaluation, Vol. 54(3), 1996, pp. 386-392

Lackey, E., Characterization of the pultrusion process using the central composite design method of statistical experimentation, Master Thesis, University of Mississippi, 1992

Lagoudas, D.M., Tadjbakhsh, Active flexible rods with embedded SMA fibers, Smart Materials and Structures, Vol. 1, 1992, pp. 162-167

Lammering, R., Schmidt, I., Experimental investigations on the damping capacity of NiTi components, Smart Materials and Structures, Vol. 10, 2001, pp. 853-859

Lane, P., Starzomski, M., Van Dommelen, R., Fiber optic connectorization procedure for FC/APC type connectors, Dalhousie University, Halifax, Nova Scotia, 1996

Lee, D.C., Lee, J.J., Fatigue behavior of composite structures with embedded optical fiber sensors, Proceedings of ICCM-10, 1995, pp. 307-314

Leka, L.G., Bayo, E., A close look at the embedment of optical fibers into composite structures, Journal of Composites Technology & Research, Vol. 11(3), 1989, pp. 106-112

Little, R.E., Mitchell, W.J., Mallick, P.K., Tensile creep and creep rupture of continuous strand mat polypropylene composites, Journal of Composite Materials, Vol. 29(16), 1995, pp. 2215-2227

MacDonald, D.O., Development and characterization of pultruded composite profiles, MASc. Thesis, Technical University of Nova Scotia, Halifax, Nova Scotia, 1989

Madill, D.R., Wang, D., Modeling and L2-Stability of a shape memory alloy position control system, IEEE Transactions on Control Systems Technology, Vol. 6(4), 1998, pp. 473-481

Mallick, P.K., Fiber reinforced composites: Materials, manufacturing, and design, Marcel Dekker, Inc., 1988

Mallick, P.K., Newman, S., Editors, Composite Materials Technology: Processes and properties, Hanser Publishers, Munich, 1990

Mantena, P.R., Vaughan, J.G., Donti, R.P., Kowsika, M.V., Influence of Process Variables on the Dynamic Characteristics of Pultruded Graphite-Epoxy Composites, Vibro-Acoustic Characterization of Materials and Structures, ASME, 14, NCA-14, 1992, pp. 147-154

Matthews, F.L., Rawlings, R.D., Composite materials: Engineering and science, Chapman & Hall, London, 1994

Maugin, G.A., Attou, D., An asymptotic theory of thin piezoelectric plates, Quarterly Journal of Mechanics and Applied Mathematics, Vol. 43, 1990, pp. 347-362

Micelli, F., Nanni, A., La Tegola, A., Effects of conditioning environments on GFRP bars, 22$^{nd}$ SAMPE Europe International Conference, CNIT Paris, March 27-29, 2001

Mufti, A.A., Bakht, B., Tadros, G., Newhook, J.P., Butt, S., Structural health monitoring of innovative bridge decks, SPIE, Vol. 4337, 2001, pp. 212-222

Nayfeh, A., Perturbation methods, John Wiley & Sons, New York, 1973

Nellen, P.M., Anderegg, P., Bronnimann, R., Sennhauser, U., Application of fiber optical and resistance strain gauges for long-term surveillance of civil engineering structures, SPIE, Vol. 3043, 1997, pp. 77-86

Newhook, J.P., Bakht, B., Mufti, A., Tadros, G., Monitoring of Hall's Harbour wharf, SPIE, Vol. 4337, 2001, pp. 234-244

Perkins, J., Hodgson, D., The two-way shape memory effect, Engineering aspects of shape memory alloys, Edited by Duerig, T.W., Melton, K.N., Stöckel, D., Wayman, C.M., Butterworth-Heinemann, 1990

Rajapakse, R.K.N.D., Plane strain/stress solutions for piezoelectric solids, Composites part B: Engineering, Vol. 28B(4), 1997, pp. 385-396

Ramkumar, R.l., Tossavainen, E.W., Strength and lifetime of bolted laminates, Fatigue in mechanically fastened composite and metallic joints, ASTM STP 927, John M Potter. Ed., American Society for Testing and Materials, Philadelphia, 1986, pp. 251-273

Reddy, J.N., Mechanics of laminated composite plates, CRC Press, New York, 1997

Reddy, J.N., On laminated composite plates with integrated sensors and actuators, Engineering Structures, Vol. 21, 1999, 568-593

Rhee, S.W., Koval, L.R., Comparison of classical with robust control for SMA smart structures, Smart Materials and Structures, Vol. 2, 1993, pp. 162-171

RocTest Ltd., Technical Information, Equipment, and Manuals, St-Lambert, Quebec, Canada, 1997

Rose, L.R.F., Wang, C.H., Modeling and optimization of passive damping for bonded repair to acoustic fatigue cracking, Proceedings of IUTAM-Symposium on Smart Structures and Structronic Systems, Magdeburg, September 26, 2000, pp. 49-57

Runtsch, E., Shape memory actuators in circuit breakers, Engineering aspects of shape memory alloys, Edited by Duerig, T.W., Melton, K.N., Stöckel, D., Wayman, C.M., Butterworth-Heinemann, 1990

Saadat, S., Davoodi, H., Hou, Z., Suzuki, Y., Masouda, A., Using NiTi SMA tendons for vibration control of coastal structures, Smart Materials and Structures, Vol. 10, 2001, pp. 695-704

Sanchez-Palencia, E., Non-Homogeneous media and vibration theory, Springer-Verlag, Berlin, 1980

Schwartz, M.M., Composite materials, Volume I: Properties, nondestructive testing, and repair, Prentice Hall, 1997

Sester, M., Poizat, Ch., On the analytical and numerical modeling of piezoelectric fiber composites, Proceedings of IUTAM-Symposium on Smart Structures and Structronic Systems, Magdeburg, September 26, 2000, pp. 103-112

Shakeri, C., Noori, M.N., Hou, Z., (2001) Smart materials and structures: A review [online]
Available:
http://me.wpi.edu/~cirrus/publications/smartmaterials/smartmaterialextension.html
[2002]

Shigley, J.E., <u>Mechanical engineering design</u>, McGraw Hill, 1986

Sirkis, J., Singh, H., Moirè-Analysis of thick composites with embedded optical fibers, Experimental Mechanics, 1994, pp. 300-305

Slowik, V., Schlattner, E., Klink, T., (1998) Fiber Bragg Grating sensors in concrete technology [online]
Available:
www.uni-leipzig.de/~massivb/institut/lacer/lacer03/103_13.pdf [2002]

Song, G., Kelly, B., Agrawal, B.N., Active position control of a shape memory alloy wire actuated composite beam, Smart Materials and Structures, Vol. 9, 2000, pp. 711-716

Srinivasan, A.V., McFarland, M.D., <u>Smart structures: Analysis and design</u>, Cambridge University Press, 2001

Stalmans R., Michaud, V., Bidaux, J-E., Gotthardt, R., Månson, J-A.E., Adaptive Composites with embedded shape memory alloy wires, Proceedings of the 4th European Conference on Smart Structures and Materials, 1998, pp. 801-804

Stöckel, D., Shape memory actuators for automotive applications, <u>Engineering aspects of shape memory alloys</u>, Edited by Duerig, T.W., Melton, K.N., Stöckel, D., Wayman, C.M., Butterworth-Heinemann, 1990

Strait, L. H., Karasek, M. L., Amateau, M. F., Effects of Seawater Immersion on the Impact Resistance of Glass Fiber Reinforced Epoxy Composites, Journal of Composite Materials, Vol. 26(14), 1992, pp. 2118-2133

Sumerak, J.E., Understanding pultrusion process variables, Modern Plastics, March 1985, pp. 58-64

Swanson, S.R., <u>Introduction to design and analysis with advanced composite materials</u>, Prentice Hall, New Jersey, 1997

Tannous, F.E., Saadatmanesh, H., Durability of AR glass fiber reinforced plastic bars, Journal of Composites for Construction, Vol. 3(1), February 1999, pp. 12-19.

Tauchert, T.R., Ashida, F., Noda, N., Adali, S., Verijenko, V., Development in thermopiezoelasticity with relevance to smart composite structures, Composite Structures, Vol. 48, 1999, pp. 31-38

Tawfik, M., Duan, B., Ro, j., Mei, C., Suppression of post-buckling deflection and panel-flutter using shape memory alloy, SPIE, Vol. 3991, 2000, pp. 346-357

Tay, A., Wilson, D.A., Strain analysis of optical fibers embedded in composite materials using finite element modeling, SPIE, Vol. 1170, 1989, pp. 521-533

Tennyson, R., Installation, use and repair of fiber optic sensors, ISIS Canada, design manual no. 1, 2001

Tennyson, R.C., Mufti, A.A., Neale, K., Fiber optic sensing for civil infrastructure, SPIE, Vol. 4337, 2001, pp. 203-211

Theobald, D., Blount, K., Vaughan, J.G., Lackey, E., Effect of Processing Parameters on the Iosipescu Shear Strength of Various Pultruded Glass/Epoxy and Graphite/Epoxy Composites, International Composites Expo '98 - Proceedings of the Composite Institute, January 19-21, 1998, pp. 1-8

Todoroki, T., Shape memory sensor and actuator for air conditioners, Engineering aspects of shape memory alloys, Edited by Duerig, T.W., Melton, K.N., Stöckel, D., Wayman, C.M., Butterworth-Heinemann, 1990

Tsai, P., Ventura, C., Waterloo Creek Bridge project instrumentation progress report No. 1, University of British Columbia, 1998

Tzou, H.S., Piezoelectric shells: Distributed Sensing and control of continua Kluwer, Dordrecht, 1993

Tzou, H.S., Bao, Y., A theory on anisotropic piezothermoelastic shell laminates with sensor/actuator applications, Journal of Sound and Vibrations, 184, 1995, pp. 453-473

Udd, E., Editor, Fiber optic sensors: An introduction for engineers and scientists, John Wiley & Sons, Inc., New York, 1991

Udd, E., Editor, Fiber optic smart structures, John Wiley and Sons, Inc., New York, 1995

Udd, E., Kunzler, M., Laylor, M., Schulz, W., Kreger, S., Corones, J., McMahon, R., Soltesz, S., and Edgar, R., Fiber grating systems for traffic monitoring, SPIE, Vol. 4337, 2001, pp. 510-516

Vaughan, J.G., Hacket, R.M., Pultrusion process characterization, NASA contract NAS8-37193, 1991

Vaughan, J.G., Robert M.H, Ellis C.S, Optimization of the Pultrusion Process for Graphite/Epoxy, Fiber-Tex 1988, NASA CP-3038, September 13-15, 1989, pp. 285-299

Vel, S.S., Batra, R.C., Cylindrical bending of laminated plates with distributed and segmented piezoelectric actuators/sensors, American Institute of Aeronautics and Astronautics Journal, Vol. 38(5), 2000a, pp. 857-867

Vel, S.S., Batra, R.C., Three-Dimensional analytical solution for hybrid multilayered piezoelectric plates, Transactions of the ASME, Vol. 67, 2000b, pp. 558-567

Vel, S.S., Batra, R.C., Analysis of piezoelectric bimorphs and plates with segmented actuators, Thin-walled Structures, Vol. 39(1), 2001a, pp. 23-44

Vel, S.S., Batra, R.C., Exact solution for rectangular sandwich plates with embedded piezoelectric shear actuators, American Institute of Aeronautics and Astronautics Journal, Vol. 39(7), 2001b, pp. 1363-1373

Ventura, C.E., Onur, T., Tsai, P.C., Dynamic characteristics of the Crowchild Trail bridge, Canadian Journal of Civil Engineering, Vol. 27(5), 2000, pp. 1046-1056

Vinson, J.R., The behavior of shells composed of isotropic and composite materials, Kluwer Academic Publishers, Dordrecht, Netherlands, 1993

Vokoun, D., Kafka, V., Mesomechanical modeling of shape memory effect, SPIE, Vol. 3667, 1999, pp. 596-601

Vurpillot, S., Inaudi, D., Ducret, J., Bridge monitoring by fiber optic deformation sensors: Design, emplacement and results, SPIE, Vol. 2719, 1996, pp. 141-150

Wang, A., Zhang, P., May, R.G., and Murphy, K.A., Sapphire fiber-based polarimetric optical sensor for high temperature applications, SPIE, Vol. 2191, 1994, pp. 13-22

Wang, Q., Quek, S.T., Flexural analysis of piezoelectric coupled structures, Proceedings of IUTAM-Symposium on Smart Structures and Structronic Systems, Magdeburg, September 26, 2000, pp. 161-168

Wayman, C.M., Duerig, T.W., An introduction to martensite and shape memory, Engineering aspects of shape memory alloys, Edited by Duerig, T.W., Melton, K.N., Stöckel, D., Wayman, C.M., Butterworth-Heinemann, 1990

Weeton, J.W., Peters, D.M., Thomas, K.L., Editors, Engineers' guide to composite materials, ASM International, Metals Park, Ohio, 1987

Wright, R.E., Molded Thermosets: A handbook for plastics engineers, molders, and designers, Hanser Publishers, Munich, 1991

Yang, X.M., Shen, Y.P., Tian, X.G., Dynamic instability of laminated piezoelectric shells, Proceedings of IUTAM-Symposium on Smart Structures and Structronic Systems, Magdeburg, September 26, 2000, pp. 153-160

# A    EQUILIBRIUM EQUATIONS

The basic differential equations used for the mathematical models in this thesis are the equilibrium equations. Because of their importance, a tensorial derivation of these equations will be given. It is based on Başar and Weichert [1999] and Holzapfel [2000].
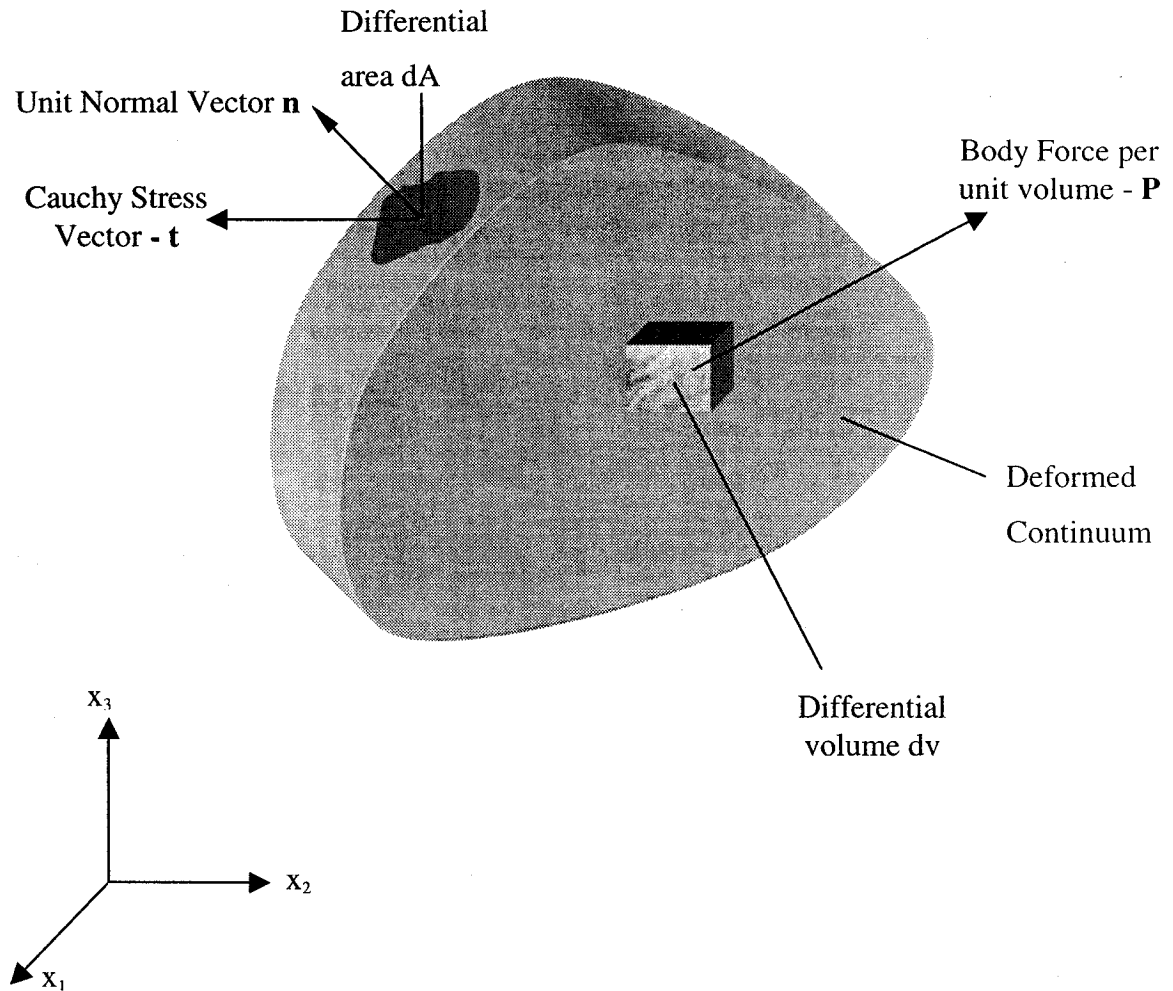


**Figure A-1:** Continuum subjected to surface tractions and body forces

Consider a body subjected to surface tractions and body forces as shown in Figure A-1. The linear momentum per unit mass of a differential element dv is given by $\dot{r}$ where $\dot{r}$ is

the position vector to that differential element measured with respect to an inertial reference frame. Hence the total momentum for the continuum is given by:

$$\mathbf{I} = \int_G \rho \dot{\mathbf{r}} \, dv \qquad\qquad (A.1)$$

Let **t** denote the traction per unit surface area of the body. This vector is commonly referred to as Cauchy stress vector [Başar and Weichert, 2000; Holzapfel, 2000]. It follows that the total surface forces acting on the body are given by:

$$\mathbf{F}_s = \int_{\partial G} \mathbf{t} \, dA \qquad\qquad (A.2)$$

Similarly, let **p** denote the resultant body force per unit volume. Thus, the total body forces acting on the continuum are:

$$\mathbf{B}_s = \int_G \mathbf{p} \, dv \qquad\qquad (A.3)$$

The net force acting on the body is therefore given by the sum of the terms in Equations (A.2) and (A.3), i.e.

$$\mathbf{F}_{net} = \int_G \mathbf{p} \, dv + \int_{\partial G} \mathbf{t} \, dA \qquad\qquad (A.4)$$

Applying Cauchy's stress theorem [Başar and Weichert, 2000; Holzapfel, 2000] to the second integral on the RHS of Equation (A.4) gives:

$$\mathbf{F}_{net} = \int_G \mathbf{p} \, dv + \int_{\partial G} \sigma \mathbf{n} \, dA \qquad\qquad (A.5)$$

Here $\sigma$ is the Cauchy stress tensor familiar from elementary stress analysis, and **n** is the unit vector normal to the boundary surface $\partial G$. Application of the divergence theorem to the second integral on the RHS of Equation (A.5) gives:

$$\mathbf{F}_{net} = \int_G \mathbf{p} \, dv + \int_G \text{div}\sigma \, dv$$
$$\therefore \mathbf{F}_{net} = \int_G (\mathbf{p} + \text{div}\sigma) dv \qquad\qquad (A.6)$$

It is known from elementary mechanics [Hibbeler, 1995] that the rate of change of linear momentum of a body equals the net external resultant force. Thus from Equations (A.1) and (A.6) one may write:

$$\frac{D}{Dt}\int_{G}\rho\dot{r}dv = \int_{G}(\mathbf{p} + div\sigma)dv \tag{A.7}$$
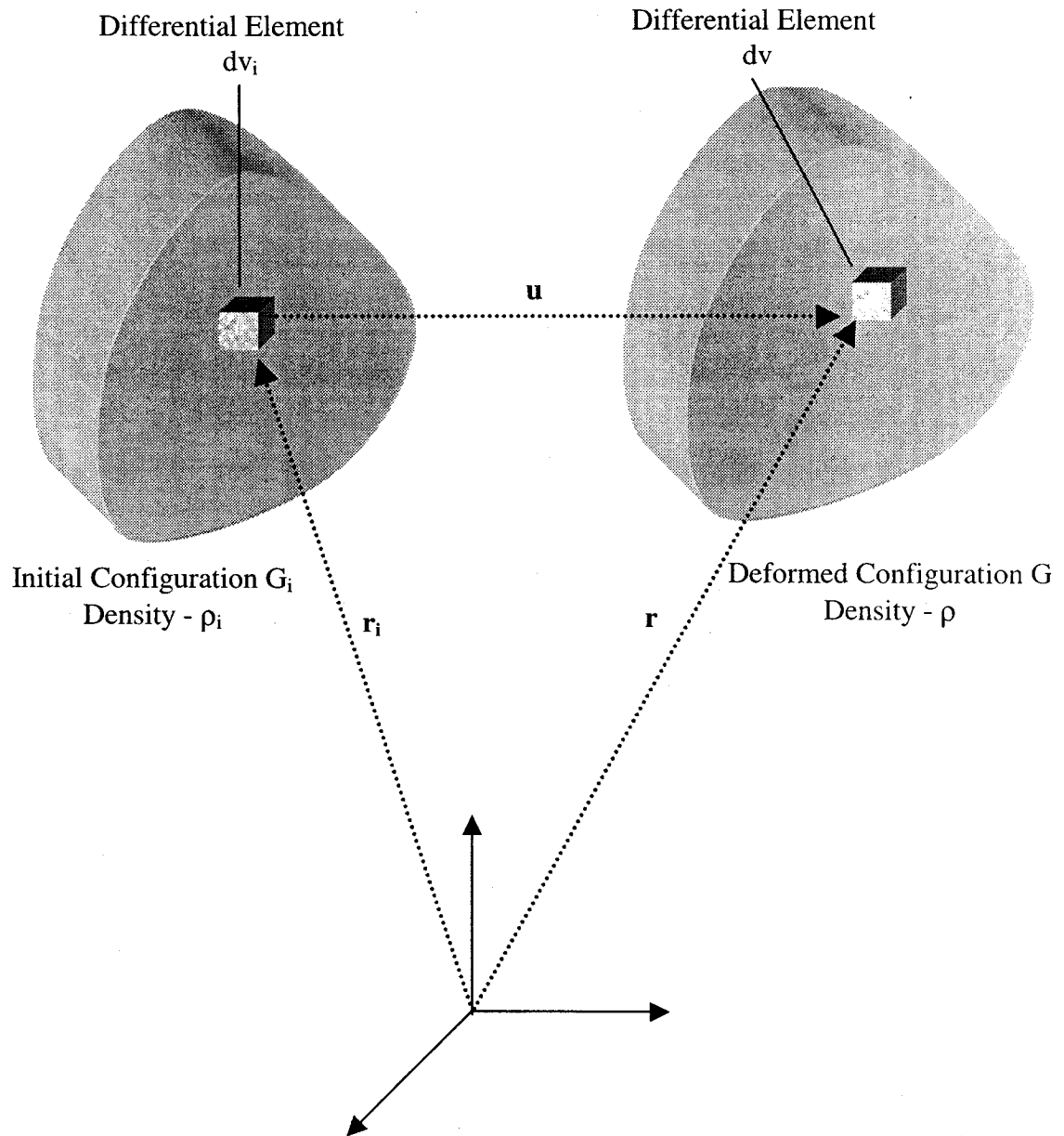


**Figure A-2:** Undeformed and deformed configurations of a continuum

To simplify the LHS of Equation (A.7), consider Figure A-2. A typical differential element is located by a position vector $\mathbf{r_i}$ before any loads are applied. After deformation, the position vector of that differential element is $\mathbf{r}$ and therefore its displacement vector, $\mathbf{u}$, is given by $\mathbf{r}$-$\mathbf{r_i}$. Thus

$$\mathbf{r} = \mathbf{u} + \mathbf{r_i}$$
$$\dot{\mathbf{r}} = \dot{\mathbf{u}}$$

(A.8)

In Equation (A.8) the derivative of the initial position vector is zero because this vector is of course not a function of time. Thus, with this result, the LHS of Equation (A.7) may be written as follows:

$$\frac{D}{Dt}\int_G \rho \dot{\mathbf{r}}\, dv = \frac{D}{Dt}\int_G \rho \dot{\mathbf{u}}\, dv = \frac{D}{Dt}\int_{G_i} \rho_i \dot{\mathbf{u}}\, dv_i$$

(A.9)

In Equation (A.9), the principle of mass conservation was invoked. The advantage of switching to the undeformed configuration $G_i$ is that it is not a function of time, and hence the time derivative can be shifted inside the integral sign. Thus the expression in Equation (A.9) becomes:

$$\frac{D}{Dt}\int_{G_i} \rho_i \dot{\mathbf{u}}\, dv_i = \int_{G_i} \frac{D}{Dt}\rho_i \dot{\mathbf{u}}\, dv_i = \int_{G_i} \rho_i \ddot{\mathbf{u}}\, dv_i = \int_G \rho \ddot{\mathbf{u}}\, dv$$

(A.10)

In the last step, the domain of integration was switched back to the deformed configuration by using mass conservation once more. Next, combining Equations (A.7) and (A.10) gives:

$$\int_G (\rho \ddot{\mathbf{u}} - \text{div}\,\sigma - \mathbf{p})\, dv = 0$$

(A.11)

Equation (A.11) is independent of the domain of integration, i.e. it is valid for the entire body, as well as for any differential element. Thus, one may write:

$$\rho \ddot{\mathbf{u}} - \text{div}\,\sigma - \mathbf{p} = 0$$
$$\therefore \rho \ddot{\mathbf{u}} = \text{div}\,\sigma + \mathbf{p}$$

(A.12)

In index form, Equation (A.12) becomes:

$$\rho \ddot{u}_i = \frac{\partial \sigma_{ij}}{\partial x_j} + p_i$$

(A.13)

If one only considers structures that are in static equilibrium then $\ddot{u}$ vanishes and Equation (A.13) reduces to:

$$\frac{\partial \sigma_{ij}}{\partial x_j} = -p_i = f_i \qquad (A.14)$$

This is the desired expression.